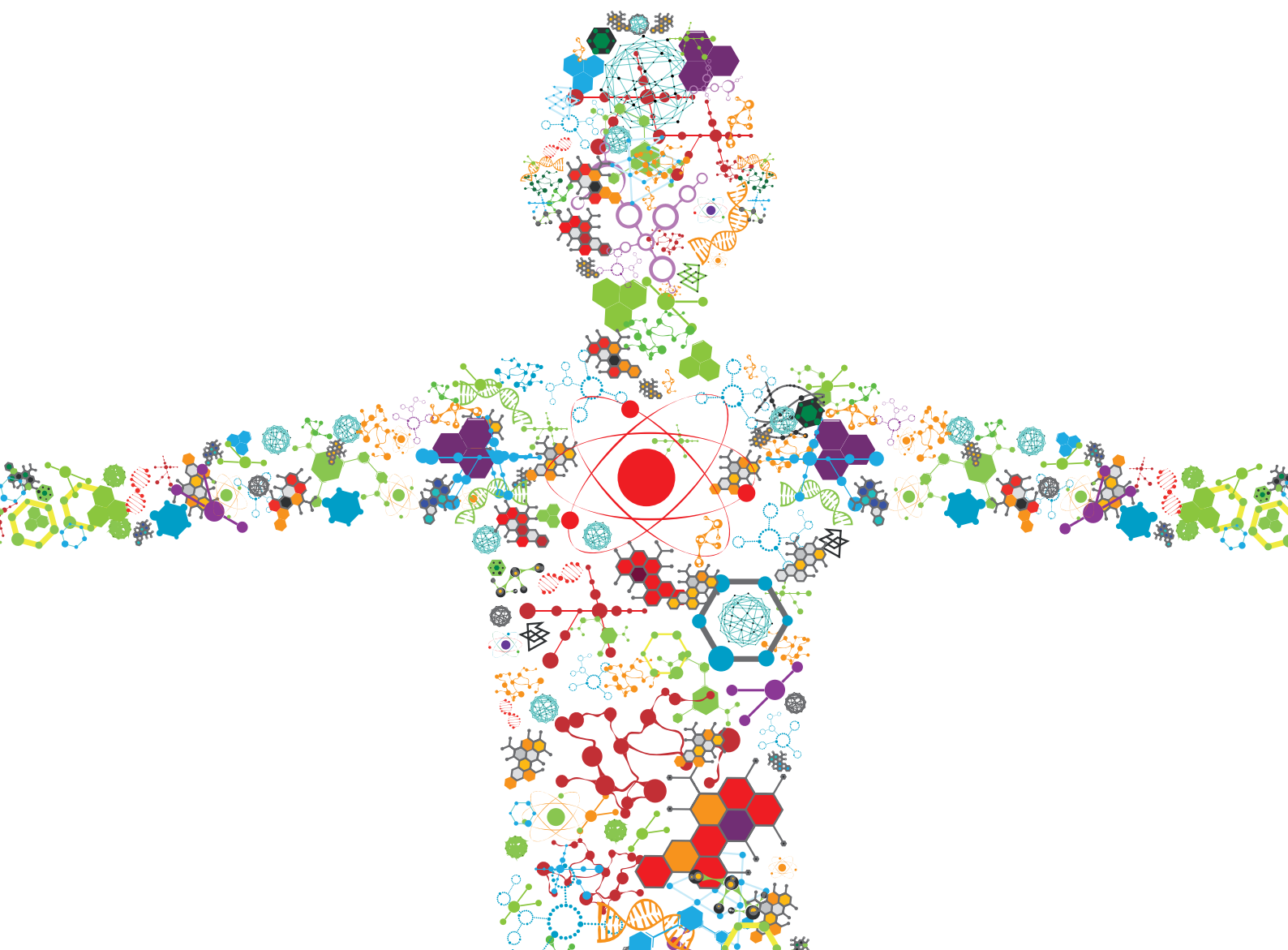


NANOMEDICINE FOR DEEP-TISSUE HIGH-RESOLUTION BIO-IMAGING AND NON-INVASIVE THERAPY

EDITED BY: Michael Ming-Yuan Wei, Yanbo Pei and Yu Gao
PUBLISHED IN: Frontiers in Bioengineering and Biotechnology





frontiers

Frontiers eBook Copyright Statement

The copyright in the text of individual articles in this eBook is the property of their respective authors or their respective institutions or funders. The copyright in graphics and images within each article may be subject to copyright of other parties. In both cases this is subject to a license granted to Frontiers.

The compilation of articles constituting this eBook is the property of Frontiers.

Each article within this eBook, and the eBook itself, are published under the most recent version of the Creative Commons CC-BY licence.

The version current at the date of publication of this eBook is CC-BY 4.0. If the CC-BY licence is updated, the licence granted by Frontiers is automatically updated to the new version.

When exercising any right under the CC-BY licence, Frontiers must be attributed as the original publisher of the article or eBook, as applicable.

Authors have the responsibility of ensuring that any graphics or other materials which are the property of others may be included in the CC-BY licence, but this should be checked before relying on the CC-BY licence to reproduce those materials. Any copyright notices relating to those materials must be complied with.

Copyright and source acknowledgement notices may not be removed and must be displayed in any copy, derivative work or partial copy which includes the elements in question.

All copyright, and all rights therein, are protected by national and international copyright laws. The above represents a summary only. For further information please read Frontiers' Conditions for Website Use and Copyright Statement, and the applicable CC-BY licence.

ISSN 1664-8714

ISBN 978-2-88966-113-8

DOI 10.3389/978-2-88966-113-8

About Frontiers

Frontiers is more than just an open-access publisher of scholarly articles: it is a pioneering approach to the world of academia, radically improving the way scholarly research is managed. The grand vision of Frontiers is a world where all people have an equal opportunity to seek, share and generate knowledge. Frontiers provides immediate and permanent online open access to all its publications, but this alone is not enough to realize our grand goals.

Frontiers Journal Series

The Frontiers Journal Series is a multi-tier and interdisciplinary set of open-access, online journals, promising a paradigm shift from the current review, selection and dissemination processes in academic publishing. All Frontiers journals are driven by researchers for researchers; therefore, they constitute a service to the scholarly community. At the same time, the Frontiers Journal Series operates on a revolutionary invention, the tiered publishing system, initially addressing specific communities of scholars, and gradually climbing up to broader public understanding, thus serving the interests of the lay society, too.

Dedication to Quality

Each Frontiers article is a landmark of the highest quality, thanks to genuinely collaborative interactions between authors and review editors, who include some of the world's best academicians. Research must be certified by peers before entering a stream of knowledge that may eventually reach the public - and shape society; therefore, Frontiers only applies the most rigorous and unbiased reviews.

Frontiers revolutionizes research publishing by freely delivering the most outstanding research, evaluated with no bias from both the academic and social point of view. By applying the most advanced information technologies, Frontiers is catapulting scholarly publishing into a new generation.

What are Frontiers Research Topics?

Frontiers Research Topics are very popular trademarks of the Frontiers Journals Series: they are collections of at least ten articles, all centered on a particular subject. With their unique mix of varied contributions from Original Research to Review Articles, Frontiers Research Topics unify the most influential researchers, the latest key findings and historical advances in a hot research area! Find out more on how to host your own Frontiers Research Topic or contribute to one as an author by contacting the Frontiers Editorial Office: researchtopics@frontiersin.org

NANOMEDICINE FOR DEEP-TISSUE HIGH-RESOLUTION BIO-IMAGING AND NON-INVASIVE THERAPY

Topic Editors:

Michael Ming-Yuan Wei, Texas Commission on Environmental Quality,
United States

Yanbo Pei, Harbin Institute of Technology, China

Yu Gao, Nanjing University of Posts and Telecommunications, China

Dr Ming-Yuan Wei currently holds a pending U.S. Patent Application entitled "Systems and Methods for High-Resolution Imaging". All other Guest Editors have no other competing interests to declare with regards to the Topic subject.

Citation: Ming-Yuan Wei, M., Pei, Y., Gao, Y., eds. (2020). Nanomedicine for Deep-Tissue High-Resolution Bio-Imaging and Non-Invasive Therapy. Lausanne: Frontiers Media SA. doi: 10.3389/978-2-88966-113-8

Table of Contents

- 05 ***Editorial: Nanomedicine for Deep-Tissue High-Resolution Bio-Imaging and Non-invasive Therapy***
Yu Gao, Yanbo Pei and Ming-Yuan Wei
- 08 ***Antibody-Functionalized MoS₂ Nanosheets for Targeted Photothermal Therapy of Staphylococcus aureus Focal Infection***
Yuqian Zhang, Weijun Xiu, Siyu Gan, Jingyang Shan, Shaokang Ren, Lihui Yuwen, Lixing Weng, Zhaogang Teng and Lianhui Wang
- 20 ***Self-Illuminating Agents for Deep-Tissue Optical Imaging***
Qing Li, Jianfeng Zeng, Qingqing Miao and Mingyuan Gao
- 32 ***Treatment of Hepatocellular Carcinoma by Intratumoral Injection of ¹²⁵I-AA98 mAb and Its Efficacy Assessments by Molecular Imaging***
Jun Zhou, Pengcheng Hu, Zhan Si, Hui Tan, Lin Qiu, He Zhang, Zhequan Fu, Wujian Mao, Dengfeng Cheng and Hongcheng Shi
- 42 ***Optically Active Nanomaterials for Bioimaging and Targeted Therapy***
Yu Yang, Li Wang, Bin Wan, Yuxin Gu and Xinxin Li
- 66 ***An Artificial Intelligent Signal Amplification System for in vivo Detection of miRNA***
Xibo Ma, Lei Chen, Yingcheng Yang, Weiqi Zhang, Peixia Wang, Kun Zhang, Bo Zheng, Lin Zhu, Zheng Sun, Shuai Zhang, Yingkun Guo, Minmin Liang, Hongyang Wang and Jie Tian
- 81 ***Characterization of Photoluminescent Polylactone-Based Nanoparticles for Their Applications in Cardiovascular Diseases***
Aneetta E. Kuriakose, Nikhil Pandey, Dingying Shan, Subhash Banerjee, Jian Yang and Kytai T. Nguyen
- 93 ***The Synergistic Effect of Nanocrystals Combined With Ultrasound in the Generation of Reactive Oxygen Species for Biomedical Applications***
Veronica Vighetto, Andrea Ancona, Luisa Racca, Tania Limongi, Adriano Troia, Giancarlo Canavese and Valentina Cauda
- 103 ***Gadolinium-Based Nanoparticles for Theranostic MRI-Guided Radiosensitization in Hepatocellular Carcinoma***
Pengcheng Hu, Zhequan Fu, Guobing Liu, Hui Tan, Jie Xiao, Hongcheng Shi and Dengfeng Cheng
- 111 ***Nanomedicines: A Potential Treatment for Blood Disorder Diseases***
Nan Zhang, Ming-Yuan Wei and Qiang Ma
- 127 ***Whole Body Vibration Triggers a Change in the Mutual Shaping State of Intestinal Microbiota and Body's Immunity***
Ning Song, Xia Liu, Qiang Feng, Mengchen Xu, Xiang Lan, Meihui Li, Rutao Liu, Caixia Li, Tianyi Dong, Deqiang Wang and Shili Liu
- 138 ***Gold Nanomaterials for Imaging-Guided Near-Infrared in vivo Cancer Therapy***
Yuanyuan Tian, Sheng Qiang and Lianhui Wang
- 147 ***Nanomedicines for Near-Infrared Fluorescent Lifetime-Based Bioimaging***
Xianhui Lian, Ming-Yuan Wei and Qiang Ma

- 163** *Recent Progress in NIR-II Contrast Agent for Biological Imaging*
Jie Cao, Binling Zhu, Kefang Zheng, Songguo He, Liang Meng, Jibin Song
and Huanghao Yang
- 184** *Ultrasound-Enhanced Chemiluminescence for Bioimaging*
Duong Le, Dinesh Dhamecha, Andrea Gonsalves and Jyothi U. Menon
- 200** *Nanozymes: A New Disease Imaging Strategy*
Peixia Wang, Tao Wang, Juanji Hong, Xiyun Yan and Minmin Liang
- 210** *The Fate of SWCNTs in Mouse Peritoneal Macrophages: Exocytosis,
Biodegradation, and Sustainable Retention*
Ping-Xuan Dong, Xinfeng Song, Jiwei Wu, Shuqin Cui, Guizhi Wang,
Lianying Zhang and Hanwen Sun



Editorial: Nanomedicine for Deep-Tissue High-Resolution Bio-Imaging and Non-invasive Therapy

Yu Gao^{1*}, Yanbo Pei^{2*} and Ming-Yuan Wei^{3*}

¹ Key Laboratory for Organic Electronics and Information Displays and Jiangsu Key Laboratory for Biosensors, Institute of Advanced Materials, Jiangsu National Synergistic Innovation Center for Advanced Materials, Nanjing University of Posts and Telecommunications, Nanjing, China, ² Department of Physics, Harbin Institute of Technology, Harbin, China, ³ Texas Commission on Environmental Quality, Austin, TX, United States

Keywords: nanomedicine, bio-imaging, drug delivery, ultrasound optical imaging, non-invasive therapy

Editorial on the Research Topic

Nanomedicine for Deep-Tissue High-Resolution Bio-imaging and Non-invasive Therapy

The interdisciplinary research of nanotechnology and biomedical application yields an emerging field of nanomedicine, which seeks to develop functional agents for *in vivo* bioimaging (diagnosis), advanced drug delivery, and innovative therapy. It's our great pleasure to have this opportunity to include 16 articles in this Research Topic, either in-depth reviews or original research articles.

Nanomedicine for bioimaging is a contrast agent modified with functional moieties to target a specific part-of-interest, such as cancer cells or tumor tissues. Valuable *in situ* diagnostic information can be obtained only when both the bioimaging nanomedicine and the imaging instrumentation are communicating. Optical bioimaging techniques demonstrate advantages of low-cost, portability, and non-invasiveness. Yang et al. surveyed recent advances in the development of optically active nanomaterials, including gold, porous silicon, up-conversion, semiconductor nanocrystal, and carbon-based nanomaterials, along with mainstream optical bioimaging modalities, such as fluorescence, luminescence, surface enhanced Raman scattering (SERS), and photoacoustic (PA). Among them, fluorescence bioimaging holds great promise for the deep-tissue imaging but is hindered by the shallow imaging depth. Near infrared (NIR) fluorescent lifetime-based imaging can suppress the scattering and self-fluorescence noise and obtain the quantitatively functional information. Lian et al. overviewed the progresses of contrast agent's development (including organic dyes and nanomaterials) and the implementation of this imaging method. Cao et al. presented a detailed review on the fluorescent nanoparticles (NPs) working in near infrared wavelength ranging from 1,000 to 1,300 nm, which is called the NIR II window and in the range of which light is less absorbed by the tissue than in the visible and near infrared range below 1,000 nm. The authors summarized the characteristics of several typical nanomaterials including single-walled carbon nanotubes, Ag₂S quantum dots, rare earth NPs, and organic fluorescent dye NPs. More recently, new bioimaging techniques that hybridize ultrasound and optics have attracted increasing attention, and deep-tissue high-resolution bioimaging has been conceived in a number of proof-of-concept studies (Pei and Wei, 2019).

The other idea to decrease the scattering and autofluorescence in the optical imaging is to use luminescent agents because the strong excitation light is eliminated. Li et al. summarized the progress on the development of NIR self-illuminating agents and the design principles. They also discussed the current challenges and future developments. Le et al. focused on the topic of

OPEN ACCESS

Edited and reviewed by:

Gianni Ciofani,
Italian Institute of Technology (IIT), Italy

*Correspondence:

Yu Gao
iamygao@njupt.edu.cn
Yanbo Pei
peiyanbo@hit.edu.cn
Ming-Yuan Wei
mingyuan.wei@tceq.texas.gov

Specialty section:

This article was submitted to
Nanobiotechnology,
a section of the journal
Frontiers in Bioengineering and
Biotechnology

Received: 29 July 2020

Accepted: 31 July 2020

Published: 02 September 2020

Citation:

Gao Y, Pei Y and Wei M-Y (2020)
Editorial: Nanomedicine for
Deep-Tissue High-Resolution
Bio-Imaging and
Non-invasive Therapy.
Front. Bioeng. Biotechnol. 8:1002.
doi: 10.3389/fbioe.2020.01002

chemiluminescence for optical imaging. The nanomaterials for bioluminescence and ultrasound enhanced chemiluminescence imaging are reviewed and the future direction is discussed.

Subsequently, a secondary nanomedicine that contains a therapeutic or regenerative drug will be deployed to the part-of-interest, and the drug release could be triggered precisely by non-invasive means, such as ultrasound, optics, magnet, or heat. Photothermal conversion agents triggers thermal therapy under the irradiation of the laser energy. Antibody (anti-protein A IgG) functionalized MoS₂ nanosheets (MPPI NSs) developed by Zhang Y. et al. were demonstrated to be effective for the treatment of *S. aureus* focal infection on a mouse model. The MPPI NSs can specifically target to the bacterial and showed inactivation efficiency larger than 99.99% in both biofilms and in infected tissues, with minimal damage to mammalian cells. Meanwhile, the high extinction coefficient of MoS₂ nanosheets in the NIR region provides the ability for real-time photoacoustic imaging. However, as mentioned previously, optical imaging and therapy usually suffer from low tissue penetration due to the absorption of the light by the tissue. For deep-seated tumor such as hepatocellular carcinoma, Zhou et al. labeled radionuclides ¹²⁵I to the AA98 monoclonal antibody (¹²⁵I-AA98 mAb) against CD146, a biomarker for angiogenesis with high expression in hepatocellular carcinoma cells. After intratumoral injection in a mouse model, the ¹²⁵I-AA98 mAb not only inhibited the early angiogenic process, but also induced apoptosis of the cancer cells, achieving higher therapeutic efficacy than treatment by free ¹²⁵I. The tumor response to the targeted therapy were monitored by single-photon emission computerized tomography (SPECT) with high sensitivity and tissue penetration. To overcome the limitation of penetration depth of light, ultrasound can be used for both imaging and therapy. In the research by Vighetto et al., the generation of reactive oxygen species (ROS) by single-crystalline zinc oxide (ZnO) NPs and ultrasound were studied. The cavitation effect of gas nanobubbles under ultrasound were responsible for the generation of hydroxyl and superoxide anions, which causing ROS-mediated apoptosis or necrosis of cells. Notably, the generated acoustic signal can be monitored by B-mode ultrasound imaging, suggesting the capability of ZnO NPs as an ultrasound aided theranostic agent. Interestingly, the health effects of non-invasive therapy on human should be carefully studied. Song et al. demonstrated that whole body vibration (WBV), a non-invasive physical therapy, significantly increased the CD4 and CD25 positive lymphocytes as well as the population of Treg cells in the spleen. Therefore, the contents of a variety of bacteria changed, such as *Lactobacillus animalis* in mice, and *Lactobacillus paraplantarum* and *Lactobacillus sanfranciscensis* in human.

In a best-case scenario, the therapy or regeneration process can be monitored real-time through the bioimaging. The interactive cooperation between these two procedures will provide accurate and effective treatment for human diseases. Kuriakose et al. developed a new biodegradable photoluminescent polylactones-co-poly (lactic-co-glycolic acid) copolymers (BPLP-PLGA) as nanocarriers for protein delivery. These NPs displayed superior stability (2 days) in physiological conditions, tunable release kinetics and

fluorescence emission, compatibility with endothelial cells, and good hemocompatibility. Thereby, the BPLP-PLGA NPs have potential to serve as optical contrast agents and nanocarriers of the drugs for cardiovascular diseases. Tian et al.'s mini-review emphasizes some recent advances of gold nanomaterials-based photothermal imaging (PTI), SERS imaging, and PA imaging-guided *in vivo* therapy in NIR region (>800 nm). Hu et al. examined the potential value of multimodality gadolinium-based NPs (AGuIX) for non-invasive theranostic MRI-guided radiotherapy in hepatocellular carcinoma (HCC). The AGuIX provide better detection of tumors in imaging, and precise identification for accurate MRI-guided radiotherapy; meanwhile, the heavy elements in this novel nanoparticle can enhance radiosensitizing effect by irradiation dose deposition.

We are extremely excited to notice that artificial intelligent (AI) has been pushing the development of nanomedicines. For instance, with the rapid development of nanotechnology in the field of biomedicine, artificial blood, or blood substitute has shown promising features for the emergency treatment of BDDs. Chemotherapy, bone marrow transplantation, and stem cell therapy have been used to treat blood disorder diseases (BDDs). However, the cure rates are still low due to the availability of the right type of bone marrow and the likelihood of recurrence and infection. Zhang N. et al. surveyed recent advances in the development of artificial blood components: gas carrier components (erythrocyte substitutes), immune response components (white blood cell substitutes), and hemostasis-responsive components (platelet substitutes). Platelet-inspired nanomedicines for cancer treatment were also discussed.

Wang et al. summarized the applications of nanozymes for disease imaging and detection to explore their potential application in disease diagnosis and precision medicine. Compared to natural enzymes, nanozymes exhibit the unique advantages including high catalytic activity, low cost, high stability, easy mass production, and tunable activity. In addition, as a new type of artificial enzymes, nanozymes not only have the enzyme-like catalytic activity, but also exhibit the unique physicochemical properties of nanomaterials, such as photothermal properties, superparamagnetism, and fluorescence, etc. Despite the remarkable advantages of nanozymes, there remains plenty of limitations while put nanozymes into practical clinical application, such as poor dispersibility, easy sedimentation after surface modification, limited catalytic types, poor substrate selectivity, and potential nanotoxicity.

Compared to detecting proteins secreted by tumors, detecting secreted miRNAs has become more attractive for monitoring tumor progression. Ma et al. designed an artificial intelligent signal amplification (AISA) system including double-stranded SQ (S, signal strand; Q, quencher strand) and FP (F, fuel strand; P, protect strand) according to thermodynamics principle for sensitive detection of miRNA *in vitro* and *in vivo*. The design features conceiving signal amplification and preventing from *in vivo* degradation and complications. Based on this detection system, the precancerous lesions of liver cancer were diagnosed and reconstructed.

The last but not the least, we should always keep in mind to take into consideration of the potential nanotoxicity of nanomedicines, which may fail the clinical trial due to severe side effects. To this end, Dong et al. investigated the candidate fate of acid-oxidized single-walled carbon nanotubes (SWNCTs) in non-activated primary mouse peritoneal macrophages (PMQ). All data showed that exocytosis, uptake, biodegradation, and sustainable retention of SWCNTs co-exist in primary macrophages.

In summary, we are pleased to witness such landmark progresses in the development of nanomedicines that are aiming to provide real-time bioimaging-guided non-invasive therapy for human diseases, along with the integration of artificial intelligence technology. The findings included in this Research

Topic will open the avenue for brighter ideas in future “Smart Nanomedicines” development. During this pandemic season of 2020, we shall keep hope and trust in science, only by which we can overcome the challenge from the COVID-19.

AUTHOR CONTRIBUTIONS

YG, YP, and M-YW wrote and edited the manuscript. All authors contributed to the article and approved the submitted version.

FUNDING

This work was supported by National Natural Science Foundation of China (81601608).

REFERENCES

Pei, Y., and Wei, M.-Y. (2019). Newly-engineered materials for bio-imaging technology: a focus on the hybrid system of ultrasound and fluorescence. *Front. Bioeng. Biotechnol.* 7:88. doi: 10.3389/fbioe.2019.00088

Conflict of Interest: The authors declare that the research was conducted in the absence of any commercial or financial relationships that could be construed as a potential conflict of interest.

Copyright © 2020 Gao, Pei and Wei. This is an open-access article distributed under the terms of the Creative Commons Attribution License (CC BY). The use, distribution or reproduction in other forums is permitted, provided the original author(s) and the copyright owner(s) are credited and that the original publication in this journal is cited, in accordance with accepted academic practice. No use, distribution or reproduction is permitted which does not comply with these terms.



Antibody-Functionalized MoS₂ Nanosheets for Targeted Photothermal Therapy of *Staphylococcus aureus* Focal Infection

Yuqian Zhang^{1,2†}, Weijun Xiu^{1†}, Siyu Gan¹, Jingyang Shan¹, Shaokang Ren¹, Lihui Yuwen^{1*}, Lixing Weng³, Zhaogang Teng⁴ and Lianhui Wang^{1*}

¹ Key Laboratory for Organic Electronics and Information Displays & Jiangsu Key Laboratory for Biosensors, Jiangsu National Synergetic Innovation Centre for Advanced Materials (SICAM), Institute of Advanced Materials (IAM), Nanjing University of Posts and Telecommunications, Nanjing, China, ² Laboratory of Immunology and Nanomedicine, Guangdong Key Laboratory of Nanomedicine, Institute of Biomedicine and Biotechnology, Shenzhen Institutes of Advanced Technology (SIAT), Chinese Academy of Sciences, Shenzhen, China, ³ School of Geography and Biological Information, Nanjing University of Posts and Telecommunications, Nanjing, China, ⁴ Department of Medical Imaging, School of Medicine, Jinling Hospital, Nanjing University, Nanjing, China

OPEN ACCESS

Edited by:

Michael Ming-Yuan Wei,
Texas Commission on Environmental
Quality, United States

Reviewed by:

Yuanyuan Su,
Soochow University, China
Daxiang Cui,
Shanghai Jiao Tong University, China
Xiaoji Xie,
Nanjing Tech University, China

*Correspondence:

Lihui Yuwen
iamhyuwen@njupt.edu.cn
Lianhui Wang
iamlhwang@njupt.edu.cn

[†]These authors have contributed
equally to this work

Specialty section:

This article was submitted to
Nanobiotechnology,
a section of the journal
Frontiers in Bioengineering and
Biotechnology

Received: 19 May 2019

Accepted: 27 August 2019

Published: 10 September 2019

Citation:

Zhang Y, Xiu W, Gan S, Shan J, Ren S,
Yuwen L, Weng L, Teng Z and Wang L
(2019) Antibody-Functionalized MoS₂
Nanosheets for Targeted
Photothermal Therapy of
Staphylococcus aureus Focal
Infection.
Front. Bioeng. Biotechnol. 7:218.
doi: 10.3389/fbioe.2019.00218

Bacterial biofilm-related diseases cause serious hazard to public health and bring great challenge to the traditional antibiotic treatment. Photothermal therapy (PTT) has been recognized as a promising alternative solution. However, the therapeutic efficacy of PTT is often compromised by the collateral damage to normal tissues due to the lack of bacteria-targeting capability. Here, a *Staphylococcus aureus* (*S. aureus*)-targeted PTT nanoagent is prepared based on antibody (anti-protein A IgG), polydopamine (PDA), and PEG-SH (thiolated poly (ethylene glycol)) functionalized MoS₂ nanosheets (MoS₂@PDA-PEG/IgG NSs, MPPI NSs). The PDA was used as bio-nano interface to facilitate the covalent conjugation of antibody and PEG-SH onto the surface of MoS₂ NSs via facile catechol chemistry. Targeted PTT of MPPI NSs shows excellent inactivation efficiency of larger than 4 log (>99.99%) to *S. aureus* both in biofilms (*in vitro*) and in infected tissues (*in vivo*) without causing damage to normal mammalian cells. By contrast, non-targeted PTT of MoS₂@PDA-PEG NSs (MPP NSs) only kills *S. aureus* by <90% *in vitro* and <50% *in vivo*. As a result, *S. aureus* focal infection in mice healed much faster after PTT of MPPI NSs than that of MPP NSs. The superiority of targeted PTT may originate from the efficient accumulation and close binding of PTT agents to bacterial cells. Therefore, MPPI NSs with bacteria-targeting capability are promising photothermal agents for effective treatment of *S. aureus* focal infection.

Keywords: targeted photothermal therapy, *Staphylococcus aureus*, infection, antibody, MoS₂ nanosheets

INTRODUCTION

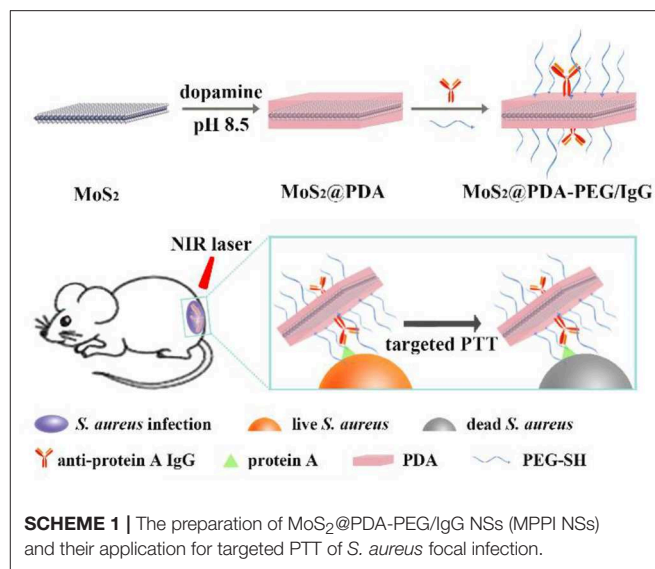
S. aureus is one of the major causes for infectious diseases, such as skin and sinus infections, endocarditis, bacteraemia, and so on, and brings severe threats to human health (van Hal et al., 2012; Wolcott et al., 2016; Hasan et al., 2017). Most of these infectious diseases are relevant to the formation of bacterial biofilms, which are organized aggregates of bacterial cells encased in

extracellular polymeric substances (EPSs) on natural or abiotic surface (Costerton et al., 1999; Davies, 2003). The bacteria in biofilms develop much higher resistance to antibiotics and the host defense system than planktonic bacterium, making it a great challenge for conventional chemotherapy to treat bacterial biofilm-related infections (Costerton et al., 1995; Lynch and Robertson, 2008; Penesyan et al., 2015). Other therapeutic methods, such as surgical remove combined with long-term antibiotic therapy, would augment patients' suffering and incur high healthcare costs (Duncan et al., 2015). Therefore, an urgent need of alternative antibiofilm strategies arises.

PTT is a simple, efficient, and non-invasive method to kill bacteria by using near-infrared (NIR) light induced local hyperthermia (Ray et al., 2012). Since bacteria in biofilms have little capability to resist the heat or stop the heat transfer, PTT is less possible to evoke bacterial resistance than antibiotics (Yuwen et al., 2018). Thus, PTT possesses great potential for the treatment of bacterial biofilm-related infections. Many nanomaterials have been used as PTT agents for the photothermal destruction of bacterial biofilms, such as various gold-based nanostructures and carbon nanomaterials (Jo and Kim, 2013; Levi-Polyachenko et al., 2014; Pallavicini et al., 2014; Ji et al., 2016; Meeker et al., 2016, 2018; Teng et al., 2016; Hu et al., 2017). However, relatively high temperature is usually needed to eliminate bacterial biofilms completely by PTT, which would cause harm to surrounding healthy tissues and limit the application of PTT (Hauck et al., 2008; Hsiao et al., 2015). In order to solve this problem, it is necessary to improve the accumulation of photothermal agents in bacterial biofilms and reduce the distance between photothermal agents and bacterial cells. The integration of bacteria-targeting moieties and photothermal agents would be a possible solution.

MoS₂ nanosheets (MoS₂ NSs) are promising photothermal agents due to their large surface area, good biocompatibility, high extinction coefficient, and high photothermal conversion efficiency in the NIR region (Robinson et al., 2011; Chou et al., 2013; Li et al., 2017). Zhang et al. (2016) have prepared chitosan functionalized MoS₂ to combat bacterial infection by NIR-triggered sterilization. Yin et al. (2016) combine the peroxidase-like activity and PTT ability of MoS₂ nanoflowers, realizing a rapid and effective killing of bacteria *in vitro* and wound disinfection *in vivo*. Yuwen et al. (2018) prepared MoS₂ NSs-silver nanoparticles composites to improve the antibiofilm efficacy via photothermal enhanced release of silver ions. Although MoS₂ NSs-based PTT has proven effective to treat bacterial infections, their further application is still hindered due to the lack of bacteria-targeting capability.

Here, MoS₂@PDA-PEG/IgG NSs (MPPI NSs) with *S. aureus*-targeting capability and photothermal properties were prepared by coating MoS₂ NSs with polydopamine (PDA) and subsequently conjugating of anti-protein A IgG and PEG-SH (Scheme 1). With good biocompatibility, colloidal stability, and high photothermal effect, MPPI NSs were used for the treatment of *S. aureus* biofilms *in vitro* and *S. aureus* focal infection *in vivo* successfully with much higher therapeutic efficacy than non-targeted PTT.



MATERIALS AND METHODS

Materials

Molybdenum disulphide (MoS₂) powder (<2 μm, 99%) and bovine serum albumin (BSA) were purchased from Sigma-Aldrich, and n-butyllithium (n-BuLi, 2.4 M hexane solution) from Amethyst. Dopamine hydrochloride (99%) was obtained from Alfa Aesar. Thiolated poly (ethylene glycol) methyl ether (PEG-SH, M_w = 5000) and rabbit anti-protein A IgG (IgG) were bought from JenKem Technology and Beijing Biosynthesis Biotechnology Co., LTD, respectively. Ultrapure water (Millipore, 18.2 MΩ) was used to prepare aqueous solutions throughout the whole study.

Preparation of MoS₂ NSs

The ultrasonication enhanced lithium intercalation (ULI) method we reported previously was used to prepare single-layer MoS₂ NSs (Zhang et al., 2017).

Preparation of MoS₂@PDA NSs (MP NSs)

Tris-HCl buffer (10 mM, pH = 8.5, 20 mL), MoS₂ NSs aqueous dispersion (1 mg/mL, 0.5 mL), and dopamine hydrochloride aqueous solution (10 mg/mL, 0.3 mL) were added into a 50 mL microwave reaction tube, and reacted in the microwave reactor (Explorer 48, CEM) at 60°C for 10 min (Yuwen et al., 2018). The reaction mixture was centrifuged at 12,000 rpm for 20 min. And the sediment was resuspended in ultrapure water. After repeating the centrifugation twice, MP NSs were resuspended in ultrapure water.

Preparation of MoS₂@PDA-PEG/IgG NSs (MPPI NSs)

Tris-HCl buffer (10 mM, pH = 8.5, 5 mL), rabbit anti-protein A IgG aqueous solution (IgG, 1 mg/mL, 1 mL), and PEG-SH aqueous solution (50 mg/mL, 0.33 mL) were added into a 50 mL centrifuge tube and mixed evenly. MP NSs aqueous dispersion

(MoS₂: 1 mg/mL, 1 mL) was added. The reaction mixture was incubated overnight in an orbital shaker at 220 rpm and 37°C. After centrifugation (12,000 rpm, 20 min) for three times, MPPI NSs were resuspended in ultrapure water.

Preparation of MoS₂@PDA-PEG NSs (MPP NSs)

The MPP NSs were prepared using the similar method with the preparation of MPPI NSs except the addition of IgG.

Quantitative Analysis of Protein Loading

Due to the cost reason, frequently-used protein bovine serum albumin (BSA) was used instead of IgG to evaluate the protein loading efficiency of MP NSs and MoS₂ NSs by using Bradford protein assay (Compton and Jones, 1985). Bradford reagent was prepared by dissolving Coomassie Brilliant Blue G-250 (10 mg) into ethanol solution (95%, 5 mL), and then adding phosphoric acid solution (85%, 10 mL) and H₂O (85 mL).

Tris-HCl buffer (10 mM, pH = 8.5, 5 mL), BSA aqueous solution (1 mg/mL, 1 mL), PEG-SH aqueous solution (50 mg/mL, 0.33 mL), and MoS₂ NSs or MP NSs aqueous dispersion (MoS₂: 1 mg/mL, 1 mL) were mixed evenly in 50 mL centrifuge tubes, respectively. The reaction mixtures were incubated overnight in an orbital shaker at 220 rpm and 37°C. After centrifugation (12,000 rpm, 20 min) for five times, the supernatant was collected.

Supernatant (50 μ L) and BSA aqueous solutions at different concentrations (8, 16, 32, and 64 μ g/mL, 50 μ L) were mixed with Bradford reagent (250 μ L), respectively. After 5 min, the absorbance at 595 nm of these mixtures was measured. A working curve of absorbance at 595 nm vs. concentration of BSA was built as followed, $C (\mu\text{g/mL}) = (\text{OD}_{595} - 0.072)/0.00456$. The amount of BSA in the supernatant was determined by using the above equation. Finally, the amount of protein integrated to MoS₂ NSs and MP NSs was calculated according to the total amount of BSA added.

Cytotoxicity Assay

Minimum essential medium (MEM, KeyGEN BioTECH, containing penicillin-streptomycin) with supplement of fetal bovine serum (FBS, Gibco, 10%) and trypsin-EDTA (0.25% w/v) were used to culture and detach the human cervical carcinoma (HeLa) cells (KeyGEN BioTECH), respectively. MoS₂ NSs, MP NSs, MPP NSs, and MPPI NSs suspended in MEM (no FBS, 200 μ L/well) were added into HeLa cells that grew in 96-well plates. After incubation for 24 h, the lactate dehydrogenase (LDH) from the supernatant was detected using the LDH-cytotoxicity colorimetric assay kit (BioVision) and the cytotoxicity of nanosheets was evaluated following the instruction described in our previous work (Zhang et al., 2017). A microtiter plate reader (PowerWave XS2, BioTek) was used to measure the optical density at 495 nm (OD₄₉₅).

Photothermal Toxicity of MPPI NSs

The PTT of MPPI NSs was carried out on the human prostatic stromal myofibroblast cell line WPMY-1 cells to evaluate the side effects. The WPMY-1 cells were seeded in 96-well plates

using DMEM (Dulbecco's modified Eagle's medium, 10% FBS, 80 U/mL penicillin, and 0.08 mg/mL streptomycin). After 24 h, WPMY-1 cells were washed with sterile saline, and incubated with different concentrations of MPPI NSs (containing 0, 40, 80, and 160 μ g/mL MoS₂) suspended in DMEM (no FBS) for another 6 h. The cells were rinsed with saline, and 50 μ L of DMEM (no FBS) was added into each well. The NIR laser irradiation was performed using a 785 nm laser at 0.58 W/cm² for 10 min. The supernatants were transferred to another 96-well plate to calculate the cell viability using the LDH-cytotoxicity colorimetric assay kit as we described above. Adherent cells were co-stained by calcein-AM and propidium iodide (PI, KeyGEN BioTECH), and imaged using an Olympus IX71 inverted fluorescence microscope.

Bacteria Culture and Biofilm Formation

S. aureus ATCC 25923 and *Pseudomonas aeruginosa* PA01 were maintained on Luria-Bertani (LB) agar and stored at 4°C. Before use, a single isolated colony was transferred into LB broth in a 50 mL centrifuge tube and incubated at 37°C in a rotary incubator with shaking at 200 rpm overnight. After rinsed with sterile saline twice, the bacteria were suspended in fresh LB medium supplemented with 1% glucose (LBG broth) at a concentration of 10⁷ colony forming units (CFU)/mL. The bacterial suspension was added into 6-well plates with ITO glass with a volume of 3 mL/well, 96-well plates with a volume of 200 μ L/well, and glass-bottomed culture dishes (confocal dishes) with a volume of 3 mL/well, respectively. Established biofilms were obtained after incubation at 37°C for 24 h (Chen et al., 2016).

In vitro PTT of *S. aureus* Biofilms

S. aureus biofilms grown in 96-well plates were rinsed softly and cultured with MPPI NSs and MPP NSs (MoS₂: 0, 40, 80, and 160 μ g/mL) suspended in saline at 37°C, respectively. After 6 h, unbound nanosheets were washed away. Sterile saline (50 μ L) was added to maintain the humidification of biofilms. NIR laser irradiation was performed by using a 785 nm continuous-wave laser at the power density of 0.58 W/cm² for 10 min. These biofilms treated with both nanosheets incubation and NIR laser irradiation were classified into MPP + NIR and MPPI + NIR groups. The biofilms with only nanosheets incubation and only NIR laser irradiation (MoS₂: 0 μ g/mL) were set as control.

The bacteria inside biofilms of each well were dispersed into saline thoroughly by pipetting. Bacterial viability was determined by serial dilution and plate counting as CFU per well.

SEM Imaging of *S. aureus* Biofilms

S. aureus biofilms grown on ITO glass after 6 h incubation with MPPI NSs or MPP NSs and *P. aeruginosa* biofilms grown ITO glass after 6 h incubation with MPPI NSs were washed with saline twice, fixed in 2.5% glutaraldehyde for 30 min, dehydrated with graded ethanol series (25%, 50%, 75%, and 100%) for 10 min each, sputter-coated with gold, and imaged by SEM.

The morphology change of *S. aureus* biofilms after PTT with MPPI NSs and MPP NSs were also observed by SEM after similar

treatments consisting of fixing with glutaraldehyde, dehydrating with graded ethanol series, and sputter coating with gold.

Quantitative Assessment of Biofilm-Binding by Energy Dispersive Spectroscopy (EDS)

After incubation with MPPI NSs or MPP NSs for 6 h, the binding affinity of MPP NSs and MPPI NSs to *S. aureus* biofilms, and that of MPPI NSs to *P. aeruginosa* biofilms were assessed. Biofilms grown on ITO glass were washed with saline twice after incubation with MPPI NSs and MPP NSs, fixed in 2.5% glutaraldehyde for 30 min, dehydrated with graded ethanol series (25, 50, 75, and 100%) for 10 min each, and examined by EDS.

Crystal Violet Staining Assay of *S. aureus* Biofilms

Crystal violet staining was used for the structure observation of *S. aureus* biofilms. The biofilms in 96-well plates treated with MPPI NSs incubation (MoS_2 : 0, 40, 80, and 160 $\mu\text{g/mL}$) and NIR laser irradiation were all fixed with 2.5% glutaraldehyde for 30 min, and stained with 0.2% crystal violet for 1 h. Excessive dye was rinsed by saline. Biofilms were imaged using an inverted microscope (Olympus IX71).

Three Dimensional (3D) Confocal Laser Scanning Microscopy (CLSM) Observation

S. aureus suspended in LBG broth at the concentration of 10^7 CFU/mL was added into confocal dishes with a volume of 3 mL/well, and cultured at 37°C for 24 h. Then, *S. aureus* biofilms were treated with different conditions: only MPP NSs incubation (MPP), only MPPI NSs incubation (MPPI), MPP NSs incubation and NIR laser irradiation (MPP + NIR), and MPPI NSs incubation and NIR laser irradiation (MPPI + NIR). Biofilms were stained by calcein-AM (KeyGEN BioTECH) for 20 min, washed with sterile saline to remove excessive dye, and imaged by Olympus IX81 confocal laser scanning microscope with an imaging area of 630×630 and 1 μm interval on z-section.

In vivo PTT of *S. aureus* Focal Infection

All animal procedures were performed in accordance with the Guidelines for Care and Use of Laboratory Animals of Nanjing University and experiments were approved by the Animal Ethics Committee of Nanjing University. Six-week-old female Balb/c mice (Nanjing Junke Biological Engineering Co. Ltd.) were first anesthetized and depilated. *S. aureus* suspended in LBG broth at the concentration of 10^9 CFU/mL was injected into the right flanks of mice subcutaneously with a volume of 40 μL each to construct subcutaneous abscesses. After 24 h, 48 mice with *S. aureus* focal infection were randomly divided into six groups and injected *in situ* (into the abscess) with 100 μL saline, 100 μL MPP NSs (suspended in saline, MoS_2 : 40 $\mu\text{g/mL}$), and 100 μL MPPI NSs (suspended in saline, MoS_2 : 40 $\mu\text{g/mL}$), respectively. The NIR laser irradiation was performed at 12 h post-injection using a 785 nm laser at the power density of 0.58 W/cm² for 10 min. The sizes of abscesses were measured by using a caliper

every other day, and photographs were taken at the same time. All mice were executed at 8th day. The infected tissues of three mice from each group were dissected and fixed in 10% neutral buffered formalin for hematoxylin and eosin (H&E) staining and Masson's trichrome staining. The stained slices were imaged by using an Olympus IX71 microscope. The *S. aureus* infected tissues of five mice from each group were transferred into sterile saline. The bacteria of abscesses were dispersed thoroughly by ultrasonication to determine the CFU by plating.

In vivo Toxicity Assessment of MPP NSs and MPPI NSs

Nine female Balb/c mice (6-week-old) were divided randomly into three groups, and were intravenously (i.v.) injected with saline, MPP NSs, and MPPI NSs suspended in saline (MoS_2 : 500 $\mu\text{g/mL}$) with a volume of 200 μL , respectively. One month after the injection, these mice were all sacrificed and their major organs (heart, liver, spleen, lung, and kidney) were collected for H&E staining.

RESULTS

Morphology and Properties

As shown in **Figures 1A,E** and **Figure S1**, the transmission electron microscopy (TEM) and atomic force microscopy (AFM) images show that the as-prepared MoS_2 NSs have uniform single-layer sheet-like morphology with sizes of 100~500 nm and thickness of about 1.2 nm, consistent with previous reports (Yuwen et al., 2016). As shown in **Figures 1A–H**, MoS_2 @PDA NSs (MP NSs), MoS_2 @PDA-PEG NSs (MPP NSs), and MoS_2 @PDA-PEG-IgG NSs (MPPI NSs) show no obvious change in terms of size and shape compared with MoS_2 NSs. After PDA coating, the thickness of MP NSs rises to about 6.6 nm (**Figure 1F**, **Figures S1D,F**). The thicknesses of MPP NSs and MPPI NSs increase to 7.8~7.9 nm (**Figures 1G,H**). The hydrodynamic sizes of MoS_2 NSs, MP NS, MPP NSs, and MPPI NSs determined by dynamic light scattering (DLS) are ~225 nm, ~246 nm, ~271 nm, and ~261 nm, respectively (**Figure S2A**). As shown in **Figure S2B**, the zeta potential of MoS_2 NSs is about -32 mV, and that of MP NSs is about -22 mV. The electroneutral PEG-SH increases the zeta potential of MPP NSs to about -17 mV, and the zeta potential of MPPI NSs is about -27 mV.

As shown in **Figure 2A**, the IR absorption band near 1,616 cm^{-1} of MP NSs can be assigned to the C=C stretching vibration and N-H bending vibration from PDA, suggesting the successful coating of PDA on the surface of MoS_2 NSs (He et al., 2014). The C-H stretching vibrations at 2,926 and 2,855 cm^{-1} demonstrate the presence of PEG-SH in both MPP NSs and MPPI NSs (Yuan et al., 2015; Uppu et al., 2016). The characteristic peaks of Amide I (1,628 and 1,624 cm^{-1}) and Amide II (1,578 and 1,542 cm^{-1}) from MPPI NSs proves the conjugation of IgG (**Figure 2A** and **Figure S3**; Islam et al., 2017). The X-ray photoelectron spectroscopy (XPS) survey spectra of MoS_2 NSs, MP NSs, MPP NSs, and MPPI NSs are shown in **Figure 2B**. The binding energy peaks of Mo 3p_{1/2} (~412 eV), Mo 3p_{3/2} (~394 eV), Mo 3d (~229 eV), and S 2p (~162 eV) can be observed in MoS_2 NSs

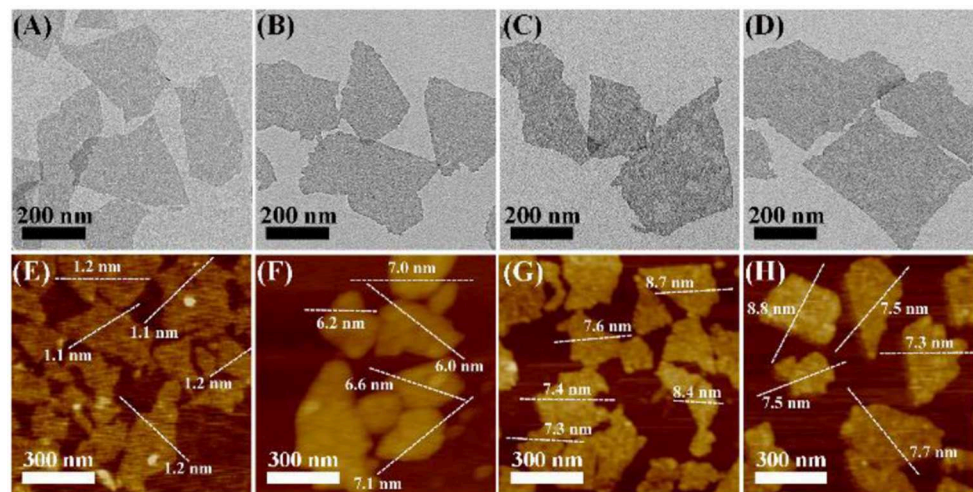


FIGURE 1 | Transmission electron microscopy (TEM) images (A–D) and atomic force microscopy (AFM) images (E–H) of MoS₂ NSs, MP NSs (MoS₂@PDA NSs), MPP NSs (MoS₂@PDA-PEG NSs), and MPPI NSs (MoS₂@PDA-PEG/IgG NSs), respectively.

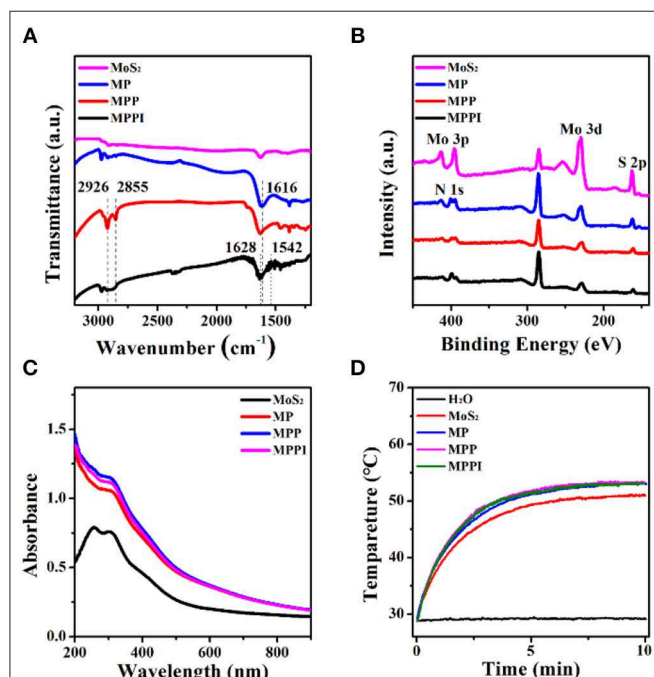


FIGURE 2 | (A) Fourier transform infrared (FT-IR) spectra, (B) X-ray photoelectron spectroscopy (XPS) spectra, and (C) Ultraviolet-visible-near infrared (UV-Vis-NIR) absorption spectra of MoS₂ NSs, MP NSs, MPP NSs, and MPPI NSs. (D) Photothermal heating curves of MoS₂ NSs, MP NSs, MPP NSs, and MPPI NSs (MoS₂: 30 μ g/mL). All samples were irradiated under 785 nm laser at the power density of 0.43 W/cm² for 10 min.

(Kibsgaard et al., 2012; Ganta et al., 2014). The intensity of these characteristic peaks of MoS₂ decrease in MP NSs, MPP NSs, and MPPI NSs after the surface modification, and N 1s (~399 eV) peak exists in all these three nanosheets, demonstrating the presence of PDA and IgG (Ryou et al., 2011).

As shown in **Figure 2C**, MoS₂ NSs have broad absorption ranging from the ultraviolet to the NIR region. The absorbance of MP NSs increases slightly due to the PDA coating (Liu et al., 2014). The ultraviolet-visible-near infrared (UV-Vis-NIR) absorption spectra of MPP NSs and MPPI NSs are almost the same as that of MP NSs. **Figure 2D** shows that the temperature of water increased < 1°C under 785 nm laser irradiation at 0.43 W/cm² for 10 min, while the temperature of MoS₂ NSs aqueous dispersion (30 μ g/mL) reached as high as 50°C. Meanwhile, the final temperatures of MP NSs, MPP NSs, and MPPI NSs aqueous dispersions containing 30 μ g/mL of MoS₂ were ~2°C higher than that of MoS₂ NSs aqueous dispersion, indicating the photothermal property of MoS₂ NSs was not significantly influenced by surface modification. What's more, MoS₂ NSs and MP NSs showed similar temperature evolution during heating (laser-on) and cooling (laser-off) processes (**Figures S4A,B**). After laser irradiation at 0.43 W/cm² for 30 min, UV-Vis-NIR absorption spectra of MoS₂ NSs and MP NSs showed no obvious change (**Figures S4C,D**), indicating good photothermal stability.

Stability, Protein Loading Ability, and Biocompatibility of MPPI NSs

The stability of MoS₂ NSs, MP NSs, MPP NSs, and MPPI NSs was studied by comparing the absorbance of MoS₂ at 785 nm at different times. As shown in **Figure 3A**, the absorbance of MoS₂ NSs aqueous dispersion (20 μ g/mL) at 785 nm decreases rapidly. The absorbance of MoS₂ NSs at 30 d is <30% of that at the beginning, due to the oxidation of MoS₂ NSs. By contrast, the absorbance of MP NSs, MPP NSs, and MPPI NSs aqueous dispersions (MoS₂: 20 μ g/mL) at 30 d stays more than 80% compared with that at 0 d, indicating greatly improved stability. As shown in **Figure 3B**, the color of MoS₂ NSs aqueous dispersion is much lighter at 30 d than that at 0 d, while the MP NSs aqueous dispersion at 30 d is almost the same as that at 0 d, suggesting the same trend as the change of absorbance.

MoS₂ NSs is stable in pure water, but usually aggregate in salt-containing buffer (Zhang et al., 2017). As shown in **Figure 3C**, MoS₂ NSs and MP NSs (MoS₂: 40 μ g/mL) aggregated completely in phosphate buffered saline (PBS) and Minimum Essential Medium (MEM) after 1 d. In contrast, MPP NSs and MPPI NSs remained well dispersed in H₂O, PBS, and MEM (MoS₂:

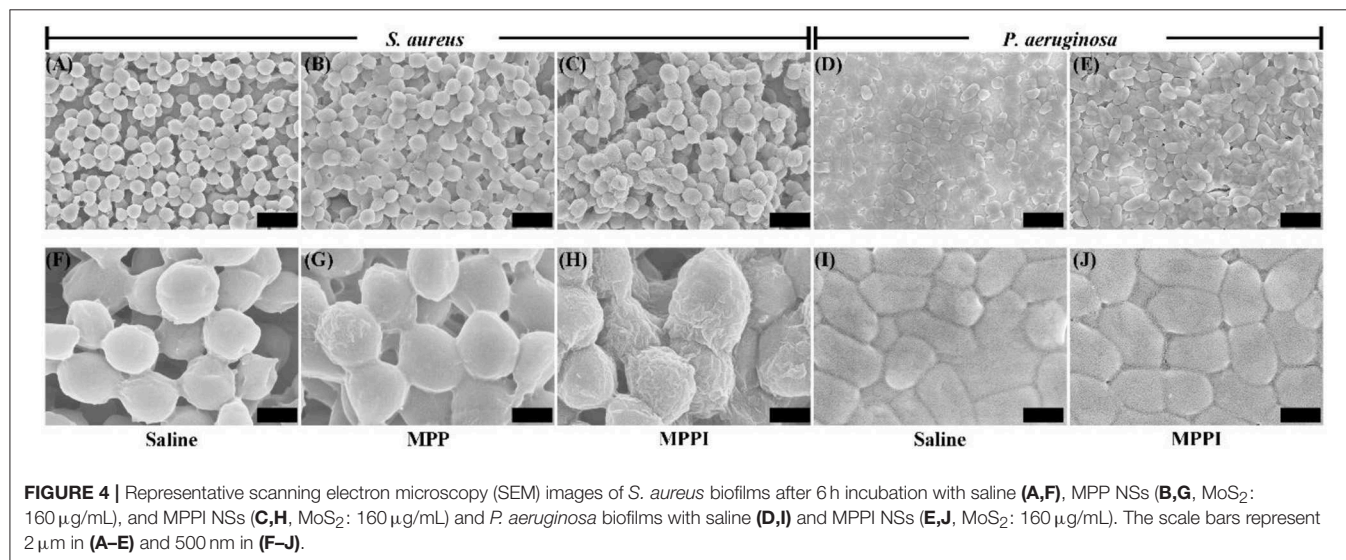
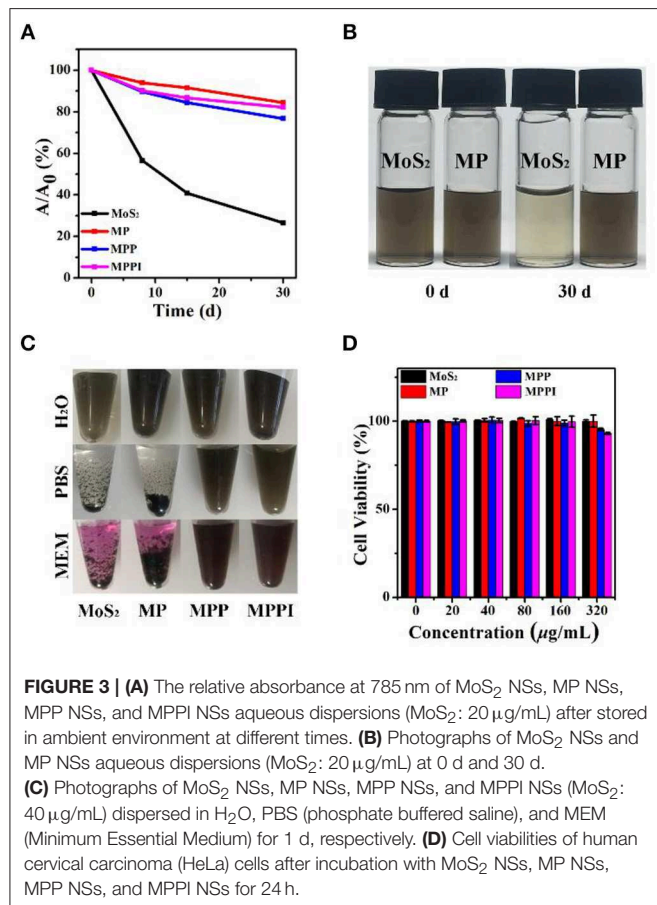
40 μ g/mL) without any obvious precipitates even after 14 d (**Figure S5**), and their hydrodynamic sizes almost remained the same (**Figure S6**), demonstrating great colloidal stability of MPP NSs and MPPI NSs.

The conjugation efficiency of protein to MP NSs was investigated by using bovine serum albumin (BSA) as an example. Determined by Bradford protein assay (Compton and Jones, 1985), 1 mg of MoS₂ NSs can load 0.012 mg of BSA, while MP NSs (containing 1 mg MoS₂) can load 0.434 mg of BSA, suggesting a 36-fold increase.

Biocompatibility is an essential factor for the biomedical application of nanomaterials. As illustrated in **Figure 3D**, HeLa cells remained almost 100% viable after incubation with MoS₂ NSs and MP NSs, and more than 90% viable with MPP NSs and MPPI NSs even at the concentration of up to 320 μ g/mL, demonstrating good biocompatibility of MPPI NSs.

Targeting Ability of MPPI NSs to *S. aureus* Biofilms

Prior to the photothermal therapy, the targeting ability of MPPI NSs to *S. aureus* biofilms was studied. As shown in **Figure S7**, the planktonic *S. aureus* cells have smooth, clear, and spherical morphology, while the surface of bacterial cells in *S. aureus* biofilms are less clear due to the enclosing of EPS (**Figures 4A,F**; Asahi et al., 2015). As indicated in **Figures 4B,G**, crumpled accumulation of nanosheets can be observed on the surface of a few *S. aureus* cells in biofilms after 6 h incubation with MPP NSs (MoS₂: 160 μ g/mL) due to the non-specific absorption. In contrast, most *S. aureus* cells in biofilms were covered by crumpled nanosheets after incubation with MPPI NSs (MoS₂: 160 μ g/mL) for 6 h (**Figures 4C,H**), suggesting effectively binding of MPPI NSs to *S. aureus*. To confirm the targeting ability of MPPI NSs to *S. aureus* biofilms, *Pseudomonas aeruginosa* (*P. aeruginosa*) biofilms was also incubated with MPPI NSs (MoS₂: 160 μ g/mL) for 6 h. SEM images show that no obvious change can be observed between the *P. aeruginosa* biofilms treated with saline (**Figures 4D,I**) and that with MPPI NSs (**Figures 4E,J**).



The specific accumulation of MPPI NSs in *S. aureus* biofilms was also analyzed by energy dispersive X-ray spectroscopy (EDS). As illustrated in **Figure S8**, the atomic percentages of Mo among all elements (C, N, O, S, P, and Mo) in *S. aureus* biofilms cultured with MPP NSs and *P. aeruginosa* biofilms cultured with MPPI NSs are very low (0.08~0.1%) even at high concentration (MoS_2 : 160 $\mu\text{g/mL}$), suggesting that limited amount of nanosheets bind to biofilms through non-specific adsorption. In contrast, the atomic percentage of Mo in *S. aureus* biofilms cultured with MPPI NSs (MoS_2 : 160 $\mu\text{g/mL}$) is 0.48%, which is about 5-fold of that with MPP NSs. These results demonstrate the excellent *S. aureus* biofilm-targeting ability of MPPI NSs.

As shown in **Figure S9**, the human prostatic stromal myofibroblast cell line (WPMY-1 cells) stayed almost 100% viable after PTT of MPPI NSs (0.58 W/cm² for 10 min), even when the concentration of MPPI NSs reached up to 160 $\mu\text{g/mL}$. The WPMY-1 cells after PTT of MPPI NSs were also co-stained by calcein-AM and propidium iodide (PI). Live cells were stained green by calcein, while dead cells were stained red by PI. **Figure S10** shows barely red fluorescence, and almost all WPMY-1 cells show green fluorescence, indicating that the targeted-PTT of MPPI NSs has little side effects to normal mammalian cells.

In vitro Targeted PTT of *S. aureus* Biofilms

Prior to the *in vivo* treatment study of *S. aureus* biofilm-related infection, the *in vitro* PTT efficacy of *S. aureus* biofilms by MPPI NSs was evaluated. As shown in **Figure 5A**, the temperature of *S. aureus* biofilms rose by 2°C under 785 nm laser irradiation (0.58 W/cm², 10 min). The *S. aureus* biofilms with MPP NSs and MPPI NSs incubation and NIR laser irradiation show temperature increase of 30 and 43°C, respectively, suggesting more MPPI NSs accumulate in *S. aureus* biofilms than MPP NSs due to the specific binding mediated by antibody.

As shown in **Figure 5B**, the colony forming units (CFU) of *S. aureus* biofilms after the treatments of MPP NSs and MPPI NSs incubation (MoS_2 : 160 $\mu\text{g/mL}$) decreases by about 0.36 log (~57.08%) and 0.77 log (~77.07%), respectively. The CFU of *S. aureus* biofilms decreases by 0.96 log (~89.14%) after PTT of MPP NSs (MoS_2 : 160 $\mu\text{g/mL}$), while that decreases by 4.46 log (>99.99%) after PTT of MPPI NSs (MoS_2 : 160 $\mu\text{g/mL}$), showing excellent targeted PTT efficacy.

Three dimensional (3D) confocal laser scanning microscopy (CLSM) was used to directly observe live bacteria in biofilms that were stained green by calcein (Chen et al., 2016). As shown in **Figure 5C**, the intensity of green fluorescence shows limited reduction in *S. aureus* biofilms of control groups, including MPP, MPPI, and MPP + NIR groups, which indicates the MPP NSs, MPPI NSs, and non-targeted PTT of MPP NSs have neglectable antibiofilm efficacy. In contrast, after targeted PTT of MPPI NSs, the green fluorescence of *S. aureus* biofilms decreases along with the increase of the concentration of MPPI NSs, and nearly vanishes at the concentration of 160 $\mu\text{g/mL}$, indicating that almost all *S. aureus* in biofilms are killed. The significant difference of the green fluorescence between MPPI + NIR group and MPP + NIR group suggests that the antibiofilm efficacy of targeted PTT is much better than the non-targeted PTT, due to

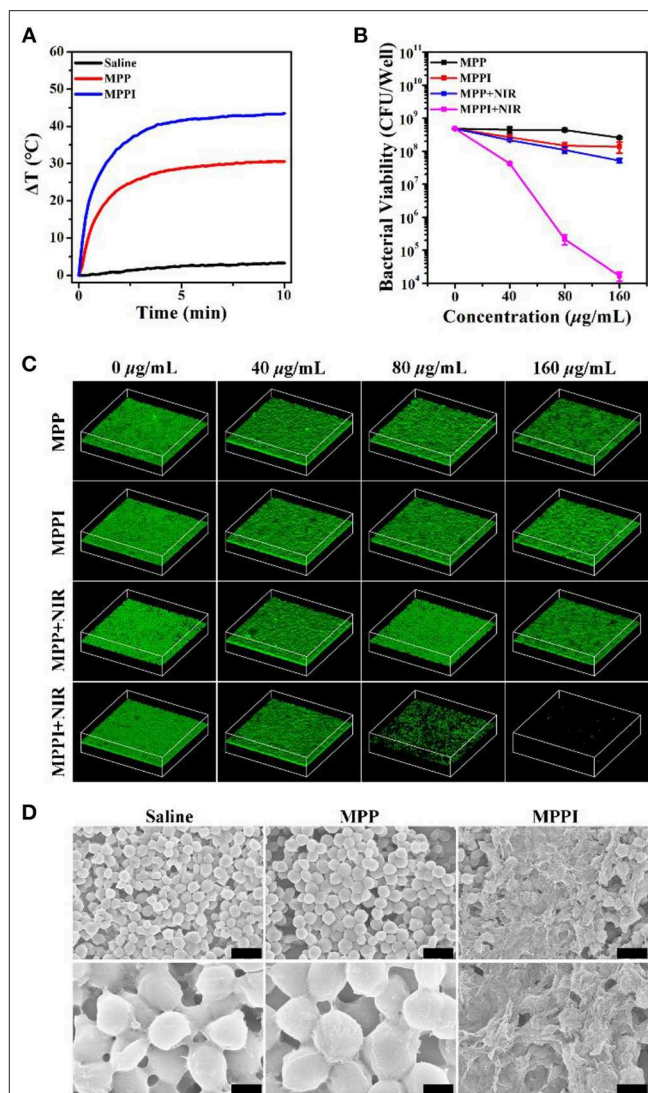
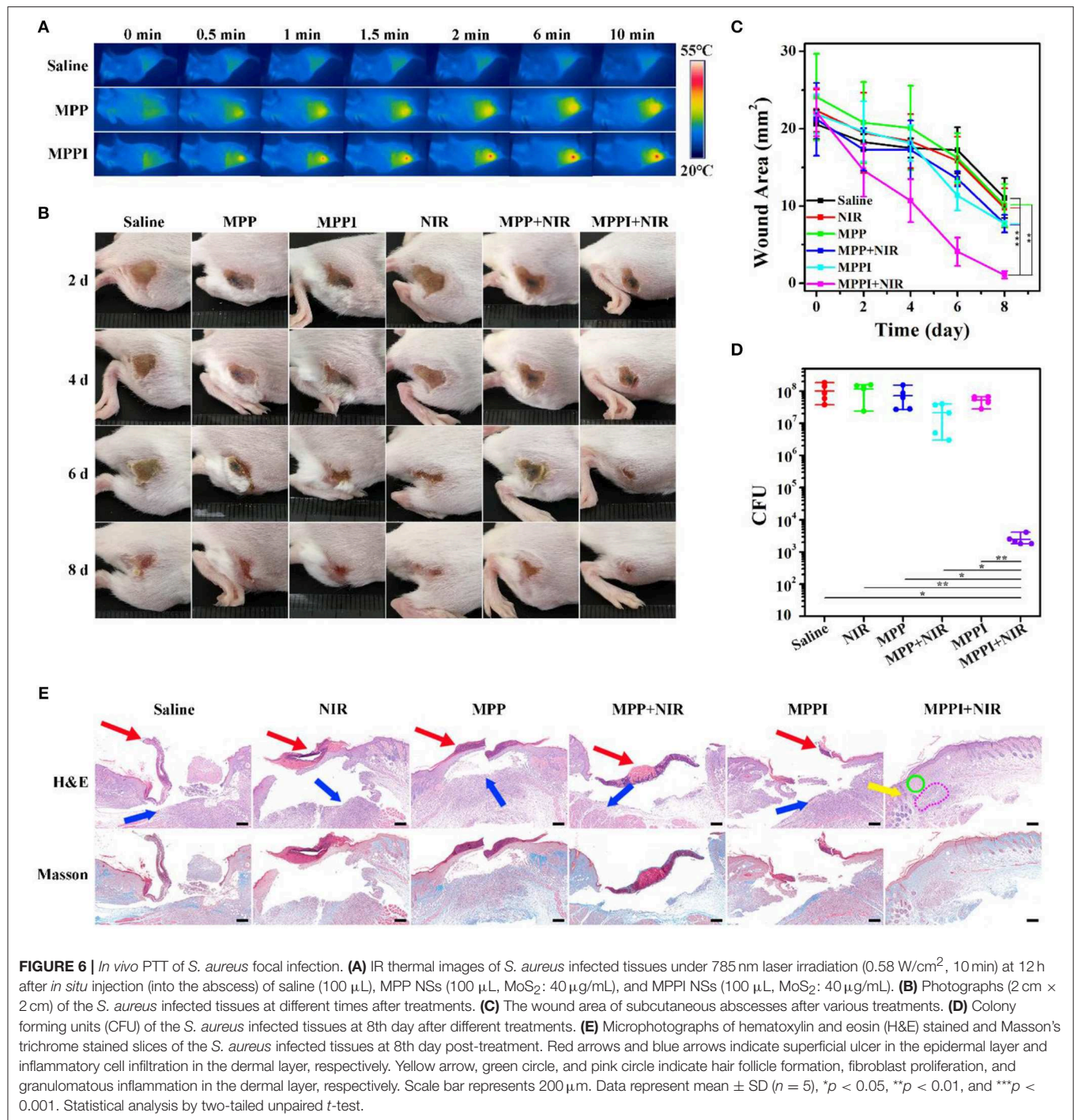


FIGURE 5 | *In vitro* targeted PTT of *S. aureus* biofilms. **(A)** Temperature changing curves of *S. aureus* biofilms under 785 nm laser irradiation (0.58 W/cm², 10 min) after 6 h incubation with saline, MPP NSs, and MPPI NSs (MoS_2 : 160 $\mu\text{g/mL}$), respectively. **(B)** Bacterial viability and **(C)** Three dimensional (3D) confocal laser scanning microscopy (CLSM) images (630 × 630 μm) of *S. aureus* biofilms with or without NIR laser irradiation after incubation with different concentrations of MPP NSs or MPPI NSs. **(D)** Representative SEM images of *S. aureus* biofilms after PTT of MPP NSs or MPPI NSs (MoS_2 : 160 $\mu\text{g/mL}$). The scale bars in upper row and lower row represent 2 μm and 500 nm, respectively.

the limited range of photo-induced thermal effect. These results are consistent with the changing trend of CFU numbers after different treatments.

As shown in **Figure 5D**, the bacteria in preformed *S. aureus* biofilms have intact morphology after NIR laser irradiation (Saline) or PTT of MPP NSs (MPP). On the contrary, after PTT of MPPI NSs (MPPI), lysed bacterial morphology and debris can be observed, suggesting serious structural damage of *S. aureus* biofilms. The structure change of *S. aureus* biofilms after PTT of MPPI NSs was also revealed by crystal violet staining (Chen



et al., 2016). As shown in **Figure S11**, the *S. aureus* biofilms after PTT of MPPI NSs become loosened, indicating that PTT of MPPI NSs can partially destroy the EPS-encased structure of biofilms. Hence, *S. aureus* biofilms can be inactivated by targeted photothermal ablation using MPPI NSs efficiently.

***In vivo* PTT of *S. aureus* Focal Infection**

To construct *S. aureus* focal infection model, *S. aureus* suspensions were subcutaneously injected into the right flanks

of Balb/c mice (Hu et al., 2017; Zhao et al., 2017). These mice with subcutaneous abscesses were randomly divided into six groups: Saline, NIR, MPP, MPP + NIR, MPPI, and MPPI + NIR. Among them, 100 µL of MPP NSs or MPPI NSs dispersed in saline were injected into the *S. aureus* focal infection sites with a dose of 4 µg (40 µg/mL), and saline was used as control. NIR laser irradiation (785 nm, 0.58 W/cm², 10 min) was carried out at 12 h post-injection. As shown in **Figure 6A** and **Figure S12**, the temperature of *S. aureus* infected skins treated with saline

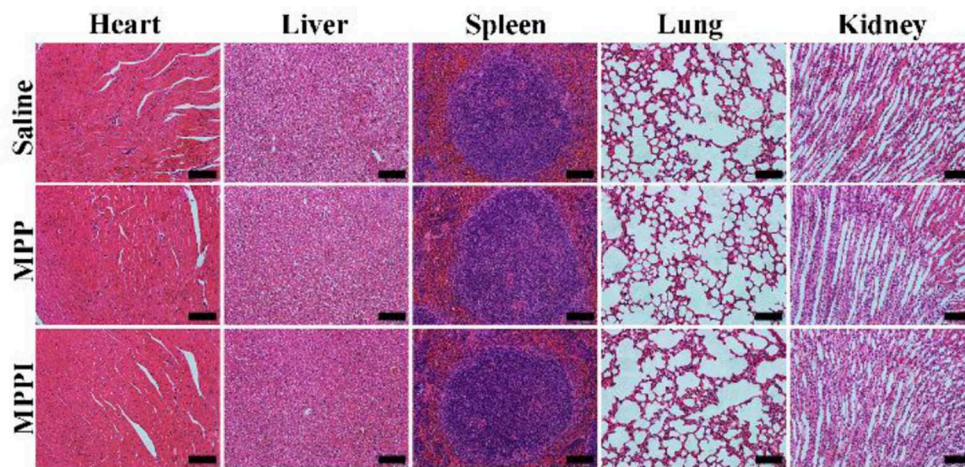


FIGURE 7 | Microphotographs of H&E stained slices of major organs of Balb/c mice at 30th day after i.v. injection of saline, MPP NSs, and MPPI NSs. The MPP NSs and MPPI NSs contained 500 $\mu\text{g/mL}$ of MoS_2 , and the injection volume was 200 μL . The scale bar represents 200 μm .

rose from 33 to 34°C under NIR laser irradiation, while the temperatures of infected tissues with PTT of MPP NSs and MPPI NSs increased to ~ 43 and $\sim 50^\circ\text{C}$, respectively. The higher temperature indicates that more MPPI NSs accumulate at the infection sites than MPP NSs.

The PTT efficacy of MPPI NSs was studied during the following 8 days after treatments. As shown in **Figures 6B,C**, the mice from MPPI + NIR group showed much earlier wound scarring and significantly faster healing than those from the other five control groups (Saline, MPP, MPPI, NIR, and MPP + NIR). Wound crust appeared at 4th day after PTT of MPPI NSs, and fell off at 6th day. After 8 d, the *S. aureus* infected tissues almost recovered with a small scar left. As to the five control groups, there were no crust formed until 6 d after treatments. At 8th day, the crust detached, but ulceration still remained, showing much slower healing. As shown in **Figure 6C**, the average area of infected tissues from MPPI + NIR group was reduced to $\sim 1 \text{ mm}^2$ at 8th day post-treatment, while those from other five control groups were still larger than 7 mm^2 .

The number of viable *S. aureus* cells from the infected tissues were obtained by standard plate counting method at 8th day post-treatment. As shown in **Figure 6D** and **Figure S13**, the CFU of the infected tissues from three groups (NIR, MPP, and MPPI), shows <0.25 log reduction compared to the Saline group, suggesting that neither MPP NSs or MPPI NSs incubation nor NIR laser irradiation can kill the bacteria effectively. The number of bacteria in infected tissues after PTT of MPPI NSs is reduced by more than 4 log ($>99.99\%$), which is significantly higher than the group treated with PTT of MPP NSs (0.57 log, $\sim 48.43\%$).

Hematoxylin and eosin (H&E) staining and Masson's trichrome staining were used to evaluate the healing status of *S. aureus* infected tissues. As shown in **Figure 6E**, the infected tissues from the five control groups (Saline, NIR, MPP, MPP + NIR, and MPPI) exhibited severe inflammation on the 8th day post-treatment, including superficial ulcer in the epidermal layer (indicated by red arrows), massive inflammatory cells infiltration

in the dermal layer (indicated by blue arrows, and also shown in **Figure S14**), and collagen layer (stained blue) disappearing. On the contrary, the infected skin of mice after PTT of MPPI NSs showed intact epidermal layer with dense collagen fibers, and proliferation of fibroblast (indicated by green circle) as well as hair follicles (indicated by yellow arrow) in the dermal layer. Although there was still a little bit of granulomatous inflammation (indicated by pink circle), the *S. aureus* focal infection almost healed at 8th day after the targeted PTT of MPPI NSs. These results demonstrate the superiority of targeted PTT for the treatment of *S. aureus* focal infection over non-targeted PTT.

In vivo Toxicity

As illustrated in **Figure 7**, the major organs (heart, liver, spleen, lung, and kidney) of mice with i.v. injection of MPP NSs or MPPI NSs have similar morphology as the healthy tissues (Saline) without noticeable organ damage or inflammatory lesion. Although more studies of long-term toxicity are still required, MPPI NSs show no obvious *in vivo* toxicity at the dose we used.

DISCUSSION

PTT is a promising alternative solution of antibiotics for the treatment of bacterial biofilm-related diseases. Targeting functionalization has great potential to improve the therapeutic efficiency and reduce the side effects. In this direction, the modification of targeting moieties to photothermal agents would be a key factor. *S. aureus* is one of the leading causes of biofilm-related infections (Otto, 2013; Tong et al., 2015). Protein A is a surface protein in the cell wall of *S. aureus*. Anti-protein A IgG has proven effective to target *S. aureus*, and used here as the targeting moiety (Meeker et al., 2016, 2018).

MoS_2 NSs is an excellent PTT agent with good biocompatibility, high extinction coefficient and photothermal

conversion efficiency in the NIR region (Robinson et al., 2011; Chou et al., 2013; Li et al., 2017). MoS₂ NSs can be functionalized by various biomolecules, such as PEG-SH, proteins, DNA, and so on, through coordination interaction and physical absorption (Li et al., 2017). These methods are easy to carry out, and the intrinsic properties of MoS₂ NSs would not be affected (Li et al., 2017). Nevertheless, because of these weak non-covalent conjugation, biomolecules tend to desorb from the surface of MoS₂ NSs, which would cause the invalidation of the functionalization and destabilization, especially in physiological environment. Therefore, a facile method for valid and stable functionalization is in demand.

It is realizable for dopamine to polymerize on the surface of MoS₂ NSs, and the *in situ* polymerization of dopamine would deposit a layer of PDA on the surface of MoS₂ NSs, yielding MP NSs (Yuwen et al., 2018). Moreover, PDA has plenty of catechol groups that can facilitate the covalent linkage with amine and thiol groups via Michael addition and/or Schiff base reactions (Liu et al., 2014). Thus, we use PDA as interface of MoS₂ NSs to conjugate PEG-SH and anti-protein A IgG covalently to form MPPI NSs, as illustrated in **Scheme 1**. The surface modification with PDA, PEG-SH, and antibody is moderate without causing any damage to the morphology of MoS₂ NSs (**Figures 1A–D**), but increases the thickness (**Figures 1E–H**). The PDA coating not only enhances the stability of MoS₂ NSs against oxidation (**Figures 3A,B**), but also greatly improves the protein-loading efficiency (36-fold increase). As a result, the MPPI NSs have better colloidal stability compared with MoS₂ NSs (**Figure 3C**, **Figures S5, S6**), good biocompatibility (**Figure 3D**), and excellent photothermal property (**Figure 2D**) and stability (**Figure S4**).

As shown in **Figure 4** and **Figure S8**, much more MPPI NSs accumulate in *S. aureus* biofilms than MPP NSs without IgG functionalization (5-fold increase), resulting higher temperature under NIR laser irradiation (**Figure 5A**). Although the amount of MPPI NSs and MPP NSs at the infection sites of mice was not measured quantitatively, the higher temperature of *S. aureus*-infected skins treated with MPPI NSs than that with MPP NSs indicates that more MPPI NSs accumulate at the infection sites than MPP NSs (**Figure 6A** and **Figure S12**). These results demonstrate that anti-protein A IgG provides MoS₂ NSs with specific binding ability to the *S. aureus* cells in both biofilms and infection sites through the antibody-antigen interaction with high binding affinity. What's more, the antibody-antigen interaction can shorten the distance between *S. aureus* cells and photothermal agents, which could enhance the ablation effect of local photothermal hyperpyrexia (Peng et al., 2018; Zhang et al., 2018). Combining the efficient accumulation and reduced distance of MPPI NSs to *S. aureus*, the targeted PTT of MPPI NSs achieved an excellent inactivation efficiency of more than 99.99% both *in vitro* and *in vivo*, and eventually accelerated the healing of *S. aureus* focal infection (**Figures 5, 6**). Meanwhile, normal mammalian cells are barely affected by the PTT of MPPI NSs (**Figures S9, S10**), indicating little side effects of the targeted-PTT. In one word,

a *S. aureus*-targeting PTT agent has been proposed with enhanced therapeutic efficiency and low side effects, suggesting the necessity of targeting functionalization when designing PTT agents.

CONCLUSIONS

In this study, MPPI NSs were prepared for targeted PTT of *S. aureus* focal infection. With PDA coating, MoS₂ NSs can be functionalized covalently with PEG-SH and IgG. As a result, MPPI NSs possess excellent colloidal stability, conjugation efficiency, photothermal property, biocompatibility, and especially *S. aureus*-targeting ability. MPPI NSs can accumulate in *S. aureus* biofilms effectively and specifically with an amount of almost 5 times more than MPP NSs without IgG. The numbers of *S. aureus* in biofilms and infected tissues were reduced by more than 4 log (>99.99%) by targeted PTT of MPPI NSs, which was significantly higher than that of MPP NSs without targeting ability (<90% *in vitro* and <50% *in vivo*). Meanwhile, the PTT of MPPI NSs show no harm to normal mammalian cells, demonstrating the low side effects of targeted PTT. Targeted PTT of MPPI NSs also shows much faster healing process for the treatment of *S. aureus* focal infection *in vivo* than non-targeted PTT. With no obvious toxicity observed both *in vitro* and *in vivo*, these results demonstrate that the MPPI NSs have great potential as a targeted PTT agent for the treatment of *S. aureus* infection.

DATA AVAILABILITY

All datasets generated for this study are included in the manuscript/Supplementary Files.

ETHICS STATEMENT

The animal study was reviewed and approved by the Animal Ethics Committee of Nanjing University.

AUTHOR CONTRIBUTIONS

LW and LY conceived and supervised the study. YZ and WX designed and carried out the experiments, and analyzed the results. SG and JS helped with the *in vivo* experiments. SR conducted the SEM and EDS measurements. YZ wrote the manuscript. All authors participated in revising the paper.

FUNDING

This work was financially supported by the National Key Research and Development Program of China (2017YFA0205302), the National Natural Science Foundation of China (51503101, 21475064), Program for Changjiang Scholars and Innovative Research Team in University (IRT_15R37), the

Priority Academic Program Development of Jiangsu Higher Education Institutions (PAPD, YX030003), the Key Research and Development Program of Jiangsu (BE2018732), and the Natural Science Key Fund for Colleges and Universities in Jiangsu Province (17KJA430011).

REFERENCES

- Asahi, Y., Miura, J., Tsuda, T., Kuwabata, S., Tsunashima, K., Noiri, Y., et al. (2015). Simple observation of *Streptococcus mutans* biofilm by scanning electron microscopy using ionic liquids. *AMB Express* 5, 6. doi: 10.1186/s13568-015-0097-4
- Chen, Z., Ji, H., Liu, C., Bing, W., Wang, Z., and Qu, X. (2016). A multinuclear metal complex based DNase-mimetic artificial enzyme: matrix cleavage for combating bacterial biofilms. *Angew. Chem. Int. Ed.* 55, 10732–10736. doi: 10.1002/anie.201605296
- Chou, S. S., Kaehr, B., Kim, J., Foley, B. M., De, M., Hopkins, P. E., et al. (2013). Chemically exfoliated MoS₂ as near-infrared photothermal agents. *Angew. Chem. Int. Ed.* 52, 4160–4164. doi: 10.1002/anie.201209229
- Compton, S. J., and Jones, C. G. (1985). Mechanism of dye response and interference in the Bradford protein assay. *Anal. Biochem.* 151, 369–374. doi: 10.1016/0003-2697(85)90190-3
- Costerton, J. W., Lewandowski, Z., Caldwell, D. E., Korber, D. R., and Lappin-Scott, H. M. (1995). Microbial biofilms. *Annu. Rev. Microbiol.* 49, 711–745. doi: 10.1146/annurev.mi.49.100195.003431
- Costerton, J. W., Stewart, P. S., and Greenberg, E. P. (1999). Bacterial biofilms: a common cause of persistent infections. *Science* 284, 1318–1322. doi: 10.1126/science.284.5418.1318
- Davies, D. (2003). Understanding biofilm resistance to antibacterial agents. *Nat. Rev. Drug Discov.* 2, 114–122. doi: 10.1038/nrd1008
- Duncan, B., Li, X., Landis, R. F., Kim, S. T., Gupta, A., Wang, L. S., et al. (2015). Nanoparticle-stabilized capsules for the treatment of bacterial biofilms. *ACS Nano* 9, 7775–7782. doi: 10.1021/acs.nano.5b01696
- Ganta, D., Sinha, S., and Haasch, R. T. (2014). 2-D material molybdenum disulfide analyzed by XPS. *Surf. Sci. Spectra* 21, 19–27. doi: 10.1116/11.20140401
- Hasan, S., Thomas, N., Thierry, B., and Prestidge, C. A. (2017). Biodegradable nitric oxide precursor-loaded micro- and nanoparticles for the treatment of *Staphylococcus aureus* biofilms. *J. Mater. Chem. B* 5, 1005–1014. doi: 10.1039/c6tb03290g
- Hauck, T. S., Jennings, T. L., Yatsenko, T., Kumaradas, J. C., and Chan, W. C. W. (2008). Enhancing the toxicity of cancer chemotherapeutics with gold nanorod hyperthermia. *Adv. Mater.* 20, 3832–3838. doi: 10.1002/adma.200800921
- He, Y. K., Wang, J. T., Zhang, H. Q., Zhang, T., Zhang, B., Cao, S. K., et al. (2014). Polydopamine-modified graphene oxide nanocomposite membrane for proton exchange membrane fuel cell under anhydrous conditions. *J. Mater. Chem. A* 2, 9548–9558. doi: 10.1039/c3ta15301k
- Hsiao, C. W., Chen, H. L., Liao, Z. X., Sureshbabu, R., Hsiao, H. C., Lin, S. J., et al. (2015). Effective photothermal killing of pathogenic bacteria by using spatially tunable colloidal gels with nano-localized heating sources. *Adv. Funct. Mater.* 25, 721–728. doi: 10.1002/adfm.201403478
- Hu, D., Li, H., Wang, B., Ye, Z., Lei, W., Jia, F., et al. (2017). Surface-adaptive gold nanoparticles with effective adherence and enhanced photothermal ablation of methicillin-resistant *Staphylococcus aureus* biofilm. *ACS Nano* 11, 9330–9339. doi: 10.1021/acs.nano.7b04731
- Islam, S., Moinuddin, Mir, A. R., Arfat, M. Y., Alam, K., and Ali, A. (2017). Studies on glycooxidatively modified human IgG: Implications in immunopathology of type 2 diabetes mellitus. *Int. J. Biol. Macromol.* 104 (Pt A), 19–29. doi: 10.1016/j.ijbiomac.2017.05.190
- Ji, H., Dong, K., Yan, Z., Ding, C., Chen, Z., Ren, J., et al. (2016). Bacterial hyaluronidase self-triggered prodrug release for chemo-photothermal synergistic treatment of bacterial infection. *Small* 12, 6200–6206. doi: 10.1002/smll.201601729
- Jo, W., and Kim, M. J. (2013). Influence of the photothermal effect of a gold nanorod cluster on biofilm disinfection. *Nanotechnology* 24, 195104. doi: 10.1088/0957-4484/24/19/195104
- Kibsgaard, J., Chen, Z., Reinecke, B. N., and Jaramillo, T. F. (2012). Engineering the surface structure of MoS₂ to preferentially expose active edge sites for electrocatalysis. *Nat. Mater.* 11, 963–969. doi: 10.1038/nmat3439
- Levi-Polyachenko, N., Young, C., MacNeill, C., Braden, A., Argenta, L., and Reid, S. (2014). Eradicating group A streptococcus bacteria and biofilms using functionalised multi-wall carbon nanotubes. *Int. J. Hypertherm.* 30, 490–501. doi: 10.3109/02656736.2014.966790
- Li, X., Shan, J., Zhang, W., Su, S., Yuwen, L., and Wang, L. (2017). Recent advances in synthesis and biomedical applications of two-dimensional transition metal dichalcogenide nanosheets. *Small* 13, 1602660. doi: 10.1002/smll.201602660
- Liu, Y., Ai, K., and Lu, L. (2014). Polydopamine and its derivative materials: synthesis and promising applications in energy, environmental, and biomedical fields. *Chem. Rev.* 114, 5057–5115. doi: 10.1021/cr400407a
- Lynch, A. S., and Robertson, G. T. (2008). Bacterial and fungal biofilm infections. *Annu. Rev. Med.* 59, 415–428. doi: 10.1146/annurev.med.59.110106.132000
- Meeker, D. G., Jenkins, S. V., Miller, E. K., Beenken, K. E., Loughran, A. J., Powless, A., et al. (2016). Synergistic photothermal and antibiotic killing of biofilm-associated *Staphylococcus aureus* using targeted antibiotic-loaded gold nanoconstructs. *ACS Infect. Dis.* 2, 241–250. doi: 10.1021/acsinfecdis.5b00117
- Meeker, D. G., Wang, T., Harrington, W. N., Zharov, V. P., Johnson, S. A., Jenkins, S. V., et al. (2018). Versatility of targeted antibiotic-loaded gold nanoconstructs for the treatment of biofilm-associated bacterial infections. *Int. J. Hyperthermia* 34, 209–219. doi: 10.1080/02656736.2017.1392047
- Otto, M. (2013). Staphylococcal infections: mechanisms of biofilm maturation and detachment as critical determinants of pathogenicity. *Annu. Rev. Med.* 64, 175–188. doi: 10.1146/annurev-med-042711-140023
- Pallavicini, P., Donà, A., Taglietti, A., Minzioni, P., Patrini, M., Dacarro, G., et al. (2014). Self-assembled monolayers of gold nanostars: a convenient tool for near-IR photothermal biofilm eradication. *Chem. Commun.* 50, 1969–1971. doi: 10.1039/c3cc48667b
- Penesyan, A., Gillings, M., and Paulsen, I. T. (2015). Antibiotic discovery: combatting bacterial resistance in cells and in biofilm communities. *Molecules* 20, 5286–5298. doi: 10.3390/molecules20045286
- Peng, B., Zhang, X., Aarts, D., and Dullens, R. P. A. (2018). Superparamagnetic nickel colloidal nanocrystal clusters with antibacterial activity and bacteria binding ability. *Nat. Nanotechnol.* 13, 478–482. doi: 10.1038/s41565-018-0108-0
- Ray, P. C., Khan, S. A., Singh, A. K., Senapati, D., and Fan, Z. (2012). Nanomaterials for targeted detection and photothermal killing of bacteria. *Chem. Soc. Rev.* 41, 3193–3209. doi: 10.1039/c2cs15340h
- Robinson, J. T., Tabakman, S. M., Liang, Y., Wang, H., Casalongue, H. S., Vinh, D., et al. (2011). Ultrasmall reduced graphene oxide with high near-infrared absorbance for photothermal therapy. *J. Am. Chem. Soc.* 133, 6825–6831. doi: 10.1021/ja2010175
- Ryou, M. H., Lee, Y. M., Park, J. K., and Choi, J. W. (2011). Mussel-inspired polydopamine-treated polyethylene separators for high-power Li-ion batteries. *Adv. Mater.* 23, 3066–3070. doi: 10.1002/adma.201100303
- Teng, C. P., Zhou, T., Ye, E., Liu, S., Koh, L. D., Low, M., et al. (2016). Effective targeted photothermal ablation of multidrug resistant bacteria and their biofilms with NIR-absorbing gold nanocrosses. *Adv. Healthc. Mater.* 5, 2122–2130. doi: 10.1002/adhm.201600346
- Tong, S. Y., Davis, J. S., Eichenberger, E., Holland, T. L., and Fowler, V. G. Jr. (2015). *Staphylococcus aureus* infections: epidemiology, pathophysiology,

SUPPLEMENTARY MATERIAL

The Supplementary Material for this article can be found online at: <https://www.frontiersin.org/articles/10.3389/fbioe.2019.00218/full#supplementary-material>

- clinical manifestations, and management. *Clin. Microbiol. Rev.* 28, 603–661. doi: 10.1128/CMR.00134-14
- Uppu, D. S., Samaddar, S., Ghosh, C., Paramanandham, K., Shome, B. R., and Haldar, J. (2016). Amide side chain amphiphilic polymers disrupt surface established bacterial bio-films and protect mice from chronic *Acinetobacter baumannii* infection. *Biomaterials* 74, 131–143. doi: 10.1016/j.biomaterials.2015.09.042
- van Hal, S. J., Jensen, S. O., Vaska, V. L., Espedido, B. A., Paterson, D. L., and Gosbell, I. B. (2012). Predictors of mortality in *Staphylococcus aureus* Bacteremia. *Clin. Microbiol. Rev.* 25, 362–386. doi: 10.1128/CMR.05022-11
- Wolcott, R. D., Hanson, J. D., Rees, E. J., Koenig, L. D., Phillips, C. D., Wolcott, R. A., et al. (2016). Analysis of the chronic wound microbiota of 2,963 patients by 16S rDNA pyrosequencing. *Wound Repair Regen.* 24, 163–174. doi: 10.1111/wrr.12370
- Yin, W., Yu, J., Lv, F., Yan, L., Zheng, L. R., Gu, Z., et al. (2016). Functionalized Nano-MoS₂ with peroxidase catalytic and near-infrared photothermal activities for safe and synergetic wound antibacterial applications. *ACS Nano* 10, 11000–11011. doi: 10.1021/acsnano.6b05810
- Yuan, Z. Q., Li, J. Z., Liu, Y., Chen, W. L., Yang, S. D., Zhang, C. G., et al. (2015). Systemic delivery of micelles loading with paclitaxel using N-succinyl-palmitoyl-chitosan decorated with cRGDyK peptide to inhibit non-small-cell lung cancer. *Int. J. Pharmaceut.* 492, 141–151. doi: 10.1016/j.ijpharm.2015.07.022
- Yuwen, L., Sun, Y., Tan, G., Xiu, W., Zhang, Y., Weng, L., et al. (2018). MoS₂@polydopamine-Ag nanosheets with enhanced antibacterial activity for effective treatment of *Staphylococcus aureus* biofilms and wound infection. *Nanoscale* 10, 16711–16720. doi: 10.1039/c8nr04111c
- Yuwen, L., Yu, H., Yang, X., Zhou, J., Zhang, Q., Zhang, Y., et al. (2016). Rapid preparation of single-layer transition metal dichalcogenide nanosheets via ultrasonication enhanced lithium intercalation. *Chem. Commun.* 52, 529–532. doi: 10.1039/c5cc07301d
- Zhang, H. H., Chen, G. H., Yu, B., and Cong, H. L. (2018). Emerging advanced nanomaterials for cancer photothermal therapy. *Rev. Adv. Mater. Sci.* 53, 131–146. doi: 10.1515/rams-2018-0010
- Zhang, W., Shi, S., Wang, Y., Yu, S., Zhu, W., Zhang, X., et al. (2016). Versatile molybdenum disulfide based antibacterial composites for in vitro enhanced sterilization and *in vivo* focal infection therapy. *Nanoscale* 8, 11642–11648. doi: 10.1039/c6nr01243d
- Zhang, Y., Xiu, W., Sun, Y., Zhu, D., Zhang, Q., Yuwen, L., et al. (2017). RGD-QD-MoS₂ nanosheets for targeted fluorescent imaging and photothermal therapy of cancer. *Nanoscale* 9, 15835–15845. doi: 10.1039/c7nr05278b
- Zhao, Z., Yan, R., Yi, X., Li, J., Rao, J., Guo, Z., et al. (2017). Bacteria-activated theranostic nanoprobe against methicillin-resistant *Staphylococcus aureus* infection. *ACS Nano* 11, 4428–4438. doi: 10.1021/acsnano.7b00041

Conflict of Interest Statement: The authors declare that the research was conducted in the absence of any commercial or financial relationships that could be construed as a potential conflict of interest.

Copyright © 2019 Zhang, Xiu, Gan, Shan, Ren, Yuwen, Weng, Teng and Wang. This is an open-access article distributed under the terms of the Creative Commons Attribution License (CC BY). The use, distribution or reproduction in other forums is permitted, provided the original author(s) and the copyright owner(s) are credited and that the original publication in this journal is cited, in accordance with accepted academic practice. No use, distribution or reproduction is permitted which does not comply with these terms.



Self-Illuminating Agents for Deep-Tissue Optical Imaging

Qing Li, Jianfeng Zeng, Qingqing Miao* and Mingyuan Gao

State Key Laboratory of Radiation Medicine and Protection, School for Radiological and Interdisciplinary Sciences (RAD-X), Collaborative Innovation Center of Radiation Medicine of Jiangsu Higher Education Institutions, Soochow University, Suzhou, China

Optical imaging plays an indispensable role in biology and medicine attributing to its noninvasiveness, high spatiotemporal resolution, and high sensitivity. However, as a conventional optical imaging modality, fluorescence imaging confronts issues of shallow imaging depth due to the need for real-time light excitation which produces tissue autofluorescence. By contrast, self-luminescence imaging eliminates the concurrent light excitation, permitting deeper imaging depth and higher signal-to-background ratio (SBR), which has attracted growing attention. Herein, this review summarizes the progress on the development of near-infrared (NIR) emitting self-luminescence agents in deep-tissue optical imaging with highlighting the design principles including molecular- and nano-engineering approaches. Finally, it discusses current challenges and guidelines to develop more effective self-illuminating agents for biomedical diagnosis and treatment.

OPEN ACCESS

Edited by:

Giada Graziana Genchi,
Italian Institute of Technology (IIT), Italy

Reviewed by:

Kanyi Pu,
Nanyang Technological
University, Singapore
Jianxiang Zhang,
Army Medical University, China

*Correspondence:

Qingqing Miao
qqmiao@suda.edu.cn

Specialty section:

This article was submitted to
Nanobiotechnology,
a section of the journal
Frontiers in Bioengineering and
Biotechnology

Received: 19 September 2019

Accepted: 28 October 2019

Published: 12 November 2019

Citation:

Li Q, Zeng J, Miao Q and Gao M
(2019) Self-Illuminating Agents for
Deep-Tissue Optical Imaging.
Front. Bioeng. Biotechnol. 7:326.
doi: 10.3389/fbioe.2019.00326

Keywords: self-luminescence, bioluminescence, chemiluminescence, afterglow, deep-tissue imaging, optical imaging

INTRODUCTION

Imaging techniques such as single-photon emission computed tomography (SPECT), positron emission computed tomography (PET), magnetic resonance imaging (MRI), computed tomography (CT), optical imaging, ultrasound imaging, and photoacoustic (PA) imaging have become powerful tools to detect and monitor the physiological or pathological processes at the molecular, subcellular, cellular, tissue and body levels (Jokerst and Gambhir, 2011; Farzin et al., 2018; Li et al., 2018; Ma et al., 2018; Ni et al., 2018a; Yin et al., 2019). Among the above-mentioned imaging modalities, optical imaging shows tremendous potential in biomedical applications due to its noninvasiveness, high sensitivity, high temporal and spatial resolution (Liu et al., 2007; Weissleder and Pittet, 2008; Choi et al., 2013; Zhu et al., 2018). Moreover, optical imaging equipment are relatively low-cost and convenient to operate (Baker, 2010; Badr and Tannous, 2011; Gnaïm et al., 2019). However, as a conventional optical imaging, fluorescence imaging has not been extensively utilized in clinical practice. The main reason is the need for concurrent light excitation in imaging process, which produces severe light-tissue interactions (i.e., light scattering, tissue absorption, and autofluorescence), consequently resulting in poor signal-to-background ratio (SBR) and low penetration depth (Shimon et al., 2009; Jones et al., 2017; Miao and Pu, 2018).

Self-luminescence imaging, which does not rely on real-time light excitation and thus eliminates the tissue autofluorescence and photo-bleaching, has attracted increasing attention in recent years. By virtue of the merits, self-luminescence imaging displays higher imaging sensitivity, higher SBR, and deeper imaging depth relative to fluorescence imaging (Table 1; Chen et al., 2017; Hananya and Shabat, 2017; Yan et al., 2019). To date, three kinds of self-luminescence imaging approaches including bioluminescence, chemiluminescence and afterglow luminescence have been developed

TABLE 1 | Comparison of the penetration depth and SBR for self-luminescence imaging modalities.

Imaging modality	Penetration depth (cm)	SBR	References
Bioluminescence	2	100	Xiong et al., 2012
Chemiluminescence	2.5	N.A.	Shuhendler et al., 2014
Afterglow	5	2,922	Jiang et al., 2019

N.A., Not applicable.

and widely applied in biology and medicine. Among the self-luminescence imaging techniques, bioluminescence and chemiluminescence imaging do not need external light source and detect photons from enzymatic- and reactive species-initiated oxidation reaction with their substrates, respectively. By contrast, instead of the combination of enzyme/reactive species with corresponding substrate to generate photons, afterglow luminescence imaging necessitates a pre-irradiation of light to store the energy in agents and then collects the slowly releasing photons from the stored energy after the cessation of light irradiation. The underlying process to generate self-luminescence is summarized in a general way **Scheme 1**. Bioluminescence, chemiluminescence, and afterglow luminescence rely on respective initiator (enzymes for bioluminescence, H_2O_2 for chemiluminescence, and light irradiation for afterglow luminescence) to generate high-energy peroxides such as 1,2-dioxetanone, 1,2-dioxetanedione, and 1,2-dioxetane firstly. Then the peroxides dissociate directly or modulating by an acceptor molecule (F) through energy transfer, leading to the production of an excited state (an excited carbonyl or acceptor molecule) and subsequent light emission.

Near-infrared (NIR) self-luminescence imaging has attracted increasing enthusiasm due to higher tissue penetration depth of NIR light than visible light, which dramatically expands the visualization scope of physiological or pathological processes in living subjects in a noninvasive way (Hasegawa et al., 2013; Li et al., 2016; Zhen et al., 2017). The publications and citations regarding NIR self-illuminating agents are increasing

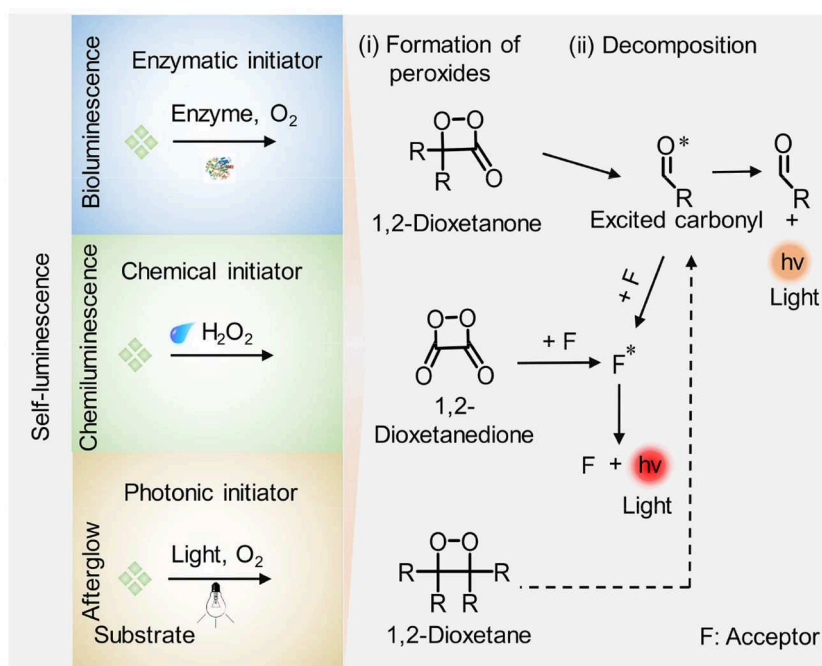
in number, and there are few reviews summarizing the recent development and advances of NIR self-illuminating agents for biomedical applications (Hananya and Shabat, 2017; Weihs and Dacres, 2019). This review will focus on the recent progress on NIR emitting self-luminescence agents for deep-tissue optical imaging, and pinpoint their contemporary molecular- and nano-engineering approaches that have been exploited in this field. As follows, the molecular construction and applications of NIR bioluminescence imaging are first described. Then, NIR chemiluminescence imaging and afterglow luminescence imaging are discussed, respectively, highlighting the strategies for red-shifting and amplifying the luminescence. Finally, it discusses current challenges and guidelines to develop more effective self-illuminating agents for biomedical diagnosis and treatment.

NIR BIOLUMINESCENCE IMAGING

Bioluminescence is the occurrence of light emission generated through oxidation reaction of a substrate catalyzed by an enzyme. The typical enzyme that is used for bioluminescence imaging is luciferase including firefly luciferase (Fluc), *Gaussia* luciferase (Gluc), *Renilla* luciferase (Rluc), and Nanoluc (Nluc) (Kaskova et al., 2016). Nevertheless, the naturally occurring bioluminescence is commonly resided in the visible region (Hai et al., 2017; Yao et al., 2018; Zhang et al., 2018). For example, the native substrate for Fluc is D-luciferin with an emission peak at 560–610 nm, the native substrate for Gluc and Rluc is coelenterazine with an emission maximum at 480 nm, and the native substrate for Nluc is furimazine with an emission peak at 460 nm (Hall et al., 2012; Tang et al., 2019b). As a result, the bioluminescence in the visible region suffers from severe tissue attenuation, compromising imaging SBR and imaging depth, which is not appropriate for *in vivo* deep-tissue imaging. To resolve this, some approaches were adopted to red-shift the light from visible into the NIR region (650–950 nm) to achieve higher imaging depth due to the decreased light scattering and tissue absorption of NIR photons through living tissues relative to that of visible light (Mezzanotte et al., 2017).

A general strategy for constructing NIR emitting bioluminescence is to elongate the π -conjugation of luciferase substrate (Miura et al., 2013). To explore the substrate with an emission wavelength in the NIR region, Pule et al. synthesized a luciferin analog (iLH₂) by inserting a carbon-carbon double bond between the thiazole group and benzothiazole group of luciferin (LH₂). The substrate iLH₂ produced light in the NIR range (λ_{\max} = 670 nm) in presence of a native Fluc (**Figure 1A**) and showed an enhanced penetration depth through blood relative to luciferin (Jathoul et al., 2014). The *in vivo* imaging ability of iLH₂ was investigated by establishing different tumor models in mice. The results revealed that the iLH₂ had less tissue attenuation and showed more imaging definition for systemic lymphoma and metastatic tumor in mice compared to LH₂. Using a similar strategy, Iwano et al. synthesized another luciferin analog, Akalumine, and utilized it for tumor imaging (λ_{\max} = 675 nm) (Iwano et al., 2013). However, Akalumine

Abbreviations: SBR, signal-to-background ratio; NIR, near-infrared; SPECT, single-photon emission computed tomography; PET, positron emission tomography; MRI, magnetic resonance imaging; CT, computed tomography; PA, photoacoustic; Fluc, firefly luciferase; Gluc, *Gaussia* luciferase; Rluc, *Renilla* luciferase; Nluc, Nanoluc; BRET, bioluminescence resonance energy transfer; QDs, quantum dots; FRET, fluorescence resonance energy transfer; MEHPPV, poly [2-methoxy-5-((2-ethylhexyl)oxy)-p-phenylenevinylene]; NCBS, silicon 2,3-naphthalocyanine bis(trihexylsilyloxy); cRGD, cyclic arginine-glycine-aspartic; ROS, reactive oxygen species; CRET, chemiluminescence resonance energy transfer; ONOO⁻, peroxynterite; H_2O_2 , hydrogen peroxide; CPPO, Bis-(2,4,5-trichloro-6-(pentyloxy-carbonyl)phenyl) oxalate; PFODBT, poly(2,7-(9,9'-diethylfluorene)-alt-4,7-bis(thiophen-2-yl)benzo-2,1,3-thiadiazole); APAP, acetaminophen; RNS, reactive nitrogen species; TCPO, bis(2,4,6-trichlorophenyl) oxalate; HOMO, highest occupied molecular orbital; LUMO, lowest unoccupied molecular orbital; CIEEL, chemically initiated electron exchange luminescence; QY, quantum yield; Ce6, chlorin e6; MPO, myeloperoxidase; DCMC, dicyanomethylene-4H-chromene; LPS, lipopolysaccharide; FA, formaldehyde; SPNs, semiconducting polymer nanoparticles; PPV, phenylenevinylene; 1O_2 , singlet oxygen; DNBS, 2,4-dinitrophenylsulfonyl; NAPQI, N-acetylparaquinonimine; AIE, aggregation-induced emission; RES, reticuloendothelial system.



SCHEME 1 | Schematic illustration of the general mechanism for generation of self-luminescence including bioluminescence, chemiluminescence, and afterglow luminescence. (i) Formation of high-energy peroxides: enzymes, reactive species (i.e., H_2O_2), and light irradiation facilitate the formation of high-energy intermediates (cyclic four-membered peroxides such as 1,2-dioxetanone, 1,2-dioxetanedione, and 1,2-dioxetane) in bioluminescence, chemiluminescence, and afterglow luminescence imaging process, respectively. (ii) A chemiexcitation process: the peroxides decompose directly or activated by an acceptor (F) through energy transfer, leading to the formation of an excited state (excited carbonyl or F^*) accompanied by light emission.

had poor water solubility, hampering its efficient accumulation to the targeted site. To resolve this, the same group reported a substituent, AkaLumine hydrochloride (AkaLumine-HCl), which had better water-solubility and emitted NIR light ($\lambda_{max} = 677$ nm) in the presence of luciferase (Kuchimaru et al., 2016). After penetrating 4- or 8-mm-thick tissue, the bioluminescence intensity of AkaLumine-HCl was 5- and 8.3-fold higher than that of D-luciferin, and 3.7- and 6.7-fold higher than that of CycLuc1, respectively (Figure 1B). As expected, AkaLumine-HCl performed imaging of lung metastases with higher sensitivity relative to CycLuc1 (Figure 1C). To further red-shift the bioluminescence, Mezzanotte developed two kinds of naphthyl-based luciferin analogs (i.e., NH_2 -NpLH₂ and OH -NpLH₂) that were matched with a mutant luciferase (CBR2), generating NIR bioluminescence (730 nm for NH_2 -NpLH₂ and 743 nm for OH -NpLH₂) (Hall et al., 2018; Figure 1D). In addition, the mutant enzyme/substrate (CBR2opt/ NH_2 -NpLH₂) system enabled stable and highly resolved NIR bioluminescence imaging of the migration of cells in the brain (Figure 1E).

To avoid the time-consuming synthetic work, bioluminescence resonance energy transfer (BRET) is an alternative approach to red-shift the light emission from visible into the NIR region. To achieve this, a NIR-emitting dye or nanoparticle was commonly selected to covalently conjugate with the natural bioluminescence system as an acceptor to allow for efficient energy transfer (Weihs and Dacres, 2019). Rao

et al. developed a series of BRET-based NIR bioluminescence inorganic systems, in which a *Renilla reniformis* luciferase (Luc8) served as an energy donor and quantum dots (QDs) acted as an energy acceptor (So et al., 2006a,b; Yao et al., 2007; Ma et al., 2010). Such QDs-based BRET systems engineering with emissions ranging from visible to the NIR were utilized for *in vivo* imaging and enzyme activity detection with high sensitivity. Except for inorganic BRET systems, Rao et al. also tried to introduce organic systems for constructing BRET-based NIR bioluminescence. For instance, self-luminescent semiconducting polymer nanoparticles (BF-SPN) were developed for *in vivo* NIR bioluminescence imaging by combining BRET and fluorescence resonance energy transfer (FRET) (Xiong et al., 2012). The nanoparticles (BF-SPNs) were designed to comprise three components: Luc8, poly [2-methoxy-5-((2-ethylhexyl)oxy)-p-phenylenevinylene] (MEHPPV) and silicon 2,3-naphthalocyanine bis(triethylsilyloxy) (NCBS) serving as the BRET donor, the BRET acceptor (and the FRET donor) and the FRET acceptor, respectively. Such BRET-FRET system produced multiple energy transfer from Luc8 to MEHPPV and then to NCBS, resulting in final NIR bioluminescence centered at 780 nm. In order to improve the targeted ability toward tumor, the cyclic arginine-glycine-aspartic (cRGD) peptides were attached to the surface of SPN to obtain BF-SPN-cRGD (Figure 2A). As shown in Figure 2B, the tumor could be clearly delineated by BF-SPN-cRGD with bioluminescence imaging

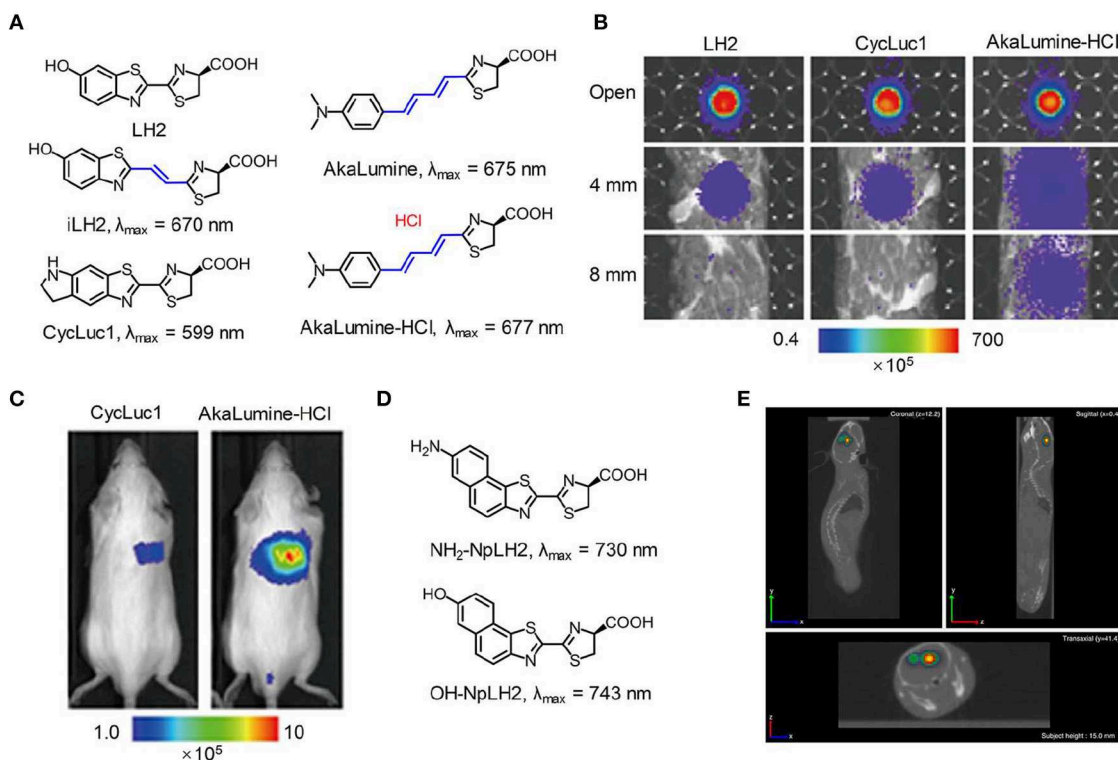


FIGURE 1 | NIR bioluminescence imaging. **(A)** Chemical structures of LH₂, iLH₂, CycLuc1, AkaLumine, and AkaLumine-HCl. **(B)** Bioluminescence imaging of LH₂, CycLuc1, or AkaLumine-HCl through biological tissues with different thickness (0, 4, and 8 mm). The penetration efficiency was calculated according to the relative bioluminescence imaging intensities. **(C)** Representative bioluminescence imaging of lung metastasis in living mice after intraperitoneal injection of substrates (5 mM, 100 μL) (reproduced with permission from Kuchimaru et al., 2016). **(D)** Chemical structures of $\text{NH}_2\text{-NpLH}_2$ and OH-NpLH_2 . **(E)** Co-registered CT and bioluminescence tomography imaging of mice brain using the bioluminescence agent CBR2opt/ $\text{NH}_2\text{-NpLH}_2$. Migration of cells could be clearly observed at day 5 after cell transplantation (reproduced with permission from Hall et al., 2018).

while it could not be achieved with NIR fluorescence imaging, attributing to negligible background of bioluminescence in living tissue. In addition, the bioluminescence imaging of BF-SPN-cRGD could detect smaller tumors (2–3 mm in diameter) with SBR over 100, which was 30-fold higher than that of fluorescence imaging (Figure 2C).

NIR CHEMILUMINESCENCE IMAGING

Compared with bioluminescence imaging, chemiluminescence imaging does not need an enzyme and detects light emission from the reaction of a substrate with reactive oxygen species (ROS), which performs a great deal of versatility and flexibility in experimental systems (Augusto et al., 2013; Ryan and Lippert, 2018; Vacher et al., 2018). The reaction commonly contains two sequential processes: oxidation of a substrate by ROS leads to the formation of a high energy intermediate and subsequently the high energy intermediate decomposes along with the generation of light. Chemiluminescence assays have been widely used in various biological and chemical applications due to their excellent sensitivity and high SBR (Suzuki and Nagai, 2017; Sun et al., 2018; Tiwari and Dhoble, 2018; Son et al.,

2019). These advantages accelerate the development of novel chemiluminescent probes. To obtain NIR chemiluminescence which is more suitable for *in vivo* imaging (Green et al., 2017a; Lippert, 2017), strategies including chemiluminescence resonance energy transfer (CRET) and chemical modifications of the chemiluminescent substrate have been utilized to achieve bright and NIR chemiluminescence probes, enabling deep-tissue imaging (Lim et al., 2010; Hananya and Shabat, 2019; Nishihara et al., 2019). Oxalate esters and luminol are the typical H_2O_2 -activated chemiluminescent compounds, which have been applied to visualize H_2O_2 -related biological situations. To improve deep-tissue imaging ability of oxalate esters and luminol, the CRET is a facile way to shift their visible chemiluminescence into the NIR region. For instance, Rao et al. exploited an organic semiconducting polymer nanoparticle-based NIR chemiluminescence probe (SPN-CF) by integrating CRET and FRET for detecting peroxynitrite (ONOO^-) and hydrogen peroxide (H_2O_2) (Shuhendler et al., 2014). In SPN-CF, bis-(2,4,5-trichloro-6-(pentyloxycarbonyl)phenyl) oxalate (CPPO) served as the chemiluminescent substrate for reaction with H_2O_2 and poly(2,7-(9,9'-dioctylfluorene)-alt-4,7-bis(thiophen-2-yl)benzo-2,1,3-thiadiazole) (PFODBT, 680 nm) acted as both the CRET acceptor and the FRET donor. A cyanine dye

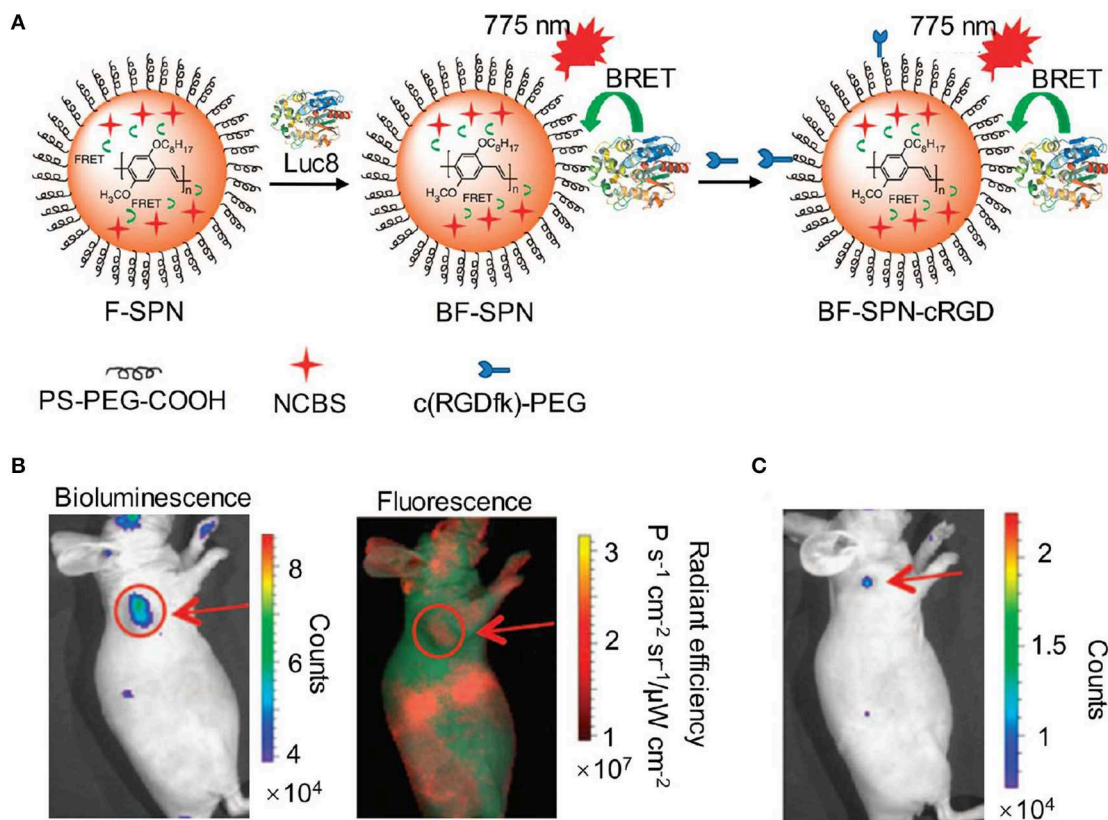


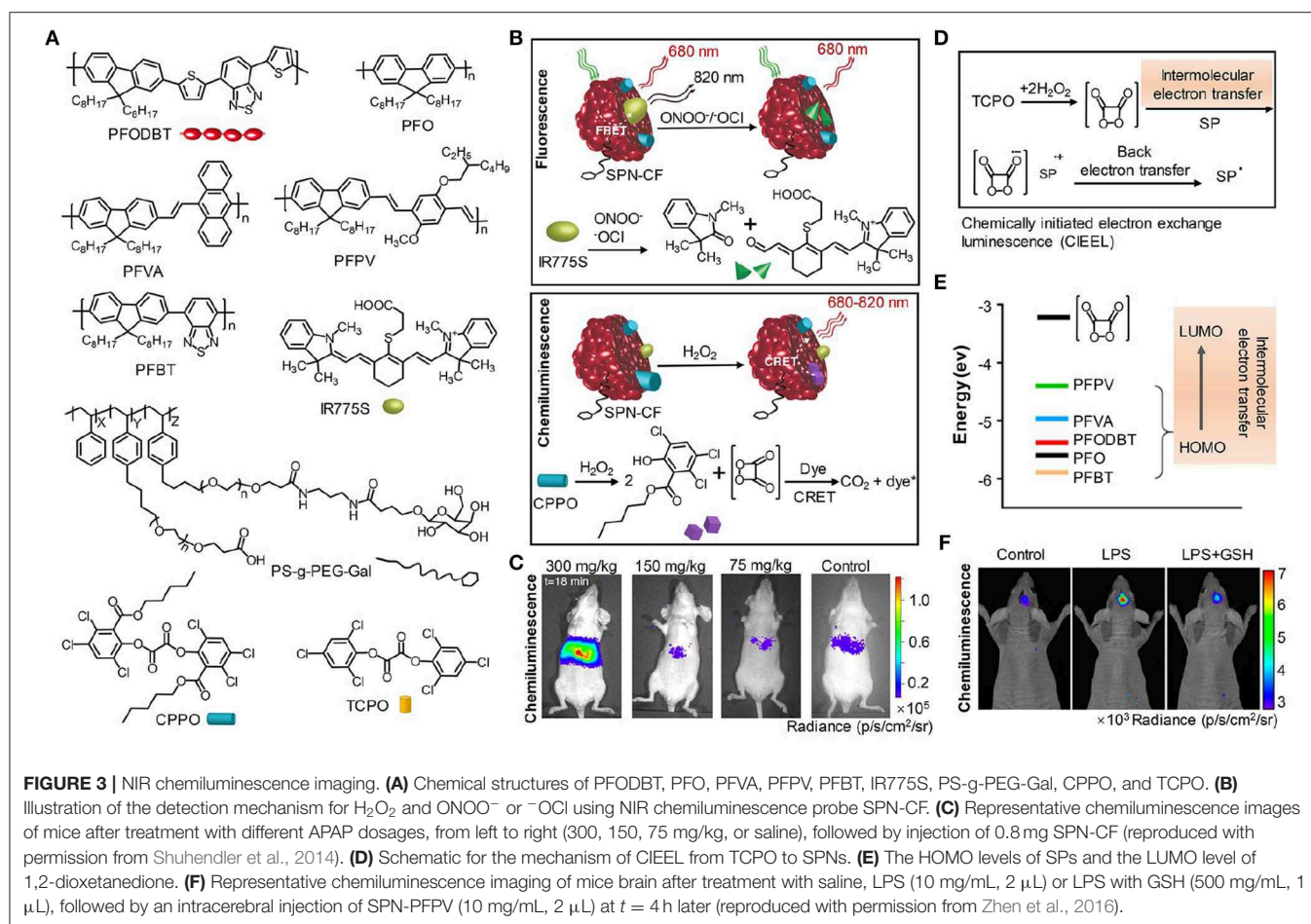
FIGURE 2 | NIR bioluminescence imaging. **(A)** Illustration of the fabrication of NIR self-luminescence nanoparticle BF-SPN-cRGD by a BRET-FRET strategy. **(B)** Bioluminescence (left) and fluorescence (right) imaging of U87MG tumor in living mice at $t = 5$ min post-injection of BF-SPN-cRGD. **(C)** Bioluminescence imaging of U87MG tumor (2 mm) at $t = 2$ h post-injection of BF-SPN-cRGD (reproduced with permission from Xiong et al., 2012).

(IR775S, 820 nm) was embedded into the nanoparticles to serve as the FRET acceptor, inducing the NIR chemiluminescence. SPN-CF was anchored with galactose-attached copolymer (PS-g-PEG-Gal) favoring hepatocytes-targeting (Hu et al., 2013; **Figure 3A**). *In vitro* experiment confirmed that the SPN-CF could detect H_2O_2 and ONOO^- with a limit of detection (LOD) of 5 and 10 nM, respectively (**Figure 3B**). The SPN-CF was further explored to detect hepatotoxicity induced by the anti-pyretic acetaminophen (APAP) (McGill and Jaeschke, 2013). Dose-dependent ROS/reactive nitrogen species (RNS) in the liver could be detected by the SPN-CF within minutes of APAP challenge (**Figure 3C**), antedating histological changes in drug-damaged tissue. This study proved that the SPN-CF could be developed for early detection of hepatotoxicity *in vivo*.

To further enhance the chemiluminescence efficacy, Pu group reported the screening of five polyfluorene derivatives-based luminescent reporters (PFO, PFVA, PFPV, PFPT, and PFODBT) to pair with the substrate bis(2,4,6-trichlorophenyl) oxalate (TCPO) (Zhen et al., 2016), as shown in **Figure 3A**. Among all the SPNs, the highest occupied molecular orbital (HOMO) of PFPV was closest to the lowest unoccupied molecular orbital (LUMO) of 1,2-dioxetanedione (**Figure 3E**), which led to the fastest

intermolecular electron transfer between them and thereby created the highest chemiluminescence intensity based on the chemically initiated electron exchange luminescence (CIEEL) mechanism (**Figure 3D**). The optimized system (SPN-PFPV) showed a quantum yield (QY) of 2.3×10^{-2} einsteins/mol, superior to the previously reported probes (Lim et al., 2010; Lee et al., 2012; Augusto et al., 2013). Furthermore, the PFPV-SPN had a high sensitivity to detect H_2O_2 with LOD as low as 5 nM. To endow this probe with NIR chemiluminescence for *in vivo* imaging, a NIR dye (NCBS) as an energy acceptor was doped into SPN-PFPV to obtain SPN-PFPV-NIR with 778 nm emission by CRET. The SPN-PFPV-NIR allowed the ultrasensitive detection of H_2O_2 *in vivo* in both peritonitis and neuroinflammation models (**Figure 3F**).

Recently, the NIR self-illuminating nanomaterials based on luminol system were developed for inflammation imaging (Liu et al., 2019; Xu et al., 2019). Zhang synthesized a biodegradable polymer nanoparticle conjugating chlorin e6 (Ce6) and luminol (CLP) (Xu et al., 2019). In the presence of myeloperoxidase (MPO) and ROS, luminol emitted luminescence at 440 nm, which was shifted to the Ce6 emission (675 nm) via energy transfer. The ROS-induced oxidation of luminol and efficient energy transfer endowed the self-illuminating CLP nanoparticle

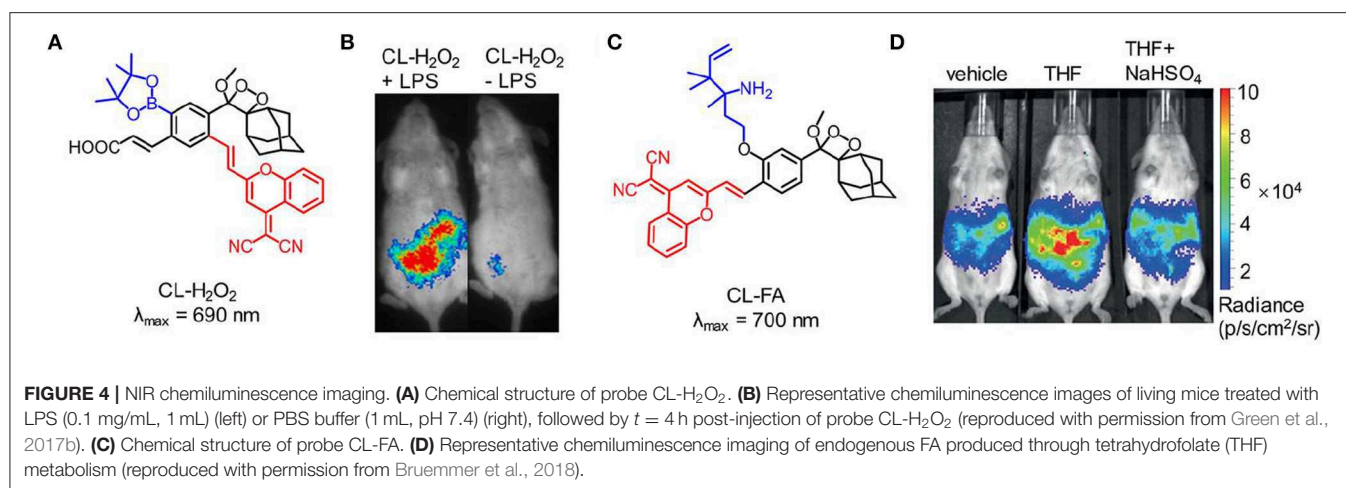


with an outstanding *in vivo* imaging capability to detect inflammation in various animal models.

Different from above-mentioned chemiluminescent compounds which require both sequential oxidation and decomposition steps in imaging process, dioxetane-based chemiluminescent agent is an oxidized high-energy species, which eliminates the ROS-oxidation step and directly generates light emission after substrate decomposition. The dioxetane can remain stable at room temperature until phenol-protecting group was removed to initiate the decomposing process, which is an ideal scaffold for designing stimulus-responsive chemiluminescent probes. To date, dioxetane-based chemiluminescent probes have been well developed for detecting enzymes and other analytes (Cao et al., 2016; Ryan and Lippert, 2018; Sun et al., 2018; Hananya and Shabat, 2019). To construct NIR dioxetane agents, Shabat et al. recently reported a “turn-on” NIR fluorophore-tethered dioxetane chemiluminescence probe for β -galactosidase imaging (Hananya et al., 2016). In the presence β -galactosidase, the protecting group of dioxetane as the CRET donor was removed to form the electronically excited benzoate and then the energy was transferred to NIR fluorophore (QCy) acting as the CRET acceptor, which resulted in efficient and bright NIR chemiluminescence (714 nm). The chemiluminescence intensity of the probe was enhanced

by 100-fold compared to the probe without tethering NIR fluorophore. Moreover, after incubation with β -galactosidase, the NIR fluorophore-tethered dioxetane probe was then injected into living mice and obtained clear chemiluminescence imaging with 6-fold increase in signal intensity than that obtained by green fluorophore-tethered dioxetane probe.

Although the NIR chemiluminescent probes based on dioxetane can be easily obtained by CRET, the chemiluminescence intensity is limited by the energy-transfer efficiency. An alternative strategy is to develop NIR chemiluminescence probe with a direct emission mode through structural modification. Recently, Shabat et al. put forward a design strategy to generate NIR chemiluminescence by extending π -conjugation length of the chemical substrate. Based on the design, a NIR-emitting phenoxy-dioxetane luminophore (690 nm) with dicyanomethylene-4H-chromene (DCMC) as an electron acceptor was synthesized (Green et al., 2017b). To achieve the ability to detect H_2O_2 , the phenol group of this luminophore was masked with aryl-boronate that can react with H_2O_2 to generate the active phenolate-dioxetane (Figure 4A). This probe was investigated to monitor H_2O_2 in living mice and the inflammation induced by lipopolysaccharide (LPS). Figure 4B shows that the inflammation for LPS-treated mice was clearly visualized with stronger chemiluminescence



signal compared with that of non-LPS-treated mice. In 2018, another NIR-emitting phenoxy-dioxetane luminophore with a 2-aza-Cope FA-reactive trigger was reported for monitoring formaldehyde (FA) (Figure 4C; Bruemmer et al., 2018). With NIR chemiluminescence at 700 nm, the luminophore was evaluated for *in vivo* FA imaging in mice, which confirmed that this probe could detect clearly endogenous FA released from the folate metabolism (Figure 4D).

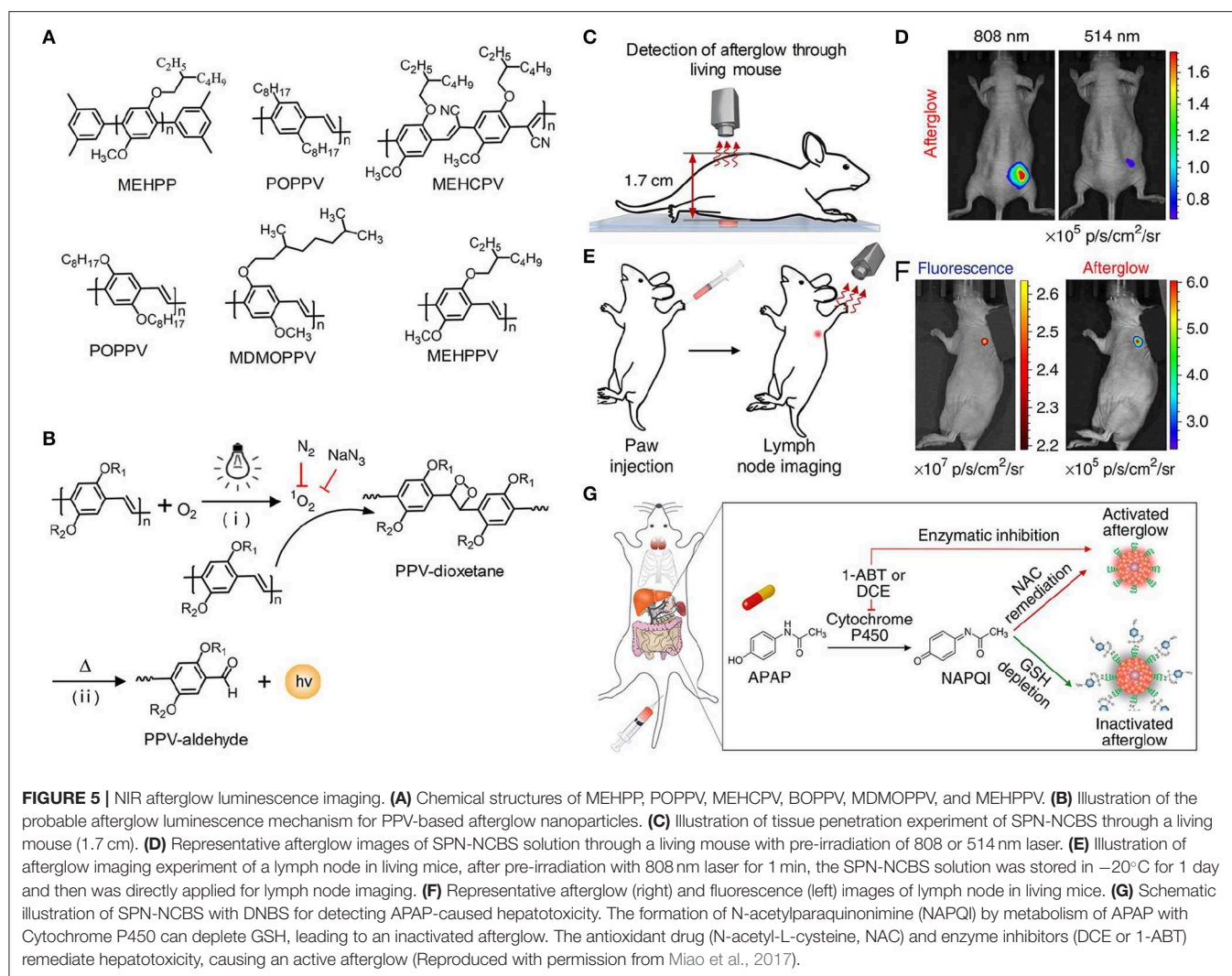
NIR AFTERGLOW IMAGING

Bioluminescence and chemiluminescence require respective enzyme or ROS to oxidize their substrate to generate luminescence, and thus the imaging signal was easily disturbed by cellular environment and substrate availability. Different from bioluminescence and chemiluminescence imaging, afterglow imaging detects slow release of photons from the chemical or energy defects stored by light pre-irradiation (Xu et al., 2016; Zhen et al., 2018; Lyu et al., 2019). The separation of light irradiation and signal collection circumvent the autofluorescence, inducing remarkable improvement of imaging sensitivity and SBR. Afterglow luminescence possesses extremely long lifetime, up to minutes to hours, which is long enough to implement time-resolved bioimaging without additional instrument. To achieve deep-tissue imaging, some afterglow nanoagents including inorganic and organic nanoparticles with NIR luminescence have been reported (Maldiney et al., 2011; Liu et al., 2013).

Inorganic persistent luminescence nanoparticles containing rare-earth metal ions have been explored as afterglow nanoagents for a long time. In the past 10 years, some advances have been made to prepare NIR emitting inorganic afterglow nanoparticles as highly sensitive tools for real-time bioimaging in living animals (Abdukayum et al., 2013; Li et al., 2014; Maldiney et al., 2014; Shi et al., 2015; Lécuyer et al., 2016; Ai et al., 2018). For instance, Han et al. employed an aqueous-phase reaction procedure to synthesize a water-soluble inorganic nanoparticle $\text{ZnGa}_2\text{O}_4\text{Cr}_{0.004}$ with sub-10 nm in size and high NIR persistent luminescence intensity (Li et al., 2015). *In vivo* imaging result

confirmed that afterglow nanoparticles had outstanding imaging ability with a SBR of 275. In addition, under the simulated deep-tissue environment created by covering a 1-cm-thick pork slab on living mouse, the renewable afterglow luminescence signal of the nanoparticle could be clearly observed. Imaging in NIR-II window (1,000–1,700 nm) possesses less light-tissue interactions (i.e., reduced light scattering) than those in NIR-I window, permitting imaging with higher SBR and sensitivity (Hong et al., 2014; Antaris et al., 2015; Sun et al., 2017; Huang et al., 2019; Tang et al., 2019a; Tian et al., 2019; Wang et al., 2019). Thus, to explore NIR-II afterglow agents, Zhang et al. synthesized a novel multifunctional nanoparticle $\text{mSiO}_2@\text{Gd}_3\text{Ga}_5\text{O}_{12}:\text{Cr}^{3+}, \text{Nd}^{3+}$ ($\text{mSiO}_2@\text{GGO}$) (Shi et al., 2018). These $\text{mSiO}_2@\text{GGO}$ nanoparticles showed excellent afterglow luminescence in the first NIR window (745 nm) and second NIR window (1,067 nm). The NIR-I luminescence of the $\text{mSiO}_2@\text{GGO}$ could penetrate through the 2 cm-thickness tissue with a SBR of 5.5. To evaluate the NIR-II imaging ability of the $\text{mSiO}_2@\text{GGO}$, the nanoparticles were subcutaneously injected into the abdomens of mice and a bright NIR-II luminescent signal was observed at the injection site. The result indicated that the $\text{mSiO}_2@\text{GGO}$ could be employed for deep-tissue imaging in NIR-II region.

Although significant achievements in deep-tissue imaging have been made, inorganic afterglow nanoparticles may suffer from potential toxicity due to the existence of heavy metal ions (Toppari et al., 1996). Furthermore, the surface of inorganic nanoparticles is difficult to modify, thereby leading to the finite targeting ability. As an alternative, organic afterglow nanoparticles have attracted increasing interest due to their high biological safety, optical tunability, facile processability, and easy functionalization (An et al., 2015; Su et al., 2018). In 2015, Rao et al. reported the semiconducting polymer nanoparticles (SPNs) with afterglow luminescence that can last for an hour (Palner et al., 2015). However, the underlying mechanism of the afterglow phenomenon remained unrevealed. To resolve it, Pu et al. screened a series of semiconducting polymers and discovered that only phenylenevinylene (PPV)-based SPNs such as BOPPV, MDMOPPV, and MEHPPV had distinct afterglow luminescence,



implying its essential role in the production of afterglow luminescence (Figure 5A; Miao et al., 2017). According to series of characterizations and analyses, the probable mechanism of afterglow luminescence for PPV-based SPNs was proposed as follows: the singlet oxygen ($^1\text{O}_2$) was generated by the light irradiation of PPVs and then oxidized the vinylene bond to form an unstable PPV-dioxetane intermediate, which could spontaneously decompose into PPV-aldehyde fragments along with photonic efflux (Figure 5B). To amplify the afterglow of SPNs and red-shift it into NIR region, NCBS, a NIR dye (778 nm) and $^1\text{O}_2$ photosensitizer, was doped into SPN-MEHPPV to yield SPN-NCBS. The afterglow of SPN-NCBS could be increased by 11-fold under pre-irradiation at 808 nm compared to 514 nm due to the higher $^1\text{O}_2$ generation ability of NCBS vs. MEHPPV. Due to the amplified brightness and lower background noise, the afterglow signal of SPN-NCBS could penetrate through a living mouse with a SBR of 237, which was 120 times higher than that of NIR fluorescence (Figures 5C,D). Then the SPN-NCBS was used for afterglow imaging of lymph nodes and

tumors in living mice (Figure 5E). The afterglow of SPN-NCBS permitted more efficient and high-contrast imaging of lymph nodes and tumor relative to NIR fluorescence imaging, demonstrating its potential in guiding intraoperative surgical resection (Figure 5F). An overdose of drugs, take acetaminophen as an example, will induce oxidative stress after metabolism and in turn deplete antioxidants (i.e., biothiols) in body. Thus, imaging of biothiol levels can be a feasible way to evaluate drug-induced hepatotoxicity. To achieve this, a biothiol-activated afterglow probe was prepared for detecting drug-induced hepatotoxicity by introducing an electron-withdrawing quencher (2,4-dinitrophenylsulfonyl, DNBS) onto the surface of SPN-NCBS (Figure 5G). In the presence of biothiols, such as Cys, Hcy and GSH, DNBS was removed from the nanoprobe and then the electron transfer between the quencher and the afterglow moiety was restrained, leading to an activated afterglow. *In vivo* data proved that the probe permitted real-time afterglow imaging of drug-caused hepatotoxicity with an excellent SBR that is 25-fold higher than that of NIR fluorescence imaging.

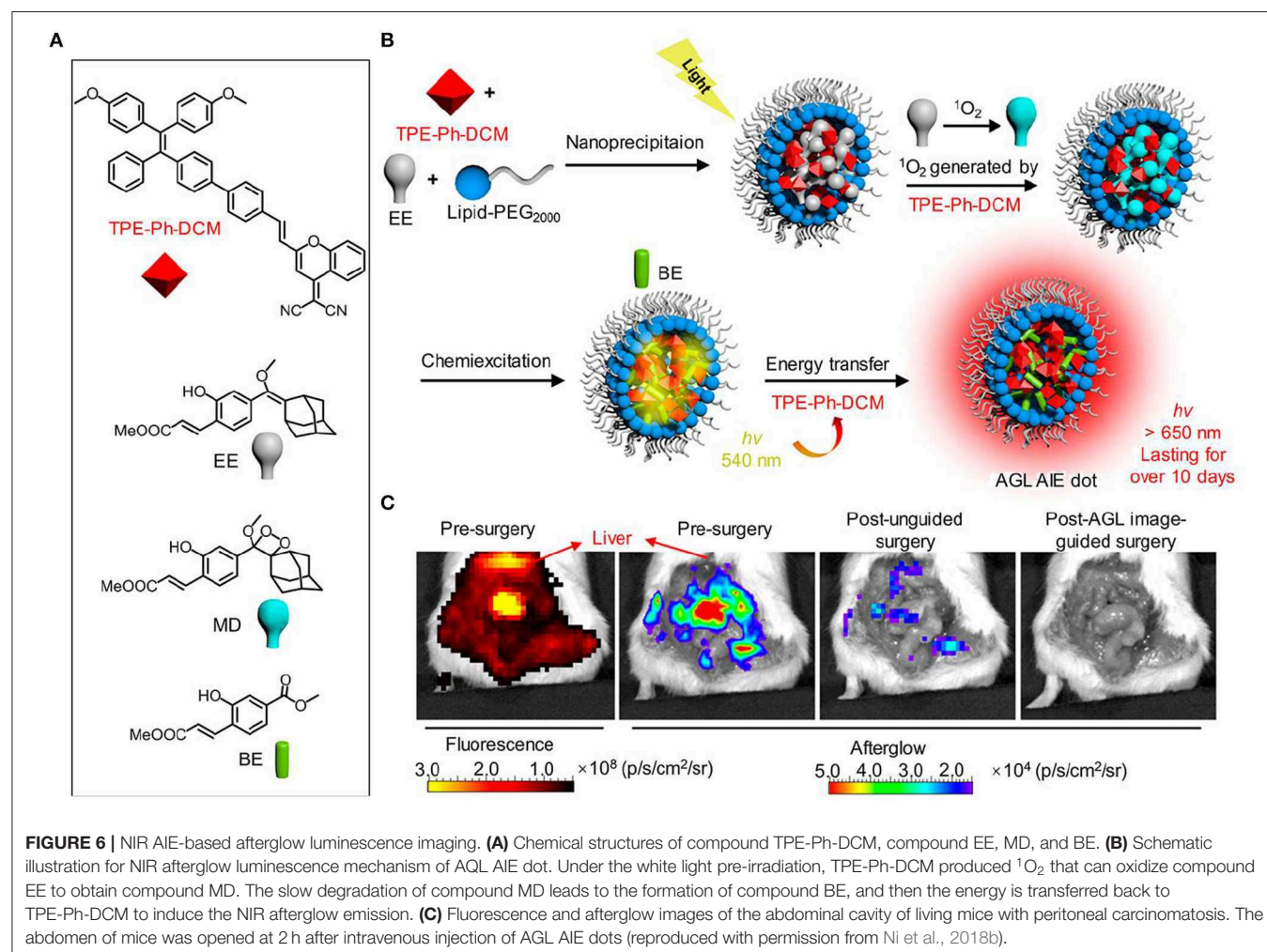
Strong hydrophobic polymer required amphiphilic polymer to form a water-soluble nanoparticle by co-precipitation, thus leading to large size (34 nm) that could be unfavorable for efficient accumulation in tumor. To solve it, Pu et al. prepared an amphiphilic PPV polymer with grafted poly(ethylene glycol) that could self-assemble into smaller nanoparticles (24 nm) in aqueous solution (Xie et al., 2018). The nanoparticles were further doped with NCBS to form SPPVN-NCBS. Compared with SPN-NCBS, SPPVN-NCBS had smaller size, stronger NIR afterglow luminescence and higher accumulation in tumor. The NIR afterglow of SPPVN-NCBS could clearly detect 1 mm³ xenografted tumors and invisible peritoneal metastatic tumors.

In a subsequent work, Pu et al. prepared a new library of afterglow luminescence agents by a generic approach that utilized an intraparticle cascade photoreaction of three main components (afterglow initiator, afterglow substrate and afterglow relay unit) (Jiang et al., 2019). By tuning the components, the afterglow emission could be adjusted from visible to NIR region. The representative NIR afterglow agents showed great imaging depth up to 5 cm, and permitted rapid detection of tumor in living mice with ultrahigh SBR ($2,922 \pm 121$). Recently, Ding et al. reported the first aggregation-induced emission (AIE)-based NIR

afterglow probe (AGL AIE dot) that could persist over 10 days (Figure 6; Ni et al., 2018b). This afterglow probe exhibited deep tissue penetration, high SBR, and ultrahigh signal ratios of tumor-to-reticuloendothelial system (RES) organs, thereby having the capability of image-guided cancer surgery in living mice. As shown in Figure 6C, the NIR afterglow imaging of AGL AIE dot could clearly differentiate the microtumors in peritoneal carcinomatosis-bearing mice, but the fluorescence imaging failed to do it. Moreover, under the guidance of the afterglow imaging, all the tiny tumor nodules could be nearly removed by surgery.

SUMMARY AND OUTLOOK

Self-luminescence including bioluminescence, chemiluminescence and afterglow have permitted imaging with higher sensitivity and deeper penetration depth than that obtained by fluorescence because it avoids the requirement of real-time light excitation and eliminates tissue autofluorescence. As NIR light possesses improved penetration depth than that obtained by visible light, many strategies via molecular- and nano-engineering approaches have been adopted to develop



NIR self-luminescence. Stimulated by the merits, NIR self-luminescence imaging has been applied for *in vivo* detection of biological and pathological processes in living systems. With the development of new self-luminescence agents, the selectivity and sensitivity of bioluminescence, chemiluminescence and afterglow imaging tools have been dramatically improved.

Because bioluminescence, chemiluminescence and afterglow agents for deep-tissue optical imaging in living system is in the infancy, some challenges still need to be addressed. Firstly, the luminescence intensity of NIR self-luminescent agents is relatively low due to the limited efficiency to red-shift luminescence emission from visible to NIR window. Thus, it is necessary to explore new agents with evolving molecular- or nano-engineering strategy to obtain brighter luminescence. Secondly, compared with NIR-I light, NIR-II light has substantially lower light scattering, and thus increases the imaging sensitivity and tissue penetration depth (Jiang and Pu, 2018; Kenry et al., 2018). However, the second NIR (NIR-II, 1,000–1,700 nm) emitting self-luminescent agents have not been reported yet. We envision that new approaches will be developed to red-shift the emission of self-luminescent agent from NIR-I to NIR-II for advances of deep-tissue optical imaging. Thirdly, the majority of the reported NIR self-luminescent

nanoagents have large size and are likely to retain in living organism for a long time, hence the long-term biosafety keeps unclear. To address this challenge, the nanoagents should be endowed with biodegradability and easily being cleared out by body. With the emergence of self-luminescent agents with high performance, it is confident that self-luminescence imaging will become a powerful tool in biology and clinical diagnosis of diseases.

AUTHOR CONTRIBUTIONS

QM and MG conceived this manuscript. QL, QM, JZ, and MG wrote and edited this manuscript.

FUNDING

This work was supported by the National Key Research Program of China (2018YFA0208800), National Natural Science Foundation of China (Grant Nos. 81901803, 21503141), Jiangsu Specially Appointed Professorship, Natural Science Foundation of Jiangsu Province (BK20191418, BK20190811, BK20190830), and Soochow University (Start-up grant: GJ12800119 and Q412800119).

REFERENCES

- Abdukayum, A., Chen, J.-T., Zhao, Q., and Yan, X.-P. (2013). Functional near infrared-emitting Cr³⁺/Pr³⁺ co-doped zinc gallogermanate persistent luminescent nanoparticles with superlong afterglow for *in vivo* targeted bioimaging. *J. Am. Chem. Soc.* 135, 14125–14133. doi: 10.1021/ja404243v
- Ai, T., Shang, W., Yan, H., Zeng, C., Wang, K., Gao, Y., et al. (2018). Near infrared-emitting persistent luminescent nanoparticles for hepatocellular carcinoma imaging and luminescence-guided surgery. *Biomaterials* 167, 216–225. doi: 10.1016/j.biomaterials.2018.01.031
- An, Z., Zheng, C., Tao, Y., Chen, R., Shi, H., Chen, T., et al. (2015). Stabilizing triplet excited states for ultralong organic phosphorescence. *Nat. Mater.* 14, 685–690. doi: 10.1038/nmat4259
- Antaris, A. L., Chen, H., Cheng, K., Sun, Y., Hong, G., Qu, C., et al. (2015). A small-molecule dye for nir-ii imaging. *Nat. Mater.* 15, 235–242. doi: 10.1038/nmat4476
- Augusto, F. A., de Souza, G. A., de Souza Junior, S. P., Khalid, M., and Baader, W. J. (2013). Efficiency of electron transfer initiated chemiluminescence. *Photochem. Photobiol.* 89, 1299–1317. doi: 10.1111/php.12102
- Badr, C. E., and Tannous, B. A. (2011). Bioluminescence imaging: progress and applications. *Trends Biotechnol.* 29, 624–633. doi: 10.1016/j.tibtech.2011.06.010
- Baker, M. (2010). Whole-animal imaging: the whole picture. *Nature* 463, 977–980. doi: 10.1038/463977a
- Bruemmer, K. J., Green, O., Su, T. A., Shabat, D., and Chang, C. J. (2018). Chemiluminescent probes for activity-based sensing of formaldehyde released from folate degradation in living mice. *Angew. Chem. Int. Ed.* 57, 7508–7512. doi: 10.1002/anie.201802143
- Cao, J., Campbell, J., Liu, L., Mason, R. P., and Lippert, A. R. (2016). *In vivo* chemiluminescent imaging agents for nitroreductase and tissue oxygenation. *Anal. Chem.* 88, 4995–5002. doi: 10.1021/acs.analchem.6b01096
- Chen, P., Zheng, Z., Zhu, Y., Dong, Y., Wang, F., and Liang, G. (2017). Bioluminescent turn-on probe for sensing hypochlorite *in vitro* and in tumors. *Anal. Chem.* 89, 5693–5696. doi: 10.1021/acs.analchem.7b01103
- Choi, H. S., Gibbs, S. L., Lee, J. H., Kim, S. H., Ashitate, Y., Liu, F., et al. (2013). Targeted zwitterionic near-infrared fluorophores for improved optical imaging. *Nat. Biotechnol.* 31, 148–153. doi: 10.1038/nbt.2468
- Farzin, L., Sheibani, S., Moassesi, M. E., and Shamsipur, M. (2018). An overview of nanoscale radionuclides and radiolabeled nanomaterials commonly used for nuclear molecular imaging and therapeutic functions. *J. Biomed. Mater. Res. Part A* 107A, 251–285. doi: 10.1002/jbm.a.36550
- Gnaim, S., Scomparin, A., Eldar-Boock, A., Bauer, C. R., Satchi-Fainaro, R., and Shabat, D. (2019). Light emission enhancement by supramolecular complexation of chemiluminescence probes designed for bioimaging. *Chem. Sci.* 10, 2945–2955. doi: 10.1039/C8SC05174G
- Green, O., Eilon, T., Hananya, N., Gutkin, S., Bauer, C. R., and Shabat, D. (2017a). Opening a gateway for chemiluminescence cell imaging: distinctive methodology for design of bright chemiluminescent dioxetane probes. *ACS Cent. Sci.* 3, 349–358. doi: 10.1021/acscentsci.7b00058
- Green, O., Gnaim, S., Blau, R., Eldar-Boock, A., Satchi-Fainaro, R., and Shabat, D. (2017b). Near-infrared dioxetane luminophores with direct chemiluminescence emission mode. *J. Am. Chem. Soc.* 139, 13243–13248. doi: 10.1021/jacs.7b08446
- Hai, Z., Wu, J., Wang, L., Xu, J., Zhang, H., and Liang, G. (2017). Bioluminescence sensing of γ -glutamyltranspeptidase activity *in vitro* and *in vivo*. *Anal. Chem.* 89, 7017–7021. doi: 10.1021/acs.analchem.7b00567
- Hall, M. P., Unch, J., Binkowski, B. F., Valley, M. P., Butler, B. L., Wood, M. G., et al. (2012). Engineered luciferase reporter from a deep sea shrimp utilizing a novel imidazopyrazinone substrate. *ACS Chem. Biol.* 7, 20127111848–20127111857. doi: 10.1021/cb3002478
- Hall, M. P., Woodroffe, C. C., Wood, M. G., Que, I., van't Root, M., Ridwan, Y., et al. (2018). Click beetle luciferase mutant and near infrared naphthyl-luciferins for improved bioluminescence imaging. *Nat. Commun.* 9:132. doi: 10.1038/s41467-017-02542-9
- Hananya, N., Eldar Boock, A., Bauer, C. R., Satchi-Fainaro, R., and Shabat, D. (2016). Remarkable enhancement of chemiluminescent signal by dioxetane-fluorophore conjugates: turn-on chemiluminescence probes with color modulation for sensing and imaging. *J. Am. Chem. Soc.* 138, 13438–13446. doi: 10.1021/jacs.6b09173
- Hananya, N., and Shabat, D. (2017). A glowing trajectory between bio- and chemiluminescence: from luciferin-based probes to triggerable dioxetanes. *Angew. Chem. Int. Ed.* 56, 16454–16463. doi: 10.1002/anie.201706969
- Hananya, N., and Shabat, D. (2019). Recent advances and challenges in luminescent imaging: bright outlook for chemiluminescence of dioxetanes in water. *ACS Cent. Sci.* 5, 949–959. doi: 10.1021/acscentsci.9b00372

- Hasegawa, M., Tsukasaki, Y., Ohyanagi, T., and Jin, T. (2013). Bioluminescence resonance energy transfer coupled near-infrared quantum dots using gsf-tagged luciferase for *in vivo* imaging. *Chem. Commun.* 49, 228–230. doi: 10.1039/C2CC36870F
- Hong, G., Zou, Y., Antaris, A. L., Diao, S., Wu, D., Cheng, K., et al. (2014). Ultrafast fluorescence imaging *in vivo* with conjugated polymer fluorophores in the second near-infrared window. *Nat. Commun.* 5:4206. doi: 10.1038/ncomms5206
- Hu, Y., Haynes, M. T., Wang, Y., Liu, F., and Huang, L. (2013). A highly efficient synthetic vector: nonhydrodynamic delivery of DNA to hepatocyte nuclei *in vivo*. *ACS Nano* 7, 5376–5384. doi: 10.1021/nn4012384
- Huang, D., Lin, S., Wang, Q., Zhang, Y., Li, C., Ji, R., et al. (2019). An nir-ii fluorescence/dual bioluminescence multiplexed imaging for *in vivo* visualizing the location, survival, and differentiation of transplanted stem cells. *Adv. Funct. Mater.* 29:1806546. doi: 10.1002/adfm.201806546
- Iwano, S., Obata, R., Miura, C., Kiyama, M., Hama, K., Nakamura, M., et al. (2013). Development of simple firefly luciferin analogs emitting blue, green, red, and near-infrared biological window light. *Tetrahedron* 69, 3847–3856. doi: 10.1016/j.tet.2013.03.050
- Jathoul, A. P., Grounds, H., Anderson, J. C., and Pule, M. A. (2014). A dual-color far-red to near-infrared firefly luciferin analogue designed for multiparametric bioluminescence imaging. *Angew. Chem. Int. Ed.* 53, 13059–13063. doi: 10.1002/anie.201405955
- Jiang, Y., Huang, J., Zhen, X., Zeng, Z., Li, J., Xie, C., et al. (2019). A generic approach towards afterglow luminescent nanoparticles for ultrasensitive *in vivo* imaging. *Nat. Commun.* 10:2064. doi: 10.1038/s41467-019-10119-x
- Jiang, Y., and Pu, K. (2018). Molecular fluorescence and photoacoustic imaging in the second near-infrared optical window using organic contrast agents. *Adv. Biosyst.* 2:1700262. doi: 10.1002/adbi.201700262
- Jokerst, J. V., and Gambhir, S. S. (2011). Molecular imaging with theranostic nanoparticles. *Acc. Chem. Res.* 44, 1050–1060. doi: 10.1021/ar200106e
- Jones, K. A., Porterfield, W. B., Rathbun, C. M., McCutcheon, D. C., Paley, M. A., and Prescher, J. A. (2017). Orthogonal luciferase-luciferin pairs for bioluminescence imaging. *J. Am. Chem. Soc.* 139, 2351–2358. doi: 10.1021/jacs.6b11737
- Kaskova, Z. M., Tsarkova, A. S., and Yampolsky, I. V. (2016). 1001 lights: luciferins, luciferases, their mechanisms of action and applications in chemical analysis, biology and medicine. *Chem. Soc. Rev.* 45, 6048–6077. doi: 10.1039/C6CS00296J
- Kenry, Duan, Y., and Liu, B. (2018). Recent advances of optical imaging in the second near-infrared window. *Adv. Mater.* 30:1802394. doi: 10.1002/adma.201802394
- Kuchimaru, T., Iwano, S., Kiyama, M., Mitsumata, S., Kadonosono, T., Niwa, H., et al. (2016). A luciferin analogue generating near-infrared bioluminescence achieves highly sensitive deep-tissue imaging. *Nat. Commun.* 7:11856. doi: 10.1038/ncomms11856
- Lécuyer, T., Teston, E., Ramirez-Garcia, G., Maldiney, T., Viana, B., Seguin, J., et al. (2016). Chemically engineered persistent luminescence nanoprobe for bioimaging. *Theranostics* 6, 2488–2524. doi: 10.7150/thno.16589
- Lee, Y. D., Lim, C.-K., Singh, A., Koh, J., Kim, J., Kwon, I. C., et al. (2012). Dye/peroxalate aggregated nanoparticles with enhanced and tunable chemiluminescence for biomedical imaging of hydrogen peroxide. *ACS Nano* 6, 6759–6766. doi: 10.1021/nn3014905
- Li, J., Wang, C., Shi, J., Li, P., Yu, Z., and Zhang, H. (2018). Porous GdAlO₃: Cr³⁺, Sm³⁺ drug carrier for real-time long afterglow and magnetic resonance dual-mode imaging. *J. Luminescence* 199, 363–371. doi: 10.1016/j.jlumin.2018.03.071
- Li, P., Liu, L., Xiao, H., Zhang, W., Wang, L., and Tang, B. (2016). A new polymer nanoprobe based on chemiluminescence resonance energy transfer for ultrasensitive imaging of intrinsic superoxide anion in mice. *J. Am. Chem. Soc.* 138, 2893–2896. doi: 10.1021/jacs.5b11784
- Li, Y., Zhou, S., Li, Y., Sharafudeen, K., Ma, Z., Dong, G., et al. (2014). Long persistent and photo-stimulated luminescence in Cr³⁺-doped Zn–Ga–Sn–O phosphors for deep and reproducible tissue imaging. *J. Mater. Chem. C* 2:2657. doi: 10.1039/c4tc00014e
- Li, Z., Zhang, Y., Wu, X., Huang, L., Li, D., Fan, W., et al. (2015). Direct aqueous-phase synthesis of sub-10 nm “luminous pearls” with enhanced *in vivo* renewable near-infrared persistent luminescence. *J. Am. Chem. Soc.* 137, 5304–5307. doi: 10.1021/jacs.5b00872
- Lim, C. K., Lee, Y. D., Na, J., Oh, J. M., Her, S., Kim, K., et al. (2010). Chemiluminescence-generating nanoreactor formulation for near-infrared imaging of hydrogen peroxide and glucose level *in vivo*. *Adv. Funct. Mater.* 20, 2644–2648. doi: 10.1002/adfm.201000780
- Lippert, A. R. (2017). Unlocking the potential of chemiluminescence imaging. *ACS Cent. Sci.* 3, 269–271. doi: 10.1021/acscentsci.7b00107
- Liu, F., Yan, W., Chuang, Y.-J., Zhen, Z., Xie, J., and Pan, Z. (2013). Photostimulated near-infrared persistent luminescence as a new optical read-out from Cr³⁺-doped ligand. *Sci. Rep.* 3:1554. doi: 10.1038/srep01554
- Liu, R., Tang, J., Xu, Y., and Dai, Z. (2019). Bioluminescence imaging of inflammation *in vivo* based on bioluminescence and fluorescence resonance energy transfer using nanobubble ultrasound contrast agent. *ACS Nano* 13, 5124–5132. doi: 10.1021/acsnano.8b08359
- Liu, Z., Cai, W., He, L., Nakayama, N., Chen, K., Sun, X., et al. (2007). *In vivo* biodistribution and highly efficient tumour targeting of carbon nanotubes in mice. *Nat. Nanotechnol.* 2, 47–52. doi: 10.1038/nnano.2006.170
- Lyu, Y., Cui, D., Huang, J., Fan, W., Miao, Y., and Pu, K. (2019). Near-infrared afterglow semiconducting nano-polycomplexes for the multiplex differentiation of cancer exosomes. *Angew. Chem. Int. Ed.* 58, 4983–4987. doi: 10.1002/anie.201900092
- Ma, N., Marshall, A. F., and Rao, J. (2010). Near-infrared light emitting luciferase via biomineralization. *J. Am. Chem. Soc.* 132, 6884–6885. doi: 10.1021/ja101378g
- Ma, T., Hou, Y., Zeng, J., Liu, C., Zhang, P., Jing, L., et al. (2018). Dual-ratiometric target-triggered fluorescent probe for simultaneous quantitative visualization of tumor microenvironment protease activity and pH *in vivo*. *J. Am. Chem. Soc.* 140, 211–218. doi: 10.1021/jacs.7b08900
- Maldiney, T., Bessière, A., Seguin, J., Teston, E., Sharma, S. K., Viana, B., et al. (2014). The *in vivo* activation of persistent nanophosphors for optical imaging of vascularization, tumours and grafted cells. *Nat. Mater.* 13, 418–426. doi: 10.1038/nmat3908
- Maldiney, T., Lécuyer, A., Viana, B., Bessière, A., Bessodes, M., Gourier, D., et al. (2011). Controlling electron trap depth to enhance optical properties of persistent luminescence nanoparticles for *in vivo* imaging. *J. Am. Chem. Soc.* 133, 11810–11815. doi: 10.1021/ja204504w
- McGill, M. R., and Jaeschke, H. (2013). Metabolism and disposition of acetaminophen: recent advances in relation to hepatotoxicity and diagnosis. *Pharm. Res.* 30, 2174–2187. doi: 10.1007/s11095-013-1007-6
- Mezzanotte, L., van ‘t Root, M., Karatas, H., Goun, E. A., and Löwik, C. W. G. M. (2017). *In vivo* molecular bioluminescence imaging: New tools and applications. *Trends Biotechnol.* 35, 640–652. doi: 10.1016/j.tibtech.2017.03.012
- Miao, Q., and Pu, K. (2018). Organic semiconducting agents for deep-tissue molecular imaging: second near-infrared fluorescence, self-luminescence, and photoacoustics. *Adv. Mater.* 30:1801778. doi: 10.1002/adma.201801778
- Miao, Q., Xie, C., Zhen, X., Lyu, Y., Duan, H., Liu, X., et al. (2017). Molecular afterglow imaging with bright, biodegradable polymer nanoparticles. *Nat. Biotechnol.* 35, 1102–1110. doi: 10.1038/nbt.3987
- Miura, C., Kiyama, M., Iwano, S., Ito, K., Obata, R., Hirano, T., et al. (2013). Synthesis and luminescence properties of biphenyl-type firefly luciferin analogs with a new, near-infrared light-emitting bioluminophore. *Tetrahedron* 69, 9726–9734. doi: 10.1016/j.tet.2013.09.018
- Ni, D., Ehlerding, E. B., and Cai, W. (2018a). Multimodality imaging agents with pet as the fundamental pillar. *Angew. Chem. Int. Ed.* 58, 2570–2579. doi: 10.1002/anie.201806853
- Ni, X., Zhang, X., Duan, X., Zheng, H.-L., Xue, X.-S., and Ding, D. (2018b). Near-infrared afterglow luminescent aggregation-induced emission dots with ultrahigh tumor-to-liver signal ratio for promoted image-guided cancer surgery. *Nano Lett.* 19, 318–330. doi: 10.1021/acsnanolett.8b03936
- Nishihara, R., Paulmurugan, R., Nakajima, T., Yamamoto, E., Natarajan, A., Afjei, R., et al. (2019). Highly bright and stable nir-bret with blue-shifted coelenterazine derivatives for deep-tissue imaging of molecular events *in vivo*. *Theranostics* 9, 2646–2661. doi: 10.7150/thno.32219
- Palner, M., Pu, K., Shao, S., and Rao, J. (2015). Semiconducting polymer nanoparticles with persistent near-infrared luminescence for *in vivo* optical imaging. *Angew. Chem. Int. Ed.* 54, 11477–11480. doi: 10.1002/anie.201502736
- Ryan, L. S., and Lippert, A. R. (2018). Ultrasensitive chemiluminescent detection of cathepsin b: insights into the new frontier of chemiluminescent imaging. *Angew. Chem. Int. Ed.* 57, 622–624. doi: 10.1002/anie.201711228

- Shi, J., Sun, X., Li, J., Man, H., Shen, J., Yu, Y., et al. (2015). Multifunctional near infrared-emitting long-persistence luminescent nanoprobes for drug delivery and targeted tumor imaging. *Biomaterials* 37, 260–270. doi: 10.1016/j.biomaterials.2014.10.033
- Shi, J., Sun, X., Zheng, S., Li, J., Fu, X., and Zhang, H. (2018). A new near-infrared persistent luminescence nanoparticle as a multifunctional nanoplateform for multimodal imaging and cancer therapy. *Biomaterials* 152, 15–23. doi: 10.1016/j.biomaterials.2017.10.032
- Shimon, G., Gammon, S. T., Moss, B. L., Rauch, D., Harding, J., Heinecke, J. W., et al. (2009). Bioluminescence imaging of myeloperoxidase activity *in vivo*. *Nat. Med.* 15, 455–461. doi: 10.1038/nm.1886
- Shuhendler, A. J., Pu, K., Cui, L., Uetrecht, J. P., and Rao, J. (2014). Real-time imaging of oxidative and nitrosative stress in the liver of live animals for drug-toxicity testing. *Nat. Biotechnol.* 32, 373–380. doi: 10.1038/nbt.2838
- So, M.-K., Loening, A. M., Gambhir, S. S., and Rao, J. (2006a). Creating self-illuminating quantum dot conjugates. *Nat. Protoc.* 1, 1160–1164. doi: 10.1038/nprot.2006.162
- So, M.-K., Xu, C., Loening, A. M., Gambhir, S. S., and Rao, J. (2006b). Self-illuminating quantum dot conjugates for *in vivo* imaging. *Nat. Biotechnol.* 24, 339–343. doi: 10.1038/nbt1188
- Son, S., Won, M., Green, O., Hananya, N., Sharma, A., Jeon, Y., et al. (2019). Chemiluminescent probe for the *in vitro* and *in vivo* imaging of cancers over-expressing nqo1. *Angew. Chem. Int. Ed.* 58, 1739–1743. doi: 10.1002/anie.201813032
- Su, Y., Phua, S. Z. F., Li, Y., Zhou, X., Jana, D., Liu, G., et al. (2018). Ultralong room temperature phosphorescence from amorphous organic materials toward confidential information encryption and decryption. *Sci. Adv.* 4:eaas9732. doi: 10.1126/sciadv.aas9732
- Sun, J., Hu, Z., Wang, R., Zhang, S., and Zhang, X. (2018). A highly sensitive chemiluminescent probe for detecting nitroreductase and imaging in living animals. *Anal. Chem.* 91, 1384–1390. doi: 10.1021/acs.analchem.8b03955
- Sun, Y., Ding, M., Zeng, X., Xiao, Y., Wu, H., Zhou, H., et al. (2017). Novel bright-emission small-molecule nir-ii fluorophores for *in vivo* tumor imaging and image-guided surgery. *Chem. Sci.* 8, 3489–3493. doi: 10.1039/C7SC00251C
- Suzuki, K., and Nagai, T. (2017). Recent progress in expanding the chemiluminescent toolbox for bioimaging. *Curr. Opin. Biotechnol.* 48, 135–141. doi: 10.1016/j.copbio.2017.04.001
- Tang, Y., Li, Y., Lu, X., Hu, X., Zhao, H., Hu, W., et al. (2019a). Bio-erasable intermolecular donor-acceptor interaction of organic semiconducting nanoprobes for activatable nir-ii fluorescence imaging. *Adv. Funct. Mater.* 29:1807376. doi: 10.1002/adfm.201807376
- Tang, Y., Parag-Sharma, K., Amelio, A. L., and Cao, Y. (2019b). A bioluminescence resonance energy transfer-based approach for determining antibody-receptor occupancy *in vivo*. *iScience* 15, 439–451. doi: 10.1016/j.isci.2019.05.003
- Tian, R., Ma, H., Yang, Q., Wan, H., Zhu, S., Chandra, S., et al. (2019). Rational design of a super-contrast nir-ii fluorophore affords high-performance nir-ii molecular imaging guided microsurgery. *Chem. Sci.* 10, 326–332. doi: 10.1039/C8SC03751E
- Tiwari, A., and Dhoble, S. J. (2018). Recent advances and developments on integrating nanotechnology with chemiluminescence assays. *Talanta* 180, 1–11. doi: 10.1016/j.talanta.2017.12.031
- Toppiari, J., Larsen, J. C., Christiansen, P., Giwerzman, A., Grandjean, P., Guillelte, L. J. J., et al. (1996). Supplement 4 || male reproductive health and environmental xenoestrogens. *Environ. Health Perspect.* 104, 741–803. doi: 10.2307/3432709
- Vacher, M., Galván, F. I., Ding, B.-W., Schramm, S., Berraud-Pache, R., Naumov, P., et al. (2018). Chemi- and bioluminescence of cyclic peroxides. *Chem. Rev.* 118, 6927–6974. doi: 10.1021/acs.chemrev.7b00649
- Wang, S., Fan, Y., Li, D., Sun, C., Lei, Z., Lu, L., et al. (2019). Anti-quenching nir-ii molecular fluorophores for *in vivo* high-contrast imaging and ph sensing. *Nat. Commun.* 10:1058. doi: 10.1038/s41467-019-09043-x
- Weih, F., and Dacres, H. (2019). Red-shifted bioluminescence resonance energy transfer: Improved tools and materials for analytical *in vivo* approaches. *TrAC Trends Anal. Chem.* 116, 61–73. doi: 10.1016/j.trac.2019.04.011
- Weissleder, R., and Pittet, M. J. (2008). Imaging in the era of molecular oncology. *Nature* 452, 580–589. doi: 10.1038/nature06917
- Xie, C., Zhen, X., Miao, Q., Lyu, Y., and Pu, K. (2018). Self-assembled semiconducting polymer nanoparticles for ultrasensitive near-infrared afterglow imaging of metastatic tumors. *Adv. Mater.* 30:1801331. doi: 10.1002/adma.201801331
- Xiong, L., Shuhendler, A. J., and Rao, J. (2012). Self-luminescing bret-fret near-infrared dots for *in vivo* lymph-node mapping and tumour imaging. *Nat. Commun.* 3:1193. doi: 10.1038/ncomms2197
- Xu, S., Chen, R., Zheng, C., and Huang, W. (2016). Excited state modulation for organic afterglow: materials and applications. *Adv. Mater.* 28, 9920–9940. doi: 10.1002/adma.201602604
- Xu, X., An, H., Zhang, D., Tao, H., Dou, Y., Li, X., et al. (2019). A self-illuminating nanoparticle for inflammation imaging and cancer therapy. *Sci. Adv.* 5:eaat2953. doi: 10.1126/sciadv.aat2953
- Yan, Y., Shi, P., Song, W., and Bi, S. (2019). Chemiluminescence and bioluminescence imaging for biosensing and therapy: *in vitro* and *in vivo* perspectives. *Theranostics* 9, 4047–4065. doi: 10.7150/thno.33228
- Yao, H., Zhang, Y., Xiao, F., Xia, Z., and Rao, J. (2007). Quantum dot/bioluminescence resonance energy transfer based highly sensitive detection of proteases. *Angew. Chem. Int. Ed.* 46, 4346–4349. doi: 10.1002/anie.200700280
- Yao, Z., Zhang, B. S., and Prescher, J. A. (2018). Advances in bioluminescence imaging: new probes from old recipes. *Curr. Opin. Chem. Biol.* 45, 148–156. doi: 10.1016/j.cbpa.2018.05.009
- Yin, L., Sun, H., Zhang, H., He, L., Qiu, L., Lin, J., et al. (2019). Quantitatively visualizing tumor-related protease activity *in vivo* using a ratiometric photoacoustic probe. *J. Am. Chem. Soc.* 141, 3265–3273. doi: 10.1021/jacs.8b13628
- Zhang, M., Wang, L., Zhao, Y., Wang, F., Wu, J., and Liang, G. (2018). Using bioluminescence turn-on to detect cysteine *in vitro* and *in vivo*. *Anal. Chem.* 90, 4951–4954. doi: 10.1021/acs.analchem.8b00682
- Zhen, X., Tao, Y., An, Z., Chen, P., Xu, C., Chen, R., et al. (2017). Ultralong phosphorescence of water-soluble organic nanoparticles for *in vivo* afterglow imaging. *Adv. Mater.* 29:1606665. doi: 10.1002/adma.201606665
- Zhen, X., Xie, C., and Pu, K. (2018). Temperature-correlated afterglow of a semiconducting polymer nanococktail for imaging-guided photothermal therapy. *Angew. Chem. Int. Ed.* 57, 3938–3942. doi: 10.1002/anie.201712550
- Zhen, X., Zhang, C., Xie, C., Miao, Q., Lim, K. L., and Pu, K. (2016). Intraparticle energy level alignment of semiconducting polymer nanoparticles to amplify chemiluminescence for ultrasensitive *in vivo* imaging of reactive oxygen species. *ACS Nano* 10, 6400–6409. doi: 10.1021/acsnano.6b02908
- Zhu, B., Tang, W., Ren, Y., and Duan, X. (2018). Chemiluminescence of conjugated-polymer nanoparticles by direct oxidation with hypochlorite. *Anal. Chem.* 90, 13714–13722. doi: 10.1021/acs.analchem.8b04109

Conflict of Interest: The authors declare that the research was conducted in the absence of any commercial or financial relationships that could be construed as a potential conflict of interest.

Copyright © 2019 Li, Zeng, Miao and Gao. This is an open-access article distributed under the terms of the Creative Commons Attribution License (CC BY). The use, distribution or reproduction in other forums is permitted, provided the original author(s) and the copyright owner(s) are credited and that the original publication in this journal is cited, in accordance with accepted academic practice. No use, distribution or reproduction is permitted which does not comply with these terms.



Treatment of Hepatocellular Carcinoma by Intratumoral Injection of ^{125}I -AA98 mAb and Its Efficacy Assessments by Molecular Imaging

Jun Zhou^{1,2,3†}, Pengcheng Hu^{1,3†}, Zhan Si^{1,3}, Hui Tan^{1,3}, Lin Qiu^{1,3}, He Zhang^{1,3}, Zhequan Fu^{1,3}, Wujian Mao^{1,3}, Dengfeng Cheng^{1,3*} and Hongcheng Shi^{1,3*}

¹ Department of Nuclear Medicine, Zhongshan Hospital, Fudan University, Shanghai, China, ² Department of Nuclear Medicine, Xuhui District Central Hospital of Shanghai, Shanghai, China, ³ Shanghai Institute of Medical Imaging, Shanghai, China

OPEN ACCESS

Edited by:

Yu Gao,
Nanjing University of Posts and
Telecommunications, China

Reviewed by:

Zhen Xu,
Nanjing University, China
Afu Fu,
Technion Israel Institute of
Technology, Israel

*Correspondence:

Dengfeng Cheng
cheng.dengfeng@zs-hospital.sh.cn
Hongcheng Shi
shi.hongcheng@zs-hospital.sh.cn

[†]These authors have contributed
equally to this work

Specialty section:

This article was submitted to
Nanobiotechnology,
a section of the journal
Frontiers in Bioengineering and
Biotechnology

Received: 19 August 2019

Accepted: 25 October 2019

Published: 14 November 2019

Citation:

Zhou J, Hu P, Si Z, Tan H, Qiu L,
Zhang H, Fu Z, Mao W, Cheng D and
Shi H (2019) Treatment of
Hepatocellular Carcinoma by
Intratumoral Injection of ^{125}I -AA98
mAb and Its Efficacy Assessments by
Molecular Imaging.
Front. Bioeng. Biotechnol. 7:319.
doi: 10.3389/fbioe.2019.00319

Objective: To investigate the therapeutic efficacy of intratumoral injection of ^{125}I -AA98 mAb for hepatocellular carcinoma (HCC) and its therapy efficacy assessment by $^{99\text{m}}\text{Tc}$ -HYNIC-duramycin and $^{99\text{m}}\text{Tc}$ -HYNIC-3PRGD2 SPECT/CT imaging.

Methods: HCC xenograft tumor mice models were injected intratumorally with a single dose of normal saline, 10 microcurie (μCi) ^{125}I -AA98 mAb, free ^{125}I , AA98 mAb, 80 μCi ^{125}I -AA98 mAb, and 200 μCi ^{125}I -AA98 mAb. $^{99\text{m}}\text{Tc}$ -HYNIC-duramycin and $^{99\text{m}}\text{Tc}$ -HYNIC-3PRGD2 micro-SPECT/CT imaging were performed on days 3 and 7, respectively. The T/M ratio for each imaging was compared with the corresponding immunohistochemical staining at each time point. The relative tumor inhibition rates were documented.

Results: In terms of apoptosis, the 200 μCi group demonstrated the highest apoptotic index ($11.8 \pm 3.8\%$), and its T/M ratio achieved by $^{99\text{m}}\text{Tc}$ -HYNIC-duramycin imaging on day 3 was higher than that of the normal saline group, 80 μCi group, 10 μCi group and free ^{125}I group on day 3, respectively (all $P < 0.05$). On day 3, there was a markedly positive correlation between T/M ratio from $^{99\text{m}}\text{Tc}$ -HYNIC-duramycin imaging and apoptotic index by TUNEL staining ($r = 0.6981$; $P < 0.05$). Moreover, the 200 μCi group showed the lowest T/M ratio on $^{99\text{m}}\text{Tc}$ -HYNIC-3PRGD2 imaging (1.0 ± 0.5) on day 7 (all $P < 0.05$) comparing to other groups. The T/M ratio on day 7 was not correlated with integrin $\alpha_v\beta_3$ staining ($P > 0.05$). The relative inhibitory rates of tumor on day 14 in the AA98 mAb, 10 μCi , 80 μCi , free ^{125}I , and 200 μCi groups were 26.3, 55.3, 60.5, 66.3, and 69.5%, respectively.

Conclusion: ^{125}I -AA98 mAb showed more effective apoptosis induced ability for CD146 high expression Hep G2 HCC cells and hold the potential for HCC treatment. Moreover, $^{99\text{m}}\text{Tc}$ -HYNIC-Duramycin (apoptosis-targeted) imaging and $^{99\text{m}}\text{Tc}$ -HYNIC-3PRGD2 (angiogenesis-targeted) imaging are reliable non-invasive methods to evaluate the efficacy of targeted treatment of HCC.

Keywords: AA98 mAb, hepatocellular carcinoma, CD146, ^{125}I , angiogenesis, apoptosis

INTRODUCTION

Hepatocellular carcinoma (HCC) is the most common primary malignant tumor of the liver in adults (Torre et al., 2015). The majority of patients diagnosed with advanced HCC and failed to meet the criteria for resection or transplantation (Thomas et al., 2010). Although locoregional therapies including transarterial chemoembolization, cryotherapy, and radiofrequency or microwave ablation can reduce tumor burden while preserving liver function, the prognosis of advanced HCC patients still remains dismal. Alternatively, intratumoral injection of radiopharmaceuticals can achieve a high therapeutic concentration at targeted sites with an extended period of time and avoid systemic exposure to radiation and the results are promising (Tian et al., 1996; Wang et al., 1998; Junfeng et al., 2000; Chi et al., 2014).

It is widely accepted that angiogenesis is essential for tumor growth and invasion (Folkman, 1971). HCC is one of the malignant hypervascular solid tumors, and inhibition of angiogenesis is one of the important methods to treat HCC. CD146 has emerged as a biomarker for angiogenesis (Zheng et al., 2009; Wang and Yan, 2013; Nomikou et al., 2015), and it has been identified as an attractive target for imaging and therapy in HCC (Thomann et al., 2014; Hernandez et al., 2016). Furthermore, high expression of CD146 predicted poor prognosis in HCC patients (Jiang et al., 2016). AA98 monoclonal antibody (mAb) is a promising mAb against CD146 by inhibition of angiogenesis and tumor growth, but it does not induce apoptosis *in vitro* (Yan et al., 2003). Anti-angiogenic mono-therapy is a powerful tool to inhibit tumor growth, but, to date, any available anti-angiogenic mono-therapies targeting cancer do not satisfy the expectation of “starving the tumor.”

One of the solutions to enhance this anti-angiogenic efficacy is to label the anti-angiogenic agents with therapeutic radionuclides, and this strategy is supported by previous reports (Tijink et al., 2006; Fujiwara et al., 2014; Park et al., 2017; Ehlerding et al., 2018). Iodine-125 (^{125}I) is a long-lived radioisotope with a half-life of 59.5 days and a short-range emitter (Cunningham et al., 1998). Its decay can produce a highly localized deposition of dose by short-range Auger electrons plus X ray and Gamma ray. ^{125}I can cause non-repairable damage to double strand DNA and then induce tumor cell death with favorable results by several possible mechanisms including apoptosis hypothesis (Hofer and Hughes, 1971; Bagshawe et al., 1991; Cunningham et al., 1998).

Molecular imaging plays a critical role in monitoring tumor response to targeted therapy. $^{99\text{m}}\text{Tc}$ is an easily accessible diagnostic radionuclide using $^{99}\text{Mo}/^{99\text{m}}\text{Tc}$ generator system, and it has a very attractive nuclear property for molecular imaging. The main targets for apoptosis are the

two common cell membrane aminophospholipids, such as the richest phosphatidylserine (PS) and the second richest phosphatidylethanolamine (PE). PE can be recognized and bound with high affinity by duramycin with a 19-amino acid peptide during cell apoptosis and necrosis (Zhao, 2011). Moreover, the stable, fast clearing, and highly specific $^{99\text{m}}\text{Tc}$ -HYNIC-duramycin can be applied to detect tumor cell death and monitor tumor response to treatment (Elvas et al., 2015; Hu et al., 2018). Integrin $\alpha_v\beta_3$ is an attractive molecular target for its highly restricted expression in tumor angiogenesis and metastasis. The $^{99\text{m}}\text{Tc}$ -HYNIC-3PRGD2 (3PEG4-cRGD dimer) with a safe, highly stable, rapid blood clearance, and easily available kit formulation has the potential for non-invasive integrin $\alpha_v\beta_3$ -targeted imaging and monitoring treatment efficacy of antiangiogenesis (Wang et al., 2009; Jia et al., 2011).

In the present study, AA98 mAb was labeled with ^{125}I to treat HCC xenograft by intratumoral injection. In the following, apoptosis-targeted imaging with $^{99\text{m}}\text{Tc}$ -HYNIC-duramycin and angiogenesis-targeted imaging with $^{99\text{m}}\text{Tc}$ -HYNIC-3PRGD2 were employed to evaluate treatment efficacy.

MATERIALS AND METHODS

Preparation of ^{125}I -AA98 mAb and Quality Control

The modified iodination protocol of AA98 mAb with ^{125}I was employed fundamentally as described previously (Visser et al., 2001; Tijink et al., 2009). Briefly, 800 μg AA98 mAb (80 μL , 10 mg/mL) was added into a tube coated with 25 μg Iodogen (Pierce Biotechnology), then 0.5- μL Na^{125}I solution (GMS Pharmaceutical Co., Ltd., Shanghai, China) with specific activity of 1.6 Ci/mL was added. After 10 min, the reaction was terminated. The radiochemical purity (RCP) of ^{125}I -AA98 mAb was assessed by radio-thin layer chromatography (radio-TLC) Imaging Scanner (Eckert & Ziegler Radiopharma, Inc., USA).

Preparation of $^{99\text{m}}\text{Tc}$ -Labeled Probes for Tumor Apoptosis and Angiogenesis

A single-step kit containing 15 μg hydrazinonicotinamide (HYNIC)-duramycin (Molecular Targeting Technologies, Inc., USA) was labeled by $\text{Na}^{99\text{m}}\text{TcO}_4$ as previously reported (Zhao et al., 2008; Hu et al., 2018). In brief, 0.5 mL freshly prepared sodium pertechnetate ($^{99\text{m}}\text{Tc}$ -pertechnetate) with specific activity of 30 millicurie (mCi), which was obtained from Mo-99/Tc-99m generator (GMS Pharmaceutical Co., Ltd., Shanghai, China), was added to the kit vial. The vial was heated at 80°C around 20 min and then cooled down to room temperature. The RCP of the $^{99\text{m}}\text{Tc}$ -HYNIC-duramycin (always beyond 95%) was analyzed by Radio-TLC.

A single-step kit containing 20 μg of the HYNIC-3PRGD2 conjugate was labeled by $\text{Na}^{99\text{m}}\text{TcO}_4$ as previously reported (Wang et al., 2009). Simply put, 1.0 mL of $\text{Na}^{99\text{m}}\text{TcO}_4$ solution (20 mCi) in saline was added into the kit vial and heated at 100°C around 20 min. After heating, the vial was cooled down to room temperature. The RCP of the $^{99\text{m}}\text{Tc}$ -HYNIC-3PRGD2 was >95%.

Abbreviations: AI, apoptosis index; DAPI, 4', 6-diamidino-2-phenylindole dihydrochloride; HCC, hepatocellular carcinoma; HE, haematoxylin and eosin; HYNIC, mAb, monoclonal antibody; IOD, integrated optical density; ^{125}I , Iodine-125; PBS, phosphate buffer solution; PE, phosphatidylethanolamine; PS, phosphatidylserine; RCP, radiochemical purity; T/M, tumor-to-contralateral muscle tissues; TUNEL, terminal deoxynucleotidyl transferase-mediated dUTP nick end labeling; VOI, volume of interest; 3PRGD2, 3PEG4-cRGD dimer.

Cell Lines

The human HCC cell line Hep G2 was obtained from the Cell Bank, Shanghai Institutes for Biological Sciences, Chinese Academy of Sciences, Shanghai. Hep G2 cells were cultured in DMEM medium (Gibco) containing 1% penicillin-streptomycin (100 U/mL penicillin; 100 µg/mL streptomycin) and 10% fetal bovine serum at 37°C with 5% CO₂. All cells were passaged and collected with trypsin-EDTA solution (0.05% trypsin; 0.02% EDTA).

Animal Care

All animal studies were performed under a protocol approved by the Institutional Animal Care and Use Committee of Zhongshan Hospital, Fudan University. All mice were acclimatized to laboratory conditions (individually ventilated cages, 20°C, 12/12 h light/dark cycle, and *ad libitum* to a standard diet) around 1 week prior to studies.

Animal Model and Intratumoral Injection

Female athymic BALB/c nu/nu mice (6–8 weeks, Shanghai SLAC Laboratory Animal Co., Ltd.) were injected s.c. into the right shoulder with Hep G2 cells (3×10^5) in 0.1 mL phosphate buffer solution (PBS). When tumors reached 6–10 mm in diameter (around 3 weeks after inoculation), 0.25% sodium iodide was fed to mice for 3 days to block the absorption of ¹²⁵I by the thyroid gland before intratumoral injection, and this treatment lasted until the end of experiments. Sixty-six athymic mice bearing s.c. Hep G2 tumor xenografts were randomized into six groups ($n = 11$ /group) to monitor tumor apoptosis ($n = 3$ /group), evaluate angiogenesis ($n = 3$ /group), and observe therapeutic efficacy ($n = 5$ /group). All mice received a single intratumoral injection in a volume up to 20 µL as follows: control (normal saline, 20 µL/mouse), 10 microcurie (µCi) ¹²⁵I-AA98 mAb (10 µCi ¹²⁵I-10 µg AA98 mAb/mouse), free ¹²⁵I (80 µCi ¹²⁵I/mouse), AA98 mAb (80 µg/mouse), 80 µCi ¹²⁵I-AA98 mAb (80 µCi ¹²⁵I-80 µg AA98 mAb/mouse), and 200 µCi ¹²⁵I-AA98 mAb (200 µCi ¹²⁵I-200 µg AA98 mAb/mouse). The injection was administered slowly into the center of the tumor using a microsyringe. The needle was left in the tumor for several seconds before withdrawal, and the injection site was pressed using cotton ball around 1 min.

In vivo Micro-SPECT/CT Imaging

Prior to micro-SPECT/CT imaging, mice were placed into a mice anesthesia chamber with 4% isoflurane mixed with 2 L/min O₂ for several minutes to induce deep anesthesia using a VETEQUIP V-1 animal anesthesia system (VetEquip Inc., USA), then mice were transferred to exam table and maintained with 1.5% isoflurane mixed with 0.4 L/min O₂ using the same anesthesia system. The Nano SPECT/CT scanner (Bioscan, USA) was employed to perform *in vivo* micro-SPECT/CT imaging with the settings (Tan et al., 2017). All 3D OSEM images were reconstructed with a HiSPECT algorithm.

Tumor responses in the tumors were evaluated with ^{99m}Tc-HYNIC-duramycin and ^{99m}Tc-HYNIC-3PRGD2. Before treatment (day 0), baseline micro-SPECT/CT imaging was performed in each of imaging groups using the two molecular probes. After intratumoral injections, micro-SPECT/CT imaging

targeting tumor apoptosis was performed using ^{99m}Tc-HYNIC-duramycin on day 3, and targeting tumor angiogenesis using ^{99m}Tc-HYNIC-3PRGD2 on day 7.

Data Analysis

All micro-SPECT/CT images were displayed with Invivo Scope software (Version 1.43, Bioscan, USA). An appropriate 3D volume of interest (VOI) was placed in the tumor with maximum molecular probe uptake included and necrotic area spared, and the contralateral muscle area was also measured. The radioactivity of tumor or contralateral muscle (in µCi/mm³) was reported by the software for each VOI. The tumor-to-contralateral muscle tissues ratio (T/M ratio) was calculated for each tumor. For assessment of tumor apoptosis and angiogenesis, the T/M ratio of each of the six groups after intratumoral injection was compared with that of the corresponding baseline imaging, and multiple comparisons of the T/M ratio were also conducted among the six groups after intratumoral injection.

Therapeutic Efficacy Study

Tumor size (length and width in mm) and body weight (gram) were measured every other day for 14 days after injection. Tumor volume (mm³) was calculated following the formula (Inaba et al., 1989): Volume = [length × (width)²]/2. The relative tumor inhibition rate was used to assess the antitumor efficacy of the different treatments as follows:

$$\text{The relative tumor inhibition rate} = [1 - (\text{average } V_{14}/V_0)_T / (\text{average } V_{14}/V_0)_C] \times 100\%.$$

Where V_{14} is the tumor volume on Day 14, V_0 is the pretreatment tumor volume before injection (Day 0), T represents each of the five treatment groups, and C means the control group. When body weight loss was >20%, or tumor volume was larger than 2 cm³, mice were sacrificed and excluded to calculate the relative tumor inhibition rate.

Histopathological and Immunohistochemistry

After imaging or treatment, all mice were sacrificed, and all tumors were harvested. Adjacent 4 µm thick paraffin-embedded sections of all tumor samples were stained with Haematoxylin and Eosin (HE) and terminal deoxynucleotidyl transferase (TdT)-mediated dUTP nick end labeling (TUNEL) fluorescence or integrin $\alpha_v\beta_3$ fluorescence. In brief, all tumors were fixed in 4% paraformaldehyde in PBS, dehydrated, and embedded in paraffin, then sliced in the maximal section of the tumor. According to the instruction of the *in situ* cell death detection kit (Roche), TUNEL fluorescence staining was performed to detect and quantify tumor cell apoptosis. To stain integrin $\alpha_v\beta_3$, the 4 µm slices were blocked with 10% goat serum at 37°C for 20 min. The sections were then incubated with rabbit anti-integrin $\alpha_v\beta_3$ antibody (1:200, Beijing Biosynthesis Biotechnology Co., Ltd.) overnight at 4°C. Then, the sections were visualized with Cy3-labeled goat anti-rabbit antibody (1:200, Abcam). Finally, tumor sections were

mounted in 4', 6-diamidino-2-phenylindole dihydrochloride (DAPI) mounting medium.

Pathological and Immunohistochemistry Analysis

The percentage of tumor necrotic area was calculated as: the area of tumor necrosis/the area of total tumor tissue (drawn manually) on HE sections using Case Viewer (3dhitech Ltd., Hungary). Apoptosis index (AI) was determined by calculating the percentage of apoptotic nuclei with green TUNEL fluorescence staining over total nuclei using Quant Center software (3dhitech Ltd., Hungary). Image-Pro Plus 6.0 software (Media Cybernetics, USA) was used to assess the integrin $\alpha_v\beta_3$ red fluorescence intensity by measuring the integrated optical density per field of view (IOD/mm²) of the images with an equivalent area.

Statistics

The numerous data were expressed as mean \pm standard deviation. The results were analyzed using the software package

(IBM SPSS version 22.0 for Mac OS, IBM, USA). A $P < 0.05$ was considered to indicate statistically significant difference.

RESULTS

The labeling rate of the ¹²⁵I-AA98 mAb molecular probe was over 95%. Both the radiochemical purity and the radiochemical yield were $95.8 \pm 0.5\%$ (Figure S1).

Apoptosis Imaging

In terms of T/M ratio, ^{99m}Tc-HYNIC-Duramycin imaging showed that the baseline scans had no statistically significant difference ($P > 0.05$, Figure 1). Three days after treatment, the T/M ratio in each group was higher than that before treatment. The T/M ratio of the 10 μ Ci group, 80 μ Ci group, free ¹²⁵I group, and 200 μ Ci group on day 3 was higher than that on the corresponding baseline scans ($P = 0.0011$, $P = 0.0002$, $P = 0.0332$, and $P = 0.0218$, respectively). There was statistically significant difference among all the 6 groups on day 3 ($P =$

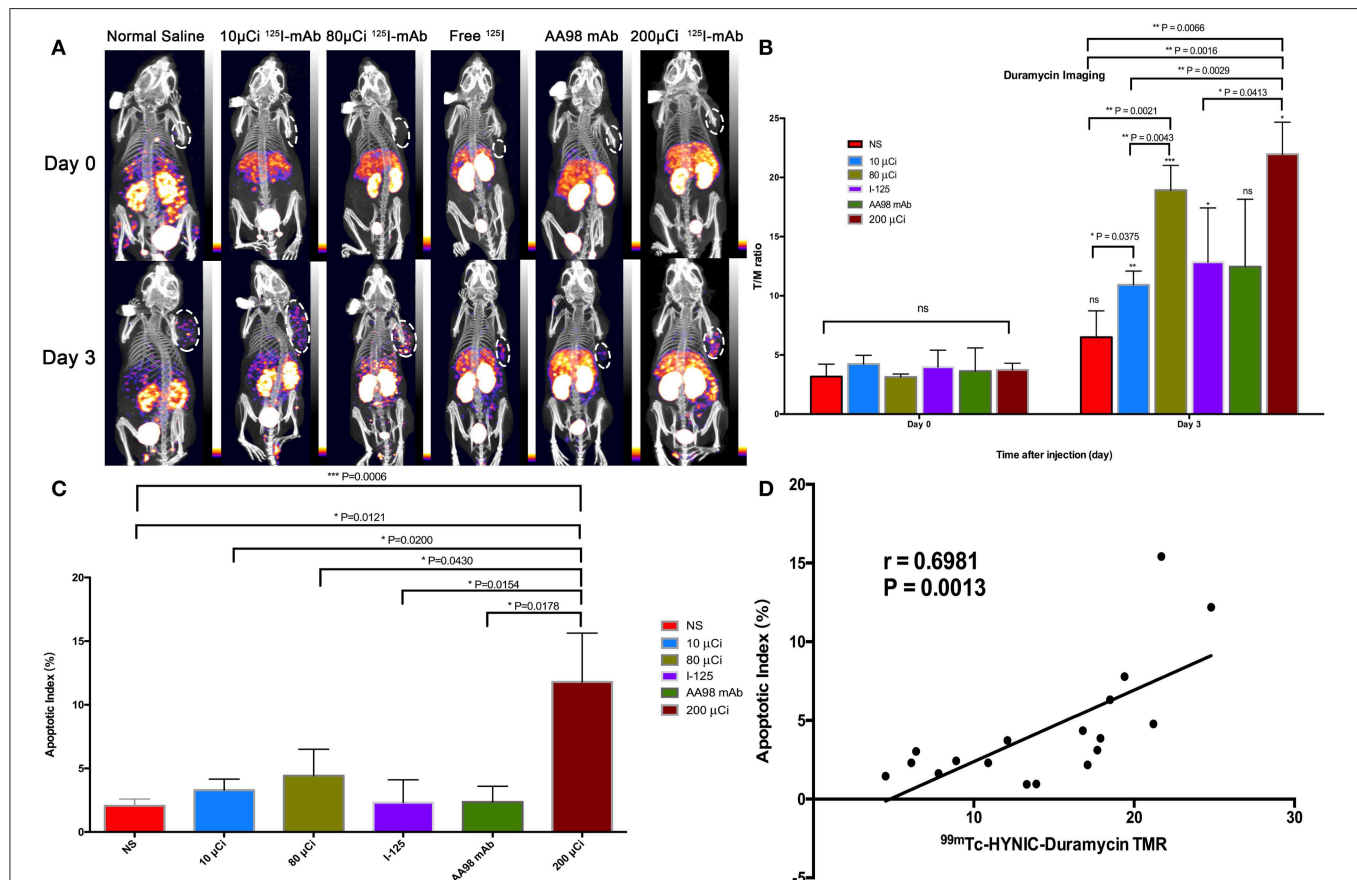


FIGURE 1 | *In vivo* SPECT/CT imaging with ^{99m}Tc-HYNIC-Duramycin and apoptosis immunofluorescence staining in HCC xenograft mice models. Tumor images were obtained with SPECT/CT before (upper row) and 3 days after (bottom row) intratumoral injection among the six groups (A). (B) T/M ratio was analyzed from ^{99m}Tc-HYNIC-Duramycin imaging at baseline scan before intratumoral injection and second scan 3 days after intratumoral injection. (C) Correlation between T/M ratio and apoptosis index. (D) Multiple comparisons of average apoptosis index were performed among the six groups. [Note: ¹²⁵I-mAb means ¹²⁵I-AA98 mAb; $n=3$, mean \pm SD, * $P < 0.05$; ** $P < 0.01$; *** $P < 0.001$; ns indicates no significance between the baseline scan on day 0 and the second scan on day 3, $P > 0.05$; μ Ci means microcurie; white dashed circled area in (A) indicates HCC tumor].

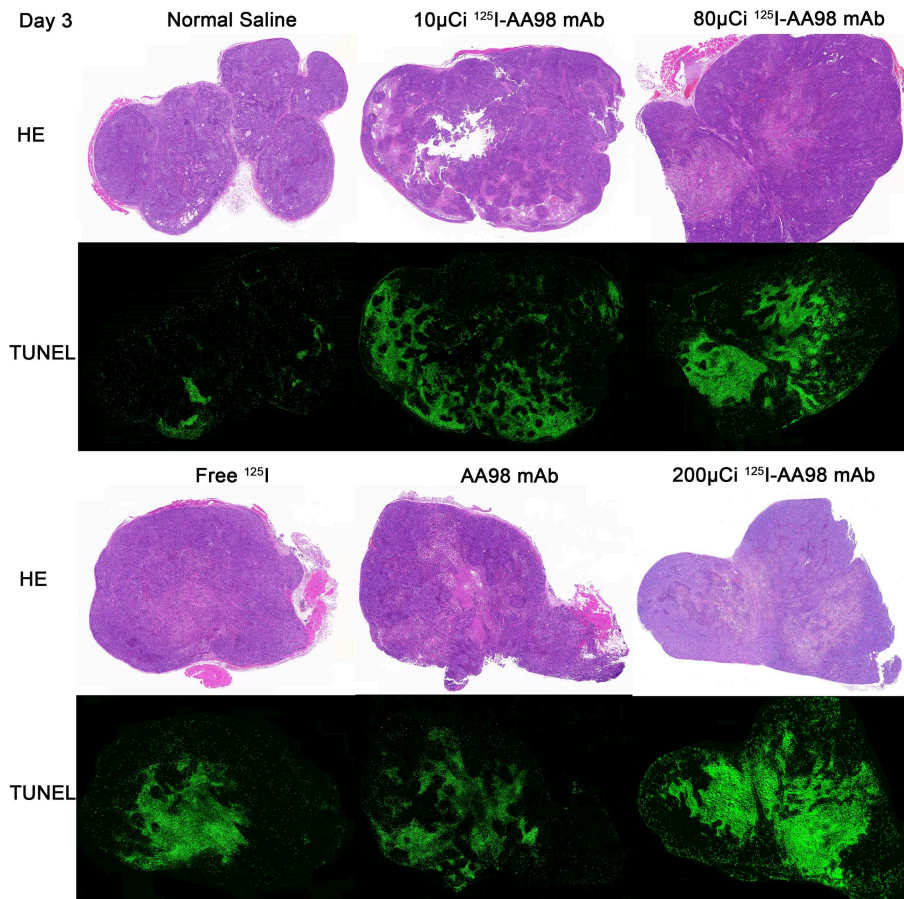


FIGURE 2 | Photographs of pair-matched HE staining and TUNEL fluorescence staining 3 days after intratumoral injection in each group.

0.0066). In terms of the degree of apoptosis, the 200 μCi group demonstrated the highest apoptotic index ($11.8 \pm 3.8\%$), and its T/M ratio on day 3 was higher than that of the normal saline, 10 μCi and free ^{125}I groups, respectively ($P = 0.0016$, $P = 0.0029$, and $P = 0.0413$, respectively). The T/M ratio in 80 μCi group on day 3 was higher than that in 10 μCi and normal groups ($P = 0.0021$ and $P = 0.0043$). In terms of T/M ratio on day 3, there was also a markedly significant difference between 10 μCi group and normal group ($P = 0.0375$). There were no significant differences among the remaining comparative studies (all $P > 0.05$). There was a markedly positive correlation ($r = 0.6981$; $P = 0.0013$) between T/M ratio and apoptotic index by TUNEL fluorescence staining (Figure 2) on day 3.

Angiogenesis Imaging

In terms of T/M ratio, $^{99\text{m}}\text{Tc}$ -HYNIC-3PRGD2 imaging showed there was no statistically significant difference among the baseline scans ($P > 0.05$) (Figure 3). Seven days after treatment, the T/M ratio was significantly lower than that before treatment, and there had no statistically significant difference among all groups ($P = 0.0001$). There was marked difference between

the baseline scan and the repeated scan on day 7 in 200 μCi group, 80 μCi group, and AA98 mAb group, respectively (all $P < 0.05$). The 200 μCi group showed the lowest T/M ratio (1.0 ± 0.5) compared with the other five groups on day 7 (all $P < 0.05$). The T/M ratio in 80 μCi group and AA98 mAb group on day 7 were both higher than that in 10 μCi group and saline control group on day 7 (all $P < 0.05$). The T/M ratio of angiogenesis-targeted imaging on day 7 was not correlated with IOD/mm^2 by integrin $\alpha_v\beta_3$ immunofluorescence staining (Figure 4) ($P = 0.1020$).

Therapeutic Efficacy

As shown in Figure 5, compared with the control group, the relative inhibitory rates of tumor in AA98 mAb group, 10 μCi group, 80 μCi group, ^{125}I group, and 200 μCi group on day 14 were 26.3%, 55.3%, 60.5%, 66.3%, and 69.5%, respectively. Fourteen days after intratumoral injection, there is no markedly statistical difference in terms of tumor volume growth rate among all the six groups ($P > 0.05$). No significant difference of the percentage of tumor necrotic area was noted among the six groups ($P > 0.05$).

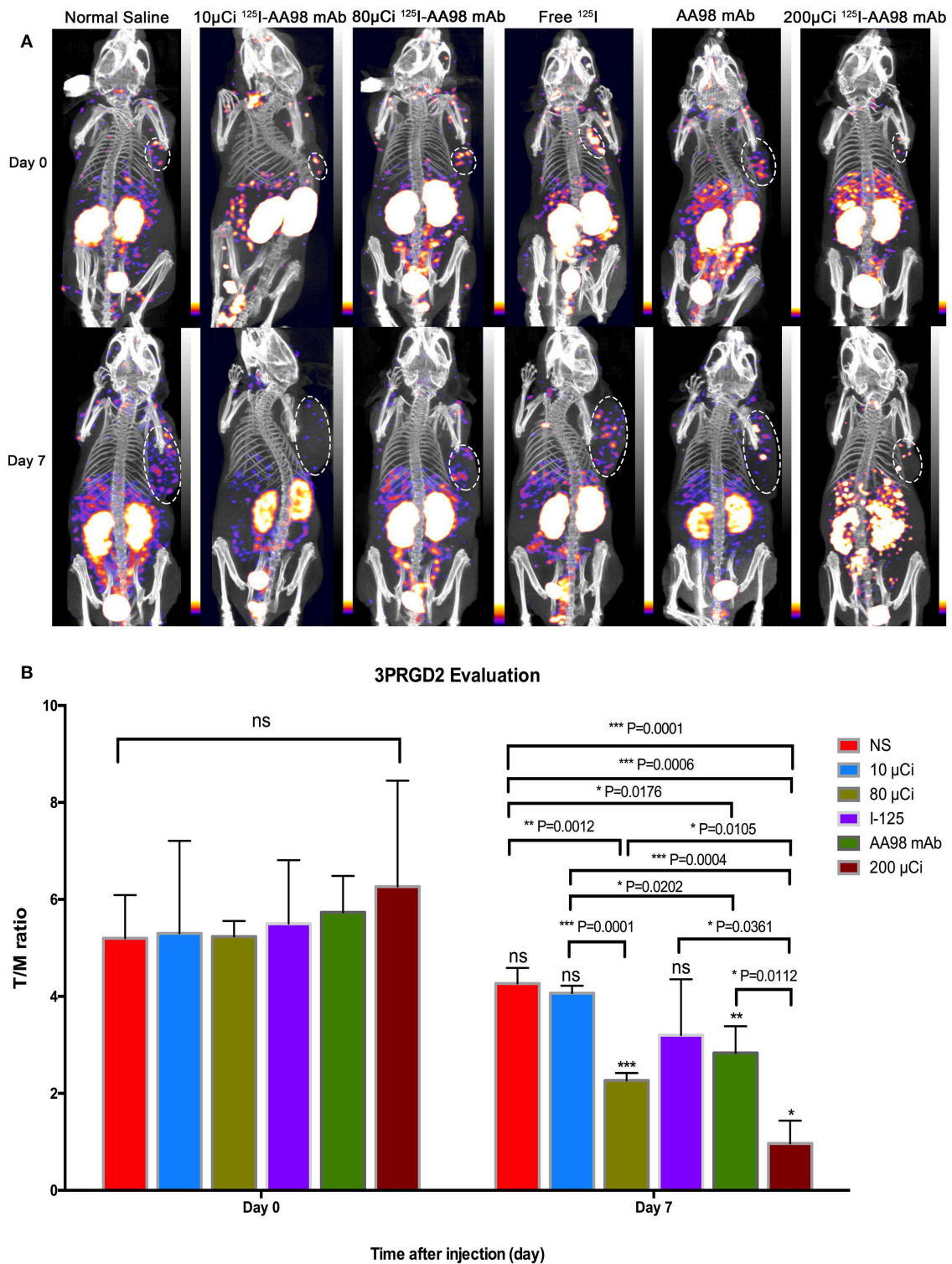


FIGURE 3 | *In vivo* SPECT/CT imaging with ^{99m}Tc -HYNIC-3PRGD2 and integrin $\alpha_v\beta_3$ immunofluorescence staining in HCC xenograft mice models. Tumor images were obtained with SPECT/CT before (upper row) and 7 days after (bottom row) intratumoral injection among the six groups **(A)**. **(B)** T/M ratio was analyzed from ^{99m}Tc -HYNIC-3PRGD2 imaging at baseline scan before intratumoral injection and second scan 7 days after intratumoral injection. ($n = 3$, mean \pm SD, * $P < 0.05$; ** $P < 0.01$; *** $P < 0.001$; ns indicates no significance between the baseline scan on day 0 and the second scan on day 7, $P > 0.05$; μCi means microcurie; white dashed circled area in **(A)** indicates HCC tumor).

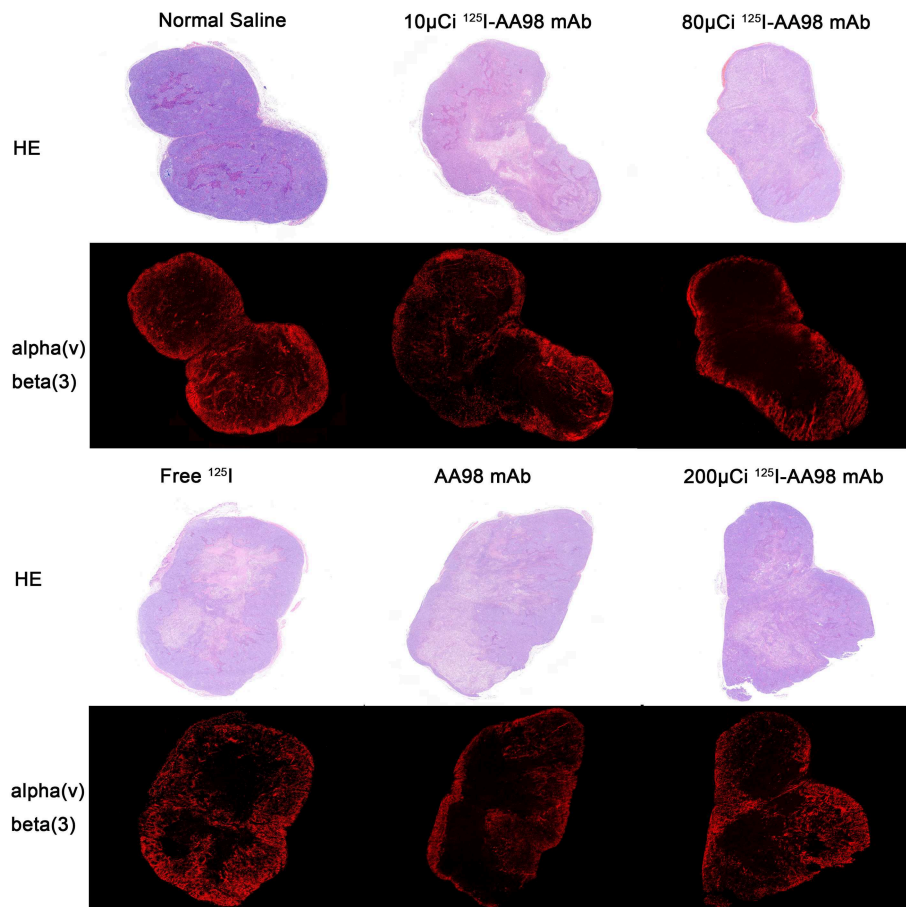


FIGURE 4 | Photographs of pair-matched HE staining and integrin $\alpha_v\beta_3$ fluorescence staining 7 days after intratumoral injection in each group.

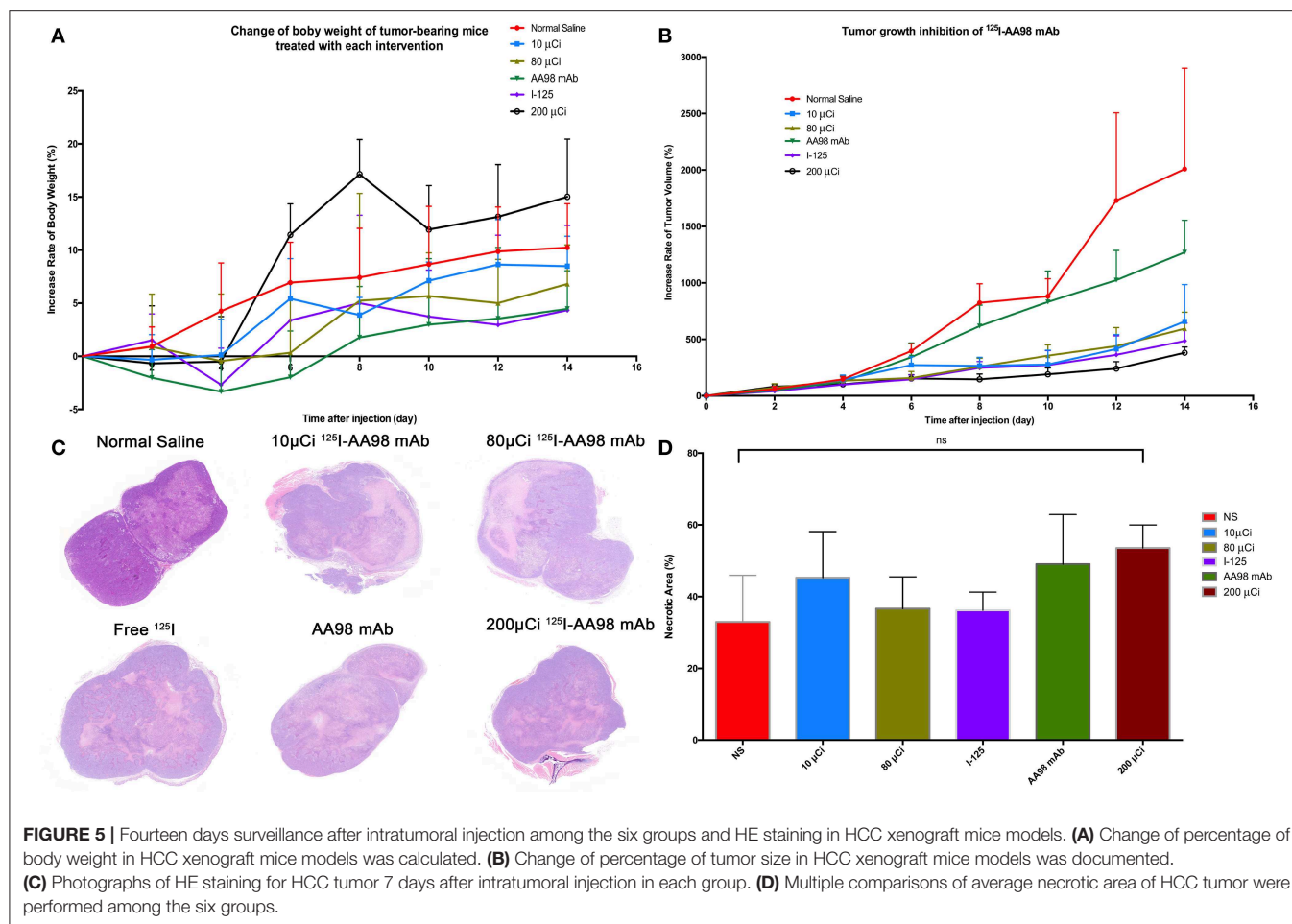
DISCUSSION

CD146 is one of adhesion molecules involving in angiogenesis (St Croix et al., 2000; Chan et al., 2005), and it also plays an essential role in tumor progression. Recently, overexpression of CD146 was found to promote migration and invasion of HCC cells and predict poor prognosis in HCC patients (Jiang et al., 2016). A novel anti-CD146 mAb AA98 has been revealed that it can block angiogenesis both *in vitro* and *in vivo*, and it alone can effectively inhibit tumor growth of HCC xenografts via intraperitoneal injections (Yan et al., 2003). In clinical settings, the usual way of treating inoperable HCC is transcatheter arterial chemoembolization (TACE), which is not easily accessible for HCC xenograft mice model. Alternatively, intratumoral injection is preferred to mimic TACE as a way of drug delivery.

AA98 mAb, as an angiogenesis inhibitor, can block the formation of new blood vessel, rather than directly damage existing blood vessel to result in secondary tumor cell apoptosis (Siemann and Horsman, 2009). Previous report also showed AA98 mAb could not directly induce cell apoptosis *in vitro* (Yan et al., 2003). However, ^{125}I can delivery longer short-range internal radiation over time to induce tumor cell apoptosis. One

of the possible molecular mechanisms of tumor cell apoptosis that ^{125}I may upregulate expression of p53 to downregulate vascular endothelial growth factor and then decrease microvessel density (Ma et al., 2014). We were motivated to try the intratumoral injection of ^{125}I -AA98 mAb to target CD146 with AA98 mAb and then to induce HCC cell apoptosis by ^{125}I with its potential mechanisms (Cunningham et al., 1998; Ma et al., 2014).

In our experiments, AA98 mAb was labeled with a high specific activity of Na^{125}I solution by Iodogen method to yield >95% of RCP. Compared with the baseline T/M ratio of *in vivo* $^{99\text{m}}\text{Tc}$ -HYNIC-Duramycin imaging before intratumoral injection, the T/M ratio of the four groups containing ^{125}I revealed marked increase of HCC cell apoptosis after 3-day treatment ($P < 0.05$), but not in AA98 mAb group ($P > 0.05$). Noticeable, ^{125}I -AA98 mAb for targeting CD146 might more efficiently induce apoptosis than free ^{125}I . The central HCC tumor apoptosis with peripheral normal HCC cells among all groups was verified by TUNEL staining. For *in vivo* $^{99\text{m}}\text{Tc}$ -HYNIC-Duramycin imaging on day 3, the T/M ratios of the 3 kinds of molecular probe groups (10 μCi group, 80 μCi group, and 200 μCi group) were significantly different from that of the control group ($P < 0.05$), but not the free ^{125}I group ($P > 0.05$).



Compared with the control group before treatment, although there was slight increase tendency of ^{99m}Tc -HYNIC-Duramycin uptake within tumor in the 3 kinds of molecular probe groups on day 3 ($P > 0.05$), the inherently spontaneous HCC tumor apoptosis in the three kinds of molecular probe groups was ruled out.

We also confirmed that ^{125}I low-energy radionuclide which resulting a highly localized irradiation can kill HCC cells via apoptosis-mediated cell death. According to dosage of ^{125}I , there is a tendency that higher dosage may induce higher apoptosis. Moreover, the 200 μCi group alone had the highest apoptotic and markedly different from the five other groups (all $P < 0.05$). It means that higher dosage of ^{125}I -AA98 mAb will cause more serious apoptosis, and the 200 and 80 μCi groups may superior to the free ^{125}I group. Finally, our results revealed that the T/M ratio of *in vivo* ^{99m}Tc -HYNIC-Duramycin imaging had a positive correlation with apoptotic index by TUNEL fluorescence staining. It indicates that *in vivo* ^{99m}Tc -HYNIC-Duramycin imaging can provide a potential tool to evaluate tumor cell apoptosis.

AA98 mAb plays an essential role in inhibiting early angiogenic processes, which control the formation of secondary

and tertiary vessel branches (Yan et al., 2003). Tumor neoangiogenesis was able to be identified by overexpression of the integrin $\alpha_v\beta_3$ receptor too, which can be visualized by radionuclide-labeled RGD analogs, such as the molecular probe ^{99m}Tc -HYNIC-3PRGD2 (Jin et al., 2016). We found that the groups containing 80 μg of AA98 mAb or more (i.e., 200 μCi group, 80 μCi group, and AA98 mAb group) showed marked difference between the baseline scan on day 0 and the repeated scan on day 7 (all $P < 0.05$). This finding indicates that AA98 mAb of $\geq 80 \mu\text{g}$ may be the optimal single dosage to achieve response detected on ^{99m}Tc -HYNIC-3PRGD2 SPECT/CT imaging during 7-day therapy. These results were consistent with previous report (Yan et al., 2003). However, our study found that only 200 μCi group was superior to the other five groups ($P < 0.05$), although the T/M ratio of *in vivo* ^{99m}Tc -HYNIC-3PRGD2 SPECT/CT imaging on day 7 was not correlated with IOD/mm^2 by integrin $\alpha_v\beta_3$ immunofluorescence staining ($P > 0.05$). The fixed dosage of AA98 mAb may be one of the reasons to limit the anti-angiogenic effects. Further work is needed to apply multiple injections for treatment to achieve better response.

In addition, our data also showed that there is a tendency of inhibiting growth of HCC xenografts using 125I-AA98 mAb for the first time, although there is no marked significant difference among the five treatment groups ($P > 0.05$). We noted that the relative inhibitory rate of tumor in the ^{125}I group was very well (66.3%). However, the average necrotic area in the ^{125}I group was just higher than the in the control group and lower than that in the other four groups. It indicates that the percentage of the tumor tissue in the ^{125}I group was only lower than that in the control group. This is the first point that we thought the ^{125}I group did not share the best anti-tumor effect. Second, the average apoptotic index in the ^{125}I group on day 3 also showed it is inferior to the three groups containing ^{125}I -AA98 mAb. Third, the evaluation of the SPECT/CT imaging in terms of anti-apoptosis and anti-angiogenesis demonstrated that the tumor-muscle rates did not indicate the ^{125}I group was the best one. Based on our study, we think our further research may focus on comparing the ^{125}I -AA98 mAb with free ^{125}I , optimal multiple injections and optimal injection interval to confirm the definite efficacy.

In conclusion, compared with free ^{125}I and unlabeled AA98 mAb, it's evident that ^{125}I -AA98 mAb showed more effective apoptosis induced ability for CD146 high expression Hep G2 HCC cells. Moreover, $^{99\text{m}}\text{Tc}$ -HYNIC-Duramycin (apoptosis-targeted) imaging and $^{99\text{m}}\text{Tc}$ -HYNIC-3PRGD2 (angiogenesis-targeted) imaging are reliable non-invasive methods to evaluate the efficacy of targeted treatment of HCC.

DATA AVAILABILITY STATEMENT

The datasets generated for this study are available on request to the corresponding author.

ETHICS STATEMENT

The animal study was reviewed and approved by the Animal Care Committee of Fudan University.

REFERENCES

- Bagshawe, K. D., Sharma, K., Southall, P. J., Boden, J. A., Boxer, G. M., Patridge, T. A., et al. (1991). Selective uptake of toxic nucleoside (^{125}I UdR) by resistant cancer. *Br. J. Radiol.* 64, 37–44. doi: 10.1259/0007-1285-64-757-37
- Chan, B., Sinha, S., Cho, D., Ramchandran, R., and Sukhatme, V. P. (2005). Critical roles of CD146 in zebrafish vascular development. *Dev. Dyn.* 232, 232–244. doi: 10.1002/dvdy.20220
- Chi, J. L., Li, C. C., Xia, C. Q., Li, L., Ma, Y., Li, J. H., et al. (2014). Effect of (^{131}I) gelatin microspheres on hepatocellular carcinoma in nude mice and its distribution after intratumoral injection. *Radiat. Res.* 181, 416–424. doi: 10.1667/RR13539.1
- Cunningham, S. H., Mairs, R. J., Wheldon, T. E., Welsh, P. C., Vaidyanathan, G., and Zalutsky, M. R. (1998). Toxicity to neuroblastoma cells and spheroids of benzylguanidine conjugated to radionuclides with short-range emissions. *Br. J. Cancer.* 77, 2061–2068. doi: 10.1038/bjc.1998.348
- Ehlerding, E. B., Lacognata, S., Jiang, D., Ferreira, C. A., Goel, S., Hernandez, R., et al. (2018). Targeting angiogenesis for radioimmunotherapy with a (^{177}Lu) -labeled antibody. *Eur. J. Nucl. Med. Mol. Imaging* 45, 123–131. doi: 10.1007/s00259-017-3793-2

AUTHOR CONTRIBUTIONS

JZ, PH, and DC were involved in the study data analysis and edited the main manuscript text. LQ, HZ, ZF, and JZ contributed to animal models. ZS and DC helped in synthesizing the probe used in this study. HT and WM deal with the pathology. JZ, PH, DC, and HS conceived and designed as well as controlled the quality of this study.

FUNDING

This work was supported by the National Natural Science Foundation of China (Nos. 11875114, 81671735 and 81871407), the Open Large Infrastructure Research of Chinese Academy of Sciences.

ACKNOWLEDGMENTS

We thank Prof. Xiyun Yan and Prof. Minmin Liang (National Laboratory of Biomacromolecules, Institute of Biophysics, Chinese Academy of Sciences) who kindly provided AA98 mAb to us for free. A single-step kit of the HYNIC-3PRGD2 conjugate was kindly provided by Prof. Fan Wang (Medical Isotopes Research Center, Peking University, Beijing, China). We want to thank for the technical supports from Dr. Yuxia Liu and Dr. Xiaobei Zheng (Institute of Applied Physics, Chinese Academy of Sciences). We thank for the imaging support from Prof. Yingjian Zhang and Mr. Jianping Zhang (Center for Biomedical Imaging, Fudan University and Department of Nuclear Medicine, Shanghai Cancer Center, Fudan University).

SUPPLEMENTARY MATERIAL

The Supplementary Material for this article can be found online at: <https://www.frontiersin.org/articles/10.3389/fbioe.2019.00319/full#supplementary-material>

Figure S1 | The radiochemical purity (96.3%) of ^{125}I -AA98 mAb was assessed by radio-thin layer chromatography.

- Elvas, F., Vangestel, C., Rapić, S., Verhaeghe, J., Gray, B., Pak, K., et al. (2015). Characterization of $[(^{99\text{m}}\text{Tc})\text{Duramycin}]$ as a SPECT imaging agent for early assessment of tumor apoptosis. *Mol. Imaging Biol.* 17, 838–847. doi: 10.1007/s11307-015-0852-6
- Folkman, J. (1971). Tumor angiogenesis: therapeutic implications. *N. Engl. J. Med.* 285, 1182–1186. doi: 10.1056/NEJM197111182852108
- Fujiwara, K., Koyama, K., Suga, K., Ikemura, M., Saito, Y., Hino, A., et al. (2014). A (^{90}Y) -labeled anti-ROBO1 monoclonal antibody exhibits antitumor activity against hepatocellular carcinoma xenografts during ROBO1-targeted radioimmunotherapy. *EJNMMI Res.* 4:29. doi: 10.1186/s13550-014-0029-3
- Hernandez, R., Sun, H., England, C. G., Valdovinos, H. F., Ehlerding, E. B., Barnhart, T. E., et al. (2016). CD146-targeted immunoPET and NIRF imaging of hepatocellular carcinoma with a dual-labeled monoclonal antibody. *Theranostics* 6, 1918–1933. doi: 10.7150/thno.15568
- Hofer, K. G., and Hughes, W. L. (1971). Radiotoxicity of intranuclear tritium, 125 iodine and 131 iodine. *Radiat. Res.* 47, 94–101. doi: 10.2307/3573291
- Hu, Y., Liu, G., Zhang, H., Li, Y., Gray, B. D., Pak, K. Y., et al. (2018). A Comparison of $[(^{99\text{m}}\text{Tc})\text{Duramycin}]$ and $[(^{99\text{m}}\text{Tc})\text{Annexin V}]$ in SPECT/CT imaging atherosclerotic plaques. *Mol. Imaging Biol.* 20, 249–259. doi: 10.1007/s11307-017-1111-9

- Inaba, M., Kobayashi, T., Tashiro, T., Sakurai, Y., Maruo, K., Ohnishi, Y., et al. (1989). Evaluation of antitumor activity in a human breast tumor/nude mouse model with a special emphasis on treatment dose. *Cancer* 64, 1577–82. doi: 10.1002/1097-0142(19891015)64:8<1577::AID-CNCR2820640803>3.0.CO;2-I
- Jia, B., Liu, Z., Zhu, Z., Shi, J., Jin, X., Zhao, H., et al. (2011). Blood clearance kinetics, biodistribution, and radiation dosimetry of a kit-formulated integrin α v β 3-selective radiotracer ^{99m}Tc -3PRGD2 in non-human primates. *Mol. Imaging Biol.* 13, 730–736. doi: 10.1007/s11307-010-0385-y
- Jiang, G., Zhang, L., Zhu, Q., Bai, D., Zhang, C., and Wang, X. (2016). CD146 promotes metastasis and predicts poor prognosis of hepatocellular carcinoma. *J. Exp. Clin. Cancer Res.* 35:38. doi: 10.1186/s13046-016-0313-3
- Jin, X., Liang, N., Wang, M., Meng, Y., Jia, B., Shi, X., et al. (2016). Integrin imaging with (^{99m}Tc) -3PRGD2 SPECT/CT shows high specificity in the diagnosis of lymph node metastasis from non-small cell lung cancer. *Radiology* 281, 958–966. doi: 10.1148/radiol.2016150813
- Junfeng, Y., Ruping, Z., Xinlan, D., Xiaofeng, M., Jianying, X., Weiqing, H., et al. (2000). Intratumoral injection with $[(188)\text{Re}]$ rhenium sulfide suspension for treatment of transplanted human liver carcinoma in nude mice. *Nucl. Med. Biol.* 27, 347–352. doi: 10.1016/S0969-8051(00)00093-7
- Ma, Z., Yang, Y., Yang, G., Wan, J., Li, G., Lu, P., et al. (2014). Iodine-125 induces apoptosis via regulating p53, microvessel density, and vascular endothelial growth factor in colorectal cancer. *World J. Surg. Oncol.* 12:222. doi: 10.1186/1477-7819-12-222
- Nomikou, E., Alexopoulou, A., Vasilieva, L., Agiasotelli, D., Pavlou, E., Theodossiadis, G., et al. (2015). Soluble CD146, a novel endothelial marker, is related to the severity of liver disease. *Scand. J. Gastroenterol.* 50, 577–583. doi: 10.3109/00365521.2014.985706
- Park, B. N., Lee, S. J., Roh, J. H., Lee, K. H., An, Y. S., Yoon, J. K. (2017). Radiolabeled anti-adenosine triphosphate synthase monoclonal antibody as a theragnostic agent targeting angiogenesis. *Mol. Imaging* 16:1536012117737399. doi: 10.1177/1536012117737399
- Siemann, D. W., and Horsman, M. R. (2009). Vascular targeted therapies in oncology. *Cell Tissue Res.* 335, 241–248. doi: 10.1007/s00441-008-0646-0
- St Croix, B., Rago, C., Velculescu, V., Traverso, G., Romans, K. E., Montgomery, E., et al. (2000). Genes expressed in human tumor endothelium. *Science* 289, 1197–1202. doi: 10.1126/science.289.5482.1197
- Tan, H., Zhou, J., Yang, X., Abudupataer, M., Li, X., Hu, Y., et al. (2017). (^{99m}Tc) -labeled bevacizumab for detecting atherosclerotic plaque linked to plaque neovascularization and monitoring antiangiogenic effects of atorvastatin treatment in ApoE(-/-) mice. *Sci. Rep.* 7:3504. doi: 10.1038/s41598-017-03276-w
- Thomann, S., Longerich, T., Bazhin, A. V., Mier, W., Schemmer, P., and Ryschich, E. (2014). Selective targeting of liver cancer with the endothelial marker CD146. *Oncotarget* 5, 8614–8624. doi: 10.18632/oncotarget.2345
- Thomas, M. B., Jaffe, D., Choti, M. M., Belghiti, J., Curley, S., Fong, Y., et al. (2010). Hepatocellular carcinoma: consensus recommendations of the National Cancer Institute Clinical Trials Planning Meeting. *J. Clin. Oncol.* 28, 3994–4005. doi: 10.1200/JCO.2010.28.7805
- Tian, J. H., Xu, B. X., Zhang, J. M., Dong, B. W., Liang, P., and Wang, X. D. (1996). Ultrasound-guided internal radiotherapy using yttrium-90-glass microspheres for liver malignancies. *J. Nucl. Med.* 37, 958–963.
- Tijink, B. M., Neri, D., Leemans, C. R., Budde, M., Dinkelborg, L. M., Stigter-van Walsum, M., et al. (2006). Radioimmunotherapy of head and neck cancer xenografts using ^{131}I -labeled antibody L19-SIP for selective targeting of tumor vasculature. *J. Nucl. Med.* 47, 1127–1135. doi: 10.1001/archotol.132.8.886-a
- Tijink, B. M., Perk, L. R., Budde, M., Stigter-van Walsum, M., Visser, G. W., Kloet, R. W., et al. (2009). (^{124}I) -L19-SIP for immuno-PET imaging of tumour vasculature and guidance of (^{131}I) -L19-SIP radioimmunotherapy. *Eur. J. Nucl. Med. Mol. Imaging* 36, 1235–1244. doi: 10.1007/s00259-009-1096-y
- Torre, L. A., Bray, F., Siegel, R. L., Ferlay, J., Lortet-Tieulent, J., and Jemal, A. (2015). Global cancer statistics, 2012. *CA Cancer J. Clin.* 65, 87–108. doi: 10.3322/caac.21262
- Visser, G. W., Klok, R. P., Gebbink, J. W., ter Linden, T., van Dongen, G. A., and Molthoff, C. F. (2001). Optimal quality (^{131}I) -monoclonal antibodies on high-dose labeling in a large reaction volume and temporarily coating the antibody with IODO-GEN. *J. Nucl. Med.* 42, 509–519. Available online at: <http://jnm.snmjournals.org/content/42/3/509.long>
- Wang, L., Shi, J., Kim, Y. S., Zhai, S., Jia, B., Zhao, H., et al. (2009). Improving tumor-targeting capability and pharmacokinetics of (^{99m}Tc) -labeled cyclic RGD dimers with PEG(4) linkers. *Mol. Pharm.* 6, 231–245. doi: 10.1021/mp800150r
- Wang, S. J., Lin, W. Y., Chen, M. N., Chi, C. S., Chen, J. T., Ho, W. L., et al. (1998). Intratumoral injection of rhenium-188 microspheres into an animal model of hepatoma. *J. Nucl. Med.* 39, 1752–1757.
- Wang, Z., and Yan, X. (2013). CD146, a multi-functional molecule beyond adhesion. *Cancer Lett.* 330, 150–162. doi: 10.1016/j.canlet.2012.11.049
- Yan, X., Lin, Y., Yang, D., Shen, Y., Yuan, M., Zhang, Z., et al. (2003). A novel anti-CD146 monoclonal antibody, AA98, inhibits angiogenesis and tumor growth. *Blood* 102, 184–191. doi: 10.1182/blood-2002-04-1004
- Zhao, M. (2011). Lantibiotics as probes for phosphatidylethanolamine. *Amino Acids* 41, 1071–1079. doi: 10.1007/s00726-009-0386-9
- Zhao, M., Li, Z., and Bugenhagen, S. (2008). ^{99m}Tc -labeled duramycin as a novel phosphatidylethanolamine-binding molecular probe. *J. Nucl. Med.* 49, 1345–1352. doi: 10.2967/jnumed.107.048603
- Zheng, C., Qiu, Y., Zeng, Q., Zhang, Y., Lu, D., Yang, D., et al. (2009). Endothelial CD146 is required for *in vitro* tumor-induced angiogenesis: the role of a disulfide bond in signaling and dimerization. *Int. J. Biochem. Cell. Biol.* 41, 2163–2172. doi: 10.1016/j.biocel.2009.03.014

Conflict of Interest: The authors declare that the research was conducted in the absence of any commercial or financial relationships that could be construed as a potential conflict of interest.

Copyright © 2019 Zhou, Hu, Si, Tan, Qiu, Zhang, Fu, Mao, Cheng and Shi. This is an open-access article distributed under the terms of the Creative Commons Attribution License (CC BY). The use, distribution or reproduction in other forums is permitted, provided the original author(s) and the copyright owner(s) are credited and that the original publication in this journal is cited, in accordance with accepted academic practice. No use, distribution or reproduction is permitted which does not comply with these terms.



Optically Active Nanomaterials for Bioimaging and Targeted Therapy

Yu Yang^{1*}, Li Wang^{1,2}, Bin Wan^{1,2}, Yuxin Gu^{1,2} and Xinxin Li³

¹ State Key Laboratory of Environmental Chemistry and Ecotoxicology, Research Center for Eco-Environmental Sciences, Chinese Academy of Sciences, Beijing, China, ² College of Resources and Environment, University of Chinese Academy of Sciences, Beijing, China, ³ Rural Energy and Environment Agency, Ministry of Agriculture, Beijing, China

OPEN ACCESS

Edited by:

Yu Gao,
Nanjing University of Posts and
Telecommunications, China

Reviewed by:

Shuai Yu,
University of Texas at Arlington,
United States
Xinyi Wang,
Shenyang Agricultural
University, China

*Correspondence:

Yu Yang
yuyang@rcees.ac.cn

Specialty section:

This article was submitted to
Nanobiotechnology,
a section of the journal
Frontiers in Bioengineering and
Biotechnology

Received: 05 August 2019

Accepted: 25 October 2019

Published: 15 November 2019

Citation:

Yang Y, Wang L, Wan B, Gu Y and Li X
(2019) Optically Active Nanomaterials
for Bioimaging and Targeted Therapy.
Front. Bioeng. Biotechnol. 7:320.
doi: 10.3389/fbioe.2019.00320

Non-invasive tracking for monitoring the selective delivery and transplantation of biotargeted agents *in vivo* has been employed as one of the most effective tools in the field of nanomedicine. Different nanoprobe have been developed and applied to bioimaging tissues and the treatment of diseases ranging from inflammatory and cardiovascular diseases to cancer. Herein, we will review the recent advances in the development of optics-responsive nanomaterials, including organic and inorganic nanoparticles, for multimodal bioimaging and targeted therapy. The main focus is placed on nanoprobe fabrication, mechanistic illustrations, and diagnostic, or therapeutical applications. These nanomedicine strategies have promoted a better understanding of the biological events underlying diverse disease etiologies, thereby facilitating diagnosis, illness evaluation, therapeutic effect, and drug discovery.

Keywords: optical, nanomaterials, bioimaging, tissues, therapy

INTRODUCTION

Molecular imaging reflects biological information on temporal and spatial scales, unveiling the dynamics of disease (Smith and Gambhir, 2017). It is a crucial diagnostic tool for monitoring *in vivo* response and assessing outcomes in targeted therapies (Fan et al., 2017). Also, integrating imaging, and therapy into theranostic systems is an efficient strategy for real-time tracking of the pharmacokinetics and biodistribution of a drug. Current imaging modalities include X-ray, magnetic resonance, optics (e.g., fluorescence, luminescence, Raman, photoacoustics), radionuclides, and mass spectrometry (Kunjachan et al., 2015). Among them, optical imaging is a common modality in preclinical research on theranostic agents.

Nanomaterials have been widely developed as therapeutic and diagnostic agents (Lim et al., 2015; Chen et al., 2016a). Research efforts have changed from developing new materials *in vitro* to exploring functional materials *in vivo*, thereby increasing the potential for clinical translation (Lamch et al., 2018). Perhaps the unique advantage of nanoparticles (NPs) for optical imaging is that their physical and optical properties are easily tunable through structural modulation. Also, some NP compositions possess inherent imaging and therapeutic properties, while others are rendered multifunctional through the manipulation of multiple structural elements. Engineering multifunctional theranostic NPs presents several challenges, including imaging quality, loading capacity, the toxicity of intrinsic ingredients, storage, and *in vivo* stability, the complexity of synthesis, batch repeatability, production costs, and regulatory hurdles (Farokhzad and Langer, 2006; Lee et al., 2012). Common nanomaterials, including inorganic and organic NPs, have demonstrated a potential for diagnosis and therapy (Brigger et al., 2002). Variations in size, shape, and surface modifications can adjust their biocompatibility and specificity with target tissues

(Wang and Thanou, 2010). Depending on their structural composition, NPs can provide an optical signal or function as nanocarriers for optically active agents. Current interests mainly involve non-invasive imaging of deep tissues and targeting drug therapy.

In this paper, we discuss recent progress in optical-sensitive NPs, their bioimaging involving fluorescence, luminescence, surface-enhanced Raman scattering (SERS), and photoacoustic (PA) signals, and their therapeutic applications in photodynamic therapy (PDT), photothermal therapy (PTT), and drug delivery. Moreover, common design considerations for advanced nanomedicines and the challenges of their application are discussed from diagnostic and therapeutic perspectives.

OPTICALLY ACTIVE NANOMATERIALS

Inorganic Nanomaterials

Due to their unique characteristics, i.e., surface plasmon resonance (SPR), gold NPs (GNPs) are usually chosen to enhance optical imaging based on their absorption, fluorescence, Raman scattering, etc. (Wu et al., 2019). Generally, GNPs are synthesized by HAuCl_4 reduction, known as the Brust et al. (1994) or Turkevich method Turkevich et al. (1951). GNPs are stabilized by a wide variety of ligands that affect their sizes and properties (Treguer-Delapierre et al., 2008; Boisselier et al., 2010). Their diameters range from 1 nm to more than 120 nm. Also, diverse shapes can be prepared, such as core-shell nanostructures (Kharlamov et al., 2015), nanorods (de la Zorda et al., 2015), or nanocages (Chen et al., 2005a) whose aspect ratios modulate their optical properties. The excellent stability of GNPs covalently bonded with thiolated ligands permits chemical modifications directly on their surfaces (Boisselier et al., 2008). The ligands for stabilizing GNPs can be specifically selected for drug encapsulation and release or targeted to tissues such as tumors (Guo et al., 2017; Her et al., 2017; Spyrtatou et al., 2017). However, the safety of GNPs in clinical application remains controversial, with more information required on their long-term toxicity *in vivo*.

Carbon-based nanomaterials (CBN) as members of the carbon family including fullerenes, carbon nanotubes (CNTs), graphene (G), graphene oxide (GO), nanodiamonds (NDDs), and carbon dots (CDs) (Bartelmess et al., 2015; Patel et al., 2019). Modifying their surfaces with functional groups (e.g., carboxylic acid, hydroxyl, or epoxy) provides the opportunity to optimize their properties. The extraordinary optical features of CBN (e.g., inherent fluorescence, high photostability, and tunable narrow emission spectra) increase their potential for imaging and diagnosis of cells or tissues (Sadegh and Shahryari-ghoshekandi, 2015; Goodarzi et al., 2017; Namdari et al., 2017; Bullock and Bussy, 2019; Tinwala and Wairkar, 2019). Fullerenes usually act as photosensitizers (PSs) to generate singlet oxygen ($^1\text{O}_2$) and hence are applied for blood sterilization and cancer PDT (Lu et al., 2019). The inherent spectroscopic features of CNTs (e.g., Raman scattering and photoluminescence) provide a valuable means of tracking *in vivo* therapeutic status, pharmacodynamic behavior, and drug delivery efficiency and imaging and detecting diseases (Tasis et al., 2006; Liu et al., 2011). Graphene and

GO-based nanocarriers have attracted significant attention for imaging and anticancer therapy because of their large drug loading and effective delivery capacity. Also, $\sim 2,600 \text{ m}^2/\text{g}$ is more than double the surface area of most nanomaterials (Mao et al., 2013; Reina et al., 2017). Recently, carbon dots (CDs, size $< 10 \text{ nm}$) have been extensively studied to gain a high fluorescence quantum yield through facile synthesis methods (Liu et al., 2015a). NDDs are nanocrystals that consist of tetrahedrally bonded carbon atoms in the form of a three-dimensional (3D) cubic lattice. The optical properties of NDDs allow their use as photoluminescent probes ($\lambda_{\text{em}} = 550\text{--}800 \text{ nm}$) due to nitrogen-vacancy defect centers (Chang et al., 2008). When functionalized, their biocompatibility is known to be superior to CNTs and carbon black (Mochalin et al., 2013). However, the toxicity of CBN is presently the key problem for their clinical use. Also, the toxicology and pharmacokinetics of CBN mainly rely on several factors, e.g., physicochemical and structural properties, exposure dose and time, cell type, mechanism, residual catalyst, and synthesis method. It is necessary to systematically evaluate CBN *in vivo* safety using more relevant animal models.

Porous silicon nanoparticles (pSiNPs) have gained intense attention in the biomedical field due to their low toxicity and potential for use in minimally invasive and focal therapies that avoid conventional side effects (Vivero-Escoto et al., 2012). pSiNPs can be degraded completely to produce non-toxic orthosilicic acid (Tzur-Balter et al., 2013), a bioavailable form of Si, and then excreted efficiently through renal clearance (Park et al., 2009). Also, their high active surface areas (up to $1,000 \text{ m}^2/\text{g}$) (Loni et al., 2015) allow Si modifications by other molecules through various surface chemical reactions (e.g., hydrosilylation, silanisation, and hydrocarbonization), which facilitate their targeted and controlled drug release into cancer cells (Wu et al., 2011a; Makila et al., 2012; Wang et al., 2014). Actually, the porous nanostructures of pSiNPs allow them to load drugs, probes, enzymes, proteins, antibodies, siRNA, or other species (Castillo and Vallet-Regi, 2019). Numerous cell-specific epitopes and biomarkers afford selective binding to certain antibodies, peptides, or other molecules and thus provide the opportunity for targeted drug delivery via vectorized pSiNPs (Li et al., 2018a). Moreover, the optical features of silicon nanostructures, i.e., intrinsic photoluminescence, afford an alternative for bioimaging, accompanied with better biocompatibility and biodegradability and lower toxicity compared with semiconductor quantum dots (Warner et al., 2005; Erogbogbo et al., 2008; Bimbo et al., 2010; Gu et al., 2010). Finally, easy handling and cost-efficient preparation through facile electrochemical anodization of crystalline silicon increase the interest in utilizing pSiNPs (Sailor, 2012). Nevertheless, the design and synthesis of smart multifunctional pSiNP nanocarriers, *in vivo* performance evaluation using animal models, and subsequent translational studies still need to be further explored.

Lanthanide (Ln)-doped upconversion nanoparticles (UCNPs) can convert two or more low-energy near-infrared (NIR) photons into high-energy emissions through a non-linear anti-Stokes process (Auzel, 2004). Due to their special upconversion luminescence feature and stable Ln-based inorganic framework,

Ln-UCNPs have been developed as promising alternatives to conventional labels (e.g., organic dyes and quantum dots) with several attractive advantages, such as being highly resistant to photobleaching and photoblinking, having negligible background autofluorescence, having deeper tissue-penetration ability, and causing minimal photodamage (Zhou et al., 2012). Also, considering the high feasibility and maneuverability of their structural design, many functional components with other imaging capabilities are introduced into these nanoparticles for diagnostic and therapeutic applications (Liu et al., 2014a, 2015b). Likewise, UCNPs with a high surface area, characteristic structures, and versatile surface functionalization can act as nanocarriers for drug delivery (Wu et al., 2015; Yang et al., 2015a). Significantly, UCNPs with a distinctive upconverted emission can double as light-transducers to activate PSs for deep-tissue PDT or as phototriggered devices for precise control of drug-payload release induced by NIR light (Wang et al., 2013a; Min et al., 2014; Idris et al., 2015). However, high upconversion efficiency is realized only upon 980- or 808-nm excitation, which has seriously hindered their practical usage in the biomedical field. Also, surface modification and bioconjugation of long-term stable and biocompatible Ln-UCNPs remain a huge challenge. Therefore, more strategies for surface modification and corresponding toxicology studies of these NPs are still needed for future pre-clinical and clinical applications.

Quantum dots (QDs) are semiconductor nanocrystals (typically with diameters <10 nm), which display dimension-dominant optical features (e.g., absorption and luminescence) (Xu et al., 2018a). Particularly, QDs of various dimensions or ingredients are excited by a single light source to separately emit diverse colors over a wide range with negligible spectral overlap, rendering them desirable for multiple imaging (Yong, 2012). Avoiding the photobleaching of organic dyes, QDs are more beneficial to imaging *in vivo* for a long time (Geszeke-Moritz and Moritz, 2013). Significantly, QDs can be tuned to emit over a broad wavelength range (e.g., 450–1,500 nm) by modulating their dimensions, configurations, and components (Pichaandi and van Veggel, 2014; Zhao et al., 2018). QDs can also be conjugated with a recognition molecule, such as antibodies, DNA, proteins, etc. (Lu and Li, 2011). Flexibility in the surface chemistry and emission peak of QDs makes them useable as optical probes or nanocarriers for bioimaging, drug discovery, diagnostics, and therapy (Probst et al., 2013; Bilan et al., 2016; Yao et al., 2018). The main QDs involved in biomedicine contain Cd-based QDs (e.g., CdSe, CdTe, CdS) or Cd-free QDs (e.g., InP, CuInS₂, AgInS₂, Ag₂S, WS₂, ZnO, silicon, GQDs, CuS) (Xu et al., 2016; Mo et al., 2017). However, the potential hazards of QDs have become a critical issue that must be further addressed prior to clinical use.

Organic Nanomaterials

Optical nanoagents (e.g., QDs, UCNPs, metal nanoclusters, carbon, and silica-based nanomaterials) have been widely employed for molecular imaging. However, inorganic NPs usually suffer from critical safety concerns, including heavy metal poisoning, and not being susceptible to fast clearance from

the body. To facilitate clinical translation, organic systems are generally preferred.

Fluorogens with aggregation-induced emission (AIEgens), the typical organic nanomaterials, exhibit very weak emission in the molecular state but high fluorescence in the aggregated state (Luo et al., 2001). They are usually arranged in a rotor-like conformation. In the free state, intermolecular collisions cause the consumption of energy in the form of non-radiative transition, while in the aggregated state, the restriction of intramolecular motion (RIM) ensures the release of exciton energy via a radiative pathway, intensifying the emission (Mei et al., 2015). Through intelligent modulation, AIEgens can emit a broad wavelength in the ultra-violet (UV) to NIR region, accompanied with certain attractive qualities. For example, they enhance the chance of intersystem crossing, thereby increasing the production of free radicals for PDT (Hong et al., 2009; Xu et al., 2015) and strengthen the conversion of non-radiative relaxation to generate thermal energy for PA imaging and PTT (Mei et al., 2014; Geng et al., 2015). Also, some biomolecules (e.g., target or chelation agents) can be integrated into AIEgens without affecting their AIE properties (Hong et al., 2011; Hu et al., 2014), which endows them with multiple performances for cancer therapy (Yuan et al., 2015). AIEgens have been successfully combined with PSs, drugs, and several imaging methods to realize efficient theranostic platforms (Chang et al., 2012; Xue et al., 2014). Most AIE systems with multiple functions (or modalities) are composed of several components through an all-in-one approach, suffering from defects in their complex molecular structure and multistep synthesis.

Owing to poor photostability of traditional NIR organic dyes, organic semiconducting agents, including semiconducting polymer nanoparticles (SPNs), and semiconducting molecule nanoparticles (SMNs), have emerged as excellent candidates (Lyu et al., 2016; Pu et al., 2016; Zhu et al., 2016). These agents possess higher absorption coefficients, more tunable optical properties, and controllable dimensions compared with inorganic agents (Hong et al., 2012a; Pu et al., 2014a). The wavelength range 650–1,000 nm of NIR fluorescence imaging is known as the first NIR window (NIR-I), which can achieve a tissue penetration depth of up to ≈1 cm (Shanmugam et al., 2014). However, when NIR-I light passes through or interacts with the tissue, it still suffers from light scattering, tissue absorption, and autofluorescence (Ntziachristos, 2010), leading to a relatively poor signal-to-noise ratio (SNR), and thus is less ideal for deep-tissue imaging. To enhance the imaging depth, the second near-infrared window (NIR-II, 1,000–1,700 nm), a more ideal region with deeper tissue-penetration depth and fewer light–tissue interactions, has been explored recently (Miao and Pu, 2018; Cai et al., 2019). To date, organic semiconducting agents have been utilized for deep-tissue imaging, including NIR-II fluorescence, self-luminescence, and PA imaging, in biomedical fields such as cell (Wu et al., 2010; Pu et al., 2014b), tumor (Wu et al., 2011b), acute edema (Pu et al., 2014b), and cardiovascular imaging (Hong et al., 2014) and in real-time evaluation of drug-toxicity (Shuhendler et al., 2014). However, they also face the major issues of high accumulation in the liver and slow removal from the body due to their large dimensions. Therefore, new designs are needed to increase their

biodegradability or reduce their sizes so that they are smaller than the renal filtration threshold (~ 5 nm) for quick clearance via urine excretion.

Polymer nanoparticles (PNPs) have been widely developed for cancer diagnosis and therapy due to their high extinction coefficients, extraordinary fluorescence intensity, good photostability, biocompatibility and biodegradability, and simple encapsulation of anticancer drugs and/or imaging probes (Pecher and Mecking, 2010; Yang et al., 2012; Feng et al., 2017). Although PNPs can accumulate in the tumor region via the enhanced permeability and retention (EPR) effect (Luk and Zhang, 2014; Tang et al., 2016), cancer-targeting moieties (e.g., proteins, peptides, and aptamers) must be modified onto the NP surface by chemical or physical interaction, resulting in functionalized PNPs with enhanced selectivity and sensitivity for cancer diagnosis and therapy (Liu et al., 2015c; Li et al., 2016; Li and Yang, 2017; Lin et al., 2017). Recently, functionalized PNPs have been designed according to specific cellular processes and disease environments and applied to selectively deliver drugs to the target regions (Vaidya et al., 2011; Krasia-Christoforou and Georgiou, 2013; Herranz-Blanco et al., 2016; Kumar et al., 2018; Wang et al., 2019). Further *in vivo* work will be required to comprehensively investigate the safety and efficacy of these novel theranostic platforms before clinical application.

OPTICALLY ACTIVE NANOMEDICINE FOR BIOIMAGING

Fluorescence Imaging

Fluorescence imaging, as a means to visualize specific organelles within cells or animals, has become a powerful tool for biological research and even for the emerging field of fluorescence-guided surgery. Additionally, fluorescence imaging can capture specific molecular information on the tumor microenvironment (Wolfbeis, 2015).

Among the commonly utilized non-viral vectors, gold nanocages (AuNCs) were investigated for microRNA (miRNA) delivery due to their biological inertness and unique physicochemical features (Skrabalak et al., 2008). Their strong and easily adjustable absorption and scattering in the NIR region demonstrate their feasibility in theranostic uses (Xia et al., 2011). The sizes, shapes or surface chemistry of NPs can mediate their cellular uptakes, macrophage clearance, and biodistribution (Huang and El-Sayed, 2010). NPs with a size of 10–100 nm are more appropriate for cancer diagnosis and therapy since they can escape from renal elimination and accumulate in tumors. Besides size, surface chemistry is another crucial factor for the cellular uptake and biodistribution of NPs *in vivo* (Chen et al., 2005b). Bao et al. (2017) have successfully fabricated a series of differently-sized miRNA delivery systems, miR-26a-loaded, hyaluronic acid (HA)-modified, polyetherimide-conjugated PEGylated AuNC ternary nanocomplexes (PPHAuNCs-TNCs), and monitored them through fluorescence and PA imaging. First, they prepared PEGylated AuNCs (PAuNCs) by employing HS-PEG-OMe (MW 5000) to replace the PVP layer through an Au-S bond to extend the circulation period of the NPs in the

blood and enhance their stability. Secondly, polyethyleneimine (PEI)-conjugated PAuNCs (PPAuNCs) were obtained by conjugation of PEI onto the surface of the PAuNCs to condense miRNAs, utilizing 11-mercaptoundecanoic acid (MUA) as a linker. Thirdly, miRNAs were encapsulated with differently-sized PPAuNCs via electrostatic interaction to obtain miRNA-loaded, PEI-conjugated PEGylated AuNC binary nanocomplexes (PPAuNCs-BNCs). Finally, to neutralize their slightly positive charge and enhance their stability and biocompatibility, a small amount of HA was added to PPAuNCs-BNCs to obtain the final product, PPHAuNC-TNC (Figure 1A).

miRNAs were labeled with Cy5.5, a NIR fluorescent dye, so as to visualize the effect of NP size on biodistribution *in vivo*. Figure 1B shows real-time images of differently-sized PPHAuNCs-TNCs in BEL-7402 tumor-bearing nude mice. Notably, the fast tumor accumulation of PPHAuNCs-30-TNCs was clearly observed at 0.5 h and approached saturation at 6 h post-injection. For the PPHAuNCs-30-TNC group, sustainable maintenance of the relatively high fluorescence density was found at the tumor site at 24 h, which was similar to the PPHAuNCs-50-TNC group. However, slower and less tumor accumulation was observed for the PPHAuNCs-50-TNC group than for the PPHAuNCs-30-TNC group. In addition, no obvious fluorescence signals were detected at the tumor site 24 h after injection in the PPHAuNCs-70-TNC and naked Cy5.5-labeled miRNA groups. This was likely due to the accumulation at the tumor site being too weak to be examined or its rapid clearance from the body. The different biodistribution profiles of the three NPs clearly indicated that NP accumulation in the tumor could be ascribed to not only the EPR effect but also diffusion, which largely relied upon the morphology, dimensions, and surface charges of the NPs and the physicochemical properties of the interstitial matrix. The above results confirmed that the PPHAuNCs-30-TNCs and PPHAuNCs-50-TNCs efficiently delivered miRNAs into the tumor.

Abraxane is the trade name of paclitaxel (PTX)-loaded human serum albumin (HSA) NPs, which is an example of clinical success of nanomedicine against cancer (Ma and Mumper, 2013). HSA is usually applied to encapsulate certain therapeutic drugs to promote their biocompatibility (Desai, 2016). Wang et al. (2016a) constructed a targeted agent by employing PTX and AIEgens for cancer imaging and therapy. The theranostic nanoplatform included four elements: (1) AIEgens conjugated with HSA for imaging; (2) cyclic arginine-glycine-aspartic acid (cRGD)-modified HSA for specific recognition; (3) HSA-functionalized polypyrrole (PPy) for thermotherapy; (4) PTX as a chemotherapy agent and mediating the protein assembly. Firstly, HSA-AIEgens was synthesized by introducing AIEgens into a hydrophobic pocket of HSA, which endowed AIEgens with strong fluorescence. Notably, due to the superb features of AIEgens, the final product exhibited strong fluorescence intensity even after conjugation with quencher-PPy. Next, the imaging performance of the AIEgens-based nanoplatform was investigated to assess tumor treatment efficacy in mice. With intravenous injection for about 1 h, AIEgens fluorescences were observed in the whole bodies of the mice, which were associated with the large amounts of NPs in blood. Thereafter,

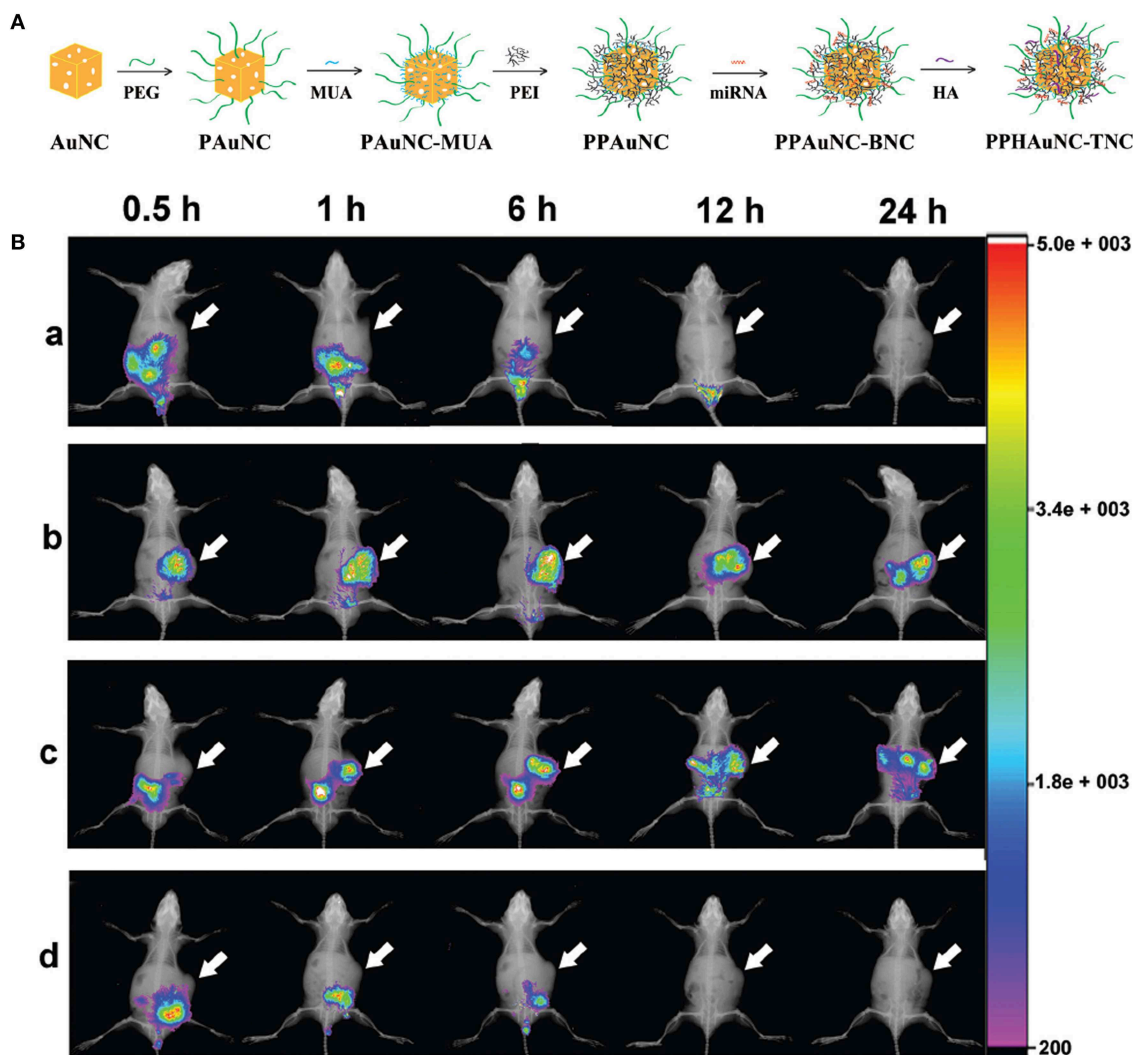


FIGURE 1 | (A) Formation of PPHAuNC-TNC. **(B)** *in vivo* biodistribution of differently-sized PPHAuNCs-TNCs. After intravenous injection with (a) naked Cy5.5-miRNAs (control group), (b) PPHAuNCs-30-TNCs, (c) PPHAuNCs-50-TNCs, and (d) PPHAuNCs-70-TNCs.

the nanoagent showed elevated accumulation in tumors with enhanced fluorescence vs. time, which verified its ability to target tumors specifically. Also, the fluorescence of the nanoagent in mice still remained strong after injection for 48 h, which indicated the superior performance of AIEgens in bioimaging and their superb long-lasting retention *in vivo*.

Persistent Luminescence Imaging

Persistent luminescence is the phenomenon whereby luminescence lasts for several seconds to even days after switching off the excitation source. Generally, two types of active centers, i.e., traps and emitters, contribute to the generation of persistent luminescence. Intrinsic lattice defects or codopants in the host material act as the traps, which are just a few electron volts (eV) below the conduction bands. The emitters are usually lanthanide or transition metal ions. The emergence of persistent luminescence covers four consecutive processes: the formation of

charge carriers, trapping of charge carriers, release of the trapped charge carriers, and recombination of the released charge carriers to generate emission.

$\text{ZnGa}_2\text{O}_4:\text{Cr}^{3+}$ is gaining considerable attention because of its strong NIR persistent luminescence upon UV excitation (Bessiere et al., 2011). Maldiney et al. (2014a) introduced the new generation of $\text{ZnGa}_2\text{O}_4:\text{Cr}^{3+}$ nanoprobe whose persistent luminescence could be directly charged *in vivo* by incident light with deep penetration and low energy. Low-temperature sintering was adopted to prepare the nanoprobe. The excitation spectrum of n-ZGO photoluminescence showed a broad spectral range from ultraviolet to red light containing four bands (Figure 2A, solid black line). The bands at 245, 290, and 425–560 nm corresponded to an exciton energy higher than the bandgap of ZnGa_2O_4 , interband excitation, and Cr^{3+} d-d transitions, respectively. The $^4A_2 \rightarrow ^4T_2$ absorption band was partly ascribed to weaker absorption of tissue domains

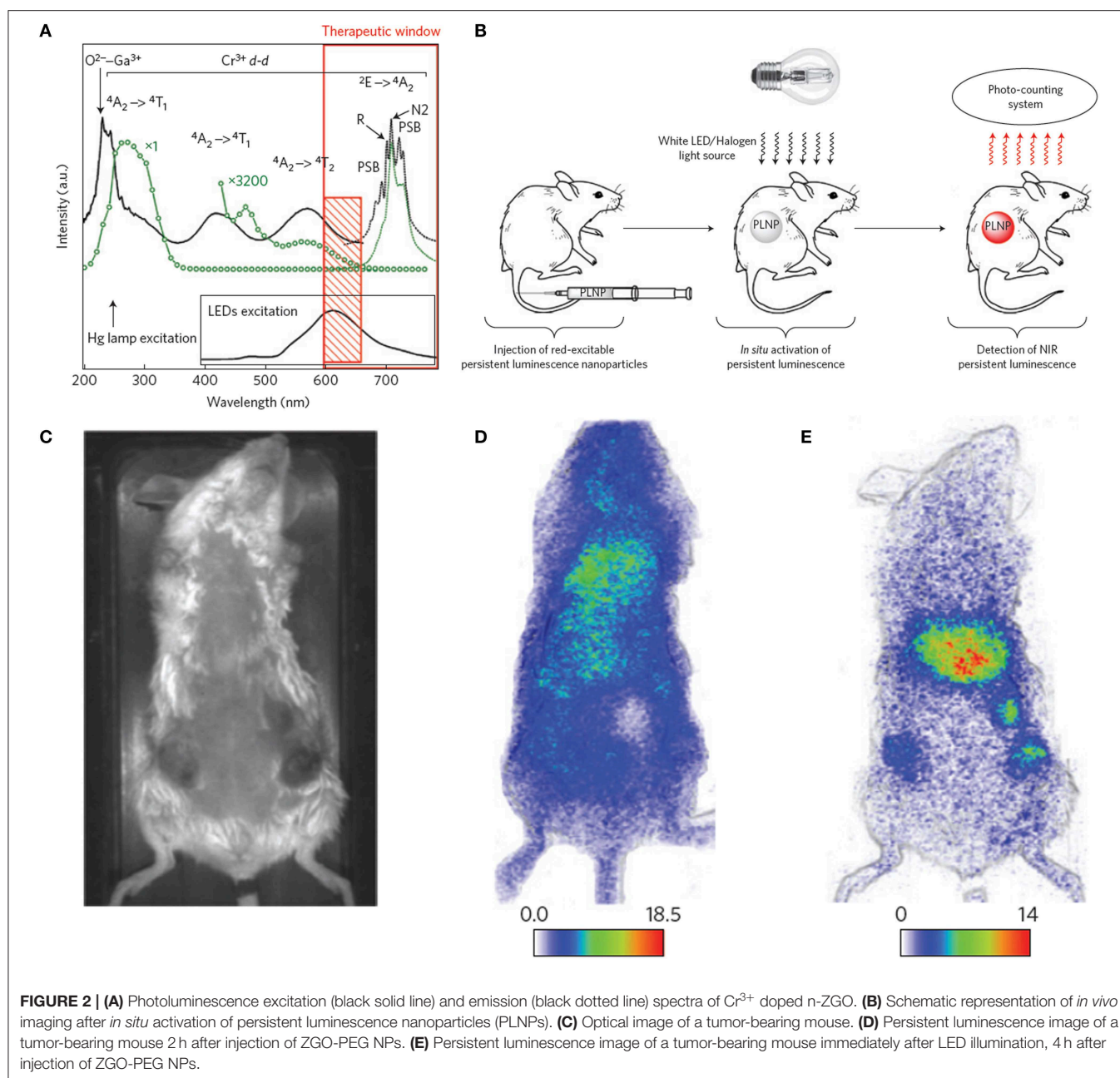


FIGURE 2 | (A) Photoluminescence excitation (black solid line) and emission (black dotted line) spectra of Cr^{3+} doped n-ZGO. **(B)** Schematic representation of *in vivo* imaging after *in situ* activation of persistent luminescence nanoparticles (PLNPs). **(C)** Optical image of a tumor-bearing mouse. **(D)** Persistent luminescence image of a tumor-bearing mouse 2 h after injection of ZGO-PEG NPs. **(E)** Persistent luminescence image of a tumor-bearing mouse immediately after LED illumination, 4 h after injection of ZGO-PEG NPs.

(red rectangle, **Figure 2A**). The n-ZGO PL emission (**Figure 2A**, dotted black line) consisted of the $2E \rightarrow 4A_2$ bandgap of Cr^{3+} . The mechanism for $\text{ZnGa}_2\text{O}_4:\text{Cr}^{3+}$ persistent luminescence under visible light was related to antisite defects around the Cr^{3+} ion. Then, $\text{ZnGa}_2\text{O}_4:\text{Cr}^{3+}$ nanoprobles were directly injected into mice without preliminary activation (**Figure 2B**). In the first 2 h, there was no difference in the biodistribution between tumor-bearing and healthy mice (**Figures 2C,D**). However, persistent luminescence images of tumor-bearing mice clearly showed the tumors 4 h after PEGylated ZGO administration and following visible activation using the orange/red LED source (**Figure 2E**).

Unfortunately, the persistent luminescence peak (around 700 nm) of $\text{ZnGa}_2\text{O}_4:\text{Cr}^{3+}$ made it difficult to use for deep tissue imaging. Also, the emissions of Near-infrared persistent luminescence NPs (NPLNPs) quickly decays over time, leading to lower SNRs. Therefore, superior nanoprobles with higher SNRs are urgently needed for bioimaging. Shi et al. (2018) fabricated a desirable NPLNP, $\text{mSiO}_2@\text{Gd}_3-\text{Ga}_5\text{O}_{12}:\text{Cr}^{3+},\text{Nd}^{3+}$ ($\text{mSiO}_2@\text{GGO}$), for bioimaging and cancer treatment. The $\text{mSiO}_2@\text{GGO}$ NPs showed an intense emission at 745 nm using 254-nm excitation. The NIR emission was ascribed to the Cr^{3+} spin-allowed $4T_2/4A_2$ transition. The 258-nm excitation band was attributed to the GGO host absorption. After the

nanoprobes were injected into mice, their luminescence signals were detected throughout the body in 5 min. An intensive luminescence was observed in the liver due to nanoprobes captured by the reticuloendothelial system (RES). The signal intensities of the nanoprobes were even still maintained in the liver after 60 min. This suggested that the nanoprobes could achieve long-duration imaging *in vivo* using their NIR-I luminescence. Also, the $\text{mSiO}_2@\text{GGO}$ NPs could realize 2-cm tissue imaging with high SNR (≈ 5.5). Three main emission peaks were detected at 888, 1,067, and 1,338 nm, corresponding to the electronic transitions of Nd^{3+} from the excitation level $^4\text{F}_{3/2}$ to the bottom states $^4\text{I}_{9/2}$, $^4\text{I}_{11/2}$, and $^4\text{I}_{13/2}$ with 808-nm irradiation, respectively. Among them, the emission peak at 1067 nm was predominant, demonstrating high NIR-II emission efficiency. After the nanoprobes were subcutaneously injected into the abdomens of mice, a remarkable NIR-II luminescence signal was detected at the injection site, while negligible intensity was determined at other abdomen areas, suggesting that the nanoprobes can be applied for *in vivo* imaging in the NIR-II region.

PLNPs have gained more attention in deep-tissue bioimaging due to their emission in the NIR region, lack of *in-situ* excitation, and high SNR (de Chermont et al., 2007; Abdulkayum et al., 2013). In particular, Cr^{3+} -doped PLNPs can produce renewable persistent luminescence under tissue-penetrating LED light, which indicates that the imaging performance of PLNPs is no longer restricted by the light-emitting lifetime (Li et al., 2015a). Chen et al. (2016b) fabricated a novel luminescence probe for bioimaging by combining PLNPs and metallic sulfide. The nanoprobe is attractive due to its ultrasensitive switch-on imaging response to targeted recognition. The PLNP, $\text{Zn}_{1.1}\text{Ga}_{1.8}\text{Ge}_{0.1}\text{O}_4:\text{Cr}^{3+}$, served as the light source due to its renewable persistent luminescence. CuS NP is not only as a PTT agent but also serves as a quenching agent for photothermal conversion and NIR absorption. A peptide catalyzed by matrix metalloproteinase (MMP) was introduced to construct the nanoprobe. Further modification with mercapto-PEG and polypeptide endows the nanoprobe with desirable biocompatibility and tumor specificity. To evaluate the activation performance of the nanoprobe, it was intravenously injected into mice after being treated by UV light for 10 min. Remarkable luminescence was clearly detected at the tumor site of mice for about 2 h, showing efficient MMP activation and the superior tumor-targeting recognition of the probe.

Some PLNPs consisting of host nanomaterials and codopants have been extensively investigated; please see details in **Table 1** (Liu et al., 2019a).

Near-Infrared Surface-Enhanced Raman Scattering (NIR SERS) Imaging

NIR optical nanoprobes have received increasing attention as multimodal therapeutic reagents for bioimaging and photothermal tumor elimination. For optical imaging, SERS has emerged as an attractive method with intense signal response and good specificity (Gandra and Singamaneni, 2013; Zhang et al., 2018). A narrow bandwidth, high resistance to

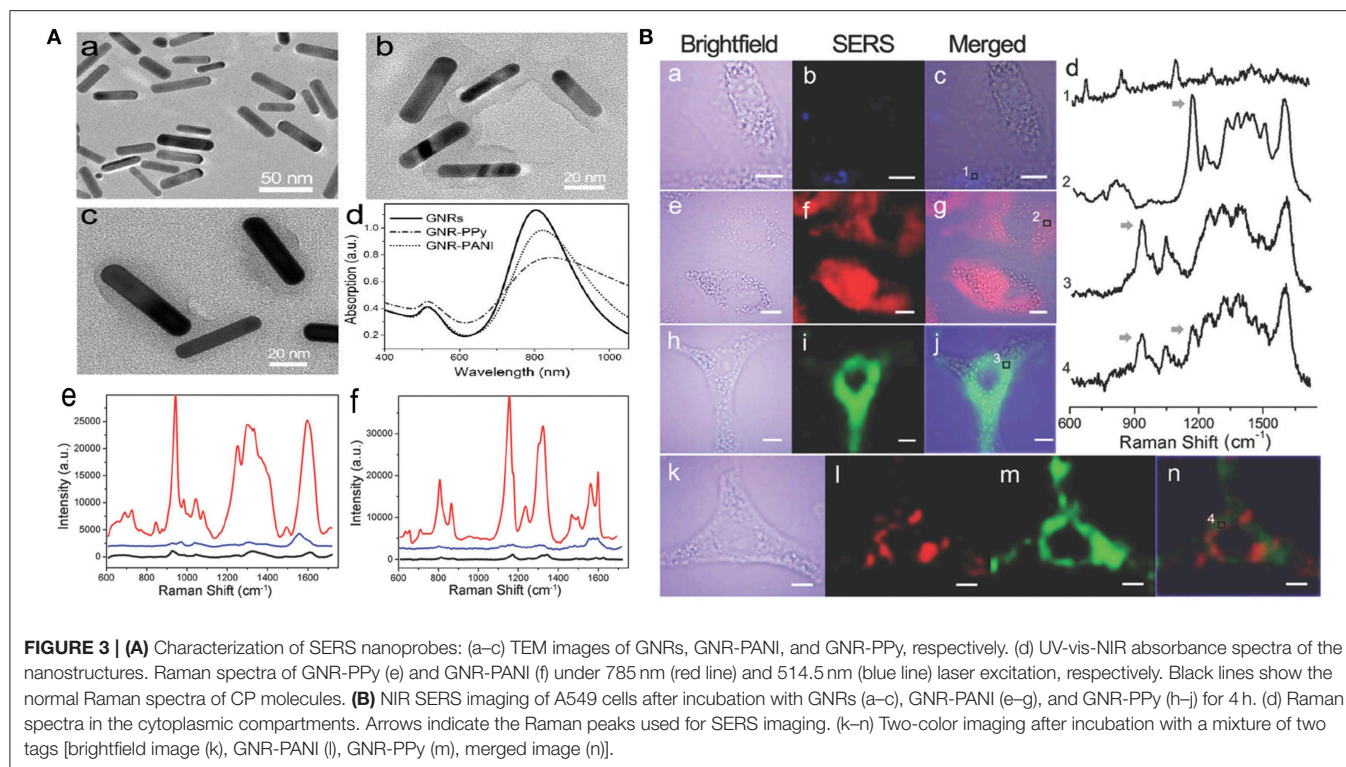
photobleaching, and autofluorescence make SERS an effective tool for non-invasive single-cell assay, rapid disease diagnosis, and nanomedical imaging (Maiti et al., 2012; Guerrini et al., 2017). Three parts, including a noble metal matrix, Raman active reporters, and a biocompatible surface coating, constitute a typical NIR SERS nanoprobe.

The NIR SERS probe is usually prepared through direct modification of a reporter molecule (e.g., a dye) onto the metal surface. However, the electrostatic force-based metal-dye framework leads to structural instability, particularly in physiological environments (Wang et al., 2013b). Strong cytotoxicity is another defect that limits the uses of dye-based SERS probes in nanomedicine. Outer covering with hydrophilic thiolated polyethylene glycol (PEG-SH) can evidently improve the biocompatibility of the metal-dye system. However, competitive binding of polymer and dye reporter with the noble metal can reduce the SERS signal intensity of probes. Also, this kind of PEG-based modification is unsuitable for PTT owing to its labile steric conformation, which is subject to morphological change (melting) upon high-power NIR irradiation (Wang et al., 2012). Liu et al. (2015d) developed environmentally friendly NIR SERS nanoprobes instead of using highly toxic organic dyes. Multifunctional conducting polymer (CP), acting as an outer modification layer and Raman-active molecule, was immobilized on the surface of gold nanorods (GNRs). The GNR-CP nanostructure was separately fabricated through oxidatively chemical polymerization, utilizing two different combinations of monomer and oxidant, namely pyrrole/ FeCl_3 and aniline/ $(\text{NH}_4)_2\text{S}_2\text{O}_8$. Rod-shaped GNRs were synthesized with average dimensions of 42.3 ± 6.9 nm long and 9.6 ± 1.4 nm wide (**Figure 3A**). Such nanoparticles are considered to have an EPR effect and long-term retention in tumors. The UV-vis-NIR absorption spectra of GNRs showed a transverse and a longitudinal SPR peak at around 515 and 800 nm, respectively. **Figure 3Ab,c** show different constructions of two probes, GNR-polyaniline(PANI) and GNR-polypyrrole(PPy). Remarkable shifts toward longer wavelengths and reductions in absorbances were observed in the absorption curves of GNR-CPs (**Figure 3Ad**). The SERS fingerprints of the nanoprobes were dependent on excitation light source. Negligible SERS signal were detected as the probes were illuminated with 514.5 nm light. In comparison, very strong SERS signals appeared upon 785 nm excitation. The strongest peaks were located at 945 cm^{-1} for GNR-PPy and $1,170\text{ cm}^{-1}$ for GNR-PANI (**Figure 3Ae,f**), which were ascribed to in-plane distortion and bending vibrations of C-H in the quinoid group, respectively.

A549 cells exposed with the probe were investigated by utilizing the above NIR SERS imaging. After cell exposure to GNRs, the SERS images exhibited a very weak response from cellular elements in the $600\text{--}1,700\text{ cm}^{-1}$ range (**Figure 3Ba-c**). However, distinct SERS signals were obtained from cells exposed to GNR-PANI (**Figure 3Be-g**) or GNR-PPy (**Figure 3Bh-j**). The results demonstrated that the probes were mainly distributed in the cytoplasm. The characteristic signals from the cytoplasm were detected clearly in the SERS spectra (**Figure 3Bd**), displaying the availability of SERS probes in the sophisticated cellular environment. Moreover, cancer cells were cotreated with the two

TABLE 1 | Persistent luminescence NPs for bio-imaging and therapy.

Hosts	Dopants	Comments and applications in bio-imaging	References
Gd ₂ O ₂ S	Eu ³⁺ , Mg ²⁺ , Ti ⁴⁺	Regular NP shape, bimodality optical/MRI	Rosticher et al., 2015
Ca ₃ (PO ₄) ₂ /hydroxyapatite	Mn ²⁺ , Tb ³⁺ , Dy ³⁺	Fully biocompatible, NPs and <i>in vivo</i> imaging	Rosticher et al., 2015
Ca ₂ Si ₅ N ₈	Eu ²⁺ , Tm ³⁺	Bioimaging applications	Maldiney et al., 2012
SrAl ₂ O ₄	Eu ²⁺ , Dy ³⁺	NPs, functionalization, Bioimaging applications, green emission	Zeng et al., 2018
Ca _{0.2} Zn _{0.9} Mg _{0.9} Si ₂ O ₆	Mn ²⁺ , Eu ²⁺ , Dy ³⁺	NPs, functionalization, pioneer work for bio-imaging: cancer cells imaging, cell targeting	de Chermon et al., 2007
Ca _{1.86} Mg _{0.14} ZnSi ₂ O ₇	Eu ²⁺ , Dy ³⁺	FRET and various bio-sensing applications	Sun et al., 2018
CaMgSi ₂ O ₆	Mn ²⁺ , Eu ²⁺ , Pr ³⁺	NPs, functionalization, bio-imaging	Maldiney et al., 2011
MAIO ₃ (M = La, Gd)	Mn ⁴⁺ /Ge ⁴⁺	Bio-imaging in pork tissue	Liu et al., 2016
GdAlO ₃	Mn ⁴⁺ , Ge ⁴⁺ , Au	Trimodality imaging	Liu et al., 2016
	Sm ³⁺ , Cr ³⁺	Optical and magnetic dual mode imaging	Li et al., 2018b
ZnGa ₂ O ₄	Cr ³⁺	NPs, functionalization, bio-imaging (cancer cells imaging), Cell targeting, cytotoxicity, visible Light NIR photostimulation X-rays activation Oral administration Breast cancer imaging Toxicology analysis Probiotic analysis	Maldiney et al., 2014a Xue et al., 2017; Liu et al., 2018a Ramirez-Garcia et al., 2017; Liu et al., 2017
ZnGa ₂ O ₄ in hollow cavity	Cr ³⁺	Photodynamic therapies	Wang et al., 2018
ZnGa ₂ O ₄	Cr ³⁺ , Gd ³⁺	NPs, functionalization, bimodality optical/NMR imaging	Maldiney et al., 2015
ZnGa ₂ O ₄ /SiO ₂	Cr ³⁺	Core-shell structure, drug delivery	Maldiney et al., 2014b
ZnGa ₂ O ₄ /Fe ₂ O ₃	Cr ³⁺	Cell labeling and magnetic vectorization	Teston et al., 2018
ZGOCS@m-SiO ₂ @Gd ₂ O ₃	Cr ³⁺	Multimodal nanoprobes	Zou et al., 2017
Zn _{1.1} Ga _{1.8} Ge _{0.1} O ₄ /SiO ₂	Cr ³⁺ , Eu ³⁺	NPs, core-shell structure, drug delivery	Shi et al., 2015a
Zn ₃ Ga ₂ Ge ₂ O ₁₀	Cr ³⁺	Imaging of pork tissue, Photostimulation, cytotoxicity	Li et al., 2014a
Zn _{1.1} Ga _{1.8} Ge _{0.1} O ₄ @SiO ₂	Cr ³⁺	Bio-imaging and drug delivery	Liu et al., 2018b
Zn _{1.25} Ga _{1.5} Ge _{0.25} O ₄	Cr ³⁺ , Yb ³⁺ , Er ³⁺	Metastasis tracking and chemo-photodynamic therapy	Li et al., 2018c
Zn _{1.1} Ga _{1.8} Ge _{0.1} O ₄	Cr ³⁺	Nanothermometry	Yang et al., 2017a
Zn ₃ Ga ₂ Sn ₁ O ₁₀	Cr ³⁺	Imaging of goldfish	Li et al., 2014b
Zn _{2.94} Ga _{1.96} Ge ₂ O ₁₀	Cr ³⁺ , Pr ³⁺	NPs, functionalization	Abdukayum et al., 2013
Zn ₃ Ga ₂ Ge ₂ O ₁₀	Cr ³⁺	Recognition of breast cancer cells	Li et al., 2015b
Zn ₃ Ga ₂ GeO ₈	Cr ³⁺ , Yb ³⁺ , Er ³⁺	Upconversion	Liu et al., 2014b
LiGa ₅ O ₈	Cr ³⁺ /PEG-OCH ₃	NPs, functionalization, bio-imaging, Visible light stimulation, photostimulation	Liu et al., 2013; Fu et al., 2014
Ca ₃ Ga ₂ Ge ₃ O ₁₂	Cr ³⁺ , Yb ³⁺ , Tm ³⁺ , Pr ³⁺ , Yb ³⁺	NIR stimulation, upconversion <i>in vivo</i> imaging	Chen et al., 2014; Dai et al., 2017
m-SiO ₂ @Gd ₃ Ga ₅ O ₁₂	Cr ³⁺ , Nd ³⁺	Multimodal imaging and cancer therapy	Shi et al., 2018
Sr ₂ SnO ₄	Nd ³⁺	Finger image	Kamimura et al., 2014
SiO ₂ /CaMgSi ₂ O ₆	Eu ²⁺ , Pr ³⁺ , Mn ²⁺	Bio-imaging, intraperitoneal injection Photostimulation imaging of pork tissue	Li et al., 2014c
Y ₃ Al ₂ Ga ₃ O ₁₂	Er ³⁺ , Cr ³⁺	Imaging in the second biological window	Xu et al., 2018b
NaYF ₄ + SrAl ₂ O ₄	Yb ³⁺ , Tm ³⁺ , Eu ²⁺ , Dy ³⁺	Upconversion & photodynamic therapy	Hu et al., 2018b
Sr ₂ MgSi ₂ O ₇	Eu ²⁺ /Yb ³⁺ , Dy ³⁺	Photodynamic activation Visualization of abdominal inflammation	Homayoni et al., 2016 Yu et al., 2018
La ₃ Ga ₅ GeO ₁₄ @SiO ₂ @Van (vancomycin)	Cr ³⁺ , Zn ²⁺	Bio-imaging-guided <i>in vivo</i> & drug delivery	Zhan et al., 2018
CaTiO ₃	Pr ³⁺ , Yb ³⁺ , Tm ³⁺	Upconverting and guided photothermal therapy	Zhao et al., 2017
ZnSn ₂ O ₄	Cr ³⁺ , Eu ³⁺	Cellular and deep tissue imaging	Li et al., 2017a
Sr ₃ Sn ₂ O ₇	Nd ³⁺	Second window imaging	Kamimura et al., 2017



probes. **Figure 3B** shows SERS images of the probes and the individual response distribution in cells. Notably, each mapping was separate, which was attributed to the narrow bandwidth of the Raman peaks.

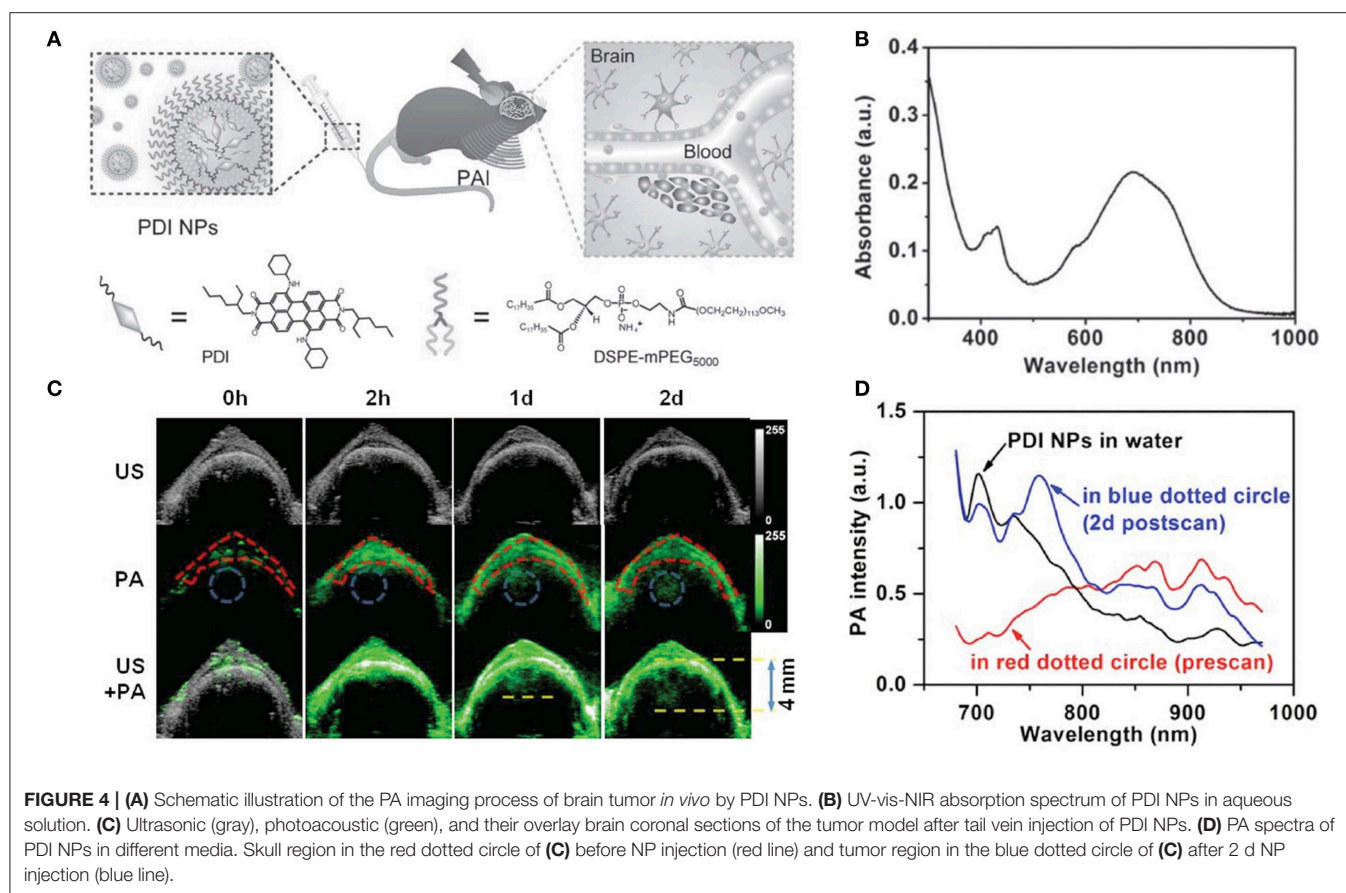
Silver bumpy nanoshell (AgNS) has been explored as a highly active NIR SERS nanoprobe for the biomedical field (Premasiri et al., 2018). AgNS has intense scattering in the NIR-region, where its SERS enhancement factor is higher than those of gold nanorods or nanospheres. Also, AgNS has strong NIR absorption, which is useful for PA imaging. Additionally, AgNS does not induce any *in vivo* toxicity, as confirmed by cytotoxicity tests (Baumberg et al., 2017). Cha et al. (2017) demonstrated dual-modal detection of sentinel lymph nodes (SLNs) using a silica-coated silver bumpy nanoshell probe (AgNS@SiO₂): imaging the SLN with a PA signal and *in vivo* multiplex identification of targets in the located region with SERS. Using the correctional Stöber approach, the surface of AgNS was covered by silica-shell and finally treated with bovine serum albumin (BSA) to enhance biocompatibility. AgNS@SiO₂ possesses some advantages, e.g., high dispersion stability, facile surface modification, and good biocompatibility. PA imaging was adopted to detect the accumulated regions of AgNS@SiO₂, and the SERS signals were analyzed to identify different ratios of several kinds of Raman-labeled AgNS@SiO₂. After three different types of Raman-labeled AgNS@SiO₂ probes were injected into rat's left front paw pad, respectively, their PA and SERS signals were monitored and analyzed to locate the SLN and identify the targeted AgNS@SiO₂. They successfully obtained PA images and SERS spectra using the portable-Raman system with a 785-nm NIR-excited laser. This dual-modal imaging system may

be utilized in diagnostic fields, e.g., multiplex cancer marker detection *in vivo*.

Photoacoustic (PA) Imaging

Photoacoustic (PA) imaging, a new method of visualization via photoacoustic response, has increasing potential in nanomedical fields (Kim et al., 2010). PA imaging has been explored to visualize biostructures from organelles to cells to organs (Wang and Hu, 2012). A contrast agent absorbs the excitation energy and converts it into thermal energy. Thus, a wideband ultrasound emission is produced due to heat-induced transient thermoelastic expansion, which is collected with an acoustic detector and transformed into PA images. PA imaging combines the good specificity of optics and the deep-tissue transmission of ultrasound (US), which overcomes the restrictions of traditional imaging (Nie and Chen, 2014).

Perylene-3,4,9,10-tetracarboxylic diimide (PDI) and its derivatives have been extensively applied to fabricate diverse electronic devices based on their extraordinary physicochemical properties, easy functionalization, and extremely low price (Perrin and Hudhomme, 2011; Birel, 2017). Fan et al. (2015) constructed an efficient PDI-based NIR-absorptive contrast nanoagent enveloped by micelle for PA imaging of deep brain tumor in living mice. To make PDI absorb in the NIR-region, tertiary amine and diimide as donor and acceptor were introduced to fabricate a classical donor- π -acceptor system for increasing redshift efficacy. Water-soluble PDI NPs were prepared by wrapping with amphiphilic PEG derivatives (**Figure 4A**). These PDI NPs displayed strong NIR absorption at around 700 nm in aqueous solution (**Figure 4B**). After 2-h



injection, the PA signal at the skull region (red dotted circle) intensified greatly due to the circulation of PDI NPs in the blood vessel. After 1-d injection, a significant PA signal appeared in the brain tumor region (blue dotted circle) of mice, but no signal was found in the control group. Also, a 4.0-mm depth of the tumor region was more clearly observed after 2-d injection compared with a shallower depth (~ 3.0 mm) after 1-d injection (**Figure 4C**), which was attributed to the enhanced tumor penetration depth of NPs with time. The biodistribution of PDI NPs in brain tumor was verified by measuring PA spectra. Strong PA intensities at 700 and 735 nm (blue line) were clearly observed in the tumor region after 2-d NP injection (**Figure 4D**), which was consistent with the NIR absorption peak of PDI NPs (**Figure 4B**). This indicated the successful accumulation of PDI NPs in the tumor.

Carbon dots (CDs) are promising carbon-based imaging probes due to their excellent biocompatibility, water solubility, and photostability (Yang et al., 2009; Li et al., 2012, 2013). However, the main challenge of CDs for practical application is guaranteeing their biodegradability (Tang et al., 2013; Ge et al., 2015; Jiang et al., 2015). Moreover, the mechanisms of the interaction between CDs and low-energy photons are being investigated to obtain high resolution and contrast for CD optical imaging. Lee et al. (2016) synthesized a biocompatible and N-doped type of CD (N-CDs) for PA imaging. N-CDs

were prepared by solvothermal carbonation using citric acid and HNO_3 as a C and N source. N-CDs showed strong absorption in the NIR region (680–800 nm). N-CDs with high contents of N atoms raised the ambient temperature more quickly upon NIR (680–808 nm) laser irradiation. This was because a high N content produced more bandgaps so that the carrier could be captured from LUMO to a bandgap and relaxed between bandgaps. N-CDs exhibited higher heat conversion efficiency than conventional PA contrast agents (e.g., GNR and methylene blue) under the same optical density. Therefore, N-CDs could produce sufficiently intense PA effects to realize non-invasive imaging and thermal therapy *in vivo*. The researchers carried out time-resolved PA imaging of SLNs of Sprague-Dawley rats and evaluated the biodegradability of N-CDs through renal clearance. The relative PA signal was suddenly enhanced in SLNs 30 min after hypodermic injection of N-CDs and reduced gradually until 180 min. Meanwhile, the PA signal from the bladder area rose intensively at 100 min, suggesting the effective removal of N-CDs to the urine. For tumor PTT, the N-CDs displayed complete tumor ablation without recurrence for Balb/c nude xenograft HepG2 tumor model mice with a tumor volume of 27 mm^3 upon 808-nm NIR laser irradiation. N-CDs, as a kind of NIR-absorbing nanomaterial, will become a potent contrast agent for PA bioimaging and for improving PTT efficacy.

A new type of optical nanoagent, semiconducting polymer NP (SPNP), provides an inspiring strategy for solving the nanotoxicity problem (Li and Pu, 2019). SPNPs with highly conjugated structures exhibit excellent photothermal conversion efficiency and photostability (Li et al., 2018d). Moreover, the molecular versatility of SPNPs is not only beneficial to facile tuning of the spectrum independent of size or morphology but also allows the skeleton or side chain to be easily modified for on-demand functionalization (Feng et al., 2013). Based on these merits, SPNPs have been used as promising PA agents for biomarkers and cancer detection (Lyu and Pu, 2017). Furthermore, preliminary investigation has revealed that SPNPs have the advantage of being degradable NIR-I nanoagents (Lyu et al., 2018). Nevertheless, whether they can perform as biodegradable NIR-II nanoagents has not been explored. Jiang et al. (2019) fabricated metabolizable NIR-II SPNP-based agents for PA imaging. By introducing the strong electron-withdrawing group benzobisthiadiazole, the synthesized SPNPs (SPNP-PT, SPNP-DT, and SPNP-OT) showed strong absorption at 1,079 nm and superior photothermal conversion efficiencies at 1,064 nm. Owing to the oxidizable thiophene group and hydrolyzable PEG-based matrix in their skeletons, three NIR-II SPNPs (~30 nm) could be effectively decomposed into smaller sizes NIR NPs (~1 nm) by myeloperoxidase or lipase with high abundance *in vivo*. Further, the SPNPs were completely eliminated in 15 days through renal or hepatobiliary metabolism in living mice. Especially, SPNP-PT demonstrated good SNRs for PA imaging of tumor or brain vasculature in mice under a systematic dosage (2.5 mg kg^{-1}) lower than that of other reported agents ($\geq 10 \text{ mg kg}^{-1}$).

Overall, various nanomaterials have been exquisitely designed for deep-tissue PA imaging. PA contrast agents are mainly categorized into inorganic and organic nanoagents based on their structures (Table 2) (Wang et al., 2016b).

OPTICALLY ACTIVE NANOMEDICINE FOR TARGETED THERAPY AND DRUG DELIVERY

Photodynamic Therapy (PDT)

Photodynamic therapy (PDT) employs photosensitizers (PSs) and light of a specific wavelength in combination with molecular oxygen to generate reactive oxygen species (ROS) that kill cancer cells through the oxidation of important biomolecules and organelles (Zhou et al., 2016a). The introduction of NPs in PSs provides the following advantages: (1) effective PS delivery to the target site, (2) easy phase transfer of hydrophobic PSs into an amphiphilic bloodstream to increase circulation time, (3) use of the EPR effect for the effective diffusion of PSs into tumors, (4) surface modification with various molecules, enhancing the cellular uptake and targeting, and (5) multiple functionality by combining the properties of NPs (e.g., multimodal imaging) with those of PSs (Lucky et al., 2015). A myriad of inorganic and organic nanostructured PSs, e.g., gold NPs (Dykman and Khlebtsov, 2012), metallic oxides (Bechet et al., 2008), carbon-based materials (Albert and Hsu, 2016),

mesoporous silica (Montalti et al., 2014), polymeric micelles (Elsababy et al., 2015), and UCNPs (Wang et al., 2017), have been developed for image-guided PDT therapies (Lan et al., 2019).

Recently, AIE PS, a new family of PSs, has been gaining more attention (Hu et al., 2018a). Owing to the inhibition of non-radiative energy consumption and RIM, AIE PSs exhibit enhanced signal intensity (Alifu et al., 2017) and produce more ROS species in the aggregate state (Gu et al., 2017). These properties of AIE-based PSs make them a better choice for image-guided PDT and tumor-killing (Wu et al., 2017a). However, PSs with NIR emissions and high ROS production still remain to be explored. Wu et al. (2017b) reported the fabrication of a kind of PS TPETCAQ (Figure 5A) with AIE characteristics for NIR image-guided PDT. Encapsulation of TPETCAQ using a DSPE-PEG-MAL matrix and subsequent surface modification with the HIV-1 transactivator were used to obtain the final product, TPETCAQ NPs (Figure 5B). The resultant product exhibited strong fluorescence emission intensity at 820 nm, accompanied by much more $^1\text{O}_2$ production than Ce6, a well-known highly efficient PSs. The bioluminescence of tumor *in vivo* progressively reduced with time, which demonstrated that the nano-PSs were efficient for image-guided PDT. Also, only very faint luminescence signals were detected from the AIE-based PSs after 14 d, suggesting their high PDT efficacy (Figure 5C). The excellent PDT efficacy of the AIE PSs was further confirmed by tumor volume changes for different groups (Figure 5D).

In addition to low toxicity, photobleaching resistance, and deep tissue penetration, UCNPs also have the unique properties of transforming from NIR emission to visible light (Gu et al., 2013; Chan et al., 2015). Notably, the long-lived red emissions from UCNPs overlap partly with the absorptions of some PSs, e.g., ZnPc or Ce6, which offers a valid energy transfer pathway to activate PSs for PDT under NIR irradiation (Idris et al., 2015; Tian et al., 2015). Huang et al. (2016) prepared $\text{Na}_{0.52}\text{YbF}_{3.52}:\text{Er}$ UCNPs with intense red emission using a simple solvothermal approach for multimodal imaging and tumor PDT. A low $[\text{Na}]/[\text{Yb}]$ ratio in UCNPs was found, owing to the lack of elemental Na, which resulted in high luminescence intensity and color purity for red UC emission of Er^{3+} . The UCNPs displayed dominant red and weak green UC emission at 655 and 522/543 nm, which were attributed to the intra-4f transitions of Er^{3+} , $^4\text{F}_{9/2} \rightarrow ^4\text{I}_{15/2}$, and $^2\text{H}_{11/2}/^4\text{S}_{3/2} \rightarrow ^4\text{I}_{15/2}$, respectively. In addition, a thin SrF_2 layer was modified on the UCNPs, and the red UC emission intensity was increased by about 17 times, while a relatively high intensity ratio (~5.8) of Red/Green was still retained. To make them utilizable *in vivo*, the $\text{Na}_{0.52}\text{YbF}_{3.52}:\text{Er}@\text{SrF}_2$ UCNPs were further modified with DSPE-PEG to obtain the final low toxicity product Lipo-UCNPs. Significantly, the PS ZnPc-loaded Lipo-UCNPs exhibited high efficacy in $^1\text{O}_2$ production and cancer cell killing under 915 nm irradiation, avoiding the overheating effect usually resulting from 980 nm excitation. After intratumoral injection of $50 \mu\text{L}$ ZnPc-Lipo-UCNPs (10 mg mL^{-1}) into HeLa tumor-bearing mice, the tumor volumes increased much more slowly, demonstrating the significant tumor growth rate inhibition effect of the

TABLE 2 | Examples of PA contrast agent explored in PA imaging.

Materials		Types of nanoagents	Advantages (+)/Disadvantages (-)	References
Inorganic	Metallic nanomaterials	Au nanorods; Au nanostars; Au nanocages; Au nanoshell; Au nanovesicles; Au nanoflowers; Ag nanoplates; Palladium nanoplates; antimony nanoparticles	(+) tunable physiochemical properties; chemically inert element with reasonable biocompatibility; able to carry cargoes. (-) non-biodegradability; suboptimal photothermal stability	Chen et al., 2015b; Zhong et al., 2015 Wang et al., 2015a Zhang et al., 2013 Topete et al., 2014 Song et al., 2015a Huang et al., 2014a Homan et al., 2012 Nie et al., 2014 Li and Chen, 2015
	Carbon-based nanomaterials	Carbon nanotubes; Graphenes; Carbon dots	(+) able to carry cargoes; good photothermal stability. (-) non-biodegradability; heterogeneity	Zhang et al., 2015 Lalwani et al., 2013; Sheng et al., 2013; Ge et al., 2015
	Transition metal chalcogenides (TMC)-based nanomaterials	CuS; WS ₂ ; MoS ₂ ; FeS; Bi ₂ S ₃ ; CuSe; Co ₉ Se ₈ ; Bi ₂ Se ₃	(+) high photothermal conversion efficiency; good photothermal stability; low cost. (-) non-biodegradability; contain heavy metal elements	Cheng et al., 2014a; Yin et al., 2014 Cui et al., 2015; Yang et al., 2015b Hessel et al., 2011; Liu et al., 2015e Song et al., 2015b
Organic	Dyes	Porphyrin- and Cyanine-based dyes, e.g., Indocyanine green (ICG), IR780, IR825, etc.	(+) good biocompatibility/biodegradability. (-) poor aqueous solubility, low photothermal stability, short bloodstream circulation half-life	Sheng et al., 2014; Wang et al., 2015b Lovell et al., 2011; Song et al., 2015c Huang et al., 2014b; Chen et al., 2015a; Rong et al., 2015
	Polymer-based nanomaterials	Polypyrrole; Polyaniline; Polydopamine; Semiconducting polymers	(+) good biocompatibility and photothermal stability; able to carry cargoes. (-) their biodegradation behaviors remain unknown	Yang et al., 2011; Lin et al., 2014 Yang et al., 2012; Pu et al., 2015

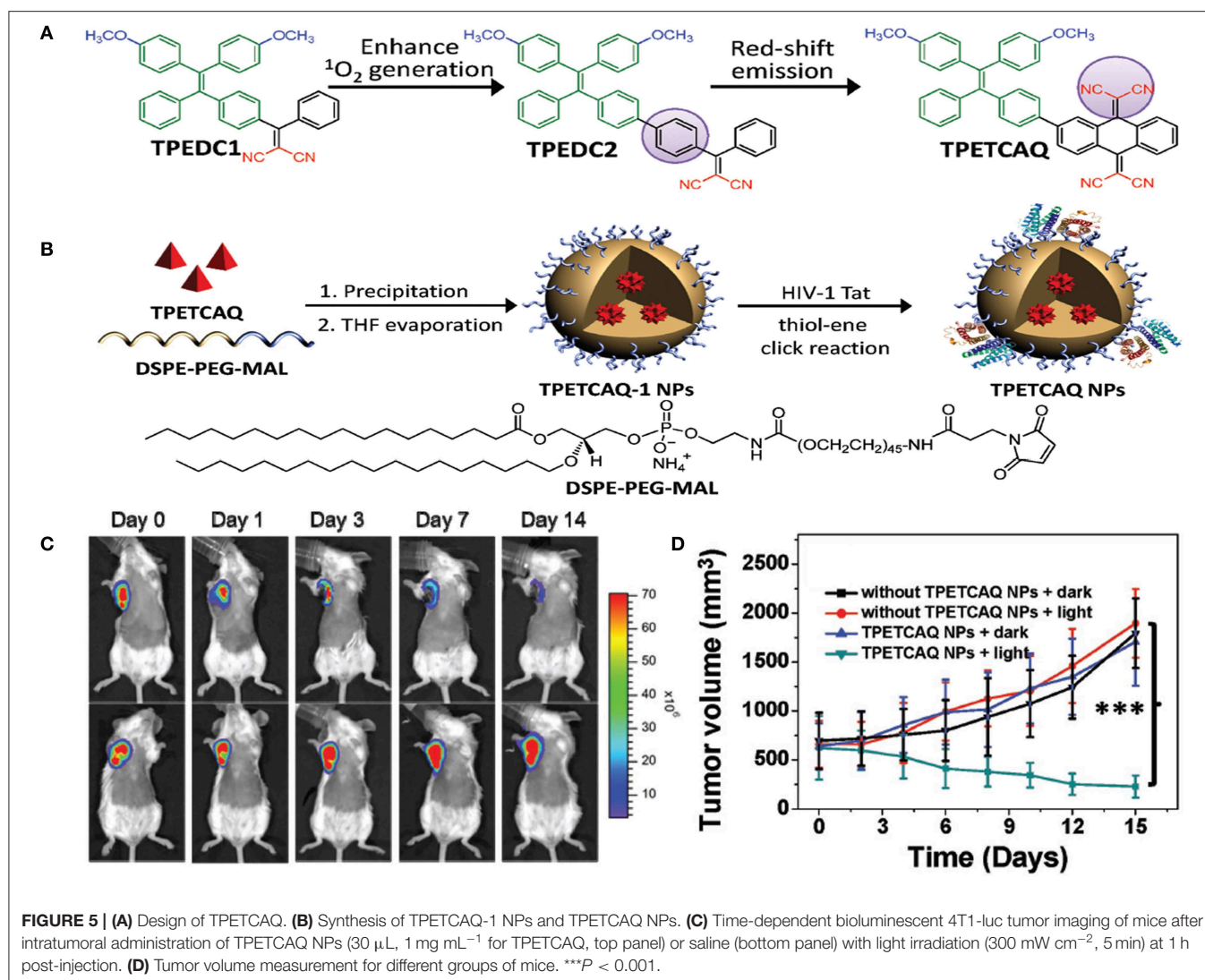
UNCP-based PDT. The results revealed the great potential of UCNP with high-purity red emission for imaging-guided PDT of tumors.

Most PSs for PDT possess poor solubility in water and suboptimal selectivity *in vivo* (Yan et al., 2015). To overcome these limitations, PSs are usually conjugated with nanocarriers with a high surface area, e.g., GO (Yang et al., 2013). Various PSs have been designed to load on the surface of GO via π - π stacking and hydrophobic forces for tumor imaging and PDT in animal models (Rong et al., 2014; Shi et al., 2014). However, most PS-GO nanoconjugates passively targeted to tumors *in vivo* via an EPR effect. Thereby, some tumor-specific molecules (e.g., peptides, ligands, and antibodies) need to be modified onto GO to increase targeting and PDT efficacy (Shi et al., 2015b). Yu et al. (2017) fabricated a PS-loaded GO nanocomplex by conjugating PEGylated GO with a tumor-selective HK peptide that can specifically bind to highly expressed integrin $\alpha\beta 6$ receptor in many tumor types and following functionalization with a PS. The tumor uptake of GO(PS)-PEG-HK was obviously higher than that of free PS and GO(PS)-PEG, demonstrating the specific intake of the nanocomplex in tumors by the recognition of integrin $\alpha\beta 6$. Tumor recurrence, especially lung metastasis, was significantly inhibited in mice for nearly a month by vaccination with necrotic 4T1 tumor cells induced by the nanocomplex PDT. The nanocomplex-treated necrotic tumor cells could activate dendritic cells and significantly

inhibit tumor growth and lung metastasis by increasing the infiltration of cytotoxic CD8⁺ T lymphocytes in tumor. Using the nanocomplex, the primary tumor, and the residual tumor cells could be efficiently killed by activating host anti-tumor immunity and stimulating the immune memory, accordingly prohibiting distant metastasis. These findings suggest that nanocomplex-based PDT is an effective strategy for eliminating residual cells after tumor resection and preventing tumor recurrence and distant metastasis.

Photothermal Therapy (PTT)

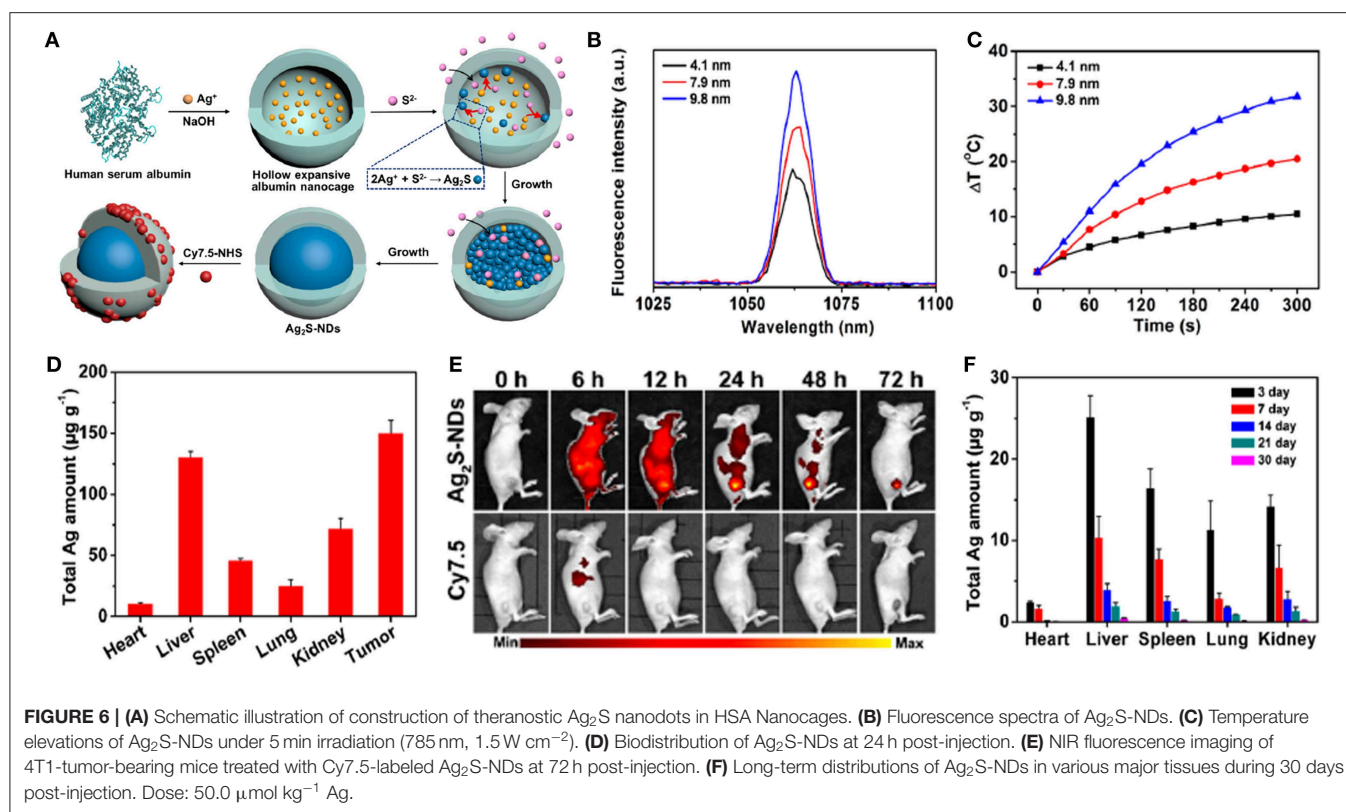
Photothermal therapy (PTT) utilizes the photothermal effect of a photothermal transduction agent (PTA) that can harvest the energy from light and transform that energy into heat to raise the surrounding temperature and induce the death of cancer cells. An ideal PTA should possess high photothermal conversion efficiency (PCE), strong absorption in the NIR region, and good accumulation in tumors without toxic side effects. In particular, nano PTAs can accumulate in tumors through the EPR effect and active targeting. Also, nano PTAs can realize higher PCE than small-molecule PTAs and can potentially be used with multiple imaging modalities and incorporate various therapeutic functions for advanced application (Cheng et al., 2014b). Nano PTAs can be divided into inorganic and organic materials (Gai et al., 2018). Inorganic materials include noble metals (Riley and Day, 2017), metal chalcogenides (Li et al., 2017b), carbon-based



materials (Hong et al., 2015), and other two-dimensional (2D) materials (e.g., black phosphorus, nanosheets, boron nitride, graphitic carbon nitride, MXenes) (Chen et al., 2015c; Augustine et al., 2017; Tan et al., 2017; Choi et al., 2018; Huang et al., 2018). Organic PTAs include semiconducting polymer NPs (SPNPs), nanomicelle-encapsulated NIR dyes, and porphyrins (Jung et al., 2018; Liu et al., 2019b).

Recently, stoichiometric semiconductor metal sulfide nanocrystals (e.g., Ag₂S and CuS) have been developed for optical imaging and PTT due to their strong absorption capacity in the NIR-region, negligible photobleaching, high photoconversion efficiency, ultrasmall size, and good inertia (e.g., the solubility product constant is $K_{sp} = 6.3 \times 10^{-50}$ for Ag₂S) (Hong et al., 2012b). Yang et al. (2017b) designed dimension-dependent Ag₂S nanodots (NDs) as a photothermal agent for PTT and multimodal imaging. These NDs are prepared by finely modulating their growth within clinically acceptable HSA nanocages (Figure 6A). They exhibited a narrow emission band (full-width at half-maximum ~ 8.0 nm) due to

their monodisperse size distribution (Figure 6B). Also, larger NDs showed a higher fluorescence response in the NIR-II range, suggesting that the fluorescence spectrum strongly depended upon their diameters. Ag₂S-NDs also displayed obvious size-dependent temperature elevations (Figure 6C), mainly originating from their size-dependent molar extinction coefficients. Additionally, strong non-radiative energy decay in the conduction band may contribute to the efficient photothermal conversion efficacy of the NDs. The improved circulation and EPR effect of NDs caused them to be mainly distributed into tumor, suggesting their high uptake in tumor (Figure 6D). The NDs showed remarkable fluorescence within tumor at 48 h after injection, whereas the control group displayed a faint signal due to fast elimination of NDs (Figure 6E). These findings indicated that the NDs could be accumulated at the tumor site for a long time, which was beneficial to flexible imaging or PTT. The NDs showed time-dependent uptakes in other tissues, including heart, liver, spleen, lung, and kidney. Moreover, the NDs were progressively excluded from the tissues

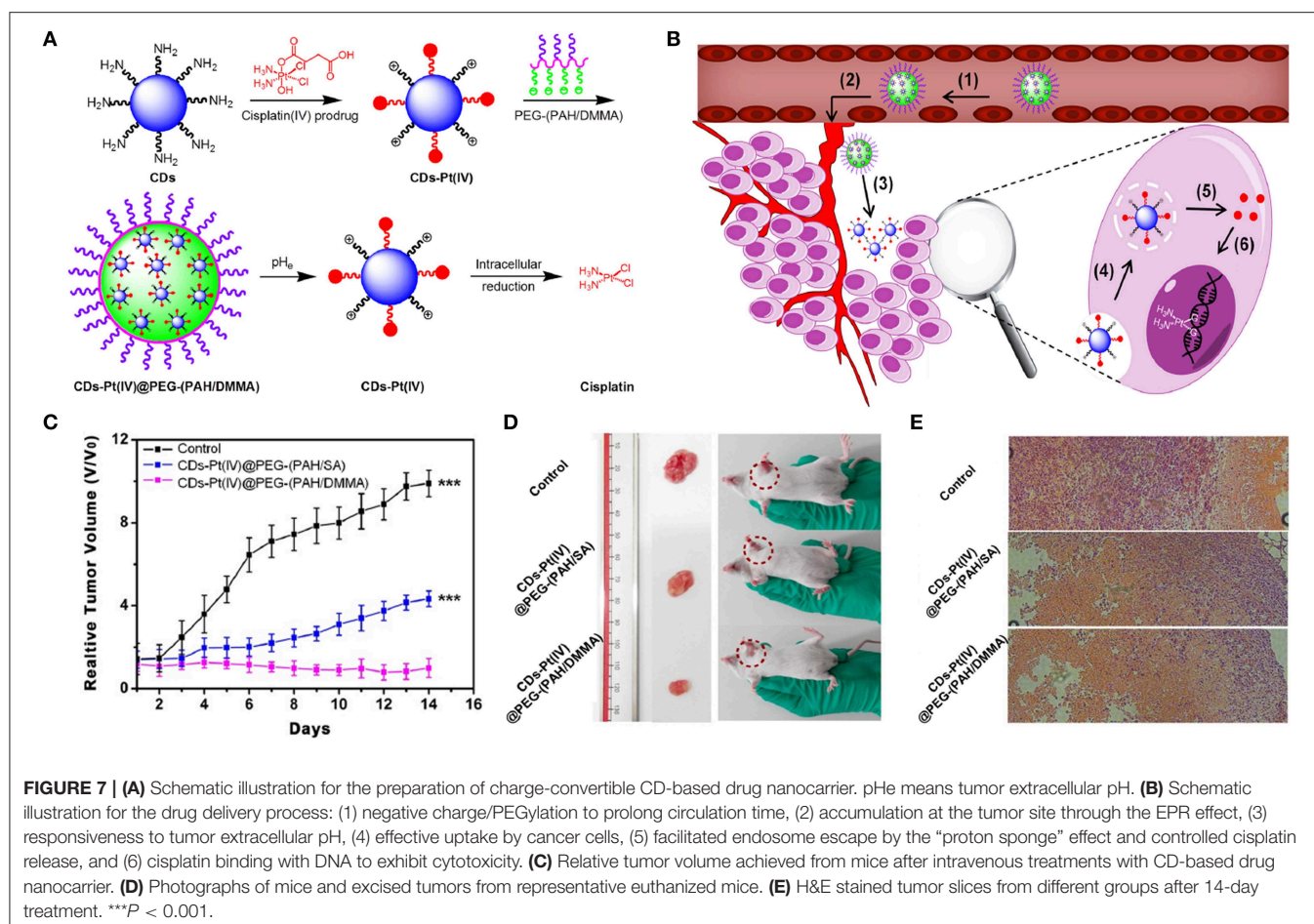


in 30 days via renal excretion (Figure 6F), thus avoiding potential toxicity concerns.

Copper chalcogenide (Cu_{2-n}R, R = S, Se, Te, 0 ≤ n ≤ 1) NPs, which possess strong localized SPRs (LSPRs) in the NIR region due to copper deficiency, have been employed for PA imaging and PTT (Coughlan et al., 2017). Cu_{2-n}R NPs may be much smaller than conventional photothermal agents such as GNPs (typically >50 nm in 1D to generate NIR LSPR). Also, their good biodegradability allows the release of the vital trace elements copper and chalcogen to maintain the health of the organism (for example, selenium or copper deficiency contributes to the incidence and mortality of some cancers [e.g., liver, prostate, and lung]) or the evolution and aggravation of some cardiovascular diseases and diabetes (Zhou et al., 2016b). Monodisperse Cu_{2-n}Se NPs are usually synthesized in organic solvents at high temperature, and they then need laboriously subsequent modification to make them utilizable in biological fields (van der Stam et al., 2015; Yan et al., 2017). Zhang et al. (2016) prepared novel ultrasmall PEGylated Cu_{2-n}Se NP in aqueous solution for multimodal imaging-guided tumor PTT. The Cu_{2-n}Se NPs were synthesized in distilled water and formed by a characteristic dark green solution and were then functionalized with dimercaptosylated PEG to enhance their solubility, dispersity, and biocompatibility after ultrafiltration. The final product displayed strong LSPRs in the NIR region (600–1,100 nm) owing to the high hole density due to copper deficiency. The high extinction coefficient (8.5 Lg⁻¹ cm⁻¹) of the PEGylated Cu_{2-n}Se NPs at 808 nm reflected a distinct

photothermal conversion capability. Also, the NPs showed good photothermal stability and long-term circulation with a half-life of 8.14 h owing to the presence of water-soluble and large sterically hindered PEG. After intravenous injection of the PEGylated Cu_{2-n}Se NPs into BALB/c mice bearing 4T1 tumors (130 mm³ volume), the tumor temperature of the mice rose steeply to 57.6°C during NIR irradiation, which was high enough to kill the cancer cells and to halt their lethal proliferation. The tumors shrank and became black scars at day 3 and were removed totally in 16 d without recurrence. These NPs might become an effective PTT agent for *in vivo* tumor therapy.

Nanodiamonds (NDDs) with diameters of 2–10 nm and a truncated octahedral framework have appeared as innovative materials for bioimaging and therapy due to their good biocompatibility, spherical morphology, high density, large surface area, and surface functionality (Mochalin et al., 2011). Ryu et al. (2016) designed folic acid (FA)-conjugated NDD (FA-NDD) nanoclusters by using the unique features of NDDs for PTT. FA was selected as a model targeting ligand for tumor and receptor-mediated endocytosis since its receptors are generally overexpressed in some types of tumor cells. Their spherical morphology and good biocompatibility enabled NDDs to act as a nanoplatform for delivery systems. Amination of NDD nanoclusters with -COOH via 1,2-ethylenediamine and subsequent modification with FA by carbodiimide chemistry were performed. After 5-min laser irradiation, the temperature of NDD (10 μg mL⁻¹) rose to 54°C. Compared with WI-38 cells (negative control), FA-NDD nanoclusters easily entered the KB



cells (positive control), indicating specificity to tumor cells that overexpress FA receptors. Cell viability assay and fluorescence microscopic imaging clearly showed that FA-NDD preferred to ablate KB cells selectively rather than WI-38 cells under NIR laser illumination. For tumor-bearing nude mice, a substantial accumulation of FA-NDD in tumor led to a significant decrease in tumor volume, and almost absent 14 d after NIR laser exposure as compared to NDD nanoclusters. These results clearly verified that the combination of the FA-NDD nanoclusters and NIR light might be an efficient and feasible tumor therapy.

Optical-Responsive Drug Delivery

The effective delivery and release of drugs to targets remains a great challenge to improving therapies for human diseases (Devadasu et al., 2013). A recognized strategy is to construct a target-specific drug delivery system (DDS) that can carry an efficient dosage of the drug to targeted cells and tissues (Wong and Choi, 2015). An ideal stimuli-responsive DDS should possess the following features: biocompatible or biodegradable composition, high drug-loading capacity, a site-specific delivery mechanism to spare normal cells and tissues, no premature drug release, and accurate release in response to exogenous or endogenous stimulus (Karimi et al., 2016; Liang et al., 2016). Various nanocarriers such as liposomes (Grimaldi et al., 2016),

polymers (Nicolas et al., 2013; Tong et al., 2014), micelles (Cabral et al., 2018), dendrimers (Astruc et al., 2010), silica (Wen et al., 2017), gold NPs (Arvizo et al., 2012), black phosphorus (Qiu et al., 2019), and carbon-based nanomaterials (Panwar et al., 2019) have been developed for medical purposes. Robust and effective nanocarriers could even be responsive to multiplex combinations of diverse stimuli to further strengthen their specificity for targeted and controlled drug delivery (Biju, 2014).

CDs can serve as imaging probes or as nanocarriers for transporting the targeted theranostic agents (e.g., PSs, drugs, genes) (Boakye-Yiadom et al., 2019). The surfaces of CDs, as the drug nanocarriers, are usually modified by negatively or positively charged PEG, which affects their therapeutic efficacy and future biological application. Owing to electrostatic repulsion from the same-charged cell membrane, negatively charged PEGylated CDs nanocarriers cannot easily enter the cancer cells, which affects intake and ultimately leads to low curative effects. Due to non-specific interactions with cellular ingredients (e.g., serum), positively charged CD carriers can be easily endocytosed through RES, resulting in quick clearance from blood circulation. Also, positively charged nanocarriers can be phagocytized by healthy cells to produce some potential toxicity via charge attraction with cell

membrane (Mishra et al., 2018). To solve the above-mentioned problems, Feng et al. (2016) developed a cisplatin-loaded charge convertible CD nanocarrier functionalized by poly-(allyamine)-modified PEG, which could sensitively distinguish the pH difference between tumor pathologic outcomes and the normal physiological environment for controllable drug delivery (**Figure 7A**). The anionic poly-(allyamine)-modified PEG polymer with dimethylmaleic acid on the constructed CD nanocarrier would experience a charge transformation into the cationic polymer under the mild acidity of tumor cells (pH \sim 6.8), resulting in intense electrostatic repulsion and “leakage” of cisplatin(IV)-CD cations. Significantly, positive cisplatin(IV)-CDs showed high affinity for negative cancer cell membrane, thus leading to the enhancement of internalization and efficient release of drug in the reductive cytosol (**Figure 7B**). Tumors growth in mice injected with the drug-loaded CDs were greatly suppressed during 14 days of treatment (**Figure 7C**). The digital images of tumor excision in mice further confirmed that the sizes of the tumors were smallest using the drug-loaded CDs, indicating their better treatment efficiency (**Figure 7D**). Also, through hematoxylin and eosin (H&E) staining analysis of tumor tissues (**Figure 7E**), the drug-loaded CD treatment groups exhibited the greatest degree of cell injury, which was consistent with the tumor growth data.

Zinc gallogermanate structured PLNPs have demonstrated superior physiochemical properties, e.g., a strong NIR signal (quantum yield \sim 10%), superlong optical lifetime (>90 h), monodisperse stability, and minimal poisoning (Abdukayum et al., 2013). The superlong sustained emission and red light renewability of the trivalence-doped zinc gallogermanate PLNPs (ZGGO:Cr³⁺, Yb³⁺, Er³⁺) are the principal basis for long circulation bioimaging and drug release in living organisms (Li and Yan, 2016). Also, the easily controllable surface modulation of ZGGO PLNPs makes them desirable alternatives for fabricating the drug carriers. Liu et al. (2018b) incorporated red blood cell membrane vesicles with NIR PLNPs to construct an erythrocyte membrane bioexcited optical nanocarrier. In order to realize the biomimetic pattern, erythrocyte membrane vesicles were isolated from RBC and then fused with mesoporous SiO₂-coated ZGGO to form the membrane bioexcited nanocarriers. Three groups of 4T1 tumor-bearing mice were individually treated with unmodified, SiO₂-coated, or membrane-fused ZGGO via tail vein injection. The NPs were mainly distributed in the two primary RES organs (i.e., liver and spleen) and the tumors due to EPR effects. Meanwhile, compared with two other NPs, the membrane-fused ZGGO exhibited a far higher proportion of retention capacity. Moreover, the amounts of membrane-fused ZGGO loaded with the drug Dox in blood were measured,

and the results indicated a long cycling period with a half-life of 9 h. Furthermore, injection of the drug-delivery vehicle into mice exhibited improved sustained-release efficacy of the NPs, strongly confirming the efficient decrease of systemic clearance and extension of circulation time caused by the biomimetic membrane coating. Employment of the drug-delivery system in the 4T1 orthotopic mammary tumor model showed the best tumor growth inhibition performance.

SUMMARY AND PERSPECTIVES

By conjugating with different functional groups, ligands, and biomolecules, multifunctional NPs have displayed superb capabilities in diagnosis and therapeutic applications. Diverse designs and synthesis strategies have been developed to achieve specific NPs offering targeted and controlled drug delivery for practical use. Multiple aspects of NP research, from investigations of the effects of different kinds of NPs and their sizes on the imaging and therapeutic efficacy in biological environments to studies of specific ligand targeted drug delivery, have been carefully performed.

Despite these exciting achievements in the last few years, the distinctive functions of multifunctional nanomaterials have influenced the injection dose in different imaging models and therapy types. Therefore, the issues around the controllable synthesis of nanoagents, synergistic theranostic effects, and short-term and long-term toxicity should be carefully investigated as a whole to realize every function (diagnosis and therapy) and to achieve the lowest side effect with single injection.

More investigations are required to improve the performance of theranostic agents, such as intensifying excretion, strengthening continuous monitoring, prolonging blood circulation time, promoting physiological barrier penetration, evading the RES, and accelerating more materials into clinical trials. Therefore, continuous innovations and development for novel theranostic approaches are necessary to meet growing clinical requirements.

AUTHOR CONTRIBUTIONS

YY designed the whole structure of the article, wrote the sections on materials, bio-imaging, PDT, and reviewed the article. LW, BW, YG, and XL wrote the sections on PTT and drug delivery.

FUNDING

This work was supported by the National Natural Science Foundation of China (Nos. 21577163, 21377142, 21477146).

REFERENCES

- Abdukayum, A., Chen, J. T., Zhao, Q., and Yan, X. P. (2013). Functional near infrared-emitting Cr³⁺/Pr³⁺ co-doped zinc gallogermanate persistent luminescent nanoparticles with superlong afterglow for *in vivo* targeted bioimaging. *J. Am. Chem. Soc.* 135, 14125–14133. doi: 10.1021/ja404243v
- Albert, K., and Hsu, H. Y. (2016). Carbon-based materials for photo-triggered theranostic applications. *Molecules* 21:1585. doi: 10.3390/molecules21111585
- Alifu, N., Dong, X., Li, D., Sun, X., Zebibula, A., Zhang, D., et al. (2017). Aggregation-induced emission nanoparticles as photosensitizer for two-photon photodynamic therapy. *Mater. Chem. Front.* 1, 1746–1753. doi: 10.1039/C7QM00092H

- Arvizo, R. R., Bhattacharyya, S., Kudgus, R. A., Giri, K., Bhattacharya, R., and Mukherjee, P. (2012). Intrinsic therapeutic applications of noble metal nanoparticles: past, present and future. *Chem. Soc. Rev.* 41, 2943–2970. doi: 10.1039/c2cs15355f
- Astruc, D., Boisselier, E., and Ornelas, C. (2010). Dendrimers designed for functions: from physical, photophysical, and supramolecular properties to applications in sensing, catalysis, molecular electronics, photonics, and nanomedicine. *Chem. Rev.* 110, 1857–1959. doi: 10.1021/cr900327d
- Augustine, S., Singh, J., Srivastava, M., Sharma, M., Das, A., and Malhotra, B. D. (2017). Recent advances in carbon based nanosystems for cancer theranostics. *Biomater. Sci.* 5, 901–952. doi: 10.1039/C7BM00008A
- Auzel, F. (2004). Upconversion and anti-stokes processes with f and d ions in solids. *Chem. Rev.* 104, 139–173. doi: 10.1021/cr020357g
- Bao, S. J., Huang, S. N., Liu, Y., Hu, Y. R., Wang, W. P., Ji, M. F., et al. (2017). Gold nanocages with dual modality for image-guided therapeutics. *Nanoscale* 9, 7284–7296. doi: 10.1039/C7NR01350G
- Bartelme, J., Quinn, S. J., and Giordani, S. (2015). Carbon nanomaterials: multi-functional agents for biomedical fluorescence and Raman imaging. *Chem. Soc. Rev.* 44, 4672–4698. doi: 10.1039/C4CS00306C
- Baumberg, J., Bell, S., and Bonifacio, A. (2017). SERS in biology/biomedical SERS: general discussion. *Faraday Discuss.* 205, 429–456. doi: 10.1039/C7FD90089A
- Bechet, D., Couleaud, P., Frochet, C., Viriot, M. L., Guillemin, F., and Barberi-Heyob, M. (2008). Nanoparticles as vehicles for delivery of photodynamic therapy agents. *Trends Biotechnol.* 26, 612–621. doi: 10.1016/j.tibtech.2008.07.007
- Bessiere, A., Jacquart, S., Priol, K. R., and Lecointre, A. (2011). ZnGa₂O₄:Cr³⁺: a new red long-lasting phosphor with high brightness. *Opt. Exp.* 19, 10131–10137. doi: 10.1364/OE.19.010131
- Biju, V. (2014). Chemical modifications and bioconjugate reactions of nanomaterials for sensing, imaging, drug delivery and therapy. *Chem. Soc. Rev.* 43, 744–764. doi: 10.1039/C3CS60273G
- Bilan, R., Nabiev, I., and Sukhanova, A. (2016). Quantum dot-based nanotools for bioimaging, diagnostics, and drug delivery. *ChemBiochem* 17, 2103–2114. doi: 10.1002/cbic.201600357
- Bimbo, L. M., Sarparanta, M., Santos, H. A., Airaksinen, A. J., Makila, E., Laaksonen, T., et al. (2010). Biocompatibility of thermally hydrocarbonized porous silicon nanoparticles and their biodistribution in rats. *ACS Nano* 4, 3023–3032. doi: 10.1021/nn901657w
- Birel, O. (2017). A review on perylene-3,4,9,10-tetracarboxylic acid diimide molecules. *CBU J. Sci.* 13, 379–386. doi: 10.18466/cbayarfe.319879
- Boakye-Yiadom, K. O., Kesse, S., Opoku-Damoah, Y., Filli, M. S., Aquib, M., Joelle, M. M. B., et al. (2019). Carbon dots: applications in bioimaging and theranostics. *Int. J. Pharmaceut.* 564, 308–317. doi: 10.1016/j.ijpharm.2019.04.055
- Boisselier, E., Diallo, A. K., Salmon, L., Ornelas, C., Ruiz, J., and Astruc, D. (2010). Encapsulation and stabilization of gold nanoparticles with “click” polyethyleneglycol dendrimers. *J. Am. Chem. Soc.* 132, 2729–2742. doi: 10.1021/ja909133f
- Boisselier, E., Salmon, L., Ruiz, J., and Astruc, D. (2008). How to very efficiently functionalize gold nanoparticles by “click” chemistry. *Chem. Commun.* 30, 5788–5790. doi: 10.1039/b812249k
- Brigger, I., Dubernet, C., and Couvreur, P. (2002). Nanoparticles in cancer therapy and diagnosis. *Adv. Drug Delivery Rev.* 54, 631–651. doi: 10.1016/S0169-409X(02)00044-3
- Brust, M., Walker, M., Bethell, D., Schiffrin, D. J., and Whyman, R. (1994). Synthesis of thiol-derivatized gold nanoparticles in a two-phase liquid-liquid system. *J. Chem. Soc.* 7, 801–802. doi: 10.1039/C39940000801
- Bullock, C. J., and Bussy, C. (2019). Biocompatibility considerations in the design of graphene biomedical materials. *Adv. Mater. Interfaces* 6:1900229. doi: 10.1002/admi.201900229
- Cabral, H., Miyata, K., Osada, K., and Kataoka, K. (2018). Block copolymer micelles in nanomedicine applications. *Chem. Rev.* 118, 6844–6892. doi: 10.1021/acs.chemrev.8b00199
- Cai, Y., Wei, Z., Song, C. H., Tang, C. C., Han, W., and Dong, X. C. (2019). Optical nano-agents in the second near-infrared window for biomedical applications. *Chem. Soc. Rev.* 48, 22–37. doi: 10.1039/C8CS00494C
- Castillo, R. R., and Vallet-Regi, M. (2019). Functional mesoporous silica nanocomposites: biomedical applications and biosafety. *Int. J. Mol. Sci.* 20:929. doi: 10.3390/ijms20040929
- Cha, M. G., Lee, S., Park, S., Kang, H., Lee, S. G., Jeong, C., et al. (2017). A dual modal silver nanoprobe for photoacoustic imaging and SERS multiplexed identification of *in vivo* lymph nodes. *Nanoscale* 9, 12556–12564. doi: 10.1039/C7NR03742B
- Chan, E. M., Levy, E. S., and Cohen, B. E. (2015). Rationally designed energy transfer in upconverting nanoparticles. *Adv. Mater.* 27, 5753–5761. doi: 10.1002/adma.201500248
- Chang, C. C., Hsieh, M. C., Lin, J. C., and Chang, T. C. (2012). Selective photodynamic therapy based on aggregation-induced emission enhancement of fluorescent organic nanoparticles. *Biomaterials* 33, 897–906. doi: 10.1016/j.biomaterials.2011.10.018
- Chang, Y. R., Lee, H. Y., Chen, K., Chang, C. C., Tsai, D. S., Fu, C. C., et al. (2008). Mass production and dynamic imaging of fluorescent nanodiamonds. *Nat. Nanotechnol.* 3, 284–288. doi: 10.1038/nnano.2008.99
- Chen, D. Q., Chen, Y., Lu, H. W., and Ji, Z. G. (2014). A bifunctional Cr/Yb/Tm:Ca₃Ga₂Ge₃O₁₂ phosphor with near-infrared long-lasting phosphorescence and upconversion luminescence. *Inorg. Chem.* 53, 8638–8645. doi: 10.1021/ic501238u
- Chen, G. Y., Roy, I., Yang, C. H., and Prasad, P. N. (2016a). Nanochemistry and nanomedicine for nanoparticle-based diagnostics and therapy. *Chem. Rev.* 116, 2826–2885. doi: 10.1021/acs.chemrev.5b00148
- Chen, J., Saeki, F., Wiley, B. J., Cang, H., Cobb, M. J., Li, Z. Y., et al. (2005a). Gold nanocages: bioconjugation and their potential use as optical imaging contrast agents. *Nano Lett.* 5, 473–477. doi: 10.1021/nl047950t
- Chen, J., Wiley, B., Li, Z. Y., and Campbell, D. (2005b). Gold nanocages: engineering their structure for biomedical applications. *Adv. Mater.* 17, 2255–2261. doi: 10.1002/adma.200500833
- Chen, L. J., Sun, S. K., Wang, Y., Yang, C. X., Wu, S. Q., and Yan, X. P. (2016b). Activatable multifunctional persistent luminescence nanoparticle/copper sulfide nanoprobe for *in vivo* luminescence imaging-guided photothermal therapy. *ACS Appl. Mater. Interfaces* 8, 32667–32674. doi: 10.1021/acsami.6b10702
- Chen, Q., Liang, C., Wang, C., and Liu, Z. (2015a). An imagable and photothermal “abraxane-like” nanodrug for combination cancer therapy to treat subcutaneous and metastatic breast tumors. *Adv. Mater.* 27, 903–910. doi: 10.1002/adma.201404308
- Chen, W. H., Yang, C. X., Qiu, W. X., Luo, G. F., Jia, H. Z., Lei, Q., et al. (2015b). Multifunctional theranostic nanoplateform for cancer combined therapy based on gold nanorods. *Adv. Healthc. Mater.* 4, 2247–2259. doi: 10.1002/adhm.201500453
- Chen, Y., Tan, C. L., Zhang, H., and Wang, L. Z. (2015c). Two-dimensional graphene analogues for biomedical applications. *Chem. Soc. Rev.* 44, 2681–2701. doi: 10.1039/C4CS00300D
- Cheng, L., Liu, J. J., Gu, X., Gong, H., Shi, X. Z., Liu, T., et al. (2014a). PEGylated WS₂ nanosheets as a multifunctional theranostic agent for *in vivo* dual-modal CT/photoacoustic imaging guided photothermal therapy. *Adv. Mater.* 26, 1886–1893. doi: 10.1002/adma.201304497
- Cheng, L., Wang, C., Feng, L. Z., Yang, K., and Liu, Z. (2014b). Functional nanomaterials for phototherapies of cancer. *Chem. Rev.* 114, 10869–10939. doi: 10.1021/cr400532z
- Choi, J. R., Yong, K. W., Choi, J. Y., Nilghaz, A., Lin, Y., Xu, J., et al. (2018). Black phosphorus and its biomedical applications. *Theranostics* 8, 1005–1026. doi: 10.7150/thno.22573
- Coughlan, C., Ibanez, M., Dobrozhan, O., Singh, A., Cabot, A., and Ryan, K. M. (2017). Compound copper chalcogenide nanocrystals. *Chem. Rev.* 117, 5865–6109. doi: 10.1021/acs.chemrev.6b00376
- Cui, J. B., Jiang, R., Xu, S. Y., Hu, G. F., and Wang, L. Y. (2015). Cu₇S₄ nanosuperlattices with greatly enhanced photothermal efficiency. *Small* 11, 4183–4190. doi: 10.1002/smll.201500845
- Dai, W. B., Lei, Y. F., Zhou, J., Xu, M., Chu, L. L., Li, L., et al. (2017). Near-infrared quantum-cutting and long-persistent phosphor Ca₃Ga₂Ge₃O₁₂:Pr³⁺, Yb³⁺ for application *in vivo* bioimaging and dye-sensitized solar cells. *J. Alloy. Compd.* 726, 230–239. doi: 10.1016/j.jallcom.2017.08.002
- de Chermont, Q. L., Chaneac, C., Seguin, J., Pelle, F., Maitrejean, S., Jolivet, J. P., et al. (2007). Nanoprobes with near-infrared persistent luminescence

- for *in vivo* imaging. *Proc. Natl. Acad. Sci. U.S.A.* 104, 9266–9271. doi: 10.1073/pnas.0702427104
- de la Zerdá, A., Prabhulkar, S., Perez, V. L., Ruggeri, M., Paranjape, A. S., Habte, F., et al. (2015). Optical coherence contrast imaging using gold nanorods in living mice eyes. *Clin. Exp. Ophthalmol.* 43, 358–366. doi: 10.1111/ceo.12299
- Desai, N. (2016). “Nanoparticle albumin-bound paclitaxel (Abraxane®),” in *Albumin in Medicine*, eds M. Otagiri and V. Chuang (Singapore: Springer Press), 101–119. doi: 10.1007/978-981-10-2116-9_6
- Devadasu, V. R., Bhardwaj, V., and Kumar, M. N. V. R. (2013). Can controversial nanotechnology promise drug delivery? *Chem. Rev.* 113, 1686–1735. doi: 10.1021/cr300047q
- Dykman, L., and Khlebtsov, N. (2012). Gold nanoparticles in biomedical applications: recent advances and perspectives. *Chem. Soc. Rev.* 41, 2256–2282. doi: 10.1039/C1CS15166E
- Elsababy, M., Heo, G. S., Lim, S. M., Sun, G. R., and Wooley, K. L. (2015). Polymeric nanostructures for imaging and therapy. *Chem. Rev.* 115, 10967–11011. doi: 10.1021/acs.chemrev.5b00135
- Erogbogbo, F., Yong, K. T., Roy, I., Xu, G. X., Prasad, P. N., and Swihart, M. T. (2008). Biocompatible luminescent silicon quantum dots for imaging of cancer cells. *ACS Nano* 2, 873–878. doi: 10.1021/nn700319z
- Fan, Q. L., Cheng, K., Yang, Z., Zhang, R. P., Yang, M., Hu, X., et al. (2015). Perylene-diimide-based nanoparticles as highly efficient photoacoustic agents for deep brain tumor imaging in living mice. *Adv. Mater.* 27, 843–847. doi: 10.1002/adma.201402972
- Fan, W. P., Yung, B., Huang, P., and Chen, X. Y. (2017). Nanotechnology for multimodal synergistic cancer therapy. *Chem. Rev.* 117, 13566–13638. doi: 10.1021/acs.chemrev.7b00258
- Farokhzad, O. C., and Langer, R. (2006). Nanomedicine: developing smarter therapeutic and diagnostic modalities. *Adv. Drug Delivery Rev.* 58, 1456–1459. doi: 10.1016/j.addr.2006.09.011
- Feng, G., Fang, Y., Liu, J., Geng, J., Ding, D., and Liu, B. (2017). Multifunctional conjugated polymer nanoparticles for image-guided photodynamic and photothermal therapy. *Small* 13:1602807. doi: 10.1002/sml.201602807
- Feng, L., Zhu, C., Yuan, H., Liu, L., Lv, F., and Wang, S. (2013). Conjugated polymer nanoparticles: preparation, properties, functionalization and biological applications. *Chem. Soc. Rev.* 42, 6620–6633. doi: 10.1039/c3cs60036j
- Feng, T., Ai, X. Z., An, G. H., Yang, P. P., and Zhao, Y. L. (2016). Charge-convertible carbon dots for imaging guided drug delivery with enhanced *in vivo* cancer therapeutic efficiency. *ACS Nano* 10, 4410–4420. doi: 10.1021/acsnano.6b00043
- Fu, X. Y., Liu, C. L., Shi, J. P., Man, H. Z., Xu, J., and Zhang, H. W. (2014). Long persistent near infrared luminescence nanoprobe $\text{LiGaS}_2\text{O}_8\text{:Cr}^{3+}\text{-PEG-OCH}_3$ for *in vivo* imaging. *Opt. Mater.* 36, 1792–1797. doi: 10.1016/j.optmat.2014.04.018
- Gai, S. L., Yang, G. X., Yang, P. P., He, F., Lin, J., Jin, D. Y., et al. (2018). Recent advances in functional nanomaterials for light-triggered cancer therapy. *Nano Today* 19, 146–187. doi: 10.1016/j.nantod.2018.02.010
- Gandra, N., and Singamaneni, S. (2013). Surface-enhanced Raman scattering for *in vivo* imaging: the future looks BRIGHT? *Nanomedicine* 8, 317–320. doi: 10.2217/nnm.13.10
- Ge, J. C., Jia, Q. Y., Liu, W. M., Guo, L., Liu, Q. Y., Lan, M. H., et al. (2015). Red-emissive carbon dots for fluorescent, photoacoustic, and thermal theranostics in living mice. *Adv. Mater.* 27, 4169–4177. doi: 10.1002/adma.201500323
- Geng, J., Liao, L. D., Qin, W., Tang, B. Z., Thakor, N., and Liu, B. (2015). Fluorogens with aggregation induced emission: ideal photoacoustic contrast reagents due to intramolecular rotation. *J. Nanosci. Nanotechnol.* 15, 1864–1868. doi: 10.1166/jnn.2015.10031
- Geszke-Moritz, M., and Moritz, M. (2013). Quantum dots as versatile probes in medical sciences: synthesis, modification and properties. *Mat. Sci. Eng. Mater.* 33, 1008–1021. doi: 10.1016/j.msec.2013.01.003
- Goodarzi, S., Da Ros, T., Conde, J., Sefat, F., and Mozafari, M. (2017). Fullerene: biomedical engineers get to revisit an old friend. *Mater. Today* 20, 460–480. doi: 10.1016/j.mattod.2017.03.017
- Grimaldi, N., Andrade, F., Segovia, N., Ferrer-Tasies, L., Sala, S., and Veciana, J. (2016). Lipid-based nanovesicles for nanomedicine. *Chem. Soc. Rev.* 45, 6520–6545. doi: 10.1039/C6CS00409A
- Gu, B., Wu, W., Xu, G., Feng, G., Yin, F., Chong, P. H. J., et al. (2017). Precise two-photon photodynamic therapy using an efficient photosensitizer with aggregation-induced emission characteristics. *Adv. Mater.* 29:1701076. doi: 10.1002/adma.201701076
- Gu, L., Park, J. H., Duong, K. H., Ruoslahti, E., and Sailor, M. J. (2010). Magnetic luminescent porous silicon microparticles for localized delivery of molecular drug payloads. *Small* 6, 2546–2552. doi: 10.1002/sml.201000841
- Gu, Z., Yan, L., Tian, G., Li, S., Chai, Z., and Zhao, Y. (2013). Recent advances in design and fabrication of upconversion nanoparticles and their safe theranostic applications. *Adv. Mater.* 25, 3758–3779. doi: 10.1002/adma.201301197
- Guerrini, L., Pazos-Perez, N., Garcia-Rico, E., and Alvarez-Puebla, R. (2017). Cancer characterization and diagnosis with SERS-encoded particles. *Cancer Nanotechnol.* 8:UNSP5. doi: 10.1186/s12645-017-0031-3
- Guo, J., Rahme, K., He, Y., Li, L. L., Holmes, J. D., and O'Driscoll, C. M. (2017). Gold nanoparticles enlighten the future of cancer theranostics. *Int. J. Nanomed.* 12, 6131–6152. doi: 10.2147/IJN.S140772
- Her, S., Jaffray, D. A., and Allen, C. (2017). Gold nanoparticles for applications in cancer radiotherapy: mechanisms and recent advancements. *Adv. Drug Deliv. Rev.* 109, 84–101. doi: 10.1016/j.addr.2015.12.012
- Herranz-Blanco, B., Shahbazi, M. A., Correia, A. R., Balasubramanian, V., Kohout, T., Hirvonen, J., et al. (2016). pH-switch nanoprecipitation of polymeric nanoparticles for multimodal cancer targeting and intracellular triggered delivery of doxorubicin. *Adv. Healthcare Mater.* 5, 1904–1916. doi: 10.1002/adhm.201600160
- Hessel, C. M., Pattani, V. P., Rasch, M., Panthani, M. G., Koo, B., Tunnell, J. W., et al. (2011). Copper selenide nanocrystals for photothermal therapy. *Nano Lett.* 11, 2560–2566. doi: 10.1021/nl201400z
- Homan, K. A., Souza, M., Truby, R., Luke, G. P., Green, C., Vreeland, E., et al. (2012). Silver nanoplate contrast agents for *in vivo* molecular photoacoustic imaging. *ACS Nano* 6, 641–650. doi: 10.1021/nn204100n
- Homayoni, H., Ma, L., Zhang, J. Y., Sahi, S. K., Rashidi, L. H., Bui, B., et al. (2016). Synthesis and conjugation of $\text{Sr}_2\text{MgSi}_2\text{O}_7\text{:Eu}^{2+}, \text{Dy}^{3+}$ water soluble afterglow nanoparticles for photodynamic activation. *Photodiagn. Photodyn. Ther.* 16, 90–99. doi: 10.1016/j.pdpdt.2016.08.012
- Hong, G., Lee, J. C., Robinson, J. T., Raaz, U., Xie, L., Huang, N. F., et al. (2012a). Multifunctional *in vivo* vascular imaging using near-infrared II fluorescence. *Nat. Med.* 18, 1841–1846. doi: 10.1038/nm.2995
- Hong, G., Robinson, J. T., Zhang, Y., Diao, S., Antaris, A. L., Wang, Q., et al. (2012b). *in vivo* fluorescence imaging with Ag_2S quantum dots in the second near-infrared region. *Angew. Chem. Int. Ed.* 51, 9818–9821. doi: 10.1002/anie.201206059
- Hong, G. S., Diao, S. O., Antaris, A. L., and Dai, H. J. (2015). Carbon nanomaterials for biological imaging and nanomedicinal therapy. *Chem. Rev.* 115, 10816–10906. doi: 10.1021/acs.chemrev.5b00008
- Hong, G. S., Zou, Y. P., Antaris, A. L., Diao, S., Wu, D., Cheng, K., et al. (2014). Ultrafast fluorescence imaging *in vivo* with conjugated polymer fluorophores in the second near-infrared window. *Nat. Commun.* 5:4206. doi: 10.1038/ncomms5206
- Hong, Y. N., Lam, J. M. Y., and Tang, B. Z. (2009). Aggregation-induced emission: phenomenon, mechanism and applications. *Chem. Commun.* 29, 4332–4353. doi: 10.1039/b904665h
- Hong, Y. N., Lam, J. W. Y., and Tang, B. Z. (2011). Aggregation-induced emission. *Chem. Soc. Rev.* 40, 5361–5388. doi: 10.1039/c1cs15113d
- Hu, F., Xu, S., and Liu, B. (2018a). Photosensitizers with aggregation-induced emission: materials and biomedical applications. *Adv. Mater.* 30:1801350. doi: 10.1002/adma.201801350
- Hu, L. D., Wang, P. Y., Zhao, M. Y., Liu, L., Zhou, L., Li, B. H., et al. (2018b). Near-infrared rechargeable “optical battery” implant for irradiation-free photodynamic therapy. *Biomaterials* 163, 154–162. doi: 10.1016/j.biomaterials.2018.02.029
- Hu, R., Leung, N. L. C., and Tang, B. Z. (2014). AIE macromolecules: syntheses, structures and functionalities. *Chem. Soc. Rev.* 43, 4494–4562. doi: 10.1039/C4CS00044G
- Huang, K., Li, Z. J., Lin, J., Han, G., and Huang, P. (2018). Two-dimensional transition metal carbides and nitrides (MXenes) for biomedical applications. *Chem. Soc. Rev.* 47, 5109–5124. doi: 10.1039/C7CS00838D
- Huang, P., Rong, P. F., Jin, A., Yan, X. F., Zhang, M. G., Lin, J., et al. (2014b). Dye-loaded ferritin nanocages for multimodal imaging and photothermal therapy. *Adv. Mater.* 26, 6401–6408. doi: 10.1002/adma.201400914

- Huang, P., Rong, P. F., Lin, J., Li, W. W., Yan, X. F., Zhang, M. G., et al. (2014a). Triphase interface synthesis of plasmonic gold bellflowers as near-infrared light mediated acoustic and thermal theranostics. *J. Am. Chem. Soc.* 136, 8307–8313. doi: 10.1021/ja503115n
- Huang, X., and El-Sayed, M. A. (2010). Gold nanoparticles: optical properties and implementations in cancer diagnosis and photothermal therapy. *J. Adv. Res.* 1, 13–28. doi: 10.1016/j.jare.2010.02.002
- Huang, Y. A., Xiao, Q. B., Hu, H. S., Zhang, K. C., Feng, Y. M., Li, F. J., et al. (2016). 915 nm light-triggered photodynamic therapy and MR/CT dual-modal imaging of tumor based on the nonstoichiometric $\text{Na}_{0.52}\text{YbF}_{3.52}\text{:Er}$ upconversion nanoprobe. *Small* 12, 4200–4210. doi: 10.1002/sml.201601023
- Idris, N. M., Jayakumar, M. K. G., Bansal, A., and Zhang, Y. (2015). Upconversion nanoparticles as versatile light nanotransducers for photoactivation applications. *Chem. Soc. Rev.* 44, 1449–1478. doi: 10.1039/C4CS00158C
- Jiang, K., Sun, S., Zhang, L., Lu, Y., Wu, A., and Cai, C. (2015). Red, green, and blue luminescence by carbon dots: full-color emission tuning and multicolor cellular imaging. *Angew. Chem. Int. Ed.* 54, 5360–5363. doi: 10.1002/anie.201501193
- Jiang, Y., Upputuri, P. K., Xie, C., Zeng, Z., Sharma, A., Zhen, X., et al. (2019). Metabolizable semiconducting polymer nanoparticles for second near-infrared photoacoustic imaging. *Adv. Mater.* 31:1808166. doi: 10.1002/adma.201808166
- Jung, H. S., Verwilt, P., Sharma, A., Shin, J., Sessler, J. L., and Kim, J. S. (2018). Organic molecule-based photothermal agents: an expanding photothermal therapy universe. *Chem. Soc. Rev.* 47, 2280–2297. doi: 10.1039/C7CS00522A
- Kamimura, S., Xu, C. N., Yamada, H., Marriott, G., Hyodo, K., and Ohno, T. (2017). Near-infrared luminescence from double-perovskite $\text{Sr}_3\text{Sn}_2\text{O}_7\text{:Nd}^{3+}$: a new class of probe for *in vivo* imaging in the second optical window of biological tissue. *J. Ceram. Soc. Jpn.* 125, 591–595. doi: 10.2109/jcersj.2.17051
- Kamimura, S., Xu, C. N., Yamada, H., Terasaki, N., and Fujihara, M. (2014). Long-persistent luminescence in the near-infrared from Nd^{3+} -doped Sr_2SnO_4 for *in vivo* optical imaging. *Jpn. J. Appl. Phys.* 53:092403. doi: 10.7567/JJAP.53.092403
- Karimi, M., Ghasemi, A., Zangabad, P. S., Rahighi, R., Basri, S. M. M., Mirshekari, H., et al. (2016). Smart micro/nanoparticles in stimulus-responsive drug/gene delivery systems. *Chem. Soc. Rev.* 45, 1457–1501. doi: 10.1039/C5CS00798D
- Kharlamov, A. N., Tyurnina, A. E., Veselova, V. S., Kovtun, O. P., Shur, V. Y., and Gabinsky, J. L. (2015). Silica-gold nanoparticles for atheroprotective management of plaques: results of the NANOM-FIM trial. *Nanoscale* 7, 8003–8015. doi: 10.1039/C5NR01050K
- Kim, C., Favazza, C., and Wang, L. H. V. (2010). *in vivo* photoacoustic tomography of chemicals: high-resolution functional and molecular optical imaging at new depths. *Chem. Rev.* 110, 2756–2782. doi: 10.1021/cr900266s
- Krasia-Christoforou, T., and Georgiou, T. K. (2013). Polymeric theranostics: using polymer-based systems for simultaneous imaging and therapy. *J. Mater. Chem.* 1, 3002–3025. doi: 10.1039/c3tb20191k
- Kumar, S., Sarita, N. M., Dilbaghi, N., and Tankeshwar, K., Kim, K. H. (2018). Recent advances and remaining challenges for polymeric nanocomposites in healthcare applications. *Prog. Polym. Sci.* 80, 1–38. doi: 10.1016/j.progpolymsci.2018.03.001
- Kunjachan, S., Ehling, J., Storm, G., Kiessling, F., and Lammers, T. (2015). Noninvasive imaging of nanomedicines and nanotheranostics: principles, progress, and prospects. *Chem. Rev.* 115, 10907–10937. doi: 10.1021/cr500314d
- Lalwani, G., Cai, X., Nie, L. M., Wang, L. H. V., and Sitharaman, B. (2013). Graphene-based contrast agents for photoacoustic and thermoacoustic tomography. *Photoacoustics* 1, 62–67. doi: 10.1016/j.pacs.2013.10.001
- Lamch, L., Pucek, A., Kulbacka, J., Chudy, M., Jastrzebska, E., Tokarska, K., et al. (2018). Recent progress in the engineering of multifunctional colloidal nanoparticles for enhanced photodynamic therapy and bioimaging. *Adv. Colloid. Interfaces* 261, 62–81. doi: 10.1016/j.cis.2018.09.002
- Lan, M., Zhao, S., Liu, W., Lee, C. S., Zhang, W., and Wang, P. (2019). Photosensitizers for photodynamic therapy. *Adv. Healthc. Mater.* 8:e1900132. doi: 10.1002/adhm.201900132
- Lee, C., Kwon, W., Beack, S., Lee, D., Park, Y., Kim, H., et al. (2016). Biodegradable nitrogen-doped carbon nanodots for non-invasive photoacoustic imaging and photothermal therapy. *Theranostics* 6, 2196–2208. doi: 10.7150/thno.16923
- Lee, D. E., Koo, H., Sun, I. C., Ryu, J. H., Kim, K., and Kwon, I. C. (2012). Multifunctional nanoparticles for multimodal imaging and theragnosis. *Chem. Soc. Rev.* 41, 2656–2672. doi: 10.1039/C2CS15261D
- Li, H., Kang, Z., Liu, Y., and Lee, S. T. (2012). Carbon nanodots: synthesis, properties and applications. *J. Mater. Chem.* 22, 24230–24253. doi: 10.1039/c2jm34690g
- Li, J., and Pu, K. (2019). Development of organic semiconducting materials for deep-tissue optical imaging, phototherapy and photoactivation. *Chem. Soc. Rev.* 48, 38–71. doi: 10.1039/C8CS00001H
- Li, J., Xie, C., Huang, J., Jiang, Y., Miao, Q., and Pu, K. (2018d). Semiconducting polymer nanoenzymes with photothermal activity for enhanced cancer therapy. *Angew. Chem. Int. Ed.* 130, 4059–4062. doi: 10.1002/ange.201800511
- Li, J. L., Shi, J. P., Shen, J. S., Man, H. Z., Wang, M. X., and Zhang, H. W. (2015b). Specific recognition of breast cancer cells *in vitro* using near infrared-emitting long-persistence luminescent $\text{Zn}_3\text{Ga}_2\text{Ge}_2\text{O}_{10}\text{:Cr}^{3+}$ nanoprobe. *Nano-Micro Lett.* 7, 138–145. doi: 10.1007/s40820-014-0026-0
- Li, J. L., Shi, J. P., Wang, C. C., Li, P. H., Yu, Z. F., and Zhang, H. W. (2017a). Five-nanometer $\text{ZnSn}_2\text{O}_4\text{:Cr}$, Eu ultra-small nanoparticles as new near infrared-emitting persistent luminescent nanoprobe for cellular and deep tissue imaging at 800 nm. *Nanoscale* 9, 8631–8638. doi: 10.1039/C7NR02468A
- Li, J. L., Wang, C. C., Shi, J. P., Li, P. H., Yu, Z. F., and Zhang, H. W. (2018b). Porous $\text{GdAlO}_3\text{:Cr}^{3+}$, Sm^{3+} drug carrier for real-time long afterglow and magnetic resonance dual-mode imaging. *J. Lumin.* 199, 363–371. doi: 10.1016/j.jlumin.2018.03.071
- Li, S. L., Wang, X. Y., Hu, R., Chen, H., Li, M., Wang, J. W., et al. (2016). Near-infrared (NIR)-absorbing conjugated polymer dots as highly effective photothermal materials for *in vivo* cancer therapy. *Chem. Mater.* 28, 8669–8675. doi: 10.1021/acs.chemmater.6b03738
- Li, W., and Chen, X. Y. (2015). Gold nanoparticles for photoacoustic imaging. *Nanomedicine* 10, 299–320. doi: 10.2217/nnm.14.169
- Li, W., Liu, Z. H., Fontana, F., Ding, Y. P., Liu, D. F., Hirvonen, J. T., et al. (2018a). Tailoring porous silicon for biomedical applications: from drug delivery to cancer immunotherapy. *Adv. Mater.* 30:1703740. doi: 10.1002/adma.201703740
- Li, W., Zhang, Z., Kong, B., Feng, S., Wang, J., Wang, L., et al. (2013). Simple and green synthesis of nitrogen-doped photoluminescent carbonaceous nanospheres for bioimaging. *Angew. Chem. Int. Ed.* 52, 8151–8155. doi: 10.1002/anie.201303927
- Li, X., Shan, J. Y., Zhang, W. Z., Su, S., Yuwen, L. H., and Wang, L. H. (2017b). Recent advances in synthesis and biomedical applications of two-dimensional transition metal selenide nanosheets. *Small* 13:1602660. doi: 10.1002/sml.201602660
- Li, Y., Zhou, S. F., Dong, G. P., Peng, M. Y., Wondraczek, L., and Qiu, J. R. (2014a). Anti-stokes fluorescent probe with incoherent excitation. *Sci. Rep.* 4:4059. doi: 10.1038/srep04059
- Li, Y., Zhou, S. F., Li, Y. Y., Sharafudeen, K., Ma, Z. J., Dong, G. P., et al. (2014b). Long persistent and photo-stimulated luminescence in Cr^{3+} -doped Zn-Ga-Sn-O phosphors for deep and reproducible tissue imaging. *J. Mater. Chem.* 2, 2657–2663. doi: 10.1039/c4tc00014e
- Li, Y. J., and Yan, X. P. (2016). Synthesis of functionalized triple-doped zinc gallogermanate nanoparticles with superlong near-infrared persistent luminescence for long-term orally administrated bioimaging. *Nanoscale* 8, 14965–14970. doi: 10.1039/C6NR04950H
- Li, Y. J., Yang, C. X., and Yan, X. P. (2018c). Biomimetic persistent luminescent nanoplatform for autofluorescence-free metastasis tracking and chemophotodynamic therapy. *Anal. Chem.* 90, 4188–4195. doi: 10.1021/acs.analchem.8b00311
- Li, Z., and Yang, Y. W. (2017). Creation and bioapplications of porous organic polymer materials. *J. Mater. Chem.* 5, 9278–9290. doi: 10.1039/C7TB02647A
- Li, Z., Zhang, Y., Wu, X., Huang, L., Li, D., Fan, W., et al. (2015a). Direct aqueous-phase synthesis of sub-10 nm “luminous pearls” with enhanced *in vivo* renewable near-infrared persistent luminescence. *J. Am. Chem. Soc.* 137, 5304–5307. doi: 10.1021/jacs.5b00872
- Li, Z. J., Shi, J. P., Zhang, H. W., and Sun, M. (2014c). Highly controllable synthesis of near-infrared persistent luminescence $\text{SiO}_2/\text{CaMgSi}_2\text{O}_6$ composite nanospheres for imaging *in vivo*. *Opt. Exp.* 22, 10509–10518. doi: 10.1364/OE.22.010509
- Liang, C., Xu, L. G., Song, G. S., and Liu, Z. (2016). Emerging nanomedicine approaches fighting tumor metastasis: animal models, metastasis-targeted drug delivery, phototherapy, and immunotherapy. *Chem. Soc. Rev.* 45, 6250–6269. doi: 10.1039/C6CS00458J

- Lim, E. K., Kim, T., Paik, S., Haam, S., Huh, Y. M., and Lee, K. (2015). Nanomaterials for theranostics: recent advances and future challenges. *Chem. Rev.* 115, 327–394. doi: 10.1021/cr300213b
- Lin, L. S., Cong, Z. X., Cao, J. B., Ke, K. M., Peng, Q. L., Gao, J. H., et al. (2014). Multifunctional Fe_3O_4 @polydopamine core-shell nanocomposites for intracellular mRNA detection and imaging-guided photothermal therapy. *ACS Nano* 8, 3876–3883. doi: 10.1021/nn500722y
- Lin, W. H., Zhang, W., Sun, T. T., Liu, S., Zhu, Y., and Xie, Z. G. (2017). Rational design of polymeric nanoparticles with tailorable biomedical functions for cancer. *ACS Appl. Mater. Interfac.* 9, 29612–29622. doi: 10.1021/acsami.7b10763
- Liu, F., Liang, Y. J., and Pan, Z. W. (2014b). Detection of up-converted persistent luminescence in the near infrared emitted by the $\text{Zn}_3\text{Ga}_2\text{GeO}_8$: Cr^{3+} , Yb^{3+} , Er^{3+} phosphor. *Phys. Rev. Lett.* 113:177401. doi: 10.1103/PhysRevLett.113.177401
- Liu, F., Yan, W. Z., Chuang, Y. J., Zhen, Z. P., Xie, J., and Pan, Z. W. (2013). Photostimulated near-infrared persistent luminescence as a new optical read-out from Cr^{3+} -doped LiGa_5O_8 . *Sci. Rep.* 3:1554. doi: 10.1038/srep01554
- Liu, F. Y., He, X. X., Chen, H. D., Zhang, J. P., Zhang, H. M., and Wang, Z. X. (2015c). Gram-scale synthesis of coordination polymer nanodots with renal clearance properties for cancer theranostic applications. *Nat. Commun.* 6:8003. doi: 10.1038/ncomms9003
- Liu, H. H., Ren, F., Zhang, H., Han, Y. B., Qin, H. Z., Zeng, J. F., et al. (2018a). Oral administration of highly bright Cr^{3+} doped ZnGa_2O_4 nanocrystals for *in vivo* targeted imaging of orthotopic breast cancer. *J. Mater. Chem.* 6, 1508–1518. doi: 10.1039/C7TB03148C
- Liu, J., Zheng, X. P., Yan, L., Zhou, L. J., Tian, G., Yin, W. Y., et al. (2015e). Bismuth sulfide nanorods as a precision nanomedicine for *in vivo* multimodal imaging-guided photothermal therapy of tumor. *ACS Nano* 9, 696–707. doi: 10.1021/nn506137n
- Liu, J. H., Cao, L., LeCroy, G. E., Wang, P., Meziari, M. J., Dong, Y. Y., et al. (2015a). Carbon “quantum” dots for fluorescence labeling of cells. *ACS Appl. Mater. Interfaces* 7, 19439–19445. doi: 10.1021/acsami.5b05665
- Liu, J. H., Lecuyer, T., Seguin, J., Mignet, N., Scherman, D., Viana, B., et al. (2019a). Imaging and therapeutic applications of persistent luminescence nanomaterials. *Adv. Drug Delivery Rev.* 138, 193–210. doi: 10.1016/j.addr.2018.10.015
- Liu, J. M., Liu, Y. Y., Zhang, D. D., Fang, G. Z., and Wang, S. (2016). Synthesis of $\text{GdAlO}_3\text{:Mn}^{4+}$, Ge^{4+} Au core-shell nanoprobe with plasmon-enhanced near-infrared persistent luminescence for *in vivo* trimodality bioimaging. *ACS Appl. Mater. Interfaces* 8, 29939–29949. doi: 10.1021/acsami.6b09580
- Liu, J. M., Zhang, D. D., Fang, G. Z., and Wang, S. (2018b). Erythrocyte membrane biopsied near-infrared persistent luminescence nanocarriers for *in vivo* long-circulating bioimaging and drug delivery. *Biomaterials* 165, 39–47. doi: 10.1016/j.biomaterials.2018.02.042
- Liu, Q., Feng, W., and Li, F. Y. (2014a). Water-soluble lanthanide upconversion nanophosphors: synthesis and bioimaging applications *in vivo*. *Coord. Chem. Rev.* 273, 100–110. doi: 10.1016/j.ccr.2014.01.004
- Liu, X. G., Yan, C. H., and Capobianco, J. A. (2015b). Photon upconversion nanomaterials. *Chem. Soc. Rev.* 44, 1299–1301. doi: 10.1039/C5CS90009C
- Liu, Y. J., Bhattarai, P., Dai, Z. F., and Chen, X. Y. (2019b). Photothermal therapy and photoacoustic imaging via nanotheranostics in fighting cancer. *Chem. Soc. Rev.* 48, 2053–2108. doi: 10.1039/C8CS00618K
- Liu, Y. Y., Liu, J. M., Zhang, D. D., Ge, K., Wang, P. H., Liu, H. L., et al. (2017). Persistent luminescence nanophosphor involved near-infrared optical bioimaging for investigation of foodborne probiotics biodistribution *in vivo*: a proof-of-concept study. *J. Agr. Food Chem.* 65, 8229–8240. doi: 10.1021/acs.jafc.7b02870
- Liu, Z., Robinson, J. T., Tabakman, S. M., Yang, K., and Dai, H. J. (2011). Carbon materials for drug delivery & cancer therapy. *Mater. Today* 14, 316–323. doi: 10.1016/S1369-7021(11)70161-4
- Liu, Z. M., Ye, B. G., Jin, M., Chen, H. L., Zhong, H. Q., Wang, X. P., et al. (2015d). Dye-free near-infrared surface-enhanced Raman scattering nanoprobe for bioimaging and high-performance photothermal cancer therapy. *Nanoscale* 7, 6754–6761. doi: 10.1039/C5NR01055A
- Loni, A., Defforge, T., Caffull, E., Gautier, G., and Canham, L. T. (2015). Porous silicon fabrication by ariodisation: progress towards the realisation of layers and powders with high surface area and micropore content. *Micropor. Mesopor. Mater.* 213, 188–191. doi: 10.1016/j.micromeso.2015.03.006
- Lovell, J. F., Jin, C. S., Huynh, E., Jin, H. L., Kim, C., Rubinstein, J. L., et al. (2011). Porphysome nanovesicles generated by porphyrin bilayers for use as multimodal biophotonic contrast agents. *Nat. Mater.* 10, 324–332. doi: 10.1038/nmat2986
- Lu, D., Tao, R., and Wang, Z. (2019). Carbon-based materials for photodynamic therapy: a mini-review. *Front. Chem. Sci. Eng.* 13, 310–323. doi: 10.1007/s11705-018-1750-7
- Lu, Z. S., and Li, C. M. (2011). Quantum dot-based nanocomposites for biomedical applications. *Curr. Med. Chem.* 18, 3516–3528. doi: 10.2174/092986711796642634
- Lucky, S. S., Soo, K. C., and Zhang, Y. (2015). Nanoparticles in photodynamic therapy. *Chem. Rev.* 115, 1990–2042. doi: 10.1021/cr5004198
- Luk, B. T., and Zhang, L. F. (2014). Current advances in polymer-based nanotheranostics for cancer treatment and diagnosis. *ACS Appl. Mater. Interfaces* 6, 21859–21873. doi: 10.1021/am5036225
- Luo, J. D., Xie, Z. L., Lam, J. W. Y., Cheng, L., Chen, H. Y., Qiu, C. F., et al. (2001). Aggregation-induced emission of 1-methyl-1,2,3,4,5-pentaphenylsilole. *Chem. Commun.* 18, 1740–1741. doi: 10.1039/b105159h
- Lyu, Y., Fang, Y., Miao, Q. Q., Zhen, X., Ding, D., and Pu, K. Y. (2016). Intraparticle molecular orbital engineering of semiconducting polymer nanoparticles as amplified theranostics for *in vivo* photoacoustic imaging and photothermal therapy. *ACS Nano* 10, 4472–4481. doi: 10.1021/acsnano.6b00168
- Lyu, Y., and Pu, K. (2017). Recent advances of activatable molecular probes based on semiconducting polymer nanoparticles in sensing and imaging. *Adv. Sci.* 4:1600481. doi: 10.1002/adv.201600481
- Lyu, Y., Zeng, J., Jiang, Y., Zhen, X., Wang, T., Qiu, S., et al. (2018). Enhancing both biodegradability and efficacy of semiconducting polymer nanoparticles for photoacoustic imaging and photothermal therapy. *ACS Nano* 12, 1801–1810. doi: 10.1021/acsnano.7b08616
- Ma, P., and Mumper, R. J. (2013). Paclitaxel nano-delivery systems: a comprehensive review. *J. Nanomed. Nanotechnol.* 4:1000164. doi: 10.4172/2157-7439.1000164
- Maiti, K. K., Dinis, U. S., Samanta, A., Vendrell, M., Soh, K. S., Park, S. J., et al. (2012). Multiplex targeted *in vivo* cancer detection using sensitive near-infrared SERS nanotags. *Nano Today* 7, 85–93. doi: 10.1016/j.nantod.2012.02.008
- Makila, E., Bimbo, L. M., Kaasalainen, M., Herranz, B., Airaksinen, A. J., Heinonen, M., et al. (2012). Amine modification of thermally carbonized porous silicon with silane coupling chemistry. *Langmuir* 28, 14045–14054. doi: 10.1021/la303091k
- Maldiney, T., Ballet, B., Bessodes, M., Scherman, D., and Richard, C. (2014b). Mesoporous persistent nanophosphors for *in vivo* optical bioimaging and drug-delivery. *Nanoscale* 6, 13970–13976. doi: 10.1039/C4NR03843F
- Maldiney, T., Bessiere, A., Seguin, J., Teston, E., Sharma, S. K., Viana, B., et al. (2014a). The *in vivo* activation of persistent nanophosphors for the optical imaging of vascularization, tumors and grafted cells. *Nat. Mater.* 13, 418–426. doi: 10.1038/nmat3908
- Maldiney, T., Doan, B. T., Alloyeau, D., Bessodes, M., Scherman, D., and Richard, C. (2015). Gadolinium-doped persistent nanophosphors as versatile tool for multimodal *in vivo* imaging. *Adv. Funct. Mater.* 25, 331–338. doi: 10.1002/adfm.201401612
- Maldiney, T., Lecoindre, A., Viana, B., Bessiere, A., Bessodes, M., Gourier, D., et al. (2011). Controlling electron trap depth to enhance optical properties of persistent luminescence nanoparticles for *in vivo* imaging. *J. Am. Chem. Soc.* 133, 11810–11815. doi: 10.1021/ja204504w
- Maldiney, T., Sraiki, G., Viana, B., Gourier, D., Richard, C., Scherman, D., et al. (2012). *in vivo* optical imaging with rare earth doped $\text{Ca}_2\text{Si}_5\text{N}_8$ persistent luminescence nanoparticles. *Opt. Mater. Exp.* 2, 261–268. doi: 10.1364/OME.2.000261
- Mao, H. Y., Laurent, S., Chen, W., Akhavan, O., Imani, M., Ashkarran, A. A., et al. (2013). Graphene: promises, facts, opportunities, and challenges in nanomedicine. *Chem. Rev.* 113, 3407–3424. doi: 10.1021/cr300335p
- Mei, J., Hong, Y. N., Lam, J. M. Y., Qin, A. J., Tang, Y. H., and Tang, B. Z. (2014). Aggregation-induced emission: the whole is more brilliant than the parts. *Adv. Mater.* 26, 5429–5479. doi: 10.1002/adma.201401356
- Mei, J., Leung, N. L. C., Kwok, R. T. K., Lam, J. W. Y., and Tang, B. Z. (2015). Aggregation-induced emission: together we shine, united

- we soar! *Chem. Rev.* 115, 11718–11940. doi: 10.1021/acs.chemrev.5b00263
- Miao, Q. Q., and Pu, K. Y. (2018). Organic semiconducting agents for deep-tissue molecular imaging: second near-infrared fluorescence, self-luminescence, and photoacoustics. *Adv. Mater.* 30:1801778. doi: 10.1002/adma.201801778
- Min, Y. Z., Li, J. M., Liu, F., Yeow, E. K. L., and Xing, B. G. (2014). Near-infrared light-mediated photoactivation of a platinum antitumor prodrug and simultaneous cellular apoptosis imaging by upconversion-luminescent nanoparticles. *Angew. Chem. Int. Ed.* 53, 1012–1016. doi: 10.1002/anie.201308834
- Mishra, V., Patil, A., Thakur, S., and Kesharwani, P. (2018). Carbon dots: emerging theranostic nanoarchitectures. *Drug Discov. Today* 23, 1219–1232. doi: 10.1016/j.drudis.2018.01.006
- Mo, D., Hu, L., Zeng, G. M., Chen, G. Q., Wan, J., Yu, Z. G., et al. (2017). Cadmium-containing quantum dots: properties, applications, and toxicity. *Appl. Microbiol. Biotechnol.* 101, 2713–2733. doi: 10.1007/s00253-017-8140-9
- Mochalin, V. N., Pentecost, A., Li, X. M., Neitzel, I., Nelson, M., Wei, C. Y., et al. (2013). Adsorption of drugs on nanodiamond: toward development of a drug delivery platform. *Mol. Pharmacol.* 10, 3728–3735. doi: 10.1021/mp400213z
- Mochalin, V. N., Shenderova, O., Ho, D., and Gogotsi, Y. (2011). The properties and applications of nanodiamonds. *Nat. Nanotechnol.* 7, 11–23. doi: 10.1038/nnano.2011.209
- Montalti, M., Prodi, L., Rampazzo, E., and Zaccheroni, N. (2014). Dye-doped silica nanoparticles as luminescent organized systems for nanomedicine. *Chem. Soc. Rev.* 43, 4243–4268. doi: 10.1039/C3CS60433K
- Namdari, P., Negahdari, B., and Eatemadi, A. (2017). Synthesis, properties and biomedical applications of carbon-based quantum dots: an updated review. *Biomed. Pharmacother.* 87, 209–222. doi: 10.1016/j.biopha.2016.12.108
- Nicolas, J., Mura, S., Brambilla, D., Mackiewicz, N., and Couvreur, P. (2013). Design, functionalization strategies and biomedical applications of targeted biodegradable/biocompatible polymer-based nanocarriers for drug delivery. *Chem. Soc. Rev.* 42, 1147–1235. doi: 10.1039/C2CS35265F
- Nie, L. M., Chen, M., Sun, X. L., Rong, P. F., Zheng, N. F., and Chen, X. Y. (2014). Palladium nanosheets as highly stable and effective contrast agents for *in vivo* photoacoustic molecular imaging. *Nanoscale* 6, 1271–1276. doi: 10.1039/C3NR05468C
- Nie, L. M., and Chen, X. Y. (2014). Structural and functional photoacoustic molecular tomography aided by emerging contrast agents. *Chem. Soc. Rev.* 43, 7132–7170. doi: 10.1039/C4CS00086B
- Ntziachristos, V. (2010). Going deeper than microscopy: the optical imaging frontier in biology. *Nat. Methods* 7, 603–614. doi: 10.1038/nmeth.1483
- Panwar, N., Soehartono, A. M., Chan, K. K., Zeng, S., Xu, G., Qu, J., et al. (2019). Nanocarbons for biology and medicine: sensing, imaging, and drug delivery. *Chem. Rev.* 119, 9559–9656. doi: 10.1021/acs.chemrev.9b00099
- Park, J. H., Gu, L., von Maltzahn, G., Ruoslahti, E., Bhatia, S. N., and Sailor, M. J. (2009). Biodegradable luminescent porous silicon nanoparticles for *in vivo* applications. *Nat. Mater.* 8, 331–336. doi: 10.1038/nmat2398
- Patel, K. D., Singh, R. K., and Kim, H. W. (2019). Carbon-based nanomaterials as an emerging platform for theranostics. *Mater. Horiz.* 6, 434–469. doi: 10.1039/C8MH00966J
- Pecher, J., and Mecking, S. (2010). Nanoparticles of conjugated polymers. *Chem. Rev.* 110, 6260–6279. doi: 10.1021/cr100132y
- Perrin, L., and Hudhomme, P. (2011). Synthesis, electrochemical and optical absorption properties of new perylene-3,4,9,10-bis(dicarboximide) and perylene-3,4,9,10-bis(benzimidazole) derivatives. *Eur. J. Org. Chem.* 2011, 5427–5440. doi: 10.1002/ejoc.201100513
- Pichaandi, J., and van Veggel, F. C. J. M. (2014). Near-infrared emitting quantum dots: recent progress on their synthesis and characterization. *Coord. Chem. Rev.* 263, 138–150. doi: 10.1016/j.ccr.2013.10.011
- Premasiri, W. R., Chen, Y., Fore, J., Brodeur, A., and Ziegler, L. D. (2018). “Chapter 10 - SERS biomedical applications: diagnostics, forensics, and metabolomics,” in *Frontiers and Advances in Molecular Spectroscopy*, ed J. Laane (Cambridge, MA: Elsevier Press), 327–367. doi: 10.1016/B978-0-12-811220-5.00010-1
- Probst, C. E., Zrazhevskiy, P., Bagalkot, V., and Gao, X. H. (2013). Quantum dots as a platform for nanoparticle drug delivery vehicle design. *Adv. Drug Deliv. Rev.* 65, 703–718. doi: 10.1016/j.addr.2012.09.036
- Pu, K., Mei, J. G., Jokerst, J. V., Hong, G. S., Antaris, A. L., Chattopadhyay, N., et al. (2015). Diketopyrrolopyrrole-based semiconducting polymer nanoparticles for *in vivo* photoacoustic imaging. *Adv. Mater.* 27, 5184–5190. doi: 10.1002/adma.201502285
- Pu, K. Y., Chattopadhyay, N., and Rao, J. H. (2016). Recent advances of semiconducting polymer nanoparticles in *in vivo* molecular imaging. *J. Control. Release* 240, 312–322. doi: 10.1016/j.jconrel.2016.01.004
- Pu, K. Y., Shuhendler, A. J., Jokerst, J. V., Mei, J. G., Gambhir, S. S., Bao, Z. N., et al. (2014a). Semiconducting polymer nanoparticles as photoacoustic molecular imaging probes in living mice. *Nat. Nanotechnol.* 9, 233–239. doi: 10.1038/nnano.2013.302
- Pu, K. Y., Shuhendler, A. J., Valt, M. P., Cui, L. N., Saar, M., Peehl, D. M., et al. (2014b). Phosphorylcholine-coated semiconducting polymer nanoparticles as rapid and efficient labeling agents for *in vivo* cell tracking. *Adv. Healthcare Mater.* 3, 1292–1298. doi: 10.1002/adhm.201300534
- Qiu, M., Singh, A., Wang, D., Qu, J. L., Swihart, M., Zhang, H., et al. (2019). Biocompatible and biodegradable inorganic nanostructures for nanomedicine: silicon and black phosphorus. *Nano Today* 25, 135–155. doi: 10.1016/j.nantod.2019.02.012
- Ramirez-Garcia, G., Gutierrez-Granados, S., Gallegos-Corona, M. A., Palma-Tirado, L., d’Orlye, F., Varenne, A., et al. (2017). Long-term toxicological effects of persistent luminescence nanoparticles after intravenous injection in mice. *Int. J. Pharmaceut.* 532, 686–695. doi: 10.1016/j.ijpharm.2017.07.015
- Reina, G., Gonzalez-Dominguez, J. M., Criado, A., Vazquez, E., Bianco, A., and Prato, M. (2017). Promises, facts and challenges for graphene in biomedical applications. *Chem. Soc. Rev.* 46, 4400–4416. doi: 10.1039/C7CS00363C
- Riley, R. S., and Day, E. S. (2017). Gold nanoparticle-mediated photothermal therapy: applications and opportunities for multimodal cancer treatment. *Wiley Interdiscip. Rev.* 9:e1449. doi: 10.1002/wnan.1449
- Rong, P., Yang, K., Srivastan, A., Kiesewetter, D. O., Yue, X., Wang, F., et al. (2014). Photosensitizer loaded nano-graphene for multimodality imaging guided tumor photodynamic therapy. *Theranostics* 4, 229–239. doi: 10.7150/thno.8070
- Rong, P. F., Huang, P., Liu, Z. G., Lin, J., Jin, A., Ma, Y., et al. (2015). Protein-based photothermal theranostics for imaging-guided cancer therapy. *Nanoscale* 7, 16330–16336. doi: 10.1039/C5NR04428F
- Rosticher, C., Chaneac, C., Viana, B., Fortin, M. A., Lagueux, J., and Faucher, L. (2015). Red persistent luminescence and magnetic properties of nanomaterials for multimodal imaging. *Oxide-Based Mater.* 9364:936419. doi: 10.1117/12.2087319
- Ryu, T. K., Baek, S. W., Kang, R. H., and Choi, S. W. (2016). Selective photothermal tumor therapy using nanodiamond-based nanoclusters with folic acid. *Adv. Funct. Mater.* 26, 6428–6436. doi: 10.1002/adfm.201601207
- Sadegh, H., and Shahryari-ghoshekandi, R. (2015). Functionalization of carbon nanotubes and its application in nanomedicine: a review. *Nanomed. J.* 2, 231–248. doi: 10.7508/NMJ.2015.04.001
- Sailor, M. J. (2012). *Porous Silicon in Practice: Preparation, Characterization and Applications*. Weinheim: Wiley-VCH Verlag GmbH & Co. KGaA.
- Shanmugam, V., Selvakumar, S., Yeh, C. S. (2014). Near-infrared light-responsive nanomaterials in cancer therapeutics. *Chem. Soc. Rev.* 43, 6254–6287. doi: 10.1039/C4CS00011K
- Sheng, Z. H., Hu, D. H., Zheng, M. B., Zhao, P. F., Liu, H. L., Gao, D. Y., et al. (2014). Smart human serum albumin-indocyanine green nanoparticles generated by programmed assembly for dual-modal imaging-guided cancer synergistic phototherapy. *ACS Nano* 8, 12310–12322. doi: 10.1021/nn5062386
- Sheng, Z. H., Song, L., Zheng, J. X., Hu, D. H., He, M., Zheng, M. B., et al. (2013). Protein-assisted fabrication of nano-reduced graphene oxide for combined *in vivo* photoacoustic imaging and photothermal therapy. *Biomaterials* 34, 5236–5243. doi: 10.1016/j.biomaterials.2013.03.090
- Shi, J. P., Sun, X., Li, J. L., Man, H. Z., Shen, J. S., Yu, Y. K., et al. (2015a). Multifunctional near infrared-emitting long-persistence luminescent nanoprobes for drug delivery and targeted tumor imaging. *Biomaterials* 37, 260–270. doi: 10.1016/j.biomaterials.2014.10.033
- Shi, J. P., Sun, X., Zheng, S. H., Li, J. L., Fu, X. Y., Zhang, H. W. (2018). A new near-infrared persistent luminescence nanoparticle as a multifunctional nanopatform for multimodal imaging and cancer therapy. *Biomaterials* 152, 15–23. doi: 10.1016/j.biomaterials.2017.10.032
- Shi, S., Chen, F., Ehlerding, E. B., Cai, W. (2014). Surface engineering of graphene-based nanomaterials for biomedical applications. *Bioconjugate Chem.* 25, 1609–1619. doi: 10.1021/bc500332c

- Shi, S., Yang, K., Hong, H., Chen, F., Valdovinos, H. F., Goel, S., et al. (2015b). VEGFR targeting leads to significantly enhanced tumor uptake of nanographene oxide *in vivo*. *Biomaterials* 39, 39–46. doi: 10.1016/j.biomaterials.2014.10.061
- Shuhendler, A. J., Pu, K. Y., Cui, L., Uetrecht, J. P., Rao, J. H. (2014). Real-time imaging of oxidative and nitrosative stress in the liver of live animals for drug-toxicity testing. *Nat. Biotechnol.* 32, 373–U240. doi: 10.1038/nbt.2838
- Skrabalak, S. E., Chen, J., Sun, Y., Lu, X., Au, L., Cobley, C. M., et al. (2008). Gold nanocages: synthesis, properties, and applications. *Acc. Chem. Res.* 41, 1587–1595. doi: 10.1021/ar800018v
- Smith, B. R., and Gambhir, S. S. (2017). Nanomaterials for *in vivo* imaging. *Chem. Rev.* 117, 901–986. doi: 10.1021/acs.chemrev.6b00073
- Song, J. B., Yang, X. Y., Jacobson, O., Huang, P., Sun, X. L., Lin, L. S., et al. (2015a). Ultrasmall gold nanorod vesicles with enhanced tumor accumulation and fast excretion from the body for cancer therapy. *Adv. Mater.* 27, 4910–4917. doi: 10.1002/adma.201502486
- Song, X. J., Chen, Q., Liu, Z. (2015c). Recent advances in the development of organic photothermal nano-agents. *Nano Res.* 8, 340–354. doi: 10.1007/s12274-014-0620-y
- Song, X. R., Wang, X. Y., Yu, S. X., Cao, J. B., Li, S. H., Li, J., et al. (2015b). Co₉Se₈ nanoplates as a new theranostic platform for photoacoustic/magnetic resonance dual-modal-imaging-guided chemo-photothermal combination therapy. *Adv. Mater.* 27, 3285–3291. doi: 10.1002/adma.201405634
- Spyratou, E., Makropoulou, M., Efstathiopoulos, E. P., Georgakilas, A. G., Sihver, L. (2017). Recent advances in cancer therapy based on dual mode gold nanoparticles. *Cancers* 9:173. doi: 10.3390/cancers9120173
- Sun, S. K., Wang, H. F., Yan, X. P. (2018). Engineering persistent luminescence nanoparticles for biological applications: from biosensing/bioimaging to theranostics. *Accounts Chem. Res.* 51, 1131–1143. doi: 10.1021/acs.accounts.7b00619
- Tan, C. L., Cao, X. H., Wu, X. J., He, Q. Y., Yang, J., Zhang, X., et al. (2017). Recent advances in ultrathin two-dimensional nanomaterials. *Chem. Rev.* 117, 6225–6331. doi: 10.1021/acs.chemrev.6b00558
- Tang, J., Kong, B., Wu, H., Xu, M., Wang, Y., Wang, Y., et al. (2013). Carbon nanodots featuring efficient FRET for real-time monitoring of drug delivery and two-photon imaging. *Adv. Mater.* 25, 6569–6574. doi: 10.1002/adma.201303124
- Tang, Z. H., He, C. L., Tian, H. Y., Ding, J. X., Hsiao, B. S., Chu, B., et al. (2016). Polymeric nanostructured materials for biomedical applications. *Prog. Polym. Sci.* 60, 86–128. doi: 10.1016/j.progpolymsci.2016.05.005
- Tasis, D., Tagmatarchis, N., Bianco, A., Prato, M. (2006). Chemistry of carbon nanotubes. *Chem. Rev.* 106, 1105–1136. doi: 10.1021/cr050569o
- Teston, E., Maldiney, T., Marangon, I., Volatron, J., Lalatonne, Y., Motte, L., et al. (2018). Nanohybrids with magnetic and persistent luminescence properties for cell labeling, tracking, *in vivo* real-time imaging, and magnetic vectorization. *Small* 14:1800020. doi: 10.1002/smll.201800020
- Tian, G., Zhang, X., Gu, Z., Zhao, Y. (2015). Recent advances in upconversion nanoparticles-based multifunctional nanocomposites for combined cancer therapy. *Adv. Mater.* 27, 7692–7712. doi: 10.1002/adma.201503280
- Tinwala, H., and Wairkar, S. (2019). Production, surface modification and biomedical applications of nanodiamonds: a sparkling tool for theranostics. *Mater. Sci. Eng. C-Mater.* 97, 913–931. doi: 10.1016/j.msec.2018.12.073
- Tong, R., Tang, L., Ma, L., Tu, C. L., Baumgartner, R., Cheng, J. J. (2014). Smart chemistry in polymeric nanomedicine. *Chem. Soc. Rev.* 43, 6982–7012. doi: 10.1039/C4CS00133H
- Topete, A., Alatorre-Meda, M., Iglesias, P., Villar-Alvarez, E. M., Barbosa, S., Costoya, J. A., et al. (2014). Fluorescent drug-loaded, polymeric-based, branched gold nanoshells for localized multimodal therapy and imaging of tumoral cells. *ACS Nano* 8, 2725–2738. doi: 10.1021/nn406425h
- Treguer-Delapierre, M., Majimel, J., Mornet, S., Duguet, E., Ravaine, S. (2008). Synthesis of non-spherical gold nanoparticles. *Gold Bull.* 41, 195–207. doi: 10.1007/BF03216597
- Turkevich, J., Stevenson, P. C., Hillier, J. (1951). A study of the nucleation and growth processes in the synthesis of colloidal gold. *Discuss. Faraday Soc.* 11, 55–75. doi: 10.1039/d4f9511100055
- Tzur-Balter, A., Gilert, A., Massad-Ivanir, N., Segal, E. (2013). Engineering porous silicon nanostructures as tunable carriers for mitoxantrone dihydrochloride. *Acta Biomater.* 9, 6208–6217. doi: 10.1016/j.actbio.2012.12.010
- Vaidya, A., Agarwal, A., Jain, A., Agrawal, R. K., Jain, S. K. (2011). Bioconjugation of polymers: a novel platform for targeted drug delivery. *Curr. Pharm. Design* 17, 1108–1125. doi: 10.2174/138161211795656873
- van der Stam, W., Berends, A. C., de Mello Donega, C. (2015). Prospects of colloidal copper chalcogenide nanocrystals. *Chemphyschem* 17, 559–581. doi: 10.1002/cphc.201500976
- Vivero-Escoto, J. L., Huxford-Phillips, R. C., Lin, W. B. (2012). Silica-based nanopores for biomedical imaging and theranostic applications. *Chem. Soc. Rev.* 41, 2673–2685. doi: 10.1039/c2cs15229k
- Wang, C., Cheng, L., Liu, Z. (2013a). Upconversion nanoparticles for photodynamic therapy and other cancer therapeutics. *Theranostics* 3, 317–330. doi: 10.7150/thno.5284
- Wang, C. F., Makila, E. M., Kaasalainen, M. H., Liu, D. F., Sarparanta, M. P., Airaksinen, A. J., et al. (2014). Copper-free azide-alkyne cycloaddition of targeting peptides to porous silicon nanoparticles for intracellular drug uptake. *Biomaterials* 35, 1257–1266. doi: 10.1016/j.biomaterials.2013.10.065
- Wang, J., Li, J. L., Yu, J. N., Zhang, H. W., Zhang, B. B. (2018). Large hollow cavity luminous nanoparticles with near-infrared persistent luminescence and tunable sizes for tumor afterglow imaging and chemo-/photodynamic therapies. *ACS Nano* 12, 4246–4258. doi: 10.1021/acsnano.7b07606
- Wang, K., Fan, X., Zhao, L., Zhang, X., Zhang, X., Li, Z., et al. (2016a). Aggregation induced emission fluorogens based nanotheranostics for targeted and imaging-guided chemo-photothermal combination therapy. *Small* 12, 6568–6575. doi: 10.1002/smll.201601473
- Wang, L. H. V., and Hu, S. (2012). Photoacoustic tomography: *in vivo* imaging from organelles to organs. *Science* 335, 1458–1462. doi: 10.1126/science.1216210
- Wang, M., and Thanou, M. (2010). Targeting nanoparticles to cancer. *Pharmacol. Res.* 62, 90–99. doi: 10.1016/j.phrs.2010.03.005
- Wang, S., Lin, J., Wang, T. F., Chen, X. Y., Huang, P. (2016b). Recent advances in photoacoustic imaging for deep-tissue biomedical applications. *Theranostics* 6, 2394–2413. doi: 10.7150/thno.16715
- Wang, S. J., Teng, Z. G., Huang, P., Liu, D. B., Liu, Y., Tian, Y., et al. (2015a). Reversibly extracellular pH controlled cellular uptake and photothermal therapy by PEGylated mixed-charge gold nanostars. *Small* 11, 1801–1810. doi: 10.1002/smll.201403248
- Wang, X., Wang, C., Cheng, L., Lee, S. T., Liu, Z. (2012). Noble metal coated single-walled carbon nanotubes for applications in surface enhanced Raman scattering imaging and photothermal therapy. *J. Am. Chem. Soc.* 134, 7414–7422. doi: 10.1021/ja300140c
- Wang, X. D., Valiev, R. R., Ohulchanskyy, T. Y., Agren, H., Yang, C. H., Chen, G. Y. (2017). Dye-sensitized lanthanide-doped upconversion nanoparticles. *Chem. Soc. Rev.* 46, 4150–4167. doi: 10.1039/C7CS00053G
- Wang, Y., Yan, B., Chen, L. (2013b). SERS tags: novel optical nanopores for bioanalysis. *Chem. Rev.* 113, 1391–1428. doi: 10.1021/cr300120g
- Wang, Y., Yang, T., Ke, H. T., Zhu, A. J., Wang, Y. Y., Wang, J. X., et al. (2015b). Smart albumin-biomimetic nanocomposites for multimodal imaging and photothermal tumor ablation. *Adv. Mater.* 27, 3874–3882. doi: 10.1002/adma.201500229
- Wang, Y. X., Feng, L. H., Wang, S. (2019). Conjugated polymer nanoparticles for imaging, cell activity regulation, and therapy. *Adv. Func. Mater.* 29:1806818. doi: 10.1002/adfm.201806818
- Warner, J. H., Hoshino, A., Yamamoto, K., Tilley, R. D. (2005). Water-soluble photoluminescent silicon quantum dots. *Angew. Chem. Int. Ed.* 44, 4550–4554. doi: 10.1002/anie.200501256
- Wen, J., Yang, K., Liu, F. Y., Li, H. J., Xu, Y. Q., Sun, S. G. (2017). Diverse gatekeepers for mesoporous silica nanoparticle based drug delivery systems. *Chem. Soc. Rev.* 46, 6024–6045. doi: 10.1039/C7CS00219J
- Wolfbeis, O. S. (2015). An overview of nanoparticles commonly used in fluorescent bioimaging. *Chem. Soc. Rev.* 44, 4743–4768. doi: 10.1039/C4CS00392F
- Wong, P. T., and Choi, S. K. (2015). Mechanisms of drug release in nanotherapeutic delivery systems. *Chem. Rev.* 115, 3388–3432. doi: 10.1021/cr5004634
- Wu, C. F., Hansen, S. J., Hou, Q. O., Yu, J. B., Zeigler, M., Jin, Y. H., et al. (2011b). Design of highly emissive polymer dot bioconjugates for *in vivo* tumor targeting. *Angew. Chem., Int. Ed.* 50, 3430–3434. doi: 10.1002/anie.201007461
- Wu, C. F., Jin, Y. H., Schneider, T., Burnham, D. R., Smith, P. B., Chiu, D. T. (2010). Ultrabright and bioorthogonal labeling of cellular targets using semiconducting

- polymer dots and click chemistry. *Angew. Chem. Int. Ed.* 49, 9436–9440. doi: 10.1002/anie.201004260
- Wu, E. C., Andrew, J. S., Cheng, L. Y., Freeman, W. R., Pearson, L., Sailor, M. J. (2011a). Real-time monitoring of sustained drug release using the optical properties of porous silicon photonic crystal particles. *Biomaterials* 32, 1957–1966. doi: 10.1016/j.biomaterials.2010.11.013
- Wu, W., Mao, D., Xu, S., Ji, S., Hu, F., Ding, D., et al. (2017a). High performance photosensitizers with aggregation-induced emission for image-guided photodynamic anticancer therapy. *Mater. Horiz.* 4, 1110–1114. doi: 10.1039/C7MH00469A
- Wu, W. B., Mao, D., Hu, F., Xu, S. D., Chen, C., Zhang, C. J., et al. (2017b). A highly efficient and photostable photosensitizer with near-infrared aggregation-induced emission for image-guided photodynamic anticancer therapy. *Adv. Mater.* 29:1700548. doi: 10.1002/adma.201700548
- Wu, X., Chen, G. Y., Shen, J., Li, Z. J., Zhang, Y. W., Han, G. (2015). Upconversion nanoparticles: a versatile solution to multiscale biological imaging. *Bioconjug. Chem.* 26, 166–175. doi: 10.1021/bc5003967
- Wu, Y., Ali, M. R. K., Chen, K. C., Fang, N., El-Sayed, M. A. (2019). Gold nanoparticles in biological optical imaging. *Nano Today* 24, 120–140. doi: 10.1016/j.nantod.2018.12.006
- Xia, Y., Li, W., Cobley, C. M., Chen, J., Xia, X., Zhang, Q., et al. (2011). Gold nanocages: from synthesis to theranostic applications. *Acc. Chem. Res.* 44, 914–924. doi: 10.1021/ar200061q
- Xu, G. X., Zeng, S. W., Zhang, B. T., Swihart, M. T., Yong, K. T., Prasad, P. N. (2016). New generation cadmium-free quantum dots for biophotonics and nanomedicine. *Chem. Rev.* 116, 12234–12327. doi: 10.1021/acs.chemrev.6b00290
- Xu, J., Murata, D., Ueda, J., Viana, B., Tanabe, S. (2018b). Toward rechargeable persistent luminescence for the first and third biological windows via persistent energy transfer and electron trap redistribution. *Inorg. Chem.* 57, 5194–5203. doi: 10.1021/acs.inorgchem.8b00218
- Xu, S. D., Yuan, Y. Y., Cai, X. L., Zhang, C. J., Hu, F., Liang, J., et al. (2015). Tuning the singlet-triplet energy gap: a unique approach to efficient photosensitizers with aggregation-induced emission (AIE) characteristics. *Chem. Sci.* 6, 5824–5830. doi: 10.1039/C5SC01733E
- Xu, Y. H., Wang, X. X., Zhang, W. L., Lv, F., Guo, S. J. (2018a). Recent progress in two-dimensional inorganic quantum dots. *Chem. Soc. Rev.* 47, 586–625. doi: 10.1039/C7CS00500H
- Xue, X. D., Zhao, Y. Y., Dai, L. R., Zhang, X., Hao, X. H., Zhang, C. Q., et al. (2014). Spatiotemporal drug release visualized through a drug delivery system with tunable aggregation-induced emission. *Adv. Mater.* 26, 712–717. doi: 10.1002/adma.201302365
- Xue, Z. L., Li, X. L., Li, Y. B., Jiang, M. Y., Liu, H. R., Zeng, S. J., et al. (2017). X-ray-activated near-infrared persistent luminescent probe for deep-tissue and renewable *in vivo* bioimaging. *ACS Appl. Mater. Interfaces* 9, 22132–22142. doi: 10.1021/acsami.7b03802
- Yan, C., Tian, Q., Yang, S. (2017). Recent advances in the rational design of copper chalcogenide to enhance the photothermal conversion efficiency for the photothermal ablation of cancer cells. *RSC Adv.* 7, 37887–37897. doi: 10.1039/C7RA05468H
- Yan, X., Niu, G., Lin, J., Jin, A. J., Hu, H., Tang, Y., et al. (2015). Enhanced fluorescence imaging guided photodynamic therapy of sinoporphyrin sodium loaded graphene oxide. *Biomaterials* 42, 94–102. doi: 10.1016/j.biomaterials.2014.11.040
- Yang, D. M., Ma, P. A., Hou, Z. Y., Cheng, Z. Y., Li, C. X., Lin, J. (2015a). Current advances in lanthanide ion (Ln(3+))-based upconversion nanomaterials for drug delivery. *Chem. Soc. Rev.* 44, 1416–1448. doi: 10.1039/C4CS00155A
- Yang, J., Choi, J., Bang, D., Kim, E., Lim, E. K., Park, H., et al. (2011). Convertible organic nanoparticles for near-infrared photothermal ablation of cancer cells. *Angew. Chem. Int. Ed.* 50, 441–444. doi: 10.1002/anie.201005075
- Yang, J., Liu, Y. X., Zhao, Y. Y., Gong, Z., Zhang, M., Yan, D. T., et al. (2017a). Ratiometric afterglow nanothermometer for simultaneous *in situ* bioimaging and local tissue temperature sensing. *Chem. Mater.* 29, 8119–8131. doi: 10.1021/acs.chemmater.7b01958
- Yang, K., Feng, L., Shi, X., Liu, Z. (2013). Nano-graphene in biomedicine: theranostic applications. *Chem. Soc. Rev.* 42, 530–547. doi: 10.1039/C2CS35342C
- Yang, K., Xu, H., Cheng, L., Sun, C. Y., Wang, J., Liu, Z. (2012). *In vitro* and *in vivo* near-infrared photothermal therapy of cancer using polypyrrole organic nanoparticles. *Adv. Mater.* 24, 5586–5592. doi: 10.1002/adma.201202625
- Yang, K., Yang, G. B., Chen, L., Cheng, L., Wang, L., Ge, C. C., et al. (2015b). FeS nanoplates as a multifunctional nano-theranostic for magnetic resonance imaging guided photothermal therapy. *Biomaterials* 38, 1–9. doi: 10.1016/j.biomaterials.2014.10.052
- Yang, S. T., Cao, L., Luo, P. G., Lu, F., Wang, X., Wang, H., et al. (2009). Carbon dots for optical imaging *in vivo*. *J. Am. Chem. Soc.* 131, 11308–11309. doi: 10.1021/ja904843x
- Yang, T., Tang, Y. A., Liu, L., Lv, X. Y., Wang, Q. L., Ke, H. T., et al. (2017b). Size-dependent Ag₂S nanodots for second near-infrared fluorescence/photoacoustics imaging and simultaneous photothermal therapy. *ACS Nano* 11, 1848–1857. doi: 10.1021/acsnano.6b07866
- Yao, J., Li, P. F., Li, L., Yang, M. (2018). Biochemistry and biomedicine of quantum dots: from biodetection to bioimaging, drug discovery, diagnostics, and therapy. *Acta Biomater.* 74, 36–55. doi: 10.1016/j.actbio.2018.05.004
- Yin, W. Y., Yan, L., Yu, J., Tian, G., Zhou, L. J., Zheng, X. P., et al. (2014). High-throughput synthesis of single-layer MoS₂ nanosheets as a near-infrared photothermal-triggered drug delivery for effective cancer therapy. *ACS Nano* 8, 6922–6933. doi: 10.1021/nn501647j
- Yong, K. T. (2012). Quantum dots for biophotonics. *Theranostics* 2, 629–630. doi: 10.7150/thno.4757
- Yu, X. H., Gao, D., Gao, L. Q., Lai, J. H., Zhang, C. R., Zhao, Y., et al. (2017). Inhibiting metastasis and preventing tumor relapse by triggering host immunity with tumor-targeted photodynamic therapy using photosensitizer-loaded functional nanographenes. *ACS Nano* 11, 10147–10158. doi: 10.1021/acsnano.7b04736
- Yu, Z. Z., Liu, B., Pan, W., Zhang, T. T., Tong, L. L., Li, N., et al. (2018). A simple approach for glutathione functionalized persistent luminescence nanoparticles as versatile platforms for multiple *in vivo* applications. *Chem. Commun.* 54, 3504–3507. doi: 10.1039/C8CC00743H
- Yuan, Y. Y., Zhang, C. J., Gao, M., Zhang, R. Y., Tang, B. Z. (2015). Specific light-up bioprobe with aggregation-induced emission and activatable photoactivity for the targeted and image-guided photodynamic ablation of cancer cells. *Angew. Chem. Int. Ed.* 54, 1780–1786. doi: 10.1002/anie.201408476
- Zeng, P., Wei, X. T., Yin, M., Chen, Y. H. (2018). Investigation of the long afterglow mechanism in SrAl₂O₄:Eu²⁺/Dy³⁺ by optically stimulated luminescence and thermoluminescence. *J. Lumin.* 199, 400–406. doi: 10.1016/j.jlumin.2018.03.088
- Zhan, D. D., Liu, J. M., Song, N., Liu, Y. Y., Dang, M., Fang, G. Z., et al. (2018). Fabrication of mesoporous La₃Ga₅GeO₁₄:Cr³⁺,Zn²⁺ persistent luminescence nanocarriers with super-long afterglow for bioimaging-guided *in vivo* drug delivery to the gut. *J. Mater. Chem.* 6, 1479–1488. doi: 10.1039/C7TB02759A
- Zhang, L. W., Rong, P. F., Chen, M. L., Gao, S., Zhu, L. (2015). A novel single walled carbon nanotube (SWCNT) functionalization agent facilitating *in vivo* combined chemo/thermo therapy. *Nanoscale* 7, 16204–16213. doi: 10.1039/C5NR03752B
- Zhang, S. H., Sun, C. X., Zeng, J. F., Sun, Q., Wang, G. L., Wang, Y., et al. (2016). Ambient aqueous synthesis of ultrasmall PEGylated Cu_{2-x}Se nanoparticles as a multifunctional theranostic agent for multimodal imaging guided photothermal therapy of cancer. *Adv. Mater.* 28, 8927–8936. doi: 10.1002/adma.201602193
- Zhang, W., Jiang, L. M., Piper, J. A., Wang, Y. L. (2018). SERS nanotags and their applications in biosensing and bioimaging. *J. Anal. Test.* 2, 26–44. doi: 10.1007/s41664-018-0053-9
- Zhang, Y. S., Wang, Y., Wang, L. D., Wang, Y. C., Cai, X., Zhang, C., et al. (2013). Labeling human mesenchymal stem cells with gold nanocages for *in vitro* and *in vivo* tracking by two-photon microscopy and photoacoustic microscopy. *Theranostics* 3, 532–543. doi: 10.7150/thno.5369
- Zhao, P., Xu, Q., Tao, J., Jin, Z. W., Pan, Y., Yu, C. M., et al. (2018). Near infrared quantum dots in biomedical applications: current status and future perspective. *Wiley Int. Rev.* 10:e1483. doi: 10.1002/wnan.1483
- Zhao, P. Q., Ji, W., Zhou, S. Y., Qiu, L. H., Li, L. F., Qian, Z. Z., et al. (2017). Upconverting and persistent luminescent nanocarriers for accurately imaging-guided photothermal therapy. *Mater. Sci. Eng.* 79, 191–198. doi: 10.1016/j.msec.2017.05.046

- Zhong, J. P., Wen, L. W., Yang, S. H., Xiang, L. Z., Chen, Q., Xing, D. (2015). Imaging-guided high-efficient photoacoustic tumor therapy with targeting gold nanorods. *Nanomedicine* 11, 1499–1509. doi: 10.1016/j.nano.2015.04.002
- Zhou, J., Liu, Z., Li, F. Y. (2012). Upconversion nanophosphors for small-animal imaging. *Chem. Soc. Rev.* 41, 1323–1349. doi: 10.1039/C1CS15187H
- Zhou, M., Tian, M., Li, C. (2016b). Copper-based nanomaterials for cancer imaging and therapy. *Bioconjugate Chem.* 27, 1188–1199. doi: 10.1021/acs.bioconjchem.6b00156
- Zhou, Z. J., Song, J. B., Nie, L. M., Chen, X. Y. (2016a). Reactive oxygen species generating systems meeting challenges of photodynamic cancer therapy. *Chem. Soc. Rev.* 45, 6597–6626. doi: 10.1039/C6CS00271D
- Zhu, H. J., Fang, Y., Zhen, X., Wei, N., Gao, Y., Luo, K. Q., et al. (2016). Multilayered semiconducting polymer nanoparticles with enhanced NIR fluorescence for molecular imaging in cells, zebrafish and mice. *Chem. Sci.* 7, 5118–5125. doi: 10.1039/C6SC01251E
- Zou, R., Gong, S. M., Shi, J. P., Jiao, J., Wong, K. L., Zhang, H. W., et al. (2017). Magnetic-NIR persistent luminescent dual-modal ZGOCS@MSNs@Gd₂O₃ core-shell nanoprobe for *in vivo* imaging. *Chem. Mater.* 29, 3938–3946. doi: 10.1021/acs.chemmater.7b00087

Conflict of Interest: The authors declare that the research was conducted in the absence of any commercial or financial relationships that could be construed as a potential conflict of interest.

Copyright © 2019 Yang, Wang, Wan, Gu and Li. This is an open-access article distributed under the terms of the Creative Commons Attribution License (CC BY). The use, distribution or reproduction in other forums is permitted, provided the original author(s) and the copyright owner(s) are credited and that the original publication in this journal is cited, in accordance with accepted academic practice. No use, distribution or reproduction is permitted which does not comply with these terms.



An Artificial Intelligent Signal Amplification System for *in vivo* Detection of miRNA

Xibo Ma^{1,2*}, Lei Chen³, Yingcheng Yang³, Weiqi Zhang^{2,4}, Peixia Wang^{2,4}, Kun Zhang^{1,5}, Bo Zheng³, Lin Zhu^{1,2}, Zheng Sun^{1,2}, Shuai Zhang^{1,2}, Yingkun Guo⁵, Minmin Liang⁶, Hongyang Wang^{3*} and Jie Tian^{1,2,7*}

¹ CAS Key Laboratory of Molecular Imaging, Institute of Automation, Chinese Academy of Sciences, Beijing, China, ² School of Artificial Intelligence, University of Chinese Academy of Sciences, Beijing, China, ³ International Co-operation Laboratory on Signal Transduction, Eastern Hepatobiliary Surgery Institute, Second Military Medical University, Shanghai, China, ⁴ National Laboratory of Biomacromolecules, CAS Center for Excellence in Biomacromolecules, Institute of Biophysics, Chinese Academy of Sciences, Beijing, China, ⁵ Department of Radiology, West China Second University Hospital, Sichuan University, Chengdu, China, ⁶ Experimental Center of Advanced Materials School of Materials Science & Engineering, School of Materials Science & Engineering, Beijing Institute of Technology, Beijing, China, ⁷ Beijing Advanced Innovation Center for Big Data-Based Precision Medicine, Beihang University, Beijing, China

OPEN ACCESS

Edited by:

Michael Ming-Yuan Wei,
Texas Commission on Environmental
Quality, United States

Reviewed by:

Filippo Causa,
University of Naples Federico II, Italy
Paola Valentini,
Italian Institute of Technology (IIT), Italy

*Correspondence:

Xibo Ma
xibo.ma@ia.ac.cn
Hongyang Wang
hywangk@vip.sina.com
Jie Tian
jie.tian@ia.ac.cn

Specialty section:

This article was submitted to
Nanobiotechnology,
a section of the journal
Frontiers in Bioengineering and
Biotechnology

Received: 15 July 2019

Accepted: 29 October 2019

Published: 21 November 2019

Citation:

Ma X, Chen L, Yang Y, Zhang W,
Wang P, Zhang K, Zheng B, Zhu L,
Sun Z, Zhang S, Guo Y, Liang M,
Wang H and Tian J (2019) An Artificial
Intelligent Signal Amplification System
for *in vivo* Detection of miRNA.
Front. Bioeng. Biotechnol. 7:330.
doi: 10.3389/fbioe.2019.00330

MicroRNAs (miRNA) have been identified as oncogenic drivers and tumor suppressors in every major cancer type. In this work, we design an artificial intelligent signal amplification (AISA) system including double-stranded SQ (S, signal strand; Q, quencher strand) and FP (F, fuel strand; P, protect strand) according to thermodynamics principle for sensitive detection of miRNA *in vitro* and *in vivo*. In this AISA system for miRNA detection, strand S carries a quenched imaging marker inside the SQ. Target miRNA is constantly replaced by a reaction intermediate and circulates in the reaction, similar to enzyme. Therefore, abundant fluorescent substances from S and SP are dissociated from excessive SQ for *in vitro* and *in vivo* visualization. The versatility and feasibility for disease diagnosis using this system were demonstrated by constructing two types of AISA system to detect Hsa-miR-484 and Hsa-miR-100, respectively. The minimum target concentration detected by the system *in vitro* (10 min after mixing) was 1/10th that of the control group. The precancerous lesions of liver cancer were diagnosed, and the detection accuracy were larger than 94% both in terms of location and concentration. The ability to establish this design framework for AISA system with high specificity provides a new way to monitor tumor progression and to assess therapeutic responses.

Keywords: *in vivo* detection of non-coding RNA, an artificial intelligent signal amplification system, early diagnosis of precancerous lesions, fluorescent molecular tomography, stem cell tracing

INTRODUCTION

Foundational to physiological programs in developmental and disease contexts is microRNA (miRNA) regulation, especially for cancer; miRNAs have been confirmed to be oncogene drivers or inhibitory factors (Anastasiadou et al., 2018). When cells become cancerous, they secrete special proteins that can be used for targeted imaging. However, the expression levels of miRNAs in cells are often changed before they become cancerous. Compared to detecting proteins secreted by tumors, detecting secreted miRNAs has become more attractive for monitoring tumor progression. The molecular biology principle of complementary base pairing for miRNA facilitates the design of a universal, highly sensitive detection system that can visualize miRNA *in vivo* to monitor tumor

progression. Based on this principle and the fluorescence quenching principle, molecular beacons have been synthesized with DNA or RNA base sequences (Yurke et al., 2000; Seelig et al., 2006; You et al., 2015, 2017; Ma et al., 2017; Fu et al., 2018), enabling their application in the detection of target RNA *in vitro* and at the cellular level (Yurke et al., 2000; Sawada et al., 2009; Auslander and Fussenegger, 2014; Green et al., 2014; Koc et al., 2015; Parolini et al., 2016; Yang et al., 2016a; Zhang et al., 2017; Li et al., 2018).

However, these reported strategies cannot achieve *in vivo* visualization of miRNA (not to mention miRNA quantification) because the fluorescence generated by the molecular beacon is not amplified; simple conjugation with one unit of target miRNA only release one unit of the fluorescent molecule. In a short period of time, chemical reactions often cannot be completely carried out, so a unit of target molecules often cannot produce a unit of fluorescent molecules. Amplification of fluorescent signal would produce a sufficient signal to meet the needs of *in vivo* detection. Recently, some amplification strategies were successfully used in logic circuits and for *in vitro* detection of the Zika virus (Pardee et al., 2016); however, these strategies cannot be directly applied to *in vivo* monitoring of miRNA because they do not adequately account for the chemical reaction that occurs within the probe itself and its *in vivo* degradation (Green et al., 2014; Hall and Macdonald, 2016; Pardee et al., 2016).

Despite its fundamental importance and theoretical achievability, as well as the aforementioned promising early efforts (Yurke et al., 2000; Seelig et al., 2006; Siuti et al., 2013; Li et al., 2016; Ma et al., 2017; You et al., 2017), it remains challenging to develop a general strategy for designing and synthesizing an artificial intelligent signal amplification (AISA) system [including double-stranded SQ (S, signal strand; Q, quencher strand) and double-stranded FP (F, fuel strand; P, protect strand)] that can react with the miRNA of interest and further amplify the generated signal (due to double-stranded FP) for the purpose of *in vivo* detection. The key design challenge is to barely achieve a reaction between the two components in the AISA system to obtain as little noise as possible in the absence of the target miRNA and to initiate a cascade in the presence of the target miRNA to obtain as many useful signals as possible. Fortunately, Song et al. designed a probe for the detection of miR-21 (Wang et al., 2017), which was the structural prototype of the amplification system and initially realized the increase in signal. However, the specificity is not considered in the design of the system and the nonspecific signal is strong, so the fluorescence of miR-21 was only detected at the tissue level. The AISA system contains two double-stranded DNA, SQ and FP, and there are many combinations of SQ and FP (kinds of terminal α , β , and γ) that can meet the corresponding three-step amplification response. Our main innovation lies in that, through experiments, we have selected the AISA system with the optimal signal/noise ratio (SNR). Meanwhile, we will further explore the relevant conditions of the AISA system with the optimal SNR in the future research.

In addition, an appropriate carrier is indispensable to transport the active components and guarantee that the detection reaction occurs. A suitable carrier must satisfy the following

three basic requirements. First, during the transportation process after injection via the tail vein, the carrier of the AISA system should load as many active components as possible and resist degradation by various enzymes in the body to achieve a sufficient concentration in the target organs. Second, after reaching the target organ, the AISA system should be able to release its active components, that is, two double-stranded DNA molecules, which should cross the cell membrane and enter the cytoplasm. Third, and most critically, the cytoplasmic concentration of the active components released and transported by the AISA system must be sufficient to guarantee an effective detection reaction, and these components should be able to distinguish the target miRNA and its analogs effectively so that we can obtain an image with a high signal/noise (SNR) ratio. In the previous studies, many researchers have innovatively prepared vectors to deliver small interfering RNA, miRNA, and immunotherapeutic antibody for molecular therapy (Zhong et al., 2015; Wang et al., 2018; Yaghini et al., 2018; Liu et al., 2019; Wu et al., 2019; Xu et al., 2019). These carriers can transport the substances into cells, but their transport efficiency varies, which will affect subsequent calculation of the relationship between fluorescence intensity and RNA concentration. Therefore, the mature carrier with stable delivery efficiency is the best choice for our study.

In this study, we designed the AISA system including two double-stranded DNAs (SQ and FP) for *in vivo* visualization of miRNA and clarified the reaction principle. We verified the detection sensitivity and specificity of the system *in vitro*. The versatility and practicability of this system were demonstrated by constructing two types of AISA system to detect Hsa-miR-484 and Hsa-miR-100, respectively. Based on this detection system, the precancerous lesions of liver cancer were diagnosed and reconstructed.

MATERIALS AND METHODS

Materials

All chemical reagents were purchased from Sigma-Aldrich (Sigma-Aldrich, Beijing, China). Lipofectamine 3000 reagent (included lipo3000 and reagent) were purchased from ThermoFisher (USA). LO2 cells were purchased from the National Infrastructure of Cell Line Resource, and miR-484-transfected LO2 normal human liver cells (LO2-miR-484) were provided by Dr. Lei Chen from the Second Military Medical University. All animals were purchased from Beijing Vital River Laboratory Animal Technology Co., Ltd., and all animal experiments were conducted in accordance with the guidelines of the Institutional Animal Care and Use Committee at Peking University and the Eastern Hepatobiliary Surgery Hospital Research Ethics Committee.

Standard Buffer Conditions

All double- and single-stranded DNA molecules were suspended and stored in Tris-HCl buffer (150 mM NaCl pH balanced to 7.4, with 1.25 mM MgCl₂) at 4°C. This buffer concentration produces 303.75 osmotic pressure, which is near that of the internal environment.

DNA Concentration

Nucleotide concentrations were calculated according to the molar extinction coefficient of single-stranded DNA. The measured extinction value at 260 nm and ultraviolet–visible spectra were obtained through a Cary UV-300 ultraviolet–visible spectrophotometer.

Preparation of Double-Stranded SQ and FP

Each strand was prepared with nominal stoichiometry at 100 μ M concentration in Tris–HCl buffer. The signal strands S were mixed with quencher strands at a 6:7 molar ratio to ensure that the signal strands were saturated by quencher strands and suppressed the background noise without miRNA. Single-stranded F was mixed with single-stranded P at a 1:1 molar ratio. The two mixtures were heated at 90°C for 10 min and then slowly cooled to room temperature (more than 2 h). The double-stranded SQ and FP were stored at 4°C for further use.

Preparation of the AISA System

Then, 100 μ l of double-stranded SQ (50 μ M), 200 μ l of double-stranded FP (50 μ M), and 5 μ l of reagent (included in the Lipofectamine 3000 kit) were mixed homogeneously. After 5 min, 5 μ l of Lipo3000 was added to the mixture to construct the AISA system.

In vitro Time-Based Fluorescence Studies

Fluorescence emission signals were acquired using an F-7000 fluorescence spectrophotometer (Hitachi High-Tech Science Corporation, Tokyo, Japan) with 649 nm excitation and 669 nm emission wavelengths for Cy5. The fluorescence intensity of 100 nM single-stranded S was set as 1,000, and the fluorescence intensity of others was normalized to that of S.

High-Speed Atomic Force Microscopy Imaging

First, 1 μ l of sample containing single-stranded miR-484 (100 μ M), double-stranded SQ, and double-stranded FP (50 μ M) was diluted with 1 μ l of 100 mM NiCl_2 and 8 μ l of Milli-Q water (final SQ/FP: 5 μ M, 10 mM NiCl_2). Two microliters of diluted DNA was dropped on cleaved mica. After 10 min, a high-speed atomic force microscopy instrument (Research Institute of Biomolecule Metrology Co., Ltd, Japan) (Kodera et al., 2010; Katan and Dekker, 2011; Miyagi et al., 2016; Shibata et al., 2017) was used to image DNA in Milli-Q water. The conditions were set as follows: cantilever, BL-AC10DS-A2 (Olympus, Japan); resolution, 200 \times 200 pixels; mode, ac mode in liquid. All images were analyzed using ImageJ (NIH) SPIP (Image Metrology A/S).

Detection of miR-484 and miR-100 at the Subcellular Level

The LO2-miR-484/MSC-miR-100 cells were seeded at $\approx 1 \times 10^4$ cells per well into uncoated and glass-bottomed confocal plates, and the seeded cells were incubated with the AISA system (100 nM) for 4 h in Dulbecco's modified Eagle medium (HyClone, Thermo Fisher Scientific, USA) and growth medium [10% FBS (Gibco), 37°C, 5% CO_2]. Fluorescein isothiocyanate-phalloidin was diluted 200 times with phosphate-buffered saline

(PBS), added to the cells, and incubated for 40 min. For dynamic fluorescence confocal observation, 4',6-diamidino-2-phenylindole was diluted 400 times with PBS and added to the cells for the subsequent image acquisition.

In vivo Detection of Injected miR-484 Based on miR-484-Injected Animal Models

Three types of animal models were prepared for evaluation of the AISA⁴⁸⁴ system. First of all, 25 μ l of miR-484-Lipo solution (5 μ l of reagent and 5 μ l of Lipo3000 per 300 μ l solution) at 20 μ M was injected into C57 mouse livers with a 2.5-mm injection depth. Then, the mice were injected with AISA system solution (100 μ l per 20 g) via the tail vein, and fluorescence images were acquired at 22 min using the fluorescence system that we developed (Figure 3).

To evaluate the ability of the AISA system to distinguish miR-484 from tumors, miR-484-injected and diethyl nitrosamine (DEN)-induced tumor-bearing mouse models were generated. First, 4 mg/ml DEN was injected into the abdomen of a 15-day-old mouse at a dose of 25 mg/kg. Seven months later, after opening the abdominal cavity, 25 μ l of miR-484 solution was injected into mouse liver at an injection depth of 4 mm, where no tumor formation had occurred. Fluorescence images were also acquired using our system under the following conditions: binning = 2, exposure time = 0.2 s, excitation wavelength = 649, emission wavelength = 680 (Figure S4). A multiple target model was established by injecting miR-484 into the rat liver at 3- and 2-mm intervals (Figure S5).

To evaluate the universality of this design strategy for the AISA system, we redesigned the AISA system to detect miR-100 and generated a miR-100 mouse model to evaluate the detection ability. A total of 25 μ l of miR-100 solution of 60, 40, and 10 μ M was injected into the femoral head of the BALB/c mice with a lateral approach. The mice were injected with 100 μ l of AISA¹⁰⁰ system solution via the tail vein, and fluorescence images were then acquired at 5, 12, 22, 32, and 60 min using our system (Figure S9). Since miR-100 is an important indicator of the progression of gastric cancer, we also established a high-expression miR-100 model of gastric cancer to evaluate the detection capability of the AISA system. SGC-7901-miR-100 tumor-bearing mice were generated by subcutaneous injection of 10^6 cells into the right upper flanks of BALB/c nude mice. The mice were imaged to detect miR-100 when the tumor volume was $< 10 \text{ mm}^3$, after ~ 10 days. The mice were treated with 100 μ l of AISA¹⁰⁰ system solution via the tail vein, and fluorescence images were acquired at 15, 40, and 60 min and 2, 6, and 12 h using the fluorescence imaging system under the same conditions as above (Figure 3D).

In vivo Detection of miR-484 With DEN-Induced Mice and Human Samples

In addition, to evaluate the practicability of the AISA system, 4 mg/ml DEN was injected into the abdomen of the 15-day-old mice at a dose of 25 mg/kg to generate a tumorigenic model with high expression of miR-484. After ~ 3 months, the mice were treated with 100 μ M AISA⁴⁸⁴ (included SQ and FP) system at a

dose of 100 $\mu\text{l/kg}$ via the tail vein, and fluorescence images were acquired using our system (Figure 4A). Three-dimensional (3D) information of miRNA were reconstructed using fluorescence molecular tomography based on sparsity adaptive correntropy matching pursuit method (Zhang et al., 2018b). Then, to evaluate the expression of miR-484, reverse transcription PCR (RT-PCR) was performed on the samples dissected from the mouse liver according to the location of fluorescence spots on the surface and the depth information derived from the 3D reconstructed results.

For detection of miR-484 in human samples, the samples were washed three times with PBS. Then, the samples were immersed in the 100 μM AISA⁴⁸⁴ solution for ~ 15 min. Then, the samples were removed, and the floating liquid was wiped off and placed in the fluorescent imaging instrument developed by ourselves. The imaging parameters were set as: exposure time = 1 s, binning = 4, excitation wavelength = 649, and emission wavelength = 680.

In vivo Reconstruction of Injected and Transfected miR-484

The surface fluorescence signal detected by our system is related to the following two processes: the reaction between miRNA and double-stranded SQ and FP in the cell leads to fluorescence; the fluorescence signal passes through a certain depth of tissue to the body surface and is acquired by our system.

When a fluorescence signal is generated inside the body, we cannot directly detect the fluorescence intensity; we can only detect the distribution and intensity of fluorescence that passes through the tissue and reaches the body surface. The transmission of fluorescence *in vivo* obeys a certain rule, which can be expressed by the following equation describing the propagation of light (Ma et al., 2013; Xue et al., 2013; Qin et al., 2014; Ye et al., 2014; Zhang et al., 2018b):

$$\nabla [D_x(r) \nabla \Phi_x(r)] - \mu_{ax}(r) \Phi_x(r) = -\Theta \delta(r - r_l) (r \in \Omega)$$

$$\nabla [D_x(r) \nabla \Phi_x(r)] - \mu_{am}(r) \Phi_m(r) = -\Phi_x(r) \eta \mu_{af}(r) (r \in \Omega)$$

$$2D_{x,m}(r) \nabla \Phi_{x,m}(r) + q \Phi_{x,m}(r) = 0 (r \in \partial\Omega)$$

where r denotes the nodes inside the problem domain Ω ; r_l is the position of point excitation sources, which are placed on one mean free path of photon transport beneath the surface of Ω ; $\mu_{ax,am}$ and $\mu_{sx,sm}$ denote the absorption and scattering coefficients, respectively; Θ is the excitation intensity; and $\Phi(r)$ is the photon flux density at node r . $\eta \mu_{af}(r)$ is the fluorophore distribution to be reconstructed, where η is the quantum yield and q denotes the optical reflective index. In the process of fluorescence tomography reconstruction, we used Robin boundary conditions to calculate the position of fluorescence source *in vivo* (Ma et al., 2013). For nearly 10 years, our research group has been working on 3D reconstruction of internal fluorescence and developed series of algorithms. Thus, according to Equation (1), the 3D distribution of the inner source can be reconstructed.

Toxicity of the AISA System

To evaluate the toxicity of the AISA system, 2×10^3 LO2 normal human liver cells per well were seeded into 96-well plates overnight. The cells were treated with seven concentrations of the AISA system (0, 1, 5, 10, 20, 40, 60, and 100 nM) for 24 h. Then, 10 μl of CCK-8 was added to each well. After incubation for 2 h at 37°C, the absorbance was measured at 450 nm using a BioTeK Synergy HT Universal Microplate Reader.

To evaluate the toxicity of the AISA system *in vivo*, 21 mice were randomly divided into three groups. Two of the groups were treated with 100 μl of the AISA system via the tail vein, and one group was treated with the same amount of PBS. For the mice in the two groups administered the AISA system, blood and tissue, including liver, muscle, heart, spleen, kidney, stomach, lung, brain, and skin tissue, were collected 1 and 2 weeks later, respectively. For the mice in the control group, serum and tissues were taken 2 weeks later. With the serum samples, creatine kinase (CK) and lactate dehydrogenase (LDH) were measured to evaluate cardiac function (Prakash, 1978; Yong et al., 2002); aspartate transaminase (AST), alanine aminotransferase (ALT), and alkaline phosphatase (ALP) were measured to evaluate liver function (Kory et al., 1959); and blood urea nitrogen (BUN) and creatinine (CREA) were measured to evaluate kidney function (Griebing, 2017). The tissue samples were embedded in wax blocks, sectioned and stained with hematoxylin and eosin (H&E) to evaluate the toxicity of the AISA system.

RESULTS

Design of the AISA System

Although various molecular beacons based on toehold-mediated reactions or nanomaterial-mediated quenching have been created, simple conjugation with one unit of target miRNA to release one unit of the fluorescent molecule would not solve a key challenge in the *in vivo* detection of miRNA: the need to produce enough fluorescence to be captured by our charge-coupled device system despite their degradation in tissues. Thus, we urgently need to focus on finding a way to make the two double-stranded DNA molecules involving in the reaction and further amplify the fluorescence signal. We designed two double-stranded DNA that can react with the target miRNA to achieve this amplification effect. To achieve the effect of cyclic reaction, the second and third reaction must maintain a kind of seesaw thermodynamic equilibrium. The length of dangling end α in double-stranded SQ determines whether the reaction can occur spontaneously, while the length of dangling end β determines its ability to distinguish between targets and their analogs, which is defined as the discrimination factor Q (Zhang et al., 2012). Here, the discrimination factor Q can be calculated based on experiments.

$$Q = \frac{\chi_M}{\chi_S}$$

where χ_M is the signal produced by SQ in response to the target miRNA, M, and χ_S is the signal produced by SQ in response to the spurious analogs, S.

The literature (Zhang and Winfree, 2009) indicates that the length of α must be ≥ 5 to ensure the occurrence of the first-step reaction, which is marked as design rule 1. In the second step, double-stranded MQ reacts with FP via dangling end β to produce stable double-stranded FQ and MP. Considering the above two reactions (Figure 1, steps 1 and 2), it is not difficult to find that dangling ends α and β correspond to each other, that is, the length of β influences the discrimination factor Q of the first step, and the length of α influences the discrimination factor of the second step. To ensure that the value of Q is acceptable, the length of dangling ends α and β should only be 5 or 6. Here, we take its length to be 5 (as design rule 2; also conforms to design rule 1), and later, we find that the length of $\beta = 6$ influences only the length of the strand P , so we will no longer discuss this value separately.

Different carriers have different delivery efficiency to minimize the effect of delivery efficiency on fluorescence intensity. In this study, Lipo3000 is favored as a carrier of biomaterials due to its high delivery efficiency and the ability to load DNA through the mutual attraction of positive and negative charges.

The Reaction Principle and Optimization of the AISA System

For the first time, we successfully achieved *in vivo* visualization of miRNA and introduce a general design framework for the AISA system and explain the reaction principle (Figures 1A,B). The key innovation is the use of a second double-stranded DNA (FP) to initiate the next two-step cascade cyclic reactions due to the thermodynamics equilibrium based on the first-step reaction. In the process of the reaction, the target M is constantly substituted to participate in the cascade reaction. Under the condition of excessive SQ and FP, a sufficiently large signal was produced through these three-step reactions. For the first-step reaction, double-stranded SQ (Cy5 at the 3' end of the S strand, BHQ2 at the 5' end of the Q strand) reacts with the target miRNA (M) via dangling end α to generate single-stranded S carrying the signal molecule Cy5 and double-stranded MQ with a new dangling end, β . This reaction can be represented by the following reversible reaction equation: $M + SQ \rightleftharpoons MQ + S$. For the second-step reaction, double-stranded MQ reacts with FP via dangling end β to produce stable double-stranded

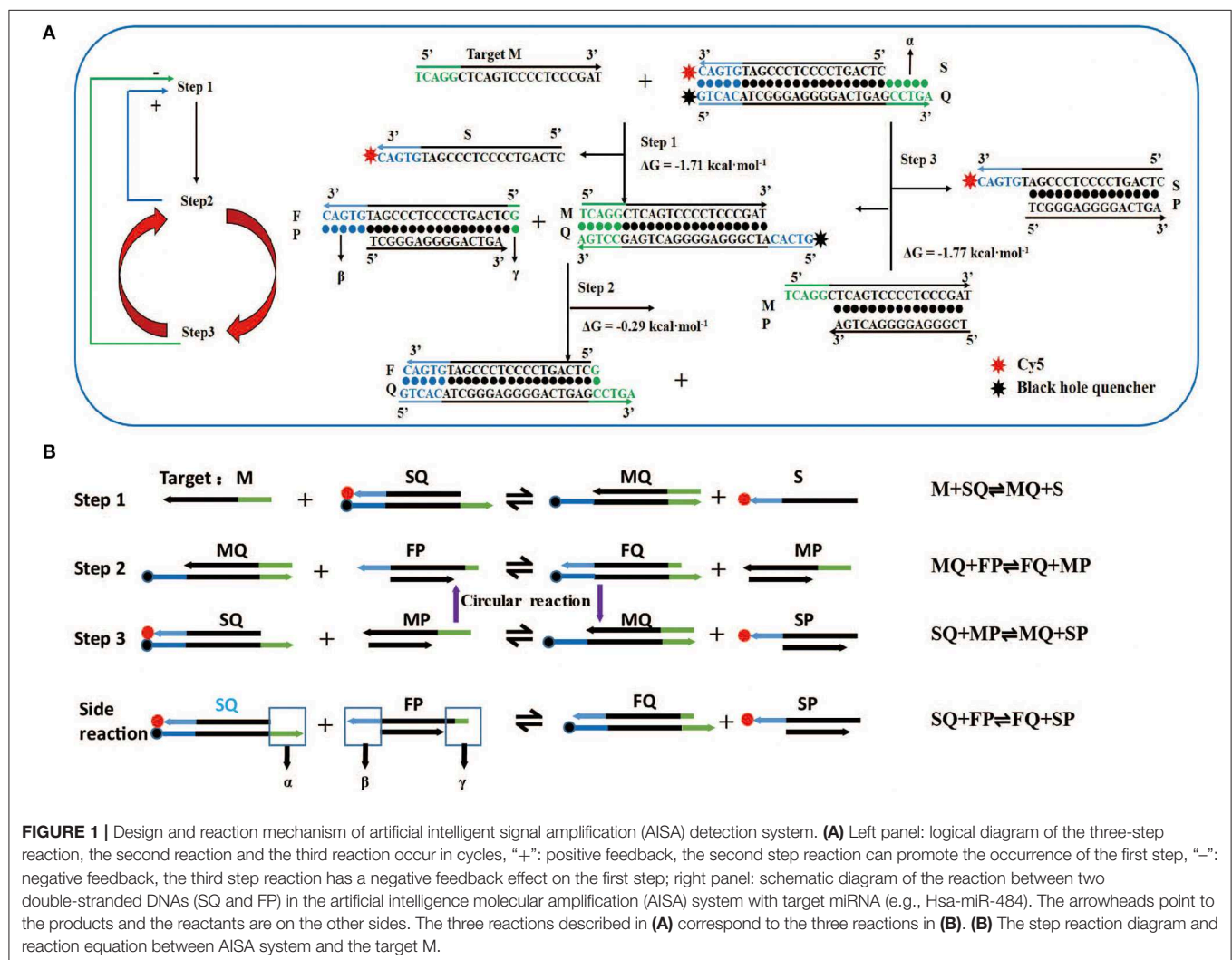


FIGURE 1 | Design and reaction mechanism of artificial intelligent signal amplification (AISA) detection system. **(A)** Left panel: logical diagram of the three-step reaction, the second reaction and the third reaction occur in cycles, "+": positive feedback, the second step reaction can promote the occurrence of the first step, "-": negative feedback, the third step reaction has a negative feedback effect on the first step; right panel: schematic diagram of the reaction between two double-stranded DNAs (SQ and FP) in the artificial intelligence molecular amplification (AISA) system with target miRNA (e.g., Hsa-miR-484). The arrowheads point to the products and the reactants are on the other sides. The three reactions described in (A) correspond to the three reactions in (B). **(B)** The step reaction diagram and reaction equation between AISA system and the target M.

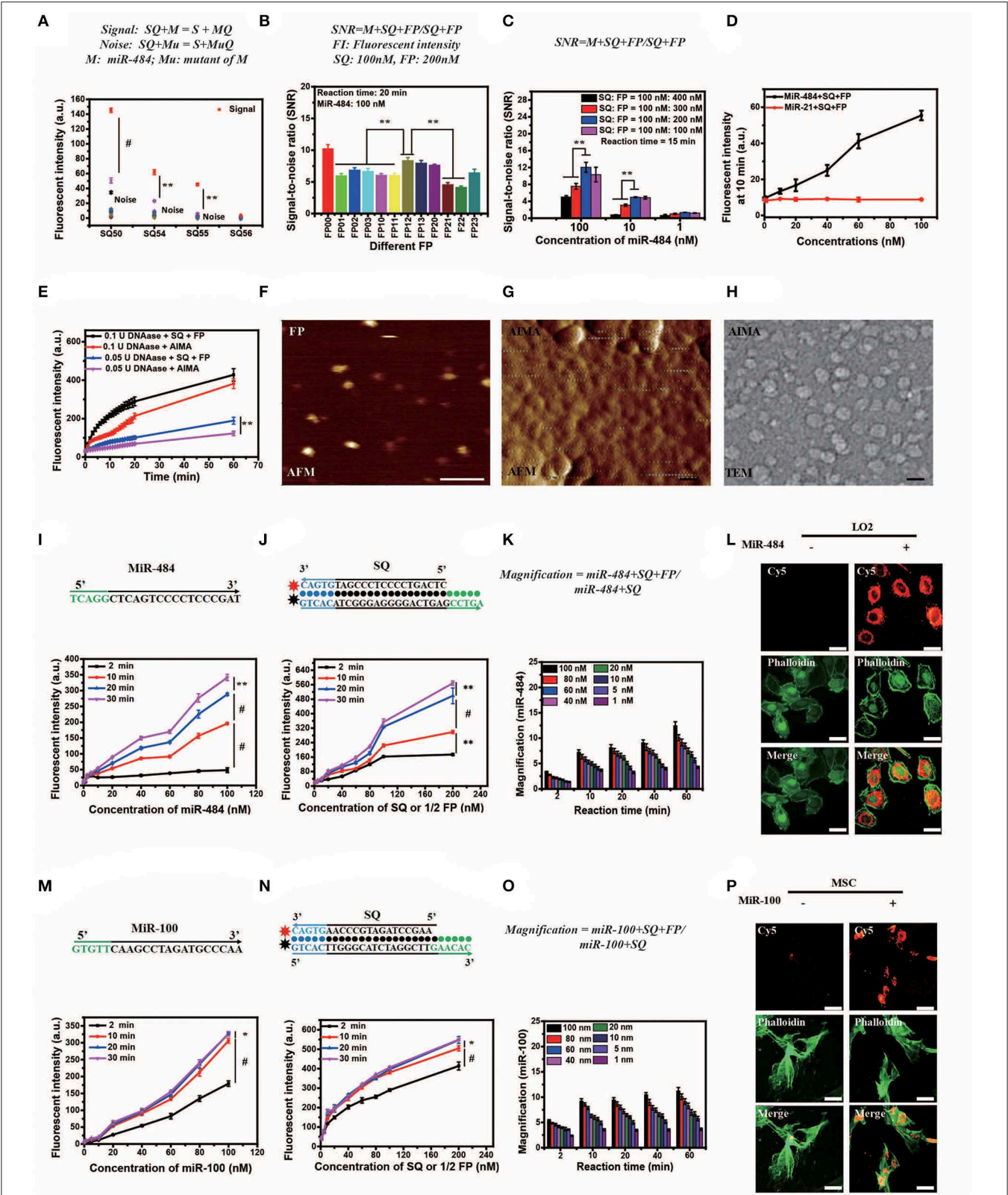


FIGURE 2 | Optimization, characterization, and *in vitro* and intracellular dynamics of artificial intelligent signal amplification (AISA) systems with target RNA. (A) Fluorescence intensity generated by different SQs and miR-484 or its 11 mutants measured using a fluorospectrophotometer [signal indicates the fluorescence intensity generated by miR-484, noise indicates the fluorescence intensity generated by its 11 mutants (shown in Table S1)]. (B) Signal/noise ratio (SNR) generated by (Continued)

FIGURE 2 | the reactions based on 12 kinds of double-stranded FP (the fluorescence intensity generated by SQ and FP with miR-484 was considered signal, while fluorescence intensity generated by SQ and FP without miR-484 was considered noise). **(C)** SNR generated by different ratios of double-stranded SQ/FP and miR-484 at 15 min after reaction (signal and noise are the same as in A). **(D)** Fluorescence intensity generated by miR-484 and miR-21 (SQ and FP is designed for detection of miR-484). **(E)** Fluorescence intensity generated by reactions between DNase (0.1 U, 0.05 U) and SQ, FP, or the AISA system. **(A–E)** Bars represent mean \pm SD, $n = 5$. **(F–H)** From left to right is the atomic force microscopy (AFM) image of double-stranded FP and the AISA system, the transmission electron microscopy (TEM) image of the AISA system; scale bar, 50 nm. Throughout the paper, ANOVA and the t -test were used to analyze the means, $*p < 0.05$, $**p < 0.01$, $##p < 0.001$. **(I)** Core sequence of miR-484; fluorescence intensity generated by the reaction between double-stranded SQ (100 nM), FP (200 nM), and different concentrations of miR-484. **(J)** Sequence of double-stranded SQ for detection of miR-484; fluorescence intensity generated by the reaction between miR-484 (100 nM) and different concentrations of double-stranded SQ and FP (SQ/FP = 1/2). **(K)** Magnification of the reaction between SQ (100 nM) and different concentrations of miR-484 with and without double-stranded FP. **(L)** Bright field microscopic image of LO2 cells transfected with or without miR-484. Fluorescence image of LO2 cells transfected with or without miR-484 after adding the AISA system. Fluorescence image of LO2 cells transfected with or without miR-484 stained with fluorescein isothiocyanate (FITC)-phalloidin. Merged image of LO2 cells transfected with or without miR-484. **(M)** Core sequence of miR-100; fluorescence intensity generated by the reaction between double-stranded SQ (100 nM), FP (200 nM), and different concentrations of miR-100. **(N)** Sequence of double-stranded SQ for detection of miR-100; fluorescence intensity generated by the reaction between miR-100 (100 nM) and different concentrations of double-stranded SQ and FP (SQ/FP = 1/2). **(O)** Magnification of the reaction between SQ (100 nM) and different concentrations of miR-100 with and without double-stranded FP. **(P)** Bright field microscopic image of mesenchymal stem cells (MSC) transfected with or without miR-100. Fluorescence image of MSC transfected with or without miR-100 after adding the AISA system. Fluorescence image of MSC transfected with or without miR-100 stained with FITC-phalloidin. Merged image of MSC transfected with or without miR-100. **(I–P)** Scale bars, 10 μ m (ANOVA and the t -test were used to analyze the means, $*p < 0.05$, $##p < 0.001$).

FQ and unstable MP: $MQ + FP \rightleftharpoons FQ + MP$. This unstable MP easily reacts with SQ through its dangling end to generate MQ and SP, which can emit fluorescence: $SQ + MP \rightleftharpoons MQ + SP$ (the third-step reaction). The reaction between the two components of the AISA system, SQ and FP, is undesirable, and the resulting fluorescence is considered noise. The side reaction is represented in the following equation: $SQ + FP \rightleftharpoons FQ + SP$ (Figures S1A,B). The most interesting thing is that the product of the third step, MQ, is a reactant in the second step; meanwhile, the second- and third-step reactions maintain a seesaw equilibrium thermodynamically; thus, these steps can occur cyclically. The above reaction principle was verified in the following experiments (Figures S1E–H).

The length of dangling end α determines whether the first-step reaction can occur spontaneously, while the length of dangling end β determines its ability to distinguish between targets and their analogs (Zhang et al., 2012). We designed 11 variants of miR-484 (miRNA usually has a high probability of point mutation at specific positions and insertion and deletion mutants in human body Table S1) and four different kinds of double-stranded SQ (Table S2) to verify the discrimination ability of SQ. Compared with others (SQ50, SQ54, and SQ56), SQ55 performed best and was ultimately selected as the first double-stranded DNA in our AISA system (Figure 2A). Notably, the length of the dangling end γ determines whether the above side reaction can occur [the side reaction refers to the reactions that occur between SQ and FP when there is no target RNA (see Figure 1B)], so we limited the length of γ to 4 or less. To further demonstrate the optimal structure of double-stranded FP, 12 double-stranded FP chains (listed in Table S3) were designed to participate in the experiments, and the SNR was tested with miR-484. SNR was defined as $SNR = \frac{FL_m}{FL_s + FL_m}$, where FL_m is the fluorescence intensity generated by the reaction among miR-484 with double-stranded SQ and FP and FL_s is the fluorescence intensity generated by the reaction between double-stranded SQ and FP. The results in Figure 2B show that the overall performance of FP00 is optimal in terms of the SNR. However, the fluorescence intensity derived by FP00 (137 a.u.) is lower than that of FP12 (152 a.u.) at the same conditions. Thus, to

ensure the miRNA detection depth, FP12 was selected as the following application. We used four different SQ/FP ratios and measured the resulting SNR. Although higher FP concentrations increased the signal intensity, the noise cannot be ignored. From the comparison of the SNR of the four reactions with different concentrations, the ratio of SQ/FP = 1/2 was selected of our AISA system (Figure 2C).

Characterization of the AISA System *in vitro*

In addition, to assess the specificity of the system, fluorescence intensity generated by miR-484 and miR-21 were detected. With the increase in RNA concentration, the fluorescence intensity generated by miR-484 was much higher than that generated by miR-21 (Figure 2D). The fluorescence intensity generated by miR-484 was about five times of that generated by miR-21 especially at high RNA concentrations. For transportation of the active components (SQ and FP) to the target to guarantee that the detection reaction will occur, a suitable carrier is also indispensable. Lipo3000 has been experimentally (Figure 2E) demonstrated to be able to resist the hydrolysis of DNase to some extent for 60 min, which may be due to the steric effect of DNase itself.

To better understand the *in vivo* detection principle, the appearance and microscopic behaviors of SQ and FP in the AISA system were observed using transmission electron microscopy (TEM) and high-speed atomic force microscopy (AFM), respectively (Kodera et al., 2010). TEM and AFM images of SQ/FP (Figures 2F–J; Movies 1,2) demonstrated that the length of the double-stranded DNA was ~ 10 nm, the width was ~ 2 nm, and the area was ~ 20 nm². When double-stranded SQ and FP were loaded onto the surface of the liposome, an ~ 50 nm sphere formed. After adding the target, miR-484, the reaction between double-stranded SQ, FP, and the target was observed by AFM (Movie S3). In addition, to obtain high-purity double-stranded DNA, all synthetic products in this work were purified by high-performance liquid chromatography. The mass spectrometry data (Figures S1I–P) showed that the purity of the

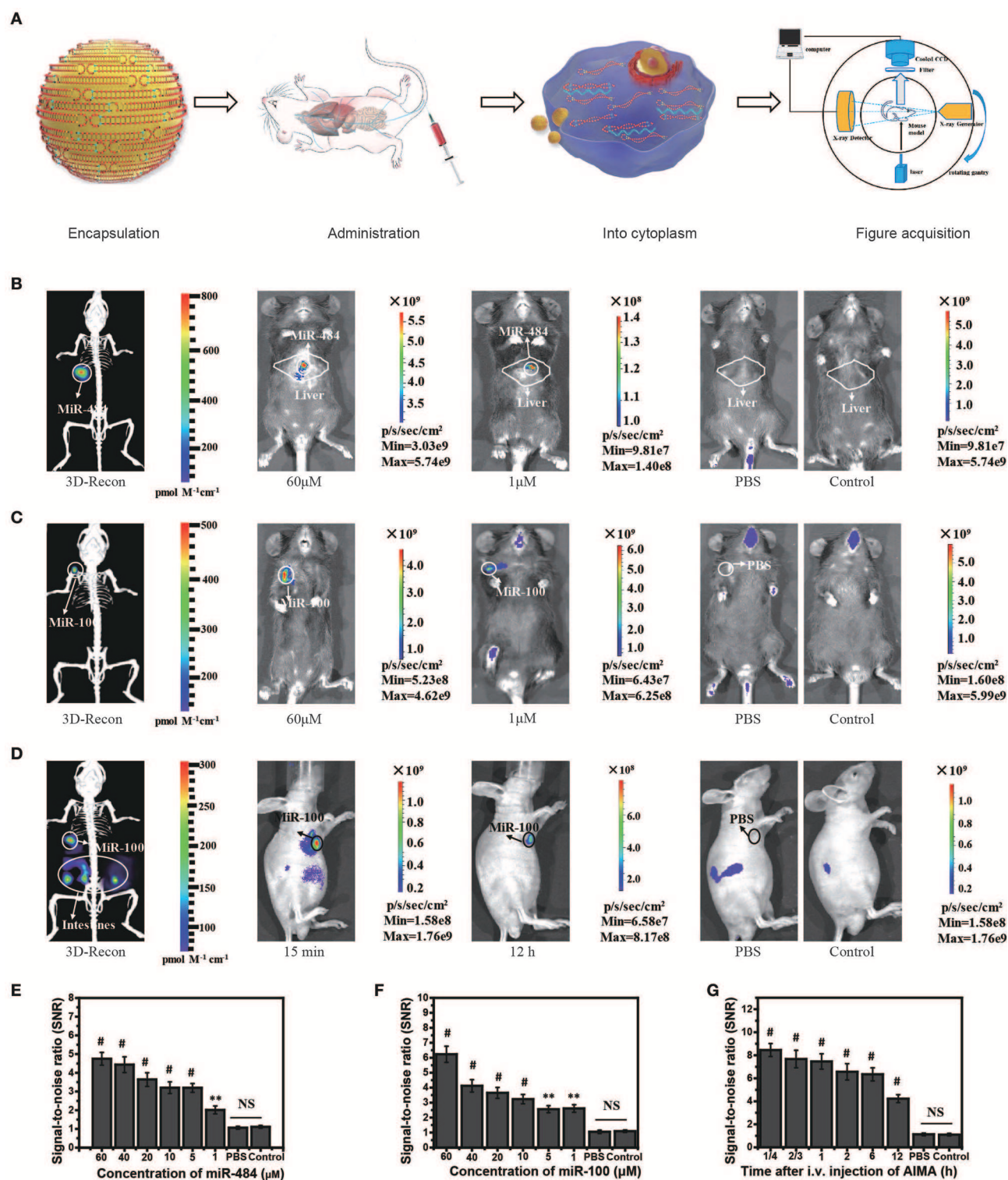


FIGURE 3 | Visualization and 3D reconstruction of microRNA (miRNA) *in vivo* based on miR-484-injected and miR-100 injection mouse models. **(A)** Flow chart of the experiments, including encapsulation of double-stranded SQ and FP in liposomes; administration of the artificial intelligent signal amplification (AISA) system; process of double-stranded SQ and FP entering the cytoplasm; and image acquisition based on a dual-modality system including a high-sensitivity fluorescence system and a microcomputed tomography system. **(B)** Fluorescence images and 3D reconstructed image of mice injected with miR-484 (25 μL , 20 μM) in the liver (depth, 2.5 mm) at 10 min after i.v. injection of the AISA⁴⁸⁴ system. **(C)** Fluorescence images and 3D reconstructed image of mice injected with miR-100 in the femoral head at 10 min (Continued)

FIGURE 3 | after i.v. injection of the AISA¹⁰⁰ system. **(D)** Fluorescence images and 3D reconstructed image of SGC-7901-miR-100 tumor-bearing mice at 15 min after i.v. injection of the AISA¹⁰⁰ system. **(E)** Signal/noise ratio (SNR) based on fluorescence images of different concentrations of miR-484-injected mice. **(F)** SNR in fluorescence images of mice injected with different concentrations of miR-100. **(G)** SNR in fluorescence images of SGC-7901-miR-100 tumor-bearing mice (ANOVA and the *t*-test were used to analyze the means, ***p* < 0.01; #*p* < 0.001; NS, no significant difference).

product we synthesized was >99%, which ensured that the noise caused by product impurity was <1%.

Visualization of miR-484 *in vitro* and in Cells

Although *in vitro* DNA hybridization kinetics based on some sequences have led to a set of mature theories (Dirks and Pierce, 2003, 2004; Dirks et al., 2004, 2007; SantaLucia and Hicks, 2004; Zhang and Winfree, 2009; Zadeh et al., 2011; Zhang et al., 2012, 2018a; Wolfe and Pierce, 2015; Wolfe et al., 2017), a basic theory for quantifying miRNA *in vivo* is still lacking, which is restricted by technologies in other related fields, such as fluorescence reconstruction (Ntziachristos and Weissleder, 2001; Dirks and Pierce, 2003; Cong and Wang, 2005; Lasser et al., 2008; Zhang et al., 2015; Shibata et al., 2017), pharmacokinetics (Brownbill et al., 2018; Caro et al., 2018; Sharma et al., 2018), and others. To quantify miRNA *in vivo*, the *in vitro* reaction kinetics of SQ, FP, and the target miRNA must be accurately modeled mathematically. The *in vitro* experimental results demonstrated that the relationship between the fluorescence intensity generated by the reactions among SQ, FP, and miR-484 in 20 min, and the miR-484 concentration was not strictly linear and instead resembled a parabola (Figures 2I,J,M,N). Compared to a single double-stranded DNA that detects miRNA at the cellular level (Siuti et al., 2013; You et al., 2015, 2017; Ma et al., 2017), the AISA system consisting of two double-stranded DNAs (SQ and FP) can effectively amplify (more than five times within 10 min) the signals of interest in a synergistic manner and hence provide the possibility for *in vivo* visualization of miRNA without an external energy input (Figure 2K). The *in vitro* detection sensitivity of this pair of double-stranded DNAs was ~0.05 nM (reaction time = 10 min, concentrations of SQ = 10 nM, FP = 20 nM). The effect of temperature on the reaction was not significant at either 25 or 37°C (Figures S1C,D). Reducing the concentration of the reactants SQ and FP did not improve the detection sensitivity, which suggested that SQ and FP have a low probability of reacting in a short period of time and that the system formed with SQ and FP is relatively stable and resistant to internal noise.

To validate the reaction kinetics of the AISA system with a target miRNA in cells, we designed an experiment in which the AISA system reacted with miR-484 in LO2 cells (miR-484 was transfected into the LO2 cells). Dynamic confocal fluorescence images showed that, along with the AISA system, double-stranded SQ and FP were rapidly delivered into the cells in several seconds and reacted with intracellular miR-484 to emit fluorescence (Figure 2L; Figure S2A; Movie S4). After correction for the fluorescence quenching effect of the laser (Figure S2B), the fluorescence intensity was found to reach the maximum within 5 min, suggesting that the relatively limited space of the cytoplasm may accelerate the reaction and that

the quenching effect must be considered when quantifying the fluorescence signal (Figure S2C).

In vivo Visualization of Transfected and Induced miRNA Based on AISA System

MiR-484 is an important biomarker expressed in the liver cells during the stage of transformation from liver cirrhosis to cancer (Yang et al., 2016b). To locate miRNA in the liver, we needed to reconstruct the 3D position of the light source based on the system (Figures 3A–D). Herein, we also experimentally validated the universality of the strategy using the AISA system to detect miR-484 in different animal models (miR-484-injected BALB/c mice in Figure S6, miR-484-injected C57 mice in Figure S7, and miR-484-injected rats in Figure S8). *In vivo* fluorescence images of the C57 mouse model demonstrated that miR-484 could be detected in the liver, and the 3D location of miRNA could be reconstructed based on our previous algorithms (Figure 3B). The above results indicated that fluorescence was generated by the reaction between miR-484 and the probe by comparing to the control group (Figures 3B,C). No fluorescence was produced without miR-484 within 30 min. Inevitably, with the extension of time, some fluorescence will be generated by the decomposition of probes such as the body's own enzymes (Figure S6E). Figure 3A shows the detection process and a schematic diagram of the dual-modality imaging system with microcomputed tomography. We can use this system to acquire enough data to reconstruct the 3D location of the internal miRNA.

To verify the ability of the AISA system to detect miRNA in a deep target, we established mouse models by injecting miR-484 at a depth of 4 mm in the liver on BALB/c mice (10 weeks, weight >25 g). The fluorescence images and 3D reconstruction results showed (Figure S3) that the AISA system also had good detection depth for targets at a depth of 4 mm. Two-photon fluorescence and microscopic images of a 60-μm slice also verified the detection capability of the AISA system.

In addition, to evaluate the ability of the AISA system to distinguish between a tumor and regions with high miR-484 expression, we established miR-484-injected and tumor-bearing mouse models by injecting 10 μl of miR-484 (100 μM; depth, 3 mm) into the liver of DEN-induced tumorigenic mice (Figure S4). The fluorescence images obtained with our system and microscope showed that the AISA system has the ability to distinguish the areas of high miR-484 expression from single or multiple tumors. The corresponding statistical data indicated that the SNR of the high miR-484 expression region to background (liver and other location) was >2. Similarly, we constructed rat models with five miR-484-injection foci to verify the horizontal spatial resolution of the AISA system. The fluorescence images demonstrated that when the distance between two of the miR-484-injected centers

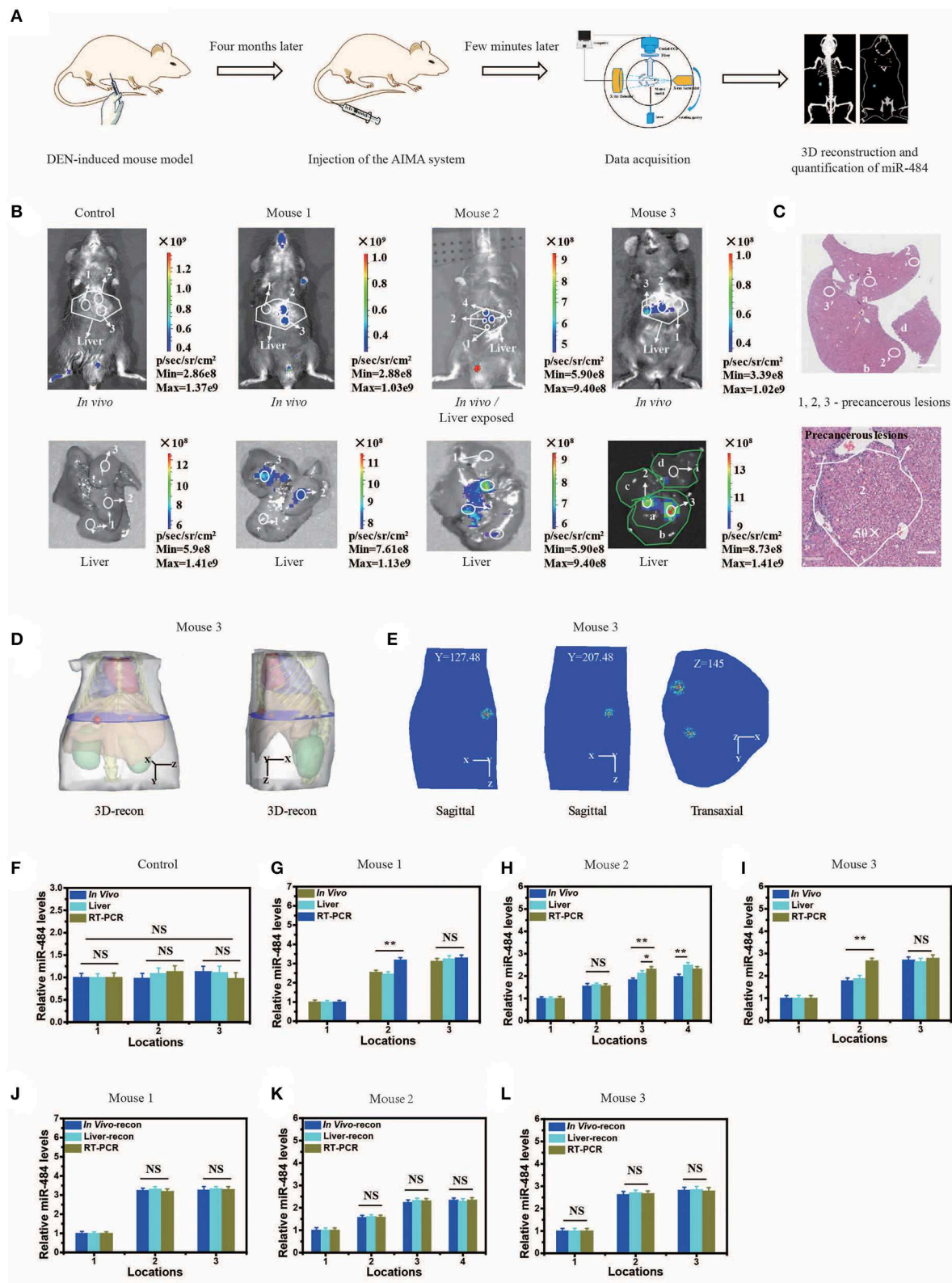


FIGURE 4 | Visualization and three-dimensional (3D) reconstruction of miRNA *in vivo* based on diethyl nitrosamine (DEN)-induced mice and the microscopic image of liver slices with hematoxylin and eosin (H&E) staining. **(A)** Schematic illustration of the quantification of miR-484, including DEN-induced mouse model; injection of the artificial intelligent signal amplification (AISA) system (included SQ and FP); data acquisition; 3D reconstruction and quantification of miR-484. **(B)** Upper panel: (Continued)

FIGURE 4 | fluorescence images of DEN-induced tumorigenic mice (for 4 months) and phosphate-buffered saline (PBS)-injected mice 15 min after i.v. injection of the AISA⁴⁸⁴ system (included SQ and FP). Lower panel: fluorescence images of livers from the above DEN-induced mice and PBS-injected mice. **(C)** Microscopic image of liver slices with H&E staining of the liver of mouse 3. The liver lobes are marked a–d, and the precancerous lesions are marked 2, 3, 2', and 3'. Scale bars are 120 and 30 μm , respectively. **(D)** 3D reconstruction results of miR-484 location in mouse 3. **(E)** Two planes of the reconstructed miRNA location. **(F–I)** Relative miR-484 levels assessed by surface fluorescence intensity and real-time RT-PCR analysis of samples with a size $<40\text{ }\mu\text{m}$ in 4-month-old PBS- or DEN-injected mice (mice 1–3). **(J–L)** Relative miR-484 levels assessed by reconstructed fluorescence intensity and real-time RT-PCR analysis of samples with a size $<40\text{ }\mu\text{m}$ in DEN-injected mice (mice 1–3) (ANOVA and the *t*-test were used to analyze the means, * $p < 0.05$; ** $p < 0.01$; NS, no significant difference).

was more than 2 mm, the AISA system could distinguish them well (Figure S5).

Scalability of the Framework for AISA System

Strikingly, to verify the scalability of the framework for AISA system, we successfully designed and synthesized AISA¹⁰⁰ with minimal adjustment to detect miR-100 *in vitro* (Figures 2M–P) [an important molecular marker of the osteogenic differentiation of mesenchymal stem cells and also a biomarker associated with the progression of gastric cancer (Ueda et al., 2010; Frith et al., 2018)] and in the femoral head and in the tumor-bearing mice (Figures 3C,D,F,G). However, different miRNAs have different base sequences, and changing the base sequences of the components in the AISA detection system would influence the reaction kinetics, and a series of experiments must be performed to validate the design of the AISA system. From Figures 2I–M, we found that the fluorescence intensity increased depending on the concentration of miRNA. However, it can be also found from the curves at different reaction times that the two systems have different velocities at the initial stage of reaction. The response speed of the AISA¹⁰⁰ system is much faster than that of the AISA⁴⁸⁴ system in 10 min (Figures 2G,N). Therefore, the magnification reached more than 10 times in the first 10 min, and the subsequent growth slowed down (Figures 2K,O).

The *in vivo* fluorescence images and their SNR demonstrated that miR-100 can be distinguished from surrounding tissues with a high SNR ratio and even at locations close to the bladder (Figure S6E). Statistical data of continuous observation experiments (Figure S6H) showed that the fluorescence intensity on the surface of the femoral head was the strongest at 60 min, which may be caused by the difference in the metabolic dynamics of the AISA¹⁰⁰ system between the femoral head and the liver. Fluorescence images of SGC-7901-miR-100 tumor-bearing mice (miR-100 transfected into SGC-7901 gastric cancer cells) demonstrated that, until 12 h, SGC-7901-miR-100 can be visualized clearly because the formation of dense tumor tissue delays the metabolism of signal-stranded S and SP to some extent (Figure 3D).

In some *in vivo* experiments performed to visualize transfected miRNA, we found that the fluorescence in the intestinal tract of mice produced a relatively large amount of noise, so we designed a suppression experiment to verify the possible influencing factors. In general, fasting inhibited the secretion of relevant digestive enzymes, and the secretion of gastrointestinal hormones may lead to the degradation of double-stranded SQ in the AISA system (Figure S7). Analysis of abdominal fluorescence intensity showed that both

fasting and somatostatin (gastrointestinal hormone secretion inhibitors) had significant inhibitory effects on fluorescence at the time points of 10 and 30 min, and the significant difference in the inhibition effect decreased with the time of administration.

Practicability of the AISA System

To evaluate the practicability of the AISA system, we detected the expression of miR-484 with DEN-induced tumorigenic mouse models and human samples using our fluorescence imaging system, and the detection results were also validated with RT-PCR for all three mice and pathological H&E staining for mouse 3 (*in vivo Detection of MiR-484 with DEN-induced Mice and Human Samples*). Figure 4B proved again that no fluorescence was emitted from the liver without the presence of miR-484. Fluorescence images, 3D-reconstructed images, and their related statistical data (Figures 4B–L) showed that the amount of miR-484 in precancerous lesions was approximately twice that in a normal liver, and the conclusions obtained from *in vivo* fluorescence images and *ex vivo* liver images were basically consistent. In addition, the SNR of miR-484 detected by RT-PCR was also consistent with the results obtained by *ex vivo* fluorescence intensity statistics (Figures 4J–L); here, all the samples used in RT-PCR were dissected according to the depth information derived from 3D-reconstructed locations. Without reconstruction guiding sample selection, the deviations among three kinds of relative miR-484 levels were $>18\%$ (Figures 4G–I), and with reconstruction guidance, the deviations were $<5\%$ (Figures 4G–L). The deviation is calculated according to the following formula:

$$D = \frac{\text{SNR}_{\text{PCR}} - \text{SNR}_{\text{FI}}}{\text{SNR}_{\text{PCR}}} \times 100\% \quad (1)$$

To demonstrate the accuracy of the location detected by the AISA system *in vivo*, the 3D location information was reconstructed, and the liver sections of mouse 3 were stained with H&E to observe the precancerous lesions (Figures 4C,D). We observed the formation of a precancerous lesion (Figure 4C), and the location of the precancerous lesion was highly consistent with the fluorescence location in *in vivo* and the *ex vivo* liver fluorescence images.

In addition, our AISA system was used to detect the precancerous lesions in five human liver samples from the Eastern Hepatobiliary Surgery Institute (Shanghai, China). The fluorescence images showed that our system was able to detect the region of high miR-484 expression in a short time (Figure 5) (~ 5 min after spraying the AISA system on the surface of the samples). The results were also verified by microscopic images

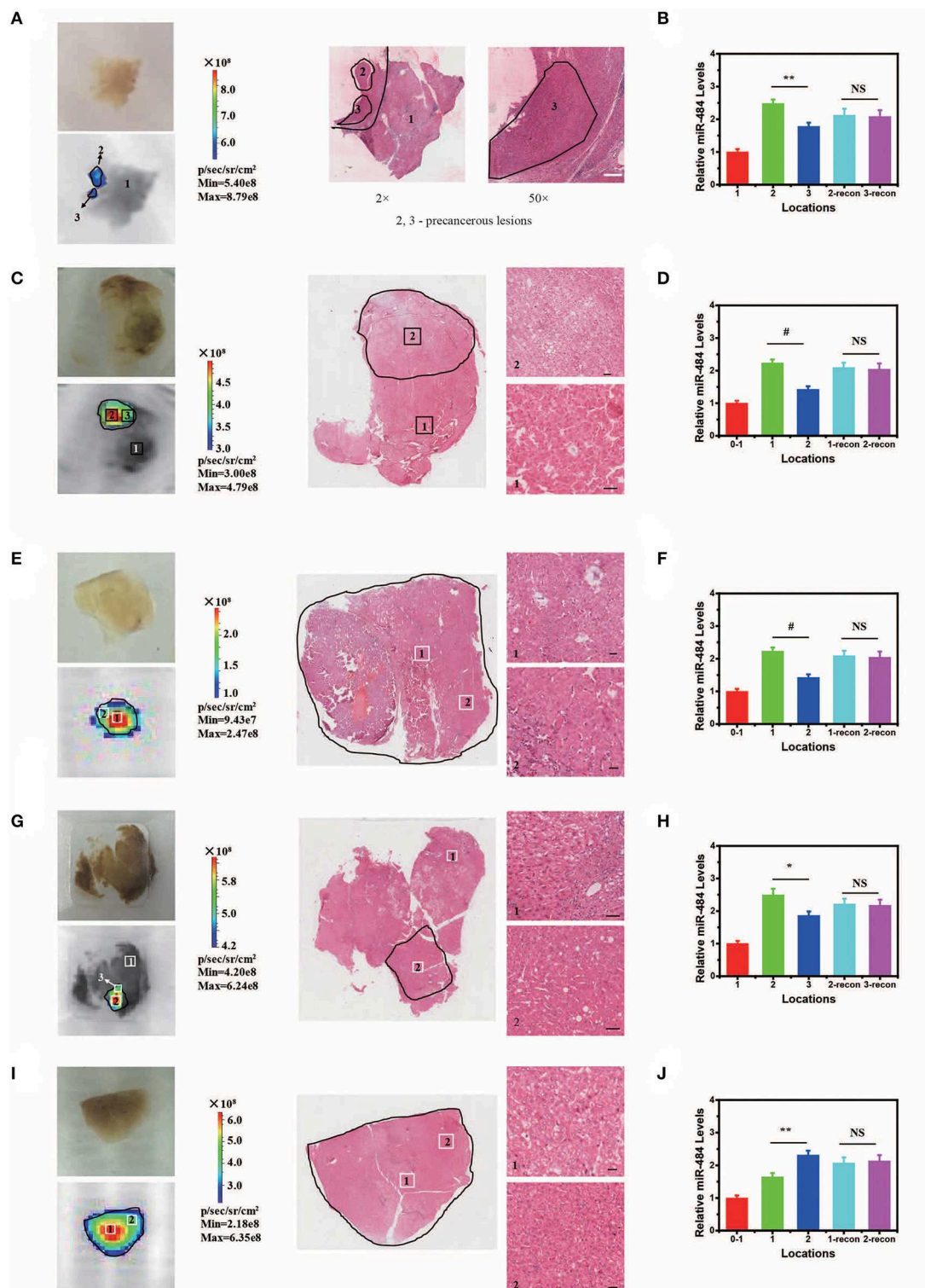


FIGURE 5 | Visualization and three-dimensional (3D) reconstruction of miRNA *in vivo* Based on Human Liver Samples. **(A,C,E,G,I)** (from left to right) Bright field image and fluorescence image of human liver samples 1–5. Microscopic image of human liver samples 1–5. In **(A,C,G)**, normal tissue and precancerous lesions are marked 1, 2, and 3. Scale bars, 90 μ m. In **(E,I)**, precancerous lesions are marked 1 and 2 according to the difference in fluorescence intensity. Scale bars, 60 μ m. **(B,D,F,H,J)** Relative miR-484 levels at different locations in human liver samples 1–5 (ANOVA and the *t*-test were used to analyze the means, #*p* < 0.001; **p* < 0.05; ***p* < 0.01; NS, no significant difference).

of the liver sections with H&E staining, in which the boundaries of precancerous lesions (high-grade dysplastic nodule) were drawn by professional pathologists (Yang et al., 2016b). To assess the similarity of precancerous lesion locations obtained by the two methods, the boundaries were outlined, and the Dice coefficients were calculated. The results (Table S4) demonstrated that Dice coefficient for all five samples were more than 0.94, which indicated that our AISA system can accurately detect the boundaries of precancerous lesions. This excellent quality indicates that it has great application potential. For example, for liver transplantation patients, the subsequent treatment strategy can be determined according to whether the dissected liver has precancerous foci.

It is worth mentioning that low toxicity is needed to make the AISA system suitable for use, so we also measured the *in vivo* clearance speed of the AISA system and its effect on various organs, including liver, muscle, heart, spleen, kidney, stomach, lung, brain, and skin (Figures S8, S9). The fluorescence images and statistical data based on BALB/c mice showed that the AISA system could be almost completely cleared from the body within 12 h (Figure S8). A cell viability assay (Figure S9A), serum test results (Figure S9B), and histopathological microscopic images (Figure S9C) all showed that the AISA system had no significant toxicity in animals (*Toxicity of the AISA System*).

DISCUSSION

The important role of miRNA in the physiological and disease development process is well known, but the *in vivo* visualization study of RNA is still almost blank. Although many strategies have been designed for the amplification of signal derived from miRNA (Yurke et al., 2000; Seelig et al., 2006; You et al., 2015, 2017; Ma et al., 2017; Fu et al., 2018), most of them amplified the miRNA signal *in vitro*. The *in vivo* visualization of miRNA will be a milestone event in the history of RNA detection, which will herald a new era of preventive medicine. However, the prerequisite is that signal derived from miRNA can be amplified *in vivo* first. The ability to design an artificial intelligent signal amplification system suitable for *in vivo* visualization of miRNA is not only interesting and significant on a fundamental basis but also offers key conceptual advantages in scalability over the current paradigm for early tumor diagnosis. In contrast to the situation for previous molecular beacon design efforts, the key design challenge in the current study was to obtain as many useful signals as possible while minimizing the introduction of noise. This seemingly contradictory demand imposes strict conditions on the dangling end of the two double-stranded DNAs to use chemical thermodynamics to promote the reaction and maintain the seesaw-type equilibrium (for the second and third reactions). Meanwhile, it also makes the reaction dynamics more regular, enabling it possible to simulate the process using mathematical models.

In addition, the experiments on human liver samples also demonstrate the practicability of the strategy, which cannot only be used for *in vitro* and *in vivo* detection of miRNA but also can be used for the evaluation of tumor prognosis and rapid intraoperative identification of tumor margins based on tissue samples. The importance of miRNA in life science applications,

as well as the practicability and universality of the principles underlying this system, will support further applications in many fields, including disease progression assessment, stem cell tracing, and disease prognosis evaluation.

Still, there are many problems with AISA system that need to be addressed. According to the restriction of dangle end α in design rule 1 ($\alpha = 5$), a total of 4^5 different AISA system can be used to detect a target RNA. In addition, considering the limitation of dangle end β on design rule 2, more different AISA system can also be used for the visualization of miRNA. How to select the most suitable system for subsequent *in vivo* visualization and quantitative research is an urgent problem to be solved in the future studies. For the mechanism research about miRNA-related diseases, the *in vivo* quantification is also imminent. This is limited by advances in a variety of technologies including fluorescence position reconstruction, fluorescence photon quantification, reaction dynamics modeling of miRNA, and so on. All in all, based on these advances, we will be able to calculate the concentration of RNA in the body in real time in the future.

DATA AVAILABILITY STATEMENT

All datasets generated for this study are included in the article/**Supplementary Material**.

ETHICS STATEMENT

The animal study was reviewed and approved by the Institutional Animal Care and Use Committee at Peking University and the Eastern Hepatobiliary Surgery Hospital Research Ethics Committee.

AUTHOR CONTRIBUTIONS

XM wrote the manuscript in addition to designing the AISA system, performing, analyzing all experiments, and build the quantitative framework. XM and KZ performing the *in vitro* kinetics experiments. XM, LC, WZ, YY, BZ, KZ, and SZ performing the animal experiments. PW and ML assisted the cell experiments. YG assisted with the imaging acquisition experiments. XM, LZ, and ZS analyzing the data and constructed the framework for *in vivo* quantification of ncRNA. HW assisted with experiment design, manuscript preparation, and data/image analysis. XM and JT designed, supervised, analyzed all experiments, and in addition to assisting with manuscript preparation.

FUNDING

This work was supported by the National Key Research programs of China (2016YFA0100900, 2016YFA0100902, and 2017YFA0205200), the National Natural Science Foundation of China (81871442, 81227901, 815270805, and 61231004), the Scientific Instrument R&D Program from the Chinese Academy of Sciences (GJJSTD20170004), and Beijing Municipal Science and Technology Commission (Z161100002616022).

ACKNOWLEDGMENTS

We thank Prof. Guanghui Liu (from Institute of Biophysics, Chinese Academy of Sciences, Beijing, China) for the discussions.

REFERENCES

- Anastasiadou, E., Jacob, L. S., and Slack, F. J. (2018). Non-coding RNA networks in cancer. *Nat. Rev. Cancer* 18, 5–18. doi: 10.1038/nrc.2017.99
- Auslander, S., and Fussenegger, M. (2014). SYNTHETIC BIOLOGY toehold gene switches make big footprints. *Nature* 516, 333–334. doi: 10.1038/516333a
- Brownbill, P., Sebire, N., McGillick, E. V., Ellery, S., and Murthi, P. (2018). *Ex vivo* dual perfusion of the human placenta: disease simulation, therapeutic pharmacokinetics and analysis of off-target effects. *Methods Mol. Biol.* 1710, 173–189. doi: 10.1007/978-1-4939-7498-6_14
- Caro, C., Carmen Munoz-Hernandez, M., Leal, M. P., and Garcia-Martin, M. L. (2018). *In vivo* pharmacokinetics of magnetic nanoparticles. *Methods Mol. Biol.* 1718, 409–419. doi: 10.1007/978-1-4939-7531-0_24
- Cong, A. X., and Wang, G. (2005). A finite-element-based reconstruction method for 3D fluorescence tomography. *Opt. Express* 13, 9847–9857. doi: 10.1364/OPEX.13.009847
- Dirks, R. M., Bois, J. S., Schaeffer, J. M., Winfree, E., and Pierce, N. A. (2007). Thermodynamic analysis of interacting nucleic acid strands. *Siam Rev.* 49, 65–88. doi: 10.1137/060651100
- Dirks, R. M., Lin, M., Winfree, E., and Pierce, N. A. (2004). Paradigms for computational nucleic acid design. *Nucleic Acids Res.* 32, 1392–1403. doi: 10.1093/nar/gkh291
- Dirks, R. M., and Pierce, N. A. (2003). A partition function algorithm for nucleic acid secondary structure including pseudoknots. *J. Comput. Chem.* 24, 1664–1677. doi: 10.1002/jcc.10296
- Dirks, R. M., and Pierce, N. A. (2004). An algorithm for computing nucleic acid base-pairing probabilities including pseudoknots. *J. Comput. Chem.* 25, 1295–1304. doi: 10.1002/jcc.20057
- Frith, J. E., Kusuma, G. D., Carthew, J., Li, F. Y., Cloonan, N., Gomez, G. A., et al. (2018). Mechanically-sensitive miRNAs bias human mesenchymal stem cell fate via mTOR signalling. *Nat. Commun.* 9:257. doi: 10.1038/s41467-017-02486-0
- Fu, T., Lyu, Y. F., Liu, H., Peng, R. Z., Zhang, X. B., Ye, M., et al. (2018). DNA-based dynamic reaction networks. *Trends Biochem. Sci.* 43, 547–560. doi: 10.1016/j.tibs.2018.04.010
- Green, A. A., Silver, P. A., Collins, J. J., and Yin, P. (2014). Toehold switches: *de-novo*-designed regulators of gene expression. *Cell* 159, 925–939. doi: 10.1016/j.cell.2014.10.002
- Griebing, T. L. (2017). Re: evaluation of the risk of nitrofurantoin lung injury and its efficacy in diminished kidney function in older adults in a large integrated healthcare system: a matched cohort study. *J. Urol.* 197, 1277–1278. doi: 10.1016/j.juro.2017.01.027
- Hall, R. A., and Macdonald, J. (2016). Synthetic biology provides a toehold in the fight against zika. *Cell Host Microbe* 19, 752–754. doi: 10.1016/j.chom.2016.05.020
- Katan, A. J., and Dekker, C. (2011). High-speed AFM reveals the dynamics of single biomolecules at the nanometer scale. *Cell* 147, 979–982. doi: 10.1016/j.cell.2011.11.017
- Koc, K. N., Stodola, J. L., Burgers, P. M., and Galletto, R. (2015). Regulation of yeast DNA polymerase delta-mediated strand displacement synthesis by 5'-flaps. *Nucleic Acids Res.* 43, 4179–4190. doi: 10.1093/nar/gkv260
- Kodera, N., Yamamoto, D., Ishikawa, R., and Ando, T. (2010). Video imaging of walking myosin V by high-speed atomic force microscopy. *Nature* 468, 72–76. doi: 10.1038/nature09450
- Kory, R. C., Bradley, M. H., Watson, R. N., Callahan, R., and Peters, B. J. (1959). A six-month evaluation of an anabolic drug, norethandrolone, in underweight persons. II. Bromsulphalein (BSP) retention and liver function. *Am. J. Med.* 26, 243–248. doi: 10.1016/0002-9343(59)90313-4
- Lasser, T., Soubret, A., Ripoll, J., and Ntziachristos, V. (2008). Surface reconstruction for free-space 360 degrees fluorescence molecular tomography and the effects of animal motion. *IEEE Trans. Med. Imaging* 27, 188–194. doi: 10.1109/TMI.2007.904662
- Li, M. X., Xu, C. H., Zhang, N., Qian, G. S., Zhao, W., Xu, J. J., et al. (2018). Exploration of the kinetics of toehold mediated strand displacement via plasmon rulers. *ACS Nano* 12, 3341–3350. doi: 10.1021/acsnano.7b08673
- Li, S., Xu, L. G., Ma, W., Wu, X. L., Sun, M. Z., Kuang, H., et al. (2016). Dual-mode ultrasensitive quantification of MicroRNA in living cells by chiropalmonic nanopyramids self-assembled from gold and upconversion nanoparticles. *J. Am. Chem. Soc.* 138, 306–312. doi: 10.1021/jacs.5b10309
- Liu, X. W., Feng, Y. L., Xu, G. C., Chen, Y., Luo, Y., Song, J. E., et al. (2019). MAPK-targeted drug delivered by a pH-sensitive MSNP nanocarrier synergizes with PD-1 blockade in melanoma without T-cell suppression. *Adv. Funct. Mater.* 29:1806916. doi: 10.1002/adfm.201806916
- Ma, W., Fu, P., Sun, M., Xu, L., Kuang, H., and Xu, C. (2017). Dual quantification of MicroRNAs and telomerase in living cells. *J. Am. Chem. Soc.* 139, 11752–11759. doi: 10.1021/jacs.7b03617
- Ma, X. B., Deng, K. X., Xue, Z. W., Liu, X. Y., Zhu, S. P., Qin, C. H., et al. (2013). Novel registration for microcomputed tomography and bioluminescence imaging based on iterated optimal projection. *J. Biomed. Opt.* 18:26013. doi: 10.1117/1.JBO.18.2.026013
- Miyagi, A., Chipot, C., Rangl, M., and Scheuring, S. (2016). High-speed atomic force microscopy shows that annexin V stabilizes membranes on the second timescale. *Nat. Nanotechnol.* 11, 783–790. doi: 10.1038/nnano.2016.89
- Ntziachristos, V., and Weissleder, R. (2001). Experimental three-dimensional fluorescence reconstruction of diffuse media by use of a normalized Born approximation. *Opt. Lett.* 26, 893–895. doi: 10.1364/OL.26.000893
- Pardee, K., Green, A. A., Takahashi, M. K., Braff, D., Lambert, G., Lee, J. W., et al. (2016). Rapid, low-cost detection of zika virus using programmable biomolecular components. *Cell* 165, 1255–1266. doi: 10.1016/j.cell.2016.04.059
- Parolini, L., Kotar, J., Di Michele, L., and Moggetti, B. M. (2016). Controlling self-assembly kinetics of DNA-functionalized liposomes using toehold exchange mechanism. *ACS Nano* 10, 2392–2398. doi: 10.1021/acsnano.5b07201
- Prakash, R. (1978). Echocardiographic evaluation of cardiac-function and drug effects in acute myocardial-infarction. *J. Am. Geriatr. Soc.* 26, 203–208. doi: 10.1111/j.1532-5415.1978.tb01959.x
- Qin, C. H., Feng, J. C., Zhu, S. P., Ma, X. B., Zhong, J. H., Wu, P., et al. (2014). Recent advances in bioluminescence tomography: methodology and system as well as application. *Laser Photon. Rev.* 8, 94–114. doi: 10.1002/lpor.201280011
- SantaLucia, J., and Hicks, D. (2004). The thermodynamics of DNA structural motifs. *Annu. Rev. Biophys. Biomol. Struct.* 33, 415–440. doi: 10.1146/annurev.biophys.32.110601.141800
- Sawada, S., Imada, I., Kato, N., and Kaihatsu, K. (2009). Regulation of duplex DNA strand displacement by visible light sensitive bis-peptide nucleic acid. *Nucleic Acids Symp. Ser.* 53, 191–192. doi: 10.1093/nass/nrp096
- Seelig, G., Soloveichik, D., Zhang, D. Y., and Winfree, E. (2006). Enzyme-free nucleic acid logic circuits. *Science* 314, 1585–1588. doi: 10.1126/science.1132493
- Sharma, A. K., Gupta, L., Sahu, H., Qayum, A., Singh, S. K., Nakhate, K. T., et al. (2018). Chitosan engineered PAMAM dendrimers as nanoconstructs for the enhanced anti-cancer potential and improved *in vivo* brain pharmacokinetics of temozolomide. *Pharm. Res.* 35:9. doi: 10.1007/s11095-017-2324-y
- Shibata, M., Nishimasu, H., Kodera, N., Hirano, S., Ando, T., Uchihashi, T., et al. (2017). Real-space and real-time dynamics of CRISPR-Cas9 visualized by high-speed atomic force microscopy. *Nat. Commun.* 8:1430. doi: 10.1038/s41467-017-01466-8
- Siuti, P., Yazbek, J., and Lu, T. K. (2013). Synthetic circuits integrating logic and memory in living cells. *Nat. Biotechnol.* 31, 448–452. doi: 10.1038/nbt.2510

SUPPLEMENTARY MATERIAL

The Supplementary Material for this article can be found online at: <https://www.frontiersin.org/articles/10.3389/fbioe.2019.00330/full#supplementary-material>

- Ueda, T., Volinia, S., Okumura, H., Shimizu, M., Taccioli, C., Rossi, S., et al. (2010). Relation between microRNA expression and progression and prognosis of gastric cancer: a microRNA expression analysis. *Lancet Oncol.* 11, 136–146. doi: 10.1016/S1470-2045(09)70343-2
- Wang, S. Y., Guo, F., Ji, Y. H., Yu, M., Wang, J. P., and Li, N. (2018). Dual-mode imaging guided multifunctional theranosomes with mitochondria targeting for photothermally controlled and enhanced photodynamic therapy *in vitro* and *in vivo*. *Mol. Pharm.* 15, 3318–3331. doi: 10.1021/acs.molpharmaceut.8b00351
- Wang, X., Nan, Y., Song, T., Bei, W., and Liang, H. J. A. B. (2017). Robust fuel catalyzed DNA molecular machine for *in vivo* MicroRNA detection. *Adv. Biosyst.* 1:1700060. doi: 10.1002/adbi.201700060
- Wolfe, B. R., and Pierce, N. A. (2015). Sequence design for a test tube of interacting nucleic acid strands. *ACS Synth. Biol.* 4, 1086–1100. doi: 10.1021/sb5002196
- Wolfe, B. R., Porubsky, N. J., Zadeh, J. N., Dirks, R. M., and Pierce, N. A. (2017). Constrained multistate sequence design for nucleic acid reaction pathway engineering constrained multistate sequence design for nucleic acid reaction pathway engineering. *J. Am. Chem. Soc.* 139, 3134–3144. doi: 10.1021/jacs.6b12693
- Wu, J., Huang, J. S., Kuang, S. C., Chen, J. B., Li, X. X., Chen, B., et al. (2019). Synergistic MicroRNA therapy in liver fibrotic rat using MRI-visible nanocarrier targeting hepatic stellate cells. *Adv. Sci.* 6:1801809. doi: 10.1002/advs.201801809
- Xu, C. F., Li, D. D., Cao, Z. T., Xiong, M. H., Yang, X. Z., and Wang, J. (2019). Facile hydrophobization of siRNA with anticancer drug for non-cationic nanocarrier-mediated systemic delivery. *Nano Lett.* 19, 2688–2693. doi: 10.1021/acs.nanolett.9b00657
- Xue, Z. W., Ma, X. B., Zhang, Q., Wu, P., Yang, X., and Tian, J. (2013). Adaptive regularized method based on homotopy for sparse fluorescence tomography. *Appl. Opt.* 52, 2374–2384. doi: 10.1364/AO.52.002374
- Yaghini, E., Dondi, R., Edler, K. J., Loizidou, M., MacRobert, A. J., and Eggleston, I. M. (2018). Codelivery of a cytotoxin and photosensitizer via a liposomal nanocarrier: a novel strategy for light-triggered cytosolic release. *Nanoscale* 10, 20366–20376. doi: 10.1039/C8NR04048F
- Yang, X. L., Tang, Y. N., Traynor, S. M., and Li, F. (2016a). Regulation of DNA strand displacement using an allosteric DNA toehold. *J. Am. Chem. Soc.* 138, 14076–14082. doi: 10.1021/jacs.6b08794
- Yang, Y. C., Lin, X. M., Lu, X. Y., Luo, G. J., Zeng, T., Tang, J., et al. (2016b). Interferon-microRNA signalling drives liver precancerous lesion formation and hepatocarcinogenesis. *Gut* 65, 1186–1201. doi: 10.1136/gutjnl-2015-310318
- Ye, J. Z., Chi, C. W., Xue, Z. W., Wu, P., An, Y., Xu, H., et al. (2014). Fast and robust reconstruction for fluorescence molecular tomography via a sparsity adaptive subspace pursuit method. *Biomed. Opt. Express* 5, 387–406. doi: 10.1364/BOE.5.000387
- Yong, Y. Q., Wu, D., Fernandes, V., Kopelen, H. A., Shimoni, S., Nagueh, S. F., et al. (2002). Diagnostic accuracy and cost-effectiveness of contrast echocardiography on evaluation of cardiac function in technically very difficult patients in the intensive care unit. *Am. J. Cardiol.* 89, 711–718. doi: 10.1016/S0002-9149(01)02344-X
- You, M. X., Lyu, Y. F., Han, D., Qiu, L. P., Liu, Q. L., Chen, T., et al. (2017). DNA probes for monitoring dynamic and transient molecular encounters on live cell membranes. *Nat. Nanotechnol.* 12, 453–459. doi: 10.1038/nnano.2017.23
- You, M. X., Zhu, G. Z., Chen, T., Donovan, M. J., and Tan, W. H. (2015). Programmable and multiparameter DNA-based logic platform for cancer recognition and targeted therapy. *J. Am. Chem. Soc.* 137, 667–674. doi: 10.1021/ja509263k
- Yurke, B., Turberfield, A. J., Mills, A. P., Simmel, F. C., and Neumann, J. L. (2000). A DNA-fuelled molecular machine made of DNA. *Nature* 406, 605–608. doi: 10.1038/35020524
- Zadeh, J. N., Wolfe, B. R., and Pierce, N. A. (2011). Nucleic acid sequence design via efficient ensemble defect optimization. *J. Comput. Chem.* 32, 439–452. doi: 10.1002/jcc.21633
- Zhang, C., Wu, R. F., Li, Y. F., Zhang, Q., and Yang, J. (2017). Programmable regulation of DNA conjugation to gold nanoparticles via strand displacement. *Langmuir* 33, 12285–12290. doi: 10.1021/acs.langmuir.7b02620
- Zhang, D. Y., Chen, S. X., and Yin, P. (2012). Optimizing the specificity of nucleic acid hybridization. *Nat. Chem.* 4, 208–214. doi: 10.1038/nchem.1246
- Zhang, D. Y., and Winfree, E. (2009). Control of DNA strand displacement kinetics using toehold exchange. *J. Am. Chem. Soc.* 131, 17303–17314. doi: 10.1021/ja906987s
- Zhang, G. L., Pu, H. S., He, W., Liu, F., Luo, J. W., and Bai, J. (2015). Bayesian framework based direct reconstruction of fluorescence parametric images. *IEEE Trans. Med. Imaging* 34, 1378–1391. doi: 10.1109/TMI.2015.2394476
- Zhang, J. X., Fang, J. Z., Duan, W., Wu, L. R., Zhang, A. W., Dalchau, N., et al. (2018a). Predicting DNA hybridization kinetics from sequence. *Nat. Chem.* 10, 91–98. doi: 10.1038/nchem.2877
- Zhang, S., Ma, X. B., Wang, Y., Wu, M., Meng, H., Chai, W., et al. (2018b). Robust reconstruction of fluorescence molecular tomography based on sparsity adaptive correntropy matching pursuit method for stem cell distribution. *IEEE Trans. Med. Imaging* 37, 2176–2184. doi: 10.1109/TMI.2018.2825102
- Zhong, X. Y., Yang, K., Dong, Z. L., Yi, X., Wang, Y., Ge, C. C., et al. (2015). Polydopamine as a biocompatible multifunctional nanocarrier for combined radioisotope therapy and chemotherapy of cancer. *Adv. Funct. Mater.* 25, 7327–7336. doi: 10.1002/adfm.201503587

Conflict of Interest: A patent application has been submitted based in part on results presented in this manuscript. XM and JT are listed as the inventors.

The remaining authors declare that the research was conducted in the absence of any commercial or financial relationships that could be construed as a potential conflict of interest.

Copyright © 2019 Ma, Chen, Yang, Zhang, Wang, Zhang, Zheng, Zhu, Sun, Zhang, Guo, Liang, Wang and Tian. This is an open-access article distributed under the terms of the Creative Commons Attribution License (CC BY). The use, distribution or reproduction in other forums is permitted, provided the original author(s) and the copyright owner(s) are credited and that the original publication in this journal is cited, in accordance with accepted academic practice. No use, distribution or reproduction is permitted which does not comply with these terms.



Characterization of Photoluminescent Polylactone-Based Nanoparticles for Their Applications in Cardiovascular Diseases

Aneetta E. Kuriakose¹, Nikhil Pandey¹, Dingying Shan², Subhash Banerjee^{3,4}, Jian Yang^{2*} and Kytai T. Nguyen^{1*}

¹ Bioengineering Department, The University of Texas at Arlington, Arlington, TX, United States, ² Department of Biomedical Engineering, Pennsylvania State University, University Park, PA, United States, ³ Division of Cardiology, VA North Texas Medical Center, Dallas, TX, United States, ⁴ Department of Internal Medicine, The University of Texas Southwestern Medical Center, Dallas, TX, United States

OPEN ACCESS

Edited by:

Michael Ming-Yuan Wei,
Texas Commission on Environmental
Quality, United States

Reviewed by:

Xiangyang Shi,
Donghua University, China
Bintian Zhang,
Arizona State University, United States

*Correspondence:

Jian Yang
jxy30@psu.edu
Kytai T. Nguyen
knguyen@uta.edu

Specialty section:

This article was submitted to
Nanobiotechnology,
a section of the journal
Frontiers in Bioengineering and
Biotechnology

Received: 19 September 2019

Accepted: 06 November 2019

Published: 22 November 2019

Citation:

Kuriakose AE, Pandey N, Shan D,
Banerjee S, Yang J and Nguyen KT
(2019) Characterization of
Photoluminescent Polylactone-Based
Nanoparticles for Their Applications in
Cardiovascular Diseases.
Front. Bioeng. Biotechnol. 7:353.
doi: 10.3389/fbioe.2019.00353

Cardiovascular diseases (CVD) affect a large number of the population across the globe and are the leading cause of death worldwide. Nanotechnology-based drug delivery has currently offered novel therapeutic options to treat these diseases, yet combination of both diagnostic and therapeutic abilities is further needed to understand factors and/or mechanisms that affect the treatment in order to design better therapies to challenge CVD. Biodegradable photoluminescent polylactones (BPLPLs) enable to bridge this gap as these materials exhibit a stable, long-term intrinsic fluorescence as well as offers excellent cytocompatibility and biodegradability properties. Herein, we formulated three different BPLPL based nanoparticles (NPs), including BPLP-co-poly (L-lactic acid) (BPLPL-PLLA), BPLP-co-poly (lactic-co-glycolic acid) copolymers with lactic acid and glycolic acid ratios of 75:25 (BPLPL-PLGA75:25) and 50:50 (BPLPL-PLGA50:50), and extensively evaluated their suitability as theranostic nanocarriers for CVD applications. All BPLPL based NPs were <160 nm in size and had photoluminescence characteristics and tunable release kinetics of encapsulated protein model depending on polylactones copolymerized with BPLP materials. Compared to BPLPL-PLLA NPs, BPLPL-PLGA NPs demonstrated excellent stability in various formulations including deionized water, serum, saline, and simulated body fluid over 2 days. *In vitro* cell studies with human umbilical vein derived endothelial cells showed dose-dependent accumulation of BPLPL-based NPs, and BPLPL-PLGA NPs presented superior compatibility with endothelial cells in terms of viability with minimal effects on cellular functions such as nitric oxide production. Furthermore, all BPLPL NPs displayed hemocompatibility with no effect on whole blood kinetic profiles, were non-hemolytic, and consisted of comparable platelet responses such as platelet adhesion and activation to those of PLGA, an FDA approved material. Overall, our results demonstrated that BPLPL-PLGA based NPs have better physical and biological properties than BPLPL-PLLA; hence they have potential to be utilized as functional nanocarriers for therapy and diagnosis of CVD.

Keywords: BPLP, bioimaging, toxicity, vascular drug carriers, endothelial cells, cardiovascular disease, theranostics

INTRODUCTION

Stenting and balloon angioplasty are common endovascular strategies used to open the occluded blood vessel. However, such interventions often damage the arterial wall, allowing activation and binding of circulating platelets to the exposed subendothelium that initiate inflammatory responses, ultimately leading to the development of restenosis. Although emerging drug eluting technologies have reduced the rates of endovascular complications, their long-term efficacy is hindered by late thrombosis and the catch-up phenomenon of restenosis (Sun et al., 2015). It is now well-known that ineffective reconstitution of the endothelial layer often results in these late stage complications. To overcome these limitations, several strategies involve with stem cell therapies and drug carriers have been developed. This includes the administration of endothelial progenitor cells (EPCs) (Povsic and Goldschmidt-Clermont, 2008; Chen et al., 2016, 2017), biodegradable superparamagnetic nanoparticles loaded endothelial cells (ECs) (Polyak et al., 2016; Vosen et al., 2016), induced pluripotent stem cells-derived ECs (Adams et al., 2013; Giordano et al., 2016) and post angioplasty strategies to restore vascular integrity. Vascular targeted nanocarriers were also employed to deliver anti-inflammatory or anti-mitogenic agents such as paclitaxel, docetaxel, simvastatin, or everolimus to inhibit intimal hyperplasia and provide a suitable environment for endothelial regeneration (Chan et al., 2010). Previously, we have developed ~400nm sized polymeric nanoscaffolds that interface with the injured arterial endothelium via glycoprotein 1b α ligand and capture circulating EPCs via anti-CD34 antibodies (Su et al., 2014). These multifunctional nanosystems cloaked the denuded endothelium, prevented platelet-mediated reactions, and reduced subsequent neointimal formation. Furthermore, they promoted rapid endothelial reconstruction by locally capturing EPCs and supporting their adhesion. Despite these achievements, the therapeutic potential of the nanoscaffolds was not fully achieved as indicated by a decreased the binding of EPCs to the injured artery after 7 and 21 days of transplantation, delayed intimal hyperplasia formation, as well as incomplete endothelial regeneration process. This might be associated with ineffective margination and retention of EPCs or nanoscaffolds on the damaged vascular wall either due to hydrodynamic dislodging forces exerted on them by circulation or their poor tissue interactions.

The real time, non-invasive monitoring of transplanted cells and nanocarriers after delivery would help us to determine their pharmacokinetics and tissue distribution *in vivo*. In addition, we can estimate the required dosing of the therapeutic candidates to be administered at the injured site, assess the outcome of the therapy and develop more efficient treatment/ delivery strategies. A common strategy employed in labeling cells or drug carriers for imaging applications is by directly incorporating fluorophores, radioisotopes, quantum dots, and paramagnetic nanoparticles within them. However, major concerns involved with these imaging agents are often associated with their poor photobleaching-resistance and substantial cytotoxicity, which limit their applications for long-term *in vivo* tracking of cells

and/or drug carriers. Another technique to image living cells involves genetic modification by introducing reporter genes into the cells' genome to express specific fluorescent/bioluminescent proteins or enzymes required for signal generation. This approach is less favorable as it produces gene alteration, and often requires viral vectors for gene transduction, which may cause immunogenicity and mutagenesis. Therefore, this strategy of imaging is only approved in terminally ill patients (Wang and Jokerst, 2016). Considering the issues associated with the tracking of cells and/or drug carriers using the aforementioned strategies, the development of biodegradable and biocompatible materials that allows non-invasive, stable and long-term imaging capabilities has become increasingly desirable.

Earlier, we have developed citrate-based biomaterials, known as biodegradable photoluminescent polymers (BPLPs) that possessed a strong and tunable photoluminescence phenomenon; and demonstrated their potential use in bioimaging, drug delivery and tissue engineering (Yang et al., 2009). Unlike other imaging agents that are not degradable, BPLPs are created from biocompatible monomers via a convenient thermal polycondensation reaction and shown to have controlled degradability properties. However, the main challenge of using BPLPs for nanoparticle fabrication was associated with their low molecular weight, which resulted in nanoparticle aggregation in physiological conditions, hence limiting their use as an imaging probe. To overcome this, we synthesized new polymers by incorporating BPLPs into the widely used biodegradable polylactones, referred to as biodegradable photoluminescent polylactones (BPLPLs) that showed higher molecular weight, improved mechanical strength, and favorable processability over BPLPs (Xie et al., 2014; Hu et al., 2016). The intrinsic and stable fluorescent property of BPLPs is well-preserved in BPLPLs. Furthermore, the BPLPLs fluorescence emission ranging from blue to red can be adjusted by varying different amino acids in the syntheses of BPLPs (Yang et al., 2009; Xie et al., 2017).

In this research, we developed three different nanoparticles based on BPLPLs including BPLP-co-poly (L-lactic acid) (BPLPL-PLLA) and BPLP-co-poly (lactic-co-glycolic acid) copolymers with lactic acid and glycolic acid ratios of 75:25 (BPLPL-PLGA75:25) as well as 50:50 (BPLPL-PLGA50:50). Furthermore, we have characterized for their physical properties and biocompatibility with the blood cells and endothelial cells and investigated for their bioimaging applications. Our preliminary characterization studies would help us to identify a suitable BPLPL-based material to synthesize theranostic NPs that can be utilized both as an imaging agent to track the EC delivery and as a vascular drug carrier to promote *in situ* reendothelialization post arterial injury.

EXPERIMENTAL PROCEDURES

Materials

Synthesis of BPLPLs such as BPLPL-PLLA (1:100), BPLPL-PLGA50:50 (1:100), BPLPL-PLGA75:25 (1:100) was described previously (Xie et al., 2014; Hu et al., 2016). The ratio of 1:100 represents the feeding molar ratio of BPLP either with lactic acid or a combination of lactic acid and glycolic acid.

PLGA50:50 of molecular weight 55–65 kDa was purchased from Akina, Inc. (West Lafayette, IN). Other reagents including bovine serum albumin (BSA) and polyvinyl alcohol (PVA) of molecular weight 31–50 kDa were brought from Sigma-Aldrich (St. Louis, MO). MTS reagent (CellTiter 96® Aqueous One Solution Cell Proliferation Assay) and Pierce BCA protein assay were obtained from Promega (Madison, WI) and ThermoFisher Scientific (Grand Island, NY), respectively. OxiSelect™ Intracellular Nitric Oxide (NO) Fluorometric Assay Kits were purchased from CellBioLabs, Inc. (San Diego, CA). Furthermore, human umbilical vein endothelial cells (HUVECs) was purchased from American Type Culture Collection (ATCC, Manassas, VA), while the culture media (Vasculife Basal Medium) and supplemental kits (Vasculife VEGF Lifefactors) were purchased from Lifeline Cell Technology (Frederick, MD). Other chemicals, if not specified were purchased from Sigma Aldrich.

Synthesis of BPLPL-Based Nanoparticles

BSA was selected as the model protein to be encapsulated into BPLPL nanoparticles, which were synthesized by a standard double emulsion technique. For this procedure, BSA solution (20 mg of BSA dissolved in 0.2 ml of DI water) was emulsified into 2% (w/v) BPLP-poly lactones solution prepared in 5 mL of chloroform and sonicated. This primary emulsion was added drop wise into 12 mL of 5% (w/v) PVA and sonicated again at 30 W for 5 min. Following the overnight stirring to evaporate organic solvents, the nanoparticles were washed and isolated by centrifugation at 15,000 rpm for 30 min, and protein (BSA)-loaded BPLPL based NPs were collected via freeze-drying. Blank BPLPL NPs as well as PLGA50:50 NPs were also fabricated using similar procedures without adding BSA to be utilized for *in vitro* cells- and blood-based studies.

Physical Characterization of BPLPL-Based Nanoparticles

The nanoparticles were characterized for their particle size, polydispersity and zeta potential via a dynamic light scattering (DLS) method using Zeta PALS zeta potential analyzer (Brookhaven Instruments, Holtsville, NY). The size and morphology of the nanoparticles were also observed using transmission electron microscopy (TEM). The stability of particles was determined by observing the variation in their size while suspended in various formulations such as DI water, saline (0.9% sodium chloride solution), 10% Fetal Bovine Serum (FBS, Atlanta Biological, Lawrenceville, GA), or simulated body fluid with similar composition of blood plasma, prepared as described previously (Marques et al., 2011). The particles were incubated at 37°C and their sizes were measured using DLS every 12 h up to 3 days. Furthermore, the amount of BSA encapsulated into BPLPL-based particles was estimated based on untrapped BSA in PVA solution after centrifugation. The percentage of loading efficiency was calculated as actual amount of BSA loaded with respect to the initial amount of BSA used to prepare NPs. For the *in vitro* release study of BSA, 1 mg/ml of particle solution in PBS suspended in a 100 kDa dialysis bag (Spectrum Laboratories Inc., Rancho Dominguez, CA) was dialyzed against phosphate buffer saline (PBS) solution. At each predetermined time points, 1 ml

of dialysate solution was collected and replaced with fresh PBS solution. BSA content in the collected solution was quantified using BCA protein assays following manufacturer's instructions, and cumulative BSA release over the time was analyzed based on BSA standards. *In vitro* degradation of nanoparticles in DI water was analyzed over a period of 4 weeks. Briefly, NPs was suspended in DI water and incubated at 37°C for predetermined times. At each time point, particles were collected and freeze dried. The degradation was determined based on the remaining mass of NPs.

In vitro Cell Studies of BPLPL-Based Nanoparticles

Cytocompatibility

To evaluate the cytotoxicity of BPLPL-based nanoparticles with human umbilical vein endothelial cells (HUVEC), cells were seeded in 96 well plates at a seeding density of 30,000 cells/cm² and incubated in 37°C for 24 h. Following incubation, cell culture media was replaced with increasing concentrations of nanoparticle suspension (in media) for 24 h. The cells were then washed and incubated with MTS assay reagents for 3 h. Absorbance readings was measured at 490 nm using UV-Vis spectrophotometer (Infinite M200 plate reader, Tecan, Durham, NC), and the percent of cell viability was determined with respect to untreated cells.

Cellular Uptake

The efficiency of HUVECs to internalize BPLPL-based nanoparticles was determined. Briefly, HUVECs of density 30,000 cells/cm² were initially seeded in to 96 well plates and allowed to attach for 24 h. The cell culture media was then replaced with nanoparticle suspensions of various concentrations, and the plates were incubated for 4 h. After treatment, cells were washed with PBS and lysed with 1% Triton X-100 for 30 min at 37°C, and lysate was utilized to measure the nanoparticles' fluorescence intensities at excitation and emission wavelength of 377 and 431 nm, respectively. These measurements were analyzed against a nanoparticle standard. These fluorescence intensity values were then normalized with the total protein content per sample using BCA assays following manufacturer's instructions. In parallel, the nanoparticle interactions with endothelial cells were imaged using a fluorescence microscope under FITC channel.

Cellular Functionality

HUVEC functionality in the presence of BPLPL-based nanoparticles was determined based on nitric oxide (NO) production. Nanoparticles (1 mg/ml) were incubated with cells for 24 h, following which nitric oxide production of exposed cells was quantified using Intracellular Nitric Oxide Fluorometric Assay kits (Cell Biolabs, Inc., San Diego, CA) following the manufacturer's instructions. In brief, a NO fluorometric probe (provided with the kit) enters the cells and deacetylates by intracellular esterase to a non-fluorescent intermediate, which is rapidly oxidized by nitric oxide into a fluorescent triazolo-fluorescein analog. The fluorescence intensity is proportional to NO levels within the cell cytosol, which can be quantified at

a wavelength of 480 nm (excitation)/530 nm (emission) using UV/vis spectrophotometer (Infinite M200 plate reader, Tecan, Durham, NC). Cells grown on tissue culture plates without any treatment served as control.

In vitro Blood Studies of BPLPL-Based Nanoparticles

Blood Collection

Whole blood was drawn from healthy adult volunteers into acid citrate dextrose anticoagulant tubes (ACD, Solution A; BD Franklin Lakes, NJ). Consent from the volunteers was obtained prior to the blood collection, and all the procedures strictly adhered to the IRB standards approved at the University of Texas at Arlington.

Whole Blood Clotting Kinetics and Hemolysis

Briefly, in hemolysis, 10 μ L of various concentrations of nanoparticles ranging from 0 to 1,000 μ g/ml were incubated with 200 μ L of blood for 2 h at 37°C. The nanoparticles were centrifuged at 1,000 rpm for 5 min and absorbance of the supernatant was obtained using UV-Vis Spectrophotometer at a wavelength of 545 nm. Blood diluted in DI water served as the positive control, whereas saline diluted blood as the negative control for hemolysis studies. Percentage of hemolysis due to each sample was quantified based on Equation (1). In the whole blood clotting study, we studied the effects of particles on normal blood clotting kinetics, which was measured as blood clotting index (BCI). Here, whole blood initially activated by adding 0.01 M of calcium chloride, and 50 μ L of activated blood was then treated with 10 μ L of 0.5 mg/ml of nanoparticles for predetermined time points. At each time point, 1.5 ml of DI water was added to lyse the un-clotted blood, and absorbance of supernatant was measured at 540 nm. Untreated blood served as a control. The absorbance of whole blood (without any addition of calcium chloride) in water at 540 nm was applied as a reference value. The BCI can be quantified from Equation (2).

$$\text{Hemolysis (\%)} = \frac{\text{Absorbance of sample} - \text{Absorbance of negative control}}{\text{Absorbance of positive control} - \text{Absorbance of negative control}} \times 100\% \quad (1)$$

$$\text{BCI} = \frac{\text{Absorbance of blood in contact with samples at set time points at 545nm}}{\text{Absorbance of whole blood in water at 545nm at time 0}} \quad (2)$$

Platelet Adhesion and Aggregation

We further investigated the hemocompatibility of BPLPL materials based on the platelet adhesion and activation. For this study, platelet rich plasma (PRP) was collected by centrifuging whole blood at 190 g for 12 min. PRP was incubated with BPLPL films for 1 h at 37°C under static conditions. After 1 h, films were rinsed carefully with PBS and attached platelets were lysed using cell lysis solution for 1 h. The LDH release corresponding to platelet adhesion was quantified by detecting the amount of lactate dehydrogenase (LDH) present in the lysate solution using CytoTox 96[®] Non-Radioactive Cytotoxicity Assays according to the manufacturer's instructions. Glass served as the positive control for comparison. The morphology of platelet adhesion on the polymer films were also visualized using scanning electron microscopy (SEM) imaging. Briefly, platelets on films were fixed

TABLE 1 | Size, charge, polydispersity of BPLPL based NPs.

Polymeric Nanoparticles	Size (nm)	PD	Zeta potential (mV)
BPLPL-PLLA NPs	145 \pm 26	0.129 \pm 0.035	−21.85 \pm 2.16
BPLPL PLGA75:25 NPs	149 \pm 37	0.116 \pm 0.032	−23.85 \pm 1.32
BPLPL-PLGA50:50 NPs	157 \pm 44	0.164 \pm 0.010	−24.72 \pm 0.82
PLGA 50:50 NPs	176 \pm 36	0.130 \pm 0.032	−15.46 \pm 1.52

with 2.5% glutaraldehyde (Electron Microscopy Science, 16536-15) for overnight, post fixed with 1% Osmium tetroxide in 0.1 M Cacodylate buffer (Electron Microscopy Sciences, 19150) for 1 h, dehydrated with graded series of ethanol (50, 75, 95, 100%) for 15 min at each step, and further dried using varying ratios of hexamethyldisilane (HMDS) in ethanol (1:2, 1:1, 2:1) for 15 min at each step. Finally, the films were dried using 100% HMDS for 30 min and then sputter-coated with the silver for SEM. In addition, after incubating PRP with polymer films for 1 h, 5 μ L of suspension was collected and incubated with saturating concentrations of CD42b-PE (platelet marker) and PAC1- FITC (activated glycoprotein GP IIb/IIIa receptor marker) for 20 min. The antibodies were obtained from BD Biosciences. The platelets were fixed with 1% paraformaldehyde for 2 h in 4°C and were analyzed on BD LSRII flow cytometer. At least 10,000 events per sample were analyzed and identified based on their forward and side scattering characteristics and by positive staining with anti-CD42b-PE antibodies. The percentage of GpIIb/IIIa expressing platelets was calculated relative to the total number of platelets (CD42b positive cells).

Statistical Analysis

All the experiments were performed with $n = 3-6$ if not specified. Data were expressed as mean \pm SEM. The statistical analysis was assessed using ANOVA followed by *post-hoc* Pairwise Multiple Comparisons using Holm-Sidak method on GraphPad Prism

(GraphPad Software Inc., CA). A significant difference was considered where P -values appeared <0.05 .

RESULTS

Physical Characterization of BPLPL-Based NPs

DLS results show that the BPLPL-PLGA50:50, BPLPL-PLGA75:25 and BPLPL-PLLA based nanoparticles suspended in DI water have hydrodynamic sizes of 157, 149, and 145 nm, respectively (Table 1).

The polydispersity values ranging from 0.10 to 0.17 suggest the particles were well-dispersed. TEM images of BPLPL nanoparticle also confirms the uniform distribution of NPs with smooth and spherical morphology (Figures 1A–C). Zeta

potential for BPLPL-PLGA 50:50, BPLPL-PLGA 75:25 and BPLPL-PLLA based nanoparticles were -24.7 , -23.9 , and -21.9 mV, respectively, suggesting that the particles might be stable in physiological solutions (Honary and Zahir, 2013). In addition, the stability of BPLPL based nanoparticles was evaluated at various formulations including DI water, 10% FBS, 0.9% saline and simulated body fluid by recording the nanoparticles diameter at fixed time intervals. We have observed that BPLPL-PLGA NPs were stable in all formulations for 48 h with no significant aggregation or change in size. Although BPLPL-PLLA NPs remained relatively stable in DI water, saline and serum, they tended to have some aggregation in simulated body fluid at 48 h (Figure 2).

To determine if these nanoparticles could be utilized for drug delivery applications, their drug release kinetics and degradation studies were conducted. BSA was chosen as the model growth factor. BPLPL-PLGA 50:50, BPLPL-PLGA 75:25 and BPLPL-PLLA showed a loading efficiency of 70, 69, and 77%, respectively. Figure 3A showed that both BPLPL-PLGA nanoparticles could release $\sim 50\%$ content within 24 h, and the complete release was achieved in 7 days. On the other hand, BPLPL-PLLA nanoparticles demonstrated comparatively lower release kinetics, and only 50% BSA release was achieved in 2 weeks. The *in vitro* degradation study also emphasizes the role of polymer composition on particle behavior (Figure 3B), where BPLPL-PLGA particles showed a similar degradation rate and almost $\sim 80\%$ degraded in 4 weeks. However, BPLPL-PLLA degraded slowly with only $\sim 30\%$ lost in weight when observed after 4 weeks. Furthermore, all BPLP-cys-poly lactone based nanoparticles showed maximum excitation and emission wavelength at 374 and 441 nm, respectively (Figure 3C).

In vitro Cell Studies With BPLPL-Based Nanoparticles

Cytocompatibility evaluation of BPLPL-based NPs at various concentrations after 24 h incubation with HUVECs was conducted. Accordingly, BPLPL NPs at all concentrations ranging from 50 to 1,000 $\mu\text{g/ml}$ was shown to be compatible with HUVECs with $>80\%$ viable cells after NP exposure (Figure 4A). In addition, the functional status of endothelial cells in the presence of BPLPL-based NPs was studied by assessing the nitric oxide (NO) production. Accordingly, we noted that NO production by HUVECs treated with BPLPL-PLLA NPs at 1,000 $\mu\text{g/ml}$ for 24 h was significantly lower than that of cells treated with BPLPL-PLGA NPs and untreated cells (Figure 4B). On the other hand, NOS activity quantified for HUVECs in the presence of both BPLPL-PLGA50:50 and BPLPL-PLGA75:25 demonstrated no negative effects on cellular function.

Lastly, the uptake of BPLPL-based NPs by vascular endothelial cells (HUVECs) was studied by incubating cells with various concentrations of NPs over 4 h. All NP formulations showed dose-dependent cellular uptake up to a concentration of 1,000 $\mu\text{g/ml}$ (Figure 5A). Fluorescence images also showed the internalization of BPLPL-based nanoparticles by endothelial cells and their subsequent localization in cytoplasmic region of cells after 4-h incubation with particles (Figure 5B).

Hemocompatibility of BPLPL-Based Nanoparticles

Hemocompatibility of nanoparticles was determined based on whole blood clotting kinetics, hemolysis study, and platelet responses. Blood clotting time reflects the thromboresistance property of nanoparticles, and high thromboresistance (Blood clot index, BCI value) means high blood compatibility. All BPLPL-based nanoparticles showed similar BCI values with each other and when compared to untreated blood samples (Figure 6A). This suggests that particles have no significant effect on the normal blood clotting kinetics. Furthermore, BPLPL-based NPs at all tested concentrations proved to be non-hemolytic with a maximum of 0.4% which was well within the standardized ISO values for non-hemolytic materials, which is 0–2% (Cerdeira-Cristerna et al., 2011) (Figure 6B). To assess the compatibility of BPLPL-based materials with platelets, BPLPL films were incubated with PRP at 37°C for 1 h. Based on the analysis, BPLPL-PLLA showed a significantly higher number of platelets adhered onto its surface than those of BPLPL-PLGA counterparts (Figure 7A). As platelets get activated, P-selectin translocate from intracellular granules to the external membrane, whereas fibrinogen aggregates platelets by bridging glycoprotein GPIIb/IIIa between adjacent platelets (Merten and Thiagarajan, 2000). Based on flow cytometric analysis, significant amount of platelet activation was seen on the glass surface as a positive control (Figure 7B). The amount of activation seen on BPLPL-PLGA surface was similar to those on PLGA surfaces. In concordance to these observations, SEM images also showed significantly higher platelet attachment on glass and BPLPL-PLLA surfaces than others. Closer observation of these images (Figure 7C) shows that platelets are spreading and aggregating on glass and BPLPL-PLLA surfaces. Other surfaces such as PLGA 50:50, BPLPL-PLGA 75:25, and BPLPL-PLGA 50:50 also presented a platelet shape change representing the early stage of platelet activation, which was characterized by transformation from discoid to spheroid form with small bulbous protrusions distributed over the platelet surface (Zilla et al., 1987).

DISCUSSION

Bioimaging holds huge potential in the field of drug delivery, tissue engineering and regenerative medicine. During the last decade, several functional polymers with imaging capabilities were investigated to understand the biological processes and their potential applications for image-guided surgery and therapy (Braeken et al., 2017; Zhang and Yao, 2018). The BPLP is one such novel biomaterial with intrinsic and excellent photoluminescent properties that can be used as a label-free *in vivo* imaging tool for disease detection and treatment. The components that are utilized to develop BPLPs including citric acid, amino acids, and aliphatic diols, which are all commonly used in many FDA-regulated devices (Yang et al., 2009; Li et al., 2017). Recently, a family of BPLPLs based on BPLP have been reported (Xie et al., 2014). This new class of materials can be utilized to fabricate

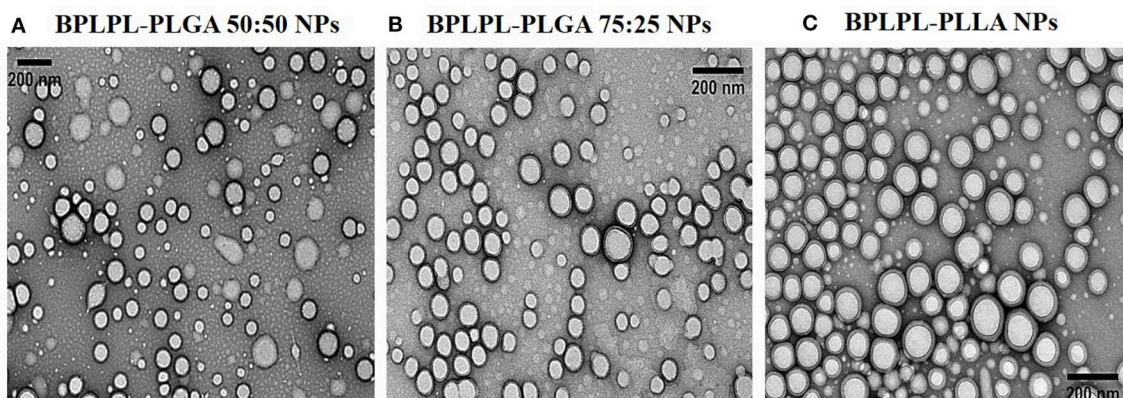


FIGURE 1 | Morphological characterization of BPLPL-based NPs. TEM images of (A) BPLPL-PLGA50:50 (1:100), (B) BPLPL-PLGA75:25(1:100), (C) BPLPL-PLLA (1:100) shows uniform sized and spherical morphology of nanoparticles. The scale bar represents 200 nm.

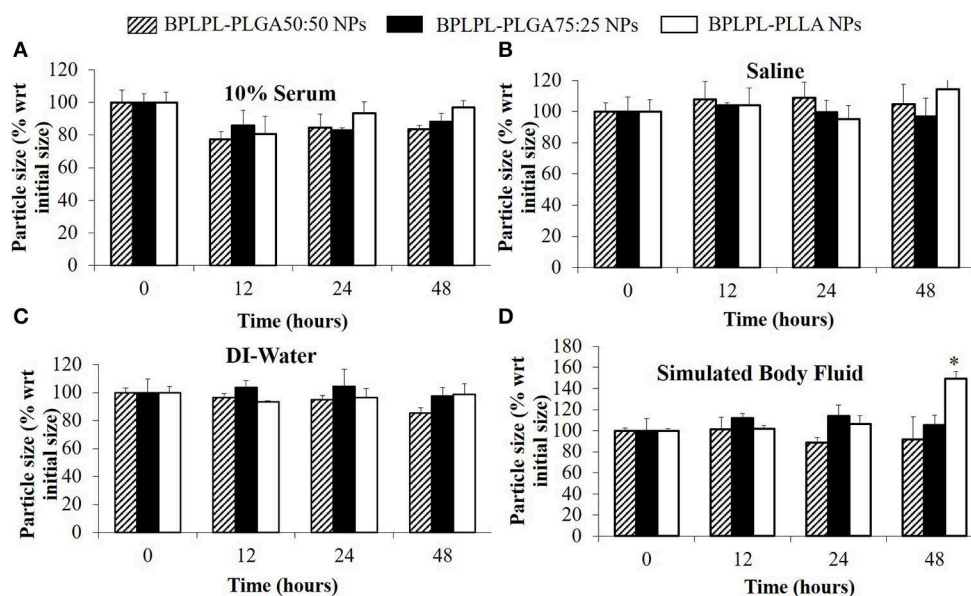


FIGURE 2 | Stability of BPLPL-based NPs. NP stability in various formulations such as (A) 10% serum, (B) Saline (0.9% NaCl), (C) DI-water, and (D) Stimulated body fluid based on particle size measured over periods of 48 h. Graph plot as average \pm SD of $n = 3$ samples. Asterisk (*) represents $p < 0.05$ in comparison to size of BPLPL-PLLA NPs at initial time point.

theranostic nanoparticles which can be tracked with a variety of microscopy techniques, including fluorescent microscopy, confocal laser scanning microscopy and two-photon microscopy (Li et al., 2017).

In our present work, we screened three different BPLPL-based nanoparticles (BPLPL-NPs) including BPLPL-PLLA, BPLPL-PLGA50:50, and BPLPL-PLGA75:25 to determine the most promising formulation that can be utilized for theranostic applications in treating cardiovascular diseases. Our characterization showed that most BPLPL-NPs maintained uniform, spherical morphology with 150 nm in diameter and higher negative zeta potential values compared to PLGA 50:50 nanoparticles due to inclusion of citric acid component

in BPLPL. This increased surface charged groups on BPLPL-based NPs not only provide additional functional motifs required for the conjugation of targeting ligands but also improve NPs stability in physiological fluids. To evaluate this, the diameter of BPLPL-NPs in various formulations including DI water, serum, saline, and simulated body fluid was monitored for 48 h. Accordingly, we found that most of BPLPL-NPs, except BPLPL-PLLA at 48 h in simulated body fluids were relatively stable with no signs of aggregations. It is plausible that with long-term incubation of BPLPL-PLLA in simulated body fluids alters the colloidal stability of particles due to enhanced interactions of these NPs with various salts and enzymes that constitute the solvent. Lazzari

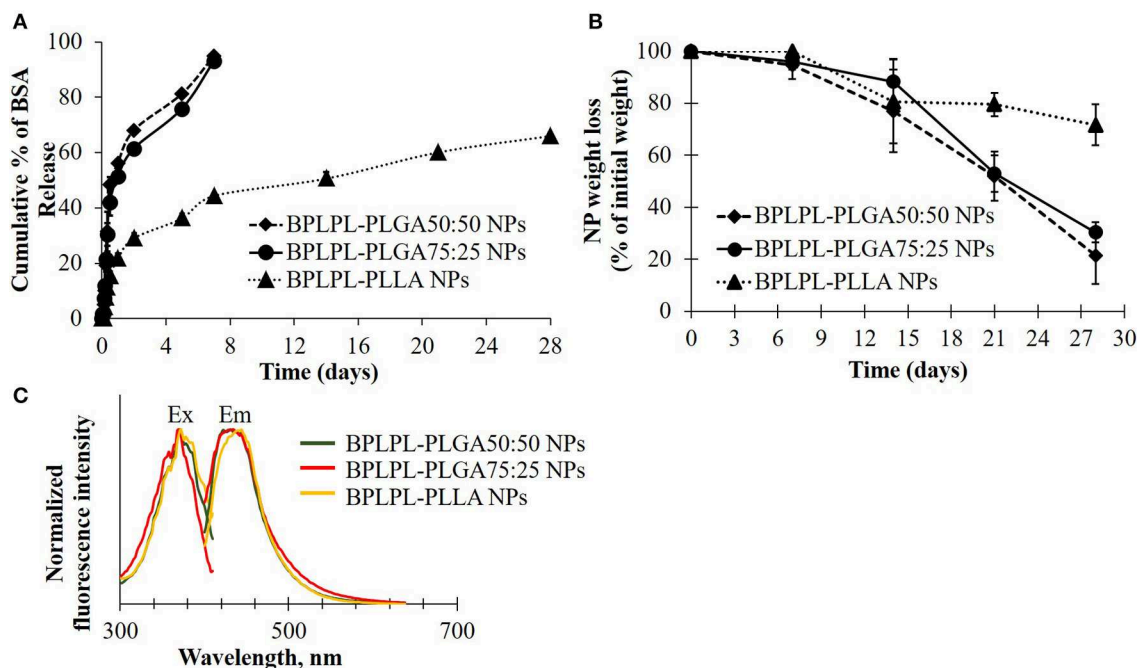


FIGURE 3 | Physical characterization of BPLPL-based NPs. **(A)** BSA release kinetics from BPLPL-based nanoparticles in PBS solution at 37°C for 2 weeks, **(B)** Degradation of NPs in water at 37°C for 4 weeks, and **(C)** Fluorescence spectrum of cysteine derived BPLPL-based NPs (1 mg/ml) has an excitation and emission at 377 and 441 nm, respectively. Graph plot as average \pm SD of $n = 3$ samples.

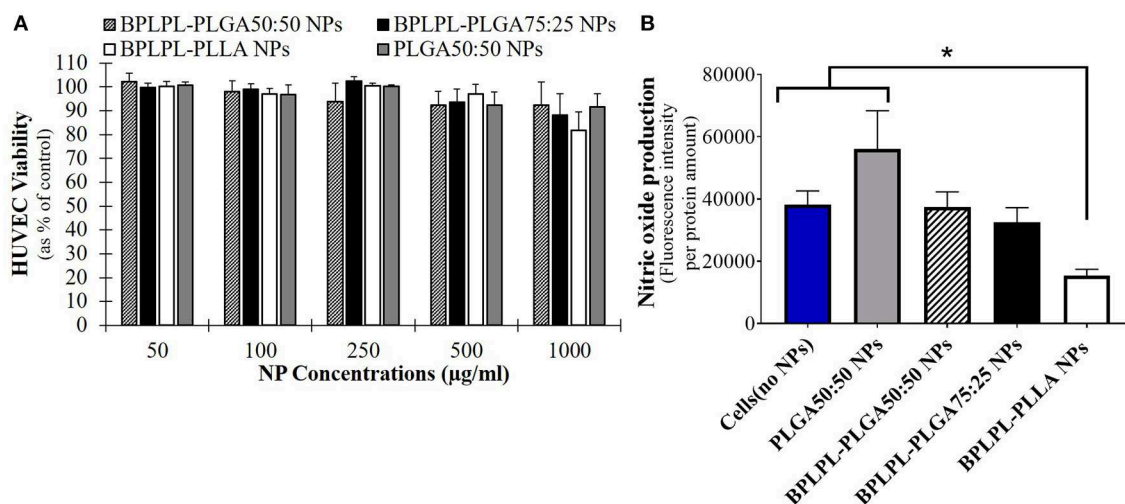


FIGURE 4 | Cytocompatibility of BPLPL-based nanoparticles. **(A)** HUVEC viability in presence of various concentrations of nanoparticles as quantified using MTS assays; **(B)** Intracellular NOS activity within HUVECs was quantified after incubation with 1,000 µg/ml of BPLPL-based NPs for 24 h. Fluorescence intensity correlates with NOS activity or NO production within cells. *Represents significance with respect to cells treated to BPLPL-PLLA. Graph plotted in terms of average \pm standard error mean (SEM).

et al. (2012) have observed similar aggregation behavior for PLLA NPs in simulated body fluids after prolonged incubation. In such instances, simple modifications of BPLPL-PLLA NPs surface with PEG chains might be able to prevent the docking of enzymes or ions on nanoparticle surfaces, thereby

improving their colloidal stability in physiological conditions (Singh et al., 2017).

The presence of PLLA in BPLPs also seem to affect the protein loading efficiency, protein release kinetics and degradation profile of BPLPL-PLLA NPs. It was noted that BPLPL-PLGA

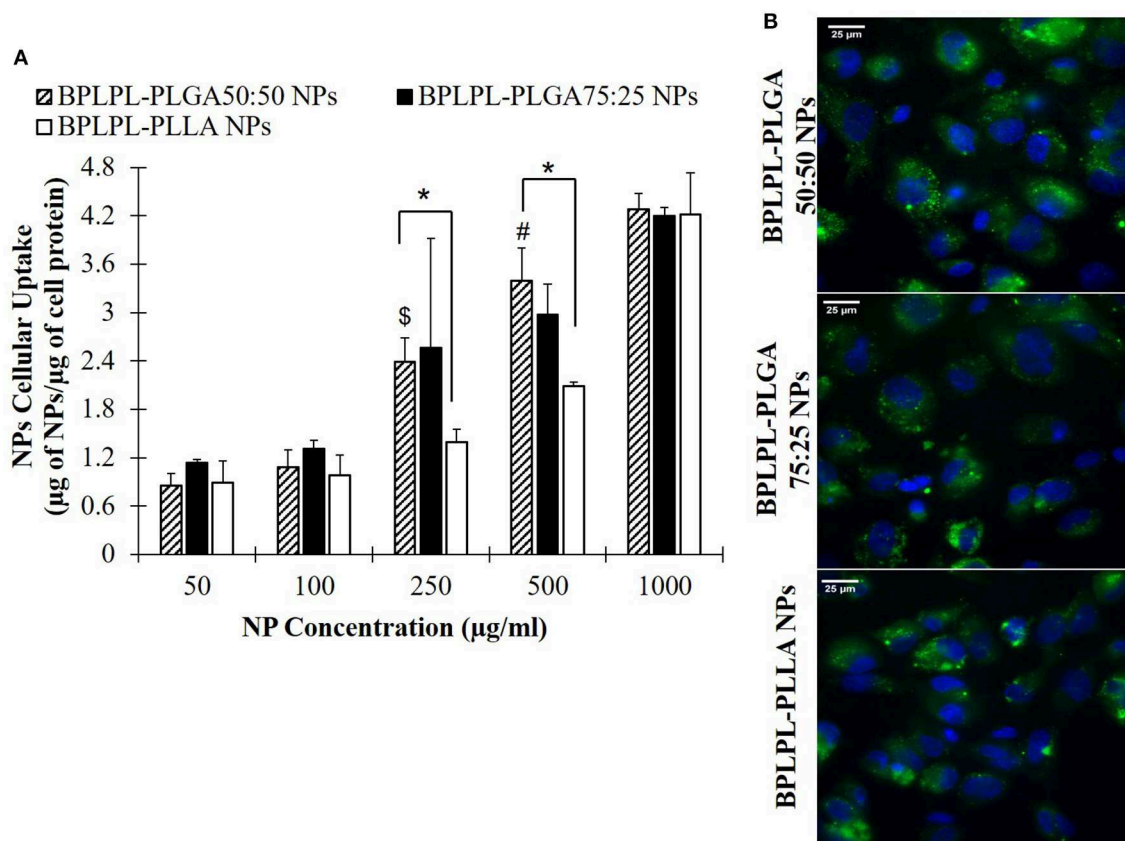


FIGURE 5 | Cellular uptake of BPLPL-based nanoparticles. **(A)** Nanoparticle uptake by endothelial cells (HUVECs) at various concentrations after incubation for 4 hr in 37°C was quantified in terms of amount of nanoparticles relative to protein amount per sample. \$ and # represents significance with respect to BPLPL-PLGA50:50 NPs at concentrations of 100 and 250 μg/ml, respectively; whereas * represents significance between BPLPL-PLGA50:50 NPs and BPLPL-PLLA NPs. **(B)** Fluorescent images of nanoparticles internalized HUVECs at 60X, green represents nanoparticles and blue for cell nuclei. The scale bar is 25 μm in length. Graph plotted in terms of average ± SEM.

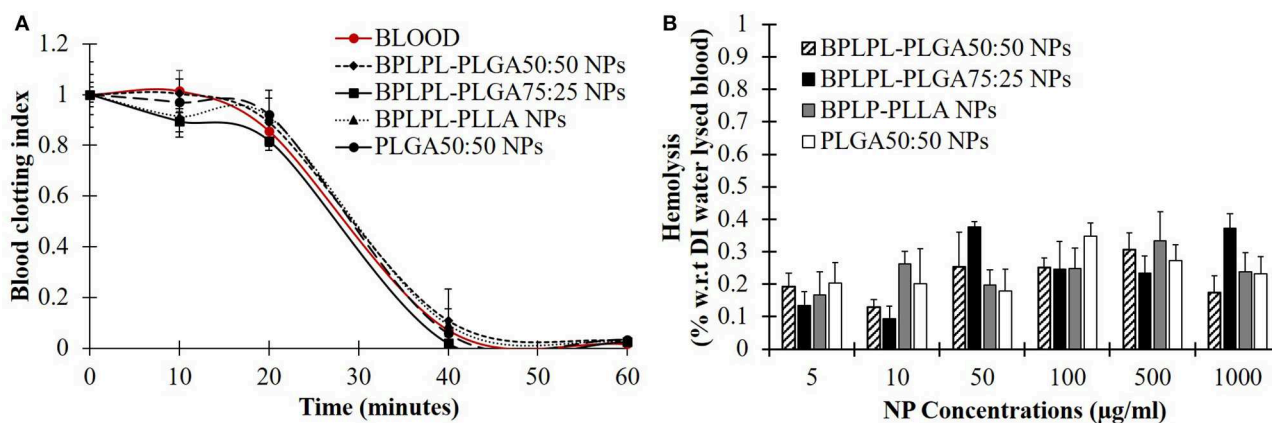


FIGURE 6 | Hemocompatibility of BPLPL-based NPs. NP compatibility in whole blood was assessed based on **(A)** clotting kinetic profile in presence of 1 mg/ml of NPs and **(B)** hemolysis after incubating with nanoparticles of various concentrations for predetermined timepoints. Graph plot as average ± SEM.

NPs released ~50% of BSA within 24 h, whereas BPLPL-PLLA achieved a similar amount of BSA release within 2 weeks. In addition, BPLPL-PLLA NPs demonstrated a slower degradation

rate with ~30% lost weight compared to BPLPL-PLGA NPs which showed ~80% degradation within 4 weeks. Hu et al. (2016) explained that BPLP incorporation into polylactones

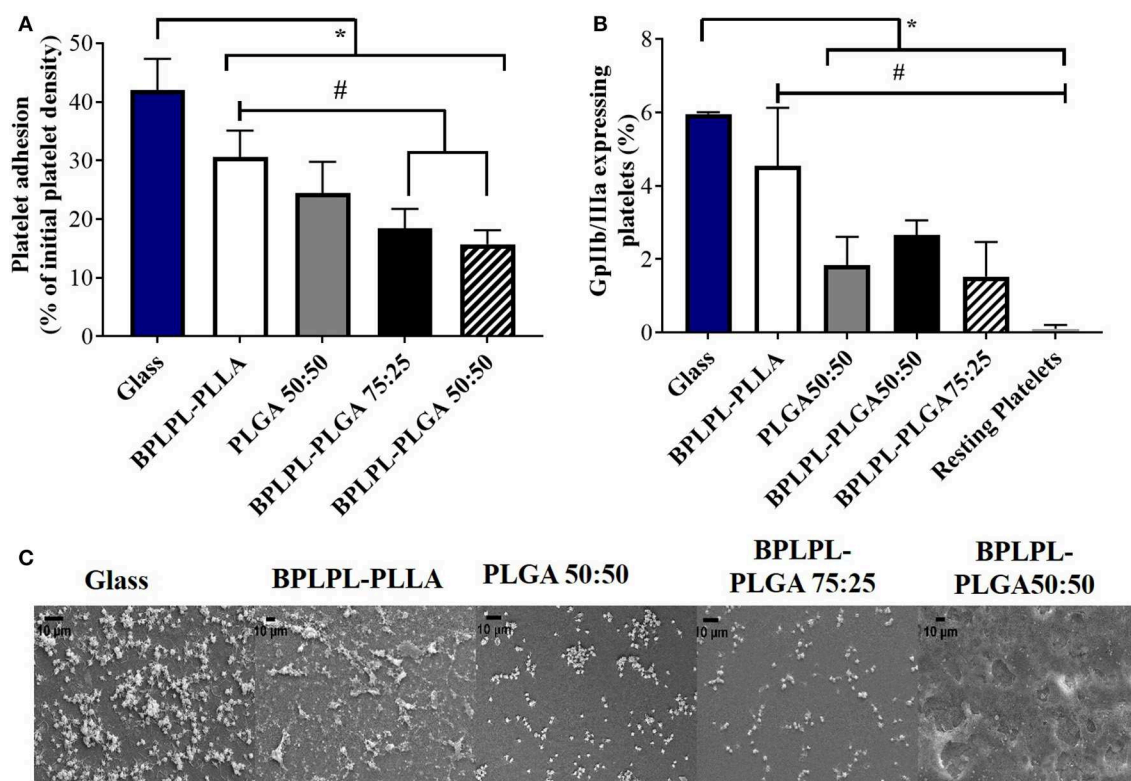


FIGURE 7 | Platelet responses to BPLPL-based materials. **(A)** Platelet adhesion to BPLPL-based materials after 1-h incubation at 37°C quantified using LDH assays, **(B)** Platelet activation quantified based on expression of GPIIb/IIIa surface markers using flow cytometry, and **(C)** SEM images to demonstrate platelet morphological changes and interactions with BPLPL-based materials. *and # represents significance value of $p < 0.05$ with respect to glass and BPLPL-PLLA, respectively. Graph plot as average \pm SEM, and scale bar for SEM images represents length of 10 μ m.

could enhance water permeability, which in turn, accelerate the drug release rate and degradation of copolymers. Also, the percentage of hydrophilic glycolic acid in BPLPL would also attribute to faster degradation and thereby drug release from the particles. We speculate that the hydrophobic nature of PLLA, may have improved their protein encapsulation compared to its PLGA counterparts by forming a hydrophobic wall to retard BSA leakage into the outer water phase during the NP synthesis (Liu et al., 2006). Furthermore, the photoluminescent property of BPLP was retained in BPLPL-based NPs, with maximum excitation and emission wavelength at 344 and 441 nm, respectively. Previously, we have shown that depending on the amino acids used in BPLP syntheses, the fluorescence emission could be broadened up to 725 nm, highlighting the versatility of these polymers for biomedical imaging (Tran et al., 2009).

Following the physical and chemical characterization of BPLPL NPs, their cytotoxicity with endothelial cells was investigated. BPLPL NPs exhibited excellent cytocompatibility with >80% of HUVECs viability post treatment with NPs at all concentrations. Xie et al. (2014) also reported similar values for cell viability using 3T3 fibroblasts exposed to BPLPL-PLLA nanoparticles at concentrations ranging from 1 to 500 μ g/ml. Due to the presence of high number of carboxylic groups on

the BPLP backbone, it was noted earlier about the reduced cell survival in presence of BPLP NPs (Zhang et al., 2013; Xie et al., 2014). In our study, BPLPL-based NPs showed similar cytocompatibility profile as seen for PLGA NPs with minimal cytotoxicity on HUVECs. Similar to our observation, Hu et al. (2016) also reported comparable *in vitro* cytotoxicity by mesenchymal stem cells as well as *in vivo* foreign body response toward BPLPL and PLGA materials. This suggests that inclusion of BPLP into commonly used polymers such as PLGA did not significantly affect the cell survival while the newly synthesized polymers can still inherit the florescent properties from BPLP, which could be possibly utilized for theranostic applications in CVD treatment.

Next, the proper functioning of endothelial cells in presence of BPLPL-based NPs in terms of nitric oxide production was evaluated. Nitric oxide (NO) is an important signaling molecule released by endothelial cells to regulate vascular inflammation, platelet function, angiogenesis and protection from ischemia reperfusion injury. Any dysregulation of NO production due to NOS uncoupling is known to cause cardiovascular diseases (e.g., atherosclerosis, diabetes, and hypertension) (Le et al., 2017). Inorganic nanoparticles including fluorescent silica NPs, superparamagnetic iron oxide NPs, titanium dioxide NPs generally investigated to be utilized for bioimaging applications

demonstrated to induce EC toxicity and dysfunction with impaired NO production (Montiel-Dávalos et al., 2012; Astanina et al., 2014; Cao, 2018). When compared to these NP types, BPLPL-PLGA NPs could be a better alternative since it demonstrated to be inert with no effect on normal cell activities. However, this is not the case with BPLPL-PLLA NPs, nitric oxide production by endothelial cells was significantly reduced when compared to cells exposed to PLGA NPs. The mechanism that influenced the cellular behavior in presence of BPLPL-PLLA NPs is not clear. However, it is plausible that the BPLPL-PLLA nanoparticles may have upregulated oxidative stress within the cells that can activate autophagy and eventually lead to endothelial dysfunction via the PI3K/Akt/mTOR pathway as seen for silica NPs (Duan et al., 2014). Similar to our observation, Wang et al. (2014) also noted that exposure of PLLA particles to human coronary artery endothelial cells decreased their NO production, and induce inflammatory adhesion molecule expression such as ICAM-1 and VCAM-1, which might facilitate immune cell adhesion and recruitment. Furthermore, several studies reported that stents coated with PLLA impairs endothelial cell functions and impaired their recovery on the luminal side of stents that promoted in stent late thrombosis (Liu and Ma, 2010; Xu et al., 2011).

To investigate the utilization of BPLPL-based NPs as an imaging probe to track HUVECs, we incubated BPLPL-based NPs with vascular endothelial cells (HUVECs) over time. Dose-dependent uptake of NPs was observed for all NP formulations. Fluorescence images demonstrated the internalization of BPLPL-based nanoparticles by endothelial cells and their subsequent localization in the cytoplasmic region of cells after a 4-h incubation. Our results agreed with previous reports from other groups that tested various nanoparticle formulations on a different cell line. For instance, Menon et al. (2014) demonstrated increasing uptake of PLGA nanoparticles by Type I alveolar epithelial cells up to 1,000 µg/ml. Kona et al. (2012) also observed dose-dependent uptake of GpIbα conjugated PLGA nanoparticles and unconjugated nanoparticles by human aortic endothelial cells, which were saturated at 300 µg/ml. Even BPLP particles were shown to have dose-dependent uptake characteristics (Wadajkar et al., 2012). In this study, they observed BPLP particles being uptake by the human dermal fibroblast without any saturation up to 500 µg/ml. It was also noted that hydrophilic and hydrophobic versions of BPLP polymers impacted the amount of nanoparticles being internalized by the different cell lines, thereby exhibiting variation in NP cellular uptake. Similarly, we have observed a significant difference in BPLPL-PLLA and BPLPL-PLGA50:50 based NPs uptake by endothelial cells, especially at concentrations of 250 and 500 µg/ml. We speculate that such difference is due to differential composition of PLLA and PLGA50:50 in BPLPLs materials, where PLLA more hydrophobic in nature than PLGA50:50 and thereby affected the NP uptake by the endothelial cells. Cells continued to exhibit significant uptake of these nanoparticles at 1,000 µg/ml, and as a result, almost similar amounts of NPs in the cells were observed at high concentrations despite of polymer types. On other hand, we did not observe cells demonstrate any dose-dependent NP

uptake for BPLPL-PLLA NPs at concentrations <250 µg/ml. In line with our results, It is plausible that the serum proteins in the media interact with the nanoparticles and modulate their uptake kinetics by the endothelial cells at low concentrations (Lesniak et al., 2010; Pelaz et al., 2015). Also, at these small concentrations, the measured levels of fluorescence intensity produced by NPs in the cells may be more difficult to discriminate.

In addition to the intrinsic fluorescence property of BPLPLs, we investigated whether the citric acid composition endows them with hemocompatibility suitable for blood contacting applications as previously seen for poly(diols-citrate) (POC) prepared from citric acid and 1,8-octanediol (Yang et al., 2004; Motlagh et al., 2007; Tran et al., 2009, 2015). First, *in vitro* hemostatic properties of BPLPL-based NPs were evaluated by whole blood clotting experiment. At various time points, absorbance of RBCs that were not trapped in clots were determined at 540 nm. Higher BCI values represent reduced blood clotting kinetics, and we have observed blood treated with BPLPL-based NPs did not exhibit a different rate of clotting when compared either with untreated blood or blood incubated with PLGA NPs. Second, hemolytic results of BPLPL-based NPs demonstrate them to be non-hemolytic material that is safe to be utilized for drug delivery applications without causing any adverse effects. Lastly, platelet behaviors toward BPLPL-based materials indicates that BPLPL-PLGA consisted of better or comparable platelet attachment and activation as seen in those of PLGA surfaces; whereas, higher number of platelets adhered and expressed GPIIb/IIIa markers on BPLPL-PLLA surfaces. Many studies previously observed that PLLA in its unmodified form or without incorporation of therapeutic agents induce increased inflammatory responses mainly due to its hydrophobic nature (Nguyen et al., 2003; Meng et al., 2004; Okamura et al., 2011; Rudolph et al., 2015). Our speculation is that since incorporating BPLPs into PLLA shown to increase the wettability of the polymer (Hu et al., 2016); the effect we have observed for platelets to BPLPL-PLLA could be minimal than its unmodified form of PLLA, which must be investigated further.

CONCLUSION

We have formulated three different photoluminescent polylactones based NPs, and characterized their physical and chemical properties, protein encapsulation, *in vitro* hemocompatibility, cytocompatibility and particle uptake. Among these formulations, BPLPL-PLGA NPs exhibited stability in physiological conditions, bi-phasic release kinetics, excellent cytocompatibility with no negative influence on cellular functions, optimal uptake characteristics, and hemocompatibility similar to PLGA nanoparticles. Most importantly, BPLPL-based NPs showed intrinsic fluorescence capability inherited from the precursor BPLP. In short, herein we have demonstrated that BPLPL-based NPs are safe, biocompatible material with imaging capability that can be potentially used to fabricate targeted, therapeutic loaded nanocarriers for theranostic applications or utilized as an imaging agent to tag transplanted cells.

DATA AVAILABILITY STATEMENT

The datasets generated for this study are available on request to the corresponding author.

AUTHOR CONTRIBUTIONS

AK, KN, and JY contributed conception and design of the study. AK performed the experiments, data collection, statistical analysis, and wrote the manuscript. NP conducted TEM imaging of nanoparticles whereas DS synthesized the BPLP based

polylactones. All authors contributed to manuscript revision, read, and approved the submitted version.

FUNDING

This project was supported in part by the National Institutes of Health Awards (T32 HL134613, F31 HL146118, and R21 EB024829). The content is solely the responsibility of the authors and does not necessarily represent the official views of the National Institutes of Health.

REFERENCES

- Adams, W. J., Zhang, Y., Cloutier, J., Kuchimanchi, P., Newton, G., Sehrawat, S., et al. (2013). Functional vascular endothelium derived from human induced pluripotent stem cells. *Stem Cell Rep.* 1, 105–113. doi: 10.1016/j.stemcr.2013.06.007
- Astanina, K., Simon, Y., Cavelius, C., Petry, S., Kraegeloh, A., and Kiemer, A. K. (2014). Superparamagnetic iron oxide nanoparticles impair endothelial integrity and inhibit nitric oxide production. *Acta Biomater.* 10, 4896–4911. doi: 10.1016/j.actbio.2014.07.027
- Braeken, Y., Cheruku, S., Ethirajan, A., and Maes, W. (2017). Conjugated polymer nanoparticles for bioimaging. *Materials* 10:1420. doi: 10.3390/ma10121420
- Cao, Y. (2018). The toxicity of nanoparticles to human endothelial cells. *Adv. Exp. Med. Biol.* 1048, 59–69. doi: 10.1007/978-3-319-72041-8_4
- Cerda-Cristerna, B. I., Flores, H., Pozos-Guillen, A., Perez, E., Sevrin, C., and Grandfils, C. (2011). Hemocompatibility assessment of poly(2-dimethylamino ethylmethacrylate) (PDMAEMA)-based polymers. *J. Control Release* 153, 269–277. doi: 10.1016/j.jconrel.2011.04.016
- Chan, J. M., Zhang, L., Tong, R., Ghosh, D., Gao, W., Liao, G., et al. (2010). Spatiotemporal controlled delivery of nanoparticles to injured vasculature. *Proc. Natl. Acad. Sci. U.S.A.* 107, 2213–2218. doi: 10.1073/pnas.0914585107
- Chen, H., Wang, X., Zhou, Q., Xu, P., Liu, Y., Wan, M., et al. (2017). Preparation of vascular endothelial cadherin loaded-amphoteric copolymer decorated coronary stents for anticoagulation and endothelialization. *Langmuir* 33, 13430–13437. doi: 10.1021/acs.langmuir.7b03064
- Chen, Z., Li, Q., Chen, J., Luo, R., Maitz, M. F., and Huang, N. (2016). Immobilization of serum albumin and peptide aptamer for EPC on polydopamine coated titanium surface for enhanced in-situ self-endothelialization. *Mater. Sci. Eng. C Mater. Biol. Appl.* 60, 219–229. doi: 10.1016/j.msec.2015.11.044
- Duan, J., Yu, Y., Yu, Y., Li, Y., Wang, J., Geng, W., et al. (2014). Silica nanoparticles induce autophagy and endothelial dysfunction via the PI3K/Akt/mTOR signaling pathway. *Int. J. Nanomed.* 9, 5131–5141. doi: 10.2147/IJN.S71074
- Giordano, S., Zhao, X., Xing, D., Hage, F., Oparil, S., Cooke, J. P., et al. (2016). Targeted delivery of human iPS-ECs overexpressing IL-8 receptors inhibits neointimal and inflammatory responses to vascular injury in the rat. *Am. J. Physiol. Heart. Circ. Physiol.* 310, H705–H715. doi: 10.1152/ajpheart.00587.2015
- Honary, S., and Zahir, F. (2013). Effect of zeta potential on the properties of nano-drug delivery systems-a review (Part 2). *Trop. J. Pharm. Res.* 12, 265–273. doi: 10.4314/tjpr.v12i2.20
- Hu, J., Guo, J., Xie, Z., Shan, D., Gerhard, E., Qian, G., et al. (2016). Fluorescence imaging enabled poly(Lactide-co-glycolide). *Acta Biomater.* 29, 307–319. doi: 10.1016/j.actbio.2015.10.010
- Kona, S., Dong, J.-F., Liu, Y., Tan, J., and Nguyen, K. T. (2012). Biodegradable nanoparticles mimicking platelet binding as a targeted and controlled drug delivery system. *Int. J. Pharm.* 423, 516–524. doi: 10.1016/j.ijpharm.2011.11.043
- Lazzari, S., Moscatelli, D., Codari, F., Salmona, M., Morbidelli, M., and Diomedea, L. (2012). Colloidal stability of polymeric nanoparticles in biological fluids. *J. Nanopart. Res.* 14:920. doi: 10.1007/s11051-012-0920-7
- Le, D. Q., Kuriakose, A. E., Nguyen, D. X., Nguyen, K. T., and Acharya, S. (2017). Hybrid nitric oxide donor and its carrier for the treatment of peripheral arterial diseases. *Sci. Rep.* 7:8692. doi: 10.1038/s41598-017-08441-9
- Lesniak, A., Campbell, A., Monopoli, M. P., Lynch, I., Salvati, A., and Dawson, K. A. (2010). Serum heat inactivation affects protein corona composition and nanoparticle uptake. *Biomaterials* 31, 9511–9518. doi: 10.1016/j.biomaterials.2010.09.049
- Li, J., Tian, Y., Shan, D., Gong, A., Zeng, L., Ren, W., et al. (2017). Neuropeptide Y Y1 receptor-mediated biodegradable photoluminescent nanobubbles as ultrasound contrast agents for targeted breast cancer imaging. *Biomaterials* 116, 106–117. doi: 10.1016/j.biomaterials.2016.11.028
- Liu, R., Huang, S.-S., Wan, Y.-H., Ma, G.-H., and Su, Z.-G. (2006). Preparation of insulin-loaded PLA/PLGA microcapsules by a novel membrane emulsification method and its release *in vitro*. *Colloids Surf. B Biointerfaces* 51, 30–38. doi: 10.1016/j.colsurfb.2006.05.014
- Liu, X., and Ma, P. X. (2010). The nanofibrous architecture of poly(L-lactic acid)-based functional copolymers. *Biomaterials* 31, 259–269. doi: 10.1016/j.biomaterials.2009.09.046
- Marques, M. R., Loebenberg, R., and Almukainzi, M. (2011). Simulated biological fluids with possible application in dissolution testing. *Dissolution Technol.* 18, 15–28. doi: 10.14227/DT180311P15
- Meng, B., Wang, X., Cui, F., Dong, H., and Yu, F. (2004). A new method of heparinizing PLLA film by surface entrapment. *J. Bioact. Compat. Pol.* 19, 131–143. doi: 10.1177/0883911504042644
- Menon, J. U., Ravikumar, P., Pise, A., Gyawali, D., Hsia, C. C. W., and Nguyen, K. T. (2014). Polymeric nanoparticles for pulmonary protein and DNA delivery. *Acta Biomater.* 10, 2643–2652. doi: 10.1016/j.actbio.2014.01.033
- Merten, M., and Thiagarajan, P. (2000). P-selectin expression on platelets determines size and stability of platelet aggregates. *Circulation* 102, 1931–1936. doi: 10.1161/01.CIR.102.16.1931
- Montiel-Dávalos, A., Ventura-Gallegos, J. L., Alfaro-Moreno, E., Soria-Castro, E., García-Latorre, E., Cabañas-Moreno, J. G., et al. (2012). TiO₂ nanoparticles induce dysfunction and activation of human endothelial cells. *Chem. Res. Toxicol.* 25, 920–930. doi: 10.1021/tx200551u
- Motlagh, D., Allen, J., Hoshi, R., Yang, J., Lui, K., and Ameer, G. (2007). Hemocompatibility evaluation of poly(diols citrate) *in vitro* for vascular tissue engineering. *J. Biomed. Mater. Res. A* 82A, 907–916. doi: 10.1002/jbm.a.31211
- Nguyen, K. T., Su, S. H., Sheng, A., Wawro, D., Schwade, N. D., Brouse, C. F., et al. (2003). *In vitro* hemocompatibility studies of drug-loaded poly-(L-lactic acid) fibers. *Biomaterials* 24, 5191–5201. doi: 10.1016/S0142-9612(03)00451-4
- Okamura, Y., Schmidt, R., Raschke, I., Hintze, M., Takeoka, S., Egner, A., et al. (2011). A few immobilized thrombins are sufficient for platelet spreading. *Biophys. J.* 100, 1855–1863. doi: 10.1016/j.bpj.2011.02.052
- Pelaz, B., Del Pino, P., Maffre, P., Hartmann, R., Gallego, M., Rivera-Fernández, S., et al. (2015). Surface functionalization of nanoparticles with polyethylene glycol: effects on protein adsorption and cellular uptake. *ACS Nano* 9, 6996–7008. doi: 10.1021/acsnano.5b01326
- Polyak, B., Medved, M., Lazareva, N., Steele, L., Patel, T., Rai, A., et al. (2016). Magnetic nanoparticle-mediated targeting of cell therapy reduces in-stent stenosis in injured arteries. *ACS Nano* 10, 9559–9569. doi: 10.1021/acsnano.6b04912

- Povsic, T. J., and Goldschmidt-Clermont, P. J. (2008). Endothelial progenitor cells: markers of vascular reparative capacity. *Ther. Adv. Cardiovasc. Dis.* 2, 199–213. doi: 10.1177/1753944708093412
- Rudolph, A., Teske, M., Illner, S., Kiefel, V., Sternberg, K., Grabow, N., et al. (2015). Surface modification of biodegradable polymers towards better biocompatibility and lower thrombogenicity. *PLoS ONE* 10:e0142075. doi: 10.1371/journal.pone.0142075
- Singh, N. A., Mandal, A. K. A., and Khan, Z. A. (2017). Fabrication of PLA-PEG nanoparticles as delivery systems for improved stability and controlled release of catechin. *J. Nanomater.* 2017:9. doi: 10.1155/2017/6907149
- Su, L.-C., Xu, H., Tran, R. T., Tsai, Y.-T., Tang, L., Banerjee, S., et al. (2014). In situ re-endothelialization via multifunctional nanoscaffolds. *ACS nano* 8, 10826–10836. doi: 10.1021/nn504636n
- Sun, J., Kang, X., and Li, T. (2015). Vascular restoration: is there a window of opportunity? *Med. Hypotheses* 85, 972–975. doi: 10.1016/j.mehy.2015.08.024
- Tran, R. T., Yang, J., and Ameer, G. A. (2015). Citrate-based biomaterials and their applications in regenerative engineering. *Annu. Rev. Mater. Res.* 45, 277–310. doi: 10.1146/annurev-matsci-070214-020815
- Tran, R. T., Zhang, Y., Gyawali, D., and Yang, J. (2009). Recent developments on citric acid derived biodegradable elastomers. *Recent Pat. Biomed. Eng.* 2, 216–227. doi: 10.2174/1874764710902030216
- Vosen, S., Rieck, S., Heidsieck, A., Mykhaylyk, O., Zimmermann, K., Bloch, W., et al. (2016). Vascular repair by circumferential cell therapy using magnetic nanoparticles and tailored magnets. *ACS Nano* 10, 369–376. doi: 10.1021/acsnano.5b04996
- Wadajkar, A. S., Kadapure, T., Zhang, Y., Cui, W., Nguyen, K. T., and Yang, J. (2012). Dual-imaging enabled cancer-targeting nanoparticles. *Adv. Healthc. Mater.* 1, 450–456. doi: 10.1002/adhm.201100055
- Wang, J., and Jokerst, J. V. (2016). Stem cell imaging: tools to improve cell delivery and viability. *Stem Cell Int.* 2016:16. doi: 10.1155/2016/9240652
- Wang, X., Zachman, A. L., Chun, Y. W., Shen, F.-W., Hwang, Y.-S., and Sung, H.-J. (2014). Polymeric stent materials dysregulate macrophage and endothelial cell functions: implications for coronary artery stent. *Int. J. Cardiol.* 174, 688–695. doi: 10.1016/j.ijcard.2014.04.228
- Xie, Z., Kim, J. P., Cai, Q., Zhang, Y., Guo, J., Dhimi, R. S., et al. (2017). Synthesis and characterization of citrate-based fluorescent small molecules and biodegradable polymers. *Acta Biomater.* 50, 361–369. doi: 10.1016/j.actbio.2017.01.019
- Xie, Z., Zhang, Y., Liu, L., Weng, H., Mason, R. P., Tang, L., et al. (2014). Development of intrinsically photoluminescent and photostable polylactones. *Adv. Mater.* 26, 4491–4496. doi: 10.1002/adma.201306070
- Xu, H., Deshmukh, R., Timmons, R., and Nguyen, K. T. (2011). Enhanced endothelialization on surface modified poly(L-lactic acid) substrates. *Tissue Eng. A* 17, 865–876. doi: 10.1089/ten.tea.2010.0129
- Yang, J., Webb, A. R., and Ameer, G. A. (2004). Novel citric acid-based biodegradable elastomers for tissue engineering. *Adv. Mater.* 16, 511–516. doi: 10.1002/adma.200306264
- Yang, J., Zhang, Y., Gautam, S., Liu, L., Dey, J., Chen, W., et al. (2009). Development of aliphatic biodegradable photoluminescent polymers. *Proc. Natl. Acad. Sci. U.S.A.* 106, 10086–10091. doi: 10.1073/pnas.0900004106
- Zhang, Y., Tran, R. T., Qattan, I. S., Tsai, Y.-T., Tang, L., Liu, C., et al. (2013). Fluorescence imaging enabled urethane-doped citrate-based biodegradable elastomers. *Biomaterials* 34, 4048–4056. doi: 10.1016/j.biomaterials.2013.02.040
- Zhang, Y. S., and Yao, J. (2018). Imaging biomaterials-tissue interactions. *Trends Biotechnol.* 36, 403–414. doi: 10.1016/j.tibtech.2017.09.004
- Zilla, P., Fasol, R., Hammerle, A., Yildiz, S., Kadletz, M., Laufer, G., et al. (1987). Scanning electron microscopy of circulating platelets reveals new aspects of platelet alteration during cardiopulmonary bypass operations. *Tex. Heart Inst. J.* 14, 13–21.

Conflict of Interest: JY and The Pennsylvania State University have a financial interest in Aleo BME, Inc. and Acuitive Technologies, Inc. These interests have been reviewed by the University's Institutional and Individual Conflict of Interest Committees and are currently being managed by the University.

The remaining authors declare that the research was conducted in the absence of any commercial or financial relationships that could be construed as a potential conflict of interest.

Copyright © 2019 Kuriakose, Pandey, Shan, Banerjee, Yang and Nguyen. This is an open-access article distributed under the terms of the Creative Commons Attribution License (CC BY). The use, distribution or reproduction in other forums is permitted, provided the original author(s) and the copyright owner(s) are credited and that the original publication in this journal is cited, in accordance with accepted academic practice. No use, distribution or reproduction is permitted which does not comply with these terms.



The Synergistic Effect of Nanocrystals Combined With Ultrasound in the Generation of Reactive Oxygen Species for Biomedical Applications

Veronica Vighetto^{††}, Andrea Ancona^{††}, Luisa Racca¹, Tania Limongi¹, Adriano Troia², Giancarlo Canavese¹ and Valentina Cauda^{1*}

OPEN ACCESS

Edited by:

Michael Ming-Yuan Wei,
Texas Commission on Environmental
Quality, United States

Reviewed by:

Ming Xi Wan,
Xi'an Jiaotong University, China
Juncai Xu,
Case Western Reserve University,
United States

*Correspondence:

Valentina Cauda
valentina.cauda@polito.it

^{††}These authors have contributed
equally to this work

Specialty section:

This article was submitted to
Nanobiotechnology,
a section of the journal
Frontiers in Bioengineering and
Biotechnology

Received: 01 August 2019

Accepted: 14 November 2019

Published: 26 November 2019

Citation:

Vighetto V, Ancona A, Racca L,
Limongi T, Troia A, Canavese G and
Cauda V (2019) The Synergistic Effect
of Nanocrystals Combined With
Ultrasound in the Generation of
Reactive Oxygen Species for
Biomedical Applications.
Front. Bioeng. Biotechnol. 7:374.
doi: 10.3389/fbioe.2019.00374

¹ Department of Applied Science and Technology, Politecnico di Torino, Turin, Italy, ² Ultrasounds and Chemistry Lab, Advanced Metrology for Quality of Life, Istituto Nazionale di Ricerca Metrologica, Turin, Italy

Reactive oxygen species (ROS) effects on living cells and tissues is multifaceted and their level or dose can considerably affect cell proliferation and viability. It is therefore necessary understand their role also designing ways able to regulate their amount inside cells, i.e., using engineered nanomaterials with either antioxidant properties or, for cancer therapy applications, capable to induce oxidative stress and cell death, through tunable ROS production. In this paper, we report on the use of single-crystalline zinc oxide (ZnO) round-shaped nanoparticles, yet ZnO nanocrystals (NCs) functionalized with amino-propyl groups (ZnO-NH₂ NCs), combined with pulsed ultrasound (US). We show the synergistic effects produced by NC-assisted US which are able to produce different amount of ROS, as a result of inertial cavitation under the pulsed US exposure. Using Passive Cavitation Detection (PCD) and Electron Paramagnetic Resonance (EPR) spectroscopy, we systematically study which are the key parameters, monitoring, and influencing the amount of generated ROS measuring their concentration in water media and comparing all the results with pure water batches. We thus propose a ROS generation mechanism based on the selective application of US to the ZnO nanocrystals in water solutions. Ultrasound B-mode imaging is also applied, proving in respect to pure water, the enhanced ecographic signal generation of the aqueous solution containing ZnO-NH₂ NCs when exposed to pulsed ultrasound. Furthermore, to evaluate the applicability of ZnO-NH₂ NCs in the biomedical field, the ROS generation is studied by interposing different tissue mimicking materials, like phantoms and *ex vivo* tissues, between the US transducer and the sample well. As a whole, we clearly proof the enhanced capability to produce ROS and to control their amount when using ZnO-NH₂ NCs in combination with pulsed ultrasound anticipating their applicability in the fields of biology and health care.

Keywords: zinc oxide, nanocrystals, ultrasound, cavitation, reactive oxygen species, contrast agent

INTRODUCTION

Reactive Oxygen Species (ROS) are the result of partial reduction of molecular oxygen (O_2) (Dabrowski, 2017). The hydroxyl radical ($HO\cdot$) is one of the strongest radicals ever described (Dabrowski, 2017) and it possesses the highest reduction potential of all the ROS that are physiologically relevant: due to its nature it can react with a large variety of different type of biological molecule (Fu et al., 2014).

Nevertheless, oxygen is the fundamental element needed for the normal metabolic activity of every aerobic organism, and so ROS are inevitably produced inside living organisms, as cells. ROS are normally involved in different cell functions as signaling system, induction of mitogenic response, and mitochondria activity (Fu et al., 2014). Nonetheless, the survival of cells is related to the ability of maintaining the redox homeostasis (Dabrowski, 2017) during all this processes. An instability in this equilibrium results in a variety of possible different diseases. When chronic low levels of ROS occurs in a biological living system indeed, it has been demonstrated that gene mutation and malignant cell transformation can appear, or a large variety of vascular diseases can be promoted (Lau et al., 2008). In addition, Shafique et al. (2013) established that the increase in ROS levels can have a protective role in endothelial homeostasis, improving the vascular function in patients affected by cardio vascular disease (CDV). It is also been proven that the ROS generation achieved by the external activation of membrane-bound NADPH oxidase can induce angiogenesis and other essential functions of endothelial cells, such as hemostasis (Kim et al., 2017; Aldosari et al., 2018). The activation of angiogenesis caused by an increase in ROS production to restore ROS physiological levels, can be beneficial not only for CVD, as occurs after ischemia (Urao et al., 2008), but can also contribute to wound healing (Osumi et al., 2017). On the other hand, an excessive production of ROS leads to a disequilibrium redox state, where the antioxidant defenses of the cell has been overcome, being responsible for damaging cellular components, as lipids, proteins and DNA. Acute high levels of ROS cause the activation of different signal pathways, involving cytokines, transcription factors, and mediators, responsible for cell death, causing ROS-mediated apoptosis or necrosis (Dabrowski, 2017). These effects generated by cellular oxidative stress can be exploited for cancer therapeutic applications (Pelicano et al., 2004; Nogueira and Hay, 2013; Tong et al., 2015).

Therefore, it is clear that the ability to regulate the amount of ROS generated inside cells plays a fundamental role in the survival or death of cells. During last years thus different ways to produce ROS in a controlled manner were investigated. Nanomaterials (NM) are largely studied with the aim to apply them in biomedical field, and one of the principal mechanisms of nanotoxicity is the production of oxidative stress due to ROS generation. It has also been demonstrated that the level of generated ROS is dependent on the physical and chemical properties of the considered engineered nanomaterial, as size, surface to volume ratio, and surface reactivity (Gonzalez et al., 2008; Abdal Dayem et al., 2017). Carlson et al. (2008) measured the amount of ROS produced in cells when Ag nanoparticles

with different dimensions were present: 10-fold increase of ROS levels was measured in cells exposed to the smallest dimension nanoparticles. In the same work, it has been assessed that not all nanomaterials with equal dimensions can produce the same amount of ROS, supporting the idea that the ROS generation from NM depends also on their chemical nature.

Oxidative stress can also be achieved by an external activation of NMs to generate ROS, leading to tumor cell death under specific conditions. An example of this mechanism is photodynamic therapy (PDT) (Dabrowski, 2017). We have previously (Ancona et al., 2018) proposed the use of hybrid nanoparticles, able to produce intracellular ROS only when remotely activated by UV light irradiation. The photogeneration of electrons (e^-) and holes (h^+) have the ability to react with the environment forming superoxide radical anions ($O_2^{\cdot-}$) when e^- reduce oxygen molecules while hydroxyl radicals ($HO\cdot$) and hydrogen peroxide (H_2O_2) molecules are produced when h^+ oxidize water molecules. In the last two decades, the use of photosensitizer materials in PDT was largely applied to cancer therapy (Dougherty et al., 1998; Dolmans et al., 2003; Dos Santos et al., 2019), but there are some limitations, as the limited tissue penetration depth of UV light used to excite the photosensitizer, that confine the application of PDT to treat superficial tumors (Dabrowski, 2017).

Ultrasound (US) is another external stimulus investigated to activate the production of ROS and sonodynamic therapy (SDT) is recently emerged as an alternative to PDT due to the higher penetration depth of ultrasound with respect to UV light (McHale et al., 2016). Additionally, under ultrasound excitation, cavitation bubbles are generated and their violent oscillation and collapse let them act as nano-chemical reactors, leading to the formation of ROS in water media. The compounds that promote ROS formation, chemically reacting or introducing a larger amount of bubbles, are named sonosensitizers (Yasuda et al., 2015). Most of the sonosensitizers, such as porphyrins, are characterized by an easy aggregation in physiological environment due to their hydrophobic nature, decreasing the therapy effectiveness, by an intrinsic toxicity and by minor selectivity to cancer tissue (Canavese et al., 2018). The effectiveness of SDT is related to the ability of efficiently generating ROS, without major drawbacks related to the nature of the implied sonosensitizer material.

A similar and most conventional technique, using photosensitizers to produce ROS is the PDT. In this treatment UV light at a specific wavelength excites the photosensitizer molecules to obtain different species of ROS and subsequent cancer cell death. PDT has been employed with promising results for the treatment of bladder, esophagus, skin, and others cancers, and is at the stage of clinical evaluation (van Straten et al., 2017). A possibility, is to combine the use of ZnO with UV in a novel PDT approach: ZnO nanoparticles have been actually employed as carrier of a photosensitizer and other chemotherapeutics (Zhang et al., 2011; Firdous, 2018) or directly as photosensitizer, as we reported recently (Ancona et al., 2018), generating superoxide, hydrogen peroxide, and hydroxyl radicals and decreasing HeLa cells viability upon irradiation. However, the main limitation of PDT is the poor tissue penetration of

light, in particular the UV, that limits PDT for the treatment of superficial tumors, as melanomas. In order to overcome this drawback, a possible solution could be “tune” ZnO absorption near visible light (with increased tissue penetration rate), enveloping ZnO nanoparticles into other metals or doping them in various manners (Hu et al., 2013).

In this study, Zinc Oxide nanocrystals with a functionalized surface of aminopropyl groups (ZnO-NH₂ NCs) have been proved able to produce ROS in a controlled manner, when stimulated by US generated by an already approved medical device (LipoZero G39).

Nanosized ZnO is a metal oxide well-known for its safety in biomedical fields (Racca et al., 2018). In this work, we demonstrated that our customized ZnO-NH₂ NCs specific monocrystalline structure, size, shape, and functionalization, are able to generate a tunable quantity of ROS according to the intensity of administered US. More in details, the ultrasound is generated through the use of a safe medical device able to generate cavitation phenomena in human tissues. Several parameters like US output power, frequency, duty cycle, sonication time, as well as ZnO-NH₂ NCs concentration in water media, were systematically examined. To push our study forward up to a possible *in vivo* application, it has also been verified that a larger amount of controllably cavitation and ROS generation occur also when tissue mimicking materials have been employed.

All the presented results are thus preliminary data which can potentially bring to the safe and reproducible use of nanocrystals-assisted ultrasounds for *in vivo* application, going from either tissue engineering proliferative effects to anticancer therapies application, thanks to the high control achieved on the amount of generated ROS.

MATERIALS AND METHODS

ZnO-NH₂ NCs Synthesis and Functionalization

ZnO nanoparticles were synthesized through a microwave-assisted synthesis, as previously reported (Garino et al., 2019a). The reaction path is based on the hydrolysis of the zinc precursors (zinc acetate dihydrate) due to the presence of sodium hydroxide as the base in methanol. The as-synthesized ZnO were then functionalized with amino-propyl groups with a post-grafting approach using 3-(AminoPropyl)-TriEthoxySilane (APTES) at 10 mol% with respect to the molar amount of ZnO, as in Dumontel et al. (2017) and Garino et al. (2019a).

The obtained nanostructures are amine-functionalized zinc oxide nanocrystals (ZnO-NH₂ NCs) stable colloidal suspensions in ethanol.

ZnO-NH₂ NCs Characterization

The morphological characterization of ZnO-NH₂ NCs was performed by both Field Emission Scanning Electron Microscopy (FESEM, Carl Zeiss Merlin) and Transmission Electron Microscopy (TEM, FEI Tecnai operating at 200 kV) by spotting a diluted ethanolic solution of the samples (100 µg/ml) on a silicon wafer for FESEM or on copper grid with 300 carbon mesh for TEM, respectively. The particles size and Z-potential

value of ZnO-NH₂ NCs in water suspension was determined by the Dynamic Light Scattering (DLS) technique (Zetasizer Nano ZS90, Malvern).

The crystalline structure of ZnO-NH₂ NCs was analyzed by X-Ray Diffraction (XRD) with a Panalytical X'Pert diffractometer in Bragg Brentano configuration (Cu-Kα radiation, λ = 1.54 Å, 40 kV, and 30 mA).

Evaluation of ROS Production

Ultrasound excitation was carried out with LipoZero G39 (GLOBUS) and the evaluation of ROS production was provided by Electron Paramagnetic Resonance (EPR) Spectroscopy (EMXNano X-Band spectrometer from Bruker) assisted by a spin-trapping technique. The formation of hydroxyl and superoxide anion radicals was actually detected in double distilled water using as a spin trap the 5,5-dimethyl-L-pyrroline-N-oxide (DMPO, Sigma) and each tested sample contained DMPO 10 mM. This compound is suitable for the study of ROS generation due to its capability to trap both hydroxy and superoxide anion radicals. After the ultrasound irradiation, the sample was promptly transferred into a quartz microcapillary tube and inserted in the EPR cavity. The spectra were recorded with the following measurement conditions: center field 3428 G, sweep time 160.0 s, sample g-factor 2.00000, number of scans 15. After acquisition, the spectrum was processed using the Bruker Xenon software (Bruker) for baseline correction. Analysis of recorded spectra was executed using the Bruker SpinFit software.

To perform sonication, 1 ml of sample was placed in a 24 well plate (Thermo Scientific) which was positioned in contact with LipoZero transducer through a thin layer of coupling gel (Stosswellen Gel Bestelle, ELvation Medical GmbH). Formation of hydroxyl and superoxide anion radicals was evaluated under a large range of different conditions. Samples were tested for three different sonication times (2, 5, and 10 min), five Duty Cycle conditions (10, 20, 30, 40, and 50%), three distinct working frequencies (150 KHz, 526 KHz, 1 MHz) and different output powers of the LipoZero device (0.3, 0.6, 0.9, 1.2, and 1.5 W/cm² corresponding to 10, 20, 30, 40, and 50% of the maximum output power). In addition to these conditions, different concentrations of amino-functionalized ZnO-NH₂ NCs were also tested (50, 100, and 200 µg/ml) for oxygen radicals production. Temperature inside the sample well was monitored by a temperature Multilogger Thermometer 502A1 (TERSID S.r.l.).

Needle Cavitometer Measurements

The acoustic pressure reached inside the well with LipoZero G39 at different output powers (0.6, 0.9, 1.2, and 1.5 W/cm²) and the acoustic cavitation activity in presence or absence of nanocrystals was monitored by recording the broad band acoustic emissions generated by collapsing bubbles by using a needle hydrophone Dapco NP 10-3 coupled to a spectrum analyzer (Agilent N9320B) and integrating the FFT area for a frequency range of 0.8–5.0 MHz. Analyses were performed at least on three spectra for each experiment.

B-Mode Ecographic Imaging

Ultrasound imaging was performed with a research ultrasonic scanner (Ultrasonix Sonic Touch) equipped with linear probe (L14-5/38) operating at 10 MHz in high resolution mode. It was coupled with the sample holder using ultrasound coupling gel and positioned along the axis of a single plastic well-filled with 1 ml of solution. The imaging transducer was focalized to the excitation transducer focus. Real-time videos of the system response to ultrasound irradiation were recorded and videos were analyzed using MATLAB script which calculated the relative average intensity of the bright spots in the region of interest (ROI) of each frame of the videos. Three videos were recorded for each sample.

Tissue-Mimicking and Ultrasound Irradiation

In order to evaluate the attenuation of ultrasound effects in the presence of tissue mimicking media, different materials, as phantom and *ex vivo* chicken-breast tissue, were interposed between the transducer and the sample.

To conduct these tests, the ultrasound source was immersed in a plexiglass tank filled up with demineralized water and a single well, previously cut and polished from a 24 well plate (Thermo Scientific), was placed at a distance of 1 cm from the transducer surface and exposed to ultrasound, as shown in **Figure 1**.

Therefore, the measurements were performed using a tissue-mimicking homogeneous phantom (based on 3% in weight of agarose and 0.4 M zinc acetate, $\text{Zn}(\text{CH}_3\text{COOH})_2$, with an ultrasound attenuation of 0.5 dB/cm-MHz, which matches the attenuation of muscle tissue as reported in Troia et al. (2017) with a diameter of 40 mm and an *ex vivo* tissue (chicken breast); both materials were characterized by a thickness of 1 cm. As a reference, the effects of ultrasound irradiation on the sample were also evaluated considering only the water bath, where the system is immersed, as medium between the piezoelectric transducer and the sample well.

Ultrasound excitation was provided by LipoZero and measurements were conducted with a frequency of 1 MHz, 50% of Duty Cycle, and a power of 3 W/cm² for 20 min. During each experiment the acoustic signal generated inside the well was recorded using a focused piezo-detector (Precision Acoustic) as a cavitometer, coupled to the Booster Amplifier (Precision Acoustic) and connected to a digital oscilloscope (TDS 2012B, Tektronix). To store the data, LabVIEW software was used and 100 μs were recorded every 2 s if the signal measured by the oscilloscope was higher than 0.001 V. Data were successively analyzed with MATLAB software. The time-domain signal was transformed in the frequency-domain by Fourier Transform and the cavitation dose was quantified with MATLAB by calculating the area subtended by the curve. The area measurements considered only values from a frequency of 2.5–12 MHz, in order to eliminate the initial 1 MHz driving signal.

At the end of sonication, EPR spectroscopy assisted by a spin-trapping technique was performed as previously described. In this set of tests, EPR measurement conditions were as follows:

center field 3428 G, sweep time 60.0 s, sample g-factor 2.00000, number of scans 15.

To evaluate the increase of ROS production in presence of ZnO-NH₂, two conditions were tested for each tissue-mimicking material and, as a reference, for water: milliQ water with 20 mM content of DMPO and milliQ water with 20 mM content of DMPO and a concentration of NCs equal to 200 $\mu\text{g}/\text{ml}$.

SigmaPlot 14.0 software was used for all statistical analyses. Data are expressed as the mean \pm standard error mean (S.E.M.). Asterisks denoting *P*-values (**p* < 0.05 and ***p* < 0.001) and sample sizes are indicated in each figure legend.

DISCUSSION

As evidenced by FESEM and TEM analysis (**Figures 2A,B**), the ZnO-NH₂ nanomaterials can be ascribed to single nanocrystalline structures, with an average diameter of 20 ± 5 nm, see also Garino et al. (2019a) for comparison. Amine-functionalized ZnO nanocrystals have an average hydrodynamic diameter of 122 nm in their original ethanolic suspension and also in water (**Figure 2C**) and a Z-Potential value of +22 mV in double distilled water. The XRD pattern in **Figure 2D** shows the typical hexagonal wurtzitic crystalline structure of zinc oxide materials, confirming also what previously reported so far (Garino et al., 2019a,b).

The EPR spectroscopy was used to evaluate the enhancement of ROS production when ZnO-NH₂ NCs are present in water (with a concentration of 200 $\mu\text{g}/\text{ml}$) and according to different US power. The results are shown in **Figure 3**. Samples were irradiated with US for 10 min, at a frequency of 1 MHz and the ultrasound stimulation was pulsed, with a Duty Cycle of 10%, Pulse Repetition Frequency 1 Hz. The concentration of DMPO-OH was then evaluated since it is directly correlated to the ROS production, in particular to the hydroxyl and superoxide anions production.

The measured acoustic pressures reached inside the well at the various output powers (0.6, 0.9, 1.2, and 1.5 W/cm²) were between 1 and 1.5 MPa, justifying the occurrence of the inertial cavitation inside the sample well, justifying the occurrence of the inertial cavitation inside the sample well. Actually, when a lower output power was used, i.e., 0.3 W/cm² (corresponding to 10% of the maximum output US power), also the threshold for ROS generation was not reached, meaning that inertial cavitation did not occur in the sample during the US irradiation. Otherwise, with 0.6 W/cm² (corresponding to the 20% of the maximum output power), a small amount of hydroxyl and superoxide anions were detected, and even if the amount of DMPO-OH was greater in presence of ZnO-NH₂ NCs (red bar) with respect to pure water (black bar), it can be noted that the 20% of power was not enough to obtain a statistical difference between samples. A different scenario is depicted when 0.9 and 1.2 W/cm² were utilized. In both cases a significant difference (both with *p* < 0.001) between the amount of ROS produced in pure water and the one obtained in the presence of ZnO-NH₂ NCs is clearly observed. The results achieved with these conditions indicate the efficacy of our ZnO-NH₂ NCs to act as an ultrasound responding

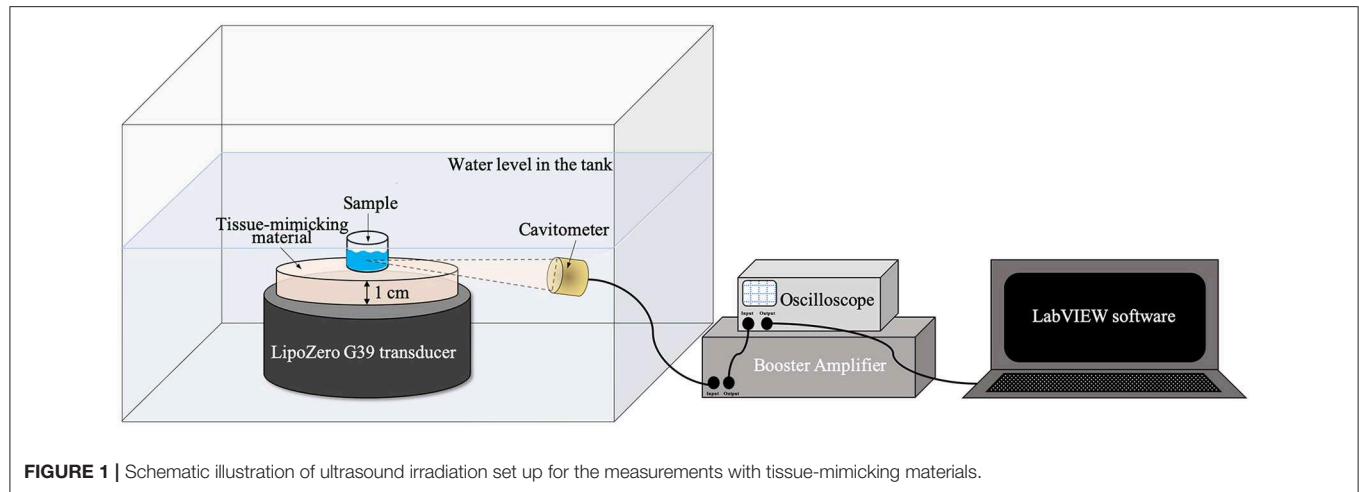


FIGURE 1 | Schematic illustration of ultrasound irradiation set up for the measurements with tissue-mimicking materials.

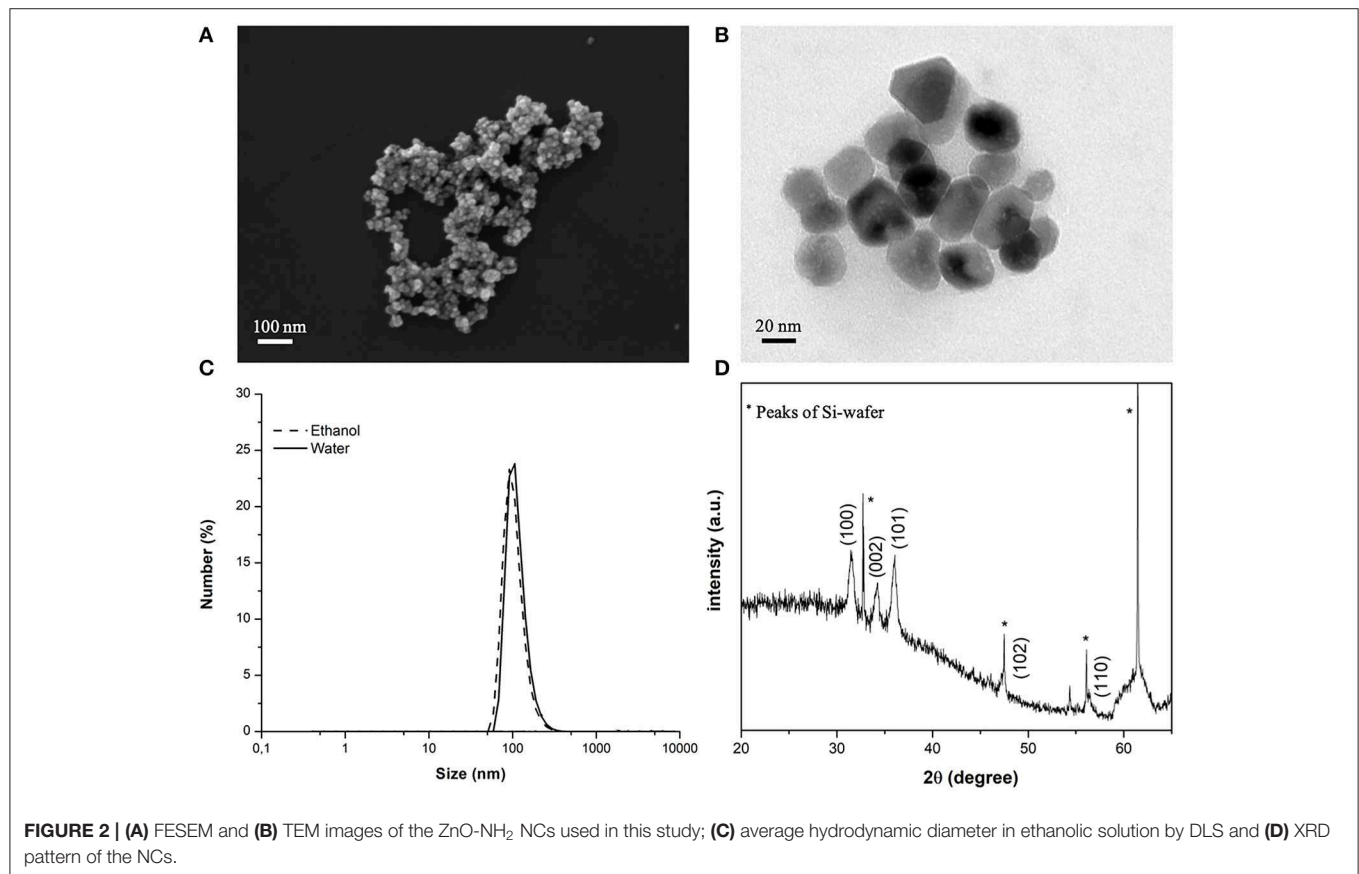


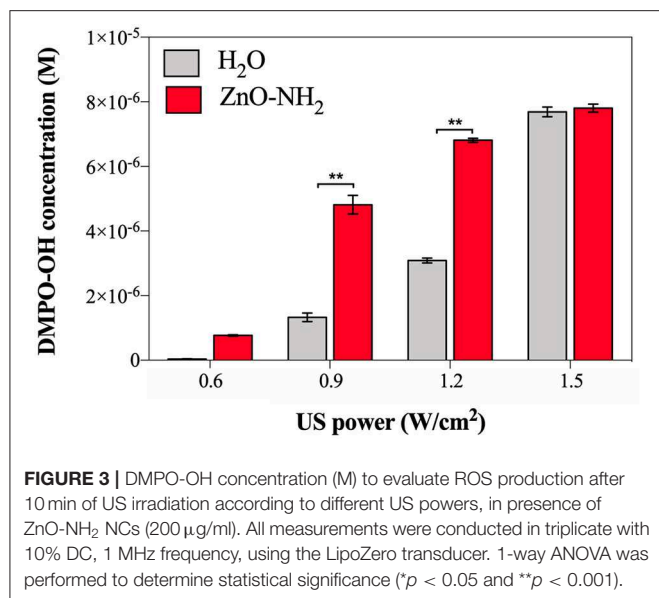
FIGURE 2 | (A) FESEM and (B) TEM images of the ZnO-NH₂ NCs used in this study; (C) average hydrodynamic diameter in ethanolic solution by DLS and (D) XRD pattern of the NCs.

nano-agent. It is interesting to observe that the power doses of 0.9 and 1.2 W/cm², corresponding to the 30 and 40% of the maximum power output of the Lipozero Transducer, were too low to generate high amount of ROS when the sonicated sample in the well was the pure water. Strikingly, both these low intensities ultrasound conditions are enough to elicit an activation of the ZnO-NH₂ NCs, widely increasing the amount of ROS produced.

The last US power tested for the sonication was 1.5 W/cm² (corresponding to the 50% of the maximum output power): the

delivered intensity of US was sufficiently high to activate the inertial cavitation in the water alone, leading to a large amount of ROS produced, comparable with the one obtained in presence of ZnO-NH₂ NCs.

From the results in **Figure 3**, it is assessed that 0.9 W/cm² (30% of US power) is the optimal condition to have ZnO-NH₂ NCs working as ultrasound responsive nano-agent: the significant difference ($p < 0.001$) in ROS production suggests that, at that power, the US irradiation was not enough intense to cause a large production of hydroxyl and superoxide anions in the



water, but it was sufficiently high to initiate the acoustic cavitation in the sample containing ZnO-NH₂ NCs due to the presence of nanobubbles the NCs surface, which act as nuclei for inertial cavitation and consequently leads to a larger ROS production.

To support these results, other parameters such as ZnO-NH₂ NCs concentration in water, time of US treatment, frequency of the US were tested to ensure the efficacy of the ZnO-NH₂ NCs, as reported in **Figure 4**.

To assess the optimal concentration of ZnO-NH₂ NCs, 50, 100, and 200 μg/ml of NCs were examined (**Figure 4A**), suggesting that the highest concentration tested, as used in all the other experiments, is the optimal one. Three different treatment times were thus evaluated, 2, 5, and 10 min, keeping fixed all the other parameters (0.9 W/cm² of power, 10% of DC, and 1 MHz of excitation frequency and 200 μg/ml of ZnO-NH₂ NCs in water). The insonation time of 10 min was confirmed to be the best treatment time condition to enhance the ultrasound responsive nano-agent capabilities of ZnO-NH₂ NCs with respect to pure water. In **Figure 4C**, three excitation frequency were also screened: 150 KHz, 526 KHz, and 1 MHz at different US output powers, with 10% DC and 200 μg/ml as NCs concentration. With the lowest frequency, a large amount of power (50% with respect to the maximum output) was needed to obtain a detectable signal with EPR instrument and DMPO spin adducts. The frequency of 1 MHz, which is the most used frequency for biomedical applications, is here confirmed to enhance the production of ROS in the presence of the ZnO-NH₂ NC under ultrasound excitation.

An hypothesis for the explanation of ROS generation capabilities of ZnO-NH₂ NCs is related to the NC surface: the high surface-to-volume ratio of ZnO-NH₂ NCs, showing a large surface area of 60 m²/g [as measured by Nitrogen Sorption isotherm elsewhere (Lops et al., 2019)] and the surface functionalization of amino-propyl groups are both capable to immobilize and promote the inertial cavitation of tiny gas

nanobubbles under such US power conditions. As inertial cavitation is produced, ROS are generated: the EPR technique detected OH· radicals, which are one of the most reactive and potentially dangerous species of ROS.

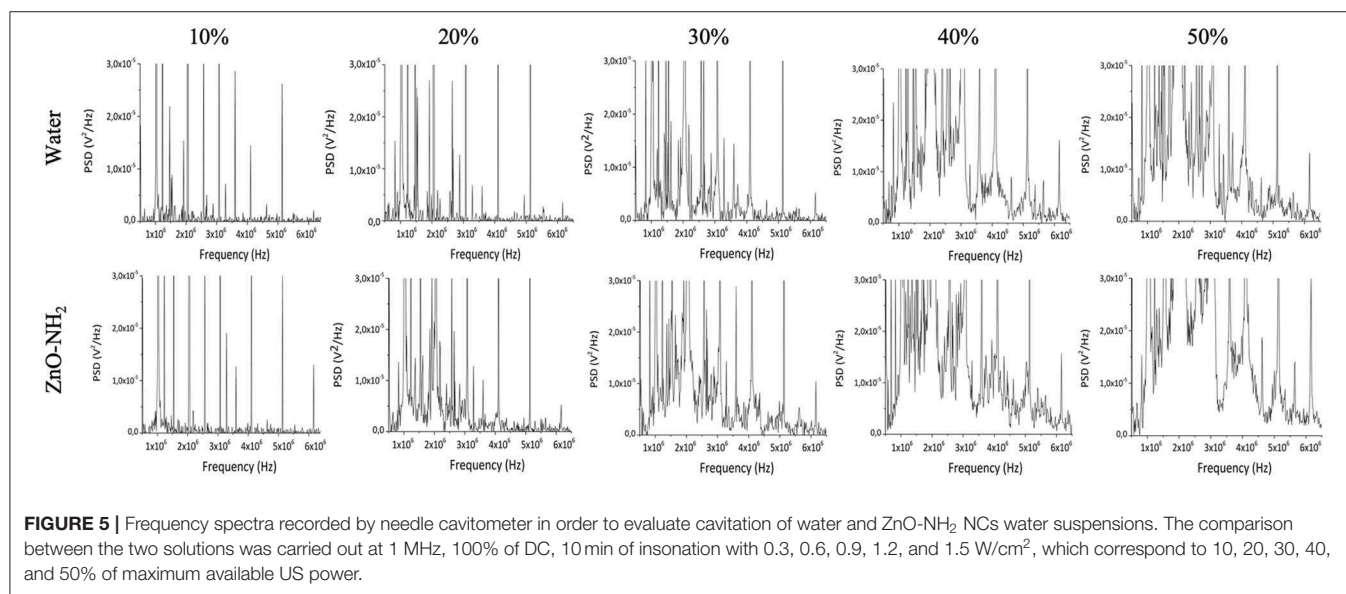
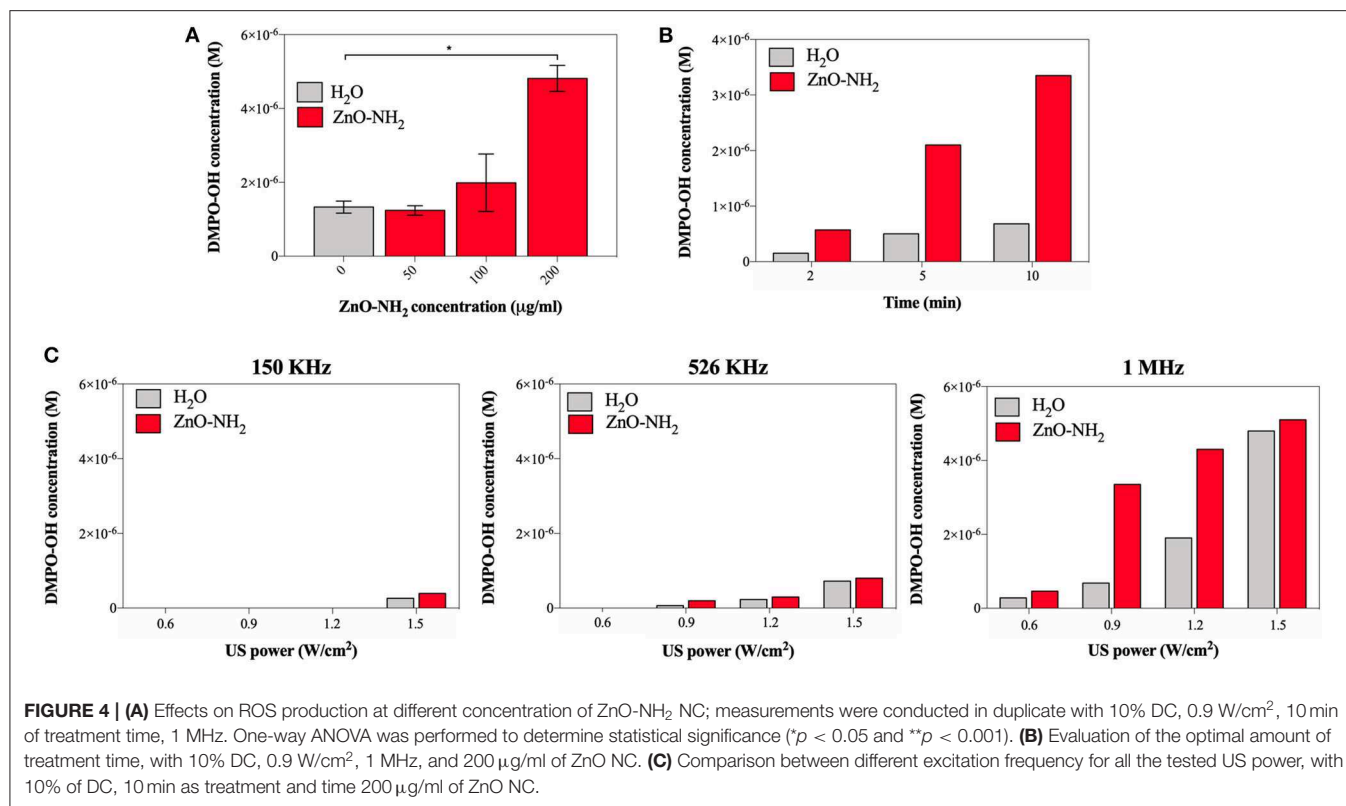
To evaluate the role of acoustic cavitation on the generation of ROS by the ultrasound exposure of ZnO-NH₂ NCs passive cavitation detection (PCD) technique was used. **Figure 5** shows the frequency spectra of the acoustic signals obtained at different ultrasound intensities with and without ZnO-NH₂ NCs in solution. At low ultrasound intensities, only harmonics and sub-harmonics signals are present: since these signals are recorded for both water and NCs samples, they are probably due to oscillation of large gas bubbles trapped in the plastic wells of the sample holder. At increasing ultrasound intensities (above 1.2 W/cm²), acoustic broadband noise typical of inertial cavitation was recorded for the water solution. When ZnO-NH₂ NCs were added to the solution, broadband noise signal was recorded at lower ultrasound intensities, suggesting that our NCs acted as nucleation site inducing inertial cavitation, thus decreasing the cavitation threshold. Since it has been shown both theoretically and experimentally that collapsing cavitating bubbles can generate sufficiently high temperatures and pressures able to induce generation of ROS in aqueous solution (The Acoustic Bubble, Leighton), PCD and EPR experiments together suggest that ZnO-NH₂ NCs generate ROS by inducing inertial cavitation upon ultrasound exposure.

In order to further study the generation of inertial cavitation by ZnO-NH₂ NCs, ultrasound B-mode imaging was used. **Figure 6A** shows the ecographic images obtained for water and ZnO-NH₂ NCs containing solutions exposed to 40% intensity ultrasound. Cavitating bubble generated by ZnO-NH₂ NCs led to bright spots in the solution, while in the absence of NCs the ecographic signal did not increase. **Figure 6B** shows the quantification of ecographic contrast obtained during the pulsed ultrasound exposure (170 s), as previously described in the Material and Methods section. ZnO-NH₂ NCs generated higher ecographic contrast over all the sonication period compared with the water containing solution. Together these results further confirm the ability of ZnO-NH₂ NCs in inducing inertial cavitation under pulsed ultrasound exposure.

ROS exert a multitude of biological effects (Lau et al., 2008; Racca et al., 2018), which also comprehend the creation of molecular damages inside cells, leading to antitumoral application (de Sá Junior et al., 2017).

In order to evaluate the future applicability of ZnO-NH₂ NCs in the biomedical field, in particular to subcutaneous *in vivo* applications, the generation of ROS, and the effects of our NCs as ultrasound responsive nano-agent was tested in Phosphate Buffered Saline (PBS) solution, cell culture medium [Minimum Essential Medium Eagle (SIGMA) completed with 10% of Fetal Bovine Serum (FBS, SIGMA) and 1% of Penicillin-Streptomycin] and finally when different tissue mimicking materials were interposed during the insonation between the LipoZero US transducer and the sample well.

The ROS evaluation in PBS and cell culture media are reported in the **Supporting Information** and confirm the ability of our ZnO-NH₂ nanocrystals to enhance inertial cavitation



and consequently ROS production also in biological media, thus leading to applications *in vitro*.

The evaluation of the cavitation and ROS generation related to the interposition of tissue-mimicking materials between the ultrasound source and the samples are shown in **Figure 7**. Different materials were tested, and for all of them the amount of cavitation of water and water with the synergistic effect of ZnO-NH₂ NCs (200 μg/ml) were evaluated. All the measurements

were performed for 20 min, with a frequency of 1 MHz, 50% of Duty Cycle, and 100% of US power available from LipoZero transducer.

Figure 7A exhibits the results of cavimeter measurements during 20 min of insonation, which are the average area under the Fourier Transform (FT) of each measured signal over time. These data correlate with the amount of occurred cavitation, and the S.E.M. is reported. It can be appreciated that, when

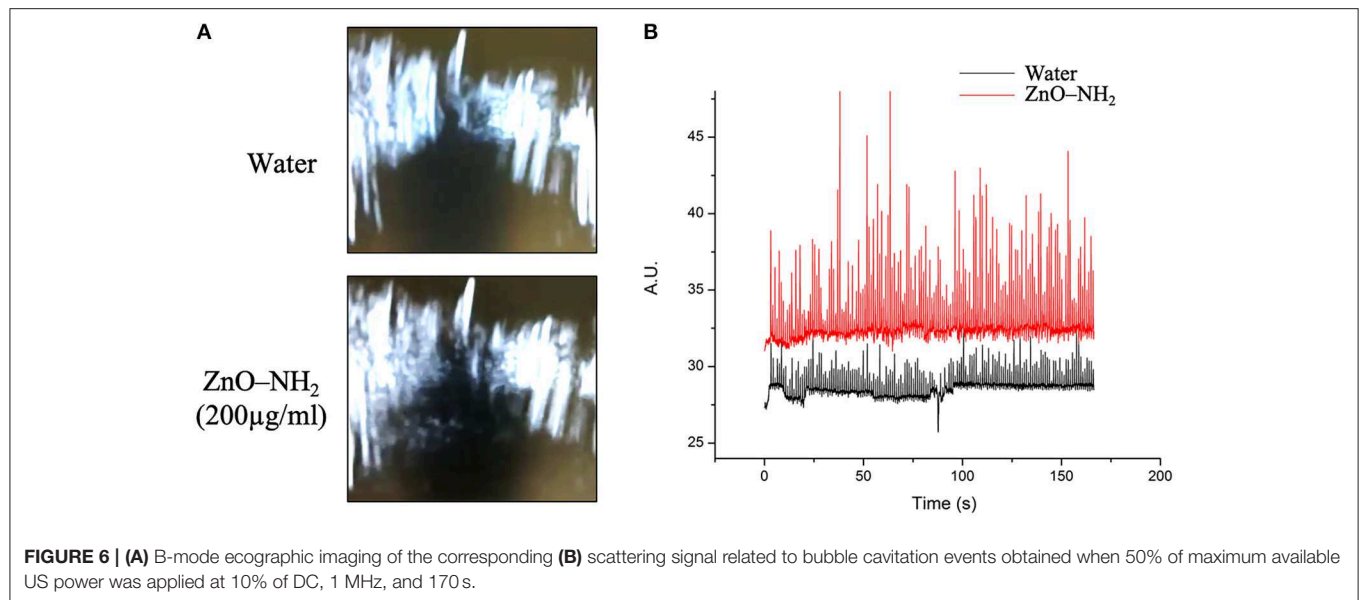


FIGURE 6 | (A) B-mode echographic imaging of the corresponding **(B)** scattering signal related to bubble cavitation events obtained when 50% of maximum available US power was applied at 10% of DC, 1 MHz, and 170 s.

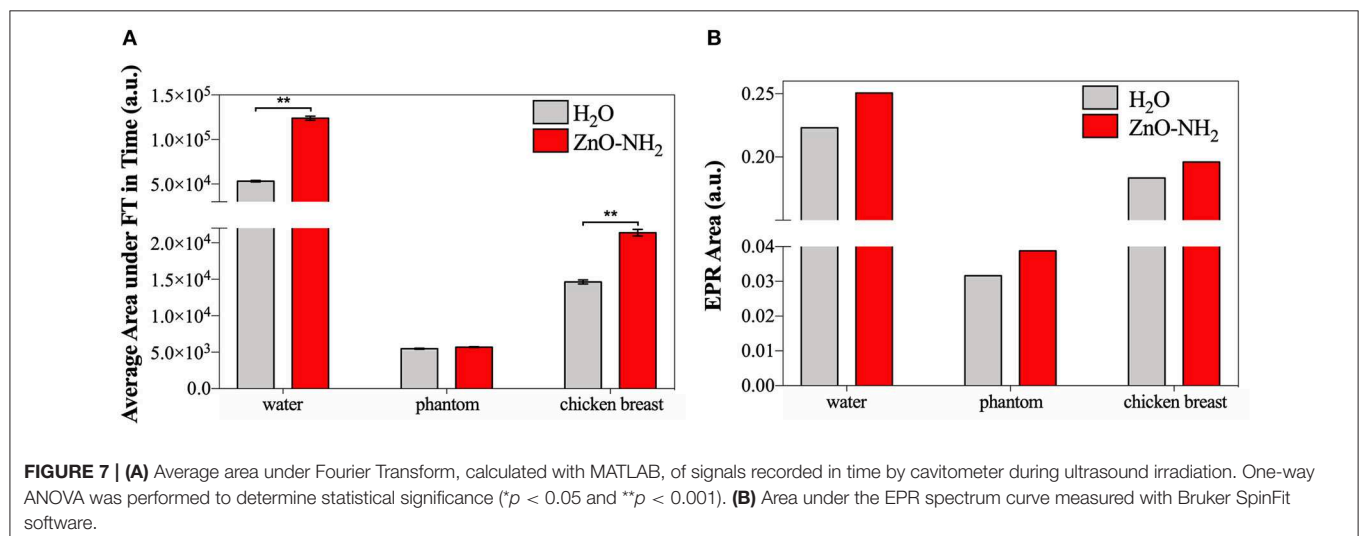


FIGURE 7 | (A) Average area under Fourier Transform, calculated with MATLAB, of signals recorded in time by cavitometer during ultrasound irradiation. One-way ANOVA was performed to determine statistical significance (* $p < 0.05$ and ** $p < 0.001$). **(B)** Area under the EPR spectrum curve measured with Bruker SpinFit software.

the ultrasound propagation medium was water, the amount of cavitation detected by the cavitometer was higher than the one measured when tissue mimicking materials were interposed. This effect can be explained considering the attenuation of power perceived inside the sample well. When the phantom and the *ex vivo* tissue are used, the real amount of US energy inside the well is lower, and the measured broadband noise, which correlates to cavitation, reflects this reduction. Nevertheless, a significant increase of cavitation is noticeable when ZnO-NH₂ NCs are present, not only when water is the transmission medium, but also when *ex vivo* tissue is interposed as the propagation medium. Even if there is not a significant difference in the presence of phantom, an increase of 4% in the generated cavitation can still be noticed when ZnO-NH₂ NCs are used.

At the end of 20 min of insonation, the amount of hydroxyl and superoxide anion radicals produced were evaluated for

all the different conditions using a spin-trapping technique involving DMPO.

Figure 7B shows areas under the EPR spectrum curve, corresponding to the integrated intensity of the radical species and reflecting the concentration of DMPO-OH, index of ROS generation. As similarly reported in Figure 7A, the results in Figure 7B demonstrate that a larger amount ROS were produced when the irradiation medium is distilled water, with respect to phantom and *ex vivo* tissue. The results obtained lead to the conclusion that we successfully generated ROS in a controlled manner even in presence of two different tissue-mimicking materials. The data open the possibility to apply this technology *in vivo* for subcutaneous ROS generation using an already approved medical device.

Despite the general difference between the attenuating media, in all the cases a largest amount of ROS was detected in presence

of ZnO-NH₂ NCs, suggesting that our nanocrystals enhance the production of free radicals under ultrasound stimulation. This phenomenon is proved here also when tissue mimicking materials were interposed between the stimulation source and the sample, suggesting the possibility of *in vivo* applications.

CONCLUSION

We report in this paper the ability of ZnO-NH₂ nanocrystals in inducing inertial cavitation under pulsed ultrasound exposure. In details, it is assessed that 0.9 W/cm² (30% of US power) is the optimal condition to have ZnO-NH₂ NCs working as ultrasound responsive nano-agent and showing the significant large production of ROS, specifically of hydroxyl and superoxide anions in the water. We proposed, as mechanism of ROS generation, that this US conditions are sufficient to initiate the acoustic cavitation of tiny gas nanobubbles trapped at the ZnO-NH₂ NCs surface. This inertial cavitation consequently leads to a large ROS production. Strikingly in the same insonating condition, lower cavitation and consequently largely lower amount of ROS are generated from the pure water control sample.

Ultrasound B-mode imaging was also used to confirm the generation of inertial cavitation by ZnO-NH₂ NCs. An enhanced ecographic signal generation was detected when ZnO-NH₂ NCs solutions were exposed to 40% intensity ultrasound with respect to pure water.

To evaluate the future applicability of ZnO-NH₂ NCs in the biomedical field, the generation of ROS and the effects of NCs as ultrasound responsive nano-agent agent were tested when different tissue mimicking materials were interposed during the insonation between the US transducer and the sample well. A significant increase of cavitation is noticeable when ZnO-NH₂ NCs are present, with respect to pure water, when phantoms and, in a larger amount, *ex vivo* tissue are interposed as the propagation medium. These measurements, together with the increased and controlled ROS production also in biological media as PBS and cell culture media (EMEM), suggest the future applicability of this technology to the *in vivo* setting.

All together these results proof the enhanced effects and controllability of ROS generation by ZnO-NH₂ NPs assisted

pulsed ultrasound, anticipating high potential in a wide range of biomedical/healthcare applications.

DATA AVAILABILITY STATEMENT

All datasets generated for this study are included in the article/**Supplementary Material**.

AUTHOR CONTRIBUTIONS

VV, AA, and LR performed most of the experiments described in the manuscript. TL designed the solution and tissue-mimicking measurements and assisted them. AT performed and evaluated critically the needle hydrophone and B-mode imaging characterization. GC designed the whole manuscript concept. VC supervised the whole work and was the recipient of the funding. All the authors contributed to the manuscript writing and corrections.

FUNDING

This work had received funding from the European Research Council (ERC) under the European Union's Horizon 2020 research and innovation programme (Grant Agreement No. 678151—Project Acronym TROJANANOHORSE—ERC starting Grant), and also from the Politecnico di Torino and the Moschini Spa Company through a seed funding of Proof-of-Concept Grant No. 16417.

ACKNOWLEDGMENTS

The authors wish to thank Eng. MD Carmine Lops and Eng. MD Federico Zagallo for setting up the preliminary measurements, Eng. MD Bianca Dumontel and Dr. Nadia Garino for the nanocrystals synthesis and preliminary characterizations, and Dr. Mauro Raimondo for FESEM and TEM imaging.

SUPPLEMENTARY MATERIAL

The Supplementary Material for this article can be found online at: <https://www.frontiersin.org/articles/10.3389/fbioe.2019.00374/full#supplementary-material>

REFERENCES

- Abdal Dayem, A., Hossain, M., Lee, S., Kim, K., Saha, S., Yang, G.-M., et al. (2017). The role of reactive oxygen species (ROS) in the biological activities of metallic nanoparticles. *Int. J. Mol. Sci.* 18:120. doi: 10.3390/ijms18010120
- Aldosari, S., Awad, M., Harrington, E. O., Sellke, F. W., and Abid, M. R. (2018). Subcellular reactive oxygen species (ROS) in cardiovascular pathophysiology. *Antioxidants* 7:E14. doi: 10.3390/antiox7010014
- Ancona, A., Dumontel, B., Garino, N., Demarco, B., Chatzitheodoridou, D., Fazzini, W., et al. (2018). Lipid-coated zinc oxide nanoparticles as innovative ROS-generators for photodynamic therapy in cancer cells. *Nanomaterials* 8:143. doi: 10.3390/nano8030143
- Canavese, G., Ancona, A., Racca, L., Canta, M., Dumontel, B., Barbaresco, F., et al. (2018). Nanoparticle-assisted ultrasound: a special focus on sonodynamic therapy against cancer. *Chem. Eng. J.* 340, 155–172. doi: 10.1016/j.cej.2018.01.060
- Carlson, C., Hussain, S. M., Schrand, A. M., Braydich-Stolle, L. K., Hess, K. L., Jones, R. L., et al. (2008). Unique cellular interaction of silver nanoparticles: size-dependent generation of reactive oxygen species. *J. Phys. Chem. B* 112, 13608–13619. doi: 10.1021/jp712087m
- Dabrowski, J. M. (2017). Reactive oxygen species in photodynamic therapy: mechanisms of their generation and potentiation. *Adv. Inorg. Chem.* 70, 343–394. doi: 10.1016/bs.adioch.2017.03.002
- de Sá Junior, P. L., Câmara, D. A. D., Porcacchia, A. S., Fonseca, P. M. M., Jorge, S. D., Araldi, R. P., et al. (2017). The roles of ROS in cancer heterogeneity and therapy. *Oxid. Med. Cell. Longev.* 2017:2467940. doi: 10.1155/2017/2467940
- Dolmans, D., Fukumura, D., and Jain, R. (2003). Photodynamic therapy for cancer. *Nat. Rev. Cancer* 3:8. doi: 10.1038/nrc1071

- Dos Santos, A. F., De Almeida, D. R. Q., Terra, L. F., Baptista, M. S., and Labriola, L. (2019). Photodynamic therapy in cancer treatment - An update review. *J. Cancer Metastasis Treat.* 5:25. doi: 10.20517/2394-4722.2018.83
- Dougherty, T. J., Gomer, C. J., Henderson, B. W., Jori, G., Kessel, D., Korbek, M., et al. (1998). Photodynamic therapy. *J. Natl. Cancer Inst.* 90:17. doi: 10.1093/jnci/90.12.889
- Dumontel, B., Canta, M., Engelke, H., Chiodoni, A., Racca, L., Ancona, A., et al. (2017). Enhanced biostability and cellular uptake of zinc oxide nanocrystals shielded with a phospholipid bilayer. *J. Mater. Chem. B* 5, 8799–8813. doi: 10.1039/C7TB02229H
- Firdous, S. (2018). Development and imaging of zinc oxide nanorods as a photosensitizer for the diagnosis and treatment of cancer using lasers. *Laser Phys. Lett.* 15:095604. doi: 10.1088/1612-202X/aad28c
- Fu, P. P., Xia, Q., Hwang, H.-M., Ray, P. C., and Yu, H. (2014). Mechanisms of nanotoxicity: generation of reactive oxygen species. *J. Food Drug Anal.* 22, 64–75. doi: 10.1016/j.jfda.2014.01.005
- Garino, N., Limongi, T., Dumontel, B., Canta, M., Racca, L., Laurenti, M., et al. (2019a). A microwave-assisted synthesis of zinc oxide nanocrystals finely tuned for biological applications. *Nanomaterials* 9:212. doi: 10.3390/nano9020212
- Garino, N., Sanvitale, P., Dumontel, B., Laurenti, M., Colilla, M., Izquierdo-Barba, I., et al. (2019b). Zinc oxide nanocrystals as a nanoantibiotic and osteoinductive agent. *RSC Adv.* 9, 11312–11321. doi: 10.1039/C8RA10236H
- Gonzalez, L., Lison, D., and Kirsch-Volders, M. (2008). Genotoxicity of engineered nanomaterials: a critical review. *Nanotoxicology* 2, 252–273. doi: 10.1080/17435390802464986
- Hu, Z., Li, J., Li, C., Zhao, S., Li, N., Wang, Y., et al. (2013). Folic acid-conjugated graphene-zno nanohybrid for targeting photodynamic therapy under visible light irradiation. *J. Mater. Chem. B* 1:5003. doi: 10.1039/c3tb20849d
- Kim, Y.-M., Kim, S.-J., Tatsunami, R., Yamamura, H., Fukai, T., and Ushio-Fukai, M. (2017). ROS-induced ROS release orchestrated by Nox4, Nox2, and mitochondria in VEGF signaling and angiogenesis. *Am. J. Physiol. Cell Physiol.* 312, C749–C764. doi: 10.1152/ajpcell.00346.2016
- Lau, A. T. Y., Wang, Y., and Chiu, J.-F. (2008). Reactive oxygen species: current knowledge and applications in cancer research and therapeutic. *J. Cell. Biochem.* 104, 657–667. doi: 10.1002/jcb.21655
- Lops, C., Ancona, A., Di Cesare, K., Dumontel, B., Garino, N., Canavese, G., et al. (2019). Sonophotocatalytic degradation mechanisms of rhodamine B dye via radicals generation by micro- and nano-particles of ZnO. *Appl. Catal. B Environ.* 243, 629–640. doi: 10.1016/j.apcatb.2018.10.078
- McHale, A. P., Callan, J. F., Nomikou, N., Fowley, C., and Callan, B. (2016). “Sonodynamic therapy: concept, mechanism and application to cancer treatment,” in *Therapeutic Ultrasound*, Vol. 880, eds J.-M. Escoffier and A. Bouakaz (Cham: Springer International Publishing), 429–450. doi: 10.1007/978-3-319-22536-4_22
- Nogueira, V., and Hay, N. (2013). Molecular pathways: reactive oxygen species homeostasis in cancer cells and implications for cancer therapy. *Clin. Cancer Res.* 19, 4309–4314. doi: 10.1158/1078-0432.CCR-12-1424
- Osumi, K., Matsuda, S., Fujimura, N., Matsubara, K., Kitago, M., Itano, O., et al. (2017). Acceleration of wound healing by ultrasound activation of TiO₂ in *Escherichia coli* -infected wounds in mice: wound healing with sonicated TiO₂. *J. Biomed. Mater. Res. B Appl. Biomater.* 105, 2344–2351. doi: 10.1002/jbm.b.33774
- Pelicano, H., Carney, D., and Huang, P. (2004). ROS stress in cancer cells and therapeutic implications. *Drug Resist. Updat.* 7, 97–110. doi: 10.1016/j.drug.2004.01.004
- Racca, L., Canta, M., Dumontel, B., Ancona, A., Limongi, T., Garino, N., et al. (2018). “Zinc oxide nanostructures in biomedicine,” in *Smart Nanoparticles for Biomedicine*, ed G. Ciofani (Amsterdam: Elsevier Inc.), 171–187. doi: 10.1016/B978-0-12-814156-4.00012-4
- Shafique, E., Choy, W. C., Liu, Y., Feng, J., Cordeiro, B., Lyra, A., et al. (2013). Oxidative stress improves coronary endothelial function through activation of the pro-survival kinase AMPK. *Aging* 5, 515–530. doi: 10.18632/aging.100569
- Tong, L., Chuang, C.-C., Wu, S., and Zuo, L. (2015). Reactive oxygen species in redox cancer therapy. *Cancer Lett.* 367, 18–25. doi: 10.1016/j.canlet.2015.07.008
- Troia, A., Cuccaro, R., and Schiavi, A. (2017). Independent tuning of acoustic and mechanical properties of phantoms for biomedical applications of ultrasound. *Biomed. Phys. Eng. Express.* 3:025011. doi: 10.1088/2057-1976/aa5ed0
- Urao, N., Inomata, H., Razvi, M., Kim, H. W., Wary, K., McKinney, R., et al. (2008). Role of Nox2-based NADPH oxidase in bone marrow and progenitor cell function involved in neovascularization induced by hindlimb ischemia. *Circ. Res.* 103, 212–220. doi: 10.1161/CIRCRESAHA.108.176230
- van Straten, D., Mashayekhi, V., de Bruijn, H., Oliveira, S., and Robinson, D. (2017). Oncologic photodynamic therapy: basic principles, current clinical status and future directions. *Cancers* 9:19. doi: 10.3390/cancers9020019
- Yasuda, J., Miyashita, T., Taguchi, K., Yoshizawa, S., and Umehara, S. (2015). Quantitative assessment of reactive oxygen sonochemically generated by cavitation bubbles. *Jpn. J. Appl. Phys.* 54 (7 S1):07HF21. doi: 10.7567/JJAP.54.07HF21
- Zhang, H., Chen, B., Jiang, H., Wang, C., Wang, H., and Wang, X. (2011). A strategy for ZnO nanorod mediated multi-mode cancer treatment. *Biomaterials* 32, 1906–1914. doi: 10.1016/j.biomaterials.2010.11.027

Conflict of Interest: The authors declare that the research was conducted in the absence of any commercial or financial relationships that could be construed as a potential conflict of interest.

Copyright © 2019 Vighetto, Ancona, Racca, Limongi, Troia, Canavese and Cauda. This is an open-access article distributed under the terms of the Creative Commons Attribution License (CC BY). The use, distribution or reproduction in other forums is permitted, provided the original author(s) and the copyright owner(s) are credited and that the original publication in this journal is cited, in accordance with accepted academic practice. No use, distribution or reproduction is permitted which does not comply with these terms.



Gadolinium-Based Nanoparticles for Theranostic MRI-Guided Radiosensitization in Hepatocellular Carcinoma

Pengcheng Hu^{1†}, Zhequan Fu^{1†}, Guobing Liu¹, Hui Tan¹, Jie Xiao¹, Hongcheng Shi^{1,2*} and Dengfeng Cheng^{1,2*}

¹ Department of Nuclear Medicine, Zhongshan Hospital, Fudan University, Shanghai, China, ² Shanghai Institute of Medical Imaging, Shanghai, China

OPEN ACCESS

Edited by:

Michael Ming-Yuan Wei,
Texas Commission on Environmental
Quality, United States

Reviewed by:

Weibo Cai,
University of Wisconsin-Madison,
United States
Xi Yang,
Fudan University, China
Lihua Wang,
Shanghai Advanced Research
Institute (CAS), China

*Correspondence:

Hongcheng Shi
shi.hongcheng@zs-hospital.sh.cn
Dengfeng Cheng
cheng.dengfeng@zs-hospital.sh.cn

[†]These authors have contributed
equally to this work

Specialty section:

This article was submitted to
Nanobiotechnology,
a section of the journal
Frontiers in Bioengineering and
Biotechnology

Received: 12 September 2019

Accepted: 13 November 2019

Published: 27 November 2019

Citation:

Hu P, Fu Z, Liu G, Tan H, Xiao J, Shi H
and Cheng D (2019)
Gadolinium-Based Nanoparticles for
Theranostic MRI-Guided
Radiosensitization in
Hepatocellular Carcinoma.
Front. Bioeng. Biotechnol. 7:368.
doi: 10.3389/fbioe.2019.00368

Background: Radiation therapy (RT) of hepatocellular carcinoma (HCC) is limited by low tolerance of the liver to radiation, whereas radiosensitizers are effective in reducing the required radiation dose. Multimodality gadolinium-based nanoparticles (AGuIX) are small and have enhanced permeability and retention effects; thus, they are very suitable for radiation sensitizer HCC RT. Here, we evaluated the potential value of AGuIX for theranostic MRI-radiosensitization in HCC.

Methods: The radiosensitization effects of AGuIX were evaluated via *in vitro* and *in vivo* experiments. Tumor growth, apoptosis imaging, and immunohistochemistry were performed to verify the antitumor effects of RT with AGuIX.

Results: *In vitro* evaluation of the efficacy of radiosensitivity of the AGuIX demonstrated that the presence of AGuIX significantly decreased HepG2 cell survival when combined with an X-ray beam. *In vivo* MRI imaging showed the ratio of tumor/liver concentration of the AGuIX was the highest 1 h after intravenous injection. For antitumor effects, we found that the tumor size decreased by RT-only and RT with AGuIX. The antitumor effects were more effective with high-dose AGuIX-mediated RT. Apoptosis imaging and immunohistochemistry both demonstrated that the degree of the cell apoptosis was highest with a high dose of AGuIX-mediated RT.

Conclusions: This study provides compelling data that AGuIX can facilitate theranostic MRI-radiosensitization in HCC.

Keywords: nanoparticles, AGuIX, hepatocellular carcinoma, MRI, theranostic, radiosensitization

INTRODUCTION

Hepatocellular carcinoma (HCC), the most common liver cancer in the world, only 20–25% can be cured by surgery alone (Torre et al., 2015). Most HCC patients require comprehensive multidisciplinary treatment because they are in advanced or first diagnosed as terminal stage (Lope et al., 2012; Waller et al., 2015). Radiotherapy (RT) based on highly penetrating MeV photons (X-rays and γ -rays) is non-invasive and useful for inoperable tumors. HCC itself is a radiotherapy-sensitive tumor, and thus, radiotherapy plays an important role in comprehensive HCC treatment (Poon, 2011). However, radiotherapy suffers from poor tumor specificity. Photons can damage all

tissues, leading to serious side effects on the normal liver tissue surrounding the tumor. These patients often have a background of cirrhosis, making them susceptible to lower doses of radiation than normal liver. The incidence of radiotherapy complications rises with increasing radiation dose in which radiation-induced liver disease (RILD) is a serious threat to patients' lives (Kalogeridi et al., 2015). Therefore, simultaneous enhancing the selectivity of tumor tissues and the bioavailability of radiation are the focus of future cancer radiotherapy.

Radiosensitizers can accumulate in the tumor tissue to increase the sensitivity of tumor cell to radiation, making tumor cells more likely to be killed by lower doses of radiation (Kwatra et al., 2013). Many drugs have been developed as HCC radiosensitizers, and the development of nanoparticles (NPs) is one important step (Kunz-Schughart et al., 2017). The use of NPs with the characteristic of preferential aggregation in tumors (even passively absorbed due to enhanced permeability and retention effects, EPR) can lead to local treatment of solid tumors (Rancoule et al., 2016). Furthermore, it has been proposed that NPs with high Z atoms are promising radiosensitizers because they may exert strong radiosensitizing effects on tumors when they are used in combination with several types of radiation of different energies (Liu et al., 2018). Gold NPs have a radiosensitizing effect on HCC (Zheng et al., 2013; Maniglio et al., 2018). However, radiotherapy in the liver region also damages normal tissues because normal liver tissue also has a high uptake of gold NPs (Balasubramanian et al., 2010). Therefore, to increase the target ratio, PEG-coated gold NPs were designed for HCC treatment. PEG-coated gold NPs increase the histocompatibility of gold NPs and prolong the circulation time *in vivo*. When galactose is coupled to gold NPs, it can recognize the asialoglycoprotein receptor (ASGPR) on the HCC, which improves its ability to bind to HCC and increase radiosensitization (Zhu et al., 2015). However, normal hepatocytes can also express ASGPR, and there is still a risk of RILD. Therefore, new nano-radiosensitizers are needed for HCC RT.

In 2013, Mignot et al. constructed a new type of multifunctional gadolinium nanoparticle, AGuIX, which is small (about 5 nm in diameter) and can be quickly excreted by the kidneys (Mignot et al., 2013). Due to the EPR effect, the liver background of AGuIX is much lower than that of AGuIX in most tumor tissues (Kamaly et al., 2012). With a high number of gadolinium atoms (atomic number 64), these nanoparticles can be used for enhanced magnetic resonance imaging (MRI), as well as a radiosensitization (Sancey et al., 2014).

In addition to the Compton effects and the photoelectric effect, the interaction between gadolinium atoms and X-rays also produces an Auger effect. The excited low-energy Auger electrons locally aggregate. There are more aggregation effects with more gadolinium atoms (Butterworth et al., 2012; Coulter et al., 2013). In addition, these materials have good biosafety and biocompatibility at conventional therapeutic concentrations (Morlieras et al., 2013; Bianchi et al., 2014; Bouziotis et al., 2017). Thus, AGuIX are NP radiosensitizers for integrated diagnosis and treatment of HCC.

Our previous research confirmed AGuIX uptake in the HepG2 cells and defined their biodistribution and pharmacokinetics in HepG2 tumor-bearing nude mice. This also indicated that the AGuIX accumulates in the HepG2 xenografts (Hu et al., 2017). Here, we evaluated the radiosensitization effect of AGuIX on HepG2 cells *in vitro* and performed MRI-guided RT using AGuIX radiosensitizer. We also conducted apoptosis Micro-SPECT/CT imaging to explore the radiosensitizing effect of AGuIX on HepG2 xenograft *in vivo*.

MATERIALS AND METHODS

AGuIX Nanoparticles

Gadolinium nanoparticles (AGuIX) were purchased from Nano-H (Lyon, France). The nanoparticles were spherical, dehydrated and sub-5 nm in diameter. Via built-in DOTA chelators the gadolinium atoms were attached to a polysiloxane shell in AGuIX nanoparticles. Rehydrated in sterile, Diethyl pyrocarbonate (DEPC)-treated water (Invitrogen, USA), AGuIX nanoparticles were stored at 4°C according to the manufacturer's instructions.

Cell Culture

The human HCC cell line, HepG2, was obtained from the Chinese Type Culture Collection (Chinese Academy of Sciences, Shanghai, China). HepG2 cells were cultured (37°C, 5% CO₂) in Dulbecco's modified Eagle's medium (Gibco) supplemented with 100 IU/ml penicillin-streptomycin and 10% fetal bovine serum.

Cell Irradiation With γ -Rays

HepG2 cells incubated in medium were first divided into four groups, and then irradiated at intensity from 1 to 6 Gy. Four different combinations were studied: A. Irradiation without AGuIX. B. AGuIX (0.5 nM) was added in the media just before the irradiation. This combination was called +IR/-incubation. C. Incubated cells with the AGuIX (0.5 nM) for 1 h and the media was changed just before the irradiation. This combination was called +IR/+washing. D. Incubated cells were with the AGuIX (0.5 nM) for 1 h and then irradiated. This combination was called +IR/- washing. The X-ray source (X-RAD 320, Precision X-Ray, North Branford, CT, USA) was used for irradiation. It was operated at 300 kV and 8 mA with a 2-mm Al filter at a dose rate of 2.0 Gy/min.

Quantification of AGuIX-Mediated Cell Radiosensitization Effects via a Clonogenic Assay

The cells were washed with PBS, trypsinized, and counted after irradiation. The irradiated cells were incubated at 300 cells per plate and grow for 10 days in 10 cm dishes. They were stained with 10% ethanol dye solution and 1% crystal violet. The clones in plates were counted, and measurements were done in triplicate. Linear-quadratic (LQ) model was used for cell survival curves fitting. The radiation doses reducing cells survival rate to 37% (D1%) on radiation survival curve divided by that on corresponding curves of radiation with AGuIX was called sensitizing enhancement ratio (SER).

Animal Models

The protocol for animal research was approved by the medical ethics committee of Zhongshan Hospital, Fudan University. This study followed the relevant guidelines and regulations of Fudan University. Six-week-old male BALB/c athymic nude mice weighing between 16 and 18 g were obtained from Slac Biotechnology (Shanghai, China). The mice were subcutaneously injected with HepG2 cells ($5 \times 10^6/100 \mu\text{l}$) in the right flank.

In vivo MRI

To observe the distribution of nanoparticles *in vivo* and choose appropriate time for radiotherapy, three groups of nude mice-bearing HepG2 tumors with AGuIX (10 mg/200 μl nanoparticles injected into the tail vein) were chosen

for MRI imaging. MRI scans were performed at four time points: before injection of nanoparticles, 1 h post injection (p.i.), 3 h p.i., and 6 h p.i. The MRI was a 7 T scanner (BioSpec 70/20 USR, Bruker Biospin MRI GmbH, Germany). We estimated the AGuIX's concentration in the tumor based on the signal of contrast-enhanced T1-weighted images ($TR = 650 \text{ ms}$, $TE = 700 \text{ ms}$, $NA = 1$, slice thickness = 0.7 mm , reconstruction voxel size = $256 \times 256 \times 700 \mu\text{m}$, $FOV = 3 \times 4.25 \text{ cm}$). According to the formula $[Gd^{3+} \propto 1/S^{T1}(t) - 1/S^{T1}(t_0)]$ where $S^{T1}(t_0)$ is the signal strength before NPs injection and $S^{T1}(t)$ is the signal strength at a determined time after NPs injection, the Gd^{3+} 's concentration was estimated based on the relaxation determined by the signal strength of contrast-enhanced T1 images (Lux et al., 2011; Detappe et al., 2017).

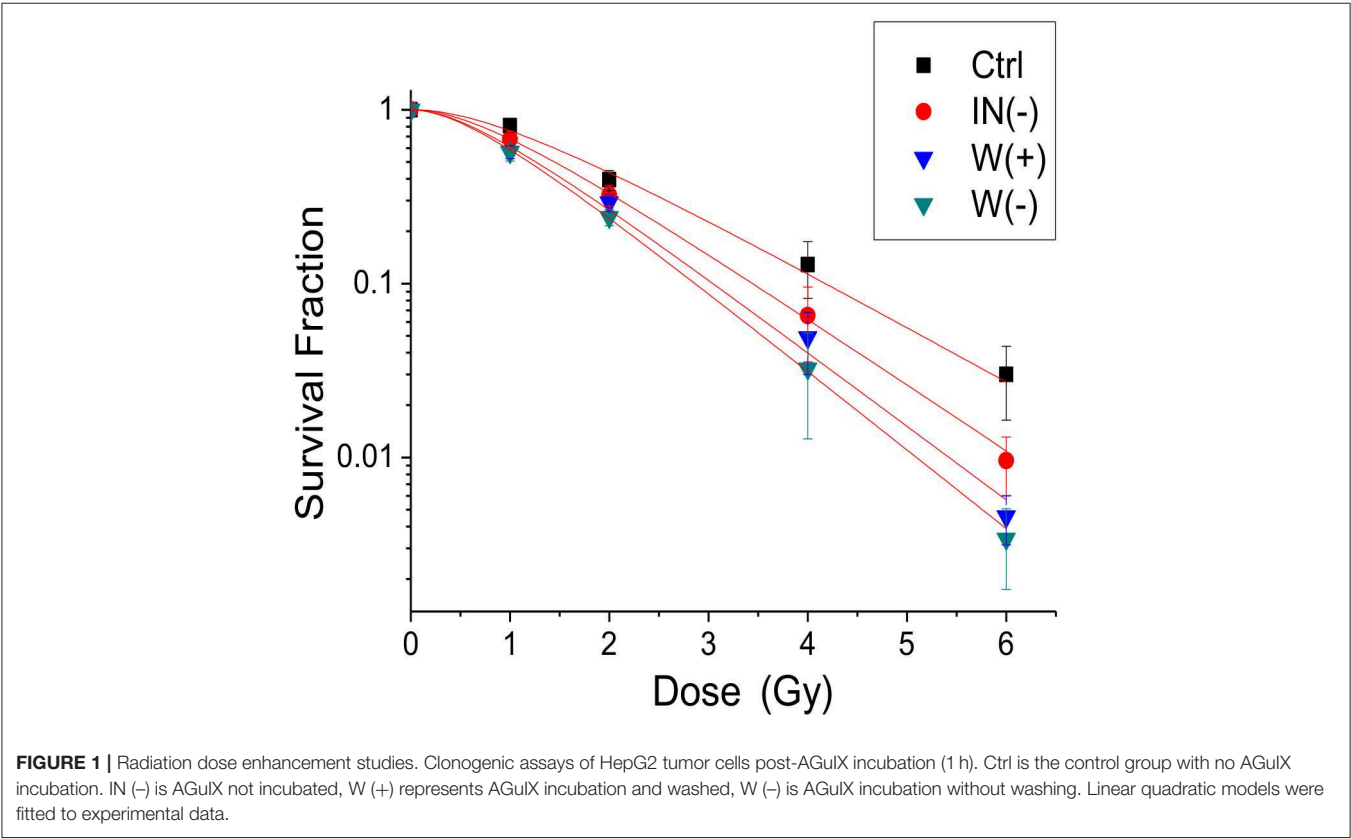


TABLE 1 | Clonogenic assays.

Dose (Gy)	Ctrl		IN (-)		W (+)		W (-)	
	Survival	SE	Survival	SE	Survival	SE	Survival	SE
0	1	1.00E-03	1	0.02	1	0.003	1	0.005
1	0.80907	0.07355	0.67502	0.055	0.57162	0.04764	0.57011	0.06335
2	0.39495	0.05247	0.32314	0.04475	0.29336	0.03154	0.24099	0.02591
4	0.12829	0.04616	0.06544	0.02993	0.04904	0.01908	0.03238	0.0196
6	0.02995	0.01357	0.00957	0.00353	0.00458	0.00144	0.0034	0.00166

Clonogenic assays of HepG2 tumor cells post-AGuIX incubation (1 h) after RT in Ctrl, IN (-), W (+) and W (-) groups.

Radiotherapy *in vivo*

To verify radiosensitization effect *in vivo*, Twenty four mice bearing subcutaneous right flank tumors were divided into four groups ($n = 6$). The diameter of the tumors were 4–6 mm. The mice in the control group and solely radio therapy group were injected with 0.5 mL of normal saline through the tail vein once a day for 2 days. The mice in the other two group were injected with 1 mg and 10 mg of AGuIX in 0.5 mL of normal saline through the tail vein, respectively. The tumor bearing mice received 6 Gy radiotherapy just 1 h after the intravenous injection on consecutive 2 days. All the mice were irradiated using an X-ray source (X-RAD 320, Precision X-Ray, North Branford, CT, USA) operating at 300 kV and 8 mA with a 2-mm Al filter at a dose rate of 2.0 Gy/min with a 2×2 cm radiation field to cover the tumor. Other parts of the body were covered with 5 mm lead shield. Tumor growth was measured over the following days.

Micro-SPECT/CT Apoptosis Imaging

Twelve HepG2 tumor bearing mice were randomly divided into four groups ($n = 3$) and injected with ^{99m}Tc -duramycin (37 MBq/2 μg /mouse) through the tail vein. Two hours after injection, mice were anesthetized using inhalation of 2% isoflurane. Then they were scanned in a simultaneous micro-single-photon emission computed tomography/computed tomography (SPECT/CT) scanner (Bioscan, Washington DC,

USA). The SPECT/CT imaging parameters were as follow: SPECT: energy peak, 140 keV; scanning time, 35 s/projection; window width, 10%; resolution, 1 mm/pixel; and matrix, 256×256 . CT: tube current, 0.15 mA; tube voltage, 45 keV; exposure time, 500 ms/frame, and frame resolution, 256×512 . The HiSPECT algorithm was used for imaging reconstruction.

InVivoScope software (Version 1.43, Bioscan, Washington DC, USA) was used for imaging post-processing. Two 3D region of interest (ROI) were drawn in the region of the tumor and similar region on the contralateral muscle as background ROI. The concentration of radioactivity of each ROI ($\mu\text{Ci}/\text{mm}^3$) was determined using this software. The tumor-to-background ratio (T/B) was regarded to express tumor signal intensity with reducing inter-mice variations.

Immunohistochemistry

Mice were sacrificed after apoptosis imaging. Tumors were harvested from the above four groups. The harvested tumors were immersed in 4% paraformaldehyde buffered solution for 24 h. Then dehydrated and embedded in paraffin. The tumor was sectioned serially to 4 mm for TUNEL staining with a TUNEL Apoptosis Assay kit (Roche Diagnostics, Indianapolis, IN, USA) following the manufacturer's protocol. The immunostaining was evaluated by determining the histochemistry score (H-SCORE). $\text{H-SCORE} = \sum(\text{PI} \times \text{I}) = (\text{percentage of cells of weak intensity} \times 1) + (\text{percentage of cells of moderate intensity} \times 2) + (\text{percentage of cells of strong intensity} \times 3)$ (Azim et al., 2015; Yeo et al., 2015).

TABLE 2 | Dose enhancement effect.

Ctrl	IN (–)	W (+)	W (–)
D0 1.44	1.14	0.99	0.95
SER	1.26	1.45	1.52

Dose enhancement effects in terms of SER for HepG2 cells incubated with 0.5 mM AGuIX in three groups. The sensitizing enhancement ratio (SER) was determined as the radiation dose reducing the survival to 37% (D0) for the radiation-only survival curve divided by that on corresponding curves of AGuIX plus radiation. $\text{SER} = \text{D0 (radiation-only group)}/\text{D0 (AGuIX plus radiation groups)}$.

Statistics

The cell growth curve was analyzed by OriginPro 8.0. Statistical analysis of image data and the tumor diameter used the Student's *t* test for comparisons between two groups by SPSS. In all cases, data were presented as mean \pm SD (standard deviation). Statistical significance (*) was set at $P < 0.05$.

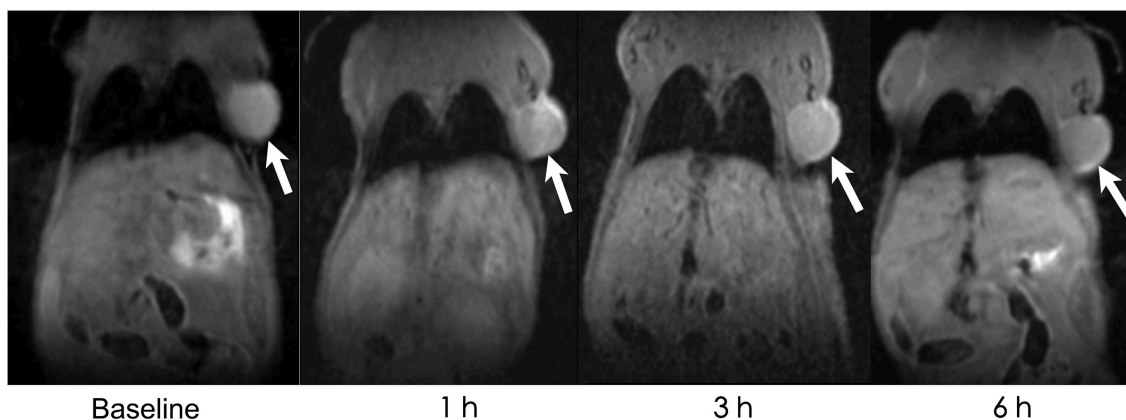
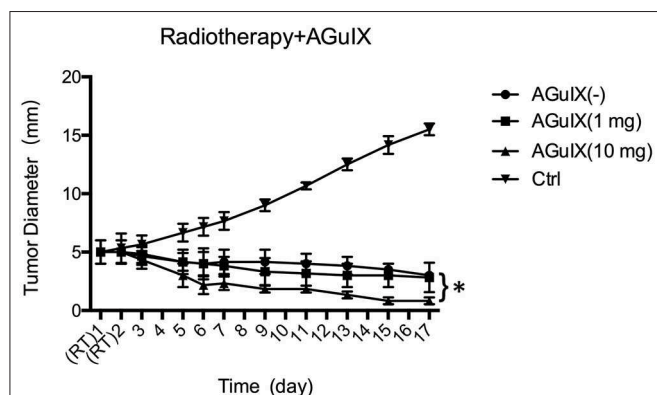
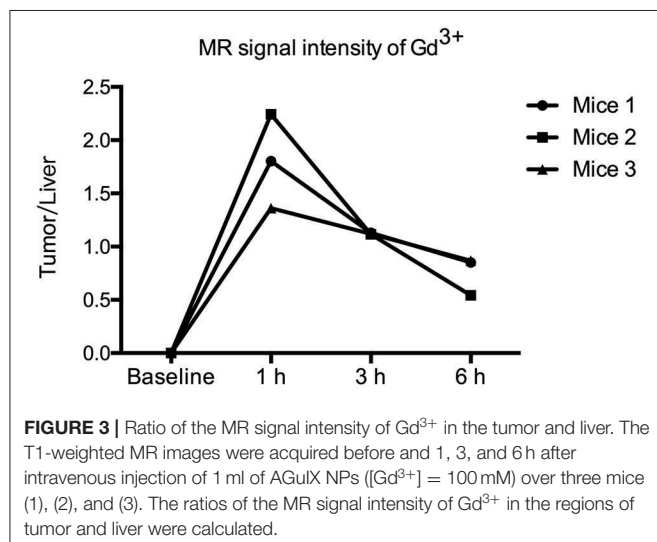


FIGURE 2 | *In vivo* MRI. *In vivo* MRI of the HepG2 tumor (white arrow)-bearing mice before AGuIX injection (baseline), 1, 3, and 6 h after AGuIX injection through the tail vein.

RESULTS

Radiosensitizing Effect Exerted by Irradiated AGuIX *in vitro*

Significant radiosensitization effect was observed in all clonogenic assays (Figure 1). The cell cloning rates of the 1-6 Gy experimental groups were lower than that of the control group ($P < 0.05$). This shows that AGuIX has radiosensitization effects on each experimental group. The results of the dose enhancement studies are summarized in Tables 1, 2. The +IR/-washing group showed the strongest radiosensitization followed by the +IR/+washing group, and finally the +IR/-incubation group. The SER values were 1.26, 1.45, and 1.52 for the cells treated with the +IR/- incubation (IN-), the +IR/+washing (W+), and the +IR/- washing (W-), respectively.

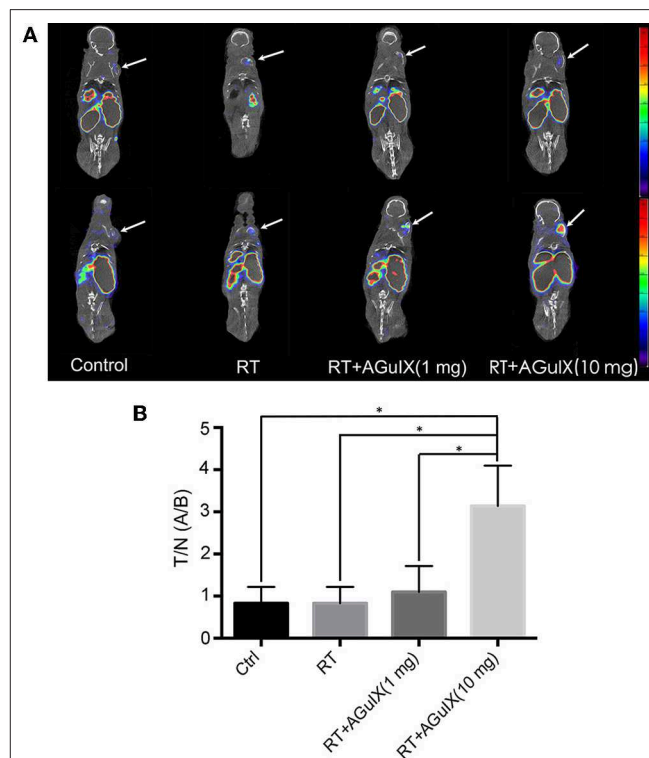


MRI Imaging of Tumors *in vivo*

AGuIXs were injected into the mice through the tail vein, and T1-weighted images were scanned at 1, 3, and 6 h (Figure 2). After injection of the AGuIX, we found that the tumor region (white arrow) became brighter than the background tissue and even the liver as seen by coronal scanning (Figure 2). With longer time, both the signal intensity of the tumor and the liver decreased gradually. The concentration of Gd^{3+} in the regions of interest (tumor, liver, muscle) was calculated according to the formula $[Gd^{3+} \propto 1/S^{T1}(t) - 1/S^{T1}(t_0)]$ (Figure 3). The Gd^{3+} concentration ratio of tumor/liver 1 h after intravenous injection is the highest among 1, 3, and 6 h.

Radiosensitization Assessment *in vivo*

The curve of tumor growth showed that the tumors size increased rapidly in the control group during the whole period of investigation and enlarging nearly 3.2-fold in 17 days (Figure 4).



In the group treated with radiotherapy alone and with AGuIX (1 mg), the tumor diameter decreased by two with a 6 Gy dose per fraction; however, it showed no statistical difference in tumor diameter throughout the period of investigation. During this process, the tumor diameter in AGuIX (–) group and AGuIX (1 mg) group decreased by ~40 and 44%, respectively. In contrast, AGuIX (10 mg) combined with the radiation group showed that the tumors size shrank by 83%. Versus radiotherapy alone, the introduction of the AGuIX caused a significant dose enhancement effect that inhibited the growth of the tumors.

Apoptosis Imaging and Immunohistochemistry

The radioactivity of the tumor increased progressively in the group of RT with AGuIX (10 mg) after therapy. The tumor-to-background ratio (T/B) was 0.83 ± 0.39 , 1.37 ± 0.31 , 1.10 ± 0.62 , and 3.87 ± 0.96 in the Control group, RT group, RT + AGuIX (1 mg) group, RT + AGuIX (10 mg) groups, respectively ($n = 3$, mean \pm SD). The T/B of the RT + AGuIX (10 mg) was the highest among four groups and showed statistical differences vs. the other three groups (Figure 5). The results of H-SCORE and TUNEL staining of tumor tissues among the 4 groups were consistent with apoptosis imaging; the score of RT + AGuIX (10 mg) was also high. There was a statistical difference between the RT + AGuIX (10 mg) group and the control group (Figure 6).

DISCUSSIONS

AGuIX nanoparticles have been proven the capability of increasing the tumor cells' sensitivity to radiation therapy in a number of tumor cells (including radiation-resistant cell lines) *in vitro*. The SERs were observed from 1.1 to 2.5 (Sancey et al., 2014). Besides, AGuIX NPs, the first nanoparticles based on multifunctional silica with a hydrodynamic diameter under 5 nm, are sufficiently small to escape hepatic clearance and allow animal imaging by four complementary techniques (SPECT, fluorescence imaging, MRI and CT) (Lux et al., 2011). Thus, AGuIX has potential to be developed into theranostic MRI-radiosensitization for HCC (Kamaly et al., 2012; Lux et al., 2015).

In order to study the radiosensitization effect of AGuIX on HCC RT, we next irradiated HepG2 cells. Our previous research showed that AGuIX can be taken up into the HepG2 cytoplasm and has a good dispersion shape in HepG2 cells, indicating that AGuIX was stable in the cells (Hu et al., 2017). The obtained of radiation dose enhancement studies in HepG2 cells (Figure 1) are similar to that by Porcel et al. in pancreatic cancer cells (Detappe et al., 2015). Irradiated AGuIX groups presented a stronger inhibition of cell clonogenic rates than the control group.

Radiosensitization was also observed in the groups with AGuIX regardless of whether AGuIX is incubated with cells for 1 h in our study. The mechanism of action of radiotherapy, in addition to the direct killing effect of the incident radiation beam, there may be other factors contributing as well. McMahon

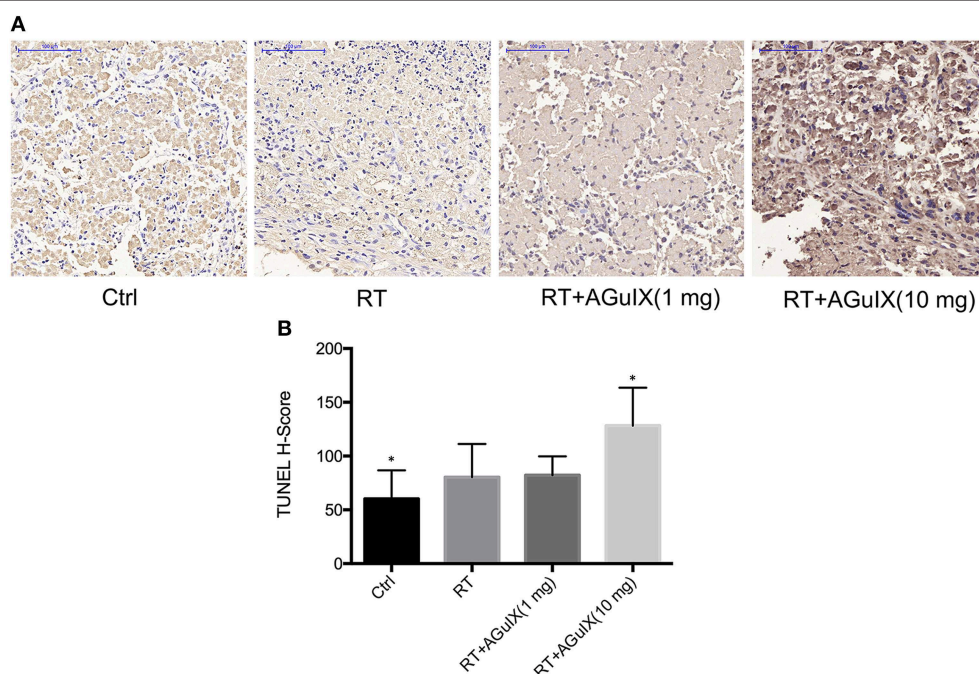


FIGURE 6 | Pathology and immunohistochemistry of tumor tissues. **(A)** Microscopic images of TUNEL ($\times 200$) staining of tumor tissues obtained from HepG2-bearing mice with no therapy were used as control. In TUNEL staining, apoptotic cells are stained brown. **(B)** Data analysis using the H-SCORE of TUNEL staining of tumor tissues to compare the four groups. Independent-sample *t* test was used for statistics. The asterisk indicates statistical significance ($P < 0.05$).

et al. demonstrated Auger electrons can create a local effect and affect nanoparticles clustering, which is the main cause of the formation of reaction oxygen species (ROS) such as OH^\bullet , H_2O_2 , or HOCl (McMahon et al., 2011). Also, a biological and chemical effect should be explored to account for the measured radiosensitization as well. Some of these ROS, with high chemical stabilities and a long-range action (few mm), may increase the cell death whether the nanoparticles are in the intercellular space or in cytoplasm. Therefore, the results of the study *in vitro* hinted that AGuIX whether in tumor intercellularly or in tumor intracellularly can both have the radiosensitization effect *in vivo*.

To evaluate the radiosensitization effect of AGuIX *in vivo*, we intravenously injected AGuIX into the HepG2 xenograft mice. For HCC, when the radiosensitizer concentration ratio of tumor/liver was the highest, it is the most suitable time point for RT to maximize therapeutic effect and minimize side effects to normal hepatic tissue. According to this hypothesis, we performed MRI on these mouse models and selected 1 h p.i. mice as the therapeutic time point for RT. The MRI data suggested that the signal intensity and contrast of the tumor lesion was significantly enhanced after 1 h AGuIX post injected. Therefore, MRI could be used for guiding the radiation process by monitoring and assisting tumor localization in real time.

The tumor growth curve in Figure 4 showed that the introduction of the AGuIX during the radiation process result in a markedly dose increasing effect compared to radiotherapy alone, thereby inhibiting the growth of solid tumors. Tumor cell apoptosis after radiotherapy is the basis of cell death (Garcia-Barros et al., 2003; Neshastehriz et al., 2018), and apoptosis imaging *in vivo* can achieve early detection of tumor post-radiation response, as well as accurate prediction of radiotherapy efficacy (Verheij, 2008). The $^{99\text{m}}\text{Tc}$ -duramycin is a relatively mature apoptosis imaging agent and has been used in apoptotic imaging of various tumors (Johnson et al., 2013; Audi et al., 2015; Elvas et al., 2016). Therefore, $^{99\text{m}}\text{Tc}$ -duramycin Micro-SPECT/CT imaging was performed to access the antitumor effects of imaging-guided RT with AGuIX. Combined with the apoptosis immunohistochemistry, both results demonstrated that the group of AGuIX-mediated RT showed the highest degree of cell apoptosis. These concurred with the tumor growth data. Thus, apoptosis imaging, pathology and tumor growth data suggest that the EPR-dependent accumulation of AGuIX within tumors can enhance the efficacy of radiation therapy.

REFERENCES

- Audi, S. H., Jacobs, E. R., Zhao, M., Roerig, D. L., Haworth, S. T., Clough, A. V., et al. (2015). *In vivo* detection of hyperoxia-induced pulmonary endothelial cell death using $^{99\text{m}}\text{Tc}$ -Duramycin. *Nucl Med Biol.* 42, 46–52. doi: 10.1016/j.nucmedbio.2014.08.010
- Azim, H. A., Peccatori, F. A., Brohée, S., Branstetter, D., Loi, S., Viale, G., et al. (2015). RANK-ligand (RANKL) expression in young breast cancer patients and during pregnancy. *Breast Cancer Res. Br.* 17:24. doi: 10.1186/s13058-015-0538-7
- Balasubramanian, S. K., Jittiwat, J., Manikandan, J., Ong, C. N., Yu, L. E., and Ong, W. Y. (2010). Biodistribution of gold nanoparticles and gene expression changes in the liver and spleen after intravenous administration

CONCLUSIONS

We describe a gadolinium-based nanoparticle AGuIX for MRI-guided radiotherapy in HCC. The AGuIX provide better detection of tumors in imaging, and precise identified for accurate MRI-guided radiotherapy. On the other hand, the heavy elements in this novel nanoparticle can enhance radiosensitizing effect by irradiation dose deposition. The preliminary results showed that the radiosensitizing effect observed *in vivo* could be translated to remarkable tumor control via AGuIX-radiosensitized radiotherapy. Thus, this study demonstrates that the AGuIX could be a promising theranostic nanoparticle for both MRI-guided and enhancement of radiosensitivity. Thus, it can overcome the limitations of RT in HCC by increasing the tolerance of the liver tumor to radiation.

DATA AVAILABILITY STATEMENT

All datasets generated for this study are included in the article/supplementary material.

ETHICS STATEMENT

The animal research protocol was approved by Zhongshan Hospital medical ethics committee, Fudan University. All experiments were conducted following the relevant guidelines and regulations of Fudan University.

AUTHOR CONTRIBUTIONS

PH, ZF, HT, and HS conceived and designed the study. PH, GL, and JX performed the experiments. PH, HT, JX, and DC were engaged in the data interpretation and analysis. PH, ZF, and DC participated in the writing of the manuscript.

ACKNOWLEDGMENTS

The authors are deeply grateful for the financial support from National Natural Science Foundation of China (Nos. 11875114, 81471706, and 81871407), and the Shanghai Municipal Health and Family Planning Commission Youth Fund of China (20164Y0113).

in rats. *Biomaterials* 31, 2034–2042. doi: 10.1016/j.biomaterials.2009.11.079

- Bianchi, A., Dufort, S., Lux, F., Courtois, A., Tillement, O., Coll, J. L., et al. (2014). Quantitative biodistribution and pharmacokinetics of multimodal gadolinium-based nanoparticles for lungs using ultrashort TE MRI. *Magma* 27, 303–316. doi: 10.1007/s10334-013-0412-5
- Bouziotis, P., Stellas, D., Thomas, E., Truillet, C., Tsoukalas, C., Lux, F., et al. (2017). (68)Ga-radiolabeled AGuIX nanoparticles as dual-modality imaging agents for PET/MRI-guided radiation therapy. *Nanomedicine* 12, 1561–1574. doi: 10.2217/nnm-2017-0032
- Butterworth, K. T., McMahon, S. J., Currell, F. J., and Prise, K. M. (2012). Physical basis and biological mechanisms of gold nanoparticle radiosensitization. *Nanoscale* 4, 4830–4838. doi: 10.1039/c2nr31227a

- Coulter, J. A., Hyland, W. B., Nicol, J., and Currell, F. J. (2013). Radiosensitising nanoparticles as novel cancer therapeutics — pipe dream or realistic prospect? *Clin. Oncol.* 25, 593–603. doi: 10.1016/j.clon.2013.06.011
- Detappe, A., Kunjachan, S., Rottmann, J., Robar, J., Tsiamas, P., Korideck, H., et al. (2015). AGuIX nanoparticles as a promising platform for image-guided radiation therapy. *Cancer Nanotechnol.* 6:4. doi: 10.1186/s12645-015-0012-3
- Detappe, A., Thomas, E., Tibbitt, M. W., Kunjachan, S., Zavidij, O., Parnandi, N., et al. (2017). Ultrasmall silica-based bismuth gadolinium nanoparticles for dual magnetic resonance-computed tomography image guided radiation therapy. *Nano Lett.* 17, 1733–1740. doi: 10.1021/acs.nanolett.6b05055
- Elvas, F., Boddaert, J., Vangestel, C., Pak, K., Gray, B., Kumar-Singh, S., et al. (2016). ^{99m}Tc -Duramycin SPECT imaging of early tumor response to targeted therapy: a comparison with ^{18}F -FDG PET. *J. Nucl. Med. Offic. Publ. Soc. Nucl. Med.* 58, 116–182014. doi: 10.2967/jnumed.116.182014
- Garcia-Barros, M., Paris, F., Cordon-Cardo, C., Lyden, D., Rafii, S., Haimovitz-Friedman, A., et al. (2003). Tumor response to radiotherapy regulated by endothelial cell apoptosis. *Science* 300, 1155–1159. doi: 10.1126/science.1082504
- Hu, P., Cheng, D., Huang, T., Banizs, A. B., Xiao, J., Liu, G., et al. (2017). Evaluation of novel 64 Cu-labeled theranostic gadolinium-based nanoprobe in HepG2 tumor-bearing nude mice. *Nanoscale Res. Lett.* 12:523. doi: 10.1186/s11671-017-2292-5
- Johnson, S. E., Li, Z., Liu, Y., Moulder, J. E., and Zhao, M. (2013). Whole-body imaging of high-dose ionizing irradiation-induced tissue injuries using ^{99m}Tc -duramycin. *J. Nucl. Med.* 54, 1397–1403. doi: 10.2967/jnumed.112.112490
- Kalogeridi, M. A., Zygiogianni, A., Kyrgias, G., Kouvaris, J., Chatziioannou, S., Kelekis, N., et al. (2015). Role of radiotherapy in the management of hepatocellular carcinoma: a systematic review. *World J. Hepatol.* 7, 101–112. doi: 10.4254/wjh.v7.i1.101
- Kamaly, N., Xiao, Z., Valencia, P. M., Radovic-Moreno, A. F., and Farokhzad, O. C. (2012). Targeted polymeric therapeutic nanoparticles: design, development and clinical translation. *Chem. Soc. Rev.* 41, 2971–3010. doi: 10.1039/c2cs15344k
- Kunz-Schughart, L. A., Dubrovskaya, A., Peitzsch, C., Ewe, A., Aigner, A., Schellenburg, S., et al. (2017). Nanoparticles for radiooncology: Mission, vision, challenges. *Biomaterials* 120, 155–184. doi: 10.1016/j.biomaterials.2016.12.010
- Kwatra, D., Venugopal, A., and Anant, S. (2013). Nanoparticles in radiation therapy: a summary of various approaches to enhance radiosensitization in cancer. *Transl. Cancer Res.* 2, 330–342.
- Liu, Y., Zhang, P., Li, F., Jin, X., Li, J., Chen, W., et al. (2018). Metal-based NanoEnhancers for Future Radiotherapy: Radiosensitizing and synergistic effects on tumor cells. *Theranostics* 8, 1824–1849. doi: 10.7150/thno.22172
- Lope, C. R., Tremosini, S., Forner, A., Reig, M., and Bruix, J. (2012). Management of HCC. *J. Hepatol.* 56, S75–S87. doi: 10.1016/S0168-8278(12)60009-9
- Lux, F., Mignot, A., Mowat, P., Louis, C., Dufort, S., Bernhard, C., et al. (2011). Ultrasmall rigid particles as multimodal probes for medical applications. *Angewandte Chemie* 123, 12299–12303. doi: 10.1002/anie.201104104
- Lux, F., Sancey, L., Bianchi, A., Crémillieux, Y., Roux, S., and Tillement, O. (2015). Gadolinium-based nanoparticles for theranostic MRI-radiosensitization. *Nanomedicine* 10, 1801–1815. doi: 10.2217/nmm.15.30
- Maniglio, D., Benetti, F., Minati, L., Jovicich, J., Valentini, A., Speranza, G., et al. (2018). Theranostic gold-magnetite hybrid nanoparticles for MRI-guided radiosensitization. *Nanotechnology* 29:315101. doi: 10.1088/1361-6528/aac4ce
- McMahon, S. J., Hyland, W. B., Muir, M. F., Coulter, J. A., Jain, S., Butterworth, K. T., et al. (2011). Biological consequences of nanoscale energy deposition near irradiated heavy atom nanoparticles. *Sci. Rep.* 1:18. doi: 10.1038/srep00018
- Mignot, A., Truillet, C., Lux, F., Sancey, L., Louis, C., Denat, F., et al. (2013). A top-down synthesis route to ultrasmall multifunctional Gd-based silica nanoparticles for theranostic applications. *Chemistry* 19, 6122–6136. doi: 10.1002/chem.201203003
- Morlieras, J., Dufort, S., Sancey, L., Truillet, C., Mignot, A., Rossetti, F., et al. (2013). Functionalization of small rigid platforms with cyclic RGD peptides for targeting tumors overexpressing $\alpha\text{v}\beta\text{3}$ -integrins. *Bioconjug. Chem.* 24, 1584–1597. doi: 10.1021/bc4002097
- Neshastehriz, A., Khosravi, Z., Ghaznavi, H., and Shakeri-Zadeh, A. (2018). Gold-coated iron oxide nanoparticles trigger apoptosis in the process of thermoradiotherapy of U87-MG human glioma cells. *Radiat. Environ. Biophys.* 57, 405–418. doi: 10.1007/s00411-018-0754-5
- Poon, R. T. (2011). Prevention of recurrence after resection of hepatocellular carcinoma: a daunting challenge. *Hepatology* 54, 757–759. doi: 10.1002/hep.24569
- Rancoule, C., Magné, N., Vallard, A., Guy, J. B., Rodriguez-Lafrasse, C., Deutsch, E., et al. (2016). Nanoparticles in radiation oncology: From bench-side to bedside. *Cancer Lett.* 375, 256–262. doi: 10.1016/j.canlet.2016.03.011
- Sancey, L., Lux, F., Kotb, S., Roux, S., Dufort, S., Bianchi, A., et al. (2014). The use of theranostic gadolinium-based nanoprobe to improve radiotherapy efficacy. *Br. J. Radiol.* 87, 527–528. doi: 10.1259/bjr.20140134
- Torre, L. A., Bray, F., Siegel, R. L., Ferlay, J., Lortet-Tieulent, J., and Jemal, A. (2015). Global cancer statistics, 2012. *Ca Cancer J. Clin.* 65, 87–108. doi: 10.3322/caac.21262
- Verheij, M. (2008). Clinical biomarkers and imaging for radiotherapy-induced cell death. *Eur. J. Cancer Suppl.* 7, 471–480. doi: 10.1007/s10555-008-9131-1
- Waller, L. P., Deshpande, V., and Pysopoulos, N. (2015). Hepatocellular carcinoma: a comprehensive review. *World J. Hepatol.* 7, 2648–2663. doi: 10.4254/wjh.v7.i26.2648
- Yeo, W., Chan, S. L., Mo, F. K., Chu, C. M., Hui, J. W., Tong, J. H., et al. (2015). Phase I/II study of temsirolimus for patients with unresectable Hepatocellular Carcinoma (HCC) – a correlative study to explore potential biomarkers for response. *BMC Cancer* 15:395. doi: 10.1186/s12885-015-1334-6
- Zheng, Q., Yang, H., Wei, J., Tong, J. L., and Shu, Y. Q. (2013). The role and mechanisms of nanoparticles to enhance radiosensitivity in hepatocellular cell. *Biomed. Pharmacother.* 67, 569–575. doi: 10.1016/j.biopha.2013.04.003
- Zhu, C. D., Zheng, Q., Wang, L. X., Xu, H. F., Tong, J. L., Zhang, Q. A., et al. (2015). Synthesis of novel galactose functionalized gold nanoparticles and its radiosensitizing mechanism. *J. Nanobiotechnol.* 13, 1–11. doi: 10.1186/s12951-015-0129-x

Conflict of Interest: The authors declare that the research was conducted in the absence of any commercial or financial relationships that could be construed as a potential conflict of interest.

Copyright © 2019 Hu, Fu, Liu, Tan, Xiao, Shi and Cheng. This is an open-access article distributed under the terms of the Creative Commons Attribution License (CC BY). The use, distribution or reproduction in other forums is permitted, provided the original author(s) and the copyright owner(s) are credited and that the original publication in this journal is cited, in accordance with accepted academic practice. No use, distribution or reproduction is permitted which does not comply with these terms.



Nanomedicines: A Potential Treatment for Blood Disorder Diseases

Nan Zhang^{1,2}, Ming-Yuan Wei³ and Qiang Ma^{1*}

¹ Chinese Academy of Inspection and Quarantine, Beijing, China, ² School of Life Science and Medicine, Dalian University of Technology, Panjin, China, ³ Texas Commission on Environmental Quality, Austin, TX, United States

OPEN ACCESS

Edited by:

Michele Lafisco,
Italian National Research Council
(CNR), Italy

Reviewed by:

Xin Li,
Institute of Materia Medica
(IMM), China
Nenad L. Ignjatovic,
Serbian Academy of Sciences and
Arts (SASA), Serbia

*Correspondence:

Qiang Ma
maqiang@caiq.org.cn

Specialty section:

This article was submitted to
Nanobiotechnology,
a section of the journal
Frontiers in Bioengineering and
Biotechnology

Received: 17 September 2019

Accepted: 13 November 2019

Published: 28 November 2019

Citation:

Zhang N, Wei M-Y and Ma Q (2019)
Nanomedicines: A Potential Treatment
for Blood Disorder Diseases.
Front. Bioeng. Biotechnol. 7:369.
doi: 10.3389/fbioe.2019.00369

Blood disorder diseases (BDDs), also known as hematologic, is one of the diseases owing to hematopoietic system disorder. Chemotherapy, bone marrow transplantation, and stem cells therapy have been used to treat BDDs. However, the cure rates are still low due to the availability of the right type of bone marrow and the likelihood of recurrence and infection. With the rapid development of nanotechnology in the field of biomedicine, artificial blood or blood substitute has shown promising features for the emergency treatment of BDDs. Herein, we surveyed recent advances in the development of artificial blood components: gas carrier components (erythrocyte substitutes), immune response components (white blood cell substitutes), and hemostasis-responsive components (platelet substitutes). Platelet-inspired nanomedicines for cancer treatment were also discussed. The challenges and prospects of these treatment options in future nanomedicine development are discussed.

Keywords: nanomedicine, blood disorder diseases, artificial blood components, treatment, emergency blood supply

INTRODUCTION

Blood disorder diseases (BDDs), also known as hematologic, is one of the diseases owing to hematopoietic system disorder. BDDs can be broadly classified into three categories, red blood cell disease, white blood cell disease, and platelet disease. Among BDDs, iron deficiency anemia, leukemia, hemophilia, and malignant lymphoma are most widely known. Taking leukemia as an example, the early stage is extremely difficult to cure, resulting in high mortality rate. In 1948, Farber et al. realized a temporary remissions in acute leukemia, providing a promising direction for leukemia treatment (Farber and Diamond, 1948).

Researchers discovered that chemotherapy may be an effective means of treating BDDs with the high risk of causality due to immune system damage. The similar challenge exists in the bone marrow transplant treatment, which transplants normal human hematopoietic stem cells into the patient and rebuilds the patient's immune and hematopoietic system. A matching donor is rare to find, and the treatment cost is not affordable. Hematopoietic stem cells are rich in cord blood (CB), which could be considered as a bone marrow substitute. CB cells can be used for infusion therapy in special situations, because it allows a certain degree of leukocyte antigen mismatch. Patient survival rate could be improved by umbilical cord blood transplantation, such as the injection of two units of cord blood cells, or *ex vitro* expansion of cord blood cells (Pelosi et al., 2012). To date, this technology has been used for BDDs treatment, but some patients died of bacterial infection due to the insufficient doses (Maeda et al., 2005).

A great variety of methods for BDDs treatment have been developed in recent years. For example, as for severe thalassemia treatment, deferoxamine, or deferiprone is often used as a chelating agent to bind unstable iron to eliminate a series of effects from excessive iron content (Maggio, 2007). It was found that rituximab, an anti-CD20 monoclonal antibody, specifically depletes B cells, and reduces their damage to blood proteins or cells (Barcellini and Zanella, 2011). In addition, the modification or deletion of the telomere gene was found beneficial for the treatment of hematological diseases resulting from random or malignant transformation of hematopoietic function due to telomere shortening (Allegra et al., 2017). Genetic engineering has been attracted increasing attention for BDDs treatment. Townes et al. derived embryonic stem cells and then performed homologous recombination *in vitro* to change the pathogenic gene of sickle-shaped anemia, replacing the normal gene copy $\beta\beta\beta A$ with the disease-causing gene $\beta\beta\beta S$ (Townes, 2008). The diseased mice returned to normal and produced high levels of human hemoglobin. Osborn et al. efficiently induced double-stranded DNA breaks by the clustered regularly interspaced short palindromic repeats/associated protein 9 (CRISPR/Cas9) method, specifically editing clinically relevant T cell receptor alpha constant (TRAC) gene targets that are highly correlated with leukemia (Osborn et al., 2016). Compared with patients with non-hematologic malignancies, hematological malignancies, such as chronic lymphocytic leukemia, acute lymphoblastic leukemia, and non-Hodgkin's lymphoma, chimeric antigen receptors T cells (CART), had shown higher overall response rate and complete response rate.

Nanomedicine is a new branch of medicine that applies nanotechnology to traditional medical development. Nanomedicine focuses on designing a specific combination of nanomaterial (e.g., nanoparticle, nanocarrier, and nanovesicle) and small molecules to conceive a biocompatible carrier for delivering drugs to cancer sites effectively (Wicki et al., 2015). The effective component could be a polypeptide, a protein, a nucleotide, or a small molecule drug. Compared with traditional medicines, nanomedicine appears to be able to avoid the body's defense mechanisms, reduce the clearance rate, prevent tissue damage through regulated drug release, and improve the pharmacokinetics and biodistribution of the drug. The nanoscale component to build a nanomedicine include: polymer nanoparticles (NPs), liposomes, metal NPs, carbon nanotubes, and molecularly targeted NPs. For instance, polymer nanoparticles are often composed of hydrophobic core and hydrophilic shell, on which specific targeting moieties were coated. Quintana et al. attached folic acid, methotrexate and fluorescein to polyamidoamine dendrimer, and the targeted delivery improved the cytotoxic response of the cells to methotrexate 100-fold over free drug (Quintana et al., 2002). In addition to conventional intravenous and oral medications, lung infection disease was treated by inhalation of NPs as an adjuvant therapy (Blum et al., 2014; Jurek et al., 2014). Marrache et al. used a targeted high-density lipoprotein (HDL)-mimicking NP with contrast agents to detect vulnerable plaque and initiate preventative therapy for atherosclerosis (Marrache and Dhar, 2013).

By 2016, 14 nano-drugs for clinical treatment was approved by U.S. Food and Drug Administration (FDA). In addition, FDA approves 18 nanomedicines for cancer chemotherapy in clinical trials, 19 nanopharmaceutical formulations for being developed and clinically tested, and 15 antibacterial nano-formulations for being developed (Caster et al., 2017). The development of common clinical nano-formulations appear to reduce toxicity rather than improve efficacy (Caster et al., 2017). The cytotoxicity and the stability in complex biological environments are still under debate and limit the progresses of nano-drug development (Lim et al., 2016). On December 21, 2018, FDA approved the first treatment for rare BDDs by granting Elzonris (tagraxofusp-erzs) infusion for the treatment of blastic plasmacytoid dendritic cell neoplasm (BPDCN) in adults and in pediatric patients (2 years or above) (FDA, 2018). Tagraxofusp-erzs is a cytotoxin that a protein is comprised of human IL-3 and truncated diphtheria toxin (DT), and it targets cells that express CD123, the alpha chain of the IL-3 receptor, which is overexpressed in BPDCN (Jen et al., 2019). The drug is preferentially accepted by CD123-overexpressed cells and initiates irreversible protein synthesis to cause cell death.

Despite of the excitement of the emerging of above-mentioned nanomedicines, direct blood transfusion of whole blood is preferred, if available, to efficiently treat BDDs. However, the storage of whole blood is challenging, due to short shelf life and the risk of infection by pathogenic bacteria (Hess, 2006; Greening et al., 2010). Most of the whole blood in the blood bank are donated by volunteers. At the beginning of the twentieth century, private blood sales led to the ravage of Human Immunodeficiency Virus (HIV) and Hepatitis B Virus (HBV) as a result of the lack of general health knowledge and safety awareness, especially in some economically backward developing countries. Taking China as an example, with the development of the country's economy, the need of blood donation, according to the National Health Service of China, has become desperately larger, but the public awareness of blood donation still falls behind. The blood banks' inventory became in shortage. Whole blood transfusion is often used for the patients after major surgeries or with BDDs, such as acute anemia. Therefore, the synthesis of blood substitutes as a supplement to the natural blood bank has become an urgent need.

Herein, we demonstrate recent advances in artificial blood components: gas carrier components (erythrocyte substitutes), immune response components (white blood cell substitutes), and hemostasis-responsive components (platelet substitutes). Moreover, the development of platelet-inspired nanomedicines was discussed. The challenges and prospects of these treatment options in future development are discussed.

NANOMEDICINES FOR THE GAS-CARRIER COMPONENT

Hemoglobin-Based Red Blood Cells Substitutes

The three key components of human blood are red blood cells (RBCs), white blood cells (WBCs), and platelets. The

main function of RBCs is to serve as a gas carrier component for transporting oxygen and carbon dioxide. As discussed, RBC substitutes may be an alternative solution for emergency blood transfusion for BDDs treatment. The advantages of RBC substitutes include: (a) no surface antigens; (b) more convenient to store than natural blood; and (c) function as effectively as hemoglobin.

More than three decades ago, researchers extracted RBCs from expiring human or animal blood samples, broke the cells and centrifuged, and collected cell-free hemoglobin (Kothe et al., 1985), which was considered as an early version of RBC substitute. This hemoglobin solution showed the capacity of expanding oxygen delivery (Kaplan and Murthy, 1975), whereas the short effective time led to hypoxia-induced poisoning of liver, kidney, brain, and other organs (Friedman et al., 1978, 1979; White et al., 1986).

Chemical crosslinking of hemoglobin monomers was reported to eliminate the adverse effects of hemoglobin. For example, Biro et al. tested the effects of whole blood, unmodified stroma-free hemoglobin solution (SFHS), and partially cross-linked hemoglobin solution on coronary vessels in anesthetized open-chest dogs (Biro et al., 1988). The results showed that unmodified SFHS significantly caused vasoconstriction compared with whole blood perfusion. Blood vessels do not shrink when SFHS is subjected to pyridyloxylolation (partial crosslinking). Infusion of adenosine in the coronary artery did not improve this condition. The results indicate that unmodified hemoglobin preparations cause coronary artery contraction in dogs and have an effect on their normal blood circulation (Biro et al., 1988). When the RBC lysate is covalently linked by adenosine triphosphate (ATP) or pyridoxal phosphate and purified by agarose nucleophilic chromatography, it can cause vasoconstriction of the coronary artery. This may be caused by the covalent modification, or that nucleophilic chromatography removes membrane phospholipids and denatured protein aggregates (Vogel et al., 1987; Lang et al., 1990).

Diaspirin cross-linked hemoglobin (DCLHb) is a modified hemoglobin that the two α helix units were crosslinked while the molecule maintains a tetramer conformation (the structure is shown in **Table 1**). DCLHb had shown a strong oxygen carrying capacity. DCLHb was in the treatment of severe traumatic hemorrhagic shock: a randomized controlled efficacy trial. Early experiments showed that DCLHb was well-tolerated and had shown no obvious functional disorders or toxicity (Przybelski et al., 1999). However, Sloan et al. found that the input of DCLHb resulted in an increase in patient mortality compared to the control group (Sloan et al., 1999). A more in-depth study found that it was well-tolerated at low doses (50–200 mg/kg) (Bloomfield et al., 1996; Przybelski et al., 1996), whereas some side effects, such as yellowing skin, hemoglobinuria, and jaundice, were observed at high doses (680–1,500 mg/kg). Taken together, DCLHb could be an alternative blood supply for patients with rare blood types or for emergency usage during the shortage of blood bank inventory (Reppucci et al., 1997; Schubert et al., 2002, 2003).



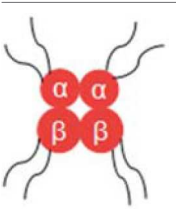
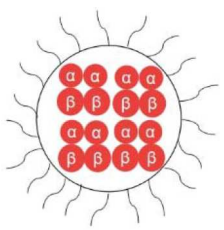
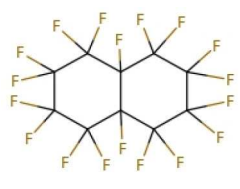
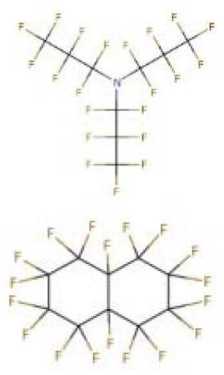
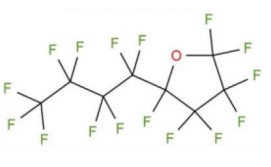
Polymerized hemoglobin (PolyHeme, the structure is shown in **Table 1**) appeared to be a safer oxygen-carrying resuscitation

fluid than DCLHb. It is a hemoglobin polymer complex formed by crosslinking adjacent α subunit and β subunit. In 1998, PolyHeme was first applied in trauma and emergency surgery, showing good tolerance and safety (Gould et al., 1998). Subsequent experiments showed that total hemoglobin level could be maintained by infusion of PolyHeme alone, thereby increasing the survival rate of patients with RBCs in critical situations (Gould et al., 2002). In addition to PolyHeme, researchers found that bovine aggregated hemoglobin (HBOC-201) was found to be able to keep up the hemoglobin level (Levy et al., 2002). In their work, a randomized, double-blind trial of HBOC-201 for patients undergoing heart surgery was conducted. After blood transfusion with HBOC-201, one third of patients survived without additional supply of RBCs. This indicates that HBOC-201 transfusion might be an alternative treatment for patients with moderate to severe anemia after cardiac surgery. Studies had shown that HBOC-201 is an effective oxygen carrier for most patients (Dong et al., 2006; Mackenzie et al., 2010); however, high vasoactivity-related adverse effects were found in the seniors with partial orthopedic surgery (Freilich et al., 2009).

Instead of cross-linking modification of hemoglobin, poly (ethylene glycol) (PEG) modified hemoglobin had attracted increasing attentions. For example, Nho et al. experimented with PEG-bovine hemoglobin in a low blood volume-bleeding shock model in dogs. The results showed that PEG-bHb has a longer half-life in blood vessels and no significant adverse effects compared to native hemoglobin (Nho et al., 1992). Björkholm et al. found that in a single-blind clinical trial of 12 volunteers they did not show any adverse symptoms at a dose of 50 mg/kg. When the dosage was increased to 100 mg/kg, the levels of amylase and lipase were slightly higher than normal (Björkholm et al., 2005). Hemospan is a PEG-modified human hemoglobin product developed by Sangart Inc and is also a widely used clinical preparation of RBCs substitutes. Eight PEG molecules were attached to the specific sites on α globulin and β globulin (Vandegriff et al., 2008), as depicted in **Table 1**. The purpose of this design is to prolong the retention time in blood vessel by increasing molecular weight, to increase the oxygen affinity, and to prevent it from early unloading (Vandegriff and Winslow, 2009). Olofsson et al. conducted a safety study in old patients undergoing selective hip arthroplasty and found that Hemospan is well-tolerated. No high frequency of adverse events from infusion to 24 h were observed along with a slight increase in liver enzymes and lipase (Olofsson et al., 2006). In a more recent study, Cooper et al. reported an PEGlated Hb engineered with tyrosine residues (Cooper et al., 2019), and it showed an increased vascular half time compared to wild type PEGlated Hb. The tyrosine residues were believed to enhance the reducibility of Hb and decrease adverse side effects, such as autooxidation.

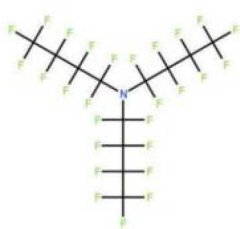
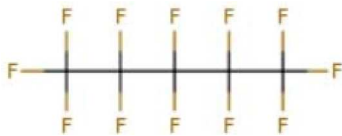
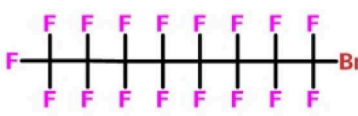
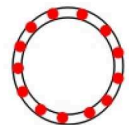
Hemoglobin molecules were encapsulated in liposome particles (see **Table 1**), and the surface of the particles was attached with PEG-conjugated phosphatidylethanolamine (Sakai et al., 1997). Such HbV-PEG were found to be less prone to flocculation than unmodified hemoglobin vesicles. Animal experiments demonstrated that in comparison with the control group greater blood flow and faster gas exchange rates were observed for the group that had a 90% exchange

TABLE 1 | Nanomedicines for the gas-carrier component.

Components	Structure information	Applications	References
	Crosslinking between two α subunits within a hemoglobin molecule	Hemorrhagic shock	Reppucci et al., 1997; Przybelski et al., 1999; Sloan et al., 1999; Schubert et al., 2002, 2003
	Crosslinking between adjacent hemoglobin α and β subunits	Emergency trauma and surgery Postoperative blood transfusion	Gould et al., 1998; Levy et al., 2002; Freilich et al., 2009
	modified by PEG molecules	Blood transfusion Hemorrhagic shock	Nho et al., 1992; Bjorkholm et al., 2005; Olofsson et al., 2006; Vandegriff et al., 2008
	Nanostructure of outer PEG-modified lipid membrane	Blood transfusion Hemorrhagic shock	Sakai et al., 1997
	Perfluorocarbonated emulsions based on perfluorodecalin and egg yolk phospholipids	Acute shock of animals	Yokoyama et al., 1975
	Fluosol-DA. Consists of perfluorodecalin, perfluorotripropylamine, hydroxyethyl starch and Krebs-Ringer bicarbonate	Increase patient oxygen delivery	Tremper et al., 1980, 1982; Suyama et al., 1981; Gould et al., 1986; Spence et al., 1994
	Perfluoro (2-n-butyltetrahydrofuran)	Provide oxygen for measuring nerve parts	Sanders and Schick, 1978

(Continued)

TABLE 1 | Continued

Components	Structure information	Applications	References
	Perfluorotributylamine	Blood exchange	Motta et al., 1981
	Dodecafluoropentane	Hemorrhagic shock Anemia Protection of the brain and heart	Woods et al., 2013; Borrelli et al., 2014; Moon-Massat et al., 2014; Strom et al., 2014; Culp et al., 2015
	Perfluorooctane bromide	Auxiliary exchange gas	Pranikoff et al., 1996
	The modified hemoglobin is embedded in the liposome bilayer	Oxygen transport	Hasegawa et al., 1982; Tsuchida et al., 1984, 1988

transfusion with HbV-PEG/albumin (Sakai et al., 1997). Other Hb encapsulation protocols include polymersomes, hydrogels, or porous microparticles (Baudin-Creuzat et al., 2008; Piras et al., 2008; Jia et al., 2016).

Devineau et al. reported a new strategy to form Hb-based oxygen carriers by directly adsorbing Hb onto the surface of silica NPs (Devineau et al., 2018). The authors claimed that the tetrameric structure of Hb was retained for carrying oxygen and the Hb-silica NPs complex has the potential to prevent the release of free Hb, which may lead to acute renal toxicity.

In summary, the development of nanomedicine for the application of Hb-based oxygen carriers should meet the four requirements (Benitez Cardenas et al., 2017): efficient oxygen delivery, low rates of NO scavenging, resistance to oxidative degradation, and high production yields. Chemical modification (such as cross-linking) and nano-carrier assistance are two main approaches to develop Hb-based nanomedicines for carrying oxygen. Prior to clinical trials, the latter requires more characterizations on structure and stability and more efforts to ensure the Hb-loading rates (Jansman and Hosta-Rigau, 2018). While site-specific mutations of Hb molecules had been engineered to enhance oxygen affinity, the intact Hb molecules that maintain the tetrameric structure were adopted and integrated into artificial nanostructures, either being attached onto nanocarrier's surface or encapsulated inside the nanocarrier. PEGylation provide a better bio-compatibility and enhance retention time. On one hand, molecular engineering would design protective pockets or formations to prevent

oxidative molecules from penetrating the Hb, which leads to the degradation of Hb. On the other hand, adding antioxidation residues, such as tyrosine, into the mutated Hb molecule could lower the chance of autooxidation of Hb.

Non-hemoglobin-Based Red Blood Cells Substitutes

Perfluorocarbon-Based Blood Substitutes

Perfluorocarbons (PFCs) emulsions are the first hemoglobin-free RBC substitutes discovered by scientists. PFCs were found to have oxygen and deoxygenation functions. Perfluoro compounds are saturated fluorocarbon molecules that have strong oxygen affinity. In early clinical practice, PFCs emulsions were administered intravenously directly or *via* a carrier and then left in the liver. However, some PFCs molecules hardly remain in the liver and are rapidly excreted through the breath and skin. Unlike hemoglobin-dependent RBC substitutes, PFCs solutions are white and are therefore referred as white blood.

In 1975, Yokoyama et al. first prepared a low-toxicity perfluorodecalin emulsion (the structure is shown in **Table 1**), which eliminated the disadvantage of the previous perfluoro compound that it accumulates in the body due to poor metabolism (Yokoyama et al., 1975). Subsequently, Naito et al. (Naito and Yokoyama, 1978) prepared a mixed emulsion, namely Fluosol-DA emulsion (the structure is shown in **Table 1**), containing perfluorodecalin, perfluorotripropylamine, hydroxyethyl starch, and Krebs-Ringer bicarbonate solution. It showed a significantly increase of the amount of oxygen delivered

to the patient. Although it was prone to accumulate in the liver and spleen, it could be cleared by the lungs for a certain period of time (Tremper et al., 1980, 1982; Suyama et al., 1981; Spence et al., 1994). Fluosol-DA showed a high oxygen-carrying capacity, but its effectiveness appeared to be insufficient in certain critical situations, such as anemia patients with moderate and severe blood loss (Gould et al., 1986). Because of low durability and stability in the blood vessel as well as the complexity of configuration and use, continuing development of Fluosol-DA was hindered (Riess, 1992). Oxygent, i.e., perfluorooctyl bromide, is the second generation of PFCs emulsions and had been with a wide range of applications. Oxygent has more outstanding advantages than Fluosol-DA. First, it has a stronger oxygen carrying capacity. Second, it is more convenient to prepare and use without mixing different components. Third, it has a longer shelf life, i.e., it can be stored for more than 1 year at 5–8°C (Riess, 1992).

Keipert et al. investigated the feasibility of applying Oxygent as a blood substitute during surgery for patients under consciousness and anesthesia (Keipert, 1995). The results showed that in the state of continuous blood loss, the low level of Oxygent was able to ensure oxygen delivery, along with two side effects at high concentrations: body temperature rises (by 1–1.5°C in 4–6 h) and platelet count reducing. The results suggested that Oxygent could be used as a blood substitute for the patient of low-blood loss surgery. In addition to being an oxygen carrier, PFCs were found to selectively increase the radiation sensitivity of tumors, which could be beneficial for an adjuvant treatment of cancer (Teicher et al., 1992; Keipert, 1995). However, flu-like side effects were documented (Lane, 1995). In 1978, Sanders et al. synthesized a new PFCs compound, FC 75 (the structure is as shown in **Table 1**). Through potential measurement and program-induced hypoxia, FC-75 supplied oxygen to the nerves at the treatment site (Sanders and Schick, 1978). Motta et al. prepared an emulsion contains 20% perfluorotributylamine (see **Table 1** for chemical structure) in 1981 for blood replacement in rabbits (Motta et al., 1981). Rabbit vital signs showed normal within 24 h of transfusion, and tissue analysis results indicated that it could act as a good oxygen carrier, despite of low toxicity.

Dodecafluoropentane (DDFPe, see **Table 1** for chemical structure) is a special oxygen carrier with high oxygen affinity and transport capacity. It showed obvious protective effects on oxygen-dependent organs, such as brain and heart (Woods et al., 2013; Strom et al., 2014). Therefore, it has been developed for the treatment of brain damage and hemorrhagic shock (Moon-Massat et al., 2014). Intravascular fluorocarbon-stabilized microbubbles were reported to protect against fatal anemia in rats, since the oxygen carried in the microbubble was supplied for the brain functions for a certain period of time (Culp et al., 2015). As a carrier, DDFPe carries oxygen but also small molecule drugs at the same time. For example, thrombolytic drug tPA in a rabbit model of ischemic stroke or ischemic stroke (Nishioka et al., 1997; Borrelli et al., 2014). After targeted binding to blood clots suspended in the flow chamber, ultrasound was used to release oxygen or drugs. DDFPe mainly accumulates in the brain, but most of them can be removed within 2 h (Arthur et al.,

2017). In a more recent study, Bonanno et al. investigated the efficacy of the DDFPe as an adjunct to prehospital resuscitation (Bonanno et al., 2018). The authors found that adding DDFPe into fresh frozen platelet does not improve survival or enhance tissue oxygenation.

The study of pulmonary mechanics in ventilator-assisted PFCs treatment in animals were conducted. In 1991, Fuhrman BP et al. used a conventional ventilator to add a normal residual volume of PFCs solution (30 ml/kg) to the piglet trachea. It was found that PFCs were able to directly participate in normal gas exchange in the lungs and did not cause significant adverse effects on piglets (Fuhrman et al., 1991). Experiments in lambs with respiratory distress syndrome have also demonstrated the feasibility of this approach. When using conventional ventilators, PFCs promoted the release of oxygen and carbon dioxide, thereby increasing blood oxygen levels in lambs (Leach et al., 1993).

In the treatment of respiratory failure in rabbits caused by saline lung lavage, the incidence and mortality rates were higher when treated with positive respiratory mechanical ventilation than that with a series of perfluoroether aeration treatments (Tutuncu et al., 1993). It had been found that adequate lung gas exchange could be maintained for hours at lower airway pressures. In 1996, Gauger et al. first conducted a PFC preliminary trial of children with acute respiratory distress syndrome (Gauger et al., 1996). The tested patients were six children extracorporeal life support (ECLS). After 2–9 days of ECLS, PFCs were added into the trachea and perform PFCs-filled lung gas ventilation (partial fluid ventilation). The cumulative amount of PFCs was 45.2 ± 6.1 mL/kg (range 30–72.5). The results showed that ECLS patients had a brief, normal respiratory exchange in the presence of PFCs. This indicates that PFCs can be safely used in the lungs of children with severe respiratory failure. Likewise, Pranikoff et al. investigated the biocompatibility of a perflubron (perfluorobromooctane) *via* a safety test in neonates with congenital diaphragmatics and severe respiratory failure (Pranikoff et al., 1996). PFCs was reported to enhance partial pressure of oxygen in animals with abnormal lungs (Hernan et al., 1994; Tutuncu et al., 1996). These studies have shown that PFCs can improve lung function and reduce the cost of intensive care for lung diseases.

PFC is a safe and mature oxygen carrier that can be directly chemically synthesized and has been widely used in medical treatment. As mentioned earlier, PFC molecules are generally emulsified to form particles (in micro level) and to be used as an oxygen carrier, and the emulsifier eventually decomposes in the body. The oxygen transport of PFC particles was well-known with a linear relationship between PaO₂ and oxygen content, which contrasts with the sigmoidal oxygen dissociation of blood (Alam et al., 2014). Two main advantages of PFC-based oxygen transport to improve efficacy are: (a) PFC particles perfuse in the microcirculation of capillaries where no RBCs may flow; and (b) the oxygen carried by PFC particles is in dissolved state. Inspired by the PFC-based oxygen transport, PFC-base NPs were developed for multi-task nanomedicines, including bioimaging contrast agents and drug delivery carriers for diagnosis and treatment of diseases (Winter, 2014).

Heme-Based Blood Cell Substitute

Heme is a cyclic molecule composed of four pyrrole subunits surrounding a ferrous ion, which are most commonly recognized as one of the key components of hemoglobin. In the early studies, a ferrous porphyrin complex was embedded in a phospholipid bilayer of liposome to synthesize a liposome-heme complex (Tsuchida et al., 1988), as shown in **Table 1**. Tsuchida et al. converted the synthetic protohemoglobin into an amphiphilic heme molecule and encapsulated it in liposome. The liposome composite has a particle size of <0.1 micron. Compared to blood, the modified liposome heme has a faster oxygen reversible binding rate, a higher oxygen solubilization volume, and better stability. It also has smaller molecular weight than RBC. Artificial lung device test results indicate that the synthesized liposome heme can successfully deliver oxygen to muscle tissue (Tsuchida et al., 1988). The liposome heme molecule reversibly binds molecular oxygen in a neutral aqueous medium at 37°C. The oxygen adduct has an oxygen binding affinity ($p_{1/2}$) of about 50 mmHg and a half-life of half a day (Tsuchida et al., 1984). In addition, the iron (II) “picket fence porphyrin” complex with one hydrophobic imidazole is also incorporated into phosphatidylcholine molecules (the component of the phospholipid bilayer). Results have shown that The liposomal iron(II) porphyrin complex can be reversible with serum in the blood of rat at 25°C.

NANOMEDICINES FOR THE IMMUNE-RESPONSIVE COMPONENT

In the blood, white blood cells (WBCs) are directly related to the immune regulation. WBCs can be deployed to the invasion site of the pathogenic microorganism, surrounded by phagocytosis, or the surface antigen being presented, and the signal is transmitted to the B cell or the T cell to exert the immune regulation function of the human body. BBDs caused by imbalances in WBCs often lead to the problems with immune response.

WBCs are a general term for a vast variety of immune cells, which generally include granulocytes, monocytes and lymphocytes. Among them, monocytes are precursors of macrophages. Macrophages have two common phenotypes, M1 (classically activated macrophage) and M2 (alternative lyactivated macrophage). M1 releases killing substances or pro-inflammatory factors from exogenous microorganisms or tumor cells, which promotes Th1 response. M1 has a distinct feature of high expression of IL-12 and low expression of IL-10. M2 repairs damaged tissues or releases anti-inflammatory factors, promoting Th2 response and expressing high IL-10 and low IL-12.

During the process of tumor growth, macrophages are mostly converted to the M2 phenotype that promotes tumor growth, and the nuclear factor- κ -gene binding (NF- κ B) signal is down-regulated (Xiang et al., 2018). The patient's immune system is unable to effectively recognize antigenic substances and initialize proinflammatory responses, thereby facilitating the proliferation and metastasis of tumor cells. Studies have shown that the differentiation of macrophages into the M2

phenotype may be caused by prostaglandin E2 (PGE 2) and interleukin 6 (IL-6) produced by tumor cells (Heusinkveld et al., 2011). However, tumor-induced M2 cells could be retransformed into activated M1 cells by stimulation (Heusinkveld et al., 2011). This provides a new idea for the treatment of tumors. M2 type macrophages (e.g., tumor-associated macrophages, TAMs) have been reported to overexpress the mannose receptor (Bhargava and Lee, 2012). Zhu et al. invented a nanoplatform targeting TAMs (Zhu et al., 2013). The preparation process and characterization results of the poly(lactic-co-glycolic acid) (PLGA)-based NPs are shown in **Figure 1**. The biodegradable PLGA NPs were modified with mannose (targeting TAM) and PEG, as shown in **Table 2**. The results indicate that the NPs can be taken up by normal macrophages and the TAMs *via* being targeted by mannose and its receptor after exfoliating PEG molecules under acidic microenvironment conditions (favorable for tumor). The platform has the potential to carry and deliver cancer drugs Doxorubicin (DOX) to treat triple-negative breast cancer (TNBC) (Niu et al., 2016). The results showed that a single intravenous injection of the NPs significantly reduced the M2 macrophage population in the tumor within 2 days, and the density of macrophages slowly recovered. It could be more effective if multiple injection of NPs or pre-treatment with zoledronic acid was carried out.

Besides mannose, the targeting moiety could be cholesterol (Chen et al., 2013) or epidermal growth factor (EGF) (Zhang et al., 2016). Chen et al. used poly (amidoamine) to graft different percentages of cholesterol (rPAA-Ch) for siRNA delivery (Chen et al., 2013). The structure of NPs is shown in **Figure 2** and **Table 2**. The results showed that the Poly(amidoamine)-cholesterol polymer forms a stable nanocomposite that was taken up by cells and had a strong *in vivo* inhibitory effect for tumor growth. Zhang et al. simultaneously delivered DOX and B-cell lymphoma-2-small interfering RNA (Bcl-2-siRNA) with an EGF-modified NPs (as shown in **Table 2**) to investigate their therapeutic effects on lung cancer (Zhang et al., 2016).

NANOMEDICINES FOR HEMOSTASIS-RESPONSIVE COMPONENT

Platelets are the smallest cells in the blood and have no nucleus, generated from megakaryocytes in the bone marrow. Molecular mechanisms of platelet-mediated hemostasis include primary and secondary hemostasis (Sen Gupta, 2017). During the primary hemostasis, platelets bind rapidly to specific proteins (e.g., von Willebrand Factor) and collagen at the bleeding site, followed by inter-platelet crosslinking *via* fibrinogen, which is recognized by the active GPIIb-IIIa on the surface of platelet molecules; on the phosphoserine-rich surface of active platelets, fibrin is formed and deposited in the process of coagulation cascade. Taken together, such coagulation process includes activation, adhesion and aggregation of platelets, as well as deposition and maturation of fibrin. Poor coagulation can cause thrombocytopenia, and hypercoagulability can lead to thrombosis. In a bleeding complication case, natural platelets or platelet-derived products are offered for transfusion. Such

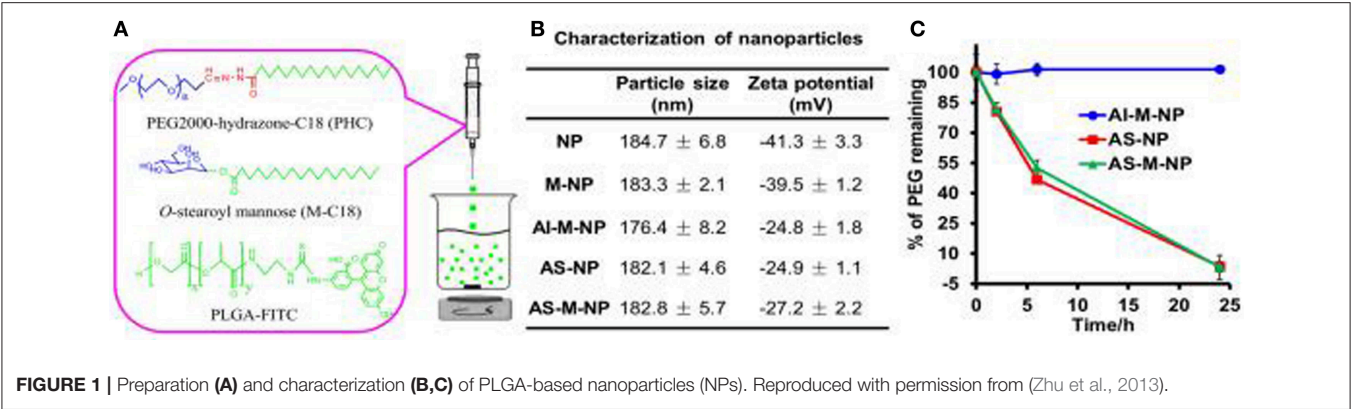


FIGURE 1 | Preparation (A) and characterization (B,C) of PLGA-based nanoparticles (NPs). Reproduced with permission from (Zhu et al., 2013).

TABLE 2 | Nanomedicines for the immune-responsive component.

Structure	Configuration	Application	References
	<p>The composite NPs consisted of PLGA and the fluorescent group FITC, which was then modified with M-C18 and PEGylated under the action of PHC</p> <p>Black spheres: nanoparticles; fold line: the modification; and yellow sphere: the fluorescent group FITC</p>	<p>Targeting tumor-associated macrophages</p> <p>Targeted drug delivery (DOX) to tumor sites for the treatment of triple-negative breast cancer</p>	<p>Zhu et al., 2013; Niu et al., 2016</p>
	<p>Polyamide-bonded NPs with a certain proportion of cholesterol molecules for siRNA delivery</p> <p>Black spheres represent nanoparticles. The black curve represents the cholesterol modification on the nanoparticles. The green helix is the siRNA carried by the nanoparticles</p>	<p>Targeting human breast cancer MCF-7 cell line and inhibiting tumor growth</p>	<p>Chen et al., 2013</p>
	<p>Carrying Dox and siRNA with synthetic PEAL polymer, and finally modifying with EGF</p> <p>Black spheres represent nanoparticles carrying siRNA and DOX. The blue curve represents the modification of the polyethylene glycol on the nanoparticles</p>	<p>Targeting mouse lung cancer cells, allowing cells to simultaneously take up siRNA and Dox, inhibiting the proliferation of cancer cells and the expression of Bcl-2 in tumor tissues</p>	<p>Zhang et al., 2016</p>

products suffer from short shelf-life, contamination, risks of infection/immunoreaction (unless prior serological testing was conducted). Artificial platelet-like biomaterials attract increasing attention to overcome such issues.

Platelet is of a micrometer size, loaded with thousands of biocomponents. Herein, scientists focus on the “platelet-inspired” nanomaterials that could function well as platelets during the hemostasis process and simplify the configuration of the nanomaterials. For instance, Jung et al. removed the content inside the platelet and obtained a natural aggregated platelet nanovesicles by using hypotonic ultrasound technology, which were then mixed with calcium chloride, thrombin, and membrane proteins to create a nano-aggregate (Jung et al., 2019) (as shown in **Table 3**). The nano-aggregate exert a hemostatic effect of platelets without causing an inflammatory reaction.

Recent developing trend would be from enhancing platelet adhesion and hemostatic plug formation to harness more platelet’s functions, such as clot contraction, and to build a

minimal system, i.e., artificial platelet (Majumder and Liu, 2017), which will be able to perform some essential functions of natural platelet, including vesicle encapsulation, attachment, fusion, and protein production. Platelet-like particles (PLPs) that are coupled to fibrin-binding antibodies had shown the capability to mimic natural platelet functions to bind the wound site, stabilize clot structure, and enhance clot formation (Brown et al., 2014). Further improvements enabled a core-shell PLP to facilitate temporal control over clot retraction (Sproul et al., 2018) and mimic the antimicrobial action of platelets by integrating with gold nanoparticles (Sproul et al., 2019), which may improve healing outcomes after hemostasis. A synthetic liposomal platelet surrogate, Syntho Plate, has shown bifunctional features, i.e., adhesion and aggregation, thanks to the integration of three peptides: von Willebrand Factor-binding peptide, collagen-binding peptide, and GPIIb-IIIa-binding fibrinogen-mimetic peptide (Shukla et al., 2017). The Syntho Plate was applied to animal testing after femoral artery injury, and the result showed

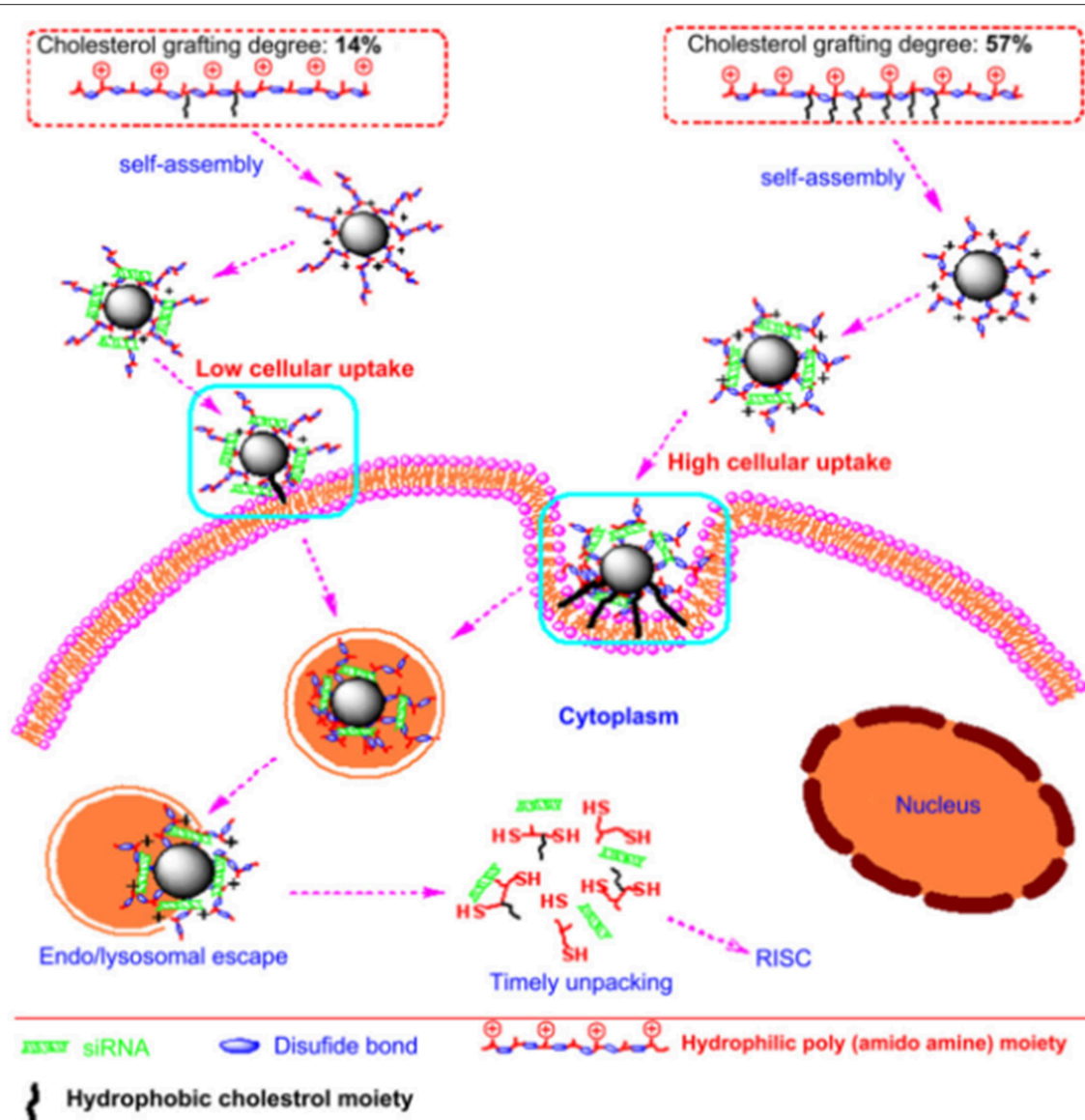


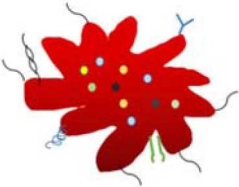
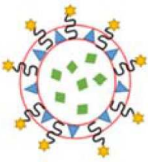

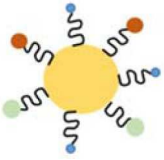
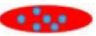
FIGURE 2 | Nanostructured siRNA-coated and mediated gene silencing. The Poly(amidoamine)-cholesterol polymer forms a stable nanocomposite that was taken up by cells and had a strong *in vivo* inhibitory effect for tumor growth. Reproduced with permission from Chen et al. (2013).

that blood loss was reduced, blood pressure was stabilized, and survival rate was improved (Hickman et al., 2018).

On the other hand, thrombosis, an abnormal aggregation of platelets, is highly likely to occur after surgery, such as coronary arteries. Ward et al. perforated platelets with high-pressure discharge, added ilocprost (drug) into the extra-platelet membrane, and then closed the membrane pores in a 37-degree warm bath for 40 min. Experiments in rabbits of atherosclerosis have shown that modified platelets can reduce platelet deposition by 64% in comparison with native platelets (Ward et al., 1995). Recently, platelet-targeting peptides- or small molecules-modified micelles/liposomes, shown in Table 3, were reported to deliver thrombolytic drugs to prevent platelet aggregation (Gupta et al., 2005; Yan et al., 2005; Modery

et al., 2011). Pan et al. developed a Amnextrin V-conjugated micelle that was synthesized with biodegradable polymer and loaded with lumbrokinase for phosphatidylserine thrombolysis (Pan et al., 2017). *In vitro* experiments have shown that such micelles are much more efficient in thrombolysis than the control group. *In vivo* experiments show that the micelles have good capability of targeting and thrombolysis. A PEGylated liposome, modified with a peptide of fibrinogen gamma chain (CQQHHLGGAKQAGDV) and loaded with thrombus-specific tissue plasminogen activator (tPA), was developed by Absar et al. (2013). *In vitro* and *in vivo* rat thrombolysis experiments demonstrated that the nano-liposomal vector targets activated platelets and rapidly releases tPA. Compared with natural tPA, such tPA-liposome complex increased the thrombus solubility

TABLE 3 | Nanomedicines for hemostatic-responsive component.

Main structure or composition	Configuration	Application	References
	Platelet-simulated NPs containing various ligands, small molecules, proteins and liposomes Radiation star when activated Various colored particles indicate that the simulated platelets contain multiple proteins and liposome small molecules (e.g., Cell mitogens, Hemostatic components, Adhesion molecules and antigens). A variety of ligands and modifications are modified on the surface of the nanoparticles (e.g., TP receptor and P-selectin)	Target cancer cells with certain adhesion	Modery-Pawlowski et al., 2013; Jung et al., 2019
	TRAL-Dox-PM-NV Dox-coated and TRAL modified on natural platelet vesicle membrane surface-modified platelet NPs Hollow round with blue double layer as platelet membrane. Green diamonds for DOX in hollow round interior. Yellow stars are modified by the platelet membrane to indicate TRAIL	Target tumor cells and induce apoptosis	Hu et al., 2015
	RGD peptide modified encapsulated melanin NPs and Dox nanoscale platelet vesicles Arrows represent RGD peptides modified on the surface of platelet nanoparticles. Black spheres represent melanin molecules Green stars represent DOX	Targeting tumor cells, supplemented by subsequent treatment, can alter multidrug resistance of tumor cells	Jing et al., 2018
	Protein or small molecule is modified on the surface of liposome NPs Yellow spheres as liposome nanoparticles. Red and green spheres represent different protein molecules modified on the nanoparticles, such as surface conjugated linear Arg-Gly-Asp (RGD) peptide moieties, fibrinogen gamma-chain. The blue sphere is represented as a small molecule modified on the nanoparticle. Such as 3'-O-Sulfated Le (a) [SO3Le (a)], integrin α (IIb) β (3), P-selectin	Delivery of thrombolytic drugs to prevent platelet aggregation	Gupta et al., 2005; Yan et al., 2005; Modery et al., 2011; Absar et al., 2013; Pan et al., 2017; Huang et al., 2019
	Inject small molecules directly into platelets by electroporation or other methods Natural platelet molecules are represented by a red ellipsoid. The blue sphere is represented by a small molecule such as DOX that is coated in platelets	Delivery of drugs Reduce platelet aggregation	Ward et al., 1995; Xu et al., 2017

by 35% and reduced the consumption of circulating protein fibrinogen by 4.3 times, which greatly improves the thrombolysis efficiency. Huang et al. synthesized a tPA-loaded PEGylated liposome, approximately 164.6 ± 5.3 nm in diameter (Huang et al., 2019). As shown in **Figure 3**, the surface was coated with cyclic arginine-glycine-aspartate (cRGD). The presence of activated platelets allows synthetic nanoliposomes to induce efficient fibrin clot lysis in the fibrin-agar plate model, and the concentration of activated platelets determines the extent of tPA release. The liposome membrane protected well the activity of tPA (retaining $97.4 \pm 1.7\%$ fibrinolytic activity) to achieve efficient thrombolysis.

On February 6, 2019, FDA approved Cablivi (caplacizumab-yhdp) injection (FDA, 2019a) in combination with plasma exchange and immunosuppressive therapy for the treatment

of adult patients with acquired thrombotic thrombocytopenic purpura (aTTP), a rare and life-threatening BDD. Patients with aTTP develop extensive blood clots in the small blood vessels throughout the body. Caplacizumab is a humanized, bivalent, variable domain-only immunoglobulin fragment, named “Nanobody” by Ablynx. It targets the A1 domain of von Willebrand factor, preventing interaction with the platelet glycoprotein Ib-IX-V receptor and the ensuing microvascular thrombosis (Callewaert et al., 2012; Scully et al., 2019).

PLATELET-INSPIRED NANOMEDICINES

The development of new nanomedicines, inspired by platelet, is beyond the two above-mentioned chapters. Some studies have shown that there is an interaction between platelets and

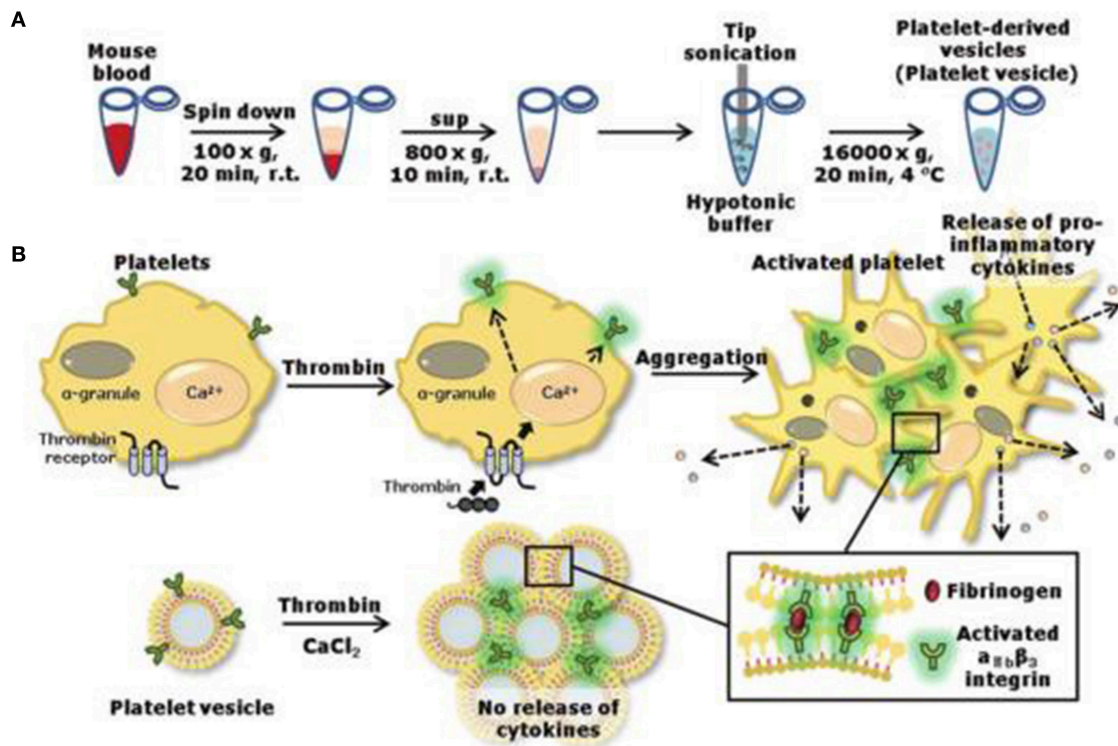


FIGURE 3 | Preparation (A) of nanovesicles and release (B) of pro-inflammatory factors. Reproduced with permission from Jung et al. (2019).

tumor cells. The formation of platelet-tumor cell aggregates and their sequestration in various end-organs may result in thrombocytopenia (Karparkin and Pearlstein, 1981; Mehta, 1984). In addition, platelet-derived factors secreted by platelets stimulate the proliferation of tumor cells, while secreting certain substances to increase vascular permeability is beneficial to the metastasis of tumor cells (Gasic et al., 1973; Karparkin and Pearlstein, 1981; Karparkin et al., 1988; Schumacher et al., 2013). Therefore, the unique interaction between platelet and tumor cells could be utilized by scientists for developing anti-cancer nanomedicines.

Modery-Pawłowski et al. designed a platelet mimetic (as shown in Table 3), loaded with ligands and other components, in order to investigate the interaction between such complex and metastatic cancer cells (Modery-Pawłowski et al., 2013). The results indicated that platelet mimics bind to cancer cells and exhibited greater cell targeting ability and adhesion for metastatic human breast cancer cell line MDA-MB-231 than cell line MCF-7. Hu et al. encapsulated the tumor-killing small molecule drug, Dox-NV, in a tumor necrosis factor-related apoptosis inducing ligand (TRAIL)-coated nanocarrier (TRAIL-Dox-PM-NV, as shown in Table 3) (Hu et al., 2015) that is formed with a platelet nanofilm, which was obtained by removing the internal contents. The results showed that the functionalized nanocarrier targeted tumor cells and induced apoptosis, as shown in Figure 4.

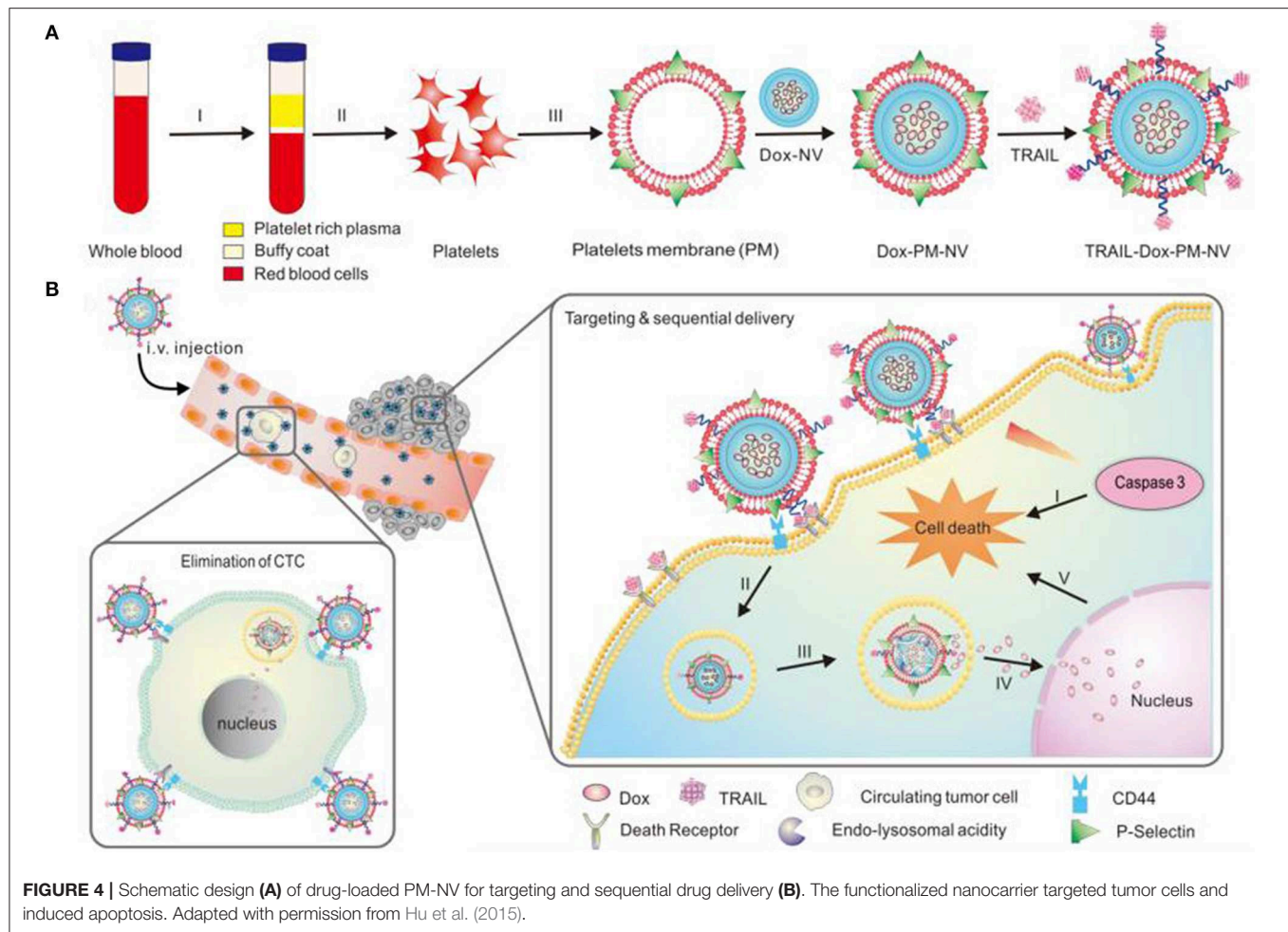
Jing et al. designed a nanoparticle, RGD-NPVs@MNPs/DOX (as shown in Table 3), for multidrug resistance (MDR) cancer

and performed *in vitro* experiments using different cell lines (Jing et al., 2018). The mixture of melanin NPs (MNPs) and RGD-modified platelet membrane was extruded by ultrasound to form a MNPs-loaded RGD-coated nano-platelet vesicle, followed by loading with DOX. The results showed that such vesicle can target and kill tumor cells.

Synthetic NPs may cause cytotoxicity to endothelial cells (Ilinskaya and Dobrovolskaia, 2013). Natural platelets therefore became an ideal drug delivery vehicle. Xu et al. encapsulated DOX in platelets through an open tubule system to make a DOX-platelet complex (as shown in Table 3) and conducted a series of experiments on Raji cells in the tumor-bearing mouse model (Xu et al., 2017). Compared to free DOX, DOX-platelets were able to target tumor cells and release more DOX at an acidic pH; the DOX-platelet stayed longer in the blood (half-life $t_{1/2} = 29.12 \pm 1.13$ h). Tissue distribution results showed that DOX released by DOX-platelet mostly exists in tumor cells, along with low residuals in the organs, such as heart, liver, spleen, kidney, and lungs. This indicates a strong anti-tumor effect.

CONCLUSIONS AND OUTLOOK

Nanomedicines is a hybrid term of nanotechnology and medicine, converting traditional small molecule medicine into a nano-sized carrier loaded with drug molecules or other therapeutic (bio)moieties and delivery system for disease treatment. As for BDDs treatment, a potential application



of nanomedicines is to offer artificial blood components, which may possess some advantages over blood: long shelf-life, good stability, and large-scale availability. On one hand, engineered or modified hemoglobin molecules, as well as hemoglobin-loaded liposome, were reported to serve as RBC substitute to carry oxygen. On the other hand, PFCs- or heme-based non-hemoglobin substitutes show different oxygen disassociation factors. The findings in the development of PFCs-base substitutes provide a mechanism guideline for future design of multifunctional PFCs nanomedicines (carrying oxygen, drug delivery, and bioimaging), as the PFCs nanoparticles had been approved by FDA for contrast agent in clinical applications. It has been realized that nanomedicines cannot replace the exact same role as the RBCs because the complicated components of the latter and the size difference. Nanomedicines may mimic the main features of the RBCs by integrating the functioning components into the nanocarrier. Likewise, artificial nanomedicines were designed to mimic the specific affinity (or binding) of WBCs or platelet in order to act as an immune- or hemostasis-responsive component. Inspired by the biocompatible platelet membrane, platelet-like functional

nanomedicines were developed and showed better drug delivery efficacy.

While scientists are dedicated to make “blood” *ex vitro* through stem cell research, it is also important to design nanomedicines for BDDs treatment. Researchers are trying to close the gap between artificial nanomedicine and natural blood components. Not only the potential toxicity of nanomedicines (e.g., activating immunoreaction), but also the complications of scale-down (from micro-size cell to nano-size system) and simplification of functioning components that may result in the lack of some comprehensive functions, shall be under consideration.

Some new drugs for BDDs treatment had been approved by FDA, including Elzonris (tagraxofusp-erzs) for BPDCN, Cablivi (caplacizumab-yhdp) for aTTP, and Jakafi (ruxolitinib) and Inrebic (fedratinib) for myelofibrosis (FDA, 2019b). These had set good examples for researchers, academic and industrial, to get a better understanding how to move forward the development and (pre)clinical trial of nanomedicine for BDDs treatment. It was 1995 that FDA approved the first nanomedicine (NPs drug), namely Doxil, yet no nanomedicines were approved for BDD treatment. A straightforward path will be to integrate the

approved drugs for BDDs treatment into a nanocarrier, forming a promising candidate of nanomedicine.

A critical step to move forward is from preclinical testing to clinical trial. Preclinical testing focuses mainly the characterization of nanomedicine. Prior to clinical trial, another challenging step for nanomedicine development for BDD treatment, as well as for other tumor/cancer treatment, is the scale-up manufacturing. It was estimated that an ~8% passing rate for nanomedicines, but only one fourth for small molecules drugs (Torrice, 2016). When used “blood disease” and “liposome” or “nanoparticles” to search on Clinicaltrials.gov, we obtained more than 150 open or active clinical trials. This is an exciting news for researchers working in this field.

A debating issue of nanomedicine development is the drug delivery efficiency of nanomedicines provoked by Chan's group (Wilhelm et al., 2016) in 2016, which documented that the number of nanomedicines reaching the tumor site was <1%. Some researchers or drug-makers argued that the retention time and maximum concentration at the tumor site are more important than the efficiency, and they, especially from a more practical perspective, were more intrigued to find ways to minimize the impact of nanomedicines on non-target organ

(Torrice, 2016), such as liver. Information gathered from this debate will also be an inevitable step for the nanomedicine development for BDDs treatment.

AUTHOR CONTRIBUTIONS

M-YW and QM oversee the content and writing of the manuscript and reviewed the finalized the manuscript. NZ wrote the draft.

FUNDING

This work was supported by the National Natural Science Foundation of China (21974129) and Natural Science Foundation of Beijing Municipality (8192049).

ACKNOWLEDGMENTS

M-YW acknowledges that all statements in this article do not represent any viewpoints from Texas Commission on Environmental Quality. All authors appreciate the constructive comments from reviewers.

REFERENCES

- Absar, S., Nahar, K., Kwon, Y. M., and Ahsan, F. (2013). Thrombus-targeted nanocarrier attenuates bleeding complications associated with conventional thrombolytic therapy. *Pharm. Res.* 30, 1663–1676. doi: 10.1007/s11095-013-1011-x
- Alam, F., Yadav, N., Ahmad, M., and Shadan, M. (2014). Blood substitutes: possibilities with nanotechnology. *Indian J. Hematol. Blood Transfus.* 30, 155–162. doi: 10.1007/s12288-013-0309-5
- Allegra, A., Innao, V., Penna, G., Gerace, D., Allegra, A. G., and Musolino, C. (2017). Telomerase and telomere biology in hematological diseases: a new therapeutic target. *Leuk. Res.* 56, 60–74. doi: 10.1016/j.leukres.2017.02.002
- Arthur, C., Song, L., Culp, W., Brown, A., Borrelli, M., Skinner, R., et al. (2017). Tissue Concentration of Dodecafluoropentane (DDEP) following repeated IV administration in the New Zealand White Rabbit. *AAPS J.* 19, 520–526. doi: 10.1208/s12248-016-0013-0
- Barcellini, W., and Zanella, A. (2011). Rituximab therapy for autoimmune haematological diseases. *Eur. J. Intern. Med.* 22, 220–229. doi: 10.1016/j.ejim.2010.12.016
- Baudin-Creuz, V., Chauvierre, C., Domingues, E., Kiger, L., Leclerc, L., Vasseur, C., et al. (2008). Octamers and nanoparticles as hemoglobin based blood substitutes. *Biochim. Biophys. Acta Proteins Proteomics* 1784, 1448–1453. doi: 10.1016/j.bbapap.2008.02.005
- Benitez Cardenas, A. S., Samuel, P. P., and Olson, J. S. (2017). Current challenges in the development of acellular hemoglobin oxygen carriers by protein engineering. *Shock* 52, 28–40. doi: 10.1097/SHK.0000000000001053
- Bhargava, P., and Lee, C. H. (2012). Role and function of macrophages in the metabolic syndrome. *Biochem. J.* 442, 253–262. doi: 10.1042/BJ20111708
- Biro, G. P., Taichman, G. C., Lada, B., Keon, W. J., Rosen, A. L., and Sehgal, L. R. (1988). Coronary vascular actions of stroma-free hemoglobin preparations. *Artif. Organs* 12, 40–50. doi: 10.1111/j.1525-1594.1988.tb01522.x
- Bjorkholm, M., Fagrell, B., Przybelski, R., Winslow, N., Young, M., Winslow, R., et al. (2005). A phase I single blind clinical trial of a new oxygen transport agent (MP4), human hemoglobin modified with maleimide-activated polyethylene glycol. *Haematologica* 90, 505–515. Available online at: <http://www.haematologica.org/content/90/4/505>
- (Torrice, 2016), such as liver. Information gathered from this debate will also be an inevitable step for the nanomedicine development for BDDs treatment.
- Bloomfield, E. L., Rady, M. Y., Popovich, M. J., Esfandiari, S., and Bedocs, N. M. (1996). Use of diaspirin cross-linked hemoglobin in critically ill patients. *Intensive Care Med.* 22:S105. doi: 10.1007/BF01921279
- Blum, J. L., Rosenblum, L. K., Grunig, G., Beasley, M. B., Xiong, J. Q., and Zelikoff, J. T. (2014). Short-term inhalation of cadmium oxide nanoparticles alters pulmonary dynamics associated with lung injury, inflammation, and repair in a mouse model. *Inhal. Toxicol.* 26, 48–58. doi: 10.3109/08958378.2013.851746
- Bonanno, A. M., Graham, T. L., Wilson, L. N., Madtson, B., and Ross, J. D. (2018). Efficacy of the perfluorocarbon dodecafluoropentane as an adjunct to pre-hospital resuscitation. *PLoS ONE* 13:e0207197. doi: 10.1371/journal.pone.0207197
- Borrelli, M. J., Hamilton, E., and Bernock, L. J. (2014). Dodecafluoropentane nanoemulsions produced with protein and lipid surfactants permit targeted oxygen and drug delivery, and help elucidate mechanisms of action. *J. Vasc. Interv. Radiol.* 25:S10. doi: 10.1016/j.jvir.2013.12.029
- Brown, A. C., Stabenfeldt, S. E., Ahn, B., Hannan, R. T., Dhada, K. S., Herman, E. S., et al. (2014). Ultrasoft microgels displaying emergent platelet-like behaviours. *Nat. Mater.* 13, 1108–1114. doi: 10.1038/nmat4066
- Callewaert, F., Roodt, J., Ulrichs, H., Stohr, T., van Rensburg, W. J., Lamprecht, S., et al. (2012). Evaluation of efficacy and safety of the anti-VWF Nanobody ALX-0681 in a preclinical baboon model of acquired thrombotic thrombocytopenic purpura. *Blood* 120, 3603–3610. doi: 10.1182/blood-2012-04-420943
- Caster, J. M., Patel, A. N., Zhang, T., and Wang, A. (2017). Investigational nanomedicines in 2016: a review of nanotherapeutics currently undergoing clinical trials. *Wiley Interdiscip. Rev. Nanomed. Nanobiotechnol.* 9:e1416. doi: 10.1002/wnan.1416
- Chen, C. J., Wang, J. C., Zhao, E. Y., Gao, L. Y., Feng, Q., Liu, X. Y., et al. (2013). Self-assembly cationic nanoparticles based on cholesterol-grafted bioreducible poly(amidoamine) for siRNA delivery. *Biomaterials* 34, 5303–5316. doi: 10.1016/j.biomaterials.2013.03.056
- Cooper, C. E., Silkstone, G. G. A., Simons, M., Rajagopal, B., Syrett, N., Shaik, T., et al. (2019). Engineering tyrosine residues into hemoglobin enhances heme reduction, decreases oxidative stress and increases vascular retention of a hemoglobin based blood substitute. *Free Radical Biol. Med.* 134, 106–118. doi: 10.1016/j.freeradbiomed.2018.12.030
- Culp, W. C., Brown, A. T., Lowery, J. D., Arthur, M. C., Roberson, P. K., and Skinner, R. D. (2015). Dodecafluoropentane emulsion extends window

- for tPA therapy in a rabbit stroke model. *Mol. Neurobiol.* 52, 979–984. doi: 10.1007/s12035-015-9243-x
- Devineau, S., Kiger, L., Galacteros, F., Baudin-Creuz, V., Marden, M., Renault, J. P., et al. (2018). Manipulating hemoglobin oxygenation using silica nanoparticles- a novel prospect for artificial oxygen carriers. *Blood Adv.* 2, 90–94. doi: 10.1182/bloodadvances.2017012153
- Dong, F., Hall, C. H., Golech, S. A., Philbin, N. B., Rice, J. P., Gurney, J., et al. (2006). Immune effects of resuscitation with HBOC-201, a hemoglobin-based oxygen carrier, in swine with moderately severe hemorrhagic shock from controlled hemorrhage. *Shock* 25, 50–55. doi: 10.1097/01.shk.0000187982.56030.94
- Farber, S., and Diamond, L. K. (1948). Temporary remissions in acute leukemia in children produced by folic acid antagonist, 4-aminopteroyl-glutamic acid. *N. Engl. J. Med.* 238, 787–793. doi: 10.1056/NEJM194806032382301
- FDA (2018). *FDA Approves First Treatment for Rare Blood Disease*. FDA Newsroom. Retrieved January 1st, 2019. Available online at: <https://www.fda.gov/news-events/press-announcements/fda-approves-first-therapy-treat-patients-rare-blood-disorder>
- FDA (2019a). *FDA Approves First Therapy for the Treatment of Adult Patients With a Rare Blood Clotting Disorder*. Available online at: <https://www.fda.gov/news-events/press-announcements/fda-approves-first-therapy-treat-patients-rare-blood-disorder>
- FDA (2019b). *FDA Approves Treatment for Patients With Rare Bone Marrow Disorder*. Available online at: <https://www.fda.gov/news-events/press-announcements/fda-approves-treatment-patients-rare-bone-marrow-disorder>
- Freilich, D., Pearce, L. B., Pitman, A., Greenburg, G., Berzins, M., Bebris, L., et al. (2009). HBOC-201 vasoactivity in a phase III clinical trial in orthopedic surgery subjects—extrapolation of potential risk for acute trauma trials. *J. Trauma* 66, 365–376. doi: 10.1097/TA.0b013e3181820d5c
- Friedman, H., DeVenuto, F., Lollini, L., Mellick, P., and Zuck, T. F. (1979). Morphologic effects following massive exchange transfusions with a stroma-free hemoglobin solution. II. Kidney. *Lab. Invest.* 40, 655–667.
- Friedman, H. I., DeVenuto, F., Lollini, L., Mellick, P., and Zuck, T. F. (1978). Morphologic effects following massive exchange transfusions with a stroma-free hemoglobin solution. I. Liver. *Lab. Invest.* 39, 167–177.
- Fuhrman, B. P., Paczan, P. R., and DeFrancis, M. (1991). Perfluorocarbon-associated gas exchange. *Crit. Care Med.* 19, 712–722. doi: 10.1097/00003246-199105000-00019
- Gasic, G. J., Gasic, T. B., Galanti, N., Johnson, T., and Murphy, S. (1973). Platelet-tumor-cell interactions in mice. The role of platelets in the spread of malignant disease. *Int. J. Cancer* 11, 704–718. doi: 10.1002/ijc.2910110322
- Gauger, P. G., Pranikoff, T., Schreiner, R. J., Moler, F. W., and Hirschl, R. B. (1996). Initial experience with partial liquid ventilation in pediatric patients with the acute respiratory distress syndrome. *Crit. Care Med.* 24, 16–22. doi: 10.1097/00003246-199601000-00006
- Gould, S. A., Moore, E. E., Hoyt, D. B., Burch, J. M., Haenel, J. B., Garcia, J., et al. (1998). The first randomized trial of human polymerized hemoglobin as a blood substitute in acute trauma and emergent surgery. *J Am Coll Surg* 187, 113–120; discussion 120–112. doi: 10.1016/S1072-7515(98)00095-7
- Gould, S. A., Moore, E. E., Hoyt, D. B., Ness, P. M., Norris, E. J., Carson, J. L., et al. (2002). The life-sustaining capacity of human polymerized hemoglobin when red cells might be unavailable. *J Am Coll Surg* 195, 445–452; discussion 452–445. doi: 10.1016/S1072-7515(02)01335-2
- Gould, S. A., Rosen, A. L., Sehgal, L. R., Sehgal, H. L., Langdale, L. A., Krause, L. M., et al. (1986). Fluosol-DA as a red-cell substitute in acute anemia. *N. Engl. J. Med.* 314, 1653–1656. doi: 10.1056/NEJM198606263142601
- Greening, D. W., Glenister, K. M., Sparrow, R. L., and Simpson, R. (2010). International blood collection and storage: clinical use of blood products. *J. Proteomics* 73, 386–395. doi: 10.1016/j.jprot.2009.07.011
- Gupta, A. S., Huang, G., Lestini, B. J., Sagnella, S., Kottke-Marchant, K., and Marchant, R. E. (2005). RGD-modified liposomes targeted to activated platelets as a potential vascular drug delivery system. *Thromb. Haemost.* 93, 106–114. doi: 10.1160/TH04-06-0340
- Hasegawa, E., Matsushita, Y., Kaneda, M., Ejima, K., and Tsuchida, E. (1982). Liposomal heme as oxygen carrier under semiphysiological condition. *Biochem. Biophys. Res. Commun.* 105, 1416–1419. doi: 10.1016/0006-291X(82)90945-7
- Hernan, L. J., Fuhrman, B. P., Papo, M. C., Leach, C. L., Thompson, A. E., Nesti, F. D., et al. (1994). Oxygenation during perfluorocarbon associated gas exchange in normal and abnormal lungs. *Artif. Cells Blood Substit. Immobil. Biotechnol.* 22, 1377–1380. doi: 10.3109/10731199409138840
- Hess, J. R. (2006). An update on solutions for red cell storage. *Vox Sang.* 91, 13–19. doi: 10.1111/j.1423-0410.2006.00778.x
- Heusinkveld, M., de Vos van Steenwijk, P. J., Goedemans, R., Ramwadhoebe, T. H., Gorter, A., Welters, M. J., et al. (2011). M2 macrophages induced by prostaglandin E2 and IL-6 from cervical carcinoma are switched to activated M1 macrophages by CD4+ Th1 cells. *J. Immunol.* 187, 1157–1165. doi: 10.4049/jimmunol.1100889
- Hickman, D. A., Pawlowski, C. L., Shevitz, A., Luc, N. F., Kim, A., Girish, A., et al. (2018). Intravenous synthetic platelet (SynthoPlate) nanoconstructs reduce bleeding and improve 'golden hour' survival in a porcine model of traumatic arterial hemorrhage. *Sci. Rep.* 8:3118. doi: 10.1038/s41598-018-21384-z
- Hu, Q., Sun, W., Qian, C., Wang, C., Bomba, H. N., and Gu Z. (2015). Anticancer platelet-mimicking nanovehicles. *Adv. Mater. Weinheim.* 27, 7043–7050. doi: 10.1002/adma.201503323
- Huang, Y., Yu, L., Ren, J., Gu, B., Longstaff, C., Hughes, A., et al. (2019). An activated-platelet-sensitive nanocarrier enables targeted delivery of tissue plasminogen activator for effective thrombolytic therapy. *J. Control. Release* 300, 1–12. doi: 10.1016/j.jconrel.2019.02.033
- Ilinskaya, A. N., and Dobrovolskaia, M. A. (2013). Nanoparticles and the blood coagulation system. Part II: safety concerns. *Nanomedicine* 8, 969–981. doi: 10.2217/nnm.13.49
- Jansman, M. M. T., and Hosta-Rigau, L. (2018). Recent and prominent examples of nano- and microarchitectures as hemoglobin-based oxygen carriers. *Adv. Colloid Interface Sci.* 260, 65–84. doi: 10.1016/j.cis.2018.08.006
- Jen, E. Y., Gao, X., Li, L., Zhuang, L., Simpson, N. E., et al. (2019). FDA approval summary: tagraxofusp-erzs for treatment of blastic plasmacytoid dendritic cell neoplasm. *Clin. Cancer Res. ClinCanres.* doi: 10.1158/1078-0432.CCR-19-2329 Available online at: <https://clincancerres.aacrjournals.org/content/early/2019/09/21/1078-0432.CCR-19-2329>
- Jia, Y., Duan, L., and Li, J. (2016). Hemoglobin-based nanoarchitectonic assemblies as oxygen carriers. *Adv. Mater. Weinheim.* 28, 1312–1318. doi: 10.1002/adma.201502581
- Jing, L., Qu, H., Wu, D., Zhu, C., Yang, Y., Jin, X., et al. (2018). Platelet-camouflaged nanococktail: Simultaneous inhibition of drug-resistant tumor growth and metastasis via a cancer cells and tumor vasculature dual-targeting strategy. *Theranostics* 8, 2683–2695. doi: 10.7150/thno.23654
- Jung, H., Kang, Y. Y., and Mok, H. (2019). Platelet-derived nanovesicles for hemostasis without release of pro-inflammatory cytokines. *Biomater. Sci.* 7, 856–859. doi: 10.1039/C8BM01480A
- Jurek, S. C., Hirano-Kobayashi, M., Chiang, H., Kohane, D. S., and Matthews, B. D. (2014). Prevention of ventilator-induced lung edema by inhalation of nanoparticles releasing ruthenium red. *Am. J. Respir. Cell Mol. Biol.* 50, 1107–1117. doi: 10.1165/rcmb.2013-0163OC
- Kaplan, H. R., and Murthy, V. S. (1975). Hemoglobin solution: a potential oxygen transporting plasma volume expander. *Fed. Proc.* 34, 1461–1465.
- Karparkin, S., and Pearlstein, E. (1981). Role of platelets in tumor cell metastases. *Ann. Intern. Med.* 95, 636–641. doi: 10.7326/0003-4819-95-5-636
- Karparkin, S., Pearlstein, E., Ambrogio, C., and Collier, B. S. (1988). Role of adhesive proteins in platelet tumor interaction *in vitro* and metastasis *in vivo*. *J. Clin. Invest.* 81, 1012–1019. doi: 10.1172/JCI113411
- Keipert, P. E. (1995). Use of Oxygent, a perfluorochemical-based oxygen carrier, as an alternative to intraoperative blood transfusion. *Artif. Cells Blood Substit. Immobil. Biotechnol.* 23, 381–394. doi: 10.3109/10731199509117954
- Kothe, N., Eichentopf, B., and Bonhard, K. (1985). Characterization of a modified, stroma-free hemoglobin solution as an oxygen-carrying plasma substitute. *Surg. Gynecol. Obstet.* 161, 563–569.
- Lane, T. A. (1995). Perfluorochemical-based artificial oxygen carrying red cell substitutes. *Transfus. Sci.* 16, 19–31. doi: 10.1016/0955-3886(94)00067-T
- Lang, M. E., Korecky, B., Anderson, P. J., and Biro, G. P. (1990). Stroma-free hemoglobin solutions prepared by crystallization and ultrafiltration methods; comparison of composition and coronary vasoconstrictor potency. *Adv. Exp. Med. Biol.* 277, 225–236. doi: 10.1007/978-1-4684-8181-5_28
- Leach, C. L., Fuhrman, B. P., Morin, F. C. 3rd, and Rath, M. G. (1993). Perfluorocarbon-associated gas exchange (partial liquid ventilation) in

- respiratory distress syndrome: a prospective, randomized, controlled study. *Crit. Care Med.* 21, 1270–1278. doi: 10.1097/00003246-199309000-00008
- Levy, J. H., Goodnough, L. T., Greilich, P. E., Parr, G. V., Stewart, R. W., Gratz, I., et al. (2002). Polymerized bovine hemoglobin solution as a replacement for allogeneic red blood cell transfusion after cardiac surgery: results of a randomized, double-blind trial. *J. Thorac. Cardiovasc. Surg.* 124, 35–42. doi: 10.1067/mtc.2002.121505
- Lim, Y. H., Tiemann, K. M., Hunstad, D. A., Elsbahy, M., and Wooley, K. L. (2016). Polymeric nanoparticles in development for treatment of pulmonary infectious diseases. *Wiley Interdiscip. Rev. Nanomed. Nanobiotechnol.* 8, 842–871. doi: 10.1002/wnan.1401
- Mackenzie, C. F., Moon-Massat, P. F., Shander, A., Javidrooz, M., and Greenburg, A. G. (2010). When blood is not an option: factors affecting survival after the use of a hemoglobin-based oxygen carrier in 54 patients with life-threatening anemia. *Anesth. Analg.* 110, 685–693. doi: 10.1213/ANE.0b013e3181cd473b
- Maeda, T., Kusumi, E., Kami, M., Kawabata, M., Le Pavoux, A., Hara, S., et al. (2005). Disseminated tuberculosis following reduced-intensity cord blood transplantation for adult patients with hematological diseases. *Bone Marrow Transplant.* 35, 91–97. doi: 10.1038/sj.bmt.1704740
- Maggio, A. (2007). Light and shadows in the iron chelation treatment of haematological diseases. *Br. J. Haematol.* 138, 407–421. doi: 10.1111/j.1365-2141.2007.06666.x
- Majumder, S., and Liu, A. P. (2017). Bottom-up synthetic biology: modular design for making artificial platelets. *Phys. Biol.* 15:013001. doi: 10.1088/1478-3975/aa9768
- Marrache, S., and Dhar, S. (2013). Biodegradable synthetic high-density lipoprotein nanoparticles for atherosclerosis. *Proc. Natl. Acad. Sci. U.S.A.* 110, 9445–9450. doi: 10.1073/pnas.1301929110
- Mehta, P. (1984). Potential role of platelets in the pathogenesis of tumor metastasis. *Blood* 63, 55–63. doi: 10.1182/blood.V63.1.55.bloodjournal63155
- Modery, C. L., Ravikumar, M., Wong, T. L., Dzuricky, M. J., Durongkaveroj, N., and Sen Gupta, A. (2011). Heteromultivalent liposomal nanoconstructs for enhanced targeting and shear-stable binding to active platelets for site-selective vascular drug delivery. *Biomaterials* 32, 9504–9514. doi: 10.1016/j.biomaterials.2011.08.067
- Modery-Pawlowski, C. L., Master, A. M., Pan, V., Howard, G. P., and Sen Gupta, A. (2013). A platelet-mimetic paradigm for metastasis-targeted nanomedicine platforms. *Biomacromolecules* 14, 910–919. doi: 10.1021/bm301996p
- Moon-Massat, P. F., Abutarboush, R., Pappas, G., Haque, A., Aligbe, C., Arnaud, F., et al. (2014). Effects of perfluorocarbon dodecafluoropentane (NVX-108) on cerebral microvasculature in the healthy rat. *Curr. Drug Discov. Technol.* 11, 220–226. doi: 10.2174/1570163811666140709110301
- Motta, G., Ratto, G. B., Spinelli, E., Burlando, F., Agati, R., Poloniato, G., et al. (1981). Experimental research on the use of fluorocarbon compounds (FC 43) as blood substitutes. *Boll. Soc. Ital. Biol. Sper.* 57, 2529–2535.
- Naito, R., and Yokoyama, K. (1978). An improved perfluorodecalin emulsion. *Prog. Clin. Biol. Res.* 19, 81–89.
- Nho, G., Glower, D., Bredehoeft, S., Shankar, H., Shorr, R., and Abuchowski, A. (1992). PEG-bovine hemoglobin: safety in a canine dehydrated hypovolemic-hemorrhagic shock model. *Biomater. Artif. Cells Immobilization Biotechnol.* 20, 511–524. doi: 10.3109/10731199209119677
- Nishioka, T., Luo, H., Fishbein, M. C., Cercek, B., Forrester, J. S., Kim, C. J., et al. (1997). Dissolution of thrombotic arterial occlusion by high intensity, low frequency ultrasound and dodecafluoropentane emulsion: an *in vitro* and *in vivo* study. *J. Am. Coll. Cardiol.* 30, 561–568. doi: 10.1016/S0735-1097(97)00182-4
- Niu, M., Valdes, S., Naguib, Y. W., Hurlsting, S. D., and Cui, Z. (2016). Tumor-associated macrophage-mediated targeted therapy of triple-negative breast cancer. *Mol. Pharm.* 13, 1833–1842. doi: 10.1021/acs.molpharmaceut.5b00987
- Olofsson, C., Ahl, T., Johansson, T., Larsson, S., Nellgard, P., Ponzer, S., et al. (2006). A multicenter clinical study of the safety and activity of maleimide-polyethylene glycol-modified Hemoglobin (Hemospan) in patients undergoing major orthopedic surgery. *Anesthesiology* 105, 1153–1163. doi: 10.1097/0000542-200612000-00015
- Osborn, M. J., Webber, B. R., Knipping, F., Lonetree, C. L., Tennis, N., DeFeo, A. P., et al. (2016). Evaluation of TCR gene editing achieved by TALENs, CRISPR/Cas9, and megaTAL nucleases. *Mol. Ther.* 24, 570–581. doi: 10.1038/mt.2015.197
- Pan, Y., Ren, X., Wang, S., Li, X., Luo, X., and Yin, Z. (2017). Annexin V-conjugated mixed micelles as a potential drug delivery system for targeted thrombolysis. *Biomacromolecules* 18, 865–876. doi: 10.1021/acs.biomac.6b01756
- Pelosi, E., Castelli, G., and Testa, U. (2012). Human umbilical cord is a unique and safe source of various types of stem cells suitable for treatment of hematological diseases and for regenerative medicine. *Blood Cells Mol. Dis.* 49, 20–28. doi: 10.1016/j.bcmd.2012.02.007
- Piras, A. M., Dessy, A., Chiellini, F., Chiellini, E., Farina, C., Ramelli, M., et al. (2008). Polymeric nanoparticles for hemoglobin-based oxygen carriers. *Biochim. Biophys. Acta* 1784, 1454–1461. doi: 10.1016/j.bbapap.2008.03.013
- Pranikoff, T., Gauger, P. G., and Hirschl, R. B. (1996). Partial liquid ventilation in newborn patients with congenital diaphragmatic hernia. *J. Pediatr. Surg.* 31, 613–618. doi: 10.1016/S0022-3468(96)90659-4
- Przybelski, R. J., Daily, E. K., Kisicki, J. C., Mattia-Goldberg, C., Bounds, M. J., and Colburn, W. A. (1996). Phase I study of the safety and pharmacologic effects of diaspirin cross-linked hemoglobin solution. *Crit. Care Med.* 24, 1993–2000. doi: 10.1097/00003246-199612000-00011
- Przybelski, R. J., Daily, E. K., Michels, J., Sloan, E., Mols, P., Corne, L., et al. (1999). A safety assessment of diaspirin cross-linked hemoglobin (DCLHb) in the treatment of hemorrhagic, hypovolemic shock. *Prehosp. Disaster Med.* 14, 251–264. doi: 10.1017/S1049023X00027722
- Quintana, A., Raczka, E., Piehler, L., Lee, I., Myc, A., Majoros, I., et al. (2002). Design and function of a dendrimer-based therapeutic nanodevice targeted to tumor cells through the folate receptor. *Pharm. Res.* 19, 1310–1316. doi: 10.1023/A:1020398624602
- Reppucci, A. J., Mattia-Goldberg, C., Przybelski, R. J., Kuczerpa, P. R., and Balma, D. L. (1997). The effects of diaspirin-crosslinked hemoglobin on the assessment of immunohematology profiles. *Transfusion* 37, 1143–1148. doi: 10.1046/j.1537-2995.1997.37111298088043.x
- Riess, J. G. (1992). Fluorocarbon emulsions as injectable oxygen carriers. Recent progress and perspectives. *Rev. Fr. Transfus. Hemobiol.* 35, 391–406. doi: 10.1016/S1140-4639(05)80146-7
- Sakai, H., Takeoka, S., Park, S. I., Kose, T., Nishide, H., Izumi, Y., et al. (1997). Surface modification of hemoglobin vesicles with poly(ethylene glycol) and effects on aggregation, viscosity, and blood flow during 90% exchange transfusion in anesthetized rats. *Bioconjug. Chem.* 8, 23–30. doi: 10.1021/bc960069p
- Sanders, K., and Schick, E. (1978). Fluorocarbon FC 75: a new bathing medium for *in vivo* recordings in neurophysiology. *Neurosci. Lett.* 8, 269–272. doi: 10.1016/0304-3940(78)90134-9
- Schubert, A., O'Hara, J. F. Jr., Przybelski, R. J., Tetzlaff, J., Marks, K. E., Mascha, E., et al. (2002). Effect of diaspirin crosslinked hemoglobin (DCLHb HemAssist) during high blood loss surgery on selected indices of organ function. *Artif. Cells Blood Substit. Immobil. Biotechnol.* 30, 259–283. doi: 10.1081/BIO-120006118
- Schubert, A., Przybelski, R. J., Eidt, J. F., Lasky, L. C., Marks, K. E., Karafa, M., et al. (2003). Diaspirin-crosslinked hemoglobin reduces blood transfusion in noncardiac surgery: a multicenter, randomized, controlled, double-blinded trial. *Anesth. Analg.* 97, 323–332. doi: 10.1213/01.ANE.0000068888.02977.DA
- Schumacher, D., Strilic, B., Sivaraj, K. K., Wettschreck, N., and Offermanns, S. (2013). Platelet-derived nucleotides promote tumor-cell transendothelial migration and metastasis via P2Y2 receptor. *Cancer Cell* 24, 130–137. doi: 10.1016/j.ccr.2013.05.008
- Scully, M., Cataland, S. R., Peyvandi, F., Coppo, P., Knöbl, P., Kremer Hovinga, J. A., et al. (2019). Caplacizumab treatment for acquired thrombotic thrombocytopenic purpura. *N. Engl. J. Med.* 380, 335–346. doi: 10.1056/NEJMoa1806311
- Sen Gupta, A. (2017). Bio-inspired nanomedicine strategies for artificial blood components. *Wiley Interdiscip. Rev. Nanomed. Nanobiotechnol.* 9:e1464. doi: 10.1002/wnan.1464
- Shukla, M., Sekhon, U. D., Betapudi, V., Li, W., Hickman, D. A., Pawlowski, C. L., et al. (2017). *In vitro* characterization of SynthoPlate (synthetic platelet) technology and its *in vivo* evaluation in severely thrombocytopenic mice. *J. Thromb. Haemost.* 15, 375–387. doi: 10.1111/jth.13579
- Sloan, E. P., Koenigsberg, M., Gens, D., Cipolle, M., Runge, J., Mallory, M. N., and Rodman, G., Jr. (1999). Diaspirin cross-linked hemoglobin (DCLHb) in the treatment of severe traumatic hemorrhagic shock: a randomized controlled efficacy trial. *JAMA* 282, 1857–1864. doi: 10.1001/jama.282.19.1857

- Spence, R. K., Norcross, E. D., Costabile, J., McCoy, S., Cernaianu, A. C., Alexander, J. B., et al. (1994). Perfluorocarbons as blood substitutes: the early years. Experience with Fluosol DA-20% in the 1980s. *Artif. Cells Blood Substit. Immobil. Biotechnol.* 22, 955–963. doi: 10.3109/10731199409138794
- Sproul, E. P., Nandi, S., Chee, E., Sivadnam, S., Igo, B. J., Schreck, L., et al. (2019). Development of biomimetic antimicrobial platelet-like particles comprised of microgel nanogold composites. *Regenerat. Eng. Transl. Med.* doi: 10.1007/s40883-019-00121-6
- Sproul, E. P., Nandi, S., Roosa, C., Schreck, L., and Brown, A. C. (2018). Biomimetic microgels with controllable deformability improve healing outcomes. *Adv. Biosyst.* 2:1800042. doi: 10.1002/adbi.201800042
- Strom, J., Swyers, T., Wilson, D., Unger, E., Chen, Q. M., and Larson, D. F. (2014). Dodecafluoropentane emulsion elicits cardiac protection against myocardial infarction through an ATP-Sensitive K⁺ channel dependent mechanism. *Cardiovasc. Drugs Ther.* 28, 541–547. doi: 10.1007/s10557-014-6557-2
- Suyama, T., Yokoyama, K., and Naito, R. (1981). Development of a perfluorochemical whole blood substitute (Fluosol-DA, 20%)—an overview of clinical studies with 185 patients. *Prog. Clin. Biol. Res.* 55, 609–628.
- Teicher, B. A., Herman, T. S., and Menon, K. (1992). Enhancement of fractionated radiation therapy by an experimental concentrated perflubron emulsion (Oxygent) in the Lewis lung carcinoma. *Biomater. Artif. Cells Immobilization Biotechnol.* 20, 899–902. doi: 10.3109/10731199209119737
- Torrice, M. (2016). Does nanomedicine have a delivery problem? *ACS Cent Sci* 2, 434–437. doi: 10.1021/acscentsci.6b00190
- Townes, T. M. (2008). Gene replacement therapy for sickle cell disease and other blood disorders. *Hematol. Am. Soc. Hematol. Educ. Program* 1, 193–196. doi: 10.1182/asheducation-2008.1.193
- Tremper, K. K., Friedman, A. E., Levine, E. M., Lapin, R., and Camarillo, D. (1982). The preoperative treatment of severely anemic patients with a perfluorochemical oxygen-transport fluid, Fluosol-DA. *N. Engl. J. Med.* 307, 277–283. doi: 10.1056/NEJM198207293070503
- Tremper, K. K., Lapin, R., Levine, E., Friedman, A., and Shoemaker, W. C. (1980). Hemodynamic and oxygen transport effects of a perfluorochemical blood substitute, fluosol-DA (20%). *Crit. Care Med.* 8, 738–741. doi: 10.1097/00003246-198012000-00009
- Tsuchida, E., Nishide, H., and Ohno, H. (1988). Liposome/heme as a totally synthetic oxygen carrier. *Biomater. Artif. Cells Artif. Organs* 16, 313–319. doi: 10.3109/10731198809132580
- Tsuchida, E., Nishide, H., Yuasa, M., Hasegawa, E., and Matsushita, Y. (1984). Liposomal heme as oxygen carrier under semi-physiological conditions. *J. Chem. Soc., Dalton Trans.* 105, 1147–1151. doi: 10.1039/DT9840001147
- Tutuncu, A. S., Akpir, K., Mulder, P., Erdmann, W., and Lachmann, B. (1993). Intratracheal perfluorocarbon administration as an aid in the ventilatory management of respiratory distress syndrome. *Anesthesiology* 79, 1083–1093. doi: 10.1097/0000542-199311000-00027
- Tutuncu, A. S., Houmes, R. J., Bos, J. A., Wollmer, P., and Lachmann, B. (1996). Evaluation of lung function after intratracheal perfluorocarbon administration in healthy animals. *Crit. Care Med.* 24, 274–279. doi: 10.1097/00003246-199602000-00016
- Vandegriff, K. D., Malavalli, A., Mkrtchyan, G. M., Spann, S. N., Baker, D. A., and Winslow, R. M. (2008). Sites of modification of hemospan, a poly(ethylene glycol)-modified human hemoglobin for use as an oxygen therapeutic. *Bioconjug. Chem.* 19, 2163–2170. doi: 10.1021/bc8002666
- Vandegriff, K. D., and Winslow, R. M. (2009). Hemospan: design principles for a new class of oxygen therapeutic. *Artif. Organs* 33, 133–138. doi: 10.1111/j.1525-1594.2008.00697.x
- Vogel, W. M., Hsia, J. C., Briggs, L. L., Er, S. S., Cassidy, G., Apstein, C. S., et al. (1987). Reduced coronary vasoconstrictor activity of hemoglobin solutions purified by ATP-agarose affinity chromatography. *Life Sci.* 41, 89–93. doi: 10.1016/0024-3205(87)90560-1
- Ward, S. R., Guzman, L. A., Sutton, J. M., Forudi, F., Wendt, M., Brewer, L., et al. (1995). 984-30 use of electroporated platelets as a novel drug delivery system in preventing complications of coronary angioplasty. *J. Am. Coll. Cardiol.* 25, 303A–4A. doi: 10.1016/0735-1097(95)92718-K
- White, C. T., Murray, A. J., Greene, J. R., Smith, D. J., Medina, F., Makovec, G. T., et al. (1986). Toxicity of human hemoglobin solution infused into rabbits. *J. Lab. Clin. Med.* 108, 121–131.
- Wicki, A., Witzigmann, D., Balasubramanian, V., and Huwyler, J. (2015). Nanomedicine in cancer therapy: challenges, opportunities, and clinical applications. *J. Control. Release* 200, 138–157. doi: 10.1016/j.jconrel.2014.12.030
- Wilhelm, S., Tavares, A. J., Dai, Q., Ohta, S., Audet, J., Harold, F., et al. (2016). Analysis of nanoparticle delivery to tumours. *Nat. Rev. Mater.* 1:16014. doi: 10.1038/natrevmats.2016.14
- Winter, P. M. (2014). Perfluorocarbon nanoparticles: evolution of a multimodality and multifunctional imaging agent. *Scientifica* 2014:746574. doi: 10.1155/2014/746574
- Woods, S. D., Skinner, R. D., Ricca, A. M., Brown, A. T., Lowery, J. D., Borrelli, M. J., et al. (2013). Progress in dodecafluoropentane emulsion as a neuroprotective agent in a rabbit stroke model. *Mol. Neurobiol.* 48, 363–367. doi: 10.1007/s12035-013-8495-6
- Xiang, W., Shi, R., Kang, X., Zhang, X., Chen, P., Zhang, L., et al. (2018). Monoacylglycerol lipase regulates cannabinoid receptor 2-dependent macrophage activation and cancer progression. *Nat. Commun.* 9:2574. doi: 10.1038/s41467-018-04999-8
- Xu, P., Zuo, H., Chen, B., Wang, R., Ahmed, A., Hu, Y., et al. (2017). Doxorubicin-loaded platelets as a smart drug delivery system: an improved therapy for lymphoma. *Sci. Rep.* 7:42632. doi: 10.1038/srep42632
- Yan, F., Xue, J., Zhu, J., Marchant, R. E., and Guo, Z. (2005). Synthesis of a lipid conjugate of SO3Le(a) and its enhancement on liposomal binding to activated platelets. *Bioconjug. Chem.* 16, 90–96. doi: 10.1021/bc049805c
- Yokoyama, K., Yamanouchi, K., Watanabe, M., Matsumoto, T., Murashima, R., Daimoto, T., et al. (1975). Preparation of perfluorodecalin emulsion, an approach to the red cells substitute. *Fed. Proc.* 34, 1478–1483.
- Zhang, X., Wang, Q., Qin, L., Fu, H., Fang, Y., Han, B., et al. (2016). EGF-modified mPEG-PLGA-PLL nanoparticle for delivering doxorubicin combined with Bcl-2 siRNA as a potential treatment strategy for lung cancer. *Drug Deliv.* 23, 2936–2945. doi: 10.3109/10717544.2015.1126769
- Zhu, S., Niu, M., O'Mary, H., and Cui, Z. (2013). Targeting of tumor-associated macrophages made possible by PEG-sheddable, mannose-modified nanoparticles. *Mol. Pharm.* 10, 3525–3530. doi: 10.1021/mp400216r

Conflict of Interest: The authors declare that the research was conducted in the absence of any commercial or financial relationships that could be construed as a potential conflict of interest.

Copyright © 2019 Zhang, Wei and Ma. This is an open-access article distributed under the terms of the Creative Commons Attribution License (CC BY). The use, distribution or reproduction in other forums is permitted, provided the original author(s) and the copyright owner(s) are credited and that the original publication in this journal is cited, in accordance with accepted academic practice. No use, distribution or reproduction is permitted which does not comply with these terms.



Whole Body Vibration Triggers a Change in the Mutual Shaping State of Intestinal Microbiota and Body's Immunity

Ning Song^{1,2†}, Xia Liu^{1,2†}, Qiang Feng^{3,4,5†}, Mengchen Xu^{6†}, Xiang Lan^{3,4†}, Meihui Li^{3,4†}, Rutao Liu⁶, Caixia Li⁷, Tianyi Dong⁸, Deqiang Wang^{1,2*} and Shili Liu^{1,2*}

¹ School of Basic Medical Science, Shandong University, Jinan, China, ² Department of Rehabilitation Medicine, Binzhou Medical University Hospital, Binzhou, China, ³ Shandong Provincial Key Laboratory of Oral Tissue Regeneration, Department of Human Microbiome, School and Hospital of Stomatology, Shandong University, Jinan, China, ⁴ Shandong Engineering Laboratory for Dental Materials and Oral Tissue Regeneration, Department of Human Microbiome, School and Hospital of Stomatology, Shandong University, Jinan, China, ⁵ State Key Laboratory of Microbial Technology, Shandong University, Qingdao, China, ⁶ School of Environmental Science and Engineering, Shandong University, Jinan, China, ⁷ Department of Evidence Identification, Institute of Forensic Science of China, Beijing, China, ⁸ Department of Breast Thyroid Surgery, Shandong Provincial Hospital, Shandong University, Jinan, China

OPEN ACCESS

Edited by:

Yu Gao,
Nanjing University of Posts and
Telecommunications, China

Reviewed by:

Guoqing Wang,
Jilin University, China
Dong Wang,
Chengdu University of Traditional
Chinese Medicine, China

*Correspondence:

Deqiang Wang
wdqzb@163.com
Shili Liu
liushili@sdu.edu.cn

†These authors have contributed
equally to this work

Specialty section:

This article was submitted to
Nanobiotechnology,
a section of the journal
Frontiers in Bioengineering and
Biotechnology

Received: 23 August 2019

Accepted: 14 November 2019

Published: 29 November 2019

Citation:

Song N, Liu X, Feng Q, Xu M, Lan X,
Li M, Liu R, Li C, Dong T, Wang D and
Liu S (2019) Whole Body Vibration
Triggers a Change in the Mutual
Shaping State of Intestinal Microbiota
and Body's Immunity.
Front. Bioeng. Biotechnol. 7:377.
doi: 10.3389/fbioe.2019.00377

Whole body vibration (WBV) is a non-invasive physical therapy that has recently been included in the hospital's patient rehabilitation training catalog, but its health effects have not been sufficiently studied. In the present study, to examine the possible effects of WBV on immune cell differentiation, the IFN, IL-4, -17, F4/80 and CD3, -4, -8, -11b, -11c, -19 markers were used to characterizing the cells in mouse spleen. The results showed that the CD4 and CD25 positive lymphocytes in the spleen were significantly increased in the WBV group, and the population of Treg cells was enhanced significantly in response to WBV. Since the differentiation in immune cells is usually associated with microbiota, therefore the intestinal flora was characterized in mice and human individuals. The results indicated that WBV significantly reduced the α -diversity of mouse intestinal microbiota. Moreover, the principal coordinate analysis (PCoA) results indicated that the β -diversities of both mice and human fecal microbiota increased after WBV. Analysis of the bacterial composition indicated that the contents of a variety of bacteria changed in mice upon the stimulation of vibration, such as *Lactobacillus animalis* in mice, and *Lactobacillus paraplantarum* and *Lactobacillus sanfranciscensis* in human. The succeeding correlation analysis revealed that some bacteria with significant content variations were correlated to the regulatory T cell differentiation in mice and physical characteristics in human. Our research will provide the basis for future non-invasive treatment of microbial and immune related diseases.

Keywords: whole body vibration, immune cell differentiation, Treg, mouse microbiota, human microbiota, correlation, physical characteristics, *Lactobacillus*

INTRODUCTION

Non-invasive therapy (NIT) refers to a therapeutic strategy that the body is not invaded or cut open during medical treatment. The risks associated with surgery, financial costs and lengthy body recovery time have led to the development of many non-invasive technologies (Kennedy et al., 2015). Whole body vibration (WBV) is a NIT method, which acts like a mild exercise on the body

(Godinez et al., 2014). WBV is a common training method for improving athletic performance and maintaining astronauts' skeletal muscle mass and strength, it has recently been included in the hospital's patient rehabilitation training catalog. WBV machines usually provide rotational or vertical vibration stimulation, where vertical vibration is more commonly used for rehabilitation. Vertical vibration produces an upward thrust on the human body (Abercromby et al., 2007), which alternates with gravity to produce a fast, up and down shock that acts on the body's bones, muscles and nerves. Thereby WBV is a stimulus to the entire body, not to a specific local muscle group (Merriman and Jackson, 2009).

A number of literatures have been published on the effects of WBV on muscle strength and performance (Osawa et al., 2013; Rogan et al., 2015). The most basic function of vertical vibration is to stimulate the contraction of a large number of muscle fibers in a short period of time, which helps increase muscle strength, balance and muscle power (Machado et al., 2010; Sitja-Rabert et al., 2012), enhance mobility (Torvinen et al., 2002), reduce chronic pain (Rittweger et al., 2002), and stimulate limb blood circulation (Cochrane, 2011). Moreover, WBV may also affect other physiological systems of the body. Maddalozzo et al. reported that mice of the vibration group had significantly lower body fat than the control group (Maddalozzo et al., 2008). At the same time, bone mineral contents and bone density had been proved to increase significantly after a certain period of vertical vibration; the internal mechanism was the acceleration of bone formation and metabolism after using vertical vibration (Bleeker et al., 2005). Additionally, Boyle et al. reported that WBV combined with exercise reduced the possible danger of thrombosis or infarct greater than simple exercise, implying its possible role in the prevention and treatment of cardiovascular disease (Boyle and Nagelkirk, 2010). Regarding the effect on diabetes, Liu et al. reported that WBV reduced oxidative stress to ameliorate liver steatosis and improved insulin resistance in db/db mice (Liu et al., 2016). The research work of Reijne et al. supported this conclusion, and their results from mice demonstrated that WBV training tended to increase blood glucose turnover rates and stimulated hepatic glycogen utilization during fasting irrespective of age (Reijne et al., 2016). Also, Park et al. and Sa-Caputo et al. showed us the effects of WBV on pulmonary rehabilitation in patients with chronic obstructive pulmonary disease and improvement of local vasodilation in the microcirculation by the stimulation of endothelium (Park et al., 2015; Sa-Caputo et al., 2016).

However, other effects of the vibration stimulus need to be examined, and the mechanism responsible for the effect of this new intervention has not been clearly identified. Microbes that live on and in the human body, such as the oral cavity, gastrointestinal tract, and urinary tract, have been recognized as the key to understand our various abnormalities (Sekirov et al., 2010; Qin et al., 2012). Chronic inflammation is the driver of many diseases, and studies have shown that intestinal microbiota is closely related to the body's immune response and the occurrence of disease (Noverr and Huffnagle, 2004). The crucial characteristics of microbiota that affect immune response include biogeographical distribution, composition, and metabolites, etc.

(Blander et al., 2017). Unfortunately, no one has yet studied the effects of WBV on the body's intestinal flora and immunity. In the present study, the effects of WBV on the immune cell differentiation and the composition of intestinal microbiota were investigated. The vibration used in the experiment was sonic vibrations. This vibration mode is adopted by most hospitals, and the vibration toward the patient is softer and less dangerous than mechanical vibration. Our results suggested that WBV may affect the immune cell differentiation by stimulating changes in intestinal bacterial composition. Our research will provide the basis for future non-invasive treatment of microbial and immune related diseases.

MATERIALS AND METHODS

Treatments Related to Mouse and Human Volunteers

The 6-week old C57BL/6 mice in the same cage were divided into two groups: Treatment and Control. The mice in the treatment group were subjected to vertical vibration for 30 min per day for 30 days (frequency at 13 and intensity at 10 for 10 min; and then frequency at 17 and intensity at 20 for 20 min) on a vibrating instrument (Weibutexun, Jinan, China); the mice in the Treatment group were in a state of visible body vibration, but they were quiet and did not panic. After a period of vibration, the intestinal microbiota of the control and treatment groups were analyzed by sequencing. All animal studies were reviewed and approved by the ethic committee of School of Basic Medical Science, Shandong University (Jinan, Shandong Province, China). The human volunteers enrolled in the experiment were all from Binzhou Medical College, China. The volunteers were all healthy people, and their basic information is illustrated in **Supplementary Table 1**. Volunteers did not receive antibiotics, chemotherapy or radiotherapy for the first 3 months before the start of the experiment, nor did they consume probiotics. Throughout the experiment, volunteers every day performed a standing body vibration for 10 min (frequency 21 HZ, intensity 40) and then sat for vibration 10 min at the same frequency and intensity. All human studies were reviewed and approved by the ethic committee of Binzhou Medical University Hospital (Binzhou, Shandong Province, China).

16S Sequencing

Total fecal genome DNA was extracted with CTAB/SDS method, concentration and purity of the extracted genome DNA was checked by agarose gels electrophoresis. DNA was diluted with sterile water to the concentration of 1 ng/ μ l. Using about 10 ng of this template DNA and 0.2 μ M of primers that had adapters and barcodes, the variable V3–V4 region of the 16S rRNA gene was amplified by PCR (25 PCR cycles) with Phusion® High-Fidelity PCR Master Mix (New England Biolabs). Subsequently, amplicons were sequenced on a 454 GS-FLX system (Roche, Mannheim, Germany).

According to the unique barcodes, the Paired-end reads were assigned to each sample, and FLASH was used to merge the Paired-end reads. R software package (Quantitative Insights Into

Microbial Ecology) was employed for analysis of the sequences, and alpha- (within samples) and beta- (among samples) diversity were produced by in-house Perl scripts. In detail, reads were quality filtered by QIIME, and *pick_de_novo_otus.py* was used to make operational taxonomic units (OTUs) table. Sequences with $\geq 97\%$ similarity were classified to an OTU. Then the representative sequence of an OTU was picked and taxonomic information was annotated using the RDP classifier. To obtain Alpha Diversity, the OTU table was rarified into three metrics: Chao1 represents the species abundance; the number of unique OTUs in each sample was represented by Observed Species and Shannon index. Based on these three metrics, Rarefaction curves were generated. The beta-diversity indexes, weighted and unweighted unifracs, were generated with QIIME.

Flow Cytometry Analysis of Immune Cells

The spleens of the mice were collected, washed with phosphate Buffered Saline (PBS), and placed on ice in a 50 ml centrifuge tube containing PBS. Then the spleens were thoroughly ground with a copper mesh, and placed in a 50 ml centrifuge tubes, the volume was adjusted to 20–30 ml. After centrifuged at 1,200 rpm for 8 min, the supernatants were discarded, and 10 ml of red blood cell lysate was added to each tube, vortex, and place on ice for 7–8 min. Then centrifuged at 1,200 rpm for 8 min and the supernatant discarded once again, 2.88 ml percol, 0.32 ml of 8.5% NaCl solution, and 4.8 ml of PBS were added. The solution was transferred to a 10 ml centrifuge tube, and centrifuged at 2,000 rpm for 20 min; after the supernatant was discarded, 5 ml of PBS was added and the cells in the solution were counted. The number of cells required per well was estimated and pipette into a centrifuge tube. The cells were subsequently centrifuged at 1,200 rpm for 8 min, re-suspending in 1,640 and 10% FBS medium, and the stimulant PMA 30–50 $\mu\text{g/ml}$, ionomycin 1 $\mu\text{g/ml}$ was added to the medium; after incubation in a 24-well plate at 1 ml/well for 1 h, $1\times$ BFA blocker was added to reduce the extracellular release of cytokines. The cells were harvested within 4 h and placed in a flow tube, then washed with PBS and centrifuged at 1,200 rpm for 8 min; after the supernatant was discarded, the tube was blotted dry with absorbent paper, and 100 μl of PBS was added to each tube.

Surface Antigen Labeling

Add 10 μl of antibody + PBS mix to each tube, repeatedly pipette and vortex to mix. The mix was wrapped with foil paper and placed in the dark at 4°C. Half an hour later, 2 ml of PBS was added and centrifuged at 1,200 rpm for 8 min. The supernatant was discarded, re-suspended in 300 μl of 1% poly-formaldehyde, and stored at 4°C.

Intracellular Antigen Labeling

Vortex the cell solution and place at 4°C for 30 min, $1\times$ permeability buffer 1 ml was added to each tube; after centrifugation at 1,200 rpm for 8 min, the supernatant was discarded, and 100 μl of membrane solution was added; vortex, placed at 4°C for 10 min and 10 μl labeled antibody + permeability buffer mix were added. After repeated pipette, the solution was placed at 4°C for 1 h in the dark, 2 ml PBS was

then add and centrifuged at 1,200 rpm for 8 min. After discarding the supernatant, the cells were re-suspended with 300 μl PBS or poly-formaldehyde, and store at 4°C for flow cytometry.

Statistical Data Analysis

The data were represented as mean \pm standard deviation (SD), and each experiment had triplicate data. The Student's *t*-tests was used to calculate the *p*-value between the groups, and $p < 0.05$ (*) was considered as statistically significant.

RESULT

WBV Did Not Cause Any Movement Disorder or Other Changes in Behavior

The vibration instrument used in the experiment was shown in **Supplementary Figure 1**; it can provide whole body vibration, forcing the body muscles to be in a state of passive exercise. To explore the possible effect of WBV on physiological function of the body, the mice were placed on the vibration instrument for 30 min vibration every day for 35 days, and their dietary consumption and body weight changes were recorded during this process, as well as behavioral characteristics were assessed at the end. The exhaustive swimming result showed that the longest swimming time of the vibration group was significantly increased, almost twice the time of the control group (**Figure 1A**); proving that WBV can increase muscle strength and endurance. Moreover, the pole test result also showed no significant difference in the time of climbing pole between the two groups (**Figure 1B**, $p = 0.36$), illustrating that WBV treatment did not cause any movement disorder. The food intake of the WBV group mice increased on days 15, and peaked on the 20th day, but returned to similar to the control group level at the 25th day (**Figure 1C**). However, the average daily food intake of the WBV group mice during the entire period was not significantly different from the control group (**Supplementary Figure 2**). In contrast to food intake, there was a significant difference in water intake between the WBV group and the control group (**Figure 1D**), and the two groups both exhibited a certain degree of fluctuations in the amount of water consumed per day (**Supplementary Figure 3**). Additionally, the body weight results showed that the mice did not undergo significant changes in body weight after WBV (**Supplementary Figure 4**). The above results demonstrated that no changes in behavior of the mice were observed during the entire vibration experimental process.

WBV Alters Regulatory T Cell Differentiation

To examine the effects of WBV on immunological development, we examined CD3, -4, -8, -11b, -11c, -19, and IFN, IL-4, -17, F4/80 markers of cells in the mouse spleen. The results showed that the CD4 (**Figure 2A**) and CD25 (**Figure 2B**) positive lymphocytes in the WBV group were significantly increased. As a result, the population of CD4⁺CD25⁺FOXP3⁺ Treg cells in the spleen was enhanced significantly (**Figure 2C**, $p < 0.01$). The above results indicate WBV alters regulatory T cell differentiation.

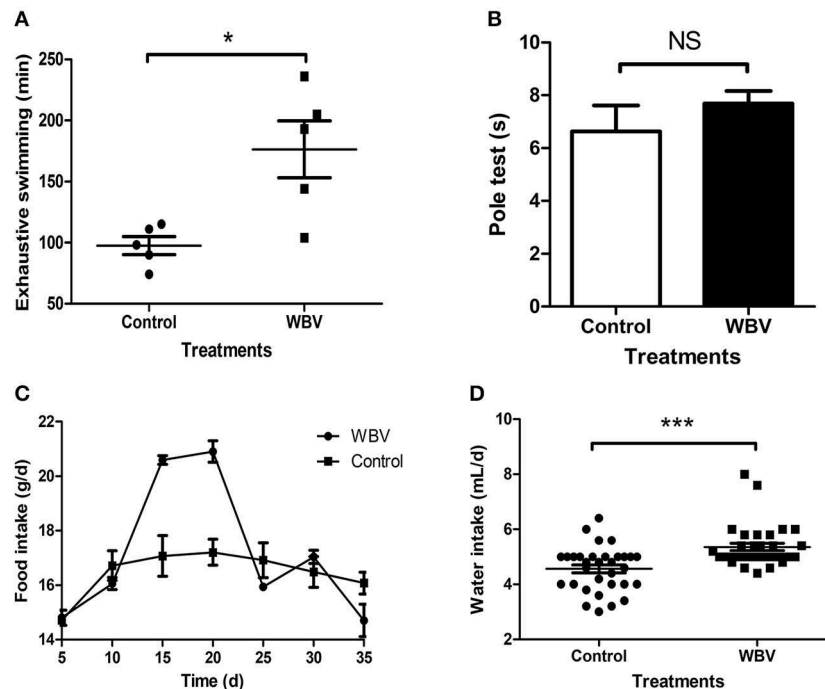


FIGURE 1 | WBV did not cause any movement disorder or other changes in behavior. The Exhaustive swimming (A) results exhibited a significant difference between the mice with vibration or not, but the Pole test (B) results showed no difference; (C,D) the food and water intake of the mice. NS, not significant; * $p < 0.05$; *** $p < 0.001$.

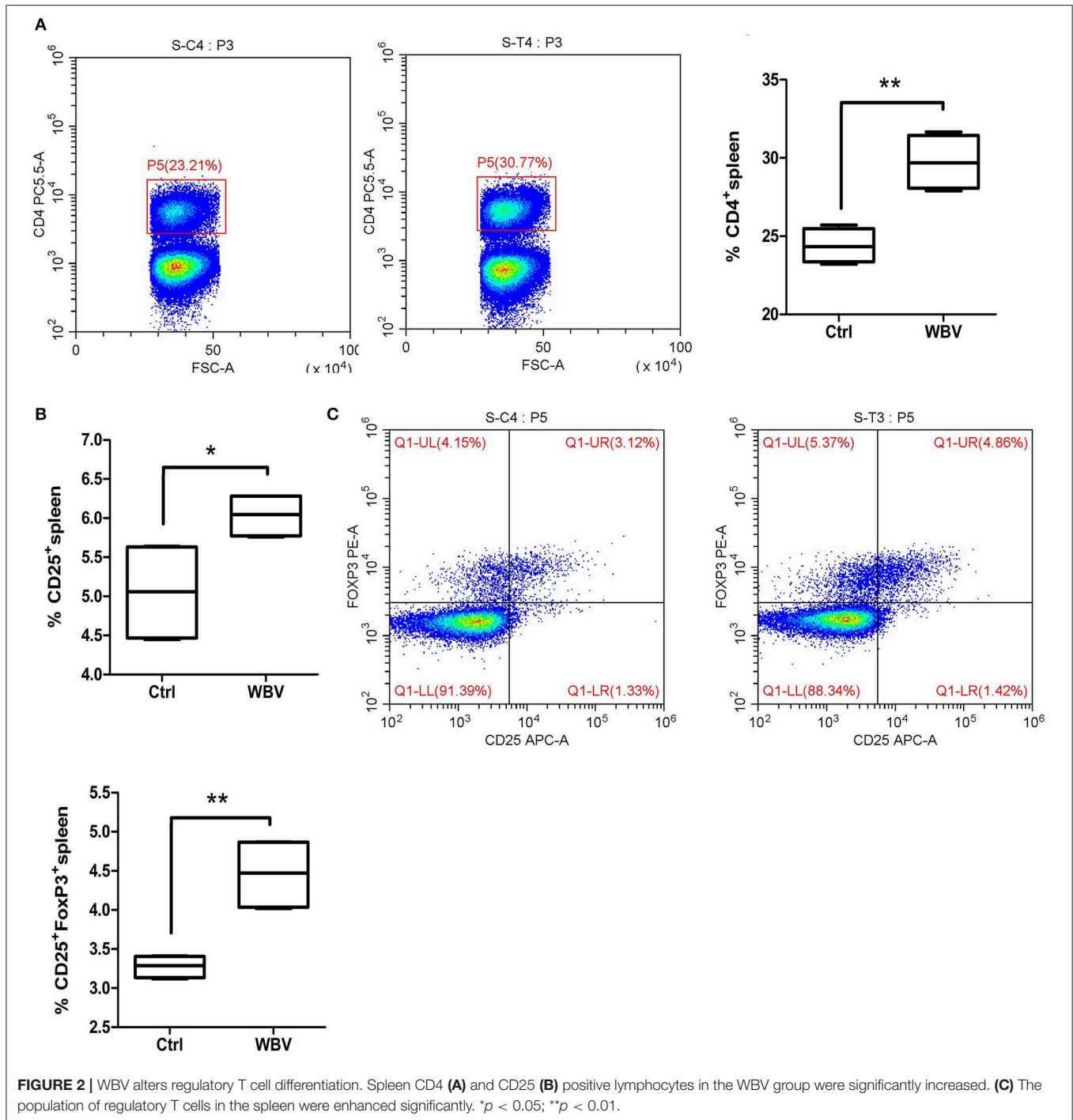
WBV Altered the Composition of the Mouse Intestinal Microbiota

Since the differentiation in immune cells in the body are usually associated with changes in the human microbiota, therefore the possible change of microbiota after WBV treatment was characterized in mice. Fecal samples of the treatment group (ST) and control group (SC) were collected and their 16S rDNA amplicons were sequenced. After quality filtering, more than 0.56 million effective tags were harvested corresponding to a mean of 56,378 effective tags and 379 OTUs per sample (Supplementary Table 2 and Supplementary Figure 5). On average, the fecal samples from treatment group had similar number of effective reads (57,384) as the control group samples (55,372, $P = 0.56$). Similarly, there was no significant difference in the OTUs identified between the two groups of samples ($p = 0.45$), although the average of the fecal microbiota in the treatment group (398) was greater than that of the control group (361, Supplementary Figure 5). Furthermore, the Rarefaction curve tended to be saturated among all samples, suggesting that the OTUs have covered most of the bacterial species that exist whether vertical vibration or not (Supplementary Figure 6).

The α -diversity of mouse intestinal microbiota indicated that WBV significantly reduced the α -diversity of the sample (Figure 3A). In contrast, the principal coordinate analysis (PCoA) showed that the distribution of the treatment group samples was more scattered relative to that of the control group (Figures 3B,C), indicating that the β -diversity of the fecal microbiota increased after WBV (Figure 3C). A clustering analysis was then performed to quantify the degree of similarity

of all the samples, and the result demonstrated that the control group samples were clustered together with a smaller Euclidean distance, while the WBV group samples were grouped in a larger Euclidean distance (Supplementary Figure 7). The results suggest that WBV affects the murine intestinal microbiome and makes the difference between individuals greater.

Then the intestinal microbial composition of the treatment and control mice were analyzed at the phylum, genus, and species levels, respectively. At the phylum level, the total amount of Firmicutes, Bacteroidetes, and Actinobacteria account for more than 90% of all fecal bacteria; meanwhile, the proportion of the most abundant phylum Firmicutes exceeded 45% of the total bacteria (Supplementary Figure 8). The observed effect of the vibration was the increased contents and variation between individuals in phylum Actinobacteria (Supplementary Figure 8). At the generic level, the genus *Lactobacillus* belonging to phylum Firmicutes, was the most abundant genus in the WBV group, covering approximately 30% of the entire bacterial mass (Supplementary Figure 9). However, its content in the control group was lower than *Turicibacter* and *Lachnospiraceae_UCG_014*, accounting for only about 5% of the total bacteria, and its content was significantly different between the two groups (Figures 3D,E). As a result, the vibration increases the content of *Lactobacillus animalis* in the intestine by more than 5 times at the species level (Figure 3F). In addition, WBV also triggered some other genera with high abundance, such as *Lachnospiraceae_UCG_014* and *Bifidobacterium*, to change their contents in intestinal microbiota (Figure 3E).



WBV Also Affects the Composition of the Human Intestinal Microbiota and Changes the Content of *Lactobacillus* spp.

To study the effects of WBV on the human intestinal microbiota, we conducted 30-day vibration training on 11 volunteers, and the fecal samples of the volunteer were collected at 0 (control), 10 (T10), 20 (T20), and 30 (T30) days after WBV and sequenced. The Rarefaction curve tended to be saturated among all samples,

suggesting that the OTUs have covered most of the bacterial species that exist in the feces (Supplementary Figure 10). Different from the results of mouse experiments, the α -diversities of the fecal microbiota of the WBV groups were not significantly different from that of the control group (Supplementary Figure 11). Unlikely, the principal components analysis (PCA) results showed that the microbial distribution of the T10 group was more scattered relative to those of the

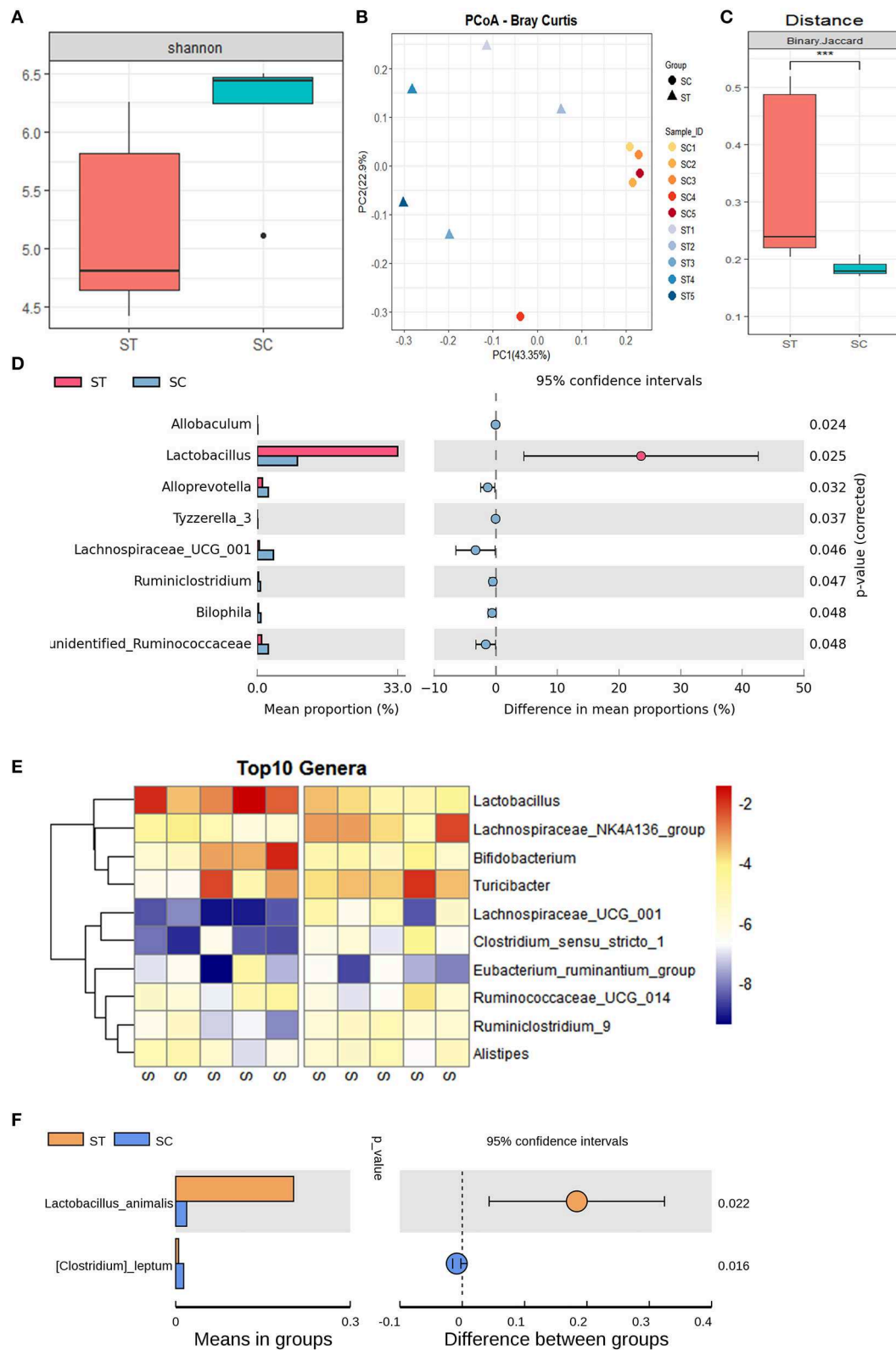


FIGURE 3 | WBV altered the composition of the mouse intestinal microbiota. **(A)** The α -diversity of mouse intestinal microbiota; the PCoA **(B)** and distance of β -diversity **(C)** analysis of the mice in the vibration and control groups; **(D)** the bacteria with significant differences between the two groups; **(E)** the Heat map of the bacteria with significant differences; **(F)** the content of *Lactobacillus animalis* in the vibration and control groups. *** $p < 0.001$.

control and the other vibration groups (Figure 4A), suggesting that the β diversity of the fecal microbiota increases after short-term of WBV, but returns to the original state as the vibration time increases (Figure 4B), which is consistent with the results of the mouse experiment.

Then the intestinal microbial structures of the treatment and control groups were analyzed at the phylum, genus and species levels, respectively. At the phylum level, Firmicutes was the only phylum that had a difference in its content caused by WBV (Figure 4C). At the generic level, the content of genus *Fusobacterium* was significantly increased solely with longer time of vibration (Figure 4D and Supplementary Figure 12). At the species level, *Intestinibacter bartlettii*, *Desulfovibrio simplex*, and *Eubacterium coprostanoligenes* varied their contents in the feces with 10 days' vibration in comparison to the control; and the differentiated bacteria changed to be *Lactobacillus paraplantarum*, *Lactobacillus sanfranciscensis*, and *Pediococcus acidilactici* at the 20 days time-point; finally only *Lactobacillus paraplantarum* maintain significant difference in content after 30 days (Figure 4E). The results from the mice and human samples indicate that the WBV can change the composition of the intestinal microbiota of mice and humans, with a significant change in the proportion of certain bacteria such as *Lactobacillus* spp.

WBV Induced Changes in Intestinal Microbiota Composition Were Correlated to the Regulatory T Cell Differentiation in Mice and Physical Characteristics in Human

The correlations between the bacterial genus with significant differences in contents before and after WBV and the amount of CD4 and CD25 positive lymphocytes as well as Tregs were investigated by Spearman correlation analysis ("Hmisc" in R package). The results showed that CD4 positive lymphocytes were correlated with 21 genera, such as *Lactobacillus*, *Bifidobacterium*, and several genera of *Lachnospiraceae* (Figure 5A). CD25 positive lymphocytes were associated with 7 genera, including *Bilophila*, *Lachnospiraceae_UCG_001*, and *Rumimicrostridium*. Therefore, the Treg-associated bacteria involved the intersection of CD4 and CD25 positive lymphocytes-associated bacteria, such as *Bilophila*, *Lachnospiraceae_UCG_001*, and *Rumimicrostridium*, as well as *Lactobacillus* and *Candidatus*. Then the relationship between the human intestinal bacteria that showed significant changes in contents after WBV and body characteristics was also explored by Spearman correlation analysis. The results demonstrated that *Eubacterium coprostanoligenes* was related to weight and height, while *Pediococcus acidilactici* was associated with BMI and weight; and *Lactobacillus paraplantarum* was related to age (Figure 5B).

Next, Spearman correlation analysis was performed toward the interrelationship between the genera with high abundance within the mice and human microbiota, the cut-off value > 0.8 and $p < 0.05$ were applied to filter the data, respectively. The constructed correlation network of mice fecal microbiota showed that the interactions between the bacteria significantly changed

in response to WBV (Figure 5C). The same phenomenon also occurred in human fecal microbiota, and the interaction between bacteria changed on the 10th and 30th day of the vibration (Figure 5D and Supplementary Figure 13). The above results suggest that WBV induced variation in regulatory T cell differentiation was correlated to changes in intestinal microbiota composition.

DISCUSSION

WBV has recently been included in the hospital's patient rehabilitation training catalog, which may play a significant role in preventing osteoporosis and losing weight (Reijne et al., 2016; Swe et al., 2016; McMillan et al., 2017), stimulating the secretion of growth hormone (GH) and testosterone in male students (Cardinale et al., 2010). Recently, some researchers reported that appropriate vibration training was a benefit to metabolic disorders such as obesity and diabetes (Yin et al., 2015; Zhang et al., 2016). In this study, the mice and human volunteers were placed on the vibration instrument for 30 min vibration every day for more than 30 days, and the immunological results in mice showed that WBV alters regulatory T cell differentiation. Since the differentiation in immune cells in the body are usually associated with changes in the human microbiota, therefore the possible changes of microbiota after WBV treatment were characterized in mice and human body. The microbiome results revealed that WBV affected the intestinal microbiome and makes the difference between individuals greater. Interestingly, it appeared that *Lactobacillus* spp. were sensitive to WBV stimulation, the content of *Lactobacillus animalis* in the intestine of mice was significantly increased in response to vibration, while the contents of *Lactobacillus paraplantarum*, and *Lactobacillus sanfranciscensis* in the human body were significantly changed concomitant with WBV. The difference of *Lactobacillus* variation occurred in the mouse and the human intestines in response to WBV may be due to the distinction in the composition of the two microbiotas, and their intestinal microenvironment is completely divergent. Finally, the correlation analysis results revealed that WBV induced changes in intestinal microbiota composition, such as *Lactobacillus* spp., were correlated to the regulatory T cell differentiation in mice and physical characteristics in human. This study implies that WBV has potential interventional effects on microbiota and immune-related diseases, so WBV-induced changes in microbiota, immune state and inflammation of the body deserve further validation and investigation in the future.

The intestinal microbiota has a profound influence on metabolism, tissue development, and homeostasis of the intestinal immune system. Components of microbiota have been shown to initiate inflammation and also regulate immune cells (Nicholson et al., 2012). A variety of mechanisms have been proposed between the gut microbes and immune response. For example, the alteration of the gut microbiome may promote the intestinal permeability, change butyrate, and lipopolysaccharide (LPS) productions, while butyrate and LPS level could modulate the immune response and inflammation (Noverr and Huffnagle, 2004). Besides, the changes of the gut microbiota could alter the energy homeostasis, modulate intestinal barrier integrity, change the gastrointestinal peptide hormone secretion, promote fat

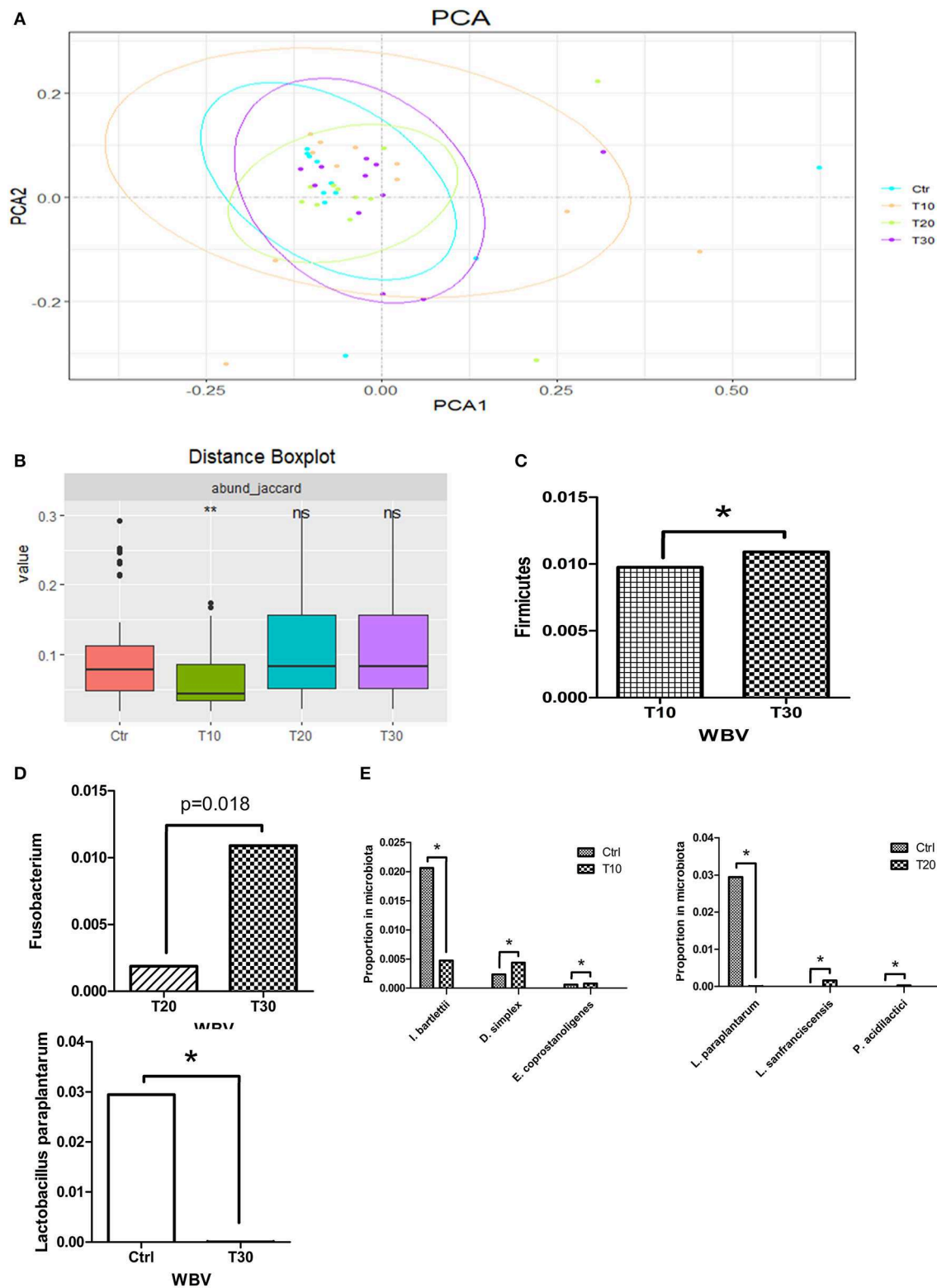
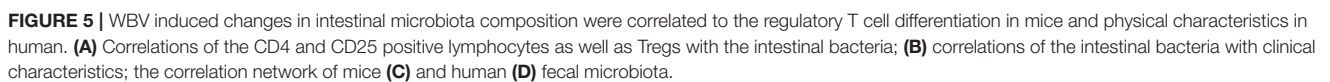


FIGURE 4 | WBV also affects the composition of the human intestinal microbiota and changes the content of *Lactobacillus* spp. **(A)** PCA result of the human intestinal microbiota; **(B)** β diversity distance of the human fecal microbiota; phyla **(C)**, genera **(D)**, and species **(E)** with significant variation concomitant with longer time of vibration. * $p < 0.05$; ** $p < 0.01$.



accumulation, and modulate host inflammatory status (Amyot et al., 2012).

Previous studies reported that Lactobacilli down-modulated the maturation of DCs and induced the *in vitro* expansion of CD4 positive T cells, which resemble regulatory T cells (von der Weid et al., 2001; Christensen et al., 2002). Lactobacillus is a Gram-positive, facultative anaerobic or microaerobic, rod-shaped, non-spore forming bacteria. They are the main part of the lactic acid bacteria family (i.e., they convert sugar to lactic acid). Members of the genus Lactobacillus have long been considered to be one of the most abundant microorganisms in the human gastrointestinal (GI) tract and are associated with good intestinal health (Heeney et al., 2018). Animal studies have shown that Lactobacilli have a wide range of roles in the prevention and treatment of infectious diseases, the reduced Interleukin-1 β -mediated inflammation and improved barrier function demonstrated the potential of lactobacilli to prevent or reverse intestinal damage during infection (Hirao et al., 2014). A report investigating the fecal microbiome of IBS patients and healthy subjects concluded that lactobacillus was depleted in patients with IBS who were predominantly diarrhea (Liu et al., 2017). The changes in microbiota and immunity triggered by WBV are in constant process of mutual shaping. Previous studies have found that certain components of the microbiota specifically affect the accumulation and activity of Treg cells, among which Lactobacilli and Bifidobacteria are involved in the induction of Treg cells (Tanoue and Honda, 2012). In the intestine, one of the most important effectors produced by Treg cells is IL-10, which is indispensable for the maintenance of intestinal immune homeostasis and micro-ecological balance. Given that autochthonous Lactobacillus plays a crucial role in the resolution of infectious disease and recovery of immune homeostasis, the correlation between WBV-induced content change in *Lactobacillus* spp. and T cell differentiation and clinical parameters might be related to disease occurrence and deserves in-depth study. A report demonstrated that vertical vibration could alleviate the severity of symptoms in patients with chronic functional constipation (Wu et al., 2012), verified the therapeutic effect of WBV. In addition, inflammation-related diseases in the body may be alleviated, although sometimes the symptoms may be less pronounced. Our research will provide the basis for future non-invasive treatment of microbial and immune related diseases.

REFERENCES

- Abercromby, A. F., Amonette, W. E., Layne, C. S., McFarlin, B. K., Hinman, M. R., and Paloski, W. H. (2007). Vibration exposure and biodynamic responses during whole-body vibration training. *Med. Sci. Sports Exerc.* 39, 1794–1800. doi: 10.1249/mss.0b013e3181238a0f
- Amyot, J., Semache, M., Ferdaoussi, M., Fontes, G., and Poirout, V. (2012). Lipopolysaccharides impair insulin gene expression in isolated islets of Langerhans via Toll-Like Receptor-4 and NF-kappaB signalling. *PLoS ONE* 7:e36200. doi: 10.1371/journal.pone.0036200

DATA AVAILABILITY STATEMENT

The sequencing data were uploaded to the NCBI website with the BioProject ID PRJNA561665 and PRJNA561686 available at <https://www.ncbi.nlm.nih.gov/sra/PRJNA561665> or <https://www.ncbi.nlm.nih.gov/sra/PRJNA561686>.

ETHICS STATEMENT

The studies involving human participants were reviewed and approved by the ethic committee of Binzhou Medical University Hospital (Binzhou, Shandong Province, China). The patients/participants provided their written informed consent to participate in this study. The animal study was reviewed and approved by the ethic committee of School of Basic Medical Science, Shandong University (Jinan, Shandong Province, China).

AUTHOR CONTRIBUTIONS

NS and MX collected the mice samples and prepared the immunological results. XLi collected the human samples and clinical characteristics of the patients. QF, XLa, and ML analyzed the sequencing data and prepared the related figures. SL designed the research and prepared the manuscript and modified the figures. RL and CL edited the manuscript. TD organized the figures. DW assisted SL in designing the research and enrolling volunteers. All authors have reviewed the final version of the manuscript and approved this submission.

ACKNOWLEDGMENTS

We gratefully acknowledge the financial support from The Cheung Kong Scholars Program, The Fundamental Research Funds of Shandong University (2018JC102), and Shandong Traditional Chinese Medicine Science and Technology Development Plan (2019-0497).

SUPPLEMENTARY MATERIAL

The Supplementary Material for this article can be found online at: <https://www.frontiersin.org/articles/10.3389/fbioe.2019.00377/full#supplementary-material>

- Blander, J. M., Longman, R. S., Iliev, I. D., Sonnenberg, G. F., and Artis, D. (2017). Regulation of inflammation by microbiota interactions with the host. *Nat. Immunol.* 18, 851–860. doi: 10.1038/ni.3780
- Bleeker, M. W., De Groot, P. C., Rongen, G. A., Rittweger, J., Felsenberg, D., Smits, P., et al. (2005). Vascular adaptation to deconditioning and the effect of an exercise countermeasure: results of the Berlin Bed Rest study. *J. Appl. Physiol.* 99, 1293–1300. doi: 10.1152/jappphysiol.00118.2005
- Boyle, L. J., and Nagelkirk, P. R. (2010). The effects of whole body vibration and exercise on fibrinolysis in men. *Eur. J. Appl. Physiol.* 110, 1057–1061. doi: 10.1007/s00421-010-1590-8

- Cardinale, M., Soiza, R. L., Leiper, J. B., Gibson, A., and Primrose, W. R. (2010). Hormonal responses to a single session of wholebody vibration exercise in older individuals. *Br. J. Sports Med.* 44, 284–288. doi: 10.1136/bjsm.2007.043232
- Christensen, H. R., Frokiaer, H., and Pestka, J. J. (2002). Lactobacilli differentially modulate expression of cytokines and maturation surface markers in murine dendritic cells. *J. Immunol.* 168, 171–178. doi: 10.4049/jimmunol.168.1.171
- Cochrane, D. J. (2011). Vibration exercise: the potential benefits. *Int. J. Sports Med.* 32, 75–99. doi: 10.1055/s-0030-1268010
- Godinez, A., Liston, D. B., Ayzenberg, R., Toscano, W. B., Cowings, P. A., and Stone, L. S. (2014). G-loading and vibration effects on heart and respiration rates. *Aviat. Space Environ. Med.* 85, 949–953. doi: 10.3357/ASEM.4015.2014
- Heeney, D. D., Gareau, M. G., and Marco, M. L. (2018). Intestinal Lactobacillus in health and disease, a driver or just along for the ride? *Curr. Opin. Biotechnol.* 49, 140–147. doi: 10.1016/j.copbio.2017.08.004
- Hirao, L. A., Grishina, I., Bourry, O., Hu, W. K., Somrit, M., Sankaran-Walters, S., et al. (2014). Early mucosal sensing of SIV infection by paneth cells induces IL-1 β production and initiates gut epithelial disruption. *PLoS Pathog.* 10:e1004311. doi: 10.1371/journal.ppat.1004311
- Kennedy, J., Verne, S., Griffith, R., Falto-Aizpurua, L., and Nouri, K. (2015). Non-invasive subcutaneous fat reduction: a review. *J. Eur. Acad. Dermatol. Venereol.* 29, 1679–1688. doi: 10.1111/jdv.12994
- Liu, H. N., Wu, H., Chen, Y. Z., Chen, Y. J., Shen, X. Z., and Liu, T. T. (2017). Altered molecular signature of intestinal microbiota in irritable bowel syndrome patients compared with healthy controls: a systematic review and meta-analysis. *Dig. Liver Dis.* 49, 331–337. doi: 10.1016/j.dld.2017.01.142
- Liu, Y., Zhai, M., Guo, F., Shi, T., Liu, J., Wang, X., et al. (2016). Whole body vibration improves insulin resistance in db/db mice: amelioration of lipid accumulation and oxidative stress. *Appl. Biochem. Biotechnol.* 179, 819–829. doi: 10.1007/s12010-016-2033-8
- Machado, A., Garcia-Lopez, D., Gonzalez-Gallego, J., and Garatachea, N. (2010). Whole-body vibration training increases muscle strength and mass in older women: a randomized-controlled trial. *Scand. J. Med. Sci. Sports.* 20, 200–207. doi: 10.1111/j.1600-0838.2009.00919.x
- Maddalozzo, G. F., Iwaniec, U. T., Turner, R. T., Rosen, C. J., and Widrick, J. J. (2008). Whole-body vibration slows the acquisition of fat in mature female rats. *Int. J. Obes.* 32, 1348–1354. doi: 10.1038/ijo.2008.111
- McMillan, L. B., Zengin, A., Ebeling, P. R., and Scott, D. (2017). Prescribing physical activity for the prevention and treatment of osteoporosis in older adults. *Healthcare* 5:E85. doi: 10.3390/healthcare5040085
- Merriman, H., and Jackson, K. (2009). The effects of whole-body vibration training in aging adults: a systematic review. *J. Geriatr. Phys. Ther.* 32, 134–145. doi: 10.1519/00139143-200932030-00009
- Nicholson, J. K., Holmes, E., Kinross, J., Burcelin, R., Gibson, G., Jia, W., et al. (2012). Host-gut microbiota metabolic interactions. *Science* 336, 1262–1267. doi: 10.1126/science.1223813
- Noverr, M. C., and Huffnagle, G. B. (2004). Does the microbiota regulate immune responses outside the gut? *Trends Microbiol.* 12, 562–568. doi: 10.1016/j.tim.2004.10.008
- Osawa, Y., Oguma, Y., and Ishii, N. (2013). The effects of whole-body vibration on muscle strength and power: a meta-analysis. *J. Musculoskelet. Neuronal Interact.* 13, 380–390. doi: 10.1590/1980-5918.030.s01.a017
- Park, S. Y., Son, W. M., and Kwon, O. S. (2015). Effects of whole body vibration training on body composition, skeletal muscle strength, and cardiovascular health. *J. Exerc. Rehabil.* 11, 289–295. doi: 10.12965/jer.150254
- Qin, J., Li, Y., Cai, Z., Li, S., Zhu, J., Zhang, F., et al. (2012). A metagenome-wide association study of gut microbiota in type 2 diabetes. *Nature* 490, 55–60. doi: 10.1038/nature11450
- Reijne, A. C., Ciapaite, J., van Dijk, T. H., Havinga, R., van der Zee, E. A., Groen, A. K., et al. (2016). Whole-body vibration partially reverses aging-induced increases in visceral adiposity and hepatic lipid storage in mice. *PLoS ONE* 11:e0149419. doi: 10.1371/journal.pone.0149419
- Rittweger, J., Just, K., Kautzsch, K., Reeg, P., and Felsenberg, D. (2002). Treatment of chronic lower back pain with lumbar extension and whole-body vibration exercise: a randomized controlled trial. *Spine* 27, 1829–1834. doi: 10.1097/00007632-200209010-00003
- Rogan, S., de Bruin, E. D., Radlinger, L., Joehr, C., Wyss, C., Stuck, N. J., et al. (2015). Effects of whole-body vibration on proxies of muscle strength in old adults: a systematic review and meta-analysis on the role of physical capacity level. *Eur. Rev. Aging Phys. Act.* 12:2. doi: 10.1186/s11556-015-0158-3
- Sa-Caputo, D., Goncalves, C. R., Morel, D. S., Marconi, E. M., Froes, P., Rufino, R., et al. (2016). Benefits of whole-body vibration, as a component of the pulmonary rehabilitation, in patients with chronic obstructive pulmonary disease: a narrative review with a suitable approach. *Evid. Based Complement. Alternat. Med.* 2016:2560710. doi: 10.1155/2016/2560710
- Sekirov, I., Russell, S. L., Antunes, L. C., and Finlay, B. B. (2010). Gut microbiota in health and disease. *Physiol. Rev.* 90, 859–904. doi: 10.1152/physrev.00045.2009
- Sitja-Rabert, M., Rigau, D., Fort, V. A., Romero-Rodriguez, D., Bonastre, S. M., and Bonfill, X. (2012). Efficacy of whole body vibration exercise in older people: a systematic review. *Disabil. Rehabil.* 34, 883–893. doi: 10.3109/09638288.2011.626486
- Swe, M., Benjamin, B., Tun, A. A., and Sugathan, S. (2016). Role of the whole body vibration machine in the prevention and management of osteoporosis in old age: a systematic review. *Malays. J. Med. Sci.* 23, 8–16. doi: 10.21315/mjms2016.23.5.2
- Tanoue, T., and Honda, K. (2012). Induction of Treg cells in the mouse colonic mucosa: a central mechanism to maintain host-microbiota homeostasis. *Semin. Immunol.* 24, 50–57. doi: 10.1016/j.smim.2011.11.009
- Torvinen, S., Sievanen, H., Jarvinen, T. A., Pasanen, M., Kontulainen, S., and Kannus, P. (2002). Effect of 4-min vertical whole body vibration on muscle performance and body balance: a randomized cross-over study. *Int. J. Sports Med.* 23, 374–9. doi: 10.1055/s-2002-33148
- von der Weid, T., Bulliard, C., and Schiffrin, E. J. (2001). Induction by a lactic acid bacterium of a population of CD4(+) T cells with low proliferative capacity that produce transforming growth factor beta and interleukin-10. *Clin. Diagn. Lab. Immunol.* 8, 695–701. doi: 10.1128/CDLI.8.4.695-701.2001
- Wu, T. J., Wei, T. S., and Chou, Y. H. (2012). Whole-body vibration for functional constipation: a single-centre, single-blinded, randomized controlled trial. *Colorectal Dis.* 14, e779–e785. doi: 10.1111/codi.12021
- Yin, H., Berdel, H. O., Moore, D., Davis, F., Liu, J., Mozaffari, M., et al. (2015). Whole body vibration therapy: a novel potential treatment for type 2 diabetes mellitus. *Springerplus* 4:578. doi: 10.1186/s40064-015-1373-0
- Zhang, B. J., Zhang, H., Kan, L., Zhang, C., and Wang, P. (2016). The effect of whole body vibration therapy on the physical function of people with type II diabetes mellitus: a systematic review. *J. Phys. Ther. Sci.* 28, 2675–2680. doi: 10.1589/jpts.28.2675

Conflict of Interest: The authors declare that the research was conducted in the absence of any commercial or financial relationships that could be construed as a potential conflict of interest.

Copyright © 2019 Song, Liu, Feng, Xu, Lan, Li, Liu, Li, Dong, Wang and Liu. This is an open-access article distributed under the terms of the Creative Commons Attribution License (CC BY). The use, distribution or reproduction in other forums is permitted, provided the original author(s) and the copyright owner(s) are credited and that the original publication in this journal is cited, in accordance with accepted academic practice. No use, distribution or reproduction is permitted which does not comply with these terms.



Gold Nanomaterials for Imaging-Guided Near-Infrared *in vivo* Cancer Therapy

Yuanyuan Tian^{1,2}, Sheng Qiang^{1*} and Lianhui Wang^{2*}

¹ Weed Research Laboratory, Nanjing Agricultural University, Nanjing, China, ² Key Laboratory for Organic Electronics and Information Displays & Jiangsu Key Laboratory for Biosensors, Institute of Advanced Materials, National Jiangsu Synergetic Innovation Center for Advanced Materials, Nanjing University of Posts and Telecommunications, Nanjing, China

OPEN ACCESS

Edited by:

Michael Ming-Yuan Wei,
Texas Commission on Environmental
Quality, United States

Reviewed by:

Raviraj Vankayala,
Independent Researcher, Irvine,
United States

Jyothi U. Menon,
University of Rhode Island,
United States

*Correspondence:

Sheng Qiang
wrl@njau.edu.cn
Lianhui Wang
iamlhwang@njupt.edu.cn

Specialty section:

This article was submitted to
Nanobiotechnology,
a section of the journal
Frontiers in Bioengineering and
Biotechnology

Received: 18 September 2019

Accepted: 22 November 2019

Published: 05 December 2019

Citation:

Tian Y, Qiang S and Wang L (2019)
Gold Nanomaterials for
Imaging-Guided Near-Infrared *in vivo*
Cancer Therapy.
Front. Bioeng. Biotechnol. 7:398.
doi: 10.3389/fbioe.2019.00398

In recent years, tremendous efforts have been devoted into the fields of valuable diagnosis and anticancer treatment, such as real-time imaging, photothermal, and photodynamic therapy, and drug delivery. As promising nanocarriers, gold nanomaterials have attracted widespread attention during the last two decades for cancer diagnosis and therapy due to their prominent properties. With the development of nanoscience and nanotechnology, the fascinating bio-applications of functionalized gold nanomaterials have been gradually developed from *in vitro* to *in vivo*. This mini-review emphasizes some recent advances of photothermal imaging (PTI), surface-enhanced Raman scattering (SERS) imaging, and photoacoustic imaging (PAI)-guided based on gold nanomaterials *in vivo* therapy in near infrared region (>800 nm). We focus on the fundamental strategies, characteristics of bio-imaging modalities involving the advantages of multiples imaging modalities for cancer treatment, and then highlight a few examples of each techniques. Finally, we discuss the perspectives and challenges in gold nanomaterial-based cancer therapy.

Keywords: gold nanomaterials, *in vivo*, photothermal therapy, surface-enhanced Raman scattering, photoacoustic imaging

INTRODUCTION

Because of the high incidence and mortality of cancer, scientists have paid long term attention to the diagnosis and treatment of cancer. Conventional cancer therapies have clear side effects (Liu et al., 2019a), thus these shortcomings have prompted researchers to look for effective diagnostic strategies to struggle against cancer (Chen et al., 2016; Ju et al., 2019). With the development of modern technology and biological medicine, diagnosis, and treatment based gold nanomaterials are emerging to improve the therapeutic effect. Particularly, photothermal therapy (PTT) based on gold nanomaterials is a promising therapeutic modality, which can be combined with the advanced imaging modalities for the multi-functional therapeutic application (Huang et al., 2017; Wu et al., 2019).

Gold nanomaterials have been widely investigated as considerable biocompatible platforms for the biological field due to the advantages of simple synthesis, large surface area, adjustable optical property, and multiple surface modification (Conde et al., 2012; Jackman et al., 2017). Over the past decade, numerous fundamental reviews have comprehensively investigated the synthesis, size, optical properties, and modification of gold nanoparticles (Daniel and Astruc, 2004; Jain et al., 2008; Sardar et al., 2009; Sau et al., 2010; Jones et al., 2011; Cao et al., 2014; Chauhan and Mukherji, 2014; Singh et al., 2014; Rai et al., 2016; Amendola et al., 2017; Pareek et al., 2017), so these characteristics

will be only briefly mentioned in this mini-review. Herein, the photothermal imaging (PTI), surface-enhanced Raman scattering (SERS), and photoacoustic imaging (PAI) guided *in vivo* cancer therapy are focused. What is worth noting is excellent photothermal effect, the localized surface plasmon resonance (LSPR) effect and enhanced electromagnetic field (SERS) of gold nanoparticles in the near infrared (NIR) region. Due to low absorption of water and hemoglobin, the NIR region (700–1,300 nm) is ideal for gold nanomaterials to have a deeper penetration depth in the tumor therapy and imaging (Bao et al., 2016). Gold nanomaterial can convert the absorbed light energy into overheating in the surrounding environment through non-radiative conversion owing to the desirable absorption cross sections and photothermal conversion efficiencies (η) in NIR region (Cao et al., 2019). Therefore, gold nanomaterials are considered as exogenous photothermal transduction agents for PTI and contrast agents for PAI, which can accumulate at tumor tissue via the enhanced permeability and retention (EPR) effect (Henry et al., 2016). Moreover, LSPR effect is a surface plasmon resonance phenomenon of the noble metal nanomaterials, which is heavily dependent on the composition, shape, size, and micro-environmental medium (Guo et al., 2015; Tian et al., 2016, 2018). In addition, SERS is generated from the strong phonon-electron interaction in the nanogaps (Girard et al., 2016). Thus, the Raman signals are enhanced by several orders of magnitude, and gold nanomaterials labeled with reporter molecules can be used as nanotags for *in vivo* imaging (Ding et al., 2016). In short, these gold nanomaterials having resonance peak within NIR (>800 nm), including gold nanorods, gold nanocages, gold nanoshells, and assemblies, can be used as photothermal agents, imaging agents, contrast agents, and therapeutic agents (Shanmugam et al., 2014). **Table 1** presents some examples of

in vivo imaging and therapeutic modalities based on different types of gold nanomaterials.

After intravenous injection, considering the pH, high ionic strength and serum concentration in the complex biological environment of organism, surface functionalization of gold nanomaterials is essential to ensure the adequate repeatability and stability (Chen et al., 2010). Basically, modulation of the surface charge, biocompatible pH values, controllable biodistribution patterns, and better aqueous dispersion of gold nanomaterials could benefit from the surface modification approaches (Huckaby and Lai, 2018; Ruiz-Muelle et al., 2019). Furthermore, the rational surface modification strategies in anticancer application can also reduce the toxicity of nanomaterials, target effectively in the cancer tissue, increase the circulatory half-life, block absorption of serum proteins, avoid unexpected side effects, escape the clearance by the reticuloendothelial system and the liver and spleen macrophages (Otsuka et al., 2003; Kooijmans et al., 2016; Dai et al., 2018; Sztandera et al., 2019). Due to the facile surface chemistry properties, functional groups can combined with gold nanomaterials through weak interactions and the stable covalent anchors (Kou et al., 2009; Moraes Silva et al., 2016; Zou et al., 2016; Wang K. et al., 2017). So far, many modification approaches have been introduced by covering and ligand exchange, so gold nanoparticles can be modified with biopolymer (e.g., polyethylene glycol (PEG), oligonucleotides, antibodies, peptides) (Loh et al., 2016; Chen Y. et al., 2017; Anantha-Iyengar et al., 2019; Delpiano et al., 2019), hydrophobic drug molecules (e.g., paclitaxel, cisplatin, tamoxifen, doxorubicin) (Avitabile et al., 2018; Ma et al., 2018), biofunctional molecules (chitosan, silica, folic acid, polyunsaturated fatty acids, and hyaluronic

TABLE 1 | Examples of different structural characteristics, optical properties, and *in vivo* imaging modality.

Structure and surface	Size (nm)	Wavelength (nm)	Laser	Models	Imaging modalities/ η	References
Nanoshells/nanomatryoshkas, thiol-PEG	150/90	~800	2 W/cm ² , 810 nm	TNBC tumor- bearing female mice	PTI, 39%/63%	Ayala-Orozco et al., 2014
Nanocages, PVP and RBC-membrane	71–89	810–817	1 W/cm ² , 850 nm	4T1 tumor- bearing BALB/c mice	PTI	Piao et al., 2014
Nanoshells, thiol-PEG	~120	780–800	4.5 W, 810 nm	Prostate cancer- patients	PTI	Rastinehad et al., 2019
Nanospheres, Au-Cu ₂ S ₅ , PMHC ₁₈ -PEG ₅₀₀₀	~20	~1,100	0.6 W/cm ² , 1064 nm	CT26 tumor- bearing mice	PTI, 37%	Ding et al., 2014
Nanospheres, Au-silica	~120		0.29 W, 785 nm	Female nude mice	SERS	Bohndiek et al., 2013
Linear gold nanospheres assemblies, rBSA-FA	71.6	~650	0.5 W/cm ² , 808/785 nm	MCF-7 tumor-bearing mice	PTI, SERS	Xia et al., 2018
Nanorods, Au-Ag-silica, PEG	80–97	~585	3 W/cm ² , 660 nm	Ovarian cancer xenograft model and RCAS/TVA GBM mouse	PTI, SERS	Pal et al., 2019
Nanovesicles (PEG-b-PCL)	145	~800	1 W/cm ² , 808 nm	MDA-MB-435 tumor-bearing mice	PTI, PAI, 37%	Huang et al., 2013
Nanorods, PDL/IR775c layered silica	400	780	795/920 nm	Female FVB/n mice	PAI	Dhada et al., 2019
Nanorods, PNIPAM	320	760	808 nm	Prostate cancer- bearing mice	PAI	Chen Y. S. et al., 2017

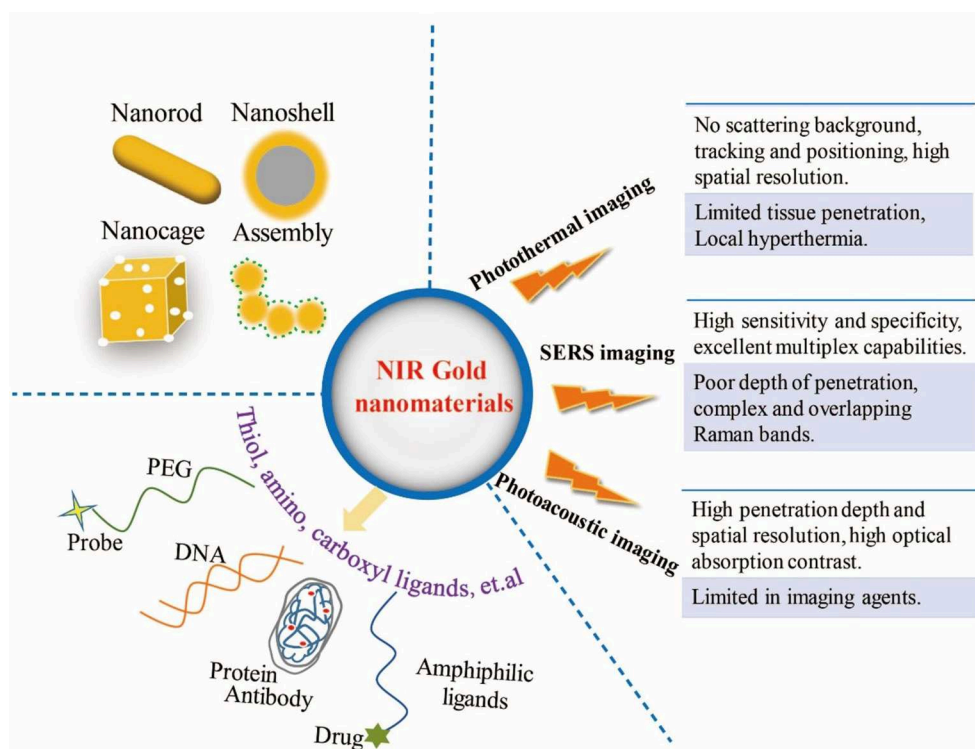


FIGURE 1 | Illustration of multifunctional NIR gold nanoparticles platform for three imaging modalities.

acid, etc.) (Vigderman and Zubarev, 2013; Sztandera et al., 2019) and other amphiphilic ligands through functional bridges, such as thiol ligands (e.g., thiolate, dithiolate, thioctic acid), amino, and carboxyl moieties (**Figure 1**) (Daraee et al., 2014; Kong et al., 2017).

Based on the physical and optical properties of gold nanomaterials, the bioimaging techniques using gold nanomaterials are beneficial to enhance the accuracy of *in vivo* treatment and effectiveness of real-time monitoring. Recently, the non-invasive imaging-guided cancer therapy based on gold nanomaterials have been applied for providing more valuable information and improving the therapy outcomes. This mini review displays some examples of gold nanomaterials-based imaging modes in NIR region for *in vivo* diagnosis and therapy, including PTI, SERS, PAI, and their multiple imaging modalities. These characteristics of the three imaging modalities are shown in **Figure 1**.

PHOTOTHERMAL IMAGING (PTI)

For PTT, gold nanomaterials can transduce the absorbed light energy into heat energy for improving the temperature of tumor cells microenvironment. When the temperature exceeds 42°C, malignant cells are destroyed without damaging the adjacent healthy tissues (Qi et al., 2019). As a result, the therapeutic effect is far superior to that of laser irradiation alone (Abadeer and Murphy, 2016). The laser safety standard establish the maximum permissible exposure (MPE) values, which is on the basis of

the damage threshold levels of laser light for skin (Jiao et al., 2019). For example, the MPE corresponding to 808 nm laser for skin is 0.33 W cm⁻², and the MPE of 1,000–1,350 nm is 1 W cm⁻² (Lin et al., 2017). Photothermal effect based on gold nanomaterials also afford a considerable imaging modality, that is, photothermal imaging (PTI), which has significant advantages over fluorescence imaging (Wang et al., 2009). PTI based on gold nanomaterials provides the accurate positioning, effective treatment, non-invasive therapy for various cancers in short time (Kang et al., 2018). Because it does not involve photobleaching or illumination saturation, and it is almost immune to background signals even accompanied with scattering (Boyer et al., 2002; Vines et al., 2019).

Conventional photothermal imaging is capable of detecting single molecules and differentiating gold nanoparticles, which is restricted by diffraction and resolution. A super-resolution photothermal imaging could be performed based on non-linear amplification signal for resolving multiple gold nanoparticles (Nedosekin et al., 2014). On account of the poor blood supply, tumors show reduced heat tolerance and thus can be destroyed in tens of minutes under hyperthermia condition (Qi et al., 2019). As known, intensive laser irradiation may lead to overheating and harm the nearby normal tissue. However, gold nanomaterials serve as the photothermal conversion agents to produce regional heating rapidly for PTT, and this method can effectively reduce irreversible tissue damage caused by laser irradiation (Ren et al., 2013). Owing to maximum transmittance in the blood and tissues in the NIR region, gold nanomaterials have deeper tissue

penetration and lower background signal (Liu et al., 2014). With inherent advantages of multi-functionalization and tunable optical properties, gold nanomaterials coated with biomolecules had been developed to increase biological stability and prolong the circulation time *in vivo* (Choi et al., 2011). For example, red blood cell membranes coated gold nanocages (RBC-Au NCs) were combined with photothermal effects from gold nanocages and biological characteristics from RBCs, which showed good biological stability, observably improved tumor uptake, and longer retention time in blood (Piao et al., 2014). This work achieved 100% survival during 45 days and facilitated the RBC-Au NCs for the *in vivo* treatment with an improved efficacy using surface engineering.

Compared with other shapes, elongated nanoparticles have better affinity, greater diffusion and transmembrane rates, and they can penetrate the tumors rapidly and accumulate extensively (Lee et al., 2017). These had been demonstrated that the multifunctional nanomaterials had a high accumulation at tumor tissue in mice, which were able to kill cancer cells effectively by producing enough heat and reactive oxygen species. Chitosan/gold nanorod nanocarriers with loading anti-cancer drug cisplatin were prepared, which improved the therapeutic efficacy via synergistic effect of combining PTT and chemotherapy (Chen et al., 2013b). It had been found that the temperature of tumor site could reach 49°C in 10 min with IR irradiation and the tumor growth was almost completely suppressed by cisplatin-loaded nanospheres. As known, lanthanide ions have the ability to convert the NIR long-wavelength into visible wavelengths in photon upconversion process (Wang and Liu, 2009). Customarily, lanthanide doped nanocrystals having novel luminescent properties are considered as upconversion luminescence nanoparticles, which exhibit superior features in biological assays, such as low auto-fluorescence signals, narrow emission bandwidths, large anti-Stokes shifts, high penetration depth, and low toxicity (Huang et al., 2014; Gnach et al., 2015; Liu et al., 2019b). In order to increase the photothermal conversion efficiency and penetration depth in biological tissues, gold nanorods combined with rare-earth ions had been designed for PTT and multimodal imaging for anti-tumor therapy, because upconversion luminescence nanoparticles displayed deeper penetration and lower autofluorescence signals by anti-Stokes emission, and they could also transfer NIR light to gold nanorods via luminescence resonance energy transfer (Wang et al., 2018). With combination of phototherapy, gene therapy, and chemotherapy, the rational treatment strategy has an overwhelming superiority of tumor shrinkage and survival rate, which also could monitor host reactions and comprehensively evaluate tumor microenvironment. Lee et al. introduced silica-coated gold nanorods modified with rabies virus glycoprotein for treating brain tumors (Lee et al., 2017). The surface-modified nanomaterials could enter the brain through central nervous system and bypass the blood-brain barrier. The rod nanostructure increased the chance of interacting with the nicotinic acetylcholine receptor and the response to hyperthermia in NIR laser irradiation.

According to the reports, drug release, and chemotherapy displayed higher cytotoxicity for enhancing the therapeutic

efficacy at raised temperatures from PTT (Vines et al., 2019; Wu et al., 2019). Indocyanine green was successfully sealed in chitosan/gold nanorod nanocapsule for PTT and photodynamic combined therapy (Chen et al., 2013a). Conde et al. adapted a triple-combination therapy that relied on drug-gold nanorods and siRNA-gold nanospheres for drug release, distinguish cancer and normal cells, and prevented cancer recurrence in a mouse model of colon cancer (Conde et al., 2016). In spite that drug-loaded nanocarriers with hyperthermia effect have therapeutic advantages for releasing targeting agents for tumor, there are still some drawbacks, such as insufficient or excessive dose by intravenous delivery (Tong et al., 2016; Wilhelm et al., 2016; Nabil et al., 2019). Recently, Lee et al. proposed a transplantable therapeutic interface based on a gold-coated nanoturf structure for on-demand hyperthermia therapy and drug delivery (Lee et al., 2018). The gold-coated polymeric nanoturf structure could not only serve as drug reservoir but also provide an induced heat under NIR irradiation, thus modulating drug releasing rate and controlling the surface temperature precisely for an esophageal cancer model. Moreover, to maximize the synergistic effects by exogenous and endogenous stimuli, two smart gold nanocages containers coated with photothermal and pH responsive polymer were designed for loading doxorubicin (Dox) and erlotinib (Erl), respectively (Feng et al., 2019). In the NIR irradiation and acidic tumor microenvironment stimulation, tumors were killed by synergistic therapy of PTT and time-staggered drug release strategy of Dox and Erl. The combination strategy obviously improved the therapy efficacy by controlling the order and continuance of drug in timing and spacing scale. These results show that it is difficult to completely ablate the tumor without any recurrence only based on PTI, because local photothermal is unable to impede the spread of cancer cells. Therefore, multiple imaging techniques need to be combined for redeeming the shortcomings of PTI.

In addition, gold nanoparticles are eliminated from the body to minimize health hazard at reasonable concentrations, which are supervised as medical devices by the Food and Drug Administration. Tremendous investigations on gold nanomaterials had been studied for biomedical sciences, and the preclinical safety of gold nanoshells had been established *in vitro* and *in vivo* (Gad et al., 2012). Recently, Halas et al. reported a study of photothermal ablation for prostate tumors in clinical trials which gold-silica nanoshells (7.5 mL/kg dose volume) were utilized in combination with imaging modality, without significant adverse events in 94% of patients (Rastinehad et al., 2019). This treatment protocol was demonstrated to be safe and feasible procedure for localized prostate cancer with low or intermediate risk, and it would open the door for gold nanomaterials in the clinical anticancer application. However, the bioinert and lack of biodegradation of gold nanomaterials bring uncertainty and toxicity to the human body. These negative feedbacks will directly affect the further clinical application of gold nanomaterials.

SERS IMAGING

In general, Raman reporter molecules are attached to the surface of gold nanomaterials, providing unique, and certain

representative peaks as the signal source (Lu et al., 2010b). The inelastic scattering of gold nanotags has narrow characteristic bandwidths with several orders of amplification, which provides sufficient structural and quantitative information for biological interactions and analyte (Maiti et al., 2010). SERS imaging is being recognized as a promising optical modality for preclinical and clinical cancer application. Compared with fluorescent imaging, SERS imaging can avoid photobleaching and photoblinking and serve as an eligible alternative with good photostability for *in vivo* imaging (Pal et al., 2019). Normally, magnetic resonance imaging (MRI) is time-consuming imaging with low sensitivity. While SERS imaging is not only fast speed and super sensitivity, but also has excellent multiplex capabilities and fine specificity for multiplex targeting (Von Maltzahn et al., 2009). In recent decades, SERS-based detection with enhanced electromagnetic field is extremely sensitive for trace analysis in nanoscale regions (Bardhan et al., 2014). More importantly, SERS imaging has weak interference signals in biological tissues, thus it is popular in high-sensitive cell tracking (Wang Z. et al., 2017).

As known, MRI has been usually used for preoperative directions and determining the macroscopic profile of the tumor. However, the typical imaging methods were limited by low sensitivity, and spatial resolution, and it was particularly difficult to describe the actual margins of tumors due to the brain shift in surgery (Orringer et al., 2010). For preoperative evaluation and intraoperative treatment, Kircher et al. showed a triple-modality to delineate the brain tumor boundaries in living mice (Kircher et al., 2012). Ideally, SERS imaging is a type of real-time imaging technique, which plays a main role in navigation for accurately delineating the brain tumor margins and guiding the tumor resection. With the development of SERS imaging for tissue in small animals, an imaging system with large area and high spatial resolution had been exploited (Bohndiek et al., 2013). This unique spectroscopic instrument showed an ultra-high sensitivity for a non-invasive imaging modality. It simplified animal handling, and thus could realize rapid and multiplex detection for the characterization of uptake dynamics *in vivo*. Gold nanoparticles covered with Raman active molecules are contrast agents with an enhanced scattering intensity. The size of core nanomaterials, the properties of Raman molecules, and the number of the molecules absorbed on the surface determine the order of magnitude of amplification. Harmsen et al. presented an administrative SERS nanoparticle for intraoperative imaging in mouse models of glioblastoma, which was composed of a gold core and a layer of Raman reporter molecules embedded in a silica shell (Harmsen et al., 2015). As a result, the limit of detection (LOD) reached femtomolar. Furthermore, Wang's group synthesized 3D flower-like hierarchical gold nanostructures and gold nanostars for cancer therapy (Song et al., 2016, 2018, 2019). The SERS-active gold nanomaterials could use as SERS tags and nanocarriers for cell imaging and drug delivery, which were suitable candidates for promising SERS-imaging.

For *in vivo* SERS mapping, gold nanostars conjugated with antibodies and Raman tags were able to detect the immunomodulators and immunomarkers simultaneously (Ou et al., 2018). With the accumulation of gold nanostars by intravenous injection, the real-time longitudinal tracking of the both biomarkers was implemented, and the sensitivity and

specificity of the relevant SERS signals displayed different levels in breast cancer tumors. Furthermore, the high-resolution SERS imaging could evaluate the distributions of gold nanostars in tumors which were closely related to vascular density. With wonderful optical properties, one-dimensional gold nanoparticle assemblies (GNAs) with good dispersion, stability, and biocompatibility were developed for *in vivo* imaging (Xia et al., 2018). The GNAs exhibited numerous ultra-small nanogaps (smaller than 1.0 nm) and flexible caterpillar-like nanostructures, which could change their morphology randomly. Due to the remarkable SERS signal and good photothermal effect, the GNAs were used as an efficient platform for SERS imaging and photothermal imaging. Currently, SERS scanners are dependent on the point-by-point acquisition, with a relatively slow speed, which could not be satisfied for real-time and rapid imaging in oncological application. Encouraged by the versatility of fluorescence imaging and the specificity of SERS detection, rational design of nanoprobe had been carried out for fluorescence and SERS imaging in ovarian cancer xenograft models (Pal et al., 2019). The bimodal nanoprobe based on DNA and gold nanorods with three consecutive layers were used successfully for imaging-guided tumor ablation and PTT. Meanwhile, aptamer-conjugated gold nanocage has also been built as the bifunctional theranostic platforms for SERS imaging and NIR-triggered PTI (Wen et al., 2019). However, the real biological environment of the human body is more intricate than animal models, and most of the modified nanoprobe are likely to be metabolized directly by immune system. Therefore, the results can lead to the reduced active targeting, the limitation of circulation time and insufficient dose of these nanoprobe that will affect the therapeutic and imaging effects.

PHOTOACOUSTIC IMAGING (PAI)

As known, contrast agents or tissue can absorb the non-ionizing laser and be heated, leading to a transient thermoelastic expansion. Subsequently, wideband acoustic waves are produced as photoacoustic waves, which can be captured on the surface of target substance (Ju et al., 2019). Usually, computed tomography (CT) imaging is high toxicity, the non-specific distribution of contrast agents, and short imaging time (Xu et al., 2019). However, PAI relies on the photoacoustic effect with high reliability, and the gold contrast agents can be purposely modified. Additionally, compared with MRI and fluorescent imaging, PAI is non-invasive, quantitative, and speedy, and it also presents high spatial-resolution of ultrasound imaging and contrast of optical imaging (Zackrisson et al., 2014). PAI has been demonstrated as a powerful tool to visualize biological tissues with the advantages of deep penetration and high spatial-resolution (Agarwal et al., 2007).

Gold nanomaterials are one kind of contrast agents for providing improved photoacoustic signals because of chemical inertness and large absorption cross sections in NIR region (Yang et al., 2015). PEG-coated Au nanocage and pegylated hollow gold nanospheres had been described as optical contrast agents for *in vivo* PAI (Yang et al., 2007; Lu et al., 2010a). Specifically, PEGylation-modified gold nanostructures with different shapes, including nanospheres, nanodisks, nanorods,

and cubic nanocages, had already been investigated for bioactivity analyses in EMT6 breast cancer model (Black et al., 2014). Furthermore, gold nanorods had been applied to image in ovarian tumor models with a multimodal imaging (Jokerst et al., 2012a). In this study, the parallel PAI and SERS imaging had complementary capabilities, where the PAI characterized the size, morphology, and stage of the tumor, and SERS imaging guided the surgical resection. The silica-coated gold nanorods as PAI agents exhibited a higher cellular up-take and had no toxic effect on normal cells. They had been prepared to quantitate and image mesenchymal stem cells for living mice in real time, and the results showed the spatial resolution of 340 μm and the temporal resolution of 0.2 s (Jokerst et al., 2012b). To track the stem cell in cardiovascular diseases, silica-gold nanorods with coating IR775c, which was a sensitive dye of reactive oxygen species, had been developed for PAI (Dhada et al., 2019). The nanoprobe had a high spatial and temporal resolution, and they displayed a 5% viability of mesenchymal stem cells after 10 days.

Due to the small size of nanoparticles with the overlap heating volume, the intensity of photoacoustic signal could be increased proportionally to the huge thermal energy which was rapidly generated from the conversion from optical absorption (Chen et al., 2012). Chen et al. synthesized small gold nanoparticle with controlled aggregation in a volume-changing nanocarrier that had photothermal stimuli-responsive behavior (Chen Y. S. et al., 2017). Overall, the PAI shows a dynamic contrast-enhancement, while the background signals from tissue is suppressed. Although the photonic nanoclusters are well-understood and have been applied in a variety of bioimaging, the bottom-up assembly based on nucleic acid scaffolds is still a challenge. As an example, the plasmonic self-assemblies had been exploited as photo-responsive probes for multimodal SERS and PAI *in vivo* (Köker et al., 2018). In this method, the discrete gold nanoparticles were functionalized with two complementary split fragments of green fluorescent protein. Park et al. manufactured a gold nanoclusters based on gold nanoparticles (about 4.5 nm) and albumin for optically visualizing and treating colon cancers via PTT, fluorescence imaging, and PAI (Park et al., 2019). By optimizing the size, shape, and optical absorption of the hybrid albumin nanostructures, the promising platform displayed a strong hyperthermic effect, as well as a balance between LSPR and fluorescence resonance energy transfer effects.

CONCLUSIONS AND PERSPECTIVES

The research on bioimaging has been mainly promoted by the systematic exploitation of nanomaterials and the combination of modern techniques. Different types of functionalized gold nanosensors have been reported with the development of the surface modification. In this review, the multifunctional gold nanomaterials have been showed for imaging-guided *in vivo* cancer therapy using photothermal, SERS, PAI, and multiples imaging modalities. Various types of gold nanostructured loading platforms have been studied for imaging and treatment of cancers. Nonetheless, there remain some challenges and opportunities for further and higher demand for

in vivo and clinical studies. Firstly, the development of gold nanomaterials is crucial for the applications of optical imaging and synergetic therapy. For ideal imaging and therapeutic results, three-dimensional structure, special configuration of assemblies and composite gold nanomaterials are popular for the bio-application. For example, some gold nanomaterials with well-defined architectures and luxuriant hot spots, including composite gold nanomaterials and self-assemblies, may generate stronger electromagnetic-field enhancement for SERS imaging. These novel nanomaterials also can be explored as excellent contrast agents for PAI to overcome the problem of penetration depth. Meanwhile, the multifunctional agents and biological responsive (accelerative or passivated) molecules also necessary to be developed with less toxic and better dispersion for the organism. Therefore, the appropriate multifunctional agents can avoid the possibility that the partial malignant cells are intact after local hyperthermia in the effective PTT. It is also possibility to enhance the NIR responsiveness, improve the accuracy of targeting, and increase the efficiency of the delivery during the cancer treatment. On the other hand, SERS possess single molecule sensitivity *in vitro* experiment, and the elaborated gold nanomaterials will be promising candidate to reach this level and free from the interference of other species in the biological system. Consequently, efficient composite gold nanoparticles with desirable surface modification agents are pressingly needed to achieve the desired effect *in vivo*. Similarly, the thermal resistance also can be reduced by modifying interfacial agents to improve the photoacoustic signal and resolution. Almost all of the experimental and theoretical researches have focused on the animal modes, while the clinical study is still lacking. Lastly, it is necessary to integrate diagnosis, multimodal imaging, and enhanced therapies for clinical application. Elaborate detecting strategies and sensitive multiplex techniques can enhance the spatial and temporal resolution, capture actual dynamic processes in real-time, and answer the fundamental biological questions in modern medicine. Finally, most of the research has focused on the biological interactions, intracellular distribution, and the transport behaviors of gold nanomaterials, while the detailed mechanism of different interaction with biomolecules and the process of internalization are still lack of deep understanding.

AUTHOR CONTRIBUTIONS

LW and SQ designed and revised this manuscript. YT wrote this manuscript.

FUNDING

This work was financially supported by the National Key Research and Development Program of China (2017YFA0205300), the National Natural Science Foundation of China (61571239), the Program for Changjiang Scholars and Innovative Research Team in University (IRT_15R37), and the Key Research and Development Program of Jiangsu (BE2018732).

REFERENCES

- Abadeer, N. S., and Murphy, C. J. (2016). Recent progress in cancer thermal therapy using gold nanoparticles. *J. Phys. Chem. C* 120, 4691–4716. doi: 10.1021/acs.jpcc.5b11232
- Agarwal, A., Huang, S. W., O'Donnell, M., Day, K. C., Day, M., Kotov, N., et al. (2007). Targeted gold nanorod contrast agent for prostate cancer detection by photoacoustic imaging. *J. Appl. Phys.* 102:064701. doi: 10.1063/1.2777127
- Amendola, V., Pilot, R., Frascioni, M., Maragò, O. M., and Iati, M. A. (2017). Surface plasmon resonance in gold nanoparticles: a review. *J. Phys. Condens. Matter* 29:203002. doi: 10.1088/1361-648X/aa60f3
- Anantha-Iyengar, G., Shanmugasundaram, K., Nallal, M., Lee, K.-P., Whitcombe, M. J., Lakshmi, D., et al. (2019). Functionalized conjugated polymers for sensing and molecular imprinting applications. *Prog. Polym. Sci.* 88, 1–129. doi: 10.1016/j.progpolymsci.2018.08.001
- Avitabile, E., Bedognetti, D., Ciofani, G., Bianco, A., and Delogu, L. G. (2018). How can nanotechnology help the fight against breast cancer? *Nanoscale* 10, 11719–11731. doi: 10.1039/C8NR02796J
- Ayala-Orozco, C., Urban, C., Knight, M. W., Urban, A. S., Neumann, O., Bishnoi, S. W., et al. (2014). Au nanomaterials as efficient near-infrared photothermal transducers for cancer treatment: benchmarking against nanoshells. *ACS Nano* 8, 6372–6381. doi: 10.1021/nn501871d
- Bao, Z., Liu, X., Liu, Y., Liu, H., and Zhao, K. (2016). Near-infrared light-responsive inorganic nanomaterials for photothermal therapy. *Asian J. Pharm. Sci.* 11, 349–364. doi: 10.1016/j.ajps.2015.11.123
- Bardhan, M., Satpati, B., Ghosh, T., and Senapati, D. (2014). Synergistically controlled nano-templated growth of tunable gold bud-to-blossom nanostructures: a pragmatic growth mechanism. *J. Mater. Chem. C* 2, 3795–3804. doi: 10.1039/C4TC00160E
- Black, K. C., Wang, Y., Luehmann, H. P., Cai, X., Xing, W., Pang, B., et al. (2014). Radioactive au-198-doped nanostructures with different shapes for *in vivo* analyses of their biodistribution, tumor uptake, and intratumoral distribution. *ACS Nano* 8, 4385–4394. doi: 10.1021/nn406258m
- Bohndiek, S. E., Wagadarikar, A., Zavaleta, C. L., Van de Sompel, D., Garai, E., Jokerst, J. V., et al. (2013). A small animal raman instrument for rapid, wide-area, spectroscopic imaging. *Proc. Natl. Acad. Sci. U.S.A.* 110, 12408–12413. doi: 10.1073/pnas.1301379110
- Boyer, D., Tamarat, P., Maali, A., Lounis, B., and Orrit, M. (2002). Photothermal imaging of nanometer-sized metal particles among scatterers. *Science* 297, 1160–1163. doi: 10.1126/science.1073765
- Cao, J., Sun, T., and Grattan, K. T. V. (2014). Gold nanorod-based localized surface plasmon resonance biosensors: a review. *Sens. Actuat.* 195, 332–351. doi: 10.1016/j.snb.2014.01.056
- Cao, W., He, Y., Zhu, R., He, Y., Hao, Z., Zhao, Q., et al. (2019). NIR light triggered size variable “remote-controlled cluster bomb” for deep penetration and tumor therapy. *Chem. Eng. J.* 375, 122080. doi: 10.1016/j.cej.2019.122080
- Chauhan, S. K., and Mukherji, S. (2014). Gold nanoparticles and nanostructures in optical biosensors. *Mater. Technol.* 30, B167–B177. doi: 10.1179/1753555714Y.0000000212
- Chen, G., Roy, I., Yang, C., and Prasad, P. N. (2016). Nanochemistry and nanomedicine for nanoparticle-based diagnostics and therapy. *Chem. Rev.* 116, 2826–2885. doi: 10.1021/acs.chemrev.5b00148
- Chen, H. J., Ming, T. A., Zhao, L., Wang, F., Sun, L. D., Wang, J. F., et al. (2010). Plasmon-molecule interactions. *Nano Today* 5, 494–505. doi: 10.1016/j.nantod.2010.08.009
- Chen, R., Wang, X., Yao, X., Zheng, X., Wang, J., and Jiang, X. (2013a). Near-ir-triggered photothermal/photodynamic dual-modality therapy system via chitosan hybrid nanospheres. *Biomaterials* 34, 8314–8322. doi: 10.1016/j.biomaterials.2013.07.034
- Chen, R., Zheng, X. C., Qian, H. Q., Wang, X., Wang, J., and Jiang, X. Q. (2013b). Combined near-ir photothermal therapy and chemotherapy using gold-nanorod/chitosan hybrid nanospheres to enhance the antitumor effect. *Biomater. Sci.* 1, 285–293. doi: 10.1039/C2BM00138A
- Chen, Y., Xianyu, Y., and Jiang, X. (2017). Surface modification of gold nanoparticles with small molecules for biochemical analysis. *Acc. Chem. Res.* 50, 310–319. doi: 10.1021/acs.accounts.6b00506
- Chen, Y. S., Frey, W., Aglyamov, S., and Emelianov, S. (2012). Environment-dependent generation of photoacoustic waves from plasmonic nanoparticles. *Small* 8, 47–52. doi: 10.1002/sml.201101140
- Chen, Y. S., Yoon, S. J., Frey, W., Dockery, M., and Emelianov, S. (2017). Dynamic contrast-enhanced photoacoustic imaging using photothermal stimuli-responsive composite nanomodulators. *Nat. Commun.* 8:15782. doi: 10.1038/ncomms15782
- Choi, W. I., Kim, J. Y., Kang, C., Byeon, C. C., Kim, Y. H., and Tee, G. (2011). Tumor regression *in vivo* by photothermal therapy based on gold-nanorod-loaded, functional nanocarriers. *ACS Nano* 5, 1995–2003. doi: 10.1021/nn103047r
- Conde, J., Doria, G., and Baptista, P. (2012). Noble metal nanoparticles applications in cancer. *J. Drug Delivery* 2012:751075. doi: 10.1155/2012/751075
- Conde, J., Oliva, N., Zhang, Y., and Artzi, N. (2016). Local triple-combination therapy results in tumour regression and prevents recurrence in a colon cancer model. *Nat. Mater.* 15, 1128–1138. doi: 10.1038/nmat4707
- Dai, Q., Wilhelm, S., Ding, D., Syed, A. M., Sindhvani, S., Zhang, Y., et al. (2018). Quantifying the ligand-coated nanoparticle delivery to cancer cells in solid tumors. *ACS Nano* 12, 8423–8435. doi: 10.1021/acsnano.8b03900
- Daniel, M. C., and Astruc, D. (2004). Gold nanoparticles: assembly, supramolecular chemistry, quantum-size-related properties, and applications toward biology, catalysis, and nanotechnology. *Chem. Rev.* 104, 293–346. doi: 10.1021/cr030698+
- Daraee, H., Eatemadi, A., Abbasi, E., Fekri Aval, S., Kouhi, M., and Akbarzadeh, A. (2014). Application of gold nanoparticles in biomedical and drug delivery. *Artif. Cells, Nanomed. Biotechnol.* 44, 410–422. doi: 10.3109/21691401.2014.955107
- Delpiano, G. R., Casula, M. F., Piludu, M., Corpino, R., Ricci, P. C., Vallet-Regí, M., et al. (2019). Assembly of multicomponent nano-bioconjugates composed of mesoporous silica nanoparticles, proteins, and gold nanoparticles. *ACS Omega* 4, 11044–11052. doi: 10.1021/acsomega.9b01240
- Dhada, K. S., Hernandez, D. S., and Suggs, L. J. (2019). *In vivo* photoacoustic tracking of mesenchymal stem cell viability. *ACS Nano* 13, 7791–7799. doi: 10.1021/acsnano.9b01802
- Ding, S. Y., Yi, J., Li, J. F., Ren, B., Wu, D. Y., Panneerselvam, R., et al. (2016). Nanostructure-based plasmon-enhanced raman spectroscopy for surface analysis of materials. *Nat. Rev. Mater.* 1:16021. doi: 10.1038/natrevmats.2016.21
- Ding, X., Liow, C. H., Zhang, M., Huang, R., Li, C., Shen, H., et al. (2014). Surface plasmon resonance enhanced light absorption and photothermal therapy in the second near-infrared window. *J. Am. Chem. Soc.* 136, 15684–15693. doi: 10.1021/ja508641z
- Feng, Y., Cheng, Y., Chang, Y., Jian, H., Zheng, R., Wu, X., et al. (2019). Time-staggered delivery of erlotinib and doxorubicin by gold nanocages with two smart polymers for reprogrammable release and synergistic with photothermal therapy. *Biomaterials* 217:119327. doi: 10.1016/j.biomaterials.2019.119327
- Gad, S. C., Sharp, K. L., Montgomery, C., Payne, J. D., and Goodrich, G. P. (2012). Evaluation of the toxicity of intravenous delivery of auroshell particles (gold-silica nanoshells). *Internet J. Toxicol.* 31, 584–594. doi: 10.1177/1091581812465969
- Girard, A., Gehan, H., Crut, A., Mermet, A., Saviot, L., and Margueritat, J. (2016). Mechanical coupling in gold nanoparticles supermolecules revealed by plasmon-enhanced ultralow frequency raman spectroscopy. *Nano Lett.* 16, 3843–3849. doi: 10.1021/acs.nanolett.6b01314
- Gnath, A., Lipinski, T., Bednarkiewicz, A., Rybka, J., and Capobianco, J. A. (2015). Upconverting nanoparticles: assessing the toxicity. *Chem. Soc. Rev.* 44, 1561–1584. doi: 10.1039/C4CS00177J
- Guo, L., Jackman, J. A., Yang, H.-H., Chen, P., Cho, N.-J., and Kim, D.-H. (2015). Strategies for enhancing the sensitivity of plasmonic nanosensors. *Nano Today* 10, 213–239. doi: 10.1016/j.nantod.2015.02.007
- Harmsen, S., Huang, R. M., Wall, M. A., Karabeber, H., Samii, J. M., Spaliviero, M., et al. (2015). Surface-enhanced resonance raman scattering nanostars for high-precision cancer imaging. *Sci. Transl. Med.* 7:11. doi: 10.1126/scitranslmed.3010633
- Henry, A. I., Sharma, B., Cardinal, M. F., Krouski, D., and Van Duyne, R. P. (2016). Surface-enhanced raman spectroscopy biosensing: *in vivo* diagnostics and multimodal imaging. *Anal. Chem.* 88, 6638–6647. doi: 10.1021/acs.analchem.6b01597

- Huang, P., Lin, J., Li, W., Rong, P., Wang, Z., Wang, S., et al. (2013). Biodegradable gold nanovesicles with an ultrastrong plasmonic coupling effect for photoacoustic imaging and photothermal therapy. *Angew. Chem.* 52, 13958–13964. doi: 10.1002/anie.201308986
- Huang, P., Zheng, W., Zhou, S., Tu, D., Chen, Z., Zhu, H., et al. (2014). Lanthanide-doped $\text{LiF}(4)$ upconversion nanoprobe for the detection of disease biomarkers. *Angew. Chem.* 53, 1252–1257. doi: 10.1002/anie.201309503
- Huang, X., Zhang, W., Guan, G., Song, G., Zou, R., and Hu, J. (2017). Design and functionalization of the nir-responsive photothermal semiconductor nanomaterials for cancer theranostics. *Acc. Chem. Res.* 50, 2529–2538. doi: 10.1021/acs.accounts.7b00294
- Huckaby, J. T., and Lai, S. K. (2018). Pegylation for enhancing nanoparticle diffusion in mucus. *Adv. Drug Deliv. Rev.* 124, 125–139. doi: 10.1016/j.addr.2017.08.010
- Jackman, J. A., Rahim Ferhan, A., and Cho, N. J. (2017). Nanoplasmonic sensors for biointerfacial science. *Chem. Soc. Rev.* 46, 3615–3660. doi: 10.1039/C6CS00494F
- Jain, P. K., Huang, X. H., El-Sayed, I. H., and El-Sayed, M. A. (2008). Noble metals on the nanoscale: optical and photothermal properties and some applications in imaging, sensing, biology, and medicine. *Acc. Chem. Res.* 41, 1578–1586. doi: 10.1021/ar7002804
- Jiao, L., Wang, J., Fan, Y., and Yang, Z. (2019). Porcine skin damage thresholds and histological damage characteristics from 1319-nm laser radiation. *J. Biomed. Opt.* 24, 1–9. doi: 10.1117/1.JBO.24.9.095003
- Jokerst, J. V., Cole, A. J., Van de Sompel, D., and Gambhir, S. S. (2012a). Gold nanorods for ovarian cancer detection with photoacoustic imaging and resection guidance via raman imaging in living mice. *ACS Nano* 6, 10366–10377. doi: 10.1021/nn304347g
- Jokerst, J. V., Thangaraj, M., Kempen, P. J., Sinclair, R., and Gambhir, S. S. (2012b). Photoacoustic imaging of mesenchymal stem cells in living mice via silica-coated gold nanorods. *ACS Nano* 6, 5920–5930. doi: 10.1021/nn302042y
- Jones, M. R., Osberg, K. D., Macfarlane, R. J., Langille, M. R., and Mirkin, C. A. (2011). Templated techniques for the synthesis and assembly of plasmonic nanostructures. *Chem. Rev.* 111, 3736–3827. doi: 10.1021/cr1004452
- Ju, Y., Dong, B., Yu, J., and Hou, Y. (2019). Inherent multifunctional inorganic nanomaterials for imaging-guided cancer therapy. *Nano Today* 26, 108–122. doi: 10.1016/j.nantod.2019.03.006
- Kang, H., Hu, S., Cho, M. H., Hong, S. H., Choi, Y., and Choi, H. S. (2018). Theranostic nanosystems for targeted cancer therapy. *Nano Today* 23, 59–72. doi: 10.1016/j.nantod.2018.11.001
- Kircher, M. F., de la Zerda, A., Jokerst, J. V., Zavaleta, C. L., Kempen, P. J., Mittra, E., et al. (2012). A brain tumor molecular imaging strategy using a new triple-modality mri-photoacoustic-raman nanoparticle. *Nat. Med.* 18, 829–834. doi: 10.1038/nm.2721
- Köcker, T., Tang, N., Tian, C., Zhang, W., Wang, X., Martel, R., et al. (2018). Cellular imaging by targeted assembly of hot-spot sers and photoacoustic nanoprobe using split-fluorescent protein scaffolds. *Nat. Commun.* 9:607. doi: 10.1038/s41467-018-03046-w
- Kong, F. Y., Zhang, J. W., Li, R. F., Wang, Z. X., Wang, W. J., and Wang, W. (2017). Unique roles of gold nanoparticles in drug delivery, targeting and imaging applications. *Molecules* 22:1445. doi: 10.3390/molecules22091445
- Kooijmans, S. A. A., Fliervoet, L. A. L., van der Meel, R., Fens, M., Heijnen, H. F. G., van Bergen En Henegouwen, P. M. P., et al. (2016). Pegylated and targeted extracellular vesicles display enhanced cell specificity and circulation time. *J. Control. Release* 224, 77–85. doi: 10.1016/j.jconrel.2016.01.009
- Kou, X., Sun, Z., Yang, Z., Chen, H., and Wang, J. (2009). Curvature-directed assembly of gold nanocubes, nanobranches, and nanospheres. *Langmuir* 25, 1692–1698. doi: 10.1021/la802883p
- Lee, C., Hwang, H. S., Lee, S., Kim, B., Kim, J. O., Oh, K. T., et al. (2017). Rabies virus-inspired silica-coated gold nanorods as a photothermal therapeutic platform for treating brain tumors. *Adv. Mater.* 29:1605563. doi: 10.1002/adma.201605563
- Lee, S., Hwang, G., Kim, T. H., Kwon, S. J., Kim, J. U., Koh, K., et al. (2018). On-demand drug release from gold nanoturf for a thermo- and chemotherapeutic esophageal stent. *ACS Nano* 12, 6756–6766. doi: 10.1021/acsnano.8b01921
- Lin, H., Gao, S., Dai, C., Chen, Y., and Shi, J. (2017). A two-dimensional biodegradable niobium carbide (mxene) for photothermal tumor eradication in nir-i and nir-ii biowindows. *J. Am. Chem. Soc.* 139, 16235–16247. doi: 10.1021/jacs.7b07818
- Liu, X., Huang, N., Li, H., Wang, H., Jin, Q., and Ji, J. (2014). Multidentate polyethylene glycol modified gold nanorods for *in vivo* near-infrared photothermal cancer therapy. *ACS Appl. Mater. Interfaces* 6, 5657–5668. doi: 10.1021/am5001823
- Liu, Y., Bhattarai, P., Dai, Z., and Chen, X. (2019a). Photothermal therapy and photoacoustic imaging via nanotheranostics in fighting cancer. *Chem. Soc. Rev.* 48, 2053–2108. doi: 10.1039/C8CS00618K
- Liu, Y., Meng, X., and Bu, W. (2019b). Upconversion-based photodynamic cancer therapy. *Coord. Chem. Rev.* 379, 82–98. doi: 10.1016/j.ccr.2017.09.006
- Loh, X. J., Lee, T. C., Dou, Q., and Deen, G. R. (2016). Utilising inorganic nanocarriers for gene delivery. *Biomater. Sci.* 4, 70–86. doi: 10.1039/C5BM00277J
- Lu, W., Huang, Q., Ku, G., Wen, X., Zhou, M., Guzatov, D., et al. (2010a). Photoacoustic imaging of living mouse brain vasculature using hollow gold nanospheres. *Biomaterials* 31, 2617–2626. doi: 10.1016/j.biomaterials.2009.12.007
- Lu, W., Singh, A. K., Khan, S. A., Senapati, D., Yu, H., and Ray, P. C. (2010b). Gold nano-popcorn-based targeted diagnosis, nanotherapy treatment, and *in situ* monitoring of photothermal therapy response of prostate cancer cells using surface-enhanced raman spectroscopy. *J. Am. Chem. Soc.* 132, 18103–18114. doi: 10.1021/ja104924b
- Ma, X., Xiong, Y., and Lee, L. T. O. (2018). Application of nanoparticles for targeting g protein-coupled receptors. *Int. J. Mol. Sci.* 19:E2006. doi: 10.3390/ijms19072006
- Maiti, K. K., Dinish, U. S., Fu, C. Y., Lee, J. J., Soh, K. S., Yun, S. W., et al. (2010). Development of biocompatible sers nanotag with increased stability by chemisorption of reporter molecule for *in vivo* cancer detection. *Biosens. Bioelectron.* 26, 398–403. doi: 10.1016/j.bios.2010.07.123
- Moraes Silva, S., Tavallaie, R., Sandiford, L., Tilley, R. D., and Gooding, J. J. (2016). Gold coated magnetic nanoparticles: from preparation to surface modification for analytical and biomedical applications. *Chem. Commun.* 52, 7528–7540. doi: 10.1039/C6CC03225G
- Nabil, G., Bhise, K., Sau, S., Atef, M., El-Banna, H. A., and Iyer, A. K. (2019). Nano-engineered delivery systems for cancer imaging and therapy: Recent advances, future direction and patent evaluation. *Drug Discov. Today* 24, 462–491. doi: 10.1016/j.drudis.2018.08.009
- Nedosekin, D. A., Galanzha, E. I., Dervishi, E., Biris, A. S., and Zharov, V. P. (2014). Super-resolution nonlinear photothermal microscopy. *Small* 10, 135–142. doi: 10.1002/smll.201300024
- Orringer, D. A., Chen, T., Huang, D. L., Armstead, W. M., Hoff, B. A., Koo, Y. E., et al. (2010). The brain tumor window model: a combined cranial window and implanted glioma model for evaluating intraoperative contrast agents. *Neurosurgery* 66, 736–743. doi: 10.1227/01.NEU.0000367631.02903.50
- Otsuka, H., Nagasaki, Y., and Kataoka, K. (2003). Pegylated nanoparticles for biological and pharmaceutical applications. *Adv. Drug Deliv. Rev.* 55, 403–419. doi: 10.1016/S0169-409X(02)00226-0
- Ou, Y. C., Webb, J. A., O'Brien, C. M., Pence, I. J., Lin, E. C., Paul, E. P., et al. (2018). Diagnosis of immunomarkers *in vivo* via multiplexed surface enhanced raman spectroscopy with gold nanostars. *Nanoscale* 10, 13092–13105. doi: 10.1039/C8NR01478G
- Pal, S., Ray, A., Andreou, C., Zhou, Y., Rakshit, T., Wlodarczyk, M., et al. (2019). DNA-enabled rational design of fluorescence-raman bimodal nanoprobe for cancer imaging and therapy. *Nat. Commun.* 10:1926. doi: 10.1038/s41467-019-09173-2
- Pareek, V., Bhargava, A., Gupta, R., Jain, N., and Panwar, J. (2017). Synthesis and applications of noble metal nanoparticles: a review. *Adv. Sci. Eng. Med.* 9, 527–544. doi: 10.1166/asem.2017.2027
- Park, S., Kim, H., Lim, S. C., Lim, K., Lee, E. S., Oh, K. T., et al. (2019). Gold nanocluster-loaded hybrid albumin nanoparticles with fluorescence-based optical visualization and photothermal conversion for tumor detection/ablation. *J. Control. Release* 304, 7–18. doi: 10.1016/j.jconrel.2019.04.036
- Piao, J. G., Wang, L., Gao, F., You, Y. Z., Xiong, Y., and Yang, L. (2014). Erythrocyte membrane is an alternative coating to polyethylene glycol for prolonging the circulation lifetime of gold nanocages for photothermal therapy. *ACS Nano* 8, 10414–10425. doi: 10.1021/nn503779d

- Qi, Z., Shi, J., Zhang, Z., Cao, Y., Li, J., and Cao, S. (2019). Pegylated graphene oxide-capped gold nanorods/silica nanoparticles as multifunctional drug delivery platform with enhanced near-infrared responsiveness. *Mater. Sci. Eng.* 104:109889. doi: 10.1016/j.msec.2019.109889
- Rai, M., Ingle, A. P., Birla, S., Yadav, A., and Santos, C. A. (2016). Strategic role of selected noble metal nanoparticles in medicine. *Crit. Rev. Microbiol.* 42, 696–719.
- Rastinehad, A. R., Anastos, H., Wajswol, E., Winoker, J. S., Sfakianos, J. P., Doppalapudi, S. K., et al. (2019). Gold nanoshell-localized photothermal ablation of prostate tumors in a clinical pilot device study. *Proc. Natl. Acad. Sci. U.S.A.* 116, 18590–18596. doi: 10.1073/pnas.1906929116
- Ren, F., Bhana, S., Norman, D. D., Johnson, J., Xu, L., Baker, D. L., et al. (2013). Gold nanorods carrying paclitaxel for photothermal-chemotherapy of cancer. *Bioconjugate Chem.* 24, 376–386. doi: 10.1021/bc300442d
- Ruiz-Muelle, A. B., Kuttner, C., Alarcón-Fernández, C., López-Romero, J. M., Uhlmann, P., Contreras-Cáceres, R., et al. (2019). Hybrid surfaces active in catalysis based on gold nanoparticles modified with redox-active pendants and polymer brushes. *Appl. Surf. Sci.* 496:143598. doi: 10.1016/j.apsusc.2019.143598
- Sardar, R., Funston, A. M., Mulvaney, P., and Murray, R. W. (2009). Gold nanoparticles: past, present, and future. *Langmuir* 25, 13840–13851. doi: 10.1021/la9019475
- Sau, T. K., Rogach, A. L., Jäckel, F., Klar, T. A., and Feldmann, J. (2010). Properties and applications of colloidal nonspherical noble metal nanoparticles. *Adv. Mater.* 22, 1805–1825. doi: 10.1002/adma.200902557
- Shanmugam, V., Selvakumar, S., and Yeh, C. S. (2014). Near-infrared light-responsive nanomaterials in cancer therapeutics. *Chem. Soc. Rev.* 43, 6254–6287. doi: 10.1039/C4CS00011K
- Singh, G., van Helvoort, A. T. J., Bandyopadhyay, S., Volden, S., Andreassen, J.-P., and Glomm, W. R. (2014). Synthesis of au nanowires with controlled morphological and structural characteristics. *Appl. Surf. Sci.* 311, 780–788. doi: 10.1016/j.apsusc.2014.05.162
- Song, C., Dou, Y., Yuwen, L., Sun, Y., Dong, C., Li, F., et al. (2018). A gold nanoflower-based traceable drug delivery system for intracellular sers imaging-guided targeted chemo-phototherapy. *J. Mater. Chem.* 6, 3030–3039. doi: 10.1039/C8TB00587G
- Song, C., Li, F., Guo, X., Chen, W., Dong, C., Zhang, J., et al. (2019). Gold nanostars for cancer cell-targeted sers-imaging and nir light-triggered plasmonic photothermal therapy (pptt) in the first and second biological windows. *J. Mater. Chem.* 7, 2001–2008. doi: 10.1039/C9TB00061E
- Song, C. Y., Yang, B. Y., Chen, W. Q., Dou, Y. X., Yang, Y. J., Zhou, N., et al. (2016). Gold nanoflowers with tunable sheet-like petals: facile synthesis, sers performances and cell imaging. *J. Mater. Chem.* 4, 7112–7118. doi: 10.1039/C6TB01046F
- Sztandera, K., Gorzkiewicz, M., and Klajnert-Maculewicz, B. (2019). Gold nanoparticles in cancer treatment. *Mol. Pharm.* 16, 1–23. doi: 10.1021/acs.molpharmaceut.8b00810
- Tian, Y., Shuai, Z., Shen, J., Zhang, L., Chen, S., Song, C., et al. (2018). Plasmonic heterodimers with binding site-dependent hot spot for surface-enhanced raman scattering. *Small* 14:e1800669. doi: 10.1002/smll.201800669
- Tian, Y., Zhang, L., Shen, J., Wu, L., He, H., Ma, D. L., et al. (2016). An individual nanocube-based plasmonic biosensor for real-time monitoring the structural switch of the telomeric g-quadruplex. *Small* 12, 2913–2920. doi: 10.1002/smll.201600041
- Tong, X., Wang, Z., Sun, X., Song, J., Jacobson, O., Niu, G., et al. (2016). Size dependent kinetics of gold nanorods in epr mediated tumor delivery. *Theranostics* 6, 2039–2051. doi: 10.7150/thno.17098
- Vigderman, L., and Zubarev, E. R. (2013). Therapeutic platforms based on gold nanoparticles and their covalent conjugates with drug molecules. *Adv. Drug. Deliv. Rev.* 65, 663–676. doi: 10.1016/j.addr.2012.05.004
- Vines, J. B., Yoon, J. H., Ryu, N. E., Lim, D. J., and Park, H. (2019). Gold nanoparticles for photothermal cancer therapy. *Front. Chem.* 7:167. doi: 10.3389/fchem.2019.00167
- Von Maltzahn, G., Centrone, A., Park, J. H., Ramanathan, R., Sailor, M. J., Hatton, T. A., et al. (2009). Sers-coded gold nanorods as a multifunctional platform for densely multiplexed near-infrared imaging and photothermal heating. *Adv. Mater.* 21, 3175–3180. doi: 10.1002/adma.200803464
- Wang, C., Chen, J., Talavage, T., and Irudayaraj, J. (2009). Gold nanorod/fe3o4 nanoparticle “nano-pearl-necklaces” for simultaneous targeting, dual-mode imaging, and photothermal ablation of cancer cells. *Angew. Chem. Int. Ed. Engl.* 48, 2759–2763. doi: 10.1002/anie.200805282
- Wang, C., Xu, C., Xu, L., Sun, C., Yang, D., Xu, J., et al. (2018). A novel core-shell structured upconversion nanorod as a multimodal bioimaging and photothermal ablation agent for cancer theranostics. *J. Mater. Chem. B* 6, 2597–2607. doi: 10.1039/C7TB02842C
- Wang, F., and Liu, X. (2009). Recent advances in the chemistry of lanthanide-doped upconversion nanocrystals. *Chem. Soc. Rev.* 38, 976–989. doi: 10.1039/b809132n
- Wang, K., Shangguan, L., Liu, Y., Jiang, L., Zhang, F., Wei, Y., et al. (2017). In situ detection and imaging of telomerase activity in cancer cell lines via disassembly of plasmonic core-satellites nanostructured probe. *Anal. Chem.* 89, 7262–7268. doi: 10.1021/acs.analchem.7b01882
- Wang, Z., Zong, S., Wu, L., Zhu, D., and Cui, Y. (2017). Sers-activated platforms for immunoassay: Probes, encoding methods, and applications. *Chem. Rev.* 117, 7910–7963. doi: 10.1021/acs.chemrev.7b00027
- Wen, S., Miao, X., Fan, G. C., Xu, T., Jiang, L. P., Wu, P., et al. (2019). Aptamer-conjugated au nanocage/sio2 core-shell bifunctional nanoprobe with high stability and biocompatibility for cellular sers imaging and near-infrared photothermal therapy. *ACS Sens.* 4, 301–308. doi: 10.1021/acssensors.8b00682
- Wilhelm, S., Tavares, A. J., Dai, Q., Ohta, S., Audet, J., Dvorak, H. F., et al. (2016). Analysis of nanoparticle delivery to tumours. *Nat. Rev. Mater.* 1:16014. doi: 10.1038/natrevmats.2016.14
- Wu, Y., Ali, M. R. K., Chen, K. C., Fang, N., and El-Sayed, M. A. (2019). Gold nanoparticles in biological optical imaging. *Nano Today* 24, 120–140. doi: 10.1016/j.nantod.2018.12.006
- Xia, Y., Ma, X., Gao, J., Chen, G., Li, Z., Wu, X., et al. (2018). A flexible caterpillar-like gold nanoparticle assemblies with ultrasmall nanogaps for enhanced dual-modal imaging and photothermal therapy. *Small* 14:e1800094. doi: 10.1002/smll.201800094
- Xu, Y., Wang, X., Cheng, L., Liu, Z., and Zhang, Q. (2019). High-yield synthesis of gold bipyramids for *in vivo* ct imaging and photothermal cancer therapy with enhanced thermal stability. *Chem. Eng. J.* 378:122025. doi: 10.1016/j.cej.2019.122025
- Yang, X., Skrabalak, S. E., Li, Z. Y., Xia, Y., and Wang, L. V. (2007). Photoacoustic tomography of a rat cerebral cortex *in vivo* with au nanocages as an optical contrast agent. *Nano Lett.* 7, 3798–3802. doi: 10.1021/nl072349r
- Yang, X., Yang, M., Pang, B., Vara, M., and Xia, Y. (2015). Gold nanomaterials at work in biomedicine. *Chem. Rev.* 115, 10410–10488. doi: 10.1021/acs.chemrev.5b00193
- Zackrisson, S., van de Ven, S. M. W. Y., and Gambhir, S. S. (2014). Light in and sound out: emerging translational strategies for photoacoustic imaging. *Cancer Res.* 74, 979–1004. doi: 10.1158/0008-5472.CAN-13-2387
- Zou, Q., Liu, K., Abbas, M., and Yan, X. (2016). Peptide-modulated self-assembly of chromophores toward biomimetic light-harvesting nanoarchitectonics. *Adv. Mater.* 28, 1031–1043. doi: 10.1002/adma.201502454

Conflict of Interest: The authors declare that the research was conducted in the absence of any commercial or financial relationships that could be construed as a potential conflict of interest.

Copyright © 2019 Tian, Qiang and Wang. This is an open-access article distributed under the terms of the Creative Commons Attribution License (CC BY). The use, distribution or reproduction in other forums is permitted, provided the original author(s) and the copyright owner(s) are credited and that the original publication in this journal is cited, in accordance with accepted academic practice. No use, distribution or reproduction is permitted which does not comply with these terms.



Nanomedicines for Near-Infrared Fluorescent Lifetime-Based Bioimaging

Xianhui Lian^{1,2}, Ming-Yuan Wei³ and Qiang Ma^{1*}

¹ Chinese Academy of Inspection and Quarantine, Beijing, China, ² School of Life Science and Medicine, Dalian University of Technology, Panjin, China, ³ Texas Commission on Environmental Quality, Austin, TX, United States

OPEN ACCESS

Edited by:

Qingxin Mu,
University of Washington,
United States

Reviewed by:

Wei Xu,
Beijing Institute of Technology, China
Shujun Cheng,
Shanghai Jiao Tong University, China

*Correspondence:

Qiang Ma
maqiang@caiq.org.cn

Specialty section:

This article was submitted to
Nanobiotechnology,
a section of the journal
Frontiers in Bioengineering and
Biotechnology

Received: 13 September 2019

Accepted: 18 November 2019

Published: 06 December 2019

Citation:

Lian X, Wei M-Y and Ma Q (2019)
Nanomedicines for Near-Infrared
Fluorescent Lifetime-Based
Bioimaging.
Front. Bioeng. Biotechnol. 7:386.
doi: 10.3389/fbioe.2019.00386

Nanomedicines refer to the application of nanotechnology in disease diagnosis, treatment, and monitoring. Bioimaging provides crucial biological information for disease diagnosis and treatment monitoring. Fluorescent bioimaging shows the advantages of good contrast and a vast variety of signal readouts and yet suffers from imaging depth due to the background noise from the autofluorescence of tissue and light scattering. Near-infrared fluorescent lifetime bioimaging (NIR- FLTB) suppresses such background noises and significantly improves signal-to-background ratio. This article gives an overview of recent advances in NIR- FLTB using organic compounds and nanomaterials as contrast agent (CA). The advantages and disadvantages of each CA are discussed in detail. We survey relevant reports about NIR-FLTB in recent years and summarize important findings or progresses. In addition, emerging hybrid bioimaging techniques are introduced, such as ultrasound-modulated FLTB. The challenges and an outlook for NIR- FLTB development are discussed at the end, aiming to provide references and inspire new ideas for future nanomedicine development.

Keywords: bioimaging, fluorescence lifetime, near-infrared, nanomaterials, contrast agents

INTRODUCTION

Nanomedicines refer to the application of nanotechnology in disease diagnosis, treatment, and monitoring (Freitas, 1999). Bioimaging is a technique that uses high-resolution and visualization methods to obtain dynamic changes of the target molecules in cells, in tissues, or *in vivo*. As the signal generator or contrast provider in biological imaging, contrast agents (CAs) have been applied in biomolecular detection, cell imaging, bacterial imaging, cell tracking, vascular imaging, *in vivo* tumor imaging, and treatment, and so on. The application of nanomaterials as CAs of bioimaging is considered one of the nanomedicines for disease diagnosis or monitoring. The success of bioimaging relies heavily on a good CA, but also the progresses of imaging technology.

Various bioimaging techniques are developed to achieve the goal of deep tissue, high resolution, and good contrast. To date, the main bioimaging methods include X-ray imaging, magnetic resonance imaging (MRI), optical bioimaging, electron microscopic imaging, and mass spectrometry imaging. X-ray imaging has larger penetration into tissues than ultraviolet/visible light (Yi Z. et al., 2014; Burdette et al., 2018), but radiation exposure limits its usage and could be a health concern. MRI provides high resolution and great depth for *in vivo* imaging yet suffers from low resolution in the cellular level (Kevadiya et al., 2018; Xu et al., 2018; Wang et al., 2019). Mass spectrometry imaging could be used to investigate the spatial distribution of molecules on complex surfaces (Amstalden van Hove et al., 2010; Bednarczyk et al., 2019; Smith et al., 2019) but not to penetrate

tissue. Optical bioimaging provides cellular- or molecular-level information with the advantages of low cost, small size, and noninvasiveness (Kumar et al., 2009; Hui et al., 2010).

Fluorescence bioimaging is one of the earliest appearances in optical bioimaging and has been widely used in biomedical research and clinical stages (Ntziachristos, 2006), thanks to the rapid development of optical technologies and a plethora of emerging fluorescent probes. Fluorescence imaging includes two methods: one imaging targets through a microscope and the other is macroscopic imaging that is based on optical tomography (Pei and Wei, 2019). Good contrast could be obtained for imaging gene, protein, and cellular processes by fluorescence bioimaging (Lv et al., 2015). It has a vast variety of signal readout mechanisms, including fluorescence intensity, lifetime, quenching, or Förster resonance energy transfer (FRET), yet it heavily relies on the function of fluorescent probes. Common fluorescent probe dyes include rhodamines, cyanine dyes, and coumarins. These organic probes may form aggregates that cause aggregation-induced quenching at high concentration, resulting in the decrease of fluorescence intensity (Lu et al., 2012). As for bioimaging in tissue, it faces the challenge that the imaging depth is limited because of the scattering light background.

Near-infrared (NIR) fluorescent probes that are of excitation and emission wavelengths in the 650–900 nm region are attractive for fluorescent bioimaging because interference from the auto-fluorescence background is significantly reduced (Li et al., 2016; Liu et al., 2016). Such bioimaging has been reported for deep-tissue *ex vivo* and *in vivo* imaging (Qian et al., 2009). New NIR fluorescent dyes of rhodamine derivatives have been developed for sensing mitochondrial membrane potential. For instance, Pastierik et al. synthesized and characterized a fluorescent probe, 9-phenylethynylpyronin analogs, conceiving the bathochromic shift to NIR region, which overcame the limits of common xanthene- or rhodamine-based fluorophores (Pastierik et al., 2014). Hang et al. developed a new NIR diketopyrrolopyrrole-based fluorescent dye for protein biosensing and other potential bioimaging (Hang et al., 2014).

Obtaining quantitative information from fluorescent bioimaging is complicated, as the signal is affected by numerous factors, including the excitation light intensity, quenching, and the distribution concentration of fluorophores. Fluorescence lifetime imaging (FLIM) is able to quantitatively obtain the functional information of samples by measuring the fluorescence lifetime of fluorophore, which is independent on the concentration (Becker, 2012). Fluorescence lifetime could be influenced by the microenvironment of the fluorophore, such as temperature, polarity, and the presence of fluorescence quenchers. Because of these advantages, FLIM along with FRET was reported to study the structures, interactions, and functional events between molecules of interest in cells or small animals (Berezin and Achilefu, 2010). Since the lifetimes of autofluorescence in tissue have been reported to be in the range of 0.1–7 ns (Berezin and Achilefu, 2010), the lifetimes of the FLIM CAs would be close to 10 ns or greater to ensure the best contrast or signal-to-background ratio.

The development of a CA that has NIR excitation/emission wavelength and long fluorescence lifetime (>7 ns) appears

a key element to the success of deep-tissue high-resolution FLTB. CAs are diverse in nature and common CAs include small molecules and nanomaterials. The latter could be nano-sized (usually <100 nm at one of the dimensions) chemical composites or biomolecules (e.g., fluorescent proteins). In this review, we surveyed the advance in the development of CAs and analyzed their properties for potential use in FLTB, followed by a brief introduction of FLTB instrumentation. Some FLTB results were presented to demonstrate the features and advantages of FLTB. The findings from the development of small molecules and nanomaterial-based CAs are summarized, which will be beneficial for further development of hybrid CAs that small molecule fluorescence dyes are encapsulated in a nano-sized carrier (“dye@nanocarrier”). Finally, a new hybrid bioimaging system that integrates ultrasound with FLTB was described, which may provide a promising platform for future FLTB development.

NIR FLUORESCENT LIFETIME BIOIMAGING (NIR-FLTB)

NIR-FLTB CA

Small Molecule-Based CAs

Serving as CAs, NIR organic dyes have been attracting wide attention in bioimaging applications. Yet only a few of them are directly available because others suffer from poor photostability, hydrophilicity, and stability, as well as low sensitivity in tissues or *in vivo* (Luo et al., 2011; Yi X. et al., 2014). Great efforts have been made to develop new dyes to overcome these issues and to obtain strong fluorescence intensity and long fluorescence lifetime (Nolting et al., 2011). The most common and frequently studied NIR organic dyes are cyanines, squaraines, phthalocyanines, and porphyrin derivatives, rhodamine analogs, and borondipyrromethane analogs (BODIPYs). The chemical structures of NIR dyes that are of potential to be used for FLTB application are shown in **Figure 1**, and their photophysical features are summarized in **Table 1**.

Cyanine dyes

Cyanine dyes were developed first by Williams in 1856 (Williams, 1856). The typical structures were composed of two aromatic nitrogen-containing heterocycle rings linked together by polymethine bridge; see the chemical structure in **Figure 1A**. The longer the polymethine bridge is (the number in the dye's name represent the number of carbon), the longer the absorption/emission wavelength is (Martinić et al., 2017). For instance, Cy5, Cy5.5, Cy7, and Cy7.5, whose maximum absorption/emission wavelengths ($\lambda_{\text{max}}/\lambda_{\text{em}}$) are 652/672, 675/694, 755/788, and 788/808 nm, respectively (Lavis and Raines, 2008; Luo et al., 2011; Martinić et al., 2017). They are widely used in the field of laser materials, paints, and bioimaging for nucleic acids and proteins, and so on; however, it has been noted that they may show poor photostability, undesired self-aggregation, small Stokes shifts, high plasma protein binding rate, and mild fluorescence and low quantum yield in aqueous solution (Levitus and Ranjit, 2011; Luo et al., 2011). There have been great challenges for

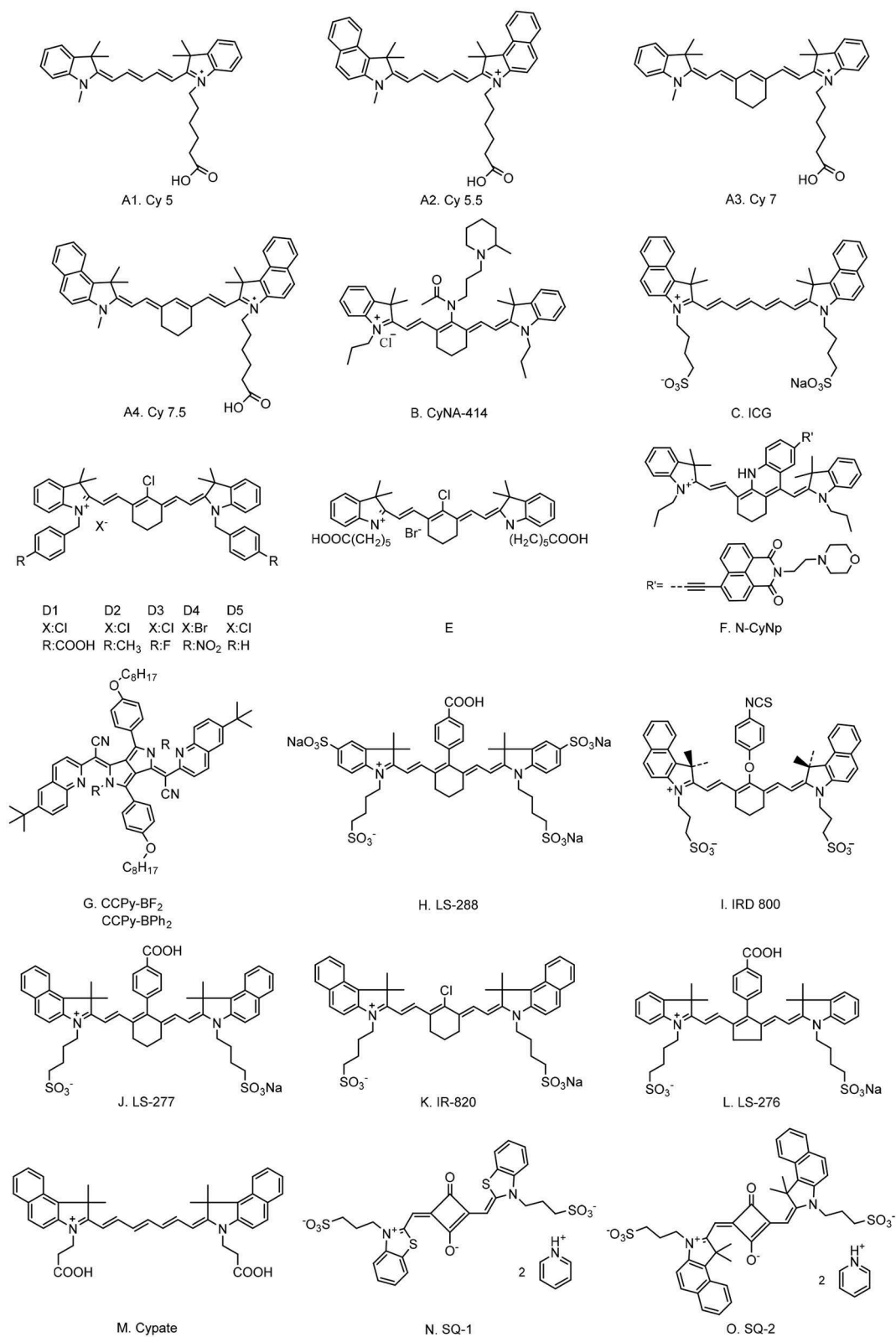


FIGURE 1 | Continued

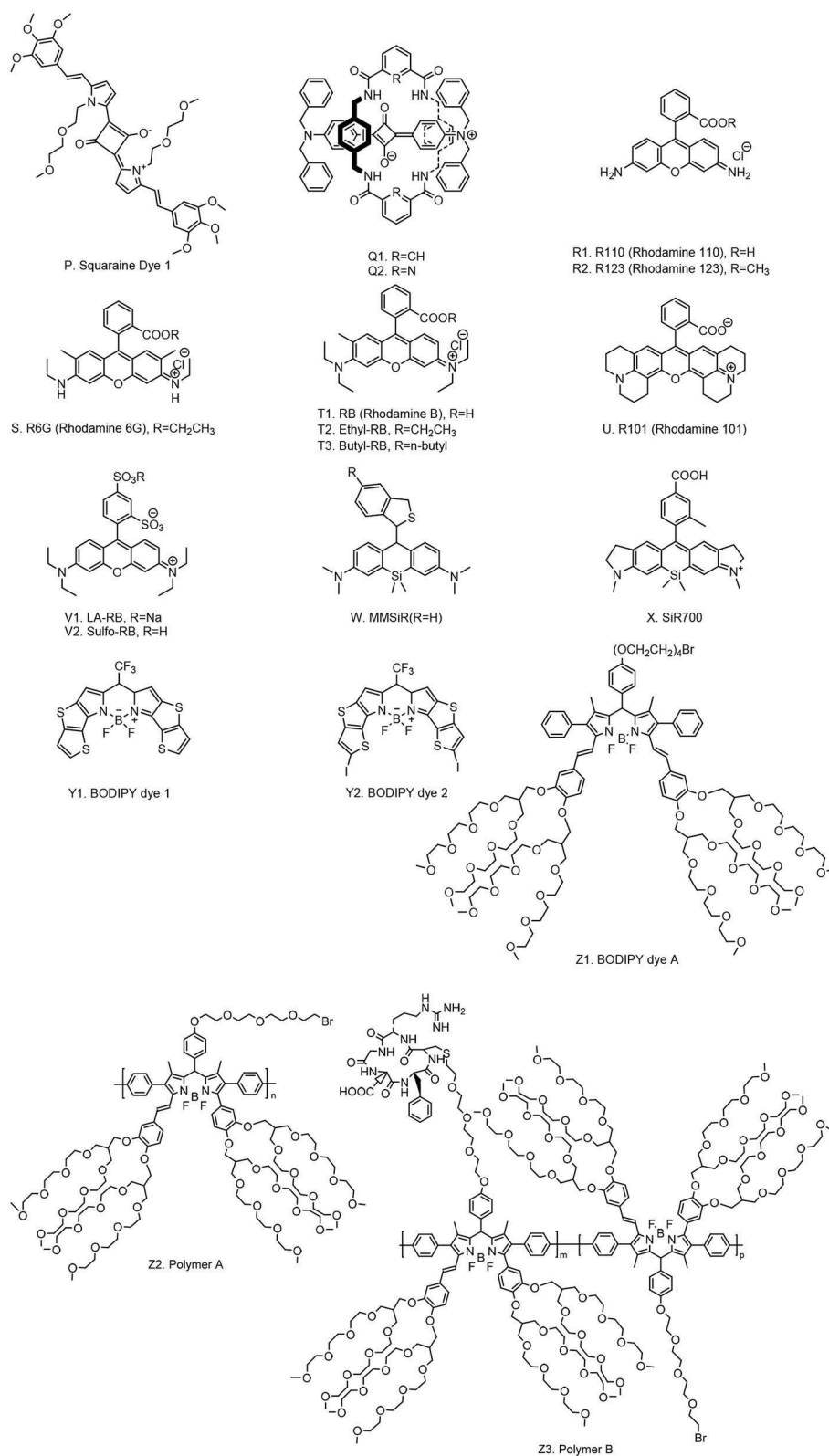


FIGURE 1 | Chemical structures of typical fluorescent lifetime organic dyes.

TABLE 1 | Photophysical features of typical fluorescent lifetime organic dyes.

Types of organic dyes	Organic dyes	Solvents	Photophysical features				References
			Absorption wavelength Abs (nm)	Emission wavelength Em (nm)	Lift time (<i>in vitro</i>) (ns)	Lift time (<i>in vivo</i>) (ns)	
Cyanine	Cy 5	H ₂ O	651	670	0.98	–	Tinnefeld et al., 2001
	Cy 5.5	–	675	694	–	–	Martinić et al., 2017
	Cy 7	–	755	788	–	–	Martinić et al., 2017
	Cy 7.5	–	788	808	–	–	Martinić et al., 2017
	CyNA-414	–	804	819	–	–	Samanta et al., 2010
	ICG	DMSO	794	831	1.11	0.60–0.84	Berezin et al., 2009a
	D1	Methanol	786	814	–	–	Chen et al., 2006
	D2	Methanol	785	813	–	–	Chen et al., 2006
	D3	Methanol	784	809	–	–	Chen et al., 2006
	D4	Methanol	785	807	–	–	Chen et al., 2006
	D5	Methanol	784	813	–	–	Chen et al., 2006
	E	Methanol	782	808	–	–	Chen et al., 2006
	N-CyNp	HEPES	–	785	–	–	Wu et al., 2017
	pyrrolopyrrole cyanine-BF2 (PPC-BF2)	DMSO	757	779	4.02	3.05–3.80	Berezin et al., 2009a
	pyrrolopyrrole cyanine-BPh2 (PPC-BPh2)	DMSO	824	840	3.35	2.50–2.88	Berezin et al., 2009a
	LS-288	Methanol	770	790	0.81	1.12	Berezin et al., 2009b
	DMSO	Methanol	782	810	0.76	–	Waddell et al., 2000
	LS-277	Methanol	800	811	0.61	0.74	Berezin et al., 2009b
	IR-820	Methanol	820	836	0.25	0.53	Berezin et al., 2009b
	LS-276	Methanol	797	816	0.83	1.12	Berezin et al., 2009b
Squaraine	Cypate	Methanol	792	817	0.46	0.63	Berezin et al., 2009b
	N-propanesulfonate- benzothiazolium squaraine (SQ-1)	Aqueous Solution (BSA)	660 ± 1	669 ± 1	3.7 ± 0.2	–	Zhang et al., 2013
	N-propanesulfonate- benzindolium squaraine (SQ-2)	Aqueous Solution (BSA)	675 ± 1	684 ± 1	2.6 ± 0.1	–	Zhang et al., 2013
	Squaraine Dye 1	DMSO	706 ± 1	719 ± 1	0.51 ± 0.07	–	Ahn et al., 2012
	Q1	THF:water (4:1)	650	676	1.24	–	Arunkumar et al., 2005
Rhodamine dyes	Q2	THF:water (4:1)	643	667	6.96	–	Arunkumar et al., 2005
	Rhodamine 110	Water	497	523	4.28	–	Zhang X.-F. et al., 2014
	Rhodamine 123	Water	497	527	4.20	–	Zhang X.-F. et al., 2014
	Rhodamine 6G	Water	525	554	4.22	–	Zhang X.-F. et al., 2014
	Rhodamine B	Water	554	580	1.75	–	Zhang X.-F. et al., 2014
	Ethyl-RB	Water	552	581	1.10	–	Zhang X.-F. et al., 2014
	Butyl-RB	Water	558	584	1.67	–	Zhang X.-F. et al., 2014
	Rhodamine 101	Water	575	604	4.91	–	Zhang X.-F. et al., 2014
	LA-RB	Water	562	588	1.49	–	Zhang X.-F. et al., 2014
	Sulfo-RB	Water	554	591	1.78	–	Zhang X.-F. et al., 2014
BODIPYs	BODIPY dye 1	Hexane	690	693	4.49	–	Sun et al., 2019
	BODIPY dye 2	Hexane	714	716	3.89	–	Sun et al., 2019
	BODIPY dye A	H ₂ O	622/665	702	2.6	–	Zhu et al., 2013
	Polymer A	H ₂ O	687	711	0.4	–	Zhu et al., 2013
	Polymer B	H ₂ O	689	712	0.6	–	Zhu et al., 2013

scientists to improve the performance of cyanine dyes, but some exciting progresses have been witnessed. For example, Samanta et al. (2010) have reported a fluorescent dye, CyNA-414 (see **Figure 1B** for chemical structure), which has stronger emission intensity and higher photostability than those of indocyanine green (ICG). They claimed that the enhancement was attributed to the introduction of the acetyl group, which is capable of withdrawing electron. Chen et al. (2006) synthesized 3H-indocyanine dyes with different N-substituents (**Figures 1D,E**), which introduce the electron-donating groups that can obtain better photochemical stability. It was believed that these dyes will be a promising CA in future biological applications. In the process of continuous searching, Stokes shift is also an important factor to be considered in addition to the photochemical stability. In 2017, Wu et al. (2017) developed a NIR cyanine dye, which is modified by naphthalimide with a Stokes shift of c.a. 165 nm and a λ_{em} at 785 nm (**Figure 1F**). The large Stokes shift mitigates the interference from the excitation light, resulting in a good signal-to-background ratio. It is a promising CA for the imaging of mouse model according to their results. Unfortunately, the fluorescence lifetimes of these modified cyanine dyes have not been studied; however, the findings from these reports will offer a meaningful strategy for future lifetime studies.

The Food and Drug Administration (FDA) of the United States approved ICG dye as the only cyanine probe for *in vivo* use in biomedical applications. However, ICG has been rarely used in fluorescence lifetime bioimaging due to its short lifetime (<2 ns). As for other cyanine dyes, increasing efforts have been taken to improve the fluorescence lifetime to meet the requirements of FLTB. It appears that none of these dyes shows a fluorescent lifetime being close to 7 ns (the background noise of the maximum fluorescence lifetime from tissue). Due to the lack of the fluorescence lifetime data of the abovementioned modified cyanine dyes, we cannot put this as a dead-end for FLTB yet.

Squaraine dyes

Squaraine dyes show intensive absorption/emission in the visible and NIR regions. These compounds belong to the subclass of polymethoxy dyes, which consist of an oxocyclobutenolate core with aromatic or heterocyclic components at both ends of these molecules (Patsenker et al., 2011). Squaraine dyes have been widely used in the fields of printing and dyeing, photo-detector, biological probe, photodynamic therapy, optical data storage, laser printing, optical-emitting effect transistor, non-linear optics, infrared photography, and solar cells (Hu et al., 2013) because of the advantages of intensive absorption bands and good photoconductivity; however, they show small Stokes shifts and poor solubility in aqueous solution (resulting in aggregate and quenching). To this end, Arunkumar et al. (2006) encapsulated dyes in the amide-containing macrocycle, and they claimed that the method could be extended to other dyes. It is believed that the fluorescence properties and the chemical robustness of squaraine dyes can be adjusted by modifying or adding moieties into the dye. A few squaraine dyes and their photophysical properties were summarized in **Table 1**.

Rhodamine dyes

Rhodamine dyes belong to the class of xanthene and have been extensively used as fluorescent probes due to their distinguishing photophysical properties, such as water solubility (Guo et al., 2014). The chemical structures of some rhodamine dyes/rhodamine analogs are shown in **Figure 1**. Although they have prodigious molar extinction coefficients and resistance, their emission wavelengths are rarely above 600 nm. For instance, rhodamine B, rhodamine 6G, and rhodamine 101 and their emission wavelengths are all in the visible region (~600 nm) (Prazeres et al., 2008; Berezin and Achilefu, 2010). This limits the application of rhodamine dyes in *in vivo* bioimaging. In recent years, developing new rhodamine analogs by modifying their xanthene core has received great attention. Koide et al. (2011) reported a far-red to NIR fluorescence probe, MMSiR, which was designed based on Si-rhodamine. Its fluorescence shows no dependence on pH and high resistance to autooxidation and photobleaching. Moreover, it had been used for real-time imaging. McCann et al. (2011) compared a silica-rhodamine-based NIR fluorophore (SiR700) with cyanine-based dyes. The absorbance (2A) and emission (2B) spectra of the dye-conjugated avidin are represented in **Figure 2**. In the presence of a surfactant, sodium dodecyl sulfate (SDS), the emission intensity of the dye-conjugated avidin was enhanced by c.a. 3-folds. This indicates that the decreased polarity (more hydrophobic) generated from the formation of SDS micelle could lead to the enhancement of fluorescence emission intensity. Their findings suggest that SiR700 could be useful for *in vivo* optical imaging.

BODIPY dyes

BODIPY dyes have a corporate structure of 4,4'-difluoro-4-bora-3a,4a-diaza-s-indacene, which were discovered by Treibs and Kreuzer in 1968 (Treibs and Kreuzer, 1968). These dyes are of high extinction coefficient, strong fluorescence intensity, good photostability, and inertness to pH and medium (Geddes and Lakowicz, 2005). Normally, BODIPYs dyes' fluorescence emission wavelengths are close to NIR range. Adjusting the absorption/emission wavelengths of these dyes to the NIR range can be realized by modifying the core of dyes. For instance, Zhu et al. (2013) prepared a polymeric BODIPY dye bearing arginine-glycine-aspartic acid (RGD) peptides (polymer B). The thiol-functionalized RGD cancer-homing peptide was conjugated with tetra(ethylene glycol) tethered spacers (polymer A) under a mild basic condition. The water-soluble BODIPY dye was used for NIR fluorescence imaging of breast cancer cells. Sun et al. (2019) designed two thieno[3,2-b]thiophene-fused BODIPY derivatives, which have an enhanced absorption in the NIR region. Study showed that BODIPY dyes are highly sensitive to microenvironment (Pei and Wei, 2019), yielding to a fact that their fluorescence intensity and lifetime dropped significantly when transferred from organic solvent to water phase. This hinders scientists using them directly in FLTB applications.

Summary of small molecule-based CAs

We summarized the chemical structures, absorbance/emission wavelengths, and fluorescence lifetime (solvents) of some

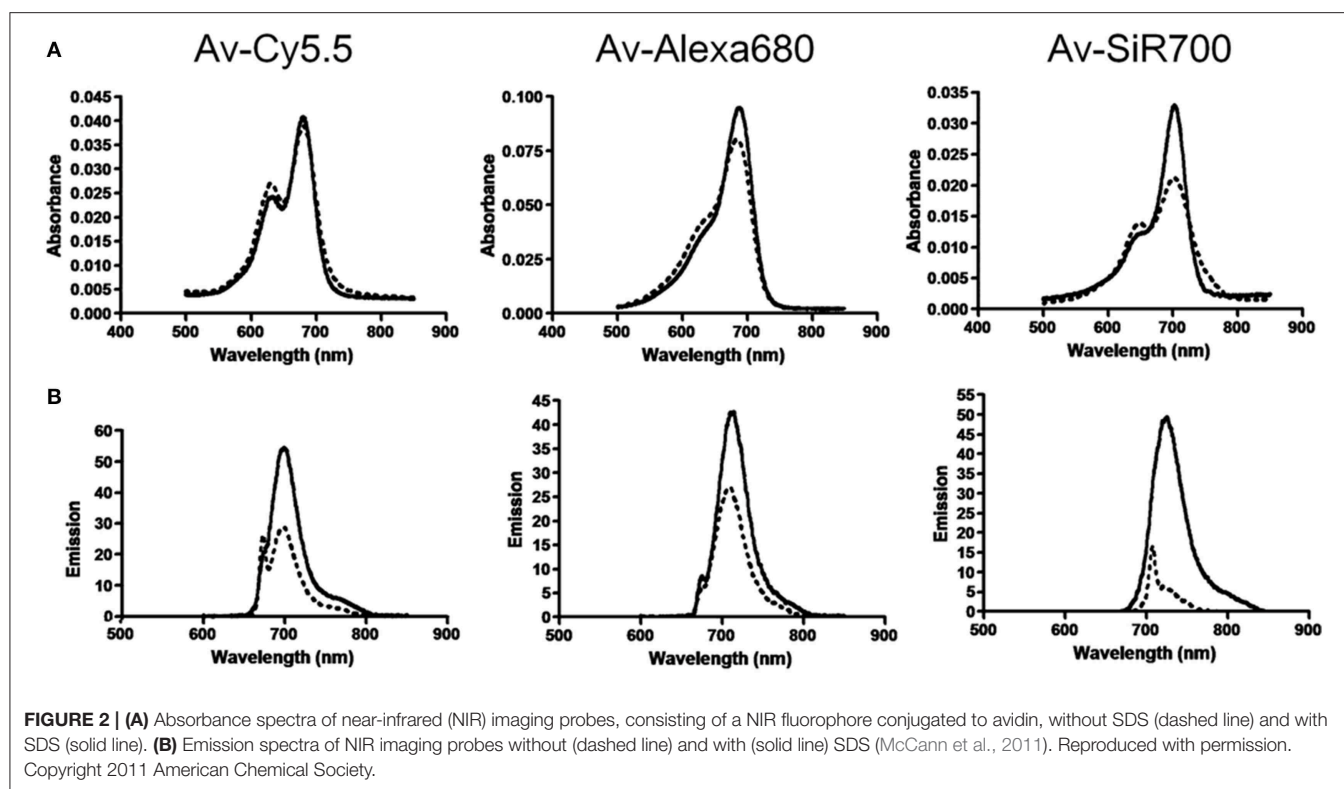


TABLE 2 | Photophysical features of selected nanomaterials[§].

	Excitation range [nm]	ϵ [$M^{-1}cm^{-1}$]	Γ [%]	Fluorescence lifetime	Time-gating	Blinking	Photostability
Quantum dots	700–1,300	10^5 – 10^6	10–90	20 ns–5 μ s	Yes	Yes	High
Polymer dots	500–800	10^6 – 10^7	10–50	≤ 1 ns	No	No	Medium
Nanodiamonds (NV)*	520–580	10^6	70–80	10–30 ns	Yes*	No	Very high
Organic dyes	600–800	10^4 – 10^5	10–50	< 1 –6 ns	No	Yes	Low
Carbon dots	500–650	10^4 – 10^5	1–10	≤ 10 ns	No	No	Medium
Gold clusters	500–650	10^4 – 10^5	< 1 –3	3–800 ns	Yes	Yes	Medium
Carbon nanotubes**	700–1,300	10^7	$< < 1$ –7	≤ 1 ns	No	No	High
Graphene oxide	400–650	10^4	< 1 –5	≤ 1 ns	No	Yes	Medium
UCNPs	980	10^3 – 10^4	< 1 –7	> 100 μ s	Yes	No	High

[§]Adapted from Reineck and Gibson (2016) with permission. Copyrights 2017 John Wiley. ϵ , the molar absorption coefficient; Γ , the fluorescence quantum yield; UCNPs, upconversion nanoparticles.

*Many nanodiamonds's lifetimes are not long enough for time-gating, except for the one that is of > 60 nm in diameter (Hui et al., 2014).

**Absorption coefficient is proportional to nanotube length. The value is based on a length of 200 nm.

representative NIR organic dyes, including cyanine, squaraine, phthalocyanines and porphyrin derivatives, rhodamine analogs, and BODIPY analogs. New dyes had been developed to improve either water solubility or fluorescence properties. These findings encourage scientists to conduct in-depth studies, one of which might be the improvement of their fluorescence lifetimes. As for NIR FLTB application, the fluorescence lifetime threshold from tissue background noise was found to be up to 7 ns. None of these dyes can be perfectly qualified to use as a CA for FLTB in tissue. As seen in Table 1, some BODIPY dyes show promising lifetimes, for example, ~ 4 ns, in organic solvent, but their lifetimes dropped significantly

in aqueous solution or buffer solutions. A trade-off between water solubility and fluorescence lifetime often exists. To this end, dye-encapsulated nanomaterials ("dyes@nanocarrier") might be a solution. The hydrophobic internal nanocore offers an environment to maintain the long lifetime of the dyes, whereas the external hydrophilic nano-shell improves the water solubility. Such composites were potentially meeting the requirements of FLTB CAs. An outstanding example is to encapsulate BODIPY dyes into a micelle (Pei and Wei, 2019). The resulting micelle-encapsulated dye shows great water solubility but also the unchanged fluorescent lifetime of the BODIPY dye.

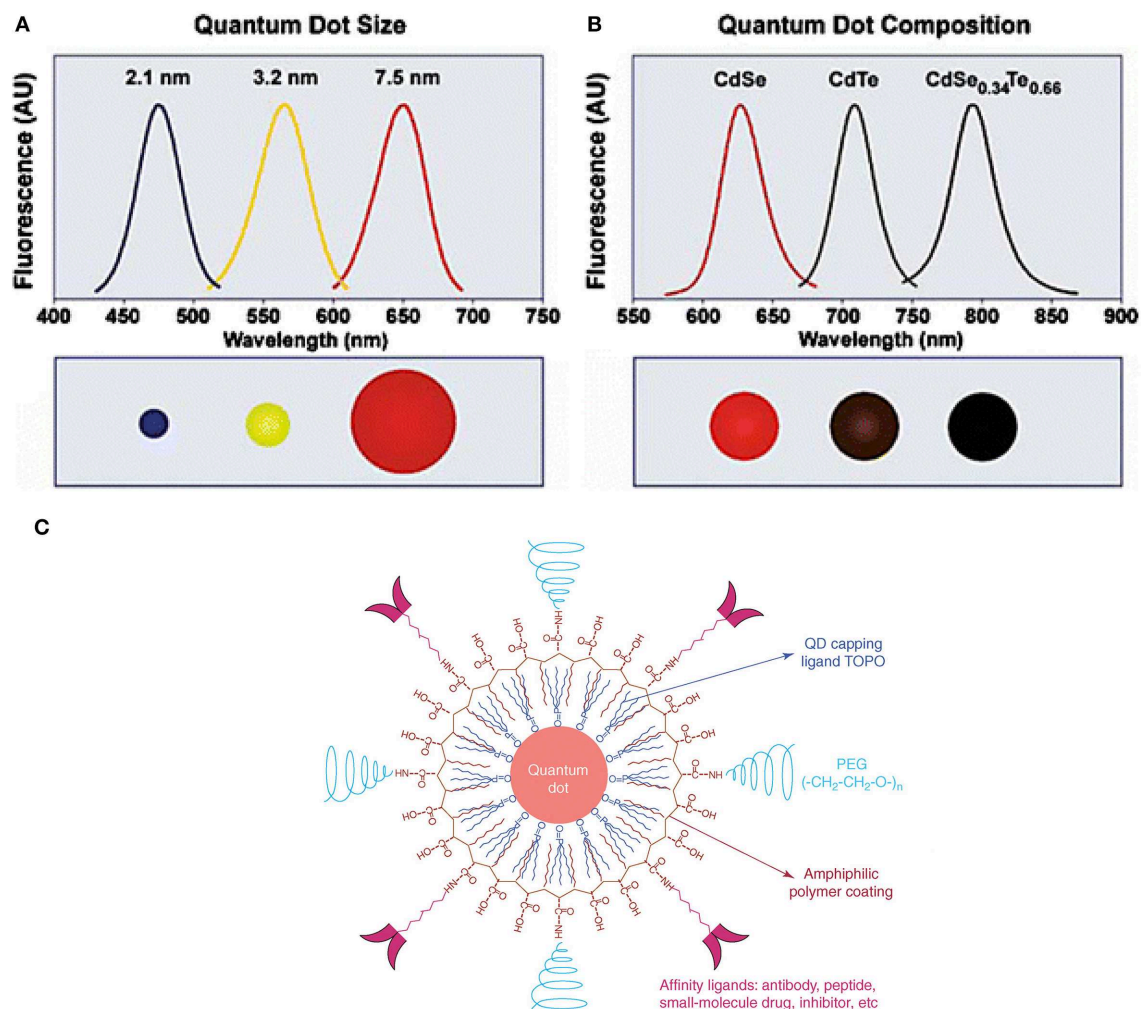
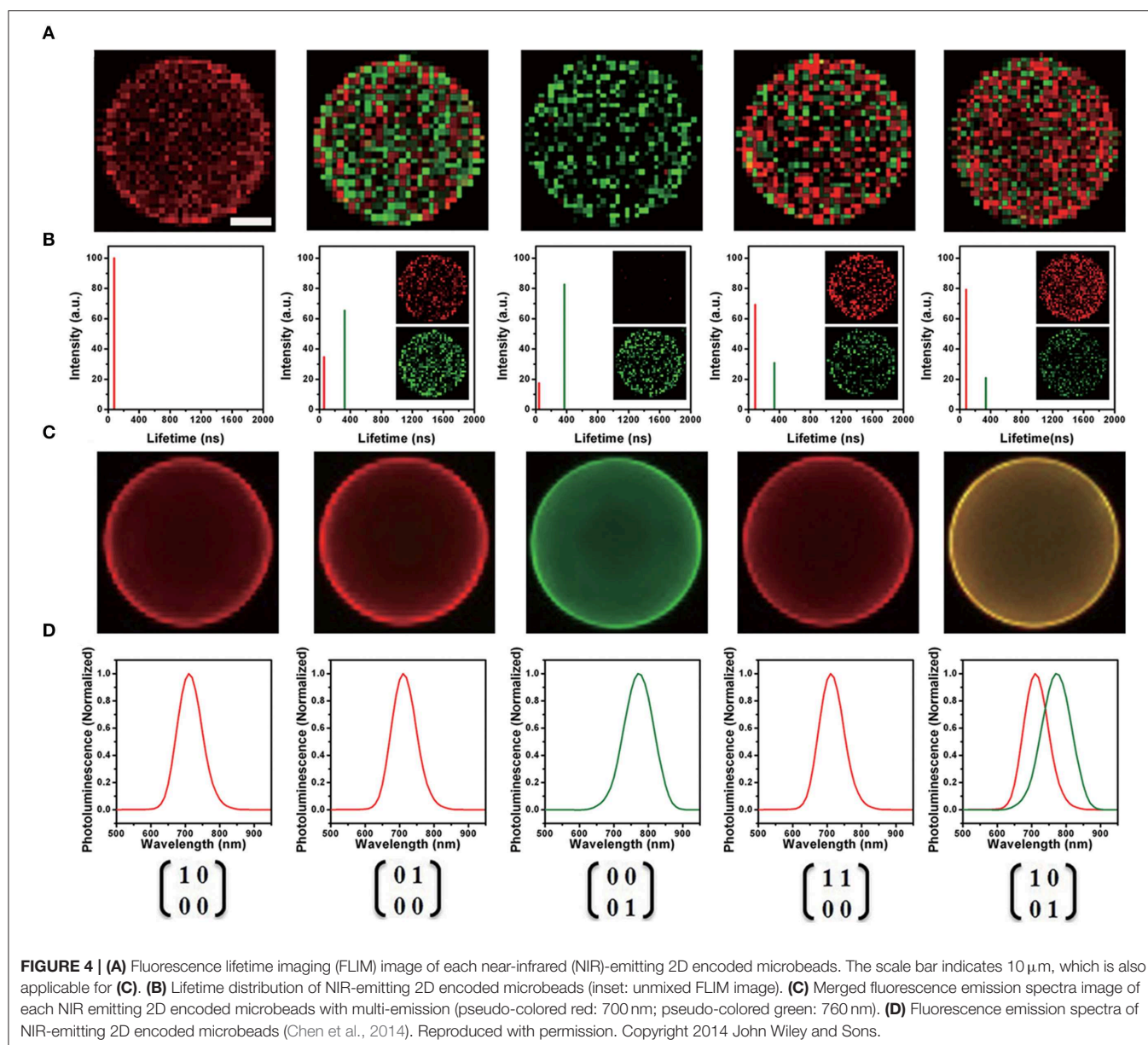


FIGURE 3 | QDs structure and novel optical properties: **(A)** Size and composition tuning of optical emission for binary CdSe and ternary CdSeTe quantum dots. A CdSe QD with various sizes (given as diameter) may be tuned to emit throughout the visible region by changing the nanoparticle size while keeping the composition constant. **(B)** The size of QD may also be held constant, and the composition may be used to alter the emission wavelength. In the above example, 5-nm-diameter quantum dots of the ternary alloy CdSe_xTe_{1-x} may be tuned to emit at longer wavelengths than either of the binary compounds CdSe and CdTe because of a non-linear relationship between the alloy bandgap energy and composition (the spectrum maximum near 790 nm corresponds to CdSe_{0.34}Te_{0.66}). **(C)** The structure of a multifunctional QD probe. Schematic illustration showing the capping ligand TOPO, an encapsulating copolymer layer, tumor-targeting ligands (such as peptides, antibodies or small-molecule inhibitors), and polyethylene glycol (PEG) (Smith et al., 2004; Gao et al., 2005). Reproduced with permission. Copyrights 2004 John Wiley and Sons and 2005 Elsevier.

Nanomaterial-Based CAs

Nanomaterials are a class of materials that are of size range from 1 to 100 nm for at least one dimension. Compared with molecular probes, nanomaterial-based fluorescence probes are not subject to nonspecific binding of proteins, so their optical properties are not affected. In recent years, the research of nanomaterial-based CAs has been developing rapidly, especially in the fields of medicine and diagnosis (Hahn et al., 2011). Their fluorescence appeared not be easily affected by solvent polarity, ionic strength, pH, and temperature. More importantly, they show high sensitivity and selectivity to the target and have good contrast (Wolfbeis, 2015). The most commonly used nanomaterial-based CAs are hydrophobic and

hydrophilic organic polymers, nanoparticles made of silica and organically modified silica, quantum dots (QDs), semiconducting organic polymers, carbonaceous nanomaterials including carbon (quantum) dots, carbon nanoclusters and carbon nanotubes, nanodiamonds, upconversion materials, metal particles, metal oxides (Wolfbeis, 2015). The photophysical features of selected nanomaterials are shown in **Table 2**. As discussed earlier, to eliminate the autofluorescence from tissue, the fluorescence lifetimes for FLTB CAs are recommended to be equal or above 10 ns. As shown in **Table 2**, QDs, nanodiamonds, gold clusters, and upconverting nanoparticles (UCNPs) are qualified for time-gated FLTB. Among them, QDs and UCNPs have unique advantages, such as NIR emission, long fluorescence lifetime, and tunable



fluorescence properties, which make them promising CAs for NIR-FLTB. The detailed features and applications of QDs and UCNP are described below. Gold cluster- and nanodiamond-based CAs are briefly introduced because of their relatively shorter excitation wavelengths (Table 2).

Quantum dots

Quantum dots (QDs), tiny light-emitting particles at nanometer-size, are extremely bright and photostable. Although QDs can be excited by a wide range of wavelengths, the NIR QDs are considered safe because they are non-ionizing. QDs are emerging as a new class of fluorescent CAs for bioimaging, thanks to the high sensitivity (brightness), high specificity (targeting), and the capability for multiple targets (narrow emission spectrum). A number of NIR fluorescent QDs have been designed, including

HgS, PbS, PbSe, Ag₂S, and so on. HgS can exhibit narrow, size-dependent transitions between 500 and 800 nm for sizes ranging from 1 to 5 nm (Goswami et al., 2012); PbS has a large exciton Bohr radii of 20 nm, whose fluorescence has a wider adjustable range (Wang et al., 2012); PbSe belongs to e IV-VI semiconductors, which has large Bohr radius, small Stokes shift, and bright luminescence (Tan et al., 2007); Ag₂S belongs to I-VI semiconductors, which has 1.0 eV of narrow band gap and low toxicity (Meherzi-Maghraoui et al., 1996). The emission wavelength of a QD is related to size, which can be adjusted through changing surface composition (Bentolila et al., 2009). For example, emission wavelength of cadmium selenide (CdSe) QDs can be tuned to cover 450–650 nm range by adjusting the size of QD from 2 to 7 nm (Figure 3A). By changing the composition of the alloy CdSe_xTe_{1-x}, emission wavelength

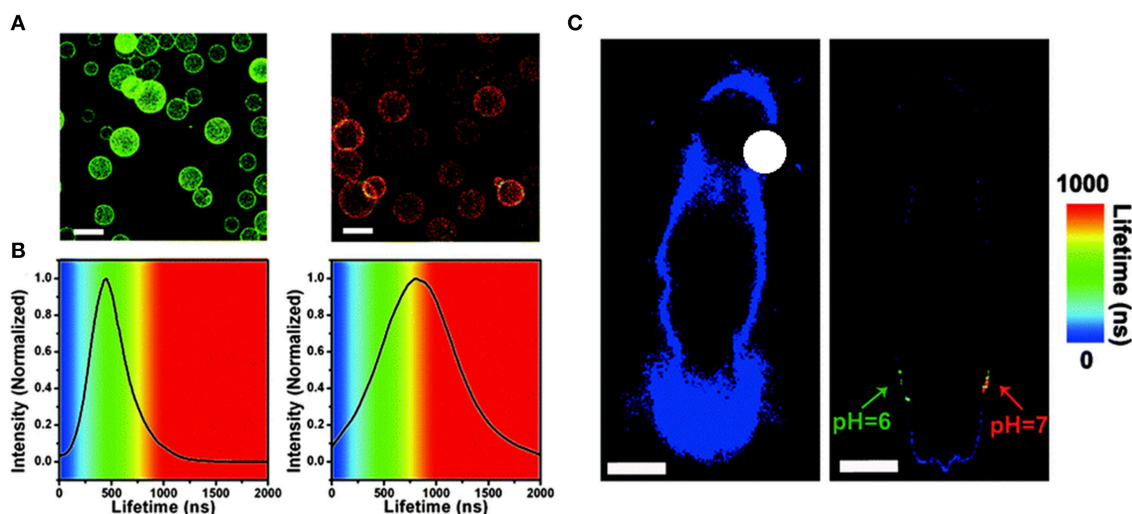


FIGURE 5 | (A) Fluorescence lifetime imaging (FLIM) images of microbeads equipped with QDs-720, dispersed in buffers with different pH values (left: pH = 6.0, right: pH = 7.0, scale bar: 100 nm) and **(B)** PL lifetime histograms collected from the images. **(C)** *In vivo* FLIM experiments of the background of the nude mouse (left) and the QDs-720 injected into adjacent locations with different pH values (green: pH = 6.0, red: pH = 7.0) on the back of the nude mouse (right), respectively (scale bar: 10 mm) (Chen et al., 2015). Reproduced with permission. Copyright 2015 Royal Society of Chemistry.

of QD with a diameter of 5 nm can be tuned from 610 to 800 nm (**Figure 3B**) (Smith et al., 2004). Compared with organic molecule-based CAs, QDs show more intriguing fluorescence properties, including adjustable emission wavelengths, high molar extinction coefficient, high fluorescence quantum yield, large effective Stokes shift, and high photobleaching resistance (Hahn et al., 2011; Zhang et al., 2012). According to the survey, the core of the most commonly used QDs is CdSe coupled with the shell layer of ZnSe or CdSe. For bioimaging applications, the core-shell structure is often coated with surfactants (e.g., stabilizer ligands, amphiphilic polymers) or affinity ligands (e.g., antibodies), as shown in **Figure 3C** (Xing and Rao, 2008). Most importantly, QDs have a long fluorescence lifetime, ranging from 20 to 50 ns or greater, which overcame the limit of organic molecules in FLTB. The relatively long fluorescence lifetime separates QDs' fluorescence from fluorescence background from tissue (<7 ns) (Smith et al., 2004). Although QDs with emission wavelengths of 450–650 nm have been well-studied, QDs that emit at NIR wavelengths are rarely explored because of the challenging synthesis (He et al., 2011).

In 2014, Chen and his collaborators (Chen et al., 2014) reported a new class of lattice-strained CdTe/CdS: Cu QDs, which have high photoluminescence quantum yield (PL QY) (50–70%), widely tunable NIR-fluorescence emission spectrum (700–910 nm), and long fluorescence lifetime (up to around 1 μ s). They used the as-prepared QDs to fabricate the NIR-emitting 2D codes based on multi-emission and multi-lifetime. The FLIM images and lifetime distribution of microbeads are presented in **Figure 4**.

In 2015, Chen et al. prepared Cu-doped CdZnS QDs that have ultra-small size (~ 3.5 nm), NIR-emission (~ 720 nm), and long lifetime (up to ~ 1 μ s) (Chen et al., 2015). The QDs-based *in vivo* pH imaging using FLIM can be seen in **Figure 5**.

Autofluorescence from the tissue was suppressed in **Figure 5C**, and the CAs showed a great selectivity toward pH. In 2019, Pons and his colleagues reported that the fluorescence lifetimes of ZnCuInSe/ZnS QDs are between 100 and 300 ns, which enable the efficient rejection of fast autofluorescence photons but also increase the sensitivity (Pons et al., 2019). With the excitement of conceiving FLTB with long fluorescence lifetime QDs, scientists also noted that such organic QDs may have toxicity *in vivo*, such as genotoxicity (Giraud et al., 2009).

UCNPs

UCNPs were first described in the early twentieth century, and UCNPs convert long-wave light into shorter-wave luminescence and have long fluorescence lifetime (Auzel, 2004). UCNPs can emit photons with higher energy than the absorbed photons. UCNPs have high photostability, deep tissue penetration (excited at NIR wavelengths), and low background interference (Liu et al., 2014), by which it attracts increasing attention in the field of bioimaging. The mechanism of energy transfer upconversion is describe in **Figure 6** (Tan et al., 2016). UCNPs are often excited at NIR wavelengths (far NIR excitation wavelength will eliminate the auto-fluorescence background), and the resulting emission occurs in visible or ultraviolet regions of the electromagnetic spectrum.

At the early stage of the development of UCNPs, efforts had been made to improve the upconversion efficiency by modifying composition, phase, and size, whereas the quantum yield of UCNPs was still limited by energy transfer between doped ions. The most exciting feature of UCNPs is that their fluorescence lifetime reaches microseconds range (Kim and Kang, 2010). In 2009, Hilderbrand et al. reported a multi-channel luminescent Y₂O₃-based UCNPs, and it was used for the *in vivo* imaging of blood vessels (Hilderbrand et al., 2009). Thanks to the

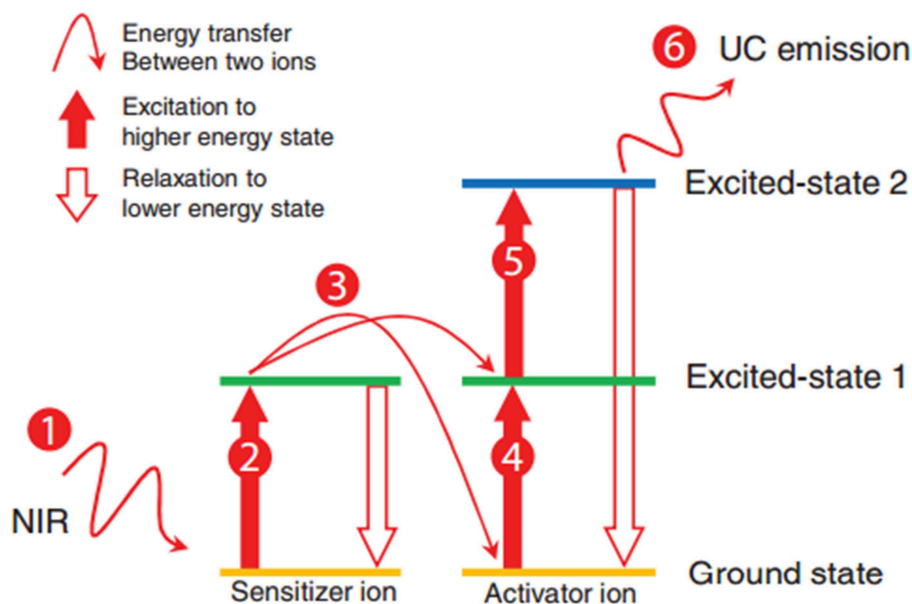


FIGURE 6 | Schematic of the energy transfer upconversion mechanism (Tan et al., 2016). Reproduced with permission. Copyright 2016 John Wiley and Sons.

long fluorescence lifetime of the UCNPs, the good contrast images were obtained after a microsecond exposure, which eliminated the background fluorescence from the tissue. Wu et al. reported lanthanide-doped UCNPs that are of NaYF_4 (β - NaYF_4) nanocrystals with multiple Yb^{3+} and Er^{3+} dopants, and the UCNPs showed no on/off emission behavior (“blinking”) down to milliseconds (Wu et al., 2009). *In vivo* and *in vitro* bioimaging results demonstrated the capability of such UCNPs toward single molecular bioimaging and future targeting bioimaging applications. Chen *et al.* described a high quantum yield UCNPs with core/shell structure of $(\alpha\text{-NaYbF}_4:\text{Tm}^{3+})/\text{CaF}_2$ (Figure 7) (Chen et al., 2012). It exhibits highly efficient NIR_{in} - NIR_{out} upconversion, and it was used for high contrast and deep bioimaging.

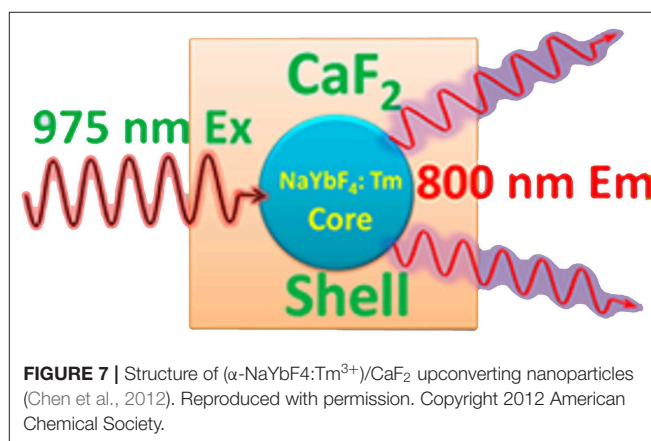


FIGURE 7 | Structure of $(\alpha\text{-NaYbF}_4:\text{Tm}^{3+})/\text{CaF}_2$ upconverting nanoparticles (Chen et al., 2012). Reproduced with permission. Copyright 2012 American Chemical Society.

Gold clusters and fluorescent nano-diamonds

Gold clusters often consist of several tens of gold atoms, prepared through the chemical reduction of gold ions in solution or the etching of large gold NPs. Their fluorescence emissions could be tuned into NIR range (usually up to ~ 700 nm) with lifetime up to ~ 800 ns (Reineck and Gibson, 2016). Thanks to the long fluorescence lifetime, they have been used for bioimaging applications (Shang et al., 2011; Liu et al., 2013; Roy et al., 2015), see Table 2. Likewise, the fluorescence lifetime of nano-diamonds could be up to ~ 20 ns (Hui et al., 2014), which makes them qualified for bioimaging application. For both cases, researchers employed time-gated fluorescence to observe fluorescence intensity after applying a 10-ns threshold.

Fluorescent proteins

The synthesis of fluorescent proteins includes two processes: the first is encoding by a cascade of DNA, including gene transcription and translation; and the second is maturation and

form fluorophore (Berezin and Achilefu, 2010). The fluorophores are protected by the protein shell, which can isolate fluorophores from the external environment, and thus their lifetimes are stable and not sensitive to external environment. However, their optical properties could be affected by pH that may cause the conformation change of the protein. A cerulean (ECFP/S72A/Y145A/H148D) fluorescent protein was reported that possesses high extinction coefficient and a fluorescence lifetime of 3.5 ns (Rizzo et al., 2004).

Summary of nanomaterial-based CAs

As shown in Table 3, both QDs and UCNPs show acceptable fluorescence lifetime (>10 ns) at NIR region, which meet the criteria of FLTB CAs. The instinct features of QDs fluorescence are the narrow emission spectrum and adjustable emission wavelength. These advantages make them promising

TABLE 3 | Photophysical features of typical nanomaterials-based contrast agents (CAs).

Type	Fluorescent component	Solvents	Photophysical features				References
			Absorption wavelength Abs (nm)	Emission wavelength Em (nm)	Lift time (<i>in vitro</i>) (ns)	Lift time (<i>in vivo</i>) (ns)	
Quantum Dots (QDs)	HgS	H ₂ O	550	730	~5.2	–	Goswami et al., 2012
		toluene	770	960	2,570	–	Cheng et al., 2017
		hexane	770	960	2,820	–	
		chloroform	770	960	2,710	–	
	PbSe	H ₂ O	–	–	8,670	–	Kigel et al., 2009
	Ag ₂ S	Chloroform	785	975–1175	57–181	–	Zhang Y. et al., 2014
		water	808	1200	~50	–	Santos et al., 2017
	CdSe	H ₂ O	425	640	1.68	–	Zhang et al., 2019
	CdSe@ZnS	PBS	–	605	~43	–	Gaigalas et al., 2014
		PBS	–	705	131	–	
		H ₂ O	–	800	160	–	
	CdTe/CdS: Cu	water	–	700–910	1,000	–	Chen et al., 2014
Upconversion nanoparticles (UCNPs)	Cu-doped CdZnS	Buffer	–	720	~800 (pH 7)	~800 (pH7)	Chen et al., 2015
	ZnCuInSe@ZnS	blood stream	–	~830	–	100–300	Pons et al., 2019
	Y ₂ O ₃ -based	Blood stream	980	795	–	~ms	Hilderbrand et al., 2009
	NaYF ₄ (β-NaYF ₄) nanocrystals with multiple Yb ³⁺ and Er ³⁺ dopants	Dulbecco's Modified Eagle Medium (DMEM)	980	540 & 650	~ms	~ms	Wu et al., 2009
	(α-NaYbF ₄ :Tm ³⁺)@CaF ₂	water	975	800	3 × 10 ⁵	> 10 ⁵ (tissue)	Chen et al., 2012
Gold Clusters	Au ₂₂	water	561	628	245.1	–	Roy et al., 2015
	Au/dihydrolipoic acid	PBS	550	684	500–800	> 600 (cell)	Shang et al., 2011
	Au/trypsine	water	520	700	~1,000	–	Liu et al., 2013
Nanodiamonds	Fluorescent nanodiamonds	water	532	700	~20	–	Hui et al., 2014

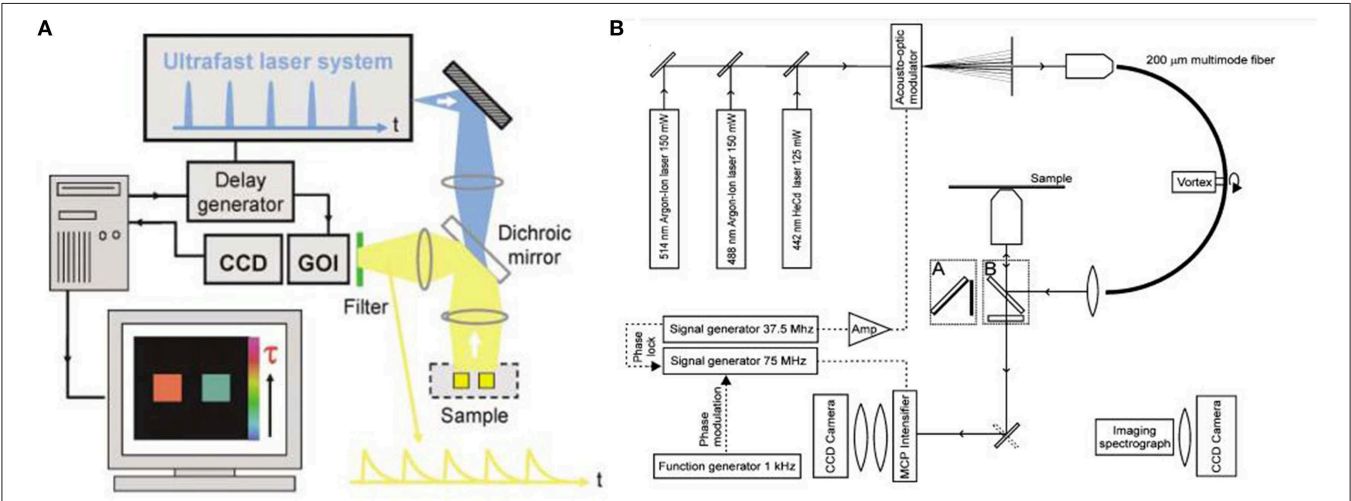
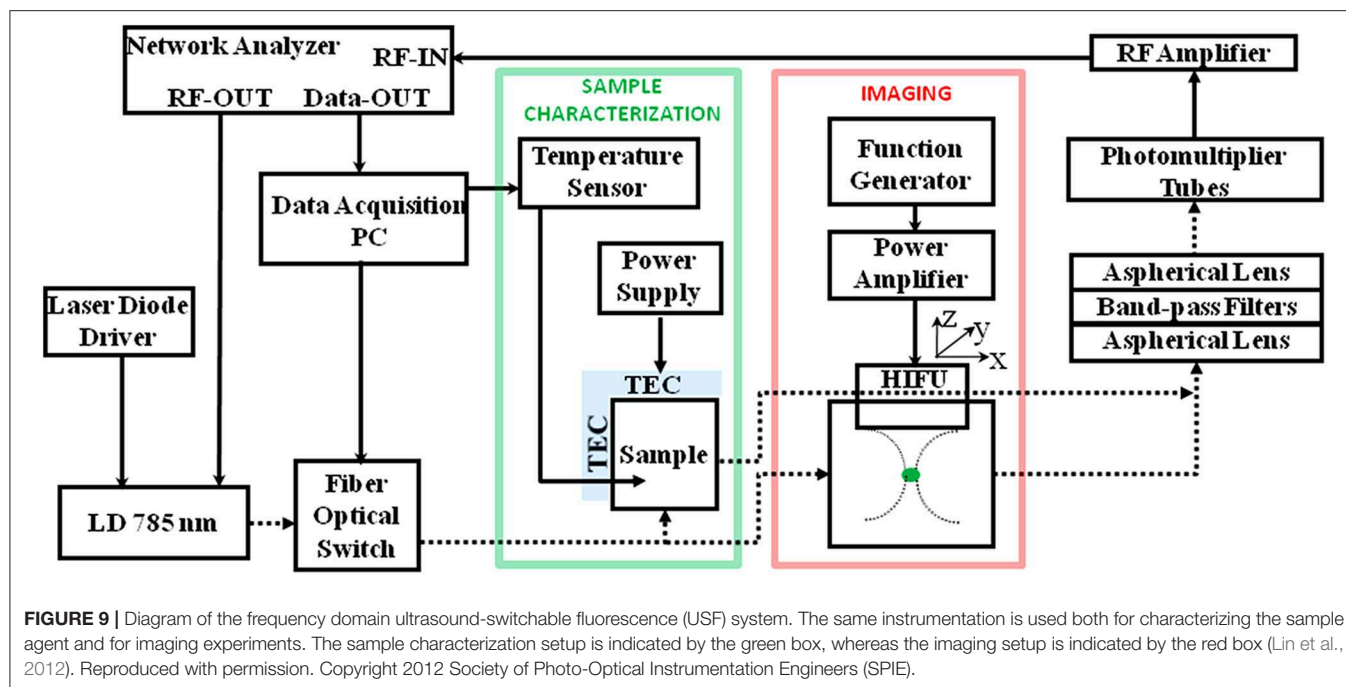


FIGURE 8 | (A) Schematic of wide-field time-domain fluorescence lifetime imaging (FLIM). (B) Setup of the frequency-domain FLIM instrumentation. (Elson et al., 2004; Van Munster and Gadella, 2004). Reproduced with permission. Copyrights 2004 Royal Society of Chemistry and 2004 John Wiley and Sons.

CAs candidates for multiple targets bioimaging. Using UCNPs as CAs allows the ease of low power excitation light source and of the elimination of auto-fluorescence background. The excitation light for UCNPs could be at far NIR, such as 950 nm, under which rare fluorescence from tissue could be generated. Not to mention that their long fluorescence lifetime offers a great tool to further improve the signal-to-background ratio (SBR). The SBR of UCNPs-based bioimaging was adequate for



fluorescence intensity-based bioimaging; thus, few studies have investigated UCNP-based FLTB. Biocompatible surfactants, such as PEG, could be coated onto the surface of QDs and UCNP, which helps in mitigating the toxicity of such CAs during *in vivo* bioimaging. However, increasing concerns have been brought up by toxicologists regarding the toxicity of the core components of QDs and UCNP. Fortunately, fluorescence protein might be a nontoxic alternative to QDs or UCNP. Yet the fluorescence lifetimes of fluorescence proteins fall short at a few nanoseconds, which is not beneficial to outstand the autofluorescence background from tissue (up to ~ 7 ns). Even though good contrasts have been conceived, light scattering in tissue is still a challenge for nanomaterial-based FLTB to improve the resolution in deep tissue.

FLTB Instrumentation

FLIM mainly includes time- and frequency-domain methods (Birch and Hungerford, 2002). Their main components can be seen in **Figure 8**. The spectroscopic configuration is mainly composed of excitation source and detection instrumentation (Leblond et al., 2010). For time-domain method, fluorophores were excited by pulsed light sources, and fluorescence lifetime measurement is conducted with time-gated detection, time correlated single photon counting (TCSPC), or streak-FLIM. Microchannel plate and intensified charge-coupled device (CCD) camera can realize full-field FLIM (Wang et al., 1992); multiphoton excitation FLIM can be performed by combination confocal microscopy or multiphoton excitation fluorescence microscopy with TCSPC (Becker, 2012); streak-FLIM can be achieved by a streak camera (Krishnan et al., 2003). As for frequency-domain method, the typical light sources are light-emitting diodes or laser diodes. Unlike time domain, it uses a co-frequency modulated CCD or photomultiplier tube (PMT)

as a detector that demodulates and receives fluorescent signals. When FLIM instrument is applied into biological samples, an inevitable issue is the scattering light in deep tissue. For instance, the imaging depth for breast could reach centimeters. In such scenarios, the resolution of optical imaging technique will be lost.

Novel Hybrid FLTB Technology

Ultrasound-based bioimaging is well-known for its great penetration in tissue and good resolution; however, it does not have the good contrast and vast detection method as fluorescence bioimaging. Theoretically, the combination of ultrasound and fluorescence could harness advantages of both and conceive deep-tissue, high-resolution, and good contrast bioimaging. Ultrasound-switchable fluorescence (USF) is a technology that uses ultrasound pulses to make fluorophores emit fluorescence in the ultrasound focus region. In 2012, USF bioimaging was first reported, and the method is about one order of magnitude better than other deep-tissue fluorescence imaging (Yuan et al., 2012). Another research group demonstrated a frequency-domain temperature-modulated fluorescence tomography system (Lin et al., 2012). This work realized a depth of 2 cm and a size of 3 mm in the biological tissue. The measurement system and experimental setup are shown in **Figure 9**.

It is noteworthy that USF CAs are a hybrid CA of small molecule and nanomaterial. NIR dyes, that is, ICG or BODIPY, were encapsulated in a polymer nano-carrier, for example, Poly(N-isopropylacrylamide) (PNIPAM) nanoparticles or Pluronic micelles. The dyes' fluorescence is highly dependent on the polarity of the microenvironment; that is, higher intensity of emission at more hydrophobic environment. The microenvironment inside the nano-carrier will become more hydrophobic through conformation change upon being heated,

namely, thermosensitive property. When the ultrasound (high-intensity focused ultrasound, HIFU) gave the energy (heat) at the focused area, the USF CAs within the area will emit higher fluorescence (turned ON). Intensity-based USF bioimaging has been explored (Pei and Wei, 2019), but no new reports of USF FTLB have been emerging yet, which is likely attributed to the unavailability of long fluorescence lifetime USF CAs.

CONCLUSIONS AND OUTLOOK

Nano-sized CAs of FLTB are one class of nanomedicines for disease diagnosis or monitoring. Small molecule-based CAs can fulfill the requirements of *in vitro* FLTB, such as cellular bioimaging, whereas they appear not applicable in tissue imaging due to the unavailability of NIR dyes. Even if a few NIR organic dyes have been developed and applied into bioimaging, scientists are still reluctant to use them in deep tissue bioimaging because of the poor imaging depth derived from large scattering light background. The use of nanomaterial-based CAs, such as QDs or UCNPs, improves the performance of *in vitro* FLTB in terms of a better quantum yield, the capability of simultaneous multiple-target imaging, and a better signal-to-background ratio (eliminating the autofluorescence), in comparison with that of small molecule-based CAs. Unfortunately, the goal of deep-tissue, high-resolution, and good contrast bioimaging appears far to reach for FTLB technique with nanomaterial-based CAs, as the optical bioimaging limit in deep tissue due to light scattering is inevitable. Thanks to their long fluorescence lifetimes, QDs- or UCNPs-CAs have been applied in tissue bioimaging with excellent contrast; however, the resolution in deep tissue is poor as a result of multiple scattering events of the emission light within tissue.

REFERENCES

- Ahn, H.-Y., Yao, S., Wang, X., and Belfield, K. D. (2012). Near-infrared-emitting squaraine dyes with high 2PA cross-sections for multiphoton fluorescence imaging. *ACS Appl. Mater. Interfaces* 4, 2847–2854. doi: 10.1021/am300467w
- Amstalden van Hove, E. R., Smith, D. F., and Heeren, R. M. (2010). A concise review of mass spectrometry imaging. *J. Chromatogr. A* 1217, 3946–3954. doi: 10.1016/j.chroma.2010.01.033
- Arunkumar, E., Forbes, C. C., Noll, B. C., and Smith, B. D. (2005). Squaraine-derived rotaxanes: sterically protected fluorescent near-IR dyes. *J. Am. Chem. Soc.* 127, 3288–3289. doi: 10.1021/ja042404n
- Arunkumar, E., Fu, N., and Smith, B. D. (2006). Squaraine-derived rotaxanes: Highly stable, fluorescent near-IR dyes. *Chem. A Eur. J.* 12, 4684–4690. doi: 10.1002/chem.200501541
- Auzel, F. (2004). Upconversion and anti-stokes processes with f and d ions in solids. *Chem. Rev.* 104, 139–174. doi: 10.1021/cr020357g
- Becker, W. (2012). Fluorescence lifetime imaging—techniques and applications. *J. Microsc.* 247, 119–136. doi: 10.1111/j.1365-2818.2012.03618.x
- Bednarczyk, K., Gawin, M., Chękan, M., Kurczyk, A., Mrukwa, G., Pietrowska, M., et al. (2019). Discrimination of normal oral mucosa from oral cancer by mass spectrometry imaging of proteins and lipids. *J. Mol. Histol.* 50, 1–10. doi: 10.1007/s10735-018-9802-3
- Bentolila, L. A., Ebenstein, Y., and Weiss, S. (2009). Quantum dots for *in vivo* small-animal imaging. *J. Nucl. Med.* 50, 493–496. doi: 10.2967/jnumed.108.053561
- Berezin, M. Y., and Achilefu, S. (2010). Fluorescence lifetime measurements and biological imaging. *Chem. Rev.* 110, 2641–2684. doi: 10.1021/cr900343z
- Berezin, M. Y., Akers, W. J., Guo, K., Fischer, G. M., Daltrozzi, E., Zumbusch, A., et al. (2009a). Long fluorescence lifetime molecular probes based on near infrared pyrrolopyrrole cyanine fluorophores for *in vivo* imaging. *Biophys. J.* 97, L22–L24. doi: 10.1016/j.bpj.2009.08.022
- Berezin, M. Y., Lee, H., Akers, W., Guo, K., Goiffon, R. J., Almutairi, A., et al. (2009b). “Engineering NIR dyes for fluorescent lifetime contrast,” in *2009 Annual International Conference of the IEEE Engineering in Medicine and Biology Society* (St. Paul, MN), 114–117.
- Birch, D. J., and Hungerford, G. (2002). “Instrumentation for red/near-infrared fluorescence,” in *Topics in Fluorescence Spectroscopy* (Boston, MA: Springer), 377–416.
- Burdette, M. K., Bandera, Y. P., Zhang, E., Trofimov, A., Dickey, A., Foulger, I., et al. (2018). Organic fluorophore coated polycrystalline ceramic LSO: Ce scintillators for x-ray bioimaging. *Langmuir* 35, 171–182. doi: 10.1021/acs.langmuir.8b03129
- Chen, C., Zhang, P., Gao, G., Gao, D., Yang, Y., Liu, H., et al. (2014). Near-infrared-emitting two-dimensional codes based on lattice-strained core/(doped) shell quantum dots with long fluorescence lifetime. *Adv. Mater.* 26, 6313–6317. doi: 10.1002/adma.201402369
- Chen, C., Zhang, P., Zhang, L., Gao, D., Gao, G., Yang, Y., et al. (2015). Long-decay near-infrared-emitting doped quantum dots for lifetime-based *in vivo* pH imaging. *Chem. Commun.* 51, 11162–11165. doi: 10.1039/C5CC03046C
- Chen, G., Shen, J., Ohulchanskyy, T. Y., Patel, N. J., Kutikov, A., Li, Z., et al. (2012). (α -NaYbF₄: Tm³⁺)/CaF₂ core/shell nanoparticles with efficient near-infrared

An intriguing breakthrough to this end was the hybrid bioimaging technique of ultrasound and fluorescence. Apart from the establishment of new ultrasound-modulated fluorescence imaging instrument, the development of CAs is a key element for the success of such hybrid bioimaging technique. Taking USF as an example, the CAs consist of a NIR dye-encapsulated nanocarrier. Intensity-base USF bioimaging have been explored, and results substantiate a proof-of-concept deep-tissue, high-resolution bioimaging. It is believed that USF-based FLTB will further improve the performance in deep tissue if a responsive lifetime-based CA is developed.

AUTHOR CONTRIBUTIONS

M-YW and QM oversaw the content, writing of the manuscript, and reviewed the finalized the manuscript. XL wrote the draft.

FUNDING

This work was supported by the National Natural Science Foundation of China (21974129) and Natural Science Foundation of Beijing Municipality (8192049).

ACKNOWLEDGMENTS

M-YW acknowledges that all statements in this article do not represent any viewpoints from Texas Commission on Environmental Quality. All authors appreciate the constructive comments from reviewers.

- to near-infrared upconversion for high-contrast deep tissue bioimaging. *ACS Nano* 6, 8280–8287. doi: 10.1021/nn302972r
- Chen, X., Peng, X., Cui, A., Wang, B., Wang, L., and Zhang, R. (2006). Photostabilities of novel heptamethine 3H-indolenine cyanine dyes with different N-substituents. *J. Photochem. Photobiol. A Chem.* 181, 79–85. doi: 10.1016/j.jphotochem.2005.11.004
- Cheng, C., Li, J., and Cheng, X. (2017). Photoluminescence lifetime and absorption spectrum of PbS nanocrystal quantum dots. *J. Lumin.* 188, 252–257. doi: 10.1016/j.jlumin.2017.04.037
- Elson, D., Requejo-Isidro, J., Munro, I., Reavell, F., Siegel, J., Suhling, K., et al. (2004). Time-domain fluorescence lifetime imaging applied to biological tissue. *Photochem. Photobiol. Sci.* 3, 795–801. doi: 10.1039/b316456j
- Freitas, R. A. (1999). *Nanomedicine: Basic Capabilities*. Vol. 1. Austin, TX: Landes Bioscience.
- Gaigalas, A. K., DeRose, P., Wang, L., and Zhang, Y. Z. (2014). Optical properties of CdSe/ZnS nanocrystals. *J. Res. Natl. Inst. Stand. Technol.* 119, 610–628. doi: 10.6028/jres.119.026
- Gao, X., Yang, L., Petros, J. A., Marshall, F. F., Simons, J. W., and Nie, S. (2005). *In vivo* molecular and cellular imaging with quantum dots. *Curr. Opin. Biotechnol.* 16, 63–72. doi: 10.1016/j.copbio.2004.11.003
- Geddes, C. D., and Lakowicz, J. R. (2005). *Reviews in Fluorescence 2005*. Boston, MA: Springer.
- Giraud, G., Schulze, H., Bachmann, T. T., Campbell, C. J., Mount, A. R., Ghazal, P., et al. (2009). Fluorescence lifetime imaging of quantum dot labeled DNA microarrays. *Int. J. Mol. Sci.* 10, 1930–1941. doi: 10.3390/ijms10041930
- Goswami, N., Giri, A., Kar, S., Bootharaju, M. S., John, R., Xavier, P. L., et al. (2012). Protein-directed synthesis of NIR-emitting, tunable hgs quantum dots and their applications in metal-ion sensing. *Small* 8, 3175–3184. doi: 10.1002/sml.201200760
- Guo, Z., Park, S., Yoon, J., and Shin, I. (2014). Recent progress in the development of near-infrared fluorescent probes for bioimaging applications. *Chem. Soc. Rev.* 43, 16–29. doi: 10.1039/C3CS60271K
- Hahn, M. A., Singh, A. K., Sharma, P., Brown, S. C., and Moudgil, B. M. (2011). Nanoparticles as contrast agents for in-vivo bioimaging: current status and future perspectives. *Anal. Bioanal. Chem.* 399, 3–27. doi: 10.1007/s00216-010-4207-5
- Hang, Y., Yang, L., Qu, Y., and Hua, J. (2014). A new diketopyrrolopyrrole-based near-infrared (NIR) fluorescent biosensor for BSA detection and AIE-assisted bioimaging. *Tetrahedron Lett.* 55, 6998–7001. doi: 10.1016/j.tetlet.2014.10.108
- He, Y., Zhong, Y., Su, Y., Lu, Y., Jiang, Z., Peng, F., et al. (2011). Water-dispersed near-infrared-emitting quantum dots of ultrasmall sizes for *in vitro* and *in vivo* imaging. *Angew. Chem. Int. Ed.* 50, 5695–5698. doi: 10.1002/anie.201004398
- Hilderbrand, S. A., Shao, F., Salthouse, C., Mahmood, U., and Weissleder, R. (2009). Upconverting luminescent nanomaterials: application to *in vivo* bioimaging. *Chem. Commun.* 4188–4190. doi: 10.1039/b905927j
- Hu, L., Yan, Z., and Xu, H. (2013). Advances in synthesis and application of near-infrared absorbing squaraine dyes. *RSC Adv.* 3, 7667–7676. doi: 10.1039/c3ra23048a
- Hui, Y. Y., Cheng, C.-L., and Chang, H.-C. (2010). Nanodiamonds for optical bioimaging. *J. Phys. D Appl. Phys.* 43:374021. doi: 10.1088/0022-3727/43/37/374021
- Hui, Y. Y., Su, L.-J., Chen, O. Y., Chen, Y.-T., Liu, T.-M., and Chang, H.-C. (2014). Wide-field imaging and flow cytometric analysis of cancer cells in blood by fluorescent nanodiamond labeling and time gating. *Sci. Rep.* 4:5574. doi: 10.1038/srep05574
- Kevadiya, B. D., Woldstad, C., Ottemann, B. M., Dash, P., Sajja, B. R., Lamberty, B., et al. (2018). Multimodal theranostic nanoformulations permit magnetic resonance bioimaging of antiretroviral drug particle tissue-cell biodistribution. *Theranostics*. 8:256–276. doi: 10.7150/thno.22764
- Kigel, A., Brumer, M., Maikov, G. I., Sashchiuk, A., and Lifshitz, E. (2009). Thermally activated photoluminescence in lead selenide colloidal quantum dots. *Small* 5, 1675–1681. doi: 10.1002/sml.200801378
- Kim, D., and Kang, J. (2010). Upconversion microscopy for biological applications. *Microsc. Sci. Technol. Appl. Educ.* 571–582.
- Koide, Y., Urano, Y., Hanaoka, K., Terai, T., and Nagano, T. (2011). Development of an Si-rhodamine-based far-red to near-infrared fluorescence probe selective for hypochlorous acid and its applications for biological imaging. *J. Am. Chem. Soc.* 133, 5680–5682. doi: 10.1021/ja111470n
- Krishnan, R. V., Biener, E., Zhang, J. H., Heckel, R., and Herman, B. (2003). Probing subtle fluorescence dynamics in cellular proteins by streak camera based fluorescence lifetime imaging microscopy. *Appl. Phys. Lett.* 83, 4658–4660. doi: 10.1063/1.1630154
- Kumar, R., Nyk, M., Ohulchanskyy, T. Y., Flask, C. A., and Prasad, P. N. (2009). Combined optical and MR bioimaging using rare earth ion doped NaYF₄ nanocrystals. *Adv. Funct. Mater.* 19, 853–859. doi: 10.1002/adfm.200800765
- Lavis, L. D., and Raines, R. T. (2008). Bright ideas for chemical biology. *ACS Chem. Biol.* 3, 142–155. doi: 10.1021/cb700248m
- Leblond, F., Davis, S. C., Valdés, P. A., and Pogue, B. W. (2010). Pre-clinical whole-body fluorescence imaging: Review of instruments, methods and applications. *J. Photochem. Photobiol. B Biol.* 98, 77–94. doi: 10.1016/j.jphotobiol.2009.11.007
- Levitus, M., and Ranjit, S. (2011). Cyanine dyes in biophysical research: the photophysics of polymethine fluorescent dyes in biomolecular environments. *Q. Rev. Biophys.* 44, 123–151. doi: 10.1017/S0033583510000247
- Li, H., Guan, L., Zhang, X., Yu, H., Huang, D., Sun, M., et al. (2016). A cyanine-based near-infrared fluorescent probe for highly sensitive and selective detection of hypochlorous acid and bioimaging. *Talanta* 161, 592–598. doi: 10.1016/j.talanta.2016.09.008
- Lin, Y., Kwong, T. C., Gulsen, G., and Bolisay, L. (2012). Temperature-modulated fluorescence tomography based on both concentration and lifetime contrast. *J. Biomed. Opt.* 17:056007. doi: 10.1117/1.JBO.17.5.056007
- Liu, J., Sun, Y.-Q., Zhang, H., Shi, H., Shi, Y., and Guo, W. (2016). Sulfone-Rhodamines: a new class of near-infrared fluorescent dyes for bioimaging. *ACS Appl. Mater. Interfaces* 8, 22953–22962. doi: 10.1021/acsami.6b08338
- Liu, J. M., Chen, J. T., and Yan, X. P. (2013). Near infrared fluorescent trypsin stabilized gold nanoclusters as surface plasmon enhanced energy transfer biosensor and *in vivo* cancer imaging bioprobe. *Anal. Chem.* 85, 3238–3245. doi: 10.1021/ac303603f
- Liu, Y., Wang, D., Li, L., Peng, Q., and Li, Y. (2014). Energy upconversion in lanthanide-doped core/porous-shell nanoparticles. *Inorg. Chem.* 53, 3257–3259. doi: 10.1021/ic403091w
- Lu, H., Su, F., Mei, Q., Tian, Y., Tian, W., Johnson, R. H., et al. (2012). Using fluorine-containing amphiphilic random copolymers to manipulate the quantum yields of aggregation-induced emission fluorophores in aqueous solutions and the use of these polymers for fluorescent bioimaging. *J. Mater. Chem.* 22, 9890–9900. doi: 10.1039/c2jm30258f
- Luo, S., Zhang, E., Su, Y., Cheng, T., and Shi, C. (2011). A review of NIR dyes in cancer targeting and imaging. *Biomaterials* 32, 7127–7138. doi: 10.1016/j.biomaterials.2011.06.024
- Lv, Y., Liu, P., Ding, H., Wu, Y., Yan, Y., Liu, H., et al. (2015). Conjugated polymer-based hybrid nanoparticles with two-photon excitation and near-infrared emission features for fluorescence bioimaging within the biological window. *ACS Appl. Mater. Interfaces* 7, 20640–20648. doi: 10.1021/acsami.5b05150
- Martinić, I., Eliseeva, S. V., and Petoud, S. (2017). Near-infrared emitting probes for biological imaging: Organic fluorophores, quantum dots, fluorescent proteins, lanthanide (III) complexes and nanomaterials. *J. Lumin.* 189, 19–43. doi: 10.1016/j.jlumin.2016.09.058
- McCann, T. E., Kosaka, N., Koide, Y., Mitsunaga, M., Choyke, P. L., Nagano, T., et al. (2011). Activatable optical imaging with a silica-rhodamine based near infrared (SiR700) fluorophore: a comparison with cyanine based dyes. *Bioconj. Chem.* 22, 2531–2538. doi: 10.1021/bc2003617
- Meherzi-Maghraoui, H., Dachraoui, M., Belgacem, S., Buhre, K. D., Kunst, R., Cowache, P., et al. (1996). Structural, optical and transport properties of Ag 2S films deposited chemically from aqueous solution. *Thin Solid Films* 288, 217–223. doi: 10.1016/S0040-6090(96)08811-6
- Nolting, D. C., Gore, J., and Pham, W. (2011). Near-infrared dyes: probe development and applications in optical molecular imaging. *Curr. Org. Synth.* 8, 521–534. doi: 10.2174/157017911796117223
- Ntziachristos, V. (2006). Fluorescence molecular imaging. *Annu. Rev. Biomed. Eng.* 8, 1–33. doi: 10.1146/annurev.bioeng.8.061505.095831
- Pastierik, T., Šebej, P., Medalov, Á, J., Štacko, P., Klán, P., et al. (2014). Near-infrared fluorescent 9-phenylethynylpyronin analogues for bioimaging. *J. Org. Chem.* 79, 3374–3382. doi: 10.1021/jo500140y
- Patsenker, L. D., Tatarts, A. L., Povrozin, Y. A., and Terpetschnig, E. A. (2011). Long-wavelength fluorescence lifetime labels. *Bioanal. Rev.* 3, 115–137. doi: 10.1007/s12566-011-0025-2

- Pei, Y., and Wei, M.-Y. (2019). Newly-engineered materials for bio-imaging technology: a focus on the hybrid system of ultrasound and fluorescence. *Front. Bioeng. Biotechnol.* 7:88. doi: 10.3389/fbioe.2019.00088
- Pons, T., Bouccara, S., Lorient, V., Lequeux, N., Pezet, S., and Fragola, A. (2019). *In vivo* Imaging of single tumor cells in fast-flowing bloodstream using near-infrared quantum dots and time-gated imaging. *ACS Nano* 13, 3125–3131. doi: 10.1021/acsnano.8b08463
- Prazeres, T. J., Alexander, F., Barbosa, S. P., Martinho, J. M., and Berberan-Santos, M. N. (2008). Accurate determination of the limiting anisotropy of rhodamine 101. Implications for its use as a fluorescence polarization standard. *J. Phys. Chem. A* 112, 5034–5039. doi: 10.1021/jp710625j
- Qian, J., Fu, T., Zhan, Q., and He, S. (2009). Using some nanoparticles as contrast agents for optical bioimaging. *IEEE J. Selected Top. Quantum Electron.* 16, 672–684. doi: 10.1109/JSTQE.2009.2030155
- Reineck, P., and Gibson, B. C. (2016). Near-infrared fluorescent nanomaterials for bioimaging and sensing. *Adv. Opt. Mater.* 5:1600446. doi: 10.1002/adom.201600212
- Rizzo, M. A., Springer, G. H., Granada, B., and Piston, D. W. (2004). An improved cyan fluorescent protein variant useful for FRET. *Nat. Biotechnol.* 22:445. doi: 10.1038/nbt945
- Roy, S., Baral, A., Bhattacharjee, R., Jana, B., Datta, A., Ghosh, S., et al. (2015). Preparation of multi-coloured different sized fluorescent gold clusters from blue to NIR, structural analysis of the blue emitting Au7 cluster, and cell-imaging by the NIR gold cluster. *Nanoscale* 7, 1912–1920. doi: 10.1039/C4NR04338C
- Samanta, A., Vendrell, M., Das, R., and Chang, Y. T. (2010). Development of photostable near-infrared cyanine dyes. *Chem. Commun.* 46, 7406–7408. doi: 10.1039/c0cc02366c
- Santos, H. D., Ruiz, D., Lifante, G., Jacinto, C., and Juarez, B. H., and Jaque, D. (2017). Time resolved spectroscopy of infrared emitting Ag2S nanocrystals for subcutaneous thermometry. *Nanoscale* 9, 2505–2513. doi: 10.1039/C6NR08534B
- Shang, L., Azadfar, N., Stockmar, F., Send, W., Trouillet, V., Bruns, M., et al. (2011). One-pot synthesis of near-infrared fluorescent gold clusters for cellular fluorescence lifetime imaging. *Small* 7, 2614–2620. doi: 10.1002/smll.201100746
- Smith, A., Galli, M., Piga, I., Denti, V., Stella, M., Chinello, C., et al. (2019). Molecular signatures of medullary thyroid carcinoma by matrix-assisted laser desorption/ionisation mass spectrometry imaging. *J. Proteomics* 191, 114–123. doi: 10.1016/j.jprot.2018.03.021
- Smith, A. M., Gao, X., and Nie, S. (2004). Quantum dot nanocrystals for *in vivo* molecular and cellular imaging. *Photochem. Photobiol.* 80, 377–385. doi: 10.1562/0031-8655(2004)080<0377:QDNFIV>2.0.CO;2
- Sun, Y., Qu, Z., Zhou, Z., Gai, L., and Lu, H. (2019). Thieno [3, 2-b] thiophene fused BODIPYs: synthesis, near-infrared luminescence and photosensitive properties. *Org. Biomol. Chem.* 17, 3617–3622. doi: 10.1039/C9OB00030E
- Tan, G. R., Wang, M., Hsu, C. Y., Chen, N., and Zhang, Y. (2016). Small upconverting fluorescent nanoparticles for biosensing and bioimaging. *Adv. Opt. Mater.* 4, 984–997. doi: 10.1002/adom.201600141
- Tan, T. T., Selvan, S. T., Zhao, L., Gao, S., and Ying, J. Y. (2007). Size control, shape evolution, and silica coating of near-infrared-emitting PbSe quantum dots. *Chem. Mater.* 19, 3112–3117. doi: 10.1021/cm061974e
- Tinnefeld, P., Hertel, D.-P., and Sauer, M. (2001). Photophysical dynamics of single molecules studied by spectrally-resolved fluorescence lifetime imaging microscopy (SFLIM). *J. Phys. Chem. A* 105, 7989–8003. doi: 10.1021/jp010365l
- Treibs, A., and Kreuzer, F. H. (1968). Difluoroboryl-Komplexe von Di- und tripyrrylmethenen. *Justus Liebigs Ann. Chem.* 718, 208–223. doi: 10.1002/jlac.19687180119
- Van Munster, E., and Gadella T. Jr. (2004). ϕ FLIM: a new method to avoid aliasing in frequency-domain fluorescence lifetime imaging microscopy. *J. Microsc.* 213, 29–38. doi: 10.1111/j.1365-2818.2004.01249.x
- Waddell, E., Wang, Y., Strykowski, W., McWhorter, S., Henry, A. C., Evans, D., et al. (2000). High-resolution near-infrared imaging of DNA microarrays with time-resolved acquisition of fluorescence lifetimes. *Anal. Chem.* 72, 5907–5917. doi: 10.1021/ac0009705
- Wang, D., Qian, J., Cai, F., He, S., Han, S., and Mu, Y. (2012). ‘Green’-synthesized near-infrared PbS quantum dots with silica-PEG dual-layer coating: ultrastable and biocompatible optical probes for *in vivo* animal imaging. *Nanotechnology* 23:245701. doi: 10.1088/0957-4484/23/24/245701
- Wang, S., He, Y., Chen, Z., Li, Y., Zhao, J., and Lyu, L. (2019). Pleiotropic action of genetic variation in ZNF804A on brain structure: a meta-analysis of magnetic resonance imaging studies. *Neuropsychiatr. Dis. Treat.* 15, 721–729. doi: 10.2147/NDT.S174728
- Wang, X. F., Periasamy, A., Herman, B., and Coleman, D. M. (1992). Fluorescence lifetime imaging microscopy (FLIM): instrumentation and applications. *Crit. Rev. Anal. Chem.* 23, 369–395. doi: 10.1080/10408349208051651
- Williams, C. H. G. (1856). XXVI.—researches on chinoline and its homologues. *Trans. R. Soc. Edinburgh* 21:377. doi: 10.1017/S0080456800032208
- Wolfbeis, O. S. (2015). An overview of nanoparticles commonly used in fluorescent bioimaging. *Chem. Soc. Rev.* 44, 4743–4768. doi: 10.1039/C4CS00392F
- Wu, D., Shen, Y., Chen, J., Liu, G., Chen, H., and Yin, J. (2017). Naphthalimide-modified near-infrared cyanine dye with a large Stokes shift and its application in bioimaging. *Chin. Chem. Lett.* 28, 1979–1982. doi: 10.1016/j.ccl.2017.07.004
- Wu, S., Han, G., Milliron, D. J., Aloni, S., Altoe, V., Talapin, D. V., et al. (2009). Non-blinking and photostable upconverted luminescence from single lanthanide-doped nanocrystals. *Proc. Natl. Acad. Sci. USA* 106, 10917–10921. doi: 10.1073/pnas.0904792106
- Xing, Y., and Rao, J. (2008). Quantum dot bioconjugates for *in vitro* diagnostics & *in vivo* imaging. *Cancer Biomarkers* 4, 307–319. doi: 10.3233/CBM-2008-4603
- Xu, M., Guo, C., Hu, G., Xu, S., and Wang, L. (2018). Organic nanoprobe for fluorescence and 19F magnetic resonance dual-modality imaging. *Chin. J. Chem.* 36, 25–30. doi: 10.1002/cjoc.201700382
- Yi, X., Wang, F., Qin, W., Yang, X., and Yuan, J. (2014). Near-infrared fluorescent probes in cancer imaging and therapy: an emerging field. *Int. J. Nanomed.* 9, 1347–1365. doi: 10.2147/IJN.S60206
- Yi, Z., Lu, W., Xu, Y., Yang, J., Deng, L., Qian, C., et al. (2014). PEGylated NaLuF4: Yb/Er upconversion nanophosphors for *in vivo* synergistic fluorescence/X-ray bioimaging and long-lasting, real-time tracking. *Biomaterials* 35, 9689–9697. doi: 10.1016/j.biomaterials.2014.08.021
- Yuan, B., Uchiyama, S., Liu, Y., Nguyen, K. T., and Alexandrakis, G. (2012). High-resolution imaging in a deep turbid medium based on an ultrasound-switchable fluorescence technique. *Appl. Phys. Lett.* 101:033703. doi: 10.1063/1.4737211
- Zhang, N., Liu, X., Wei, Z., Liu, H., Peng, J., Zhou, L., et al. (2019). Cell imaging using two-photon excited CdS fluorescent quantum dots working within the biological window. *Nanomaterials* 9:369. doi: 10.3390/nano9030369
- Zhang, X., Bloch, S., Akers, W., and Achilefu, S. (2012). Near-infrared molecular probes for *in vivo* imaging. *Curr. Protoc. Cytometry* 12:12.27. doi: 10.1002/0471142956.cy1227s60
- Zhang, X.-F., Zhang, Y., and Liu, L. (2014). Fluorescence lifetimes and quantum yields of ten rhodamine derivatives: Structural effect on emission mechanism in different solvents. *J. Lumin.* 145, 448–453. doi: 10.1016/j.jlumin.2013.07.066
- Zhang, Y., Liu, Y., Li, C., Chen, X., and Wang, Q. (2014). Controlled synthesis of Ag2S quantum dots and experimental determination of the exciton Bohr radius. *J. Phys. Chem. C* 118, 4918–4923. doi: 10.1021/jp501266d
- Zhang, Y., Yue, X., Kim, B., Yao, S., Bondar, M. V., and Belfield, K. D. (2013). Bovine serum albumin nanoparticles with fluorogenic near-IR-emitting squaraine dyes. *ACS Appl. Mater. Interfaces* 5, 8710–8717. doi: 10.1021/am402361w
- Zhu, S., Zhang, J., Janjanam, J., Bi, J., Vegesna, G., Tiwari, A., et al. (2013). Highly water-soluble, near-infrared emissive BODIPY polymeric dye bearing RGD peptide residues for cancer imaging. *Anal. Chim. Acta.* 758, 138–144. doi: 10.1016/j.aca.2012.10.026

Conflict of Interest: The authors declare that the research was conducted in the absence of any commercial or financial relationships that could be construed as a potential conflict of interest.

Copyright © 2019 Lian, Wei and Ma. This is an open-access article distributed under the terms of the Creative Commons Attribution License (CC BY). The use, distribution or reproduction in other forums is permitted, provided the original author(s) and the copyright owner(s) are credited and that the original publication in this journal is cited, in accordance with accepted academic practice. No use, distribution or reproduction is permitted which does not comply with these terms.



Recent Progress in NIR-II Contrast Agent for Biological Imaging

Jie Cao^{1,2,3*}, Binling Zhu^{3,4,5}, Kefang Zheng^{2,3}, Songguo He^{2,3}, Liang Meng^{4,5}, Jibin Song^{6*} and Huanghao Yang^{6*}

¹ Fuzhou University Postdoctoral Research Station of Chemical Engineering and Technology, Fuzhou University, Fuzhou, China, ² Scientific Research and Experiment Center, Fujian Police College, Fuzhou, China, ³ Fujian Police College Judicial Expertise Center, Fuzhou, China, ⁴ Department of Forensic Science, Fujian Police College, Fuzhou, China, ⁵ Engineering Research Center, Fujian Police College, Fuzhou, China, ⁶ The Key Lab of Analysis and Detection Technology for Food Safety of the MOE and Fujian Province, State Key Laboratory of Photocatalysis on Energy and Environment, College of Chemistry, Fuzhou University, Fuzhou, China

OPEN ACCESS

Edited by:

Yanbo Pei,
Harbin Institute of Technology, China

Reviewed by:

Shuai Yu,
University of Texas at Arlington,
United States
Guangcun Chen,
Chinese Academy of Sciences, China

*Correspondence:

Jie Cao
caojie@fjpsc.edu.cn
Jibin Song
jibinsong@fzu.edu.cn
Huanghao Yang
hhyang@fzu.edu.cn

Specialty section:

This article was submitted to
Nanobiotechnology,
a section of the journal
Frontiers in Bioengineering and
Biotechnology

Received: 17 September 2019

Accepted: 30 December 2019

Published: 30 January 2020

Citation:

Cao J, Zhu B, Zheng K, He S,
Meng L, Song J and Yang H (2020)
Recent Progress in NIR-II Contrast
Agent for Biological Imaging.
Front. Bioeng. Biotechnol. 7:487.
doi: 10.3389/fbioe.2019.00487

Fluorescence imaging technology has gradually become a new and promising tool for *in vivo* visualization detection. Because it can provide real-time sub-cellular resolution imaging results, it can be widely used in the field of biological detection and medical detection and treatment. However, due to the limited imaging depth (1–2 mm) and self-fluorescence background of tissue emitted in the visible region (400–700 nm), it fails to reveal biological complexity in deep tissues. The traditional near infrared wavelength (NIR-I, 650–950 nm) is considered as the first biological window, because it reduces the NIR absorption and scattering from blood and water in organisms. NIR fluorescence bioimaging's penetration is larger than that of visible light. In fact, NIR-I fluorescence bioimaging is still interfered by tissue autofluorescence (background noise), and the existence of photon scattering, which limits the depth of tissue penetration. Recent experimental and simulation results show that the signal-to-noise ratio (SNR) of bioimaging can be significantly improved at the second region near infrared (NIR-II, 1,000–1,700 nm), also known as the second biological window. NIR-II bioimaging is able to explore deep-tissues information in the range of centimeter, and to obtain micron-level resolution at the millimeter depth, which surpass the performance of NIR-I fluorescence imaging. The key of fluorescence bioimaging is to achieve highly selective imaging thanks to the functional/targeting contrast agent (probe). However, the progress of NIR-II probes is very limited. To date, there are a few reports about NIR-II fluorescence probes, such as carbon nanotubes, Ag₂S quantum dots, and organic small molecular dyes. In this paper, we surveyed the development of NIR-II imaging contrast agents and their application in cancer imaging, medical detection, vascular bioimaging, and cancer diagnosis. In addition, the hotspots and challenges of NIR-II bioimaging are discussed. It is expected that our findings will lay a foundation for further theoretical research and practical application of NIR-II bioimaging, as well as the inspiration of new ideas in this field.

Keywords: fluorescence imaging technology, the second region near infrared (NIR-II), biological imaging, contrast agents, biomedical applications

INTRODUCTION

Optical imaging technology has become a very important research method in the field of biomedicine, especially for its ability to monitor biomolecules, cells, tissues, and living organisms in real-time and multi-dimensional visualization. Optical imaging technology has many advantages, in that it is non-invasive and safe, has visualization capabilities and high spatial resolution, has high rapid output, and is a low-cost method. It has been widely used in biomolecular detection imaging, drug distribution metabolic tracking, disease detection and diagnosis (Sevick-Muraca et al., 2002; Hilderbrand and Weissleder, 2010; Chen et al., 2014). Especially in early cancer diagnosis and imaging-guided treatment, optical imaging technology have a good application prospect.

In the process of optical *in vivo* bioimaging, the penetration depth of photons primarily depends on the absorption and scattering of tissue elements. Meanwhile, the fluorescence and scattering photons generated by tissue itself will cause interference noise and background radiation to the photon penetration process. Therefore, fluorescence imaging technology also has limitation in its practical applications in that some active components in organisms (such as melanin, hemoglobin, cytochrome, etc.) have higher light absorption and light scattering within the visible band (400–700 nm), which will reduce the penetration depth of visible light. Because organisms are rich in many luminescent macromolecules (usually located in the visible region), these biomolecules can also produce non-specific fluorescence emissions under visible light excitation, thus interfering with imaging results (Weissleder, 2001).

Because near-infrared light (NIR) is less absorbed and scattered in biological tissues than visible light, the former can penetrate biological tissues, such as skin, more effectively. As shown in **Figure 1A** (top), the effective attenuation coefficients (EACs) of tissue components, such as whole blood (oxygenated or deoxygenated), skin, and fat are significantly lower in the range of 650–950 nm than that in visible light range, which is considered as the “first (optical) window” (NIR-I) (Frangioni, 2003; Smith et al., 2009). In the practice of NIR-I biological imaging, the imaging quality in deep tissue is far from adequate resolution. Due to the large amount of background noise generated by tissue's auto-fluorescence, the tissue penetration depth of photons in NIR-I is only 1–2 cm (Croce and Bottirol, 2014).

Typically, the NIR-II window that may be suitable for bioimaging application is from 1,000 to 1,700 nm. Tissue components show a strong EAC from 1,350 to 1,700 nm, as shown in **Figure 1A** (top). We herein narrowed down the wavelength range to 1,000–1,350 nm, as labeled as “second window” in **Figure 1A** (top). In this review, the “NIR-II” in this manuscript only refers to the wavelength range of 1,000–1,350 nm. The relationship between wavelength and the absorption coefficient or the light scattering coefficient in the skin is shown in **Figures 1B,C** respectively. The absorption to the skin in NIR-I decreases slowly with the increase of wavelength, and the trend continues into NIR-II. It reaches the lowest point at ~1,125 nm and starts spiking after 1,250 nm. No significant

difference is found for the light scattering coefficients in NIR-I and NIR-II regions. The penetration depth of light to the skin can be seen from **Figure 1D**, from which we could find a sweet spot (largest penetration depth) of 1,125 nm in NIR-II. Overall, the range of 1,000–1,125 nm in NIR-II shows a better performance than NIR-I for skin. We may get the similar conclusions for human subcutaneous fat tissue (**Figures 1E,F**) and human subcutaneous adipose tissue (**Figures 1G–I**). Again, it is difficult to compare directly the performance of NIR-I and NIR-II because the absorption coefficients in the latter shows a turning point in the middle of NIR-II (at ~1,125 nm). The sweet spot of 1,000–1,125 nm of NIR-II shows the lowest absorption coefficients for both red blood cells (RBCs) and hemoglobin with or without saturated oxygen, which is also applicable for water (see **Figure 1J**). In fact, it can be seen from **Figure 1J** of the relationship between water absorption coefficient with wavelength that the wavelength below 800 nm is the least absorbed by water, which is the optimal excitation wavelength. The closest point in NIR-II to eliminate the absorption from water is at 1,100 nm. It also can be seen from **Figure 1K** that the effective light scattering of 100% and 0% oxygen saturation RBCs shows no significant differences in NIR-I and NIR-II. However, the autofluorescence from tissue or endogenous compounds limits the signal-to-noise ratio (SNR) of NIR-I fluorescence imaging. The SNR of NIR-II fluorescence imaging, on the other hand, is enhanced due to the elimination of autofluorescence noises. For example, Lim et al. (2003) studied the optical imaging process in different biological media (including tissue and blood) and simulated the process and established relevant models. From the results of this study, it can be concluded that the SNR of quantum dot fluorescent clusters emitting at 1,320 nm is more than 100 times higher than that of quantum dots emitting at 850 nm. This result aroused great interest of the researchers in exploring biocompatible NIR-II fluorescence probes. Therefore, compared with visible light (400–700 nm) and traditional NIR-I window, NIR-II can avoid background interference such as spontaneous fluorescence and photon scattering (Smith et al., 2009; Welsher et al., 2011). In 2009, Welsher et al. (2009) first reported on a class of single-walled carbon nanotubes (SWCNTs), whose fluorescence emission wavelength is 950–1,600 nm. Further experiments show that such material can be used for imaging in living mice. The fluorescence signal of SWCNTs at 950–1,400 nm can be detected to obtain high-resolution imaging of blood vessels under deep skin tissue. Since then, more and more NIR-II fluorescent probes have been successfully developed and have been applied to biomedical imaging field.

At present, the application of NIR-II imaging window is still not fully utilized, due to the lack of research on probe materials and the restriction of imaging equipment. The **Figure 1A** (bottom) shows the relationship between incident light wavelength and quantum efficiency when cameras with different sensors are used, including silicon (Si), InGaAs, and HgCdTe. Furthermore, Si camera is the most sensitive to the light of NIR-I, while InGaAs camera is the most sensitive to the light of NIR-II. In addition, HgCdTe camera is less sensitive to the light of these two windows although it has a higher resolution array, and

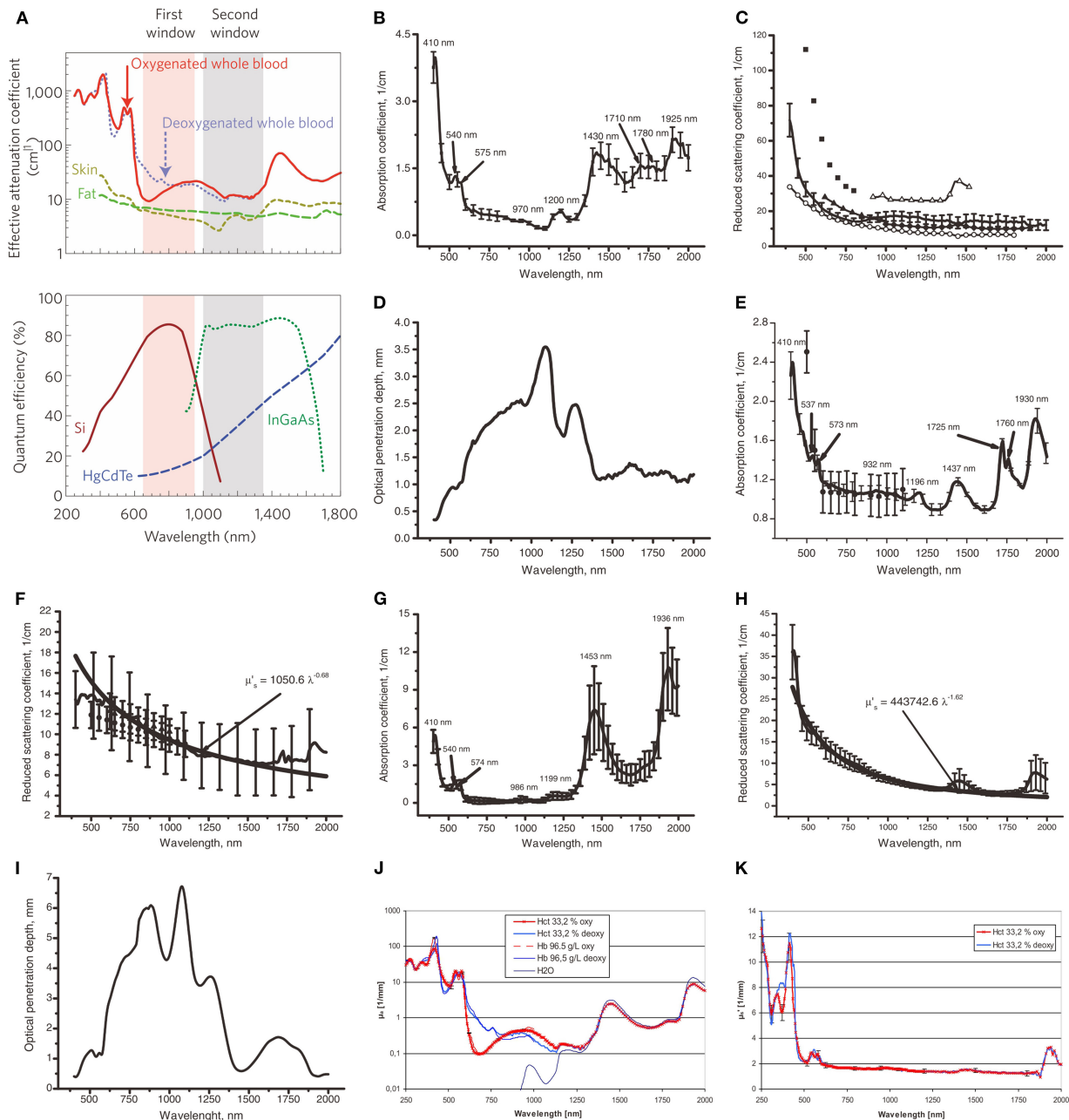


FIGURE 1 | Pahl et al. (1993) reported the inverse double increase (IAD) method and the power law approximation are used to process experimental data and determine the optical properties of tissues. In this figure, μ'_s is calculated as $\mu'_s = \mu_s (1-g)$, where μ_s is the scattering coefficient and g is the anisotropic coefficient of scattering. The solid line corresponds to the average experimental data, and the vertical line shows the SD value. (A Top) NIR-I (first window) and NIR-II (second window) imaging windows (Smith et al., 2009). The effective attenuation coefficient represents the how easily a volume of material can be penetrated by a beam of light. (A Bottom) The sensitivity curves of the sensor in the signal detector camera with silicon (Si), indium gallium arsenic (InGaAs), and mercury telluride cadmium (HgCdTe). Unlike the charge coupled device (CCD) camera using silicon sensor, the core component of near infrared camera is semiconductor alloy sensor, including InGaAs and HgCdTe, which has a narrower band gap. In particular, InGaAs cameras exhibit high quantum efficiency when used in the NIR-II window, i.e., high sensitivity. Adapted from Smith et al. (2009) written by Smith, A.M., etc. with permission. (B,C) Show the relationship between the incident light wavelength and absorption coefficient (μ_a) or the reduced light scattering coefficient (μ'_s) in human skin *in vitro*, respectively. (B) Adapted from Bashkatov et al. (2005) with permission. In (C), except for the solid line, the remaining data marker points correspond to the experimental data obtained in reference (Chan et al., 1996; Simpson et al., 1998; Du et al., 2001; Troy and Thennadi, 2001; Bashkatov et al., 2005). Adapted from Chan et al. (1996), Simpson et al. (1998), Du et al. (2001), Troy and Thennadi (2001), and Bashkatov et al. (2005) with permission. (D,I) Show the penetration depth (δ) of light to skin and human mucosal tissue in the range of incident light wavelength from 400 to 2,000 nm, respectively. Adapted from Bashkatov et al. (2005) with permission. (E,F) Show the relationship between wavelength and μ_a or μ'_s in subcutaneous adipose tissue, respectively. In (E), all the data markers except the solid line correspond to the experimental data obtained in Peters et al. (1990).

(Continued)

FIGURE 1 | Adapted from Peters et al. (1990) with permission. In **(F)**, all the data markers except the solid line correspond to the experimental data obtained in Peters et al. (1990) and Simpson et al. (1998). Adapted from Peters et al. (1990) and Simpson et al. (1998). with permission. **(G,H)** Show the relationship between wavelength and μ_a or μ_s in human mucosa, respectively. Adapted from Bashkatov et al. (2005) with permission. **(J)** Shows the relationship between wavelength and μ_a for red blood cells (RBC) with or without saturated oxygen in the 33.2% hematocrit (HCT) brine solution, as well as the relationship between wavelength and μ_a for hemoglobin with or without saturated oxygen in the 96.5 g/dl hemoglobin solution. Adapted from Friebel et al. (2009) with permission. **(J)** Shows the relationship between wavelength and μ_s for RBC with or without saturated oxygen in the 33.2% HCT brine solution. Adapted from Friebel et al. (2009) with permission.

it is most sensitive to the light of longer wavelength. Silicon-based CCD (Si-CCD) is usually used to collect fluorescence signals from NIR-I window. However, the quantum yield of this kind of CCD in NIR-II window is low, which is not sufficient for signal acquisition. Near infrared CCD based on InGaAs is commonly used as a NIR-II window detector, but the high cost of use restricts its widespread use in research (Smith et al., 2009).

In recent years, there have been a few successful applications of Nanofluorescent probes developed by NIR-II technology in bioimaging, which include the use of carbon nanotubes (Hong et al., 2014; Diao et al., 2015), Ag₂S quantum dots (Hong et al., 2012b; Zhang et al., 2012) and small organic molecules (Antaris et al., 2016). Next, the applications of various near infrared nanomaterials and bioimaging will be introduced in detail.

CATEGORIES OF REPORTED NIR-II NANOMATERIALS

Single-Walled Carbon Nanotubes

Semiconductor-based single-walled carbon nanotubes (SWCNTs) have unique optical properties due to the existence of the bandgap. When photons interact with SWCNTs, they are absorbed and released as fluorescence. It is worth noting that the absorption wavelength of SWCNTs is generally in the visible region (400–700 nm) and NIR-I (650–950 nm). However, their emission wavelength is in NIR-II (1,000–1,700 nm), and the energy from absorbed photons is not released by radiation relaxation in the form of heat (O'Connell et al., 2002). SWCNTs has been widely used in the fields of photothermal and photodynamic therapy (Robinson et al., 2010; Murakami et al., 2012), fluorescence labeling, and fluorescence imaging of deep tissue *in vivo* (Welsher et al., 2011; Hong et al., 2012a, 2014). In addition, the use of SWCNT surface functionalization (Zheng et al., 2003) using coating surfactants, polymers, DNA, proteins, and even viruses can greatly enrich the scope of application for SWCNTs in the biological field. However, the characteristically low fluorescence quantum efficiency (<1%) of SWCNTs is a major issue still needing to be addressed.

SWCNTs are used *in vivo* imaging because of their inherently wide NIR-II fluorescence emissions (Yi et al., 2012; Ghosh et al., 2014). In 2014, Belcher's research team coated SWCNTs with an M13 virus, using the M13 virus surface polypeptide, which targets tumor cells, to specifically bind SWCNTs to tumor tissue. Using SWCNTs, Belcher was able to achieve targeted fluorescence imaging of tumor tissues in mice, which proved that the system could be applied to clinical diagnosis (Ghosh et al., 2014). In the same year, Hong et al. combined an IRDye-800 fluorescent group with SWCNTs and intravenously injected the IRDye-800 fluorescent group into mice. Using a NIR-II fluorescence imaging

in vivo (Hong et al., 2014), they found that the fluorescence of carbon nanotubes could penetrate 2.6 mm deep into a mouse skull, which not only provided imaging of the distribution of blood vessels in the head of mice, but also clearly showed the fine structure of the brain capillaries. In 2019, Toshiya Okazaki and other Japanese scholars used oxygen-doped SWCNTs and enveloped it with phospholipid polyethylene glycol (o-SWCNT-PEG). They found that it has special potential and can emit 1,300 nm NIR-II fluorescence under 980 nm light excitation. Therefore, it is considered to be a promising angiographic imaging probe (Takeuchi et al., 2019). In addition, o-SWCNTs were injected intravenously into living mice as a contrast agent for vascular imaging. The biological factors of the angiographic probe *in vivo*, including retention time, biological distribution, and toxicity, were studied. The results showed that o-SWCNT-PEG, an angiographic probe, had low toxicity *in vivo*, and that it can be successfully used in angiographic imaging within the NIR-II wavelength range.

Semiconductor Quantum Dots

A second successful application of Nanofluorescent probes developed by NIR-II technology is the use of semiconductor quantum dots. Among the many kinds of semiconductor fluorescent quantum dots available, Ag₂S quantum dots have been most widely used in near infrared imaging because of their strong NIR-II fluorescence and low biological toxicity. Their biological toxicity is lower than other quantum dots containing Se, Te, Cd, Pb, As, and other acute or chronic toxic elements, and the fluorescence can be tuned from 687 nm in NIR-I to 1,294 nm in NIR-II (Yang et al., 2013; Gui et al., 2014a,b; Zhao and Song, 2014). At the same time, it also has high fluorescence stability and fluorescence quantum efficiency. Ag₂S quantum dots have smaller particle sizes [3.7 nm (Zhao and Song, 2014), 1.6–6.8 nm (Yang et al., 2013), 2.6–3.7 nm (Gui et al., 2014b), 3.5 nm (Gui et al., 2014a)], which are very suitable for bioimaging applications.

For example, in 2012 Wang's and Dai's research teams collaborated to report on NIR-II Ag₂S quantum dots with a fluorescence of 1,200 nm. The solubility of Ag₂S QDs was changed by using a surface modification of water-soluble PEG molecules. And then Ag₂S QDs can be dissolved in water. Ag₂S was first used in NIR-II cell imaging and non-specific tumor detection (Hong et al., 2012b). Additionally, in 2012, they applied PEG modified Ag₂S quantum dots with high quantum efficiency to NIR-II imaging *in vivo* (Zhang et al., 2012), using nude mice inoculated with 4T1 tumors. Not only did the Ag₂S quantum dots were proven to be a good NIR-II fluorescence contrast agent, but interestingly, after injection into the tail of nude mice, Ag₂S quantum dots gradually accumulated in the tumors of

nude mice as the circulation time increases. They believe that the reason for above observation is the non-specific enhanced permeability and retention effect (EPR effect) of cancer tissue. Subsequently, Wang's team did an in-depth study on the long period cytotoxicity of Ag₂S quantum dots *in vivo* (Zhang et al., 2013). The reticuloendothelial system (RES), such as liver and spleen, is the main accumulation site of Ag₂S QDs *in vivo*, but it can be gradually metabolized or excreted over time. Additionally, the results of the blood biochemical analysis and histological examination of the rats given the Ag₂S quantum dots for 2 months showed that Ag₂S quantum dots had no obvious toxicity.

Nanoparticle Alloys

In materials science, mixing various metal elements to form intermetallic compounds or alloys can greatly expand the properties of metals. Binary or ternary metal nanoparticles (or nanoalloys) can synthesize intermetallic compounds with controllable properties and structures on a nanoscale, which has attracted extensive attention from researchers (Ferrando et al., 2008). The main reason why alloy nanoparticles are fascinating is that the chemical and physical properties of alloy materials change with changes in composition, atom distribution, and particle size.

Researchers who have devoted themselves to in-depth studies of these metal nanoalloys have found that metal alloy materials not only have excellent catalytic properties, but also have excellent fluorescence properties. Further research shows that these fluorescent alloy nanoparticles inherit many advantages of the original metal nanoparticles, such as fluorescence properties, water solubility, and biocompatibility. They also can adjust the optical properties of the main metal nanoparticles or develop new functions through the introduction of another metal. For example, in 2013, Millstone's team (Andolina et al., 2013) introduced copper into fluorescent Au nanodots to form Au/Cu alloy nanodots. By adjusting the content of copper in the alloy nanodots, the fluorescence of Au/Cu alloy nanodots gradually shifted from NIR-I to NIR-II. Their group further introduced the Co element into fluorescent Au nanodots to prepare Au/Co alloy nanodots, which had both magnetic and near infrared fluorescence tunable functions (Marbella et al., 2014). Compared to the traditional near infrared quantum dots, the multi-functional alloy nanodots with near infrared fluorescence not only free of toxic elements, such as heavy metals, but also have many functions in the same material. These multi-functional alloy nanodots have wide prospects for application in bioimaging, especially in the field of multi-mode imaging.

Down-Conversion Rare Earth Nanoparticles

Recent research results have shown that rare earth nanomaterials have the ability of down-conversion luminescence, which is, when near-infrared light (980 nm) is used as excitation light to irradiate nanoparticles, its emission light is in the NIR-II spectrum range (Tan et al., 2009). The structure of these nano-materials is very similar to that of up-conversion nanoparticles. Nanocrystals such as lanthanide nanocrystals (NaYF₄) are used as primary materials, which doped with lanthanide

elements such as Ho³⁺, Tm³⁺, and Nd³⁺ (Naczynski et al., 2013; van Saders et al., 2013). Using the basic structure of rare earth nanocrystals, multi-shell complex core-shell rare earth nanoparticles have been developed. For example, in 2013, Moghe team reported on a core-shell structure nanoparticle of NaYF₄ which had been regenerated on the surface of existing NaYF₄ Yb:Ln nanocrystals (Naczynski et al., 2013). By changing the doped lanthanides (Er, Ho, Tm, Pr), NIR-II fluorescence with different wavelengths can be obtained under 800 nm excitation, and the longest wavelength can reach up to 1,500 nm. Compared with up-conversion rare earth nanoparticles, down-conversion nanoparticles have received less attention, but they are still widely applied *in vivo* bioimaging research (Naczynski et al., 2013, 2014; Jiang et al., 2016). Li et al. reported on a dual-function particle system using up-conversion and down-conversion (Li et al., 2013), where the particle can emit visible (800 nm) and near-infrared light (980 nm) according to the excitation light of different wavelengths and can be used in biological imaging.

In recent years, it has been found that Nd ion not only has NIR-II fluorescence emission with wavelength of 1,050 or 1,300 nm, but also has the sensitization effect on Ytterbium ion. It is excited at a biocompatibility wavelength below 800 nm, which has the lowest absorption of water. Nd³⁺ has been recognized gradually as a photosensitizer (Hemmer et al., 2016), and Nd³⁺ doped near infrared fluorescent nanoparticles have attracted great interest from researchers who study lanthanide-doped biological probes. One kind of Nd³⁺ doped near infrared fluorescent materials is an NaYF₄ type down-conversion lanthanide nanocrystal (Chen et al., 2012), and the other is an Nd³⁺ doped fluoride nanoparticle (Pokhrela et al., 2014). For example, in 2015, Garca's group synthesized Nd³⁺ doped SrF₂ nanoparticles and used them reduce background fluorescence (Villa et al., 2015), since minimizing any background fluorescence is essential for high contrast bioimaging. The excitation wavelength of the nanoparticles is 808 nm, and the emission wavelength is 1,100 nm, which belongs to NIR-II fluorescence. The nanoparticles are mixed into the feed and fed to mice. After the nanoparticles enter the mice through the digestive system, *in vivo* fluorescence imaging is performed. It was found that an NIR-II fluorescence of 1,300 nm generated by the ⁴F_{3/2}-⁴I_{13/2} orbital transition of Nd³⁺ effectively eliminated the background fluorescence. It can realize the NIR-II imaging of deeper structure, inorganic spontaneous fluorescence and high distinguishability *in vivo*. In addition, in 2016 Prasad's team prepared a hybrid organic-inorganic system to form an epitaxy of NaYF₄: Yb³⁺/X³⁺@NaYbF₄@NaYF₄:Nd³⁺ (X = null, Er, Ho, Tm or Pr) core/shell/shell (CSS) nanocrystals, and coated ICG on the external layer of CSS nanocrystals. This hybrid system can capture NIR light in a wide excitation spectrum range (700–860 nm) by ICG and produce effective polychromatic narrow-band NIR-II emission light from 1,000 to 1,600 nm according to the different doping elements in the nucleus. Further experiments show that the NIR-II emission fluorescence can be used to image clearly at a tissue depth of 9 mm and detect optical signal at a tissue depth of 23 mm (Shao et al., 2016).

Nanoparticles Based on Organic Fluorescent Dyes

Until now, organic fluorescent dyes are still the most widely used luminescent markers in fluorescence imaging. Organic fluorescent dyes have attracted much attention due to their high fluorescence quantum efficiency, easy functionalization, and adjustable luminescence spectra (Thekkekk and Richards-Kortum, 2008; Willmann et al., 2008; Kobayashi et al., 2010; Sinkeldam et al., 2010). The commonly used organic fluorescent dyes presently include naphthalimides, coumarins, fluoresceins, rhodamine, anthocyanins, BODIPY (Lu et al., 2014), porphyrin phthalocyanine, and other macrocyclic molecules. The absorption and emission wavelengths of these commonly used organic fluorescent dyes cover the ultraviolet, visible, and near infrared regions (Mishra et al., 2000; Lavis and Raines, 2008; Ma and Su, 2010).

Over the years, how to convert NIR-I fluorescent probes directly into NIR-II fluorescent probes by molecular engineering methods and design principles has been a highly discussed topic among investigators. According to the available literature (Yang et al., 2017; Zhu et al., 2018, 2019; Wu et al., 2019), the specific design principles are as follows: (1) The typical structure of NIR-II small molecule fluorescent dyes is a molecular structure composed of donor-acceptor-donor (D-A-D) (e.g., CH1055-PEG), which is modified to form a class of dyes with similar properties and emission wavelengths. The specific emission principle uses aromatic π -bridge connectors as molecular wiring. These electron-supplying groups can produce enhanced electron shifts and low energy gaps to the central electron acceptor, resulting with the dye molecule having the capability of NIR-II emission. (2) By systematically adjusting the electronic donor part, the π -bridge connector and the functional groups at the end of the fluorescent dye molecule promote quantum yield. Specific strategies to improve the brightness of small molecular dyes include enhancing intramolecular charge transfer and molecular stiffness, creating complexes with serum proteins, such as human serum albumin (HSA), and introducing a protecting group (S) to produce a S-D-A-D-S structure at the end of the dye, which protects the dye's pillars from intermolecular interactions and fluorescence quenching polymerization. (3) By increasing the conjugate length to separate electron donor/acceptor and heteroatom substitution, the fluorescence emission of existing polymethine dyes (i.e., cyanine dye) can be re-shifted to produce a new fluorescent dye that can emit NIR-II fluorescence with high quantum yield and absorption coefficient (ϵ) (Figure 2). At present, polymethine molecular dyes with emission wavelength more than 1,000 nm are available on the market, including IR-1040, IR-1048, IR-1051, and IR-1061. Unlike the previous method of for red-shifting anthocyanin dyes by simply increasing the length of polymethine chain, by Cosco et al. (2017) propose of a new method of extending heterocyclic conjugation and adding new electron donor groups. This new method has been proven as a feasible method for red-shifting anthocyanin dyes. In addition, most of the NIR-II small molecule fluorescent dyes mentioned

above are organic products with low water solubility, which need to be encapsulated in a hydrophilic matrix to enhance biocompatibility *in vivo* imaging. Recently, Li et al. (2018) developed a novel small molecule fluorescent dye FD-1080 through a structural redesign of a typical anthocyanin dye. Its excitation and emission wavelength are both in the range of NIR-II. Besides there are reports about indocyanine green (ICG). ICG is a NIR fluorescent dye with strong absorption, low toxicity, no involvement in biological transformation *in vivo* and rapid excretion. It is the only NIR optical imaging contrast agent approved by the US Food and Drug Administration (FDA) for clinical use. Because the absorption and fluorescence spectra of ICG are in the NIR-I window (650–950 nm), ICG has been widely used in cardiovascular system, liver function evaluation, visualization of retina and choroid, ophthalmic angiography, cerebral angiography, and other clinical fields. Recently Starosolski et al. (2017) found that ICG dye also has NIR-II fluorescence characteristics in the NIR-II window. This discovery has opened up new uses of ICG and will greatly expand the application scope of ICG. In the experiment, the absorbance and NIR-II fluorescence emission of ICG were detected in different concentrations of ICG media, including PBS, plasma and ethanol. The customized spectral NIR module is used for *in vitro* and *in vivo* tests, and the images of NIR-I and NIR-II windows are obtained at the same time. The results show that ICG has a significant fluorescence emission in the NIR-II window at the wavelength of about 1,100 nm, and this emission (similar to the absorption curve) is essentially affected by the molecular environment of ICG. The results of *in vivo* imaging further illustrated that ICG can be used as NIR-II fluorescent dye and the contrast-to-noise ratios (CNR) value was twice that in NIR-I window. Clinical transformation of NIR-II imaging technology can be accelerated when ICG, an FDA approved imaging agent, is used. Later, the research team published another paper on NIR-II fluorescence imaging using indocyanine green nanoparticles (Bhavane et al., 2018). In this study, they collected the fluorescence spectra of ICG liposomes in PBS and plasma. *In vivo* imaging research was carried out to observe the vascular structure of the hind limbs and the intracranial region in real time. Free ICG, NIR-I imaging and cross-sectional imaging (MRI and CT) were used as controls. The results showed that the liposome ICG had strong NIR-II fluorescence, similar to the free ICG in plasma. *In vitro* studies have shown that liposome ICG has better performance than free ICG in the NIR-II imaging of deep (≥ 4 mm) vascular analog structure. *In vivo*, NIR-II fluorescence imaging with liposome ICG can significantly improve the contrast ($P < 0.05$) compared with long-term free ICG, and make the hind limbs and intracranial vessels visualized within 4 h after injection. Compared with NIR-I imaging, liposome ICG enhanced NIR-II imaging has better vascular clarity. Subsequently, several research papers on tumor imaging using Second-Window-ICG (SWIG) technique were published, and this field has become the latest research hotspot of NIR-II imaging (Zeh et al., 2017; Cho et al., 2019a,b; Suo et al., 2019; Wang et al., 2019b).

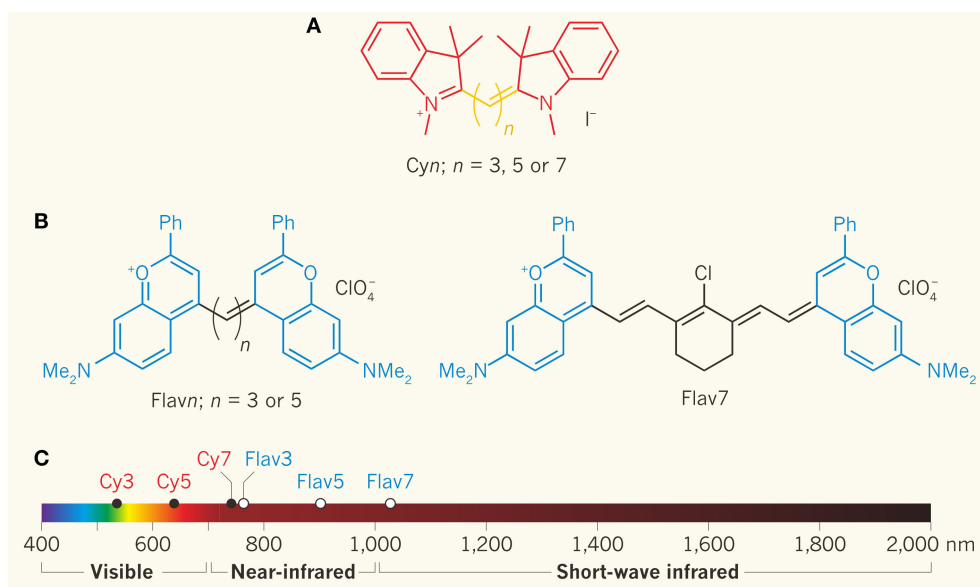


FIGURE 2 | Increasing the length of polymethine chain was proved to result in the red shift of cyanine dye's emission. Cosco et al. developed new methods of heterocyclic conjugation and added new electron donor groups (Cosco et al., 2017; Zhu et al., 2018). **(A)** Molecular structure of cyanine dye series of compounds for optical fluorescence imaging. **(B)** The blue structure is the compound of dimethyl-flavium heterocycles, which can be used to replace the indolenines to prepare flavium polymethine fluorophores. **(C)** The emission and absorption of Flav7, the modified organic small molecule fluorescent dye, was in the NIR-II window. Adapted from Cosco et al. (2017) and Schnermann (2017) with permission.

APPLICATIONS OF NIR-II WINDOW BIOIMAGING IN BIOMEDICINE

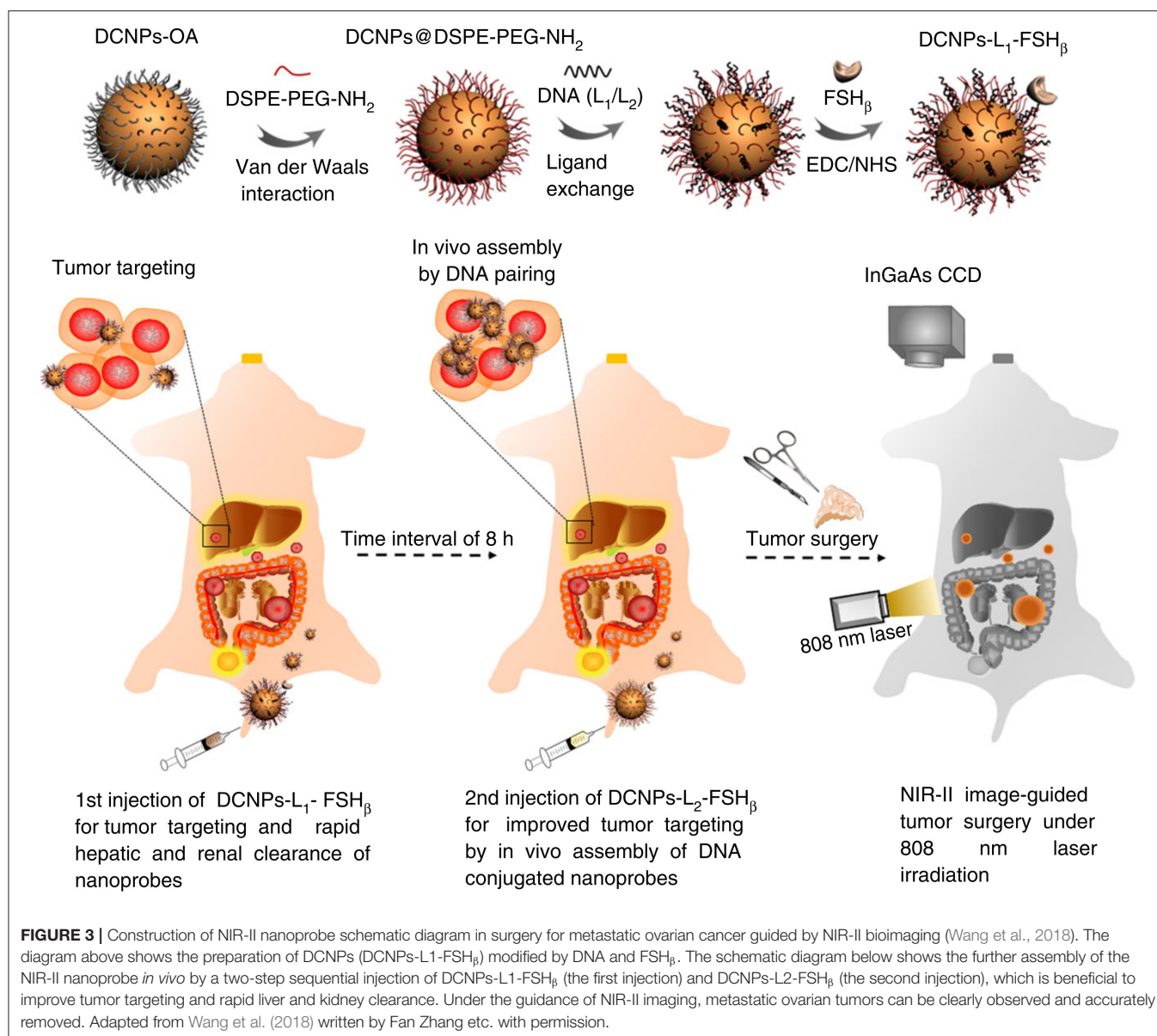
Tumor Imaging and Image-Guided Surgery

Solid tumor patients often fail in treatment due to local recurrence. Cytopenic surgery is targeted to improve staging and reduce tumors using fluorescence imaging to guide the specific resection of tumors and significantly improve the prognosis. Recently, this application field has become a high-interest topic in research, resulting in the publishing of many high-level papers.

Papers published by Wang et al. (2018) in Nature Communications, for example, report on a novel down conversion nanoparticle emitted in the NIR-II window for living assembly. In metastatic ovarian cancer, fluorescent nanoprobes modified with DNA and targeted polypeptides are used to ensure the precision of cytoreduction surgery. The image distinguishability of NIR-II nanoparticles is better than that of clinically recognized ICG, mainly due to its better light resistance and deeper tissue penetration (8 mm). After the nanoprobe is assembled *in vivo*, the stable preservation time of the nanoprobe on tumors is up to 6 h, so the nanoprobe can be used in precise tumor resection surgeries. The probe successfully obtained a superior ratio of tumors to normal tissues, which can help to delineate the resection profile in the surgery for metastatic abdominal ovarian cancer. The results also showed that metastases <1 mm could be completely removed under the guidance of NIR-II bioimaging. This novel method provides a new idea

for the design of nanomaterials for medical applications in the future.

The key to the implementation of above-mentioned study is the *in vivo* assembly of novel NIR-II fluorescent nanoparticles, which is also the ingenuity of this research design. The specific assembly principle is shown in Figure 3. At the top of Figure 3 is a schematic of the step-by-step construction of DNA and FSH β modified down-conversion nanoparticles (DCNPs-L₁-FSH β). The core of the nanoprobe are lanthanide doped core-shell nanoparticles, consisting of a 5.0 nm luminescent gadolinium tetrafluoride sodium doped 5% neodymium (NaGdF₄:5% Nd) encapsulated by a 2.5 nm thick homogeneous gadolinium sodium inert shell. This type of a structure can avoid fluorescence quenching by water and bind complementary DNA (L₁ or L₂) on its surface. FSH β is a follicle stimulating hormone peptide that specifically binds to ovarian cancer epithelium to enhance the targeting efficiency of the fluorescent nanoprobe. Because of the great potential of DNA complementary strand hybridization, the nanoprobe can be stable hybridized on the surface of tumors *in vivo* for bioimaging. Next, a process diagram of the fluorescent nanoprobe assembly *in vivo* is presented in the lower part of Figure 3. It greatly enhances the tumor targeting of the probe, but also enables the probe to be excluded from the body by the liver and kidney more quickly after the operation. The specific process is to implement two-step injection of DCNPs-L₁-FSH β and DCNPs-L₂-FSH β , in succession. In order to verify the performance of two-step *in vivo* simultaneous assembly of fluorescent nanoprobes, the fluorescent dye Cy5 was grafted into the probe assembly structure of the first needle, i.e.,



DCNPs-L₁-(Cy5)-FSH_β, and Cy7 were combined to the probe assembly structure of the second needle, i.e., DCNPs-L₂-(Cy7)-FSH_β. When the complementary DNA fragments L1 and L2 in the two components of the probe are hybridized close to each other, the two dyes will cause fluorescence resonance transfer (FRET), which is more than twice as strong as two dyes without FRET. The results show that the two components of the probe can be specifically assembled on the surface of tumors *in vivo*. Ultimately, surgery guided by NIR-II imaging can clearly observe metastatic ovarian cancer and precisely resection it.

Other recent representative work includes the development of Ag₂Te quantum dots by Zhang et al. (2019), which can emit fluorescence at 1,300 nm wavelength after assembly. The assembly process is divided into two steps; first, polymerization is conducted with polylactic-co-glycolic acid (PLGA), and

second, further packaging is completed with the cancer cell membrane. The fabricated biomimetic nano-biological probes have a bright and highly stable fluorescence in the NIR-II window. Through the second step of surface encapsulation of active homologous tumor membranes, the probe enhances the ability to target tumors. Tumor targeting occurs through the passive enhancement of permeability and retention of homologous cancer cell membranes, which can increase the accumulation of probes in the tumor sites. Zhang et al. successfully prepared a novel biomimetic NIR-II fluorescence nanoprobe which showed characteristics of ultra-bright, stable fluorescence, homologous targeting and high biocompatibility, which can significantly enhance the imaging of living tumors. In 2018, Yang et al. (2018) reported on a NIR-II lanthanide complex (Nd-DOTA) probe that can be rapidly excreted. Within

3 h after injection, more than 50% of the probe can be excreted through the kidney. The molecular weight of the probe is only 0.54 kDa, and in terms of light resistance and tissue penetration, the NIR-II imaging quality of the new probe is much better than that of the clinically approved ICG. Yang et al. also demonstrated the ability to obtain an excellent tumor-to-normal tissue ratio, which can help to accurately mark the profile of micro-tumors in surgery for abdominal metastatic ovarian cancer. Metastatic tumors <1 mm can be completely removed under the guidance of NIR-II bioimaging. In addition, the probe Nd-DOTA has the same structure as Gd-DOTA, and Gd-DOTA is a clinically recognized MRI contrast agent. Therefore, it may be a straightforward path for the clinical transformation of the new NIR-II probe. In 2018, Shou et al. (2018) prepared a semiconductor polymer nanoparticle of diketopyrrolopyrrole (PDFT1032) and developed it as a NIR-II (near infrared window 1,000–1,700 nm) fluorescent probe for *in vivo* tumor imaging and image-guided tumor re-sectioning. The NIR-II probe has many advantages, including stable fluorescence emission, high absorption efficiency at 809 nm, large Stokes shifting, biocompatibility, and lower toxicity *in vivo*. Moreover, research has shown this NIR-II probe has a wide range of applications in the biomedical field. For example, tumor imaging in terms of subcutaneous osteosarcoma patterns, evaluating vascular embolization treatment on tumors, *in-situ* cytotoreduction surgery guided by NIR-II images, and sentinel lymph node biopsy with superior temporal-spatial resolution (SLNB). In general, PDFT1032 not only has good biocompatibility and hydrophilicity, but also excellent chemical and optical properties. The NIR-II fluorescent probe has a wide application prospect in the imaging of malignant tumors and cytotoreduction surgery.

Medical Testing

Fluorescence bioimaging can detect deep tissues in the NIR-II window, and it has the smallest self-fluorescence and tissue scattering. Nevertheless, *in vivo* NIR-II fluorophores detection is merely concentrated on direct disease lesions or living organ imaging, and producing real-time dynamic NIR-II fluorescence biosensor has been challenging. In recent years, new methods and breakthroughs have been emerging in this field, such as the conception and progress of quantitative detection with fluorescent probe of ratio meter.

In Fan Zhang's paper (Liu et al., 2018) published in *Angewandte Chemie International Edition* in 2018, he reports a novel Erbium-sensitized up-conversion of nanoparticles, which have the characteristics of both 1,530 nm excitation and 1,180 nm emission in the NIR-II window, which can be used *in vivo* biosensors. This research studies a micro-manipulation needle debris sensor for *in vivo* inspection of inflammation in real time, where the detection principle of the sensor is based on the ratio meter fluorescence combined with efficient NIR-II fluorescent emission and the organic probe sensitive to hydrogen peroxide under the action of Fenton catalyst Fe^{2+} . Finally, the dynamic detection of inflammation *in vivo* is successfully produced. This NIR-II radiometric probe has the following advantages: large anti-Stokes displacement, low background fluorescence, low absorption, and scattering in biological tissues. Therefore,

the probe can detect and evaluate inflammation *in vivo* in real time with high imaging quality. The specific process of *in vivo* inspection of inflammation in real time by the fluorescence sensor of the ratio meter is shown in **Figure 4**, including the device diagram of fluorescence probe used for confirmatory testing *in vivo*, the fluorescence value of the ratio meter (I_{980}/I_{1180}) channel at different times, the quantitative curve of ratiometer fluorescence (I_{980}/I_{1180}), and the corresponding concentration of hydrogen dioxide at different times.

Figure 4A is the device diagram of the ratiometer fluorescent probe used for confirmatory testing *in vivo*, and **Figure 4B** is a photograph of a mouse treated with fragments of a micromanipulator needle. **Figures 4C–E** show the 980, 1,180, and ratio gauge (I_{980}/I_{1180}) channels, respectively. The micromanipulator needle fragments obtained fluorescence values at different times after LPS-induced inflammation. **Figure 4F** is a quantitative curve of the ratio meter fluorescence (I_{980}/I_{1180}) of the micromanipulation needle fragments and the corresponding concentration of hydrogen peroxide at different times. It can be used to quantify the degree of actual inflammation in clinical tests.

Other recent studies in this field include Zhao et al. (2019) which reported on an original method for the accurate imaging of inflammation *in vivo* using *in situ* cross bonding of glutathione-combined ultrafine lanthanum nanoparticles with NIR-II fluorescent emission. Although nanoprobe have been proven to be promising bioimaging platforms by reason of their EPR effects, to the inability to enrich nanoprobe at target position has been a key bottleneck to improve detection ability and effect. While cross bonding of nanoparticles *in vivo* can increase the enrichment of EPR region (e.g., inflammatory areas), nanoparticles are absorbed by RES, resulting in unidirectional cross bonding in non-target organs. Based on these difficulties, the principle of this strategy was developed to enhance the *in vivo* imaging by using sub-10 nanometer glutathione (GSH) combined lanthanide nanoparticles, which react with reactive oxygen species (ROS) in the inflammation region to locate and image reactive oxygen species rapidly in the NIR-II window. At the same time, these nanoprobe can be excreted quickly because of their ultrafine magnitude. Based on the *in-situ* crosslinking and rapid excretion ability of the probe, this method can achieve accurate biological imaging and is suitable for other ultrafine contrast agents.

In 2019, Wang et al. (2019a) developed a reverse quenched NIR-II molecular fluorophore and applied it to high contrast imaging and pH sensing *in vivo*. Currently, the molecular fluorophore with contrast and sensitivity in NIR-II window (1,000–1,700 nm) have both been developed *in vivo* fluorescence imaging. However, the solvation of long-wavelength absorbed fluorophore in aqueous solution, results in quenching, which is challenging to avoid. Therefore, a series of reverse-quenched pentamethine cyanine fluorophore have been developed, which significantly overcome the serious solvation coloration, thus providing a stable absorption/emission of fluorescence over 1,000 nm in aqueous solution. The fluorescence intensity increases up to ~44 times and has excellent photostability. The conditions for lymphatic imaging can be met thanks to these

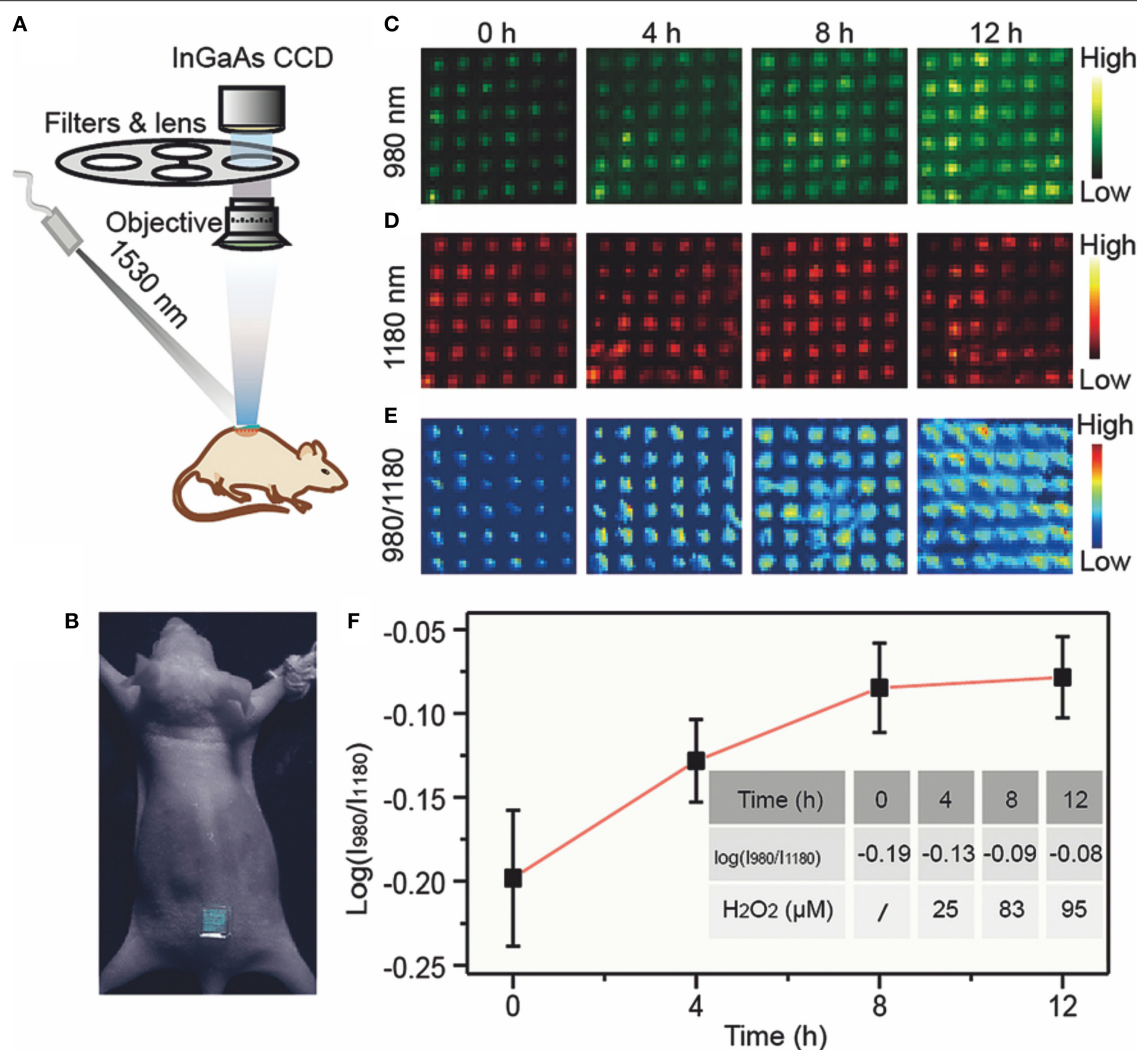


FIGURE 4 | Operational diagram of ratiometer fluorescence sensor (Liu et al., 2018). **(A)** *In vivo* bioimaging experimental apparatus. **(B)** Pictures of mice treated with microneedle patches. After lipopolysaccharide was used to induce inflammation in mice, the upconversion luminescent images of microneedle patch at 980 nm **(C)**, 1,180 nm **(D)**, and ratio (I_{980}/I_{1180}) **(E)** channels were detected at different times. **(F)** Ratiometric fluorescence (I_{980}/I_{1180}) of microneedle patches at different time and corresponding H_2O_2 concentration. Adapted from Liu et al. (2018) written by Fan Zhang etc. with permission.

advantages, including the need for tissue penetration up to 8 mm, high definition, and optical stability. Its imaging effect is better than the clinically approved indocyanine green. In addition, the fluorophore display pH-responsive fluorescence allows for non-invasive ratio meter fluorescence imaging and gastric pH quantification *in vivo*. The results show that this method is consistently accurate when tissue depth is 4 mm compared to the standard pH electrode method. This work opens up the potential of reverse quenching pentamethylene cyanine in NIR-II biological applications.

In 2019, Li et al. (2019c) developed a NIR-II fluorescence molecular probe activated by peroxynitrate for drug-induced hepatotoxicity detection. Drug-generated liver injury is a key problem to the safety of drug research and use. The emergence of peroxynitrite ($ONOO^-$) is considered to be an initial

signal of drug-generated liver injury. Therefore, the structure of the fluorescent probe is designed as the combination of benzothienopyrrole cyanine skeleton and phenyl borate group. The NIR-II fluorescence of this probe can be activated by $ONOO^-$ and can detect $ONOO^-$ sensitively. When the probe IRBTP-B and the target $ONOO^-$ exist at the same time, the structure of probe changes to produce the fluorescent group IRBTP-O to turn on the NIR-II fluorescence. The linear relationship between the NIR-II fluorescence intensity and the concentration of $ONOO^-$ is acceptable. Tissue model studies confirm that reliable activation signals can be obtained at penetration depths up to 5 mm. With this probe, the up-regulation of $ONOO^-$ in the model of incubation period drug-generated hepatotoxicity and the repair effect of N-acetylcysteine (NAC) *in vivo* could be seen. In conclusion, this method will

be used as a general method to develop activated NIR-II probes triggered by specific analytes based on hydroxyl functionalization reaction sites.

Vascular Biological Imaging

The number of people with cardiovascular and cerebrovascular diseases has increased, as has the ability to detect these diseases using examination technology, which, in turn, has led to an increase in incidence of cardiovascular and cerebrovascular diseases. The commonly used techniques in clinical angiography include B-mode ultrasonography, CT scans, and nuclear magnetic resonance (NMR). However, these techniques are non-tumor-specific, have low-sensitivity and high-cost, and can't be used for real-time detection or clinical practice in surgical operations. In recent years, some research groups have designed NIR-II fluorescence probes and injected them into mice intravenously, after which the NIR-II fluorescence is used to perform vascular imaging *in vivo*. The results showed that the NIR-II fluorescence could penetrate the skull of mice to a deeper level, not only imaging the distribution of blood vessels in the heads of mice, but also clearly showing the fine structure of capillaries.

In 2018, Li et al. (2018) published papers within this field of study in the *Angewandte Chemie*, regarding the successful synthetization of a small molecule fluorescent probe FD-1080, which has excitation and emission both in the NIR-II region and it has excellent bioimaging capability of the vascular system *in vivo*. The structure of heptamethine in fluorescent probe FD-1080 has been ingeniously designed as a key group for the conversion of absorption and emission into the NIR-II region. An acidic sulfuric acid group and cyclohexene group were applied to intensify the water dissolvability and chemical durability of the probe. The quantum yield of FD-1080 was 0.31% and improved to 5.94% when combined with bovine fetal serum (FBS). It is noteworthy that compared with the excitation wavelength from 650 to 980 nm in NIR-I region in the previous work, the excitation wavelength at 1,064 nm in NIR-II region has proved to have stronger penetration in biological media and excellent imaging quality. FD-1080 can not only achieve non-invasive, high-resolution, in-depth tissue bioimaging of the vascular and cerebrovascular systems, but it also quantifies respiratory frequencies of awake and anesthetized mice according to dynamic images of respiratory craniocaudal motion within the liver. The key steps in this study included the schematic diagram of the vascular imaging device, the fluorescence imaging of the rat cerebral vascular system with the NIR-II fluorescence probe FD-1080, and the breathing rate detection graph of the rat, as shown in **Figure 5**.

Figure 5A is a device diagram of NIR-II fluorescence penetrating the scalp and skull brain tissue for an angiography. **Figure 5B** is the disappearance spectra of the scalp (black) and skull (red). It has been found that the strongest penetration is at 1,064 nm. **Figure 5C** contrasts the fluorescence images of FD-1080-FBS complex in a rat brain vasculature system under different excitation lengths (1,300 nm long pass filter), where it was found that the clearest angiogram was at the wavelength of 1,064 nm in NIR-II region. In **Figure 5D**, a red line of interest

is marked at the Gaussian fitting fluorescence intensity profile at the 808 and 1,064 nm excitation wavelengths, respectively. It is obvious that at 1,064 nm the fluorescence intensity is higher and the peak is narrower. When stimulated at 1,064 nm (1,300 nm long pass filter), the clear emission of the FD-1080-FBS complex enables the imaging of an alert or anesthetized mouse to detect the signal fluctuations produced by liver movement (**Figure 5E**). **Figure 5F** is a spectrogram of the breathing rate of alert (above) and anesthetized (below) anesthetized mice. The graph shows that there are obvious differences in the spectrogram of breathing rate between the two groups of mice, which can be used to quantify the respiratory rate of mice under different conditions.

Other studies have also been recently conducted in this field, including Li et al. (2019a) in 2019, who developed a rare earth nanoprobe triggered by 808 nm laser, which emitted NIR-II fluorescence for small tumor detection and angiography. In this study, polyacrylic acid (PAA) modified sodium tetrafluorolutetium: gadolinium/neodymium nanorods (PAA-NRs) were prepared into single crystal hexagonal phase and unified magnitude, and then further developed as a highly sensitive NIR-II imaging probe for optical imaging navigated detection of tiny tumors, angiogenesis-related diseases, and angiogenesis diagnosis. The NIR-II emission wavelength with sodium tetrafluorolutetium: gadolinium as the main body can be easily adjusted by changing neodymium doping, which makes it hopeful that the emission center will have high optical stability at 1,056 and 1,328 nm. The probe has a high spatial resolution ($\sim 105 \mu\text{m}$) for small blood vessels *in vivo* and can detect them clearly. The *in vivo* tracking experiments with time changes confirmed that PAA-NRs probe was mostly collected in the RES, and discharged from the body by the liver. Histological examination revealed that the hydrophilic nanorods had very low toxicity and great biological compatibility in living animals.

In the same year, Li et al. (2019b) reported a polydopamine-coated multifunctional lanthanide diagnostic agent, which can be used for angiography of vascular malformations and tumors, as well as photothermal therapy guided by imaging at wavelengths above 1,500 nm. NIR-II optical imaging with emission wavelengths $> 1,500 \text{ nm}$ can be used as the next generation fluorescence imaging technology to guide the display technology of tumor vessels and vascular malformations, which can then be used for early tumor diagnosis and recognition of tumor-related vascular characteristics. This study is based on the core-shell structure of NaLuF_4 nanorods@polydopamine (NRs@PDA), which combines advanced NIR-II fluorescence imaging ultra 1,500 nm wavelength and photothermal (PTT) functions. This is a high-performance integrated nano-platform for diagnosis and treatment developed for visualization of tumor-related vascular malformations and imaging-guided photothermal therapy.

In 2018, Wan et al. (2018) developed a bright organic NIR-II fluorescent nanocluster (p-FE) for three-dimensional imaging of biological tissues, which can provide bright NIR-II fluorescent emission light with a wavelength $> 1,100 \text{ nm}$ for non-invasive *in vivo* blood flow tracking in the rat cerebrovascular system. Moreover, p-FE can produce a layer-by-layer image of the

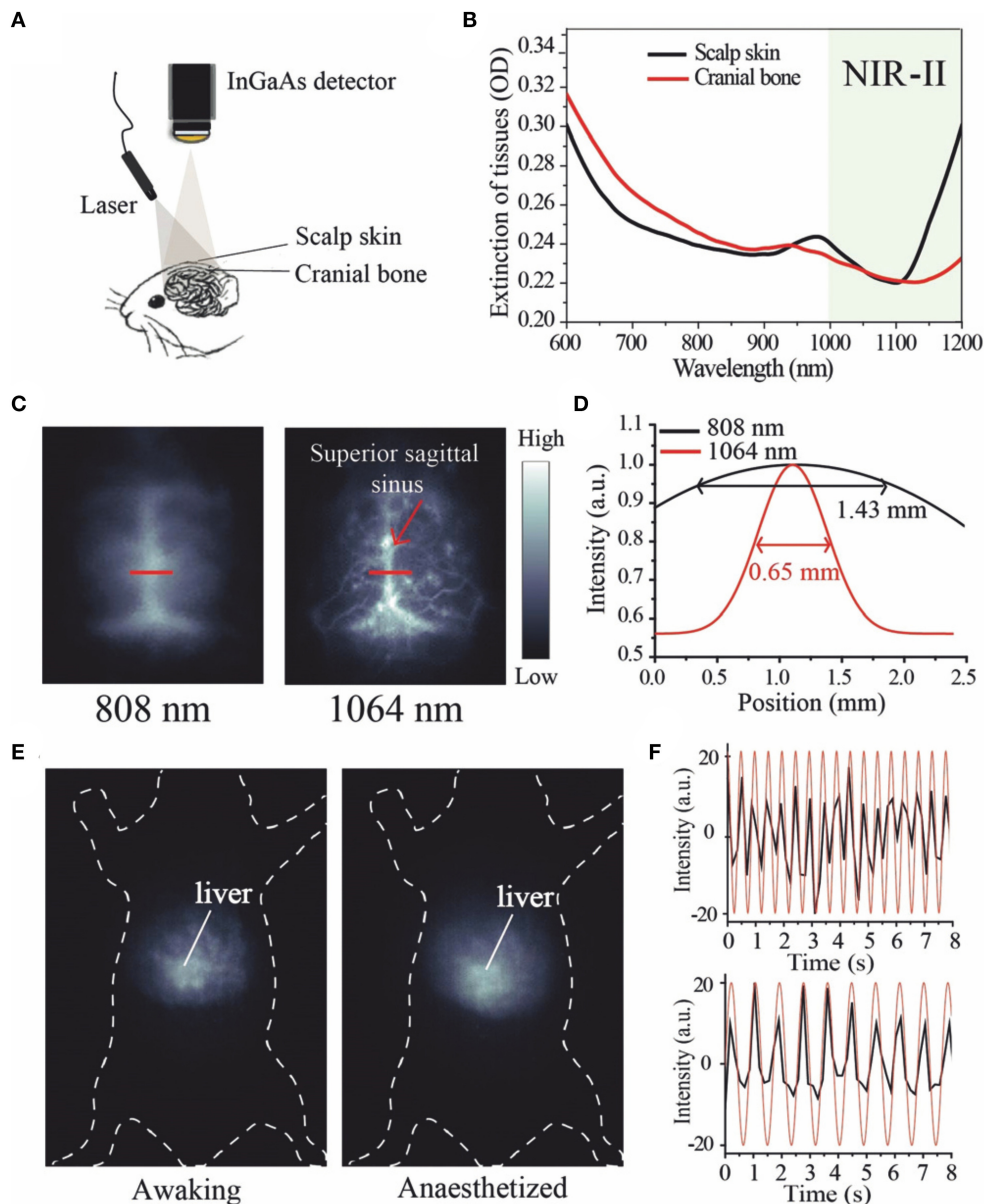


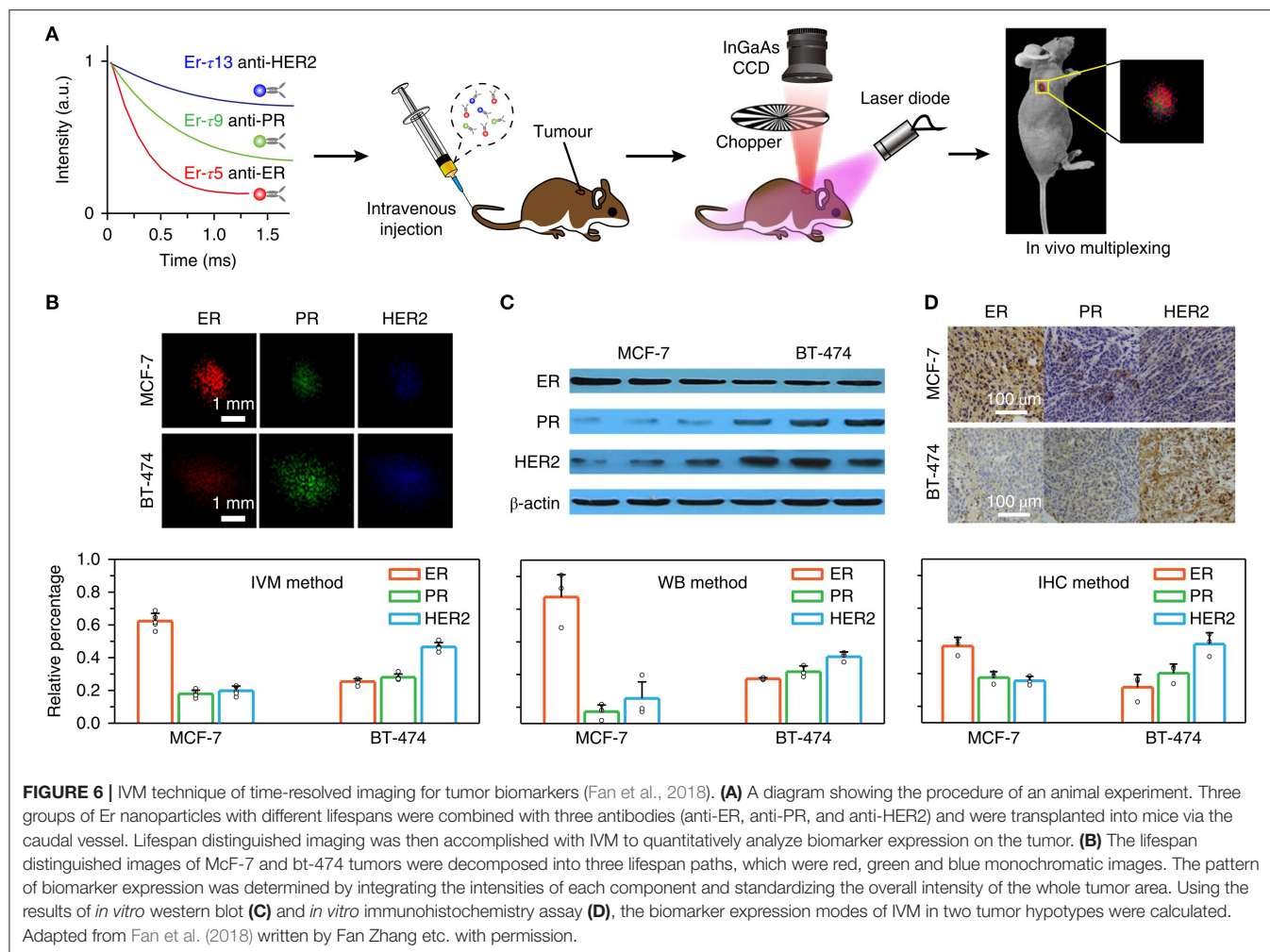
FIGURE 5 | Fluorescence imaging of rat brain vascular system and breathing rate of mice using NIR-II fluorescence probe FD-1080 (Li et al., 2018). **(A)** Schematic diagram of NIR-II optical imaging through brain tissue scalp and cranial bone. **(B)** Extinction spectra of scalp skin and skull. The black curve represents the scalp skin and the red curve represents the skull. **(C)** Fluorescence images of FD-1080-FBS complex were compared under different excitation conditions as indicated. **(D)** The fluorescence intensity profile fitted by gaussian was distributed on a red line of interest, with excitation wavelengths of 808 and 1,064 nm, respectively. **(E)** The distinct emission of the FD-1080-FBS complex made the awake and anesthetized mice imaged, and under the excitation of 1,064 nm detected the signal fluctuations generated by the liver movement. **(F)** Respiratory rates in awake (upper) and anesthetized (lower) mice. Adapted from Li et al. (2018) written by Fan Zhang etc. with permission.

vascular system based on single-photon and three-dimensional confocal imaging in a fixed rats brain tissue. Its depth is up to 1.3 mm, and it has a spatial resolution of up to 10 microns. The study also completed *in vivo* dual-color fluorescence imaging in the NIR-II window, using p-FE emitted between 1,100 and 1,300 nm as a vascular imaging reagent, as well as single-walled carbon nanotubes (CNTs), which emitted more than 1,500 nm as a contrast agent to highlight tumors in mice. Ultimately, the

results demonstrated excellent dual imaging of vascular system and tumors.

Diagnosis and Treatment of Cancer

Each imaging technology has its own unique advantages and inherent limitations. For example, fluorescence imaging has excellent sensitivity, but low tissue penetration and spatial resolution in turbid media. MRIs, CT scans, and ultrasound



imaging have better spatial resolution, but their sensitivity is limited. The sensitivity of PET-CT scan is relatively high, but it can't provide the structural information of the imaging material. Therefore, multi-mode imaging, which integrates two or more imaging technologies, can supplement the imaging information and diagnose diseases with reliable accuracy. In order to meet the needs of multi-mode imaging, researchers usually combine fluorescent nanomaterials with functionalized small molecules or particles by doping, bonding and coating to make them multi-functional nanoparticles, which can be used in multi-mode biological imaging.

Deep tissue imaging within the NIR-II window has great prospects in physiological research and biomedical applications. However, the inhomogeneous signal attenuation in biological material limits the application of multi-wavelength NIR-II probes in the imaging of various biomarkers and cancer diagnoses. For example, Fan et al. reported in 2018 (Fan et al., 2018), that NIR-II nanoparticles doped with lanthanides have the ability to design the luminescence time for quantitative imaging *in vivo* after using multiplexing in the time domain. To achieve this, a systematic research method based on controllable energy transfer

was designed to create an adjustable lifetime range of nanoprobe, which had a luminescence time spanning three orders of magnitude and had only one emission band. When the depth of the NIR-II nanoparticle probe in biological tissue reached 8 mm, the selected nanoparticle duration was continuously resolved, and the SNR was taken from the time node when light intensity was <1.5 . Powerful time-length editors have been shown to be independent of tissue penetration depth, and *in vivo* multiplexing technology (IVM) has been used to diagnose tumor hypotype in living animals. The data in this paper are in good agreement with those of a standard *ex vivo* immunohistochemistry assay, which proves that the luminescent time-length imaging can serve as a microinvasive method for tumor definite diagnosis. The research process and key points of IVM for tumor biomarkers using specific luminescence time-length imaging are shown in **Figure 6**.

Figure 6A illustrates the schematic diagram of conducted animal experiments. Three batches of Erbium nanoparticles were bound to three different kinds of antibodies (anti-ER, anti-PR, anti-HER2) and were transplanted into mice via the caudal vessel and resulted showed that each had a different luminescence

duration. Then, time-resolved images using *in vivo* multiple techniques were used to quantitatively analyze the expression of biomarkers in the tumors. *In vivo* multiple technology devices include CCD and charge coupling devices. **Figure 6B** shows the time-processing image, which decomposes MCF-7 and BT-474 tumors into three time-long paths, indicated by the red, green, and blue monochrome image collections. The expression of biomarkers was determined by integrating the intensity of each component and normalizing the total intensity to synthesize all tumor regions. **Figures 6C,D** are the results of *in vitro* protein imprinting; **Figure 6C** shows the result of immunohistochemical experiment of indirect *in vitro* therapy, While **Figure 6D** shows the result of determined biomarker expression modes of the two tumor hypotypes by using IVM.

At present, this field has become a vital resource for biomedical diagnosis and treatment, and many research groups are competing to continue pushing forward in expanding its study. Several high-level research papers and reviews have been reported recently, such as Guo et al. (2019), who used NIR-II fluorescence and photoacoustic imaging to study the precise identification of the vascular system and micro-tumors in 2019. It is well-known that the diagnosis of cerebrovascular structure with complete blood-brain barrier and microtumors is of great significance for the timely treatment of patients with nervous system diseases. The combined diagnosis and treatment of NIR-II fluorescence and photoacoustic imaging (PAI) is anticipated to provide improving performance, for instance, excellent spatial and temporal distinguishability, large penetration depth and great SNR, and accurate brain diagnosis. In this study, conjugated polymer nanoparticles (CP NPs) with biocompatibility and photostability were prepared, and bimodal brain imaging was achieved using its NIR-II window. The nanoparticles with a uniform size of 50 nm can be prepared by microfluidic device. The emission peak was at 1,156 nm and had strong absorption of $35.2 \text{ Lg}^{-1} \text{ cm}^{-1}$ is at 1,000 nm. NIR-II fluorescence imaging provides a solution to the depth and resolution issues previously experienced with the hemodynamic and cerebral vascular systems, providing an imaging depth of 600 microns and a spatial resolution of 23 microns. After an ultrasound-induced opening of the blood-brain barrier, NIR-II PAI could successfully perform non-invasive imaging of deep micro-brain tumors (2.4 mm below dense skull and scalp <2 mm) with a SNR of 7.2. This study showed that CP-NPs is a promising brain diagnostic contrast agent.

In 2019, Fan et al. (2019) published an overview of optical multiplex techniques for biological detection to improve biomedical diagnosis, arguing that traditional methods according to the detection of single disease markers may not be precise enough, since disease progression usually involves a variety of chemicals and biomolecules. Multi-target simultaneous analysis is of great importance in basic biomedical research and clinical application, promoting simultaneous multi-target analysis that requires the development of a high-throughput multi-target biological analysis technology. In order to improve the level of biomedical diagnosis, this paper reviewed the research progress of optical multiplexing analysis technology used in biomedical diagnosis over the recent years. The review primarily focused

on the Fluorescence and Surface Enhanced Raman Scattering (SERS) technique which has unique optical characteristics as a main signal reader. The paper also focused on the review of the multiplexing strategy in biomedical field and the recent advances in biosensors from multi-analyte and multi-color cell tracking to multi-channel bioimaging *in vivo*. Finally, the paper provided forecasting of future challenges and opportunities of multi-bio-analysis.

In 2018, He et al. (2018) proposed that the structural design and synthesis of fluorophores emitted in NIR-II biological window are moving toward multi-mode imaging, as well as toward multimodal diagnosis and treatment. He et al. reviewed some progress of NIR-II fluorophores and molecular probes and considered the synthesis of NIR-II fluorescent group fit for multimode imaging will become a new way to obtain high-resolution images through the structural design. NIR-II fluorophores can convert NIR-II photons into heat required for photothermal therapy and can also be stimulated by NIR-II light to generate singlet oxygen for photodynamic therapy. The single probe has both diagnostic and therapeutic functions which can be used for precise treatment. He et al. details the latest development in structural design and synthesis of various NIR-II fluorophores and provides a discussion on the similarities and differences in known NIR-II imaging systems and the recent research on NIR-II imaging in biomedical applications.

Tracking the Transplanted Stem Cells

Stem cell (SC) is one type of pluripotent cells with self-replication ability, which can differentiate into a variety of functional cells under certain conditions. SC therapy is showing the hope of curing major human diseases. In the process of SC therapy, how to observe the transplanted SCs non-invasively in real time has become a challenge in experimental and clinical research. NIR imaging based on exogenous markers has always been one of the best methods to trace stem cells *in vivo*.

In recent years, NIR fluorescent probes, with their strong biological penetration ability, low photon detection domain value, high detection sensitivity, relatively simple operation, and advantages of real-time imaging during surgery, have made the shift of emission from NIR-I window to NIR-II window to track transplanted stem cells. For instance, Chen et al. (2018b) has reviewed the research progress of tracking transplanted SCs with NIR fluorescence NPs. The latest development of NIR-II window fluorescence imaging technology was introduced. The emergence of new fluorescent functional NPs (QDs, RE-doped NPs, organic fluorescent NPs, etc.) makes stem cells easy to be labeled and tracked, greatly promoting the further development of stem cell therapy. NIR-II fluorescence emission is absorbed little by tissues, and the scattering and spontaneous fluorescence in NIR-II region are the least in tissues. Therefore, the signal-to-background ratio can be greatly improved, yielding to a large tissue penetration depths and a good spatial-temporal resolution. Moreover, NIR-II fluorescence imaging technology for accurate optical tracking can improve our comprehending of the fate and regeneration ability of transplanted SCs and provide immense potential development of SC-based regenerative medicine. Up to now, only a few research labs are exploring the feasibility of

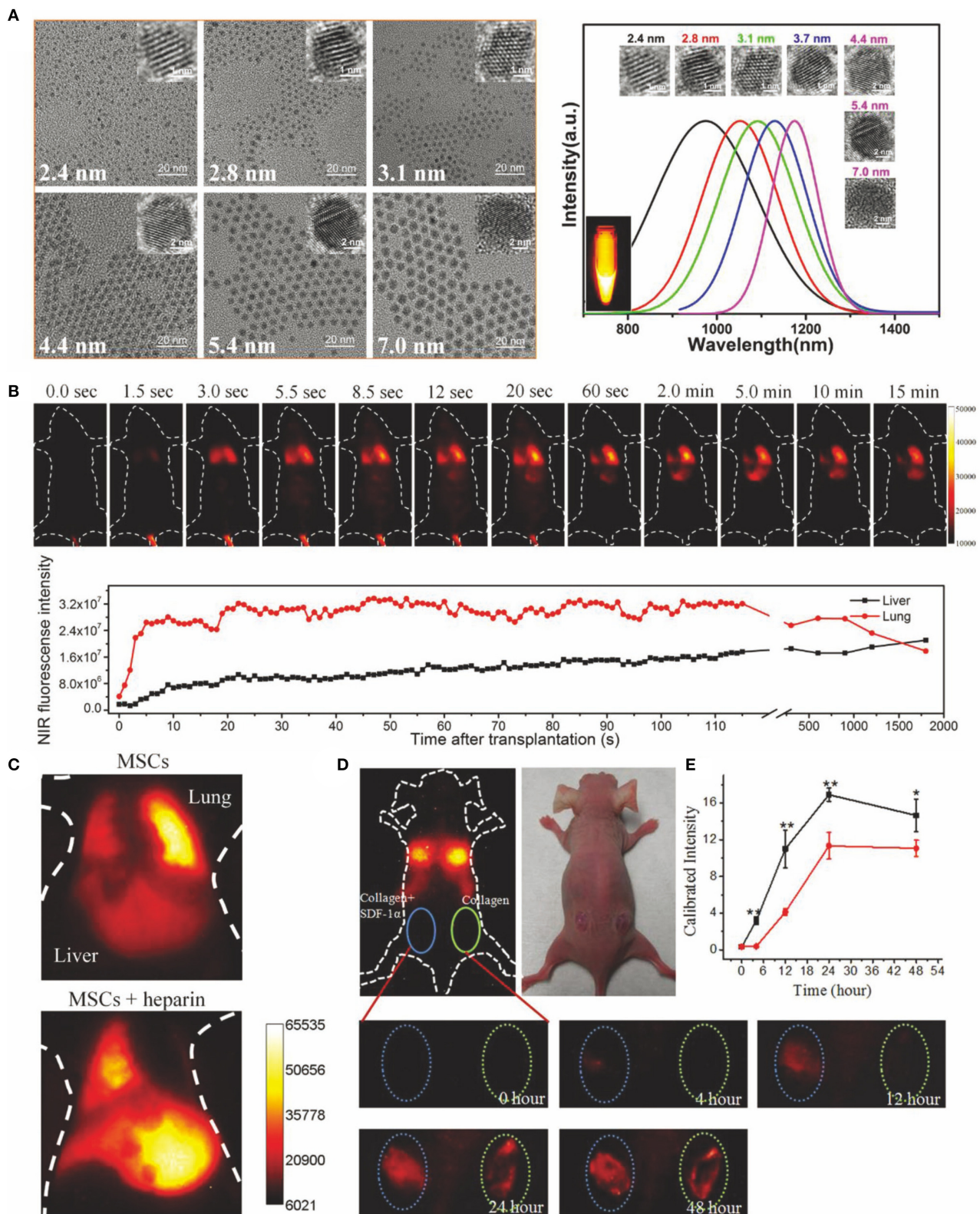


FIGURE 7 | Ag₂S quantum dots of NIR-II emitting were used to track the transplanted MSCs (Chen et al., 2018b). **(A)** Representative TEM pictures and fluorescence emission spectra of Ag₂S QDs with diverse sizes. Adapted from Zhang et al. (2014) written by Qiangbin Wang etc. with permission. **(B)** Ag₂S QDs labeled MSCs were

(Continued)

FIGURE 7 | injected into mice by vein, and NIR-II fluorescence imaging was accomplished on the mice with 100 ms exposure. When excited at 808 nm, the InGaAs/SWIR camera was used to obtain the NIR-II image. NIR-II fluorescence signal value in liver and lung of mice at diverse time points was quantitatively analyzed. Adapted from Chen et al. (2018a) written by Qiangbin Wang etc. with permission. **(C)** MSCs were tracked in mice with acute liver failure and labeled by Ag₂S quantum dots. MSCs were injected into mice in combination with or without heparin and imaged. Adapted from Chen et al. (2013) written by Qiangbin Wang etc. with permission. Homing of MSCs was studied by **(D)** *in vivo* imaging and **(E)** fluorescence quantification. The MSCs were transplanted intravenously into a mouse model with skin trauma. The left trauma was cured with a collagen scaffold loaded with SDF1- α . The right trauma was cured with collagen scaffold. The data are shown as mean \pm SD values from $n = 3$, * $p < 0.05$, ** $p < 0.01$. Adapted from Chen et al. (2015) written by Qiangbin Wang etc. with permission.

using NPs emitted in NIR-II to track SCs *in vivo*. Ag₂S QDs-based NIR-II imaging is currently the only method that has succeeded in SC tracking research *in vivo*. In order to greater improve the performance of NPs emitted in NIR-II in SC-based regeneration research, more efforts should be made to conquer the defects (such as water solubility, physiological stability, biocompatibility, and metabolic capacity) of current NIR-II NP-based imaging technology. In addition, new strategies are needed to take full advantage of NIR-II excitation and emission. The comparison diagram of transplanted mesenchymal stem cells (MSCs) tracked by Ag₂S quantum dots emitted NIR-II fluorescence is shown in **Figure 7**.

Figure 7A shows typical TEM pictures and fluorescence emission spectrum of Ag₂S quantum dots with different particle sizes. **Figure 7B** shows the real-time NIR-II fluorescence imaging of Ag₂S QDs labeled MSCs after intravenous injection into mice exposed for 100 ms. When excited at 808 nm, NIR-II fluorescence images were collected with InGaAs/SWIR camera. The fluorescence intensity of NIR-II in liver and lung of mice at diverse time points was measured, and then quantitative analysis was performed. In **Figure 7C**, Ag₂S quantum dots were labeled on MSCs and then injected into mice with acute liver failure for tracking study. MSCs were combined with or without heparin and then transplanted intravenously into mice and imaged. **Figures 7D,E**, respectively show *in vivo* imaging and fluorescence quantitative homing behavior of MSCs to the wound in a mouse model with skin trauma. MSCs were transplanted intravenously into model mice. The left and right wounds were treated with SDF1- α -loaded collagen scaffolds and collagen scaffolds, respectively.

Other related researches on the tracking of transplanted CS with NIR-II quantum dots include an article published in 2019 by Chen's team about the fate of intraarticular injection of MSCs *in vivo* for the useful treatment of supraspinatus tendon tears (Yang et al., 2019). This paper reports that MSCs have a strong therapeutic potential in the treatment of supraspinatus tendon tears. However, by reason of the finite evidence of dynamic visualization of cell behavior *in vivo*, MSC therapy has not been fully utilized and may even be underestimated. Here, PbS QD labeled MSCs can treat supraspinatus tendon tears in mice. PbS QD is a biocompatible NIR-II fluorescence imaging probe, which can provide a cell migration map and information about the biological distribution and clearance process of MSCs injected into the joints with three densities. Intra-articular injection can avoid MSCs being wrapped by filtered organs and reduces organ toxicity induced by quantum dots. It is worth noting that MSCs have similar migration directions, but the migration efficiency of the medium density group is higher. In the repair stage, MSCs

stay around the footprint for the longest time, with the highest cell retention rate. In addition, quantitative kinetics studies showed that labeled MSCs were cleared by feces and urine. Histomorphological analysis showed that therapeutic effect of the medium density group was the best, and the labeled MSCs showed no damage or inflammatory response to the main organs, suggesting that too much or too little MSCs administration might reduce its efficacy. This imaging method provides spatio-temporal evidence for the response of MSCs therapy *in vivo*, which is helpful for the optimization of MSCs therapy.

Moreover, in 2018, Huang et al. published a paper on NIR-II fluorescence and bioluminescence multiple imaging for *in vivo* observation of the location, survival and differentiation of transplanted stem cells (Huang et al., 2019). An NIR-II fluorescence/bioluminescence composite imaging method is successfully developed covering 400–1,700 nm visible light and NIR-II window for *in vivo* monitoring of location, survival, and osteogenic differentiation of human bone marrow mesenchymal stem cells (hMSCs) in a mouse model of skull defect. The long-term biological distribution of transplanted hMSCs was observed by using Ag₂S quantum dot with NIR-II window. Bioluminescent imaging (BLI) based on endogenous red firefly luciferase (rfluc) and gaussian luciferase (gluc) driven by collagen type 1 promoter were used to report the survival and osteogenic differentiation status of transplanted hMSCs. At the same time, by combining the three imaging channels, they can not only directly observe the various dynamic biological behaviors of the transplanted hMSCs, but also further observe the promoting effects of immunosuppression and bone morphogenetic protein 2 on the survival and osteogenic differentiation of the transplanted hMSCs. This new multifunctional imaging technique can widely extend the analysis of the fate and therapeutic capacity of transplanted stem cells and help to promote stem cell-based regenerative therapy and its transformation in the clinical applications.

CONCLUSION

In summary, compared with traditional NIR-I imaging technology and other medical imaging methods, NIR-II bioimaging technology not only has a deeper imaging depth, but also can better avoid background interference such as spontaneous fluorescence and photon scattering of tissue. So far, a variety of NIR-II dyes, such as inorganic nanomaterials (single-walled carbon nanotubes, semiconductor quantum dots, rare earth nanomaterials), conjugated polymers and organic small-molecule materials, have been successfully synthesized and prepared. Because of its special properties, NIR-II dyes can

TABLE 1 | NIR-II contrast agent and its biomedical application.

Fluorophore	Fluorescence property	Biomedical applications	References
SWCNTs	808/950–1,400 nm (excitation/emission)	High-resolution imaging of blood vessels	Welsher et al., 2009
M13-SWCNTs	808/950–1,100 nm (excitation/emission)	Targeted fluorescence imaging of tumor tissues in mice	Ghosh et al., 2014
IRDye-800- SWCNTs	808/1,300–1,400 nm (excitation/emission)	Imaging of the distribution of veins in the head of mice and the fine structure of the brain capillaries	Hong et al., 2014
A synthetic organic molecule (CH1055)	750/1,055 nm (excitation/emission)	Tumor imaging and precise image-guided tumor-removal surgery	Antaris et al., 2016
o-SWCNT-PEG	980/1,300 nm (excitation/emission)	Used in angiographic imaging	Takeuchi et al., 2019
Ag ₂ S QD	800/1,200 nm (excitation/emission)	Used in NIR-II cell imaging and non-specific tumor detection	Hong et al., 2012b; Zhang et al., 2012, 2013
Au/Cu alloy nanodots or Au/Co alloy nanodots	808/950–1,100 nm (excitation/emission)	It is a non-toxic and multifunctional nanodots for used in biological imaging, especially in multi-mode imaging	Andolina et al., 2013; Marbella et al., 2014
NaYF ₄ :Yb/Ln@NaYF ₄ (Ln= Er, Ho, Tm, Pr)nanocrystals	800/~1,500 nm (excitation/emission)	Widely applied <i>in vivo</i> bioimaging research	Naczynski et al., 2013
SrF ₂ :Nd ³⁺ NP	808/1,100 nm (excitation/emission)	<i>In vivo</i> NIR-II optical imaging	Villa et al., 2015
NaYF ₄ :Yb ³⁺ /X ³⁺ @NaYbF ₄ @NaYF ₄ :Nd ³⁺ (X = null, Er, Ho, Tm or Pr)	700–860/1,000–1,600 nm (excitation/emission)	NIR-II <i>in vivo</i> imaging of deep tissue	Shao et al., 2016
FD-1080	1,046/1,080 nm (excitation/emission)	non-intrusive high distinguishability deep tissue hindlimb vascular system and brain veins biological imaging	Li et al., 2018
Free ICG	810–830/1,100 nm (excitation/emission)	Utility in NIR-II navigated cytoreductive surgery of cerebral cancers and accelerate the clinical translation of NIR-II imaging technology	Starosolski et al., 2017; Zeh et al., 2017; Cho et al., 2019a,b; Wang et al., 2019b
liposomal-ICG (Lip-ICG)	782/950–1500 nm (excitation/emission)	Long-term imaging of hind limb and intracranial vessels <i>in vivo</i>	Bhavane et al., 2018
ICG conjugated bevacizumab (Bev-ICG)	808 nm/>900 nm (excitation/emission)	Immensely facilitate the application of NIR-II clinical bioimaging	Suo et al., 2019
Core:DCNPs(NaGdF ₄ :5%Nd@NaGdF ₄) <i>In vivo</i> assembly nanoprobe: DCNPs-L ₁ /L ₂ -FSH ₈ (L1 and L2 are conjugated DNA; FSH ₈ is a follicle stimulating hormone peptide)	808/1,060 nm (excitation/emission)	Tumor imaging and image-guided surgery	Wang et al., 2018
Ag ₂ Te quantum dots (QDs)	808/1,300 nm (excitation/emission)	Tumor imaging and image-guided surgery	Zhang et al., 2019
lanthanide complex (Nd-DOTA)	808/1,060 and 1,330 nm (excitation/emission)	Accurately mark the profile of micro-tumors in surgery and thoroughly removed under the guidance of NIR-II biological imaging	Yang et al., 2018
semiconductor polymer nanoparticle of diketopyrrolopyrrole (PDFT1032)	809/1,032 nm (excitation/emission)	Widely used in clinical imaging and surgical treatment of malignant tumors	Shou et al., 2018
NaErF ₄ :2%Ho@NaYF ₄ UCNPs the sensor is based on the ratio meter fluorescence	1,530/1,180 nm (excitation/emission)	Used to quantify the degree of actual inflammation in clinical tests	Liu et al., 2018
DCNPs(NaGdF ₄ :5%Nd@NaGdF ₄)@GSH	808/1,060 nm (excitation/emission)	Accurate imaging of inflammation <i>in vivo</i>	Zhao et al., 2019
pentamethine cyanine NIR-II molecular fluorophore	1,015/1,065 nm (excitation/emission)	high-quality imaging and pH sensing <i>in vivo</i>	Wang et al., 2019a
Peroxynitrate NIR-II molecular fluorophore IRBTP-O	575 and 905/>1,000 nm (excitation/emission)	Drug-induced hepatotoxicity detection	Li et al., 2019c
Polyacrylic acid (PAA) modified NaLuF ₄ :Gd/Nd nanorods (PAA-NRs)	808/1,056 and 1,328 nm (excitation/emission)	For Fluorescence imaging-guided detection of small tumors, angiogenesis-related diseases, and angiogenesis diagnosis	Li et al., 2019a
NaLuF ₄ : Gd/Yb/Er NRs@PDA	980/1,525 nm (excitation/emission)	Visualization of tumor-related vascular malformations and imaging-guided photothermal therapy	Li et al., 2019b
A bright organic NIR-II fluorescent nanocluster (p-FE)	980/1,100 nm (excitation/emission)	As a vascular imaging reagent for non-invasive <i>in vivo</i> blood flow tracking in the rat cerebrovascular system	Wan et al., 2018

(Continued)

TABLE 1 | Continued

Fluorophore	Fluorescence property	Biomedical applications	References
NaGdF ₄ @NaGdF ₄ :Yb,Er@NaYF ₄ :Yb@NaNdF ₄ :Yb	808 nm/Er ³⁺ at 1,525 nm. Ho ³⁺ at 1,155 nm, Pr ³⁺ at 1,289 nm, Tm ³⁺ at 1,475 nm Nd ³⁺ at 1,060 nm (excitation/emission)	As a microinvasive probes for disease diagnosis	Fan et al., 2018
Conjugated polymer nanoparticles (CP NPs)	980/1,156 nm (excitation/emission)	Accurate brain diagnosis	Guo et al., 2019
Ag ₂ S QDs	808/From 900 to 1,700 nm (excitation/emission)	Tracking the transplanted stem cells	Chen et al., 2013, 2015, 2018a; Zhang et al., 2014; Huang et al., 2019
C ₁₈ -PMH-PEG-Ag ₂ Se	808/1,300 nm (excitation/emission)	Tracking the transplanted stem cells	Dong et al., 2013; Chen et al., 2018b
PbS QDs	808/1,100 nm (excitation/emission)	Tracking the transplanted stem cells <i>in vivo</i> to provide evidence for therapy and promote the optimization of therapy	Yang et al., 2019
AgInTe ₂ QDs	700 nm/between 1,095 and 1,160 nm (excitation/emission)	<i>In vivo</i> bioimaging and solar energy conversion systems	Langevin et al., 2015; Kameyama et al., 2016; Chen et al., 2018b

be used not only as biomedical contrast agent, but also in the fields of photothermal and photodynamic therapy, drug delivery, surgical guidance and tracking the transplanted stem cells. In this article, the reported NIR-II fluorescent probes and their biomedical applications are summarized in **Table 1**.

With the development of molecular design theory and nanomaterials, more and more NIR-II imaging systems will be designed, developed and promoted into clinical trials. It is worth noting that at present, most of NIR-II fluorescent molecules have poor water solubility and physiological stability, and low fluorescence quantum yield. For polymers and inorganic nano systems, problems, such as slow metabolism, high toxicity, and lack of specific tissue targeting, still exist. New methods and materials will be helpful to promote the application of NIR-II imaging technology in the field of biology. In general, the following points should be paid attention to in the development and design of NIR-II dyes. Firstly, in order to improve the water solubility and physiological stability of organic NIR-II fluorescent dyes, reduce the band gap when choosing the appropriate space configuration, and consider the influence of the group on the water solubility of dyes when modifying the group. Secondly, in order to improve the biocompatibility and metabolic capacity of the probe, the molecular structure should be designed reasonably. In particular, when the probe is a polymer molecule dye and nanoparticles, the design and synthesis of the degradation of NIR-II dye probe is the best. Thirdly, dye is endowed with specific

functions, such as combining dye with targeted molecules, improving the aggregation ability of dye in specific parts of the organism, and promoting the development of disease targeting and early diagnosis in clinical practice.

AUTHOR CONTRIBUTIONS

JC wrote the draft and corresponded to submittal, revision, and coordination. BZ, KZ, SH, LM, JS, and HY participated in manuscript revision. JS and HY oversaw the design, quality assurance, and finalization of the manuscript.

FUNDING

This work was supported by the National Natural Science Foundation of China [grant number 21874024], Young and middle-aged teacher foundation of Education Department of Fujian Province [grant number JAT160157], the start-up funds for new teachers in Fujian Agriculture And Forestry University [grant numbers 61201400908, 61201400916], the Science and Technology Program of Fujian Entry-Exit Inspection and Quarantine Bureau of P.R.C. [grant numbers FK2013-29, FK2014-01], the National Natural Science Foundation of Fujian Province [2017J05019], Young Scientist Natural Science Foundation of Universities in Fujian, and Chinese Scholarship Council granted fund [No: 201700930062].

REFERENCES

- Andolina, C. M., Dewar, A. C., Smith, A. M., Marbella, L. E., Hartmann, M. J., and Millstone, J. E. (2013). Photoluminescent gold-copper nanoparticle alloys with composition-tunable near-infrared emission. *J. Am. Chem. Soc.* 135, 5266–5269. doi: 10.1021/ja400569u
- Antaris, A. L., Chen, H., Cheng, K., Sun, Y., Hong, G. S., Qu, C. R., et al. (2016). A small-molecule dye for NIR-II imaging. *Nat. Mater.* 15, 235–242. doi: 10.1038/nmat4476
- Bashkatov, A. N., Genina, E. A., Kochubey, V. I., and Tuchin, V. V. (2005). Optical properties of human skin, subcutaneous and mucous tissues in the wavelength range from 400 to 2000 nm.

- J. Phys. D Appl. Phys.* 38: 2543–2555. doi: 10.1088/0022-3727/38/15/004
- Bhavane, R., Starosolski, Z., Stupin, I., Ghaghada, K. B., and Annapragada, A. (2018). NIR-II fluorescence imaging using indocyanine green nanoparticles. *Sci. Rep.* 8:14455. doi: 10.1038/s41598-018-32754-y
- Chan, E. K., Sorg, B., Protsenko, D., O'Neil, M., Motamedi, M., and Welch, A. J. (1996). Effects of compression on soft tissue optical properties. *IEEE J. Sel. Top. Quantum Electron.* 2, 943–950. doi: 10.1109/2944.577320
- Chen, G. C., Lin, S. Y., Huang, D. H., Zhang, Y. J., Li, C. Y., Wang, M., et al. (2018a). Revealing the fate of transplanted stem cells *in vivo* with a novel optical imaging strategy. *Small* 14:1702679. doi: 10.1002/smll.201702679
- Chen, G. C., Tian, F., Li, C. Y., Zhang, Y. J., Weng, Z., Zhang, Y., et al. (2015). *In vivo* real-time visualization of mesenchymal stem cells tropism for cutaneous regeneration using NIR-II fluorescence imaging. *Biomaterials* 53, 265–273. doi: 10.1016/j.biomaterials.2015.02.090
- Chen, G. C., Tian, F., Zhang, Y., Zhang, Y. J., Li, C. Y., and Wang, Q. B. (2013). Tracking of transplanted human mesenchymal stem cells in living mice using near-infrared Ag₂S quantum dots. *Adv. Funct. Mater.* 24, 2481–2488. doi: 10.1002/adfm.201303263
- Chen, G. C., Zhang, Y. J., Li, C. Y., Huang, D. H., Wang, Q. W., and Wang, Q. B. (2018b). Recent advances in tracking the transplanted stem cells using near-infrared fluorescent nanoprobe: turning from the first to the second near-infrared window. *Adv. Funct. Mater.* 7, 1–18. doi: 10.1002/adfm.201800497
- Chen, G. Y., Ohulchanskyy, T. Y., Liu, S., Law, W. C., Wu, F., Swihart, M. T., et al. (2012). Core/shell NaGdF₄: Nd³⁺/NaGdF₄ nanocrystals with efficient near-infrared to near-infrared downconversion photoluminescence for bioimaging applications. *ACS Nano* 6, 2969–2977. doi: 10.1021/nn2042362
- Chen, G. Y., Qiu, H. L., Prasad, P. N., and Chen, X. Y. (2014). Upconversion nanoparticles: design, nanochemistry, and applications in theranostics. *Chem. Rev.* 114, 5161–5214. doi: 10.1021/cr400425h
- Cho, S. S., Salinas, R., De Ravin, E., Teng, C. W., Li, C., Abdullah, K. G., et al. (2019a). Near-infrared imaging with second-window indocyanine green in newly diagnosed high-grade gliomas predicts gadolinium enhancement on postoperative magnetic resonance imaging. *Mol. Imaging Biol.* 21, 1–11. doi: 10.1007/s11307-019-01455-x
- Cho, S. S., Salinas, R., and Lee, J. Y. K. (2019b). Indocyanine-green for fluorescence-guided surgery of brain tumors: evidence, techniques, and practical experience. *Front. Surg.* 6:11. doi: 10.3389/fsurg.2019.00011
- Cosco, E. D., Caram, J. R., Bruns, O. T., Franke, D., Day, R. A., Farr, E. P., et al. (2017). Flavylium polymethine fluorophores for near-and shortwave infrared imaging. *Angew. Chem. Int. Ed. Engl.* 56, 13126–13129. doi: 10.1002/anie.201706974
- Croce, A. C., and Bottiroli, G. (2014). Autofluorescence spectroscopy and imaging: a tool for biomedical research and diagnosis. *Eur. J. Histochem.* 58:2461. doi: 10.4081/ejh.2014.2461
- Diao, S., Blackburn, J. L., Hong, G. S., Antaris, A. L., Chang, J. L., Wu, J. Z., et al. (2015). Fluorescence imaging *in vivo* at wavelengths beyond 1500 nm. *Angew. Chem. Int. Ed. Engl.* 54, 14758–14762. doi: 10.1002/anie.201507473
- Dong, B. H., Li, C. Y., Chen, G. C., Zhang, Y. J., Zhang, Y., Deng, M. J., et al. (2013). Facile synthesis of highly photoluminescent Ag₂Se quantum dots as a new fluorescent probe in the second near-infrared window for *in vivo* imaging. *Chem. Mater.* 25, 2503–2509. doi: 10.1021/cm400812v
- Du, Y., Hu, X. H., Cariveau, M., Ma, X., Kalmus, G. W., and Lu, J. Q. (2001). Optical properties of porcine skin dermis between 900 nm and 1500 nm. *Phys. Med. Biol.* 46, 167–181. doi: 10.1088/0031-9155/46/1/312
- Fan, Y., Wang, P. Y., Lu, Y. Q., Wang, R., Zhou, L., Zheng, X. L., et al. (2018). Lifetime-engineered NIR-II nanoparticles unlock multiplexed *in vivo* imaging. *Nat. Nanotechnol.* 13, 941–946. doi: 10.1038/s41565-018-0221-0
- Fan, Y., Wang, S. F., and Zhang, F. (2019). Optical multiplexed bioassays for improve biomedical diagnostics. *Angew. Chem. Int. Ed. Engl.* 58, 13208–13219. doi: 10.1002/anie.201901964
- Ferrando, R., Jellinek, J., and Johnston, R. L. (2008). Nanoalloys: from theory to applications of alloy clusters and nanoparticles. *Chem. Rev.* 108, 845–910. doi: 10.1021/cr040090g
- Frangioni, J. V. (2003). *In vivo* near-infrared fluorescence imaging. *Curr. Opin. Chem. Biol.* 7, 626–634. doi: 10.1016/j.cbpa.2003.08.007
- Friebe, M., Helfmann, J., Netz, U., and Meinke, M. (2009). Influence of oxygen saturation on the optical scattering properties of human red blood cells in the spectral range 250 to 2000 nm. *J. Biomed. Opt.* 14:034001. doi: 10.1117/1.3127200
- Ghosh, D., Bagley, A. F., Na, Y. J., Birrer, M. J., Bhatia, S. N., and Belcher, A. M. (2014). Deep, noninvasive imaging and surgical guidance of submillimeter tumors using targeted M13-stabilized single-walled carbon nanotubes. *Proc. Natl. Acad. Sci. U.S.A.* 111, 13948–13953. doi: 10.1073/pnas.1400821111
- Gui, R. J., Sun, J., Liu, D. X., Wang, Y. F., and Jin, H. (2014a). A facile cation exchange-based aqueous synthesis of highly stable and biocompatible Ag₂S quantum dots emitting in the second near-infrared biological window. *Dalton Trans.* 43, 16690–16697. doi: 10.1039/C4DT00699B
- Gui, R. J., Wan, A. J., Liu, X. F., Yuan, W., and Jin, H. (2014b). Water-soluble multidentate polymers compactly coating Ag₂S quantum dots with minimized hydrodynamic size and bright emission tunable from red to second near-infrared region. *Nanoscale* 6, 5467–5473. doi: 10.1039/c4nr00282b
- Guo, B., Feng, Z., Hu, D. H., Xu, S. D., Middha, E., Pan, Y. T., et al. (2019). Precise deciphering of brain vasculatures and microscopic tumors with dual NIR-II fluorescence and photoacoustic imaging. *Adv. Mater.* 31:e1902504. doi: 10.1002/adma.201902504
- He, S. Q., Song, J., Qu, J. L., and Cheng, Z. (2018). Crucial breakthrough of second near-infrared biological window fluorophores: design and synthesis toward multimodal imaging and theranostics. *Chem. Soc. Rev.* 47, 4258–4278. doi: 10.1039/C8CS00234G
- Hemmer, E., Benayas, A., Légaré, F., and Vetrone, F. (2016). Exploiting the biological windows: current perspectives on fluorescent bioprobes emitting above 1000 nm. *Nanoscale Horiz.* 1, 168–184. doi: 10.1039/C5NH00073D
- Hilderbrand, S. A., and Weissleder, R. (2010). Near-infrared fluorescence: application to *in vivo* molecular imaging. *Curr. Opin. Chem. Biol.* 14, 71–79. doi: 10.1016/j.cbpa.2009.09.029
- Hong, G. S., Diao, S., Chang, J. L., Antaris, A. L., Chen, C. X., Zhang, B., et al. (2014). Through skull fluorescence imaging of the brain in a new near-infrared window. *Nat. Photonics* 8, 723–730. doi: 10.1038/nphoton.2014.166
- Hong, G. S., Lee, J. C., Robinson, J. T., Raaz, U., Xie, L. M., Huang, N. F., et al. (2012a). Multifunctional *in vivo* vascular imaging using near-infrared II fluorescence. *Nat. Med.* 18, 1841–1846. doi: 10.1038/nm.2995
- Hong, G. S., Robinson, J. T., Zhang, Y. J., Diao, S., Antaris, A. L., Wang, Q. B., et al. (2012b). *In vivo* fluorescence imaging with Ag₂S quantum dots in the second near-infrared region. *Angew. Chem. Int. Ed. Engl.* 51, 9818–9821. doi: 10.1002/anie.201206059
- Huang, D. H., Lin, S. Y., Wang, Q. W., Zhang, Y. J., Li, C. Y., Ji, R., et al. (2019). An NIR-II fluorescence/dual bioluminescence multiplexed imaging for *in vivo* visualizing the location, survival, and differentiation of transplanted stem cells. *Adv. Funct. Mater.* 29, 1–11. doi: 10.1002/adfm.201806546
- Jiang, X. Y., Cao, C., Feng, W., and Li, F. Y. (2016). Nd³⁺-doped LiYF₄ nanocrystals for bio-imaging in the second near-infrared window. *J. Mater. Chem. B* 4, 87–95. doi: 10.1039/C5TB02023A
- Kameyama, T., Ishigami, Y., Yukawa, H., Shimada, T., Baba, Y., Ishikawa, T., et al. (2016). Crystal phase-controlled synthesis of rod-shaped AgInTe₂ nanocrystals for *in vivo* imaging in the near-infrared wavelength region. *Nanoscale* 8, 5435–5440. doi: 10.1039/C5NR07532G
- Kobayashi, H., Ogawa, M., Alford, R., Choyke, P. L., and Urano, Y. (2010). New strategies for fluorescent probe design in medical diagnostic imaging. *Chem. Rev.* 110, 2620–2640. doi: 10.1021/cr900263j
- Langevin, M. A., Pons, T., Ritcey, A. M., and Allen, C. N. (2015). Near-infrared emitting AgInTe₂ and Zn-Ag-In-Te colloidal nanocrystals. *Nanoscale Res. Lett.* 10:255. doi: 10.1186/s11671-015-0951-y
- Lavis, L. D., and Raines, R. T. (2008). Bright ideas for chemical biology. *ACS Chem. Biol.* 3, 142–155. doi: 10.1021/cb700248m
- Li, B. H., Lu, L. F., Zhao, M. Y., Lei, Z. H., and Zhang, F. (2018). Efficient 1064-nm NIR-II excitation fluorescent molecular dye for deep-tissue high-resolution dynamic bioimaging. *Angew. Chem. Int. Ed. Engl.* 57, 7483–7487. doi: 10.1002/anie.201801226
- Li, D. D., Wang, S. F., Lei, Z. H., Sun, C. X., El-Toni, A. M., Alhoshan, M. S., et al. (2019c). Peroxynitrite activatable NIR-II fluorescent molecular probe for drug-induced hepatotoxicity monitoring. *Anal. Chem.* 91, 4771–4779. doi: 10.1021/acs.analchem.9b00317
- Li, X. L., Jiang, M. Y., Li, Y. B., Xue, Z. L., Zeng, S. J., and Liu, H. R. (2019a). 808 nm laser-triggered NIR-II emissive rare-earth nanoprobe for small tumor

- detection and blood vessel imaging. *Mater. Sci. Eng. C Mater. Biol. Appl.* 100, 260–268. doi: 10.1016/j.msec.2019.02.106
- Li, X. L., Jiang, M. Y., Zeng, S. J., and Liu, H. R. (2019b). Polydopamine coated multifunctional lanthanide theranostic agent for vascular malformation and tumor vessel imaging beyond 1500 nm and imaging-guided photothermal therapy. *Theranostics* 9, 3866–3878. doi: 10.7150/thno.31864
- Li, X. M., Wang, R., Zhang, F., Zhou, L., Shen, D. K., Yao, C., et al. (2013). Nd³⁺ sensitized up/down converting dual-mode nanomaterials for efficient *in-vitro* and *in-vivo* bioimaging excited at 800 nm. *Sci. Rep.* 3:3536. doi: 10.1038/srep03536
- Lim, Y. T., Kim, S., Nakayama, A., Stott, N. E., Bawendi, M. G., and Frangioni, J. V. (2003). Selection of quantum dot wavelengths for biomedical assays and imaging. *Mol. Imaging* 2, 50–64. doi: 10.1162/153535003765276282
- Liu, L., Wang, S. F., Zhao, B. Z., Pei, P., Fan, Y., Li, X. M., et al. (2018). Er³⁺ sensitized 1530 nm to 1180 nm second near-infrared window upconversion nanocrystals for *in vivo* biosensing. *Angew. Chem. Int. Ed. Engl.* 57, 7518–7522. doi: 10.1002/anie.201802889
- Lu, H., Mack, J., Yang, Y. C., and Shen, Z. (2014). Structural modification strategies for the rational design of red/NIR region BODIPYs. *Chem. Soc. Rev.* 43, 4778–4823. doi: 10.1039/C4CS00030G
- Ma, Q., and Su, X. G. (2010). Near-infrared quantum dots: synthesis, functionalization and analytical applications. *Analyst* 135, 1867–1877. doi: 10.1039/c0an00233j
- Marbella, L. E., Andolina, C. M., Smith, A. M., Hartmann, M. J., Dewar, A. C., Johnston, K. A., et al. (2014). Gold-cobalt nanoparticle alloys exhibiting tunable compositions, near-infrared emission, and high T-2 relaxivity. *Adv. Funct. Mater.* 24, 6532–6539. doi: 10.1002/adfm.201400988
- Mishra, A., Behera, R. K., Behera, P. K., Mishra, B. K., and Behera, G. B. (2000). Cyanines during the 1990s: A Review. *Chem. Rev.* 100, 1973–2011. doi: 10.1021/cr990402t
- Murakami, T., Nakatsuiji, H., Inada, M., Matoba, Y., Umeyama, T., Tsujimoto, M., et al. (2012). Photodynamic and photothermal effects of semiconducting and metallic-enriched single-walled carbon nanotubes. *J. Am. Chem. Soc.* 134, 17862–17865. doi: 10.1021/ja3079972
- Naczynski, D. J., Tan, M. C., Riman, R. E., and Moghe, P. V. (2014). Rare earth nanoprobes for functional biomolecular imaging and theranostics. *J. Mater. Chem. B* 2, 2958–2973. doi: 10.1039/C4TB00094C
- Naczynski, D. J., Tan, M. C., Zevon, M., Wall, B., Kohl, J., Kulesa, A., et al. (2013). Rare-earth-doped biological composites as *in vivo* shortwave infrared reporters. *Nat. Commun.* 4:2199. doi: 10.1038/ncomms3199
- O'Connell, M. J., Bachilo, S. M., Huffman, C. B., Moore, V. C., Strano, M. S., Haroz, E. H., et al. (2002). Band gap fluorescence from individual single-walled carbon nanotubes. *Science* 297, 593–596. doi: 10.1126/science.1072631
- Peters, V. G., Wyman, D. R., Patterson, M. S., and Frank, G. L. (1990). Optical properties of normal and diseased human breast tissues in the visible and near infrared. *Phys. Med. Biol.* 35, 1317–1334. doi: 10.1088/0031-9155/35/9/010
- Pokhrela, M., Mimun, L. C., Yust, B., Kumar, G. A., Dhanale, A., Tang, L., et al. (2014). Stokes emission in GdF₃:Nd³⁺ nanoparticles for bioimaging probes. *Nanoscale* 6, 1667–1674. doi: 10.1039/C3NR03317A
- Prahl, S. A., van Gemert, M. J. C., and Welch, A. J. (1993). Determining the optical properties of turbid media by using the adding-doubling method. *Appl. Opt.* 32, 559–568. doi: 10.1364/AO.32.000559
- Robinson, J. T., Welsher, K., Tabakman, S. M., Sherlock, S. P., Wang, H. L., Luong, R., et al. (2010). High performance *in vivo* near-IR (> 1 μ m) imaging and photothermal cancer therapy with carbon nanotubes. *Nano Res.* 3, 779–793. doi: 10.1007/s12274-010-0045-1
- Schnermann, M. J. (2017). Organic dyes for deep bioimaging. *Nature* 551, 176–177. doi: 10.1038/nature24755
- Sevick-Muraca, E. M., Houston, J. P., and Gurfinkel, M. (2002). Fluorescence-enhanced, near infrared diagnostic imaging with contrast agents. *Curr. Opin. Chem. Biol.* 6, 642–650. doi: 10.1016/S1367-5931(02)00356-3
- Shao, W., Chen, G. Y., Kuzmin, A., Kutscher, H. L., Pliss, A., Ohulchanskyy, T. Y., et al. (2016). Tunable narrow band emissions from dye-sensitized core/shell/shell nanocrystals in the second near-infrared biological window. *J. Am. Chem. Soc.* 138, 16192–16195. doi: 10.1021/jacs.6b08973
- Shou, K. Q., Tang, Y. F., Chen, H., Chen, S., Zhang, L., Zhang, A., et al. (2018). Diketopyrrolopyrrole-based semiconducting polymer nanoparticles for *in vivo* second nearinfrared window imaging and image-guided tumor surgery. *Chem. Sci.* 9, 3105–3110. doi: 10.1039/C8SC00206A
- Simpson, C. R., Kohl, M., Essenpreis, M., and Cope, M. (1998). Near-infrared optical properties of *ex vivo* human skin and subcutaneous tissues measured using the Monte Carlo inversion technique. *Phys. Med. Biol.* 43, 2465–2478. doi: 10.1088/0031-9155/43/9/003
- Sinkeldam, R. W., Greco, N. J., and Tor, Y. (2010). Fluorescent analogs of biomolecular building blocks: design, properties, and applications. *Chem. Rev.* 110, 2579–2619. doi: 10.1021/cr900301e
- Smith, A. M., Mancini, M. C., and Nie, S. (2009). Bioimaging: second window for *in vivo* imaging. *Nat. Nanotechnol.* 4, 710–711. doi: 10.1038/nnano.2009.326
- Starosolski, Z., Bhavane, R., Ghaghada, K. B., Vasudevan, S. A., Kaay, A., and Annapragada, A. (2017). Indocyanine green fluorescence in second near-infrared (NIR-II) window. *PLoS ONE* 12, 1–14. doi: 10.1371/journal.pone.0187563
- Suo, Y. K., Wu, F. X., Xu, P. F., Shi, H., Wang, T. Z., Liu, H. G., et al. (2019). NIR-II fluorescence endoscopy for targeted imaging of colorectal cancer. *Adv. Health. Mater.* 8:1900974. doi: 10.1002/adhm.201900974
- Takeuchi, T., Iizumi, Y., Yudasaka, M., Kizaka-Kondoh, S., and Okazaki, T. (2019). Characterization and biodistribution analysis of oxygen-doped single-walled carbon nanotubes used as *in vivo* fluorescence imaging probes. *Bioconjugate Chem.* 30, 1323–1330. doi: 10.1021/acs.bioconjchem.9b00088
- Tan, M. C., Kumar, G. A., Riman, R. E., Brik, M. G., Brown, E., and Hommerich, U. (2009). Synthesis and optical properties of infrared-emitting YF₃: Nd nanoparticles. *J. Appl. Phys.* 106:063118. doi: 10.1063/1.3168442
- Thekkekk, N., and Richards-Kortum, R. (2008). Optical imaging for cervical cancer detection: solutions for a continuing global problem. *Nat. Rev. Cancer* 8, 725–731. doi: 10.1038/nrc2462
- Troy, T. L., and Thennadil, S. N. (2001). Optical properties of human skin in the near infrared wavelength range of 1000 to 2200 nm. *J. Biomed. Opt.* 6, 167–176. doi: 10.1117/1.1344191
- van Saders, B., Al-Baroudi, L., Tan, M. C., and Riman, R. E. (2013). Rare-earth doped particles with tunable infrared emissions for biomedical imaging. *Opt. Mater. Express* 3, 566–573. doi: 10.1364/OME.3.000566
- Villa, I., Vedda, A., Cantarelli, I. X., Pedroni, M., Piccinelli, F., Bettinelli, M., et al. (2015). 1.3 μ m emitting SrF₂: Nd³⁺ nanoparticles for high contrast *in vivo* imaging in the second biological window. *Nano Res.* 8, 649–665. doi: 10.1007/s12274-014-0549-1
- Wan, H., Yue, J. Y., Zhu, S. J., Uno, T., Zhang, X. D., Yang, Q. L., et al. (2018). A bright organic NIR-II nanofluorophore for three-dimensional imaging into biological tissues. *Nat. Commun.* 9, 1171–1180. doi: 10.1038/s41467-018-03505-4
- Wang, P. Y., Fan, Y., Lu, L. F., Liu, L., Fan, L. L., Zhao, M. Y., et al. (2018). NIR-II nanoprobes *in-vivo* assembly to improve image-guided surgery for metastatic ovarian cancer. *Nat. Commun.* 9, 2898–2908. doi: 10.1038/s41467-018-05113-8
- Wang, P. Y., Wang, X. D., Luo, Q., Li, Y., Lin, X. X., Fan, L. L., et al. (2019b). Fabrication of red blood cell-based multimodal theranostic probes for second near-infrared window fluorescence imaging-guided tumor surgery and photodynamic therapy. *Theranostics* 9, 369–380. doi: 10.7150/thno.29817
- Wang, S. F., Fan, Y., Li, D. D., Sun, C. X., Lei, Z. H., Lu, L. F., et al. (2019a). Anti-quenching NIR-II molecular fluorophores for *in vivo* high-contrast imaging and pH sensing. *Nat. Commun.* 10, 1–11. doi: 10.1038/s41467-019-09043-x
- Weissleder, R. (2001). A clearer vision for *in vivo* imaging. *Nat. Biotechnol.* 19, 316–317. doi: 10.1038/86684
- Welsher, K., Liu, Z., Sherlock, S. P., Robinson, J. T., Chen, Z., Daranciang, D., et al. (2009). A route to brightly fluorescent carbon nanotubes for near-infrared imaging in mice. *Nat. Nanotechnol.* 4, 773–780. doi: 10.1038/nnano.2009.294
- Welsher, K., Sherlock, S. P., and Dai, H. J. (2011). Deep-tissue anatomical imaging of mice using carbon nanotube fluorophores in the second near-infrared window. *Proc. Natl. Acad. Sci. U.S.A.* 108, 8943–8948. doi: 10.1073/pnas.1014501108
- Willmann, J. K., van Bruggen, N., Dinkelborg, L. M., and Gambhir, S. S. (2008). Molecular imaging in drug development. *Nat. Rev. Drug Discov.* 7, 591–607. doi: 10.1038/nrd2290
- Wu, W., Yang, Y. Q., Yang, Y., Yang, Y. M., Zhang, K. Y., Guo, L., et al. (2019). Molecular engineering of an organic NIR-II fluorophore with aggregation-induced emission characteristics for *in vivo* imaging. *Small* 15, 1–10. doi: 10.1002/smll.20190106

- Yang, H. Y., Zhao, Y. W., Zhang, Z. Y., Xiong, H. M., and Yu, S. N. (2013). One-pot synthesis of water-dispersible Ag₂S quantum dots with bright fluorescent emission in the second near-infrared window. *Nanotechnology*. 24:055706. doi: 10.1088/0957-4484/24/5/055706
- Yang, Q. L., Ma, Z. R., Wang, H. S., Zhou, B., Zhu, S. J., Zhong, Y. T., et al. (2017). Rational design of molecular fluorophores for biological imaging in the NIR-II window. *Adv. Mater.* 29:1605497. doi: 10.1002/adma.201605497
- Yang, Y. L., Wang, P. Y., Lu, L. Y., Fan, Y., Sun, C. X., Fan, L. L., et al. (2018). Small-molecule lanthanide complexes probe for second near-infrared window bioimaging. *Anal. Chem.* 90, 7946–7952. doi: 10.1021/acs.analchem.8b00603
- Yang, Y. M., Chen, J., Shang, X. L., Feng, Z. J., Chen, C., Lu, J. Y., et al. (2019). Visualizing the fate of intra-articular injected mesenchymal stem cells *in vivo* in the second near-infrared window for the effective treatment of supraspinatus tendon tears. *Adv. Sci.* 6, 1–12. doi: 10.1002/advs.201901018
- Yi, H. J., Ghosh, D., Ham, M. H., Qi, J. F., Barone, P. W., Strano, M. S., et al. (2012). M13 phage-functionalized single-walled carbon nanotubes as nanoprobe for second near-infrared window fluorescence imaging of targeted tumors. *Nano Lett.* 12, 1176–1183. doi: 10.1021/nl2031663
- Zeh, R., Sheikh, S., Xia, L., Pierce, J., Newton, A., Predina, J., et al. (2017). The second window ICG technique demonstrates a broad plateau period for near infrared fluorescence tumor contrast in glioblastoma. *PLoS ONE* 12:e0182034. doi: 10.1371/journal.pone.0182034
- Zhang, J. J., Lin, Y., Zhou, H., He, H., Ma, J. J., Luo, M. Y., et al. (2019). Cell membrane-camouflaged NIR II fluorescent Ag₂Te quantum dots-based nanobioprobes for enhanced *in vivo* homotypic tumor imaging. *Adv. Healthc. Mater.* 8:e1900341. doi: 10.1002/adhm.201900341
- Zhang, Y., Hong, G. H., Zhang, Y. J., Chen, G. C., Li, F., Dai, H. J., et al. (2012). Ag₂S quantum dot: a bright and biocompatible fluorescent nanoprobe in the second near-infrared window. *ACS Nano* 6, 3695–3702. doi: 10.1021/nn301218z
- Zhang, Y., Zhang, Y. J., Hong, G. S., He, W., Zhou, K., Yang, K., et al. (2013). Biodistribution, pharmacokinetics and toxicology of Ag₂S near-infrared quantum dots in mice. *Biomaterials* 34, 3639–3646. doi: 10.1016/j.biomaterials.2013.01.089
- Zhang, Y. J., Liu, Y. S., Li, C. Y., Chen, X. Y., and Wang, Q. B. (2014). Controlled synthesis of Ag₂S quantum dots and experimental determination of the exciton bohr radius. *J. Phys. Chem. C* 118, 4918–4923. doi: 10.1021/jp501266d
- Zhao, M. Y., Wang, R., Li, B. H., Fan, Y., Wu, Y. F., Zhu, X. Y., et al. (2019). Precise *in vivo* inflammation imaging using *in-situ* responsive cross-linking of glutathione modified ultra-small NIR-II lanthanide nanoparticles. *Angew. Chem. Int. Ed. Engl.* 58, 2050–2054. doi: 10.1002/anie.201812878
- Zhao, Y. X., and Song, Z. M. (2014). Phase transfer-based synthesis of highly stable, biocompatible and the second near-infrared-emitting silver sulfide quantum dots. *Mater. Lett.* 126, 78–80. doi: 10.1016/j.matlet.2014.04.014
- Zheng, M., Jagota, A., Semke, E. D., Diner, B. A., Mclean, R. S., Lustig, S. R., et al. (2003). DNA-assisted dispersion and separation of carbon nanotubes. *Nat. Mater.* 2, 338–342. doi: 10.1038/nmat877
- Zhu, S. J., Tian, R., Antaris, A. L., Chen, X. Y., and Dai, H. J. (2019). Near-infrared-II molecular dyes for cancer imaging and surgery. *Adv. Mater.* 31:1900321. doi: 10.1002/adma.201900321
- Zhu, S. J., Yung, B. C., Chandra, S., Niu, G., Antaris, A. L., and Chen, X. Y. (2018). Near-infrared-II (NIR-II) bioimaging via off-peak NIR-I fluorescence emission. *Theranostics* 8,4141–4151. doi: 10.7150/thno.27995

Conflict of Interest: The authors declare that the research was conducted in the absence of any commercial or financial relationships that could be construed as a potential conflict of interest.

Copyright © 2020 Cao, Zhu, Zheng, He, Meng, Song and Yang. This is an open-access article distributed under the terms of the Creative Commons Attribution License (CC BY). The use, distribution or reproduction in other forums is permitted, provided the original author(s) and the copyright owner(s) are credited and that the original publication in this journal is cited, in accordance with accepted academic practice. No use, distribution or reproduction is permitted which does not comply with these terms.



Ultrasound-Enhanced Chemiluminescence for Bioimaging

Duong Le, Dinesh Dhamecha, Andrea Gonsalves and Jyothi U. Menon*

Department of Biomedical and Pharmaceutical Sciences, College of Pharmacy, The University of Rhode Island, Kingston, RI, United States

OPEN ACCESS

Edited by:

Michael Ming-Yuan Wei,
Texas Commission on Environmental
Quality, United States

Reviewed by:

Fernando Soto,
University of California, San Diego,
United States
Lixia Zhao,
Research Center
for Eco-Environmental Sciences
(CAS), China

*Correspondence:

Jyothi U. Menon
jmenon@uri.edu

Specialty section:

This article was submitted to
Nanobiotechnology,
a section of the journal
Frontiers in Bioengineering and
Biotechnology

Received: 05 September 2019

Accepted: 13 January 2020

Published: 06 February 2020

Citation:

Le D, Dhamecha D, Gonsalves A
and Menon JU (2020)
Ultrasound-Enhanced
Chemiluminescence for Bioimaging.
Front. Bioeng. Biotechnol. 8:25.
doi: 10.3389/fbioe.2020.00025

Tissue imaging has emerged as an important aspect of theragnosis. It is essential not only to evaluate the degree of the disease and thus provide appropriate treatments, but also to monitor the delivery of administered drugs and the subsequent recovery of target tissues. Several techniques including magnetic resonance imaging (MRI), computational tomography (CT), acoustic tomography (AT), biofluorescence (BF) and chemiluminescence (CL), have been developed to reconstruct three-dimensional images of tissues. While imaging has been achieved with adequate spatial resolution for shallow depths, challenges still remain for imaging deep tissues. Energy loss is usually observed when using a magnetic field or traditional ultrasound (US), which leads to a need for more powerful energy input. This may subsequently result in tissue damage. CT requires exposure to radiation and a high dose of contrast agent to be administered for imaging. The BF technique, meanwhile, is affected by strong scattering of light and autofluorescence of tissues. The CL is a more selective and sensitive method as stable luminophores are produced from physiochemical reactions, e.g. with reactive oxygen species. Development of near infrared-emitting luminophores also bring potential for application of CL in deep tissues and whole animal studies. However, traditional CL imaging requires an enhancer to increase the intensity of low-level light emissions, while reducing the scattering of emitted light through turbid tissue environment. There has been interest in the use of focused ultrasound (FUS), which can allow acoustic waves to propagate within tissues and modulate chemiluminescence signals. While light scattering is decreased, the spatial resolution is increased with the assistance of US. In this review, chemiluminescence detection in deep tissues with assistance of FUS will be highlighted to discuss its potential in deep tissue imaging.

Keywords: chemiluminescence, bioluminescence, focused ultrasound, deep tissue, imaging

INTRODUCTION

Imaging has become an essential component of biomedical research and patient treatment. There has been tremendous improvement in imaging techniques and their application in last 30 years. These imaging tools help clinicians not only to diagnose diseases but also to visualize the expression of the reaction, and interactions within the human body (Weissleder and Pittet, 2008). *In vivo* molecular imaging has significantly revolutionized modern medical diagnostics. In order to evaluate the complex nature of tissues/organs, there is a need for advanced and versatile imaging techniques which are not only capable of analyzing the structure and morphology of

tissues/organs but can also efficiently monitor the functions and molecular reactions in the cells (Nam et al., 2014). Each of the imaging modalities available today work on different principles and methods, and the outcome are largely variable depending on interfaces, samples and the imaging technique used (Nam et al., 2014). Therefore, based on the experiments and the clinical application, the most appropriate imaging technique must be carefully chosen from among the range of available methods.

Tissue imaging can be done using spectroscopic signal detection techniques such as magnetic resonance imaging (MRI), computational tomography (CT), acoustic tomography (AT), biofluorescence (BF), and chemiluminescence (CL). Based on the unique principle of each technique, imaging methods have their exclusive range of applications. In most imaging methods, the physical interaction of X-rays, radiofrequencies or sound waves with the target/imaged object (tissues or organs) results in a change in the energy, which is transmitted to form an image. Based on the source and intensity of the energy, the various imaging modalities differ in their specific properties such as resolution, exogenous and endogenous contrast component, penetration depth, cost, and safety (Pysz et al., 2010; Appel et al., 2013). Due to the high energy source, CT and MRI have the best imaging depth and resolution when compared to luminescence and AT. MRI uses radio frequencies coupled with strong magnetic field as the source of energy, which rebounds off the body fat and water molecules, and the transmitted energy is detected and translated into an image. Hence, it is generally used for imaging of soft tissues like brain, wrists, heart and blood vessels (Miwa and Otsuka, 2017). In comparison to CT, MRI has two disadvantages, namely loud machine noises during imaging and longer imaging time (Weissleder and Pittet, 2008). CT uses X-ray energy to image the target tissue and is quick, painless and non-invasive. It is generally used to image bone fractures, tumors progression and internal bleeding (Pysz et al., 2010). However, one of the constraints of CT imaging is the use of radiation and the generation of less detailed images of soft tissues when compared to MRI (Nam et al., 2014). AT has evolved as a hybrid imaging method which can possibly overcome some of the disadvantages of MRI and CT. AT imaging is based on the acoustic wave signals which are generated when the absorbed optical energy is converted to acoustic energy. These waves scatter less than the optical waves in tissue, leading to generation of high-resolution images of deeper tissues. This imaging technique has several advantages. For example, in comparison with CT, it uses non-X-ray laser energy source for imaging, and in comparison to MRI, it is less expensive. However, it faces some disadvantages like poor deep tissue imaging and imaging speed (Xia et al., 2014). Luminescent imaging is another method of imaging. Bioluminescence (BL) is excellent for molecular level imaging without using an external contrast agent, and it has the capacity for real time imaging (Zhang et al., 2006; Weissleder and Pittet, 2008). BL is a unique optical imaging method in that it depends on an internal biological light source (based on a reaction) unlike other imaging systems which require external energy source. Luciferase are a group of enzymes commonly used in BL imaging as they can emit light in the presence of oxygen and a substrate (typically luciferin) (Contag and Ross, 2002).

The released light generated from the live cells is assessed by a photon detector with high sensitivity (Weissleder and Pittet, 2008). Similarly, CL (first generation), without the need of external light sources, advances luminescent imaging further by using luminescent enhancers listed and described in detail in **Table 1**. CL avoids the need for the enzyme luciferase for imaging, thus circumventing the need for genetic modification to produce BL for imaging (Lippert, 2017). CL also allows imaging of whole tissues. Recently, ultrasound (US) modulated fluorescence and US switchable fluorescence (UF) have advanced deep tissue imaging. Although these techniques are new and still under investigation, they are supposed to have advantage over CT and MRI in terms of deep tissue imaging. The key element in these types of imaging is the design of the external contrast agent, which determines the success of the imaging (Pei and Wei, 2019). With the exponential increase in research into the medical applications of US, second generation CL, i.e., ultrasound-enhanced chemiluminescence (UECL), has been developed. In UECL, CL's limitations in deep tissue imaging is attenuated. The attributes of CL and UECL is discussed in detail below.

FIRST GENERATION OF CHEMILUMINESCENCE AND BIOLUMINESCENCE

Luminescence in general is defined as the emission of visible light without increase in the temperature. Luminescence emerging from a chemical reaction is known as CL. One form of CL is bioluminescence, which is basically the production and release of light by a living organism (Créton and Jaffe, 2001). BL and CL are the results of a chemical reaction in which a product at an electronically excited state returns to the ground state by emitting a photon, which is seen as light. This BL and CL light lasts for few seconds as the reaction is very fast and continues for a very short time frame. However, literature reveals that certain suitable supplementary chemicals can modify the emission kinetics in the range of 10 s to 30 min (Aslan and Geddes, 2009). This leads to the improvement in the analytical signal output with significant reproducibility (Roda et al., 2003a).

Bioluminescence is observed in vertebrates and invertebrates (fireflies) and in some microorganisms like fungi and bacteria (Viviani, 2002). The key component involved in the generation of BL is the light emitting chemical luciferin, which is generated by a series of reactions involving the enzyme luciferase. As numerous organisms secrete luciferase and luciferin, this enzyme and molecule respectively are generally named along with the organism/species or group, for example – firefly luciferin (White et al., 1961). The enzyme luciferase catalyzes the oxidation of the luciferin to yield luminescence (Yagur-Kroll et al., 2010). There is huge variation in the reactions occurring in different organisms for the generation of luciferin. However, one of the key and common factors is the requirement of molecular oxygen and other cofactors along with luciferase, to complete the reaction. For example, the generation of firefly luciferin involves a chemical reaction involving luciferase, magnesium

TABLE 1 | Summary of CL materials.

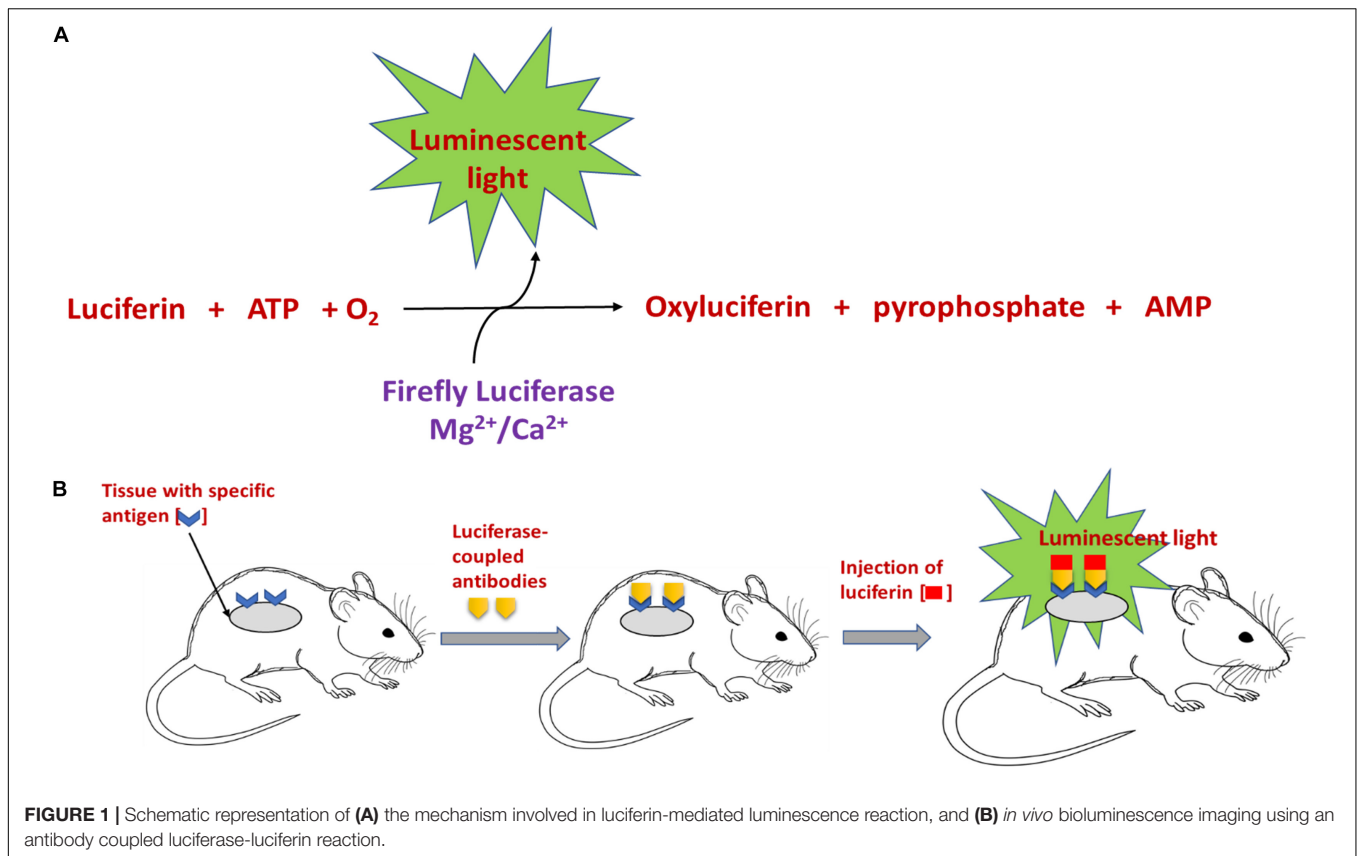
CL dye	Chemical structure	Mechanism of CL	Application	Advantages	Limitations	Reference
Luminol		Generated by pulsed laser light or optically pumped CL	Detection of myeloperoxidase activity by light emitting reaction of luminol, BL imaging of inflammation and tumors	Free state luminol is efficiently used in enzyme labeled immunoassays	CL depends solely on the pH of the system	Dodeigne et al., 2000; Bedouhène et al., 2017; Jancinová et al., 2017; Liu et al., 2019
Coelenterazine		Superoxide anion present in structure causes CL	Detection of cellular function and mass, deep tissue and whole body imaging, molecular imaging of live cells	Selective and sensitive chemiluminescent probe for the study of reactive oxygen metabolite release by neutrophils	CL efficiency is relatively low	Dubuisson et al., 2005; Mu, 2005; Diaz et al., 2018; Nishihara et al., 2018; Nomura et al., 2019
Peroxyoxalic acid and its derivatives		CL is produced through energy transfer to a fluorophore from a fluorescent sensitizer, which is excited in a S1 state.	Wide applications in the quantitative and qualitative determination of drugs, nucleic and amino acids and hydrogen peroxide forming enzymes	Flexibility to select oxalate derivative and the fluorescent sensitizer independently	Efficiency of CL is relatively low. High background is observed.	Dodeigne et al., 2000; Delafresnaye et al., 2019; Li et al., 2019
FCLA		Reaction with singlet oxygen (1O_2) or superoxide anion (O_2^-)	Used as a carrier for cancer drug therapy, optical reporter for ROS production following PDT	pH obtained during generation of CL resembles the acidic to near-neutral range of tumor and normal tissue	The degree of penetration into biological tissue is relatively low due to shorter emission wavelength of FCLA (532 nm)	Wang J. et al., 2002; Qin et al., 2005; Wei et al., 2011, 2016

and adenosine triphosphate (ATP), to yield luminescent luciferin and by-products like adenosine monophosphate, CO_2 , and pyrophosphate (Marques and Esteves da Silva, 2009; Kim et al., 2015). The mechanism of this reaction is addressed in **Figure 1**. For generation of another luminescent molecule – photoprotein aequorin, co-factors like divalent calcium or magnesium ion are required (Brown et al., 2019). A well-known application of BL based on these reactions is the cloning of genes for the enzyme firefly luciferase and the photoprotein from the jellyfish *Aequorea*. This gene can be transferred into a variety of organisms including bacteria, plants, and human cells. Luminous tobacco plants and *Escherichia coli* (expression of genes of luciferases resulted in visible shades of orange, yellow and green bacterial cells) are some of the well-known examples (McCapra, 1990).

Chemiluminescent reactions have a great role in molecular and cellular based assessment due to its high sensitivity (Créton and Jaffe, 2001). For example, CL indicators are used for immunoassays, western blots, northern (nucleic acid detection) and southern blots. One of the key features of CL is its capacity to evaluate the specimen at the cellular level wherein the cells can be either live, in fixed state or hybridized with the CL probes (Roda et al., 2000a; Sala-Newby et al., 2000). CL has great potential to analyze *in vivo* systems because of the absence of the use of heat or exciting light which aids in measurements without any disturbance to the living system. This is an improvement over regular fluorescence imaging which requires high intensity emitting light and long exposure to short wavelength lights which may subsequently damage the living cells (Créton and Jaffe, 2001).

Bioluminescence and CL imaging are interesting tools for biomedical studies, clinical diagnosis, and drug development research. They have the potential to identify and analyze (quantitatively and qualitatively) enzymes, drug and drug metabolites, nucleic acids such as DNA (Qi et al., 2018), micro RNA (Ling et al., 2018), proteins (Li et al., 2015), and antigens (Mao et al., 2019) in various specimens. These specimens can be living cells in experiments, or fixed, cryo- and paraffin-embedded cells/tissues samples and sections (Roda et al., 1996, 2000b). The resolving power of the CL is capable of penetrating to the subcellular level and image the tissue section or a single cell (Roda et al., 2003a). BL and CL offer substantial advantages over other fluorescence imaging methods, which mainly includes its broad range and sensitivity in imaging samples in both micro and macro scale. In addition, the imaging is not affected by the sample matrix, because the luminescence is generated by specific set of chemicals involved in the reaction (Roda et al., 2003b).

Recently, CL intensity has been further improved by using colloidal enhancers that have enabled improvement to not only imaging and but also therapies. Colloidal enhancers can include gold (Li et al., 2008; Yan et al., 2019), silver (Chen et al., 2007; Haghighi and Bozorgzadeh, 2010), platinum (Xu and Cui, 2007), and magnetic (Yang et al., 2019) nanoparticles (NPs). For *in vivo* imaging, peroxalate nanoparticles specific are known for their high specificity and selectivity against



hydrogen peroxide, and they have therefore been used for deep tissue CL imaging of the inflammatory response of mice (Lee et al., 2007). Similarly, polystyrene nanoparticles stained with squaraine catenane endoperoxide dyes, which are concurrently chemiluminescent and fluorescent, displayed significantly higher CL than fluorescence, which helped in the imaging of distribution of nanoparticles in mice (Lee et al., 2013). Similar to colloidal and inorganic NPs, enhancement to CL has been investigated with the help of quantum dots (QDs), including both metallic (Song et al., 2019) and non-metallic (Wang D. M. et al., 2019) QDs. Subsequently, enhancement effects such as chemiluminescence resonance energy transfer (CRET) has been discovered (Yao et al., 2017). CRET allows transfer of energy from a chemiluminescent donor to a fluorophore acceptor (e.g. QDs) without the need for an external excitation source, and with low background signal. Although QDs have several advantages, concerns regarding toxicity and environmental contamination have been raised (Ron, 2006; Wang et al., 2015; Li et al., 2016; Zhang et al., 2016). Chemiluminescence can also be triggered using electrochemical techniques, and this method is called electro-chemiluminescence (ECL). Upconversion nanoparticles, which are generally lanthanide- or rare earth- doped materials, have been identified and developed as ECL emitters. Unlike QDs, these particles have low toxicity, good ECL intensity, and low autofluorescence background. Detailed description of the use of upconversion nanoparticles in ECL is already available in literature (Liu et al., 2014; Gao et al., 2017; Zhai et al., 2017;

Gu et al., 2019). Alternative approaches for safe enhancement of CL will be discussed below.

CHEMILUMINESCENT MATERIALS

Some of the most commonly used materials in CL imaging have been described in detail below.

Luminol

Luminol is synthesized in the presence of triethylene glycol by a reaction involving cyclocondensation of 3-nitrophthalic acid with hydrazine to produce 5-nitro-1,4(2H,4H)phthalazinedione. The resultant product is further reacted with sodium dithionite in the presence of heat, followed by treatment with acetic acid to produce luminol on cooling (Maynard, 1997). CL probes consisting of luminol are known to successfully detect and quantify intracellular and extracellular reactive oxygen species (ROS) produced by phagocytosing cells in the blood (Jancinová et al., 2017). Luminol and its derivatives possess an intermediate called α -hydroxyperoxide, which is derived by the oxidation of the heterocyclic ring, and this reaction depends solely on the pH of the system (Dodeigne et al., 2000). Masking or structural modification of this heterocyclic ring (Jancinová et al., 2017) results in a complete loss of these chemiluminescent properties (Dodeigne et al., 2000). Kwon et al. (2014) took advantage of this property to develop a CL chemodosimeter, in which a

masking group was incorporated to prevent formation of the α -hydroxyperoxide intermediate, thereby preventing CL. When the masking group was selectively removed using a target analyte, the CL could be turned on to get a highly selective and sensitive signal (Kwon et al., 2014). CL is emitted solely due to the presence of oxygen and a strong base in an aprotic media such as DMSO, while protic solvents are capable of oxidizing luminol derivatives only with the assistance of either enzymes or mineral catalyst (Giussani et al., 2019).

Luminol has been used to generate CL via numerous techniques, for instance, by pulsed laser light or optically pumped CL. A dye absorbing red light is generated by a pulsed laser light and this light is capable of oxidizing luminol, thus generating CL (Khan et al., 2014). Luminol and its derivatives have found wide applications in diagnostic and monitoring techniques of non-immunoassay or immunoassays. Isoluminol derivatives have displayed increased efficiency and have been found to be the sole tracers used in substrate-labeled immunoassays (Dodeigne et al., 2000). Luminol has displayed a higher efficiency when its present in the free state. It has found wide applications in enzyme labeled immunoassays, detection of hydrogen peroxide, metal ions, amines, carbohydrates, vitamins, nitrate, enzymes and enzyme substrates, amino acids, cyanides and carbohydrates (Kugimiya and Fukada, 2015). Luminol has also been extensively used as a forensic tool in the form of aerosols by many police agencies in the U.S. for detecting trace blood patterns at crime scenes (Stoica et al., 2016). Luminol reacts with the reactive ROS and emits light via luminol CL (Chen et al., 2004). ROS are produced by defensive cells like macrophages and monocytes that are highly populated in a cancerous environment. Alshetaiwi et al. (2013) successfully demonstrated that luminol administration in tumorous mice allowed early stage imaging of the tumors. Inflammation produces myeloperoxidase (MPO) released by neutrophils and these superoxides react with Luminol emitting luminescence which enables investigation of different stages of inflammation (Tseng and Kung, 2013). Bedouhène et al. (2017) showed that in the presence of horseradish peroxidase, luminol-based CL can be used to detect superoxide anions and hydrogen peroxide. This method can therefore be used to detect ROS production by neutrophils, with high sensitivity. Luminol has also been incorporated within nanoparticles for CL imaging. Xu et al. (2019) recently developed a self-illuminating nanoparticle using an amphiphilic Ce6-luminol-polyethylene glycol (CLP) polymer. The Ce6 (chlorin e6), a photosensitizer, can be excited by the BL from luminol in the presence of excess ROS and myeloperoxidase. This excitation leads to generation of fluorescence and $^1\text{O}_2$ by the Ce6 via bioluminescence resonance energy transfer (BRET), and can be used for detecting inflammation and for tumor photodynamic therapy (PDT) (Xu et al., 2019).

Coelenterazine

Coelenterazine is derived from a protein called coelenterate, which has been synthesized by several methods described elsewhere (Dodeigne et al., 2000). This compound possesses a superoxide anion in its structure, which is responsible for causing coelenterazine to give out CL. Unlike luminol, coelenterazine

does not require any catalyst to trigger CL (Silva et al., 2012). CLA (2-methyl-6-phenyl-3,7-dihydroimidazo[1,2-a]pyrazin-3-one) and specifically MCLA probe (2-methyl-6-(4-methoxyphenyl)-3,7-dihydroimidazo[1,2-a]pyrazin-3-one) which is more efficient are some of the several coelenterazine analogs that have been prepared and used (Dubuisson et al., 2005; Wang et al., 2012; Diaz et al., 2018). In contrast to luminol, MCLA is cell impermeable, and is therefore useful for detection of superoxides outside the cell (Diaz et al., 2018). Besides being widely employed for monitoring of superoxide, coelenterazine and its analogs have found wide applications as prosthetic groups of various photoproteins like mnemiopsin, aequorin, phialidin obelin, and beroverin. Of all the above mentioned photoproteins, aequorin is widely used for measuring intracellular calcium and in immunoassay applications (Nguyen et al., 2018; Feno et al., 2019). Coelenterazine has been used often in cancer imaging. CL produced by coelenterazine are used to estimate the elevated levels of ROS that are produced by cancer cells (Bronsart et al., 2016a). Coelenterazine has also been used to detect and image chronic inflammation associated with conditions like inflammatory bowel disease, as it produces CL upon reaction with ROS associated with inflammation (Bronsart et al., 2016b). Bronsart et al. (2016a) were able to detect chemiluminescence *in vivo* at 3 and 6 days after intravenous administration of coelenterazine in tumorous mice. Wang Y. et al. (2002) successfully combined coelenterazine with a fusion gene construct which enabled real-time imaging of gene expression both in cell culture and animal models.

Peroxyoxalic Acid and Their Derivatives

Peroxyoxalate CL is achieved in the presence of a base catalyst and an appropriate fluorophore by combining hydrogen peroxide with oxalate ester (Dodeigne et al., 2000). Peroxyoxalic acid and their derivatives undergo oxidation in the presence of hydrogen peroxide producing high-energy intermediates which is dioxetanedione. Peroxyoxalate and its derivatives have found wide applications in determining selective fluorophores especially after separation by high performance liquid chromatography (Huertas-Pérez et al., 2016). However, as compared to the previously mentioned compounds, fluorescence is not emitted by the high-energy intermediate itself. Light emission is produced by energy transfer to a fluorescer, which gets excited in a S1 state (Smellie et al., 2017). The oxalate compound and the fluorescent sensitizer can be chosen independently. However, as compared to other chemiluminescent producing compounds, the efficiency of the peroxyoxalic acid and their derivatives are reportedly low. The efficiency of this fluorescent material is higher in organic solvents as compared to aqueous solvent mixtures (Dodeigne et al., 2000).

Another limitation is the observance of high background in peroxyoxalate CL which is produced due to the blending of hydrogen peroxide and peroxyoxalate (Cepas et al., 1995; Romanyuk et al., 2017). This background emission can be suppressed by addition of continuous reagent like *bis*(2,4,6-trichlorophenyl)oxalate (TCPO)-hydrogen peroxide system (Niu et al., 2006). The TCPO system have been used to detect the protein labeled 2-methoxy-2,4-diphenyl-3(2H)-furanone

(MDPF) (Salerno and Daban, 2003). Another disadvantage of this material is the poor stability of the compound in water or aqueous solutions since partial water hydrolysis results in the decomposition by decarboxylation and decarbonylation, limiting its application in diagnostics (Delafresnaye et al., 2019). Peroxyoxalate chemiluminescence (POCL) has also found wide applications in detecting hydrogen peroxide-forming enzymes namely cholesterol oxidase, uricase, xanthine oxidase, glucose oxidase, and choline oxidase (Nozaki and Kawamoto, 2003). It has also been used to eliminate tumor cells, where the CL can be absorbed by photosensitizers accumulating within the tumor, resulting in singlet oxygen generation and subsequent cell death (Romanyuk et al., 2017). POCL-containing nanoparticles have also been studied, which are sensitive to endogenous hydrogen peroxide and can be used to study inflammation, where overproduction of hydrogen peroxide is expected (Lee et al., 2007). Peroxalate loaded nanoparticles injected into the peritoneal cavity demonstrated high specificity and selective imaging of hydrogen peroxide-related inflammatory diseases (Lee et al., 2007). POCL has been used in literature frequently in nanoparticle and hydrogel preparations. Li et al. (2019) developed a POCL nanoparticle – glucose oxidase-doped alginate hydrogel, in order to determine glucose levels in the tumor periphery to study tumor metabolism. Following glucose permeation into the system, it will be oxidized by glucose oxidase to produce H_2O_2 , which will be detected by peroxyoxalate. Following subcutaneous injection of the solution into CT-26 tumor bearing mice, the gel allowed localization of the nanoparticles to provide a high signal-to-noise ratio at the tumor site (Li et al., 2019).

Acridinium Esters

Acridinium esters possess high quantum yields that can be detected in the attomole range (Weeks et al., 1983; Natrajan et al., 2010). In comparison with other materials, simple chemical triggers of acridinium derivatives display quick light emission with their minute size permitting easy labeling protocols of nucleic acids and proteins. Acridinium phenyl esters display greater luminescence than simple alkyl esters (Natrajan et al., 2010). Unlike the other chemiluminescent materials, acridinium do not require a catalyst to produce CL. Hydrogen peroxide and a strong base are sufficient to cause them to produce chemiluminescence (Dodeigne et al., 2000). Another advantage is their ability to exhibit faster light emission with simple chemical triggers (Natrajan et al., 2010). The main disadvantage of this chemiluminescent material is its instability in aqueous medium as the ester bond that is present between the acridinium ring and the phenol undergoes hydrolysis (Brown et al., 2009; Natrajan et al., 2010).

Despite this limitation, acridinium derivatives have found wide applications in immunoassays. Acridinium ester has been successfully used to perform ultrasensitive immunoassays of various proteins and antibodies. tumor markers (a-fetoprotein), thyroid stimulating hormone (TSH) and immunoglobulins (Ma et al., 2017; Min et al., 2018; Chen et al., 2019). Acridinium ester is also able to successfully label strands of DNA to produce DNA probes to emit CL (Komori et al., 2019). In a study, wild-type

p53 was immobilized on the surface of gold-functionalized magnetic nanoparticles. 2',6'-dimethylcarbonylphenyl-10-sulfofropylacridinium-9-carboxylate 4'-NHS ester was mixed with the complementary sequence of wild-type p53. The two samples were mixed and the gold-conjugated magnetic nanoparticles were subsequently separated. CL imaging showed ultrahigh sensitivity and selectivity in detecting the p53 tumor suppressor gene up to a limit of 0.001 ng/mL (Wang L. et al., 2019). Several other applications include estimating thermodynamic affinities of oligonucleotide probes that are bound to simple synthetic as well as complex biological targets and hybridization rate constants (Créton and Jaffe, 2001; Nakazono et al., 2019).

FCLA (3,7-Dihydro-6-[4-[2-[N0 -(5-Fluoresceinyl)thioureido]-Ethoxy]phenyl]- 2-Methylimidazo[1,2-a]pyrazin-3-One Sodium Salt)

FCLA is a highly efficient water soluble chemiluminescent agent (He et al., 2002a). FCLA is an analog belonging to *Cypridina* luciferin that efficiently reacts with superoxide anion (O_2^-) or singlet oxygen (1O_2) that emits luminescence via a dioxytane intermediate (He et al., 2002a). $OH^- + NaOCl + H_2O_2$, a typical reaction system is involved in generating a singlet oxygen which produces emission at about 532 nm (Wang Y. et al., 2002). Researchers have developed a novel method to diagnose superficial tumors by photodynamic diagnosis mediated by CL probe containing FCLA (Wang J. et al., 2002). Wei et al. (2011) utilized FCLA CL to monitor tumor necrosis in response to photodynamic therapy. First the FCLA was injected subcutaneously in mice, and light irradiation was provided after a 1 h. A near linear relationship was observed between the extent of damage from PDT, and the CL (Wei et al., 2011). FCLA CL was also used recently to detect ROS generation following DNA duplex-based photodynamic therapy against retinoblastoma (Wei et al., 2016).

There are several examples in literature of coupling chemiluminescent probes with enhancers such as US. Due to US' ability to penetrate deep within the tissues and remain targeted to a small region, undesirable side effects can be minimized and greater spatial information of the CL molecules can be obtained (He et al., 2002b; Kobayashi and Iwasa, 2018). Ultrasonic irradiation of water results in acoustic cavitation producing $\bullet OH$ and $\bullet H$, which form active oxygen species. These oxygen species react with FCLA producing CL (He et al., 2002b). He and colleagues observed that, when a sonosensitizer (hematoporphyrin derivative) accumulating in tumor tissues was exposed to ultrasound *in vivo*, FCLA reacted with the resulting active oxygen species to emit CL. This CL was stronger from the tumor region in comparison from other regions. He reported that the application of US increased the intensity of chemiluminescence emitted by FCLA (He et al., 2002b; Wei et al., 2016) and it resulted in excellent signal-to-noise ratio of a sonoluminescence image of tumorous mice on subcutaneous injection of FCLA solution (He et al., 2002a).

SECOND GENERATION OF CHEMILUMINESCENCE: ULTRASOUND-ENHANCED CHEMILUMINESCENCE

There are many advantages to using US and CL simultaneously. Since both US and CL are imaging techniques, they can be used for dual imaging in order to accurately visualize the tissue of interest. In addition, US can enhance the intensity of CL by reducing light scattering while increasing spatial resolution. Both of these approaches are described below.

Combination of US and CL for Dual Imaging

In an *in vivo* study by Alhasan et al. (2012) on tumor (luciferase-transfected PC3 cancer cell lines) bearing nude mice, *D*-luciferin-based bioluminescent imaging (BLI), fluorescence imaging and doppler ultrasound imaging techniques were simultaneously and independently conducted. Both BLI and US were able to correctly indicate time-dependent percent reduction in tumor blood flow following the injection of arsenic trioxide (ATO) – a model vascular disrupting agent (Figures 2A,B), and a correlation was obtained (Figure 2C) with $R^2 > 0.77$ (Alhasan et al., 2012). On the other hand, fluorescence imaging did not show any changes in the first 24 h following ATO administration. Jung et al. (2018) developed curcumin-containing antioxidant vanillyl alcohol-incorporated copolyoxalate (PVAX) nanoparticles, which can be simultaneously used for anti-cancer therapy, peroxalate CL, and amplification of ultrasound signals through generation of H_2O_2 triggered CO_2 bubbles at ischemic sites. More recently, Liu et al. (2019) used nanobubbles doped with luminol, 1,1'-Diiodododecyl-3,3',3'-tetramethylindocarbocyanine perchlorate (DiI) and 1,1'-diiodododecyl-3,3',3'-tetramethylindocarbocyanine perchlorate (DiD) dyes for dual BLI and US imaging. The luminol could detect myeloperoxidase activity in areas of inflammation and emit a blue light. By integrating BRET and fluorescence resonance energy transfer (FRET) using the DiI-DiD, the light can be shifted into red light. This method was used in combination with ultrasound imaging to get more information on anatomical structure and vasculature (Liu et al., 2019). This shows that US and BLI are useful tools that may be used independently or simultaneously to obtain important vasculature-related and anatomical information while providing therapy. However, in majority of the cases described in recent literature, US has been chiefly used as a tool for enhancing CL.

Mechanism of UECL

Although CL is widely used in tissue imaging, a chief concern raised in literature is that the scattering light increases noises of the detection. The increase in noises could be explained using the following redox reaction, similar to the Fenton reaction (McMurray and Wilson, 1999):

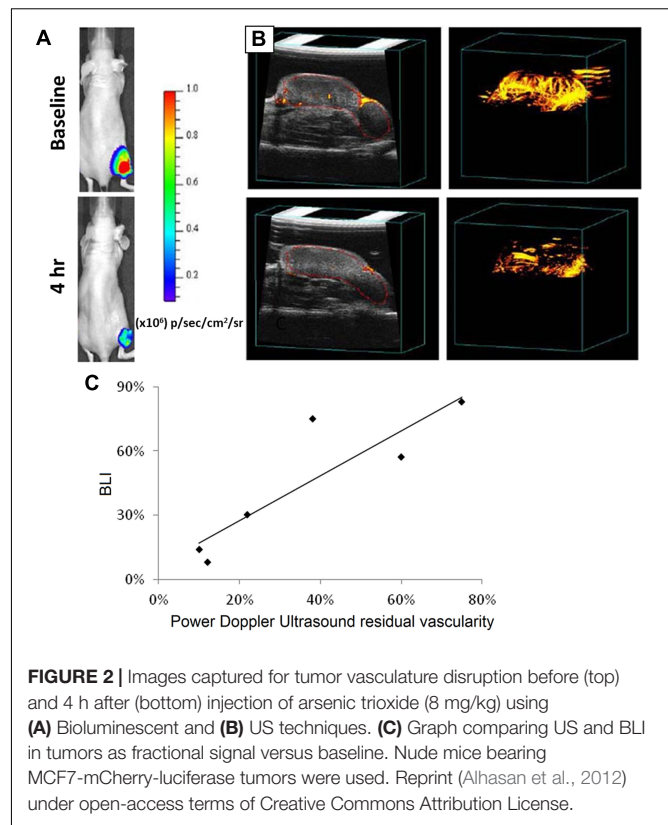
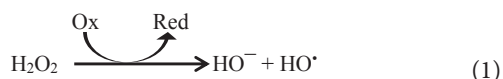


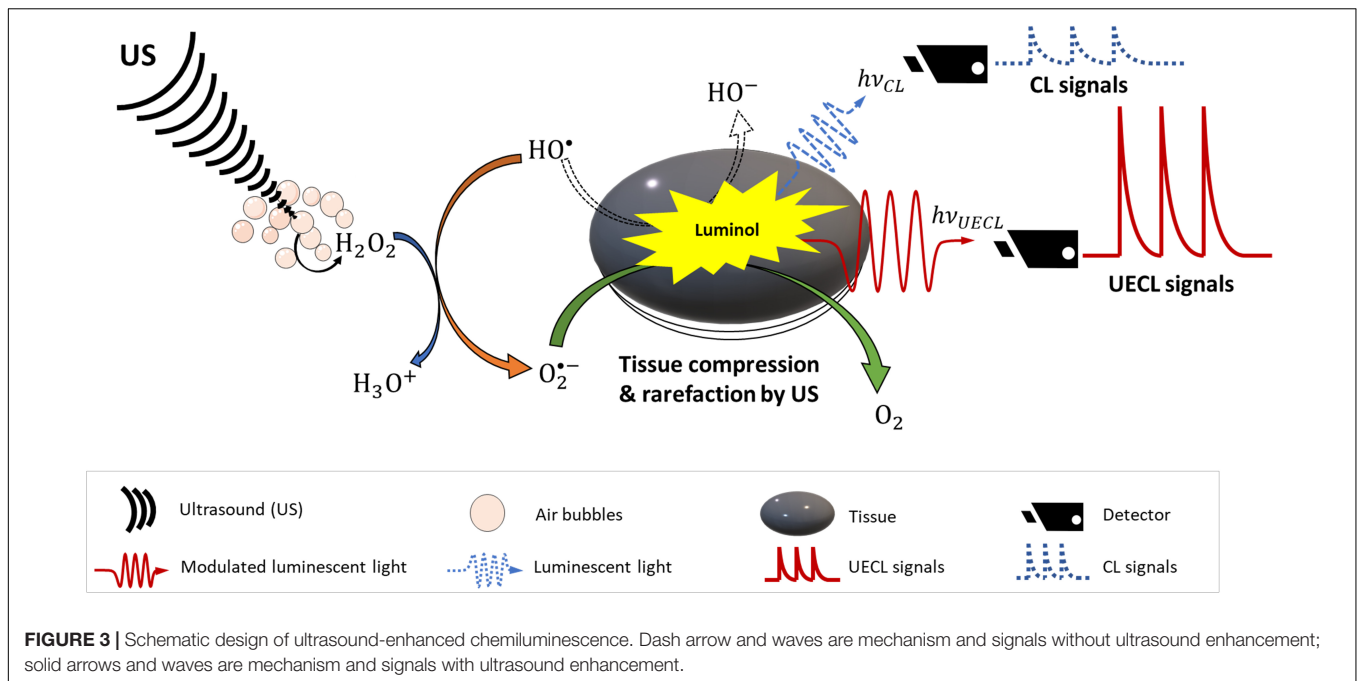
FIGURE 2 | Images captured for tumor vasculature disruption before (top) and 4 h after (bottom) injection of arsenic trioxide (8 mg/kg) using (A) Bioluminescent and (B) US techniques. (C) Graph comparing US and BLI in tumors as fractional signal versus baseline. Nude mice bearing MCF7-mCherry-luciferase tumors were used. Reprint (Alhasan et al., 2012) under open-access terms of Creative Commons Attribution License.

From Eq. (1), it could be interfered that, with the ubiquitous appearance of oxidizing agents in tissues, free HO^\bullet are also commonly produced within tissues. Subsequently, to increase signal to noise ratios, one could reduce the background signals by locally increasing production of H_2O_2 or free HO^\bullet of the target tissue while reducing those amounts in the nearby medium.

The possibility of using US to enhance sensitivity of CL was first discussed two decades ago in a non-tissue mechanistic study by McMurray and Wilson (1999). Although their system was non-tissue, it was proven that the intensity of sonochemiluminescence, I_{SCL} , was linearly increased with the increase of US power up to 100 W. The study was conducted at 10^{-3} M luminol and 10^{-4} M H_2O_2 . McMurray proposed that, at the air-liquid interface of the cavitation bubbles, water and oxygen molecules were freed and more local free radicals were created.



In term of mechanical and physical properties of tissues, it has been shown that focused ultrasound (FUS) creates periodic compression and rarefaction of tissues, which changes refractive indices of tissues locally and allows less optical absorption and scattering (Li and Wang, 2004; Murray et al., 2004). Laser light can also be modulated with frequency of US. It has been discussed in literature that tissues oscillate with US frequency that subsequently produce harmonic interference to



laser light (Li and Wang, 2004; Murray et al., 2004; Jarrett et al., 2014). Meanwhile, a phenomenon called photon-phonon interaction (Kempe et al., 1997; Jarrett et al., 2014) modulates the frequency of the transmitted laser light. Consequently, laser light is modulated to transverse deeper into tissues with less reflection. A detailed schematic of the mechanism of UECL is shown in Figure 3.

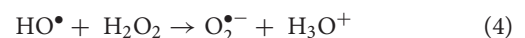
Effects of Ultrasound on Chemiluminescent Signals

Since observing that chemiluminescent signals can be modulated by US, there have been more research conducted to understand this concept. A detail mechanism was proposed (McMurray and Wilson, 1999), who suggested that I_{SCL} was correlated to free radical HO^\bullet concentration, which was confirmed to be linearly proportional to γ -ray pulse radiolytic dose or US power. More interestingly, the authors reported that effective distances were strongly dependent on the alignment of US waves. This means that the more focused the US delivered, the more aligned or less scattered the luminescent light was, and therefore the higher the resolution of the CL signal recorded.

From Figures 4A,B, it can be clearly observed that, with increased focus of US, the CL signals were also correspondingly increased. This result indicates FUS can significantly enhance sensitivity of CL (Figure 4C) by enhancing the distance that the CL laser can travel (Figure 3). The mechanism behind this is unclear; however, it might be due to the fact that the temperature of focal points was increased locally by the US, and it has been noted elsewhere in literature that increases in temperature could increase sensitivity of CL. Aslan et al. (2006) has previously reported

that all red, blue and green CLs were increased up to 75-fold through heating although in this case the heat was introduced by microwaves.

In correlation with the findings by McMurray and Wilson (1999) and Greenway et al. (2006) studied the effects of US power and the distance of US probe from the sample, on CL signals (Figure 5). The signals were reported to be significantly enhanced with the distance of 2–8 mm, and was dependent on the US power (between 60 and 126 W) (Greenway et al., 2006). In agreement with McMurray and Wilson (1999) and Greenway et al. (2006) suggested a mechanism where ultrasonication produces H_2O_2 that subsequently stabilized the short-lived free radicals HO^\bullet as below:



The stabilized $O_2^{\bullet-}$ would then react with luminol and produce increased signals. This mechanism is supported by the fact that CL intensity has been reported to increase in alkaline solutions (McMurray and Wilson, 1999; Miyoshi et al., 2001) where reaction (4) is accelerated to the right and produce more $O_2^{\bullet-}$. Recently, similar mechanism of $O_2^{\bullet-}$ enhancing CL has been proposed by Chen et al. (2014), where quantum dots utilized $O_2^{\bullet-}$ to enhance the signals of CL. For FUS, it is able to control the power and focal point, thus it concretes for the potential of US in enhancing sensitivity of CL.

Recently, researchers have been studying UECLs on tissue environment mimics. Huynh et al. (2013) studied FUS enhancing CLs through a gel tissue phantom as a scattering medium. Using 1 MHz US transducer and creating cavitation pressure 0.42 MPa, the authors detected luminescent objects at depth of 7 mm with 10 times more sensitivity than traditional luminescent methods (Huynh et al., 2013). The resolution was reported at 3 mm. Huynh et al. (2013) also indicated that

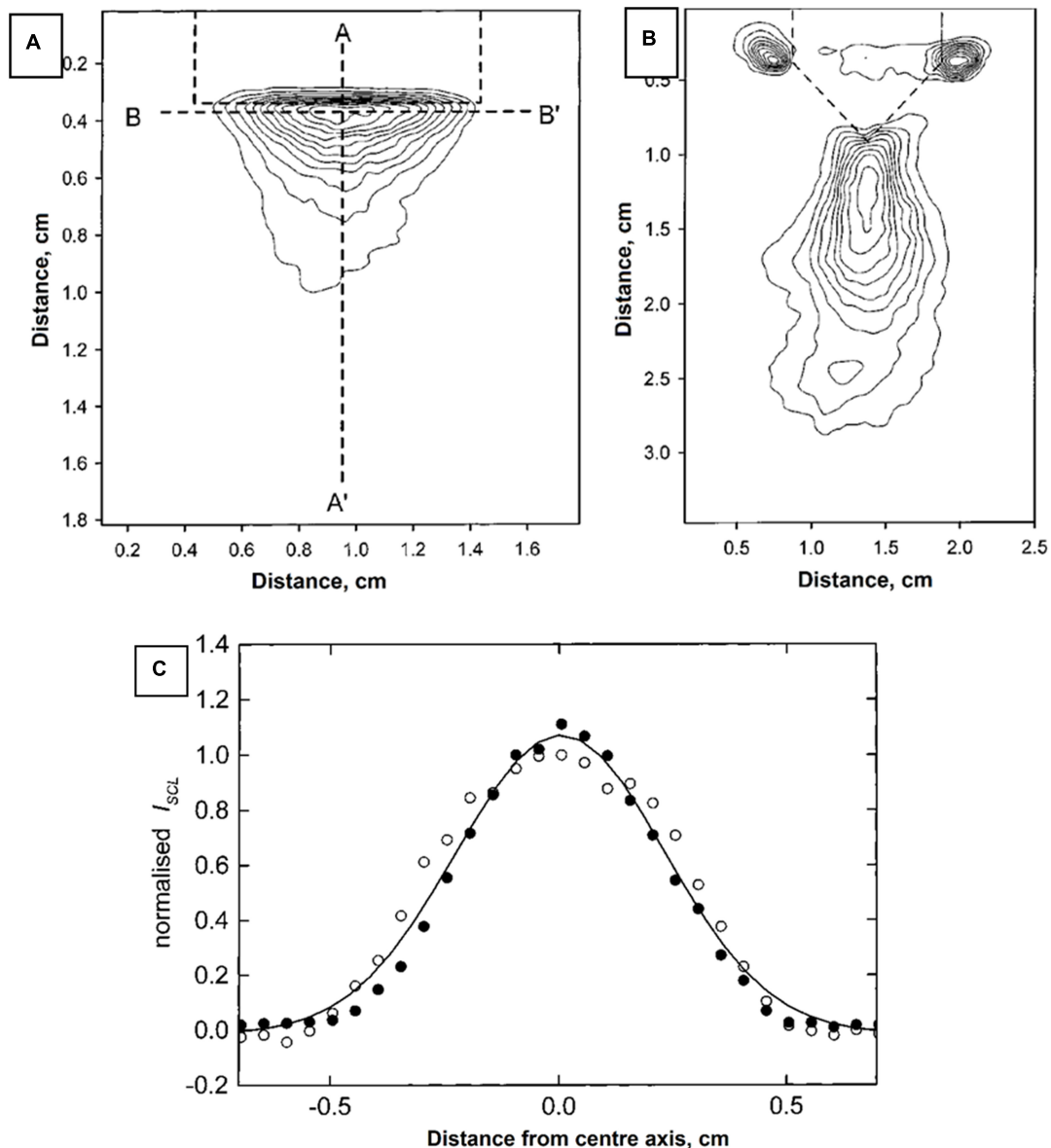


FIGURE 4 | US-dependent luminal CL when using (A) flat and (B) wedge-ended sonoprobe tips. Bell-shape distribution (C) indicated highly penetration of US in supporting CL. Reproduced with permission from McMurray and Wilson (1999).

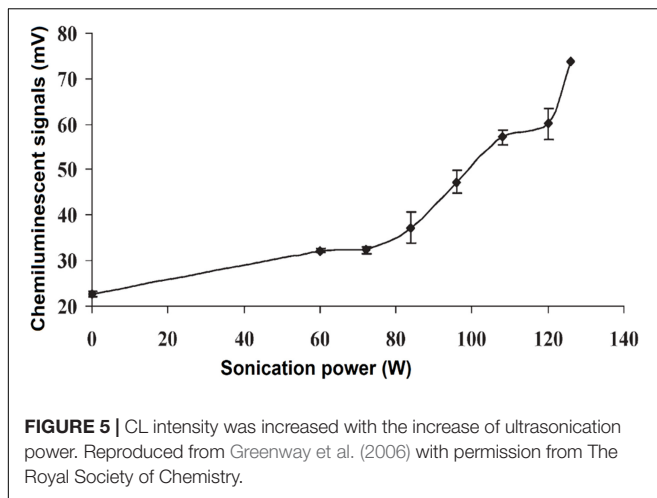
the application of microbubbles, which were FUS contrast agents, could enhance CL. In agreement with this research, Kobayashi et al. (2015) also reported that the sensitivity of POCL was increased along with the increase of inner pressure up to 6 MPa created from FUS. A clear increase and decrease in CL signals were recorded with on and off stimulation of FUS (Figure 6).

We can see from the research reviewed above that theoretical studies and lab bench experiments have proven that US, especially FUS, does have beneficial effects on increasing the sensitivity of CL. However, there is a need for evidence of efficacy on tissue-based systems. For this, scientists have mimicked tissue

microenvironments using turbid medium and *ex vivo* tissues for their studies.

FUS-CL in Turbid Microenvironments

In order to mimic tissue environments, agarose phantom is usually used as it has similar scattering coefficient as that of native tissues following Monte Carlo model (Wang et al., 1995). Since native tissues may vary from species to species, phantoms typically have a scattering coefficient from 1 to 80 cm^{-1} (Kobayashi et al., 2016; Ahmad et al., 2017; Zhu et al., 2018). Through phantoms, transparent silicon tubes were run at different depths. CL solutions passing through the silicon tubes were recorded with or without stimulation of US that is



focused at the center of the tubes. Minimum distance between two tubes that generate non-identical signals are considered as resolution. Schematic design of UECL imaging system is illustrated in **Figure 7**.

Using FUS at different stimulation levels, authors not only observed 10 times higher signal-to-noise ratio (Zhu et al., 2018) for 1064 nm luminescent laser but also increased sensitivity or better spatial resolution. The best resolution was reported at 2 mm (Ahmad et al., 2017; Klein et al., 2018) using 640 nm laser or ^{18}F lasers. The deepest penetration were obtained at 25–30 mm (Kobayashi et al., 2016) recorded on agarose phantom using POCL system. Interestingly, focused US at a low power could enhance POCL using indocyanine green (ICG) as the fluorophore (Kobayashi et al., 2016). In most cases in literature, we can see that the more powerful the FUS, the greater the penetration and resolution. For instance, once FUS was increased from 1 to 2 MHz, signals were 10 times stronger as normalized to background (Klein et al., 2018; Zhu et al.,

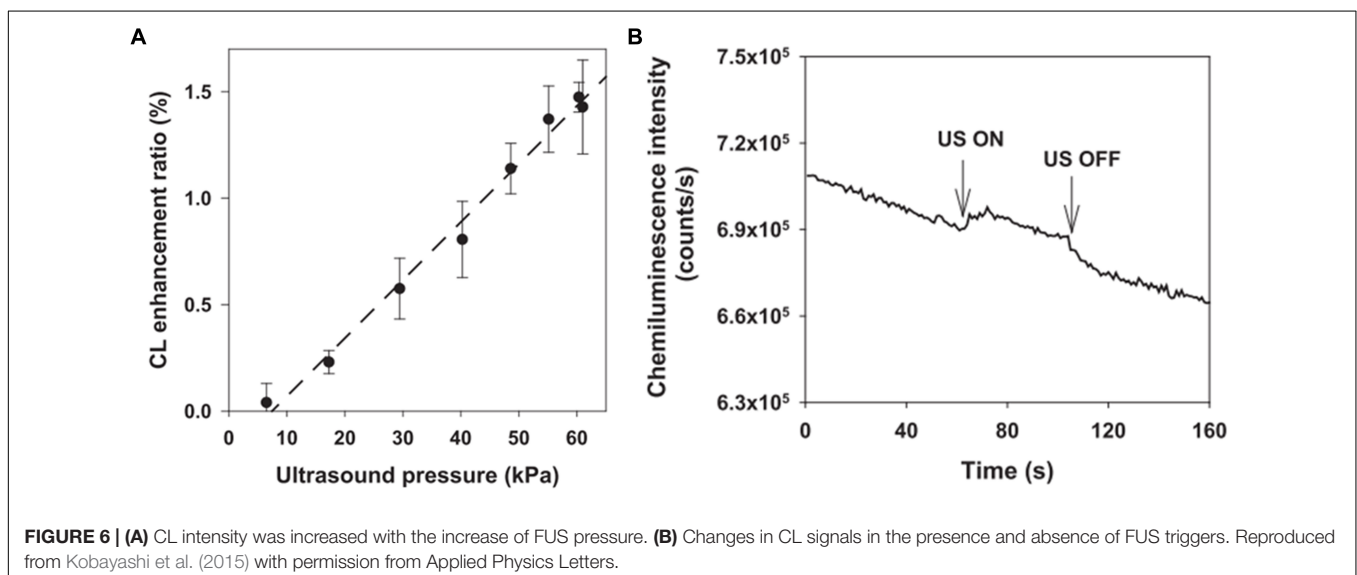
2018) while increasing FUS from 2 to 3 MHz allowed fourfold deeper penetration and 33% better resolution (Ahmad et al., 2017; Zhu et al., 2018).

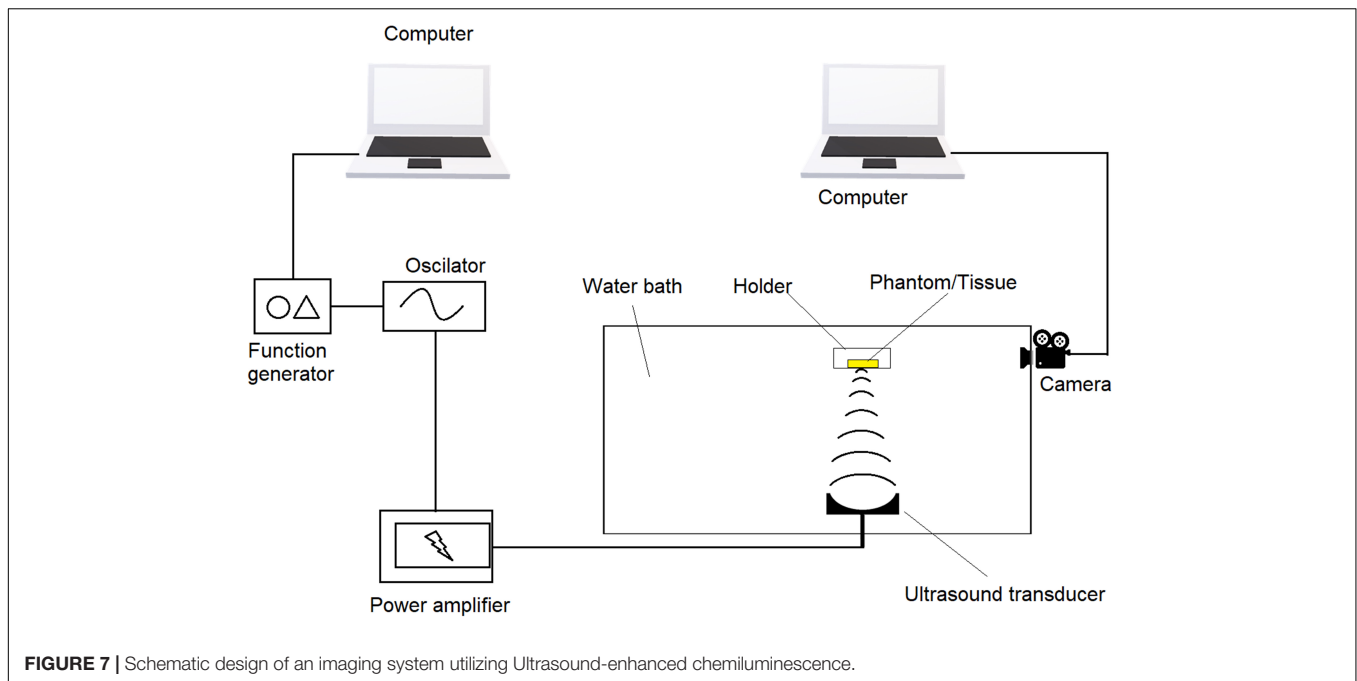
FUS-CL in *ex vivo* Studies

FUS-enhanced CL have also been studied *ex vivo* on dissected tissues and outcomes have been promising. Ahmad et al. (2017) observed clear peaks of two chemiluminescent sources (encapsulated inside plastic tubes) placed at 10 mm distance in chicken breast tissue at depth of 20 mm. Meanwhile, the experiments of Kobayashi et al. (2016) were even more interesting that they reached resolvable signals at a depth of 25 mm (**Figure 8**) in porcine tissues. On the other hand, Dawood (2016) demonstrated that greater penetration depth of lasers [637, 808, or 1064 nm Nd:YAG (Neodymium-doped Yttrium-Aluminum-Garnet (Julian, 2016) laser probes] was achieved through 10 mm bovine tissue with help of FUS (Dawood, 2016) for the fact output intensity was increased by 35–45% while attenuation was decreased 3–10%. The more powerful the FUS, the greater the penetration depth of the laser light in the tissue, without having to increase the laser power (Dawood, 2016). This clearly indicates the potential of US to enhance CL by allowing greater penetration of laser through decreasing their attenuation coefficient while passing through the tissues. To summarize, we can see from literature that US at high power (typically 3 MHz and above or 5 W/cm²) can enhance CL signals and can enable imaging of tissues as deep as 30 mm at a resolution as high as 2 mm. Summary of FUS enhanced CL is provided in **Table 2** above.

CONCLUSION AND FUTURE OUTLOOK

The significant enhancement of CL with the help of US has been proven by theoretical demonstration, using tissue mimics, and by *ex vivo* studies. The enhanced spatial information and reduced light scattering observed when combining ultrasound with CL is promising for deeper imaging of biological tissues. Among all the





mechanisms being studied for CL enhancement using US, the use of US modulated laser light has shown most promise for practical medical imaging. The more focused and powerful the US, the deeper the penetration, and better the resolution CL signals that is obtained. US at 3 MHz or 5 W/cm² and above has given the most enhancement to CL according to literature, as described above. At this setting, tissues have been imaged up to a depth of 30 mm with a good resolution of 2 mm. Additionally, US also has the advantage of providing computational data for data processing, and this may also advance the UECL further (Pei and Wei, 2019).

There are, however, a few drawbacks to this technology. A major cause of concern is the local heat generated by US. The more the focus, the greater the heat generated. Although local heat generated by US enhances intensity and resolution of CL images, generation of heat beyond the endurance of cells and can lead to tissue damage. According to a review of previous literature by Yarmolenko et al. (2011), the threshold damage temperature is 42°C, and cumulative equivalent minutes at 43°C (CEM₄₃) of more than 1 usually causes damage to tissues. To avoid the risks of overheating the tissues under consideration, the exposure duration should be optimized. For example, in a research by Pei et al. (2014), a short HIFU exposure of 0.3 s or 300 ms limited the temperature to below 43°C. According to their calculations, the CEM₄₃ was 0.0013 (Pei et al., 2014). Since primary cells in tissues are vulnerable to heat, and focused UECL is limited in its ability to control local heat, there needs to be detailed investigation into methods to overcome this limitation of FUS so that it can be used broadly without tissue damage.

With the emerging interest in FUS studies and the development of sophisticated technology, UECL is expected to play a greater role in tissue and molecular imaging in the coming years. In the future, we can expect to see more sophisticated formulations involving drug-loaded microbubbles tagged with CL probes, for theranostic applications. The microbubbles can be used not only for imaging but also for delivering therapeutics for treatment. This would mean that under stimulation of US, laser light can be modulated to penetrate deeper into tissues while microbubbles will deliver the therapeutics in response to the US stimuli. In return, the chemiluminescent images may give *in situ* feedback about the delivery process. The electroluminescence upconversion particles, which are already gaining significant attention in recent years, can also be combined with ultrasound to further



FIGURE 8 | (A) Images of an incised porcine muscle tissue in which a CL target capsule consisting of a 0.5 mm silicone tube, was embedded. **(B)** Two-dimensional tomographic image obtained with the slab of porcine muscle. The tissue, measuring 50 mm (X) × 50 mm (Y), had a CL target embedded within it to a depth of 25 mm. Reproduced with permission from Kobayashi et al. (2016).

TABLE 2 | Summary of *ex vivo* and *in vivo* applications of UECL.

Ultrasound type	Power	CL probe	Increased signal ^ξ (folds)	Tested environment	Depth ^ξ	Spatial resolution ^λ	Reference
FUS	2 MHz	Nd:YVO ₄ (Neodymium-doped yttrium orthovanadate) laser with 1064 nm wavelength; Embedding aluminum foil as target	10 less signal-to-noise	Agarose phantom from 20% w/v intralipid. Scattering coefficient 1–4 cm ⁻¹	5 mm	3 mm	Zhu et al., 2018
FUS	3.5 MHz; 1 MPa	640 nm emitting CL probe	~7-folds	Agar phantom from agar and polystyrene microspheres. Scattering coefficient 80 cm ⁻¹	~20 mm	2 mm	Ahmad et al., 2017
FUS	1 MHz; 10 MPa	¹⁸ F, tracking Cerenkov photons	N/A	Agarose phantom containing 250 μM voxels. Scattering coefficient 10 cm ⁻¹	5 mm	2 vs. 6 mm without US	Klein et al., 2018
Low power FUS	< 0.14 W/cm ²	POCL system		Agarose phantom from 10% w/v intralipid, 20% w/v glycerol and 2% w/v agarose; Scattering coefficient 15 cm ⁻¹	25–30 mm	6 mm	Kobayashi et al., 2016
Low power FUS	<0.14 W/cm ²	POCL system	~1.5	Porcine muscle	25 mm		Kobayashi et al., 2016
FUS	3.5 MHz; 1 MPa	640 nm emitting CL probe	~9–11-folds	Chicken breast	~20 mm	10 mm	Ahmad et al., 2017
FUS	3.3 MHz;	637 nm diode, 808 nm diode, and 1064 nm	~1.35–1.45-fold in power output;	Bovine muscles	10 mm		Dawood, 2016
	5 W/cm ²	Nd:YAG lasers	~7–10% decrease in attenuation (637 and 808 nm lasers); ~3% decrease in attenuation (Nd:YAG lasers)				

ξ: larger is better; λ: smaller is better.

enhance their properties for imaging. These particles possess good biocompatibility but low toxicity, high photostability and low photobleaching (Jin et al., 2018; Gu et al., 2019), and they are able to convert near infra-red (NIR) at deep penetration up to 10 mm (Yang et al., 2012; Jin et al., 2018; Gu et al., 2019) into visible radiation. Their photostability plus penetration ability and the aforementioned UECL ability to modulate NIR lasers *ex vivo* could possibly return in synergistic effects. Additionally, a label-free imaging technique called non-linear optical microscopy (NLOM), has been studied for both precision and safety advantages. The principle of label-free non-linear optical microscopy is based on two-photon excited fluorescence (TPEF) from cofactors nicotinamide adenine dinucleotide (NADH) and flavin adenine dinucleotide (FAD⁺) that provides high-resolution cellular redox imaging (Hou et al., 2018). More interestingly, this technique shares the same redox reactions to CL and UECL, therefore the two techniques could possibly image the tissues simultaneously and complement each other. Another technique that could also complement CL and UECL for imaging of shallow tissues is surface-enhanced Raman scattering (SERS). It has been reported that SERS have been successfully applied in small animal *in vivo* diagnostic and cancer detection (Henry et al., 2016). When using nanotags as enhancers, SERS alone or in combination with Spatially offset Raman Spectroscopy (SESOR), could be used to image at different depths [~ 5 mm with SERS (Stone et al., 2010) and 45–50 mm with Sesor (Stone et al., 2011)] on porcine tissues. This combination is therefore expected to provide complementary information to make the imaging more comprehensive.

High intensity focused US, or HIFU, is also attracting more interest from researchers and we can expect to see more research into the use of HIFU combined with CL in the

future. The development of this technology allows scientists to have greater control on the focus and localization, besides controlling the heat generated. Several versions of HIFU, namely ultrasound-guided and MRI-guided HIFU, have been tested preclinically and in pilot studies, for breast cancer, liver cancer, pancreatic cancer (Maloney and Hwang, 2015) and prostate cancer (van Velthoven et al., 2016). MRI-guided HIFU is clinically approved in the European Union for palliative treatment of bone lesions (Maloney and Hwang, 2015). The UECL technique by HIFU therefore has high translational potential. It will significantly enhance physiological imaging of living organisms by providing high resolution images, which will aid in providing accurate diagnosis and therapy in the future.

AUTHOR CONTRIBUTIONS

DL prepared the outline, wrote and edited the manuscript, and prepared figures and tables. DD and AG wrote the manuscript, and prepared figures and tables. JM edited and revised the manuscript. All authors approved the manuscript for publication.

ACKNOWLEDGMENTS

We gratefully acknowledge funding support from the Rhode Island Institutional Development Award (IDeA) Network of Biomedical Research Excellence from the National Institute of General Medical Sciences of the National Institutes of Health under grant number P20GM103430.

REFERENCES

- Ahmad, J., Jayet, B., Hill, P. J., Mather, M. L., Dehghani, H., and Morgan, S. P. (2017). "Ultrasound modulation of bioluminescence generated inside a turbid medium," in *SPIE 10064, Photons Plus Ultrasound: Imaging and Sensing*, eds A. A. Oraevsky, and L. V. Wang, (San Francisco, CA: International Society for Optics and Photonics), doi: 10.1117/12.2251349
- Alhasan, M. K., Liu, L., Lewis, M. A., Magnusson, J., and Mason, R. P. (2012). Comparison of optical and power doppler ultrasound imaging for non-invasive evaluation of arsenic trioxide as a vascular disrupting agent in tumors. *PLoS One* 7:e46106. doi: 10.1371/journal.pone.0046106
- Alshetia, H. S., Balivada, S., Shrestha, T. B., Pyle, M., Basel, M. T., Bossmann, S. H., et al. (2013). Luminol-based bioluminescence imaging of mouse mammary tumors. *J. Photochem. Photobiol. B Biol.* 127, 223–228. doi: 10.1016/j.jphotobiol.2013.08.017
- Appel, A. A., Anastasio, M. A., Larson, J. C., and Brey, E. M. (2013). Imaging challenges in biomaterials and tissue engineering. *Biomaterials* 34, 6615–6630. doi: 10.1016/j.biomaterials.2013.05.033
- Aslan, K., and Geddes, C. D. (2009). Metal-enhanced chemiluminescence: advanced chemiluminescence concepts for the 21st century. *Chem. Soc. Rev.* 38, 2556–2564. doi: 10.1039/b807498b
- Aslan, K., Malyn, S. N., and Geddes, C. D. (2006). Multicolor microwave-triggered metal-enhanced chemiluminescence. *J. Am. Chem. Soc.* 128, 13372–13373. doi: 10.1021/ja065571r
- Bedouhène, S., Mouti-Mati, F., Hurtado-Nedelec, M., Dang, P. M.-C., and El-Benna, J. (2017). Luminol-amplified chemiluminescence detects mainly superoxide anion produced by human neutrophils. *Am. J. Blood Res.* 7, 41–48.
- Bronsart, L. L., Stokes, C., and Contag, C. H. (2016a). Multimodality imaging of cancer superoxide anion using the small molecule coelenterazine. *Mol. Imaging Biol.* 18, 166–171. doi: 10.1007/s11307-015-0896-897
- Bronsart, L., Nguyen, L., Habtezion, A., and Contag, C. (2016b). Reactive oxygen species imaging in a mouse model of inflammatory bowel disease. *Mol. Imaging Biol.* 18, 473–478. doi: 10.1007/s11307-016-0934-930
- Brown, J. E., De Weer, P., and Salzberg, B. M. (2019). Optical measurement of changes in intracellular calcium. *Biophys. J.* doi: 10.1016/j.bpj.2019.06.034 [Epub ahead of print].
- Brown, R., Li, Z., Rutter, A., Mu, X., Weeks, O., Smith, K., et al. (2009). Development and application of a novel acridinium ester for use as a chemiluminescent emitter in nucleic acid hybridisation assays using chemiluminescence quenching. *Org. Biomol. Chem.* 7, 386–394. doi: 10.1039/b811947c
- Cepas, J., Silva, M., and Pérez-Bendito, D. (1995). Evaluation of peroxyoxalate chemiluminescence for the sensitive determination of hallucinogenic alkaloids. *Anal. Chim. Acta* 314, 87–94. doi: 10.1016/0003-2670(95)00257-Z
- Chen, C., Guo, X., Liang, H., Ning, B., Li, J., Zhong, S., et al. (2019). Determination of parvovirus antibodies in canine serum using magnetic bead-based chemiluminescence immunoassay. *Biotechnol. Appl. Biochem.* 66, 586–590. doi: 10.1002/bab.1758
- Chen, H., Gao, F., He, R., and Cui, D. (2007). Chemiluminescence of luminol catalyzed by silver nanoparticles. *J. Colloid Interface Sci.* 315, 158–163. doi: 10.1016/j.jcis.2007.06.052
- Chen, H., Lin, L., Li, H., and Lin, J.-M. (2014). Quantum dots-enhanced chemiluminescence: mechanism and application. *Coord. Chem. Rev.* 26, 86–100. doi: 10.1016/j.ccr.2013.07.013

- Chen, W.-T., Tung, C.-H., and Weissleder, R. (2004). Imaging reactive oxygen species in arthritis. *Mol. Imaging* 3:15353500200404124. doi: 10.1162/15353500200404124
- Contag, C. H., and Ross, B. D. (2002). It's not just about anatomy: in vivo bioluminescence imaging as an eyepiece into biology. *J. Magn. Reson. Imaging* 16, 378–387. doi: 10.1002/jmri.10178
- Créton, R., and Jaffé, L. F. (2001). Chemiluminescence microscopy as a tool in biomedical research. *Biotechniques* 31, 1098–1105. doi: 10.2144/01315rv01
- Dawood, M. S. (2016). The effects of ultrasound and alternating current on the laser penetration in the tissue. *Lasers Med. Sci.* 31, 955–964. doi: 10.1007/s10103-016-1937-4
- Delafresnaye, L., Bloesser, F. R., Kockler, K. B., Schmitt, C. W., Irshadeen, I. M., and Barner-Kowollik, C. (2019). All eyes on visible light peroxyoxalate chemiluminescence read-out systems. *Chem. A Eur. J.* 26, 114–127. doi: 10.1002/chem.201904054
- Diaz, J. M., Plummer, S., Tomas, C., and Alves-de-Souza, C. (2018). Production of extracellular superoxide and hydrogen peroxide by five marine species of harmful bloom-forming algae. *J. Plankton Res.* 40, 667–677. doi: 10.1093/plankt/fby043
- Dodeigne, C., Thunus, L., and Lejeune, R. (2000). Chemiluminescence as diagnostic tool. A review. *Talanta* 51, 415–439. doi: 10.1016/S0039-9140(99)00294-295
- Dubuisson, M. L. N., Rees, J.-F., and Marchand-Brynaert, J. (2005). Coelenterazine (Marine Bioluminescent Substrate): a source of inspiration for the discovery of novel antioxidants. *Drug Dev. Ind. Pharm.* 31, 827–849. doi: 10.1080/03639040500271803
- Feno, S., Di Marco, G., De Mario, A., Monticelli, H., and Reane, D. V. (2019). “High-throughput screening using photoluminescence probe to measure intracellular calcium levels,” in *Calcium Signalling: Methods and Protocols*, eds A. Raffaello, and D. Vecellio Reane, (New York, NY: Springer New York), 1–14. doi: 10.1007/978-1-4939-9018-4_1
- Gao, N., Ling, B., Gao, Z., Wang, L., and Chen, H. (2017). Near-infrared-emitting NaYF₄:Yb,Tm/Mn upconverting nanoparticle/gold nanorod electrochemiluminescence resonance energy transfer system for sensitive prostate-specific antigen detection. *Anal. Bioanal. Chem.* 409, 2675–2683. doi: 10.1007/s00216-017-0212-212
- Giussani, A., Farahani, P., Martínez-Muñoz, D., Lundberg, M., Lindh, R., and Roca-Sanjuán, D. (2019). Molecular basis of the chemiluminescence mechanism of luminol. *Chem. A Eur. J.* 25, 5202–5213. doi: 10.1002/chem.201805918
- Greenway, G. M., Leelasattarakul, T., Liawruangrath, S., Wheatley, R. A., and Youngvises, N. (2006). Ultrasound-enhanced flow injection chemiluminescence for determination of hydrogen peroxide. *Analyst* 131, 501–508. doi: 10.1039/B513735G
- Gu, Y., Wang, J., Shi, H., Pan, M., Liu, B., Fang, G., et al. (2019). Electrochemiluminescence sensor based on upconversion nanoparticles and oligoaniline-crosslinked gold nanoparticles imprinting recognition sites for the determination of dopamine. *Biosens. Bioelectron.* 128, 129–136. doi: 10.1016/j.bios.2018.12.043
- Haghighi, B., and Bozorgzadeh, S. (2010). Flow injection chemiluminescence determination of isoniazid using luminol and silver nanoparticles. *Microchem. J.* 95, 192–197. doi: 10.1016/j.microc.2009.11.012
- He, Y., Xing, D., Tan, S., Tang, Y., and Ueda, K. (2002a). In vivo sonoluminescence imaging with the assistance of FCLA. *Phys. Med. Biol.* 47, 1535–1541. doi: 10.1088/0031-9155/47/9/308
- He, Y., Xing, D., Yan, G., and Ueda, K. (2002b). FCLA chemiluminescence from sonodynamic action in vitro and in vivo. *Cancer Lett.* 182, 141–145. doi: 10.1016/S0304-3835(02)00070-78
- Henry, A.-I., Sharma, B., Cardinal, M. F., Kurouski, D., and Van Duyne, R. P. (2016). Surface-enhanced Raman spectroscopy biosensing: in vivo diagnostics and multimodal imaging. *Anal. Chem.* 88, 6638–6647. doi: 10.1021/acs.analchem.6b01597
- Hou, J., Williams, J., Botvinick, E. L., Potma, E. O., and Tromberg, B. J. (2018). Visualization of breast cancer metabolism using multimodal nonlinear optical microscopy of cellular lipids and redox state. *Cancer Res.* 78, 2503–2512. doi: 10.1158/0008-5472.CAN-17-2618
- Huertas-Pérez, J. F., Moreno-González, D., Airado-Rodríguez, D., Lara, F. J., and García-Campaña, A. M. (2016). Advances in the application of chemiluminescence detection in liquid chromatography. *TrAC Trends Anal. Chem.* 75, 35–48. doi: 10.1016/j.trac.2015.07.004
- Huynh, N. T., Hayes-Gill, B. R., Zhang, F., and Morgan, S. P. (2013). Ultrasound modulated imaging of luminescence generated within a scattering medium. *J. Biomed. Opt.* 18, 20505. doi: 10.1117/1.Jbo.18.2.020505
- Jancinová, V., Nosal, R., Payer, J., and Killinger, Z. (2017). Increased intracellular and extracellular oxidant production in phagocytes of rheumatic patients treated with biological therapy - Whole blood quantification. *Interdiscip. Toxicol.* 10, 52–55. doi: 10.1515/intox-2017-2018
- Jarrett, C. W. W., Caskey, C. F. F., and Gore, J. C. C. (2014). Detection of a novel mechanism of acousto-optic modulation of incoherent light. *PLoS One* 9:e104268. doi: 10.1371/journal.pone.0104268
- Jin, X., Fang, G., Pan, M., Yang, Y., Bai, X., and Wang, S. (2018). A molecularly imprinted electrochemiluminescence sensor based on upconversion nanoparticles enhanced by electrodeposited rGO for selective and ultrasensitive detection of clenbuterol. *Biosens. Bioelectron.* 102, 357–364. doi: 10.1016/J.BIOS.2017.11.016
- Julian, J. (2016). “7 - lasers in implant dentistry,” in *Principles and Practice of Laser Dentistry*, eds R. A. Convissar, (St. Louis: Mosby), 107–130. doi: 10.1016/B978-0-323-29762-2.00007-3
- Jung, E., Noh, J., Kang, C., Yoo, D., Song, C., and Lee, D. (2018). Ultrasound imaging and on-demand therapy of peripheral arterial diseases using H₂O₂-Activated bubble generating anti-inflammatory polymer particles. *Biomaterials* 179, 175–185. doi: 10.1016/J.BIOMATERIALS.2018.07.003
- Kempe, M., Larionov, M., Zaslavsky, D., and Genack, A. Z. (1997). Acousto-optic tomography with multiply scattered light. *J. Opt. Soc. Am. A* 14:1151. doi: 10.1364/JOSAA.14.001151
- Khan, P., Idrees, D., Moxley, M. A., Corbett, J. A., Ahmad, F., von Figura, G., et al. (2014). Luminol-based chemiluminescent signals: clinical and non-clinical application and future uses. *Appl. Biochem. Biotechnol.* 173, 333–355. doi: 10.1007/s12010-014-0850-851
- Kim, J. E., Kalimuthu, S., and Ahn, B.-C. (2015). In vivo cell tracking with bioluminescence imaging. *Nucl. Med. Mol. Imaging* 49, 3–10. doi: 10.1007/s13139-014-0309-x
- Klein, J. S., Mitchell, G. S., Stephens, D. N., and Cherry, S. R. (2018). Theoretical investigation of ultrasound-modulated Cerenkov luminescence imaging for higher-resolution imaging in turbid media. *Opt. Lett.* 43:3509. doi: 10.1364/OL.43.003509
- Kobayashi, M., and Iwasa, T. (2018). Ultrasound-tagged chemiluminescence tomography in Turbid media. in cleo pacific rim conference 2018 osa technical digest. (Hong Kong: Optical Society of America). W2K 4:45. doi: 10.1364/CLEOPR.2018.W2K.4
- Kobayashi, M., Kikuchi, N., and Sato, A. (2015). Optical tomography of fluorophores in dense scattering media based on ultrasound-enhanced chemiluminescence. *Appl. Phys. Lett.* 106:21103. doi: 10.1063/1.4905660
- Kobayashi, M., Kikuchi, N., and Sato, A. (2016). Ultrasound-enhanced chemiluminescence tomography in biological tissue. *Ultrason. Sonochem.* 31, 1–6. doi: 10.1016/J.ULTSONCH.2015.11.027
- Komori, M., Komiya, K., Shirakawa, T., Morikawa, T. J., and Yoshimura, T. (2019). Measurement of microRNA with isothermal DNA amplification on fully automated immunoassay analyzers. *Anal. Bioanal. Chem.* 411, 3789–3800. doi: 10.1007/s00216-019-01878-z
- Kugimiya, A., and Fukada, R. (2015). Chemiluminescence detection of Serine, Proline, Glycine, Asparagine, Leucine, and Histidine by using corresponding Aminoacyl-tRNA synthetases as recognition elements. *Appl. Biochem. Biotechnol.* 176, 1195–1202. doi: 10.1007/s12010-015-1639-1636
- Kwon, M., Jang, G., Bilby, D., Milián-Medina, B., Gierschner, J., Lee, T., et al. (2014). Design principles of Chemiluminescence (CL) chemodosimeter for self-signaling detection: luminol protective approach. *RSC Adv.* 4, 46488–46493. doi: 10.1039/C4RA08182J
- Lee, D., Khaja, S., Velasquez-Castano, J. C., Dasari, M., Sun, C., Petros, J., et al. (2007). In vivo imaging of hydrogen peroxide with chemiluminescent nanoparticles. *Nat. Mater.* 6:765. doi: 10.1038/nmat1983
- Lee, J.-J., White, A. G., Rice, D. R., and Smith, B. D. (2013). In vivo imaging using polymeric nanoparticles stained with near-infrared chemiluminescent and fluorescent squaraine catenane endoperoxide. *Chem. Commun.* 49, 3016–3018. doi: 10.1039/C3CC40630J

- Li, J., and Wang, L. V. (2004). Ultrasound-modulated optical computed tomography of biological tissues. *Appl. Phys. Lett.* 84, 1597–1599. doi: 10.1063/1.1651330
- Li, S., Li, X., Xu, J., and Wei, X. (2008). Flow-injection chemiluminescence determination of polyphenols using luminol–NaIO₄–gold nanoparticles system. *Talanta* 75, 32–37. doi: 10.1016/j.talanta.2007.10.001
- Li, W., Zhang, Q., Zhou, H., Chen, J., Li, Y., Zhang, C., et al. (2015). Chemiluminescence detection of a protein through the aptamer-controlled catalysis of a porphyrin probe. *Anal. Chem.* 87, 8336–8341. doi: 10.1021/acs.analchem.5b01511
- Li, X., Yang, X., Yuwen, L., Yang, W., Weng, L., Teng, Z., et al. (2016). Evaluation of toxic effects of CdTe quantum dots on the reproductive system in adult male mice. *Biomaterials* 96, 24–32. doi: 10.1016/j.biomaterials.2016.04.014
- Li, Z., Zhu, B., Duan, X., and Tang, W. (2019). The imaging of local glucose levels in tumor periphery via peroxyoxalate chemiluminescent nanoparticle–glucose oxidase–doped alginate hydrogel. *Anal. Methods* 11, 2763–2768. doi: 10.1039/c9ay00625g
- Ling, K., Jiang, H., Huang, X., Li, Y., Lin, J., and Li, F.-R. (2018). Direct chemiluminescence detection of circulating microRNAs in serum samples using a single-strand specific nuclease-distinguishing nucleic acid hybrid system. *Chem. Commun.* 54, 1909–1912. doi: 10.1039/c7cc09087k
- Lippert, R. A. (2017). Unlocking the Potential of Chemiluminescence Imaging. *ACS Cent. Sci.* 3, 269–271. doi: 10.1021/acscentsci.7b00107
- Liu, M., Ye, Y., Yao, C., Zhao, W., and Huang, X. (2014). Mn²⁺-doped NaYF₄:Yb/Er upconversion nanoparticles with amplified electrogenerated chemiluminescence for tumor biomarker detection. *J. Mater. Chem. B* 2, 6626–6633. doi: 10.1039/C4TB00717D
- Liu, R., Tang, J., Xu, Y., and Dai, Z. (2019). Bioluminescence Imaging of Inflammation in Vivo Based on Bioluminescence and Fluorescence Resonance Energy Transfer Using Nanobubble Ultrasound Contrast Agent. *ACS Nano* 13, 5124–5132. doi: 10.1021/acsnano.8b08359
- Ma, T., Zhang, M., Wan, Y., Cui, Y., and Ma, L. (2017). Preparation of an Acridinium Ester-Labeled antibody and its application in GoldMag nanoparticle-based, ultrasensitive Chemiluminescence immunoassay for the detection of human Epididymis Protein 4. *Micromachines* 8:149. doi: 10.3390/mi8050149
- Maloney, E., and Hwang, J. H. (2015). Emerging HIFU applications in cancer therapy. *Int. J. Hyperth.* 31, 302–309. doi: 10.3109/02656736.2014.969789
- Mao, Y., Wang, N., Yu, F., Yu, S., Liu, L., Tian, Y., et al. (2019). Simultaneous detection of carcinoembryonic antigen and neuron specific enolase in human serum based on time-resolved chemiluminescence immunoassay. *Analyst* 144, 4813–4819. doi: 10.1039/c9an00910h
- Marques, S. M., and Esteves da Silva, J. C. G. (2009). Firefly bioluminescence: a mechanistic approach of luciferase catalyzed reactions. *IUBMB Life* 61, 6–17. doi: 10.1002/iub.134
- Maynard, R. L. (1997). The Merck Index: 12th edition 1996. *Occup. Environ. Med.* 54:288. doi: 10.1136/oem.54.4.288
- McCapra, F. (1990). Chemiluminescence and bioluminescence. *J. Photochem. Photobiol. A Chem.* 51, 21–28. doi: 10.1016/1010-6030(90)87037-C
- McMurray, H. N., and Wilson, B. P. (1999). Mechanistic and spatial study of ultrasonically induced luminol chemiluminescence. *J. Phys. Chem. A* 103, 3955–3962. doi: 10.1021/jp984503r
- Min, X., Fu, D., Zhang, J., Zeng, J., Weng, Z., Chen, W., et al. (2018). An automated microfluidic chemiluminescence immunoassay platform for quantitative detection of biomarkers. *Biomed. Microdevices* 20:91. doi: 10.1007/s10544-018-0331-3
- Miwa, S., and Otsuka, T. (2017). Practical use of imaging technique for management of bone and soft tissue tumors. *J. Orthop. Sci.* 22, 391–400. doi: 10.1016/j.jos.2017.01.006
- Miyoshi, N., Hatanaka, S., Yasui, K., Mitome, H., and Fukuda, M. (2001). Effects of pH and surfactant on the ultrasound-induced chemiluminescence of luminol. *Jpn. J. Appl. Phys.* 40, 4097–4100. doi: 10.1143/jjap.40.4097
- Mu, X. (2005). *Synthesis of Novel Chemiluminescent Compounds*. Wales: Swansea University.
- Murray, T. W., Sui, L., Maguluri, G., Roy, R. A., Nieva, A., Blonigen, F., et al. (2004). Detection of ultrasound-modulated photons in diffuse media using the photorefractive effect. *Opt. Lett.* 29, 2509–2511. doi: 10.1364/OL.29.002509
- Nakazono, M., Nanbu, S., Akita, T., and Hamase, K. (2019). Synthesis, chemiluminescence, and application of 2,4-disubstituted phenyl 10-methyl-10λ,4-acridine-9-carboxylates. *Dye. Pigment.* 170:107628. doi: 10.1016/j.dyepig.2019.107628
- Nam, S. Y., Ricles, L. M., Suggs, L. J., and Emelianov, S. Y. (2014). Imaging strategies for tissue engineering applications. *Tissue Eng. Part B Rev.* 21, 88–102. doi: 10.1089/ten.TEB.2014.0180
- Natrajan, A., Sharpe, D., Costello, J., and Jiang, Q. (2010). Enhanced immunoassay sensitivity using chemiluminescent acridinium esters with increased light output. *Anal. Biochem.* 406, 204–213. doi: 10.1016/j.ab.2010.07.025
- Nguyen, H. T. H., Bouteau, F., Mazars, C., Kuse, M., and Kawano, T. (2018). The involvement of calmodulin and protein kinases in the upstream of cytosolic and nuclear calcium signaling induced by hyposmotic shock in tobacco cells. *Plant Signal. Behav.* 13:e1494467. doi: 10.1080/15592324.2018.1494467
- Nishihara, R., Hoshino, E., Kakudate, Y., Kishigami, S., Iwasawa, N., Sasaki, S., et al. (2018). Azide- and dye-conjugated coelenterazine analogues for a multiplex molecular imaging platform. *Bioconjug. Chem.* 29, 1922–1931. doi: 10.1021/acs.bioconjchem.8b00188
- Niu, W., Feng, N., Nie, F., and Lu, J. (2006). Investigating the post-chemiluminescence behavior of phenothiazine medications in the luminol–potassium ferricyanide system: molecular imprinting–post-chemiluminescence method for the determination of chlorpromazine hydrochloride. *Anal. Bioanal. Chem.* 385, 153–160. doi: 10.1007/s00216-006-0365-x
- Nomura, N., Nishihara, R., Nakajima, T., Bae Kim, S., Iwasawa, N., Hiruta, Y., et al. (2019). Biorthol-activatable bioluminescent coelenterazine derivative for molecular imaging in vitro and in vivo. *Anal. Chem.* 91, 9546–9553. doi: 10.1021/acs.analchem.9b00694
- Nozaki, O., and Kawamoto, H. (2003). Reactivation of inactivated horseradish peroxidase with ethyleneurea and allantoin for determination of hydrogen peroxide by micro-flow injection horseradish peroxidase-catalyzed chemiluminescence. *Anal. Chim. Acta* 495, 233–238. doi: 10.1016/S0003-2670(03)00899-897
- Pei, Y., and Wei, M.-Y. (2019). Newly-engineered materials for bio-imaging technology: a focus on the hybrid system of ultrasound and fluorescence. *Front. Bioeng. Biotechnol.* 7:88. doi: 10.3389/fbioe.2019.00088
- Pei, Y., Wei, M.-Y., Cheng, B., Liu, Y., Xie, Z., Nguyen, K., et al. (2014). High resolution imaging beyond the acoustic diffraction limit in deep tissue via ultrasound-switchable NIR fluorescence. *Sci. Rep.* 4:4690. doi: 10.1038/srep04690
- Pysz, M. A., Gambhir, S. S., and Willmann, J. K. (2010). Molecular imaging: current status and emerging strategies. *Clin. Radiol.* 65, 500–516. doi: 10.1016/j.crad.2010.03.011
- Qi, Y., Xiu, F., and Weng, Q. (2018). A novel and convenient chemiluminescence sensing of DNA: nanometer interface effect and DNA action mechanism. *Sensors Actuators B Chem.* 260, 303–310. doi: 10.1016/j.snb.2018.01.014
- Qin, Y., Xing, D., Luo, S., Zhou, J., Zhong, X., and Chen, Q. (2005). Feasibility of using Fluoresceinyl Cypridina luciferin analog in a novel chemiluminescence method for real-time photodynamic therapy dosimetry. *Photochem. Photobiol.* 81, 1534–1538. doi: 10.1562/2005-05-20-RA-536
- Roda, A., Guardigli, M., Michelini, E., Mirasoli, M., and Pasini, P. (2003a). Peer reviewed: analytical bioluminescence and chemiluminescence. *Anal. Chem.* 75, 462A–470A.
- Roda, A., Guardigli, M., Pasini, P., and Mirasoli, M. (2003b). Bioluminescence and chemiluminescence in drug screening. *Anal. Bioanal. Chem.* 377, 826–833. doi: 10.1007/s00216-003-2096-6
- Roda, A., Musiani, M., Pasini, P., Baraldini, M., and Crabtree, J. E. (2000a). In situ hybridization and immunohistochemistry with enzyme-triggered chemiluminescent probes. *Methods Enzymol.* 305, 577–590. doi: 10.1016/s0076-6879(00)05514-2
- Roda, A., Pasini, P., Musiani, M., and Baraldini, M. (2000b). Chemiluminescence imaging systems for the analysis of macrosamples: Microtiter format, blot membrane, and whole organs. *Methods Enzymol.* 305, 120–132. doi: 10.1016/s0076-6879(00)05482-3
- Roda, A., Pasini, P., Musiani, M., Girotti, S., Baraldini, M., Carrea, G., et al. (1996). Chemiluminescent low-light imaging of biospecific reactions on macro- and microsamples using a videocamera-based luminograph. *Anal. Chem.* 68, 1073–1080. doi: 10.1021/ac951062o

- Romanyuk, A. V., Grozdova, I. D., Ezhov, A. A., and Melik-Nubarov, N. S. (2017). Peroxyoxalate chemiluminescent reaction as a tool for elimination of tumour cells Under Oxidative stress. *Sci. Rep.* 7:3410. doi: 10.1038/s41598-017-03527-w
- Ron, H. (2006). A toxicologic review of quantum dots: toxicity depends on physicochemical and environmental factors. *Environ. Health Perspect.* 114, 165–172. doi: 10.1289/ehp.8284
- Sala-Newby, G. B., Badminton, M. N., Evans, W. H., George, C. H., Jones, H. E., Kendall, J. M., et al. (2000). Targeted bioluminescent indicators in living cells. *Methods Enzymol.* 305, 479–498.
- Salerno, D., and Daban, J.-R. (2003). Comparative study of different fluorescent dyes for the detection of proteins on membranes using the peroxyoxalate chemiluminescent reaction. *J. Chromatogr. B* 793, 75–81. doi: 10.1016/S1570-0232(03)00365-369
- Silva, R., Agustini, B., da Silva, A. L., and Frigeri, H. (2012). Luminol in the forensic science. *J. Biotechnol. Biodivers.* 3, 172–177. doi: 10.20873/jbb.uft.cemaf.v3n4.rogiskisilva
- Smellie, I. A., Aldred, J. K. D., Bower, B., Cochrane, A., Macfarlane, L., McCarron, H. B., et al. (2017). Alternative hydrogen peroxide sources for peroxyoxalate “glowstick” chemiluminescence demonstrations. *J. Chem. Educ.* 94, 112–114. doi: 10.1021/acs.jchemed.6b00536
- Song, H., Su, Y., Zhang, L., and Lv, Y. (2019). Quantum dots-based chemiluminescence probes: an overview. *Luminescence* 34, 530–543. doi: 10.1002/bio.3633
- Stoica, B. A., Bunesco, S., Neamtu, A., Bulgaru-Iliescu, D., Foia, L., and Botnariu, E. G. (2016). Improving luminol blood detection in forensics. *J. Forensic Sci.* 61, 1331–1336. doi: 10.1111/1556-4029.13141
- Stone, N., Faulds, K., Graham, D., and Matousek, P. (2010). Prospects of deep raman spectroscopy for noninvasive detection of conjugated surface enhanced resonance raman scattering nanoparticles buried within 25 mm of mammalian tissue. *Anal. Chem.* 82, 3969–3973. doi: 10.1021/ac100039c
- Stone, N., Kerssens, M., Lloyd, G. R., Faulds, K., Graham, D., and Matousek, P. (2011). Surface enhanced spatially offset Raman spectroscopic (SESORS) imaging – the next dimension. *Chem. Sci.* 2, 776–780. doi: 10.1039/C0SC00570C
- Tseng, J.-C., and Kung, A. L. (2013). In vivo imaging method to distinguish acute and chronic inflammation. *J. Vis. Exp.* 78:e50690. doi: 10.3791/50690
- van Velthoven, R., Aoun, F., Marcellis, Q., Albinini, S., Zanaty, M., Lemort, M., et al. (2016). A prospective clinical trial of HIFU hemiablation for clinically localized prostate cancer. *Prostate Cancer Prostatic Dis.* 19, 79–83. doi: 10.1038/pcan.2015.55
- Viviani, V. R. (2002). The origin, diversity, and structure function relationships of insect luciferases. *Cell. Mol. Life Sci.* C. 59, 1833–1850. doi: 10.1007/pl00012509
- Wang, D. M., Lin, K. L., and Huang, C. Z. (2019). Carbon dots-involved chemiluminescence: recent advances and developments. *Luminescence* 34, 4–22. doi: 10.1002/bio.3570
- Wang, J., Xing, D., He, Y., and Hu, X. (2002). Experimental study on photodynamic diagnosis of cancer mediated by chemiluminescence probe. *FEBS Lett.* 523, 128–132. doi: 10.1016/S0014-5793(02)02961-2967
- Wang, J., Xu, M., Chen, M., Jiang, Z., and Chen, G. (2012). Study on sonodynamic activity of metallophthalocyanine sonosensitizers based on the sonochemiluminescence of MCLA. *Ultrason. Sonochem.* 19, 237–242. doi: 10.1016/j.ultsonch.2011.06.021
- Wang, L., Jacques, S. L., and Zheng, L. (1995). MCML—Monte Carlo modeling of light transport in multi-layered tissues. *Comput. Methods Programs Biomed.* 47, 131–146. doi: 10.1016/0169-2607(95)01640-F
- Wang, L., Yao, M., Fang, X., and Yao, X. (2019). Novel competitive chemiluminescence DNA assay based on Fe₃O₄@SiO₂@Au-functionalized magnetic nanoparticles for sensitive detection of p53 Tumor suppressor gene. *Appl. Biochem. Biotechnol.* 187, 152–162. doi: 10.1007/s12010-018-2808-2801
- Wang, Y., Yu, Y., Shabahang, S., Wang, G., and Szalay, A. (2002). Renilla luciferase-Aequorea GFP (Ruc-GFP) fusion protein, a novel dual reporter for real-time imaging of gene expression in cell cultures and in live animals. *Mol. Genet. Genomics* 268, 160–168. doi: 10.1007/s00438-002-0751-759
- Wang, Z. G., Zhou, R., Jiang, D., Song, J. E., Xu, Q., Si, J., et al. (2015). Toxicity of graphene quantum dots in zebrafish embryo. *Biomed. Environ. Sci.* 28, 341–351. doi: 10.3967/bes2015.048
- Weeks, I., Beheshti, I., McCapra, F., Campbell, A. K., and Woodhead, J. S. (1983). Acridinium esters as high-specific-activity labels in immunoassay. *Clin. Chem.* 29, 1474–1479. doi: 10.1093/clinchem/29.8.1474
- Wei, Y., Lu, C., Chen, Q., and Xing, D. (2016). DNA duplex-based photodynamic molecular Beacon for targeted killing of retinoblastoma cell. *Invest. Ophthalmol. Vis. Sci.* 57, 6011–6019. doi: 10.1167/iovs.15-18723
- Wei, Y., Song, J., and Chen, Q. (2011). In vivo detection of chemiluminescence to monitor photodynamic threshold dose for tumor treatment. *Photochem. Photobiol. Sci.* 10, 1066–1071. doi: 10.1039/c0pp00346h
- Weissleder, R., and Pittet, M. J. (2008). Imaging in the era of molecular oncology. *Nature* 452:580. doi: 10.1038/nature06917
- White, E. H., McCapra, F., Field, G. F., and McElroy, W. D. (1961). The structure and synthesis of firefly luciferin. *J. Am. Chem. Soc.* 83, 2402–2403. doi: 10.1021/ja01471a051
- Xia, J., Yao, J., and Wang, L. V. (2014). Photoacoustic tomography: principles and advances. *Electromagn. Waves* 147, 1. doi: 10.2528/pier14032303
- Xu, S.-L., and Cui, H. (2007). Luminol chemiluminescence catalysed by colloidal platinum nanoparticles. *Luminescence* 22, 77–87. doi: 10.1002/bio.929
- Xu, X., An, H., Zhang, D., Tao, H., Dou, Y., Li, X., et al. (2019). A self-illuminating nanoparticle for inflammation imaging and cancer therapy. *Sci. Adv.* 5, eaat2953. doi: 10.1126/sciadv.aat2953
- Yagur-Kroll, S., Bilic, B., and Belkin, S. (2010). Strategies for enhancing bioluminescent bacterial sensor performance by promoter region manipulation. *Microb. Biotechnol.* 3, 300–310. doi: 10.1111/j.1751-7915.2009.00149.x
- Yan, Y., Shi, P., Song, W., and Bi, S. (2019). Chemiluminescence and bioluminescence imaging for biosensing and therapy: in vitro and in vivo perspectives. *Theranostics* 9, 4047–4065. doi: 10.7150/thno.33228
- Yang, N., Huang, Y., Ding, G., and Fan, A. (2019). In situ generation of prussian blue with potassium ferrocyanide to improve the sensitivity of chemiluminescence immunoassay using magnetic nanoparticles as label. *Anal. Chem.* 91, 4906–4912. doi: 10.1021/acs.analchem.9b01091
- Yang, Y., Shao, Q., Deng, R., Wang, C., Teng, X., Cheng, K., et al. (2012). In vitro and in vivo uncaging and bioluminescence imaging by using photocaged upconversion nanoparticles. *Angew. Chemie Int. Ed.* 51, 3125–3129. doi: 10.1002/anie.201107919
- Yao, J., Li, L., Li, P., and Yang, M. (2017). Quantum dots: from fluorescence to chemiluminescence, bioluminescence, electrochemiluminescence, and electrochemistry. *Nanoscale* 9, 13364–13383. doi: 10.1039/C7NR05233B
- Yarmolenko, P. S., Moon, E. J., Landon, C., Manzoor, A., Hochman, D. W., Viglianti, B. L., et al. (2011). Thresholds for thermal damage to normal tissues: an update. *Int. J. Hyperthermia* 27, 320–343. doi: 10.3109/02656736.2010.534527
- Zhai, Q., Li, J., and Wang, E. (2017). Recent advances based on nanomaterials as electrochemiluminescence probes for the fabrication of sensors. *ChemElectroChem* 4, 1639–1650. doi: 10.1002/celc.201600898
- Zhang, H. F., Maslov, K., Stoica, G., and Wang, L. V. (2006). Functional photoacoustic microscopy for high-resolution and noninvasive in vivo imaging. *Nat. Biotechnol.* 24:848. doi: 10.1038/nbt1220
- Zhang, W., Yang, L., Kuang, H., Yang, P., Aguilar, Z. P., Wang, A., et al. (2016). Acute toxicity of quantum dots on late pregnancy mice: effects of nanoscale size and surface coating. *J. Hazard. Mater.* 318, 61–69. doi: 10.1016/j.jhazmat.2016.06.048
- Zhu, K., Lu, Y., Zhang, S., Ruan, H., Usuki, S., and Tan, Y. (2018). Ultrasound modulated laser confocal feedback imaging inside turbid media. *Opt. Lett.* 43:1207. doi: 10.1364/OL.43.001207

Conflict of Interest: The authors declare that the research was conducted in the absence of any commercial or financial relationships that could be construed as a potential conflict of interest.

Copyright © 2020 Le, Dhamecha, Gonsalves and Menon. This is an open-access article distributed under the terms of the Creative Commons Attribution License (CC BY). The use, distribution or reproduction in other forums is permitted, provided the original author(s) and the copyright owner(s) are credited and that the original publication in this journal is cited, in accordance with accepted academic practice. No use, distribution or reproduction is permitted which does not comply with these terms.



Nanozymes: A New Disease Imaging Strategy

Peixia Wang^{1,2,3†}, Tao Wang^{4†}, Juanji Hong², Xiyun Yan^{1,3*} and Minmin Liang^{2*}

¹ CAS Engineering Laboratory for Nanozyme, Key Laboratory of Protein and Peptide Pharmaceutical, Institute of Biophysics, Chinese Academy of Sciences, Beijing, China, ² Experimental Center of Advanced Materials School of Materials Science & Engineering, School of Materials Science & Engineering, Beijing Institute of Technology, Beijing, China, ³ College of Life Sciences, University of Chinese Academy of Sciences, Beijing, China, ⁴ Department of Neurosurgery, Peking University Third Hospital, Beijing, China

OPEN ACCESS

Edited by:

Michael Ming-Yuan Wei,
Texas Commission on Environmental
Quality, United States

Reviewed by:

Rocktotpal Konwarh,
Addis Ababa Science and Technology
University, Ethiopia
Raviraj Vankayala,
Independent Researcher,
Irvine, United States

*Correspondence:

Xiyun Yan
yanxy@ibp.ac.cn
Minmin Liang
mmliang@bit.edu.cn

[†] These authors have contributed
equally to this work

Specialty section:

This article was submitted to
Nanobiotechnology,
a section of the journal
Frontiers in Bioengineering and
Biotechnology

Received: 28 September 2019

Accepted: 09 January 2020

Published: 06 February 2020

Citation:

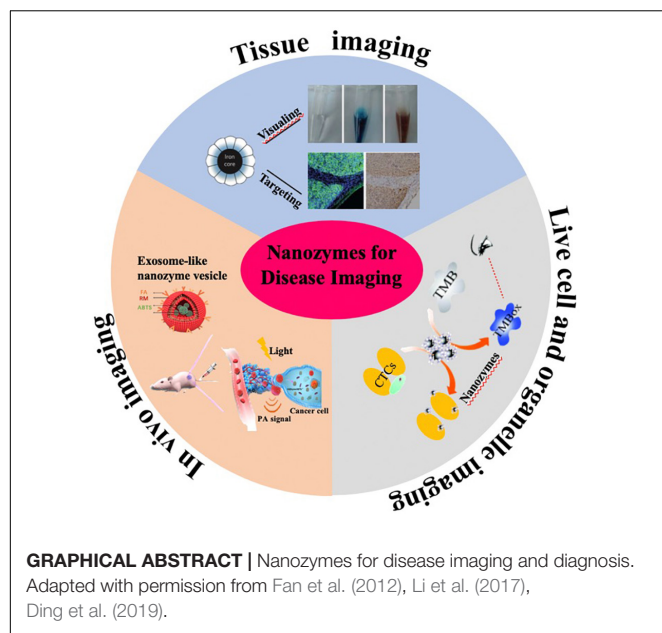
Wang P, Wang T, Hong J, Yan X
and Liang M (2020) Nanozymes:
A New Disease Imaging Strategy.
Front. Bioeng. Biotechnol. 8:15.
doi: 10.3389/fbioe.2020.00015

Nanozymes are nanomaterials with intrinsic enzyme-like properties. They can specifically catalyze substrates of natural enzymes under physiological condition with similar catalytic mechanism and kinetics. Compared to natural enzymes, nanozymes exhibit the unique advantages including high catalytic activity, low cost, high stability, easy mass production, and tunable activity. In addition, as a new type of artificial enzymes, nanozymes not only have the enzyme-like catalytic activity, but also exhibit the unique physicochemical properties of nanomaterials, such as photothermal properties, superparamagnetism, and fluorescence, etc. By combining the unique physicochemical properties and enzyme-like catalytic activities, nanozymes have been widely developed for *in vitro* detection and *in vivo* disease monitoring and treatment. Here we mainly summarized the applications of nanozymes for disease imaging and detection to explore their potential application in disease diagnosis and precision medicine.

Keywords: nanozyme, natural enzyme, disease imaging, precision medicine, tumor

INTRODUCTION

Nanozyme is a new type of artificial enzyme with intrinsic enzyme-like characteristics. In 2007, we reported the landmark paper that Fe₃O₄ nanoparticles (NPs) have intrinsic peroxidase-like activity (Gao et al., 2007), and since that time nanozymes have increasingly attracted attention from a broad spectrum of scientists and technologists because of their high catalytic activity, low cost, and high stability (Gao and Yan, 2016). To date, there are more than 300 types of nanomaterials that have been found to possess the intrinsic enzyme-like activity, including the peroxidase activity of Fe₃O₄ (Gao et al., 2007), Co₃O₄ (Mu et al., 2012), CuO (Liu et al., 2014), V₂O₅ (André et al., 2011), MnFeO₃ (Chi et al., 2018), FeS (Dai et al., 2009), graphene quantum dots (Nirala et al., 2017), CeO₂ (Xue et al., 2012), BiFeO₃ (Wei et al., 2010), CoFe₂O₄ (He et al., 2010), FeTe (Roy et al., 2012), gold@carbon dots (Zheng et al., 2016); oxidase activity of Au (Comotti et al., 2004), Pt (Yu et al., 2014), CoFe₂O₄ (Zhang et al., 2013), MnO₂ (Xing et al., 2012), CuO NPs (Hu et al., 2017) and NiCo₂O₄ (Su et al., 2017); catalase activity of CeO₂ NPs (Talib et al., 2010), Pt-Ft NPs (Fan et al., 2011), Ir NPs (Su et al., 2015), MoS₂ nanosheets (Chen et al., 2018), Prussian Blue NPs (Zhang W. et al., 2016); superoxide oxidase activity of CeO₂ (Tarnuzzer et al., 2005), Fullerene (Ali et al., 2004), FePO₄ microflowers (Wang W. et al., 2012), Gly-Cu (OH)₂ NPs (Korschelt et al., 2017), N-PCNs (Fan et al., 2018); haloperoxidase activity of V₂O₅ nanowire (Natalio et al., 2012), CeO_{2x} Nanorods (Herget et al., 2017); sulfite oxidase activity of MoO₃ NPs (Ragg et al., 2014); phosphatase activity of CeO₂ (Kuchma et al., 2010), Fe₂O₃ NPs (Huang, 2018); phosphotriesterase



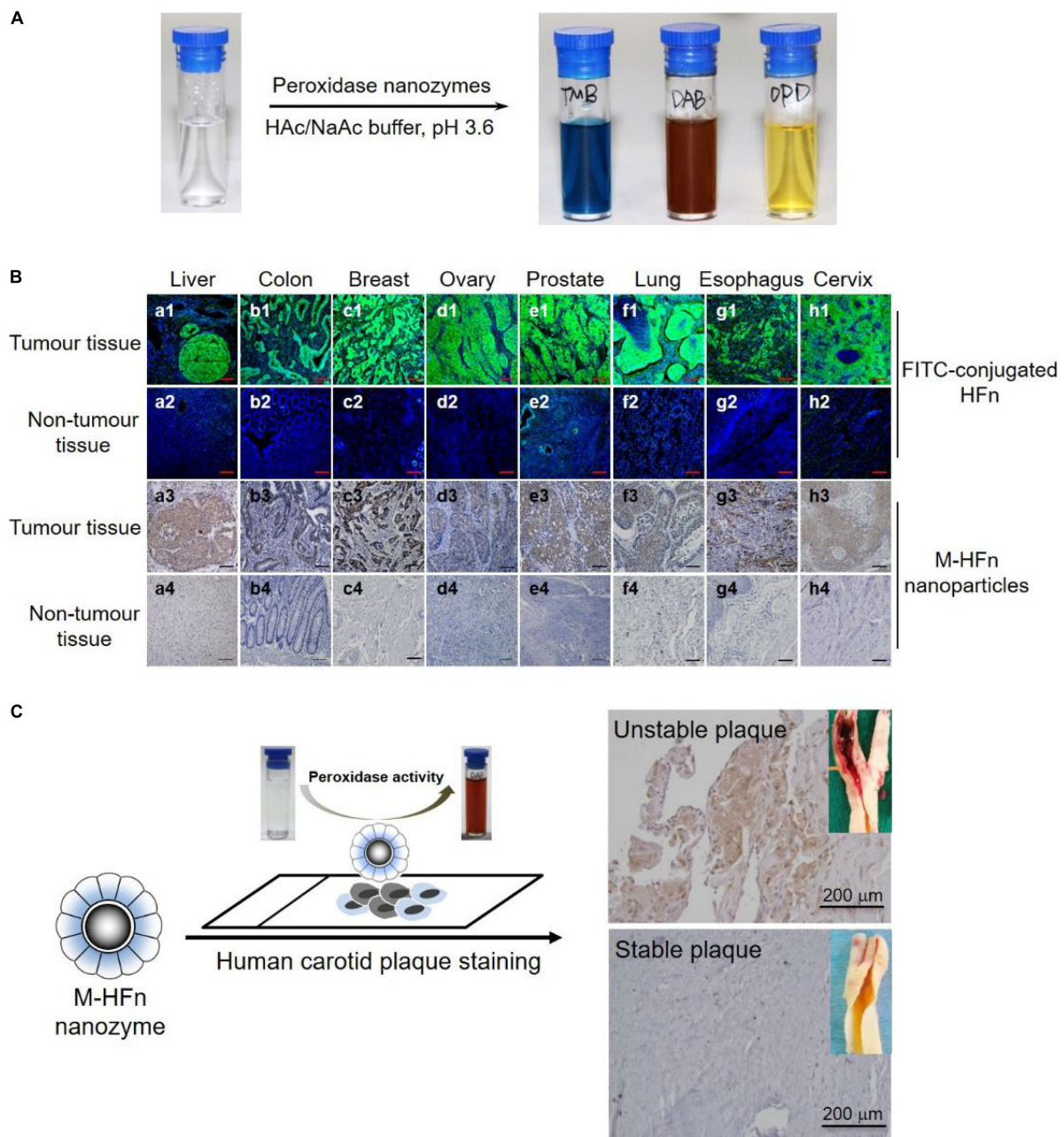
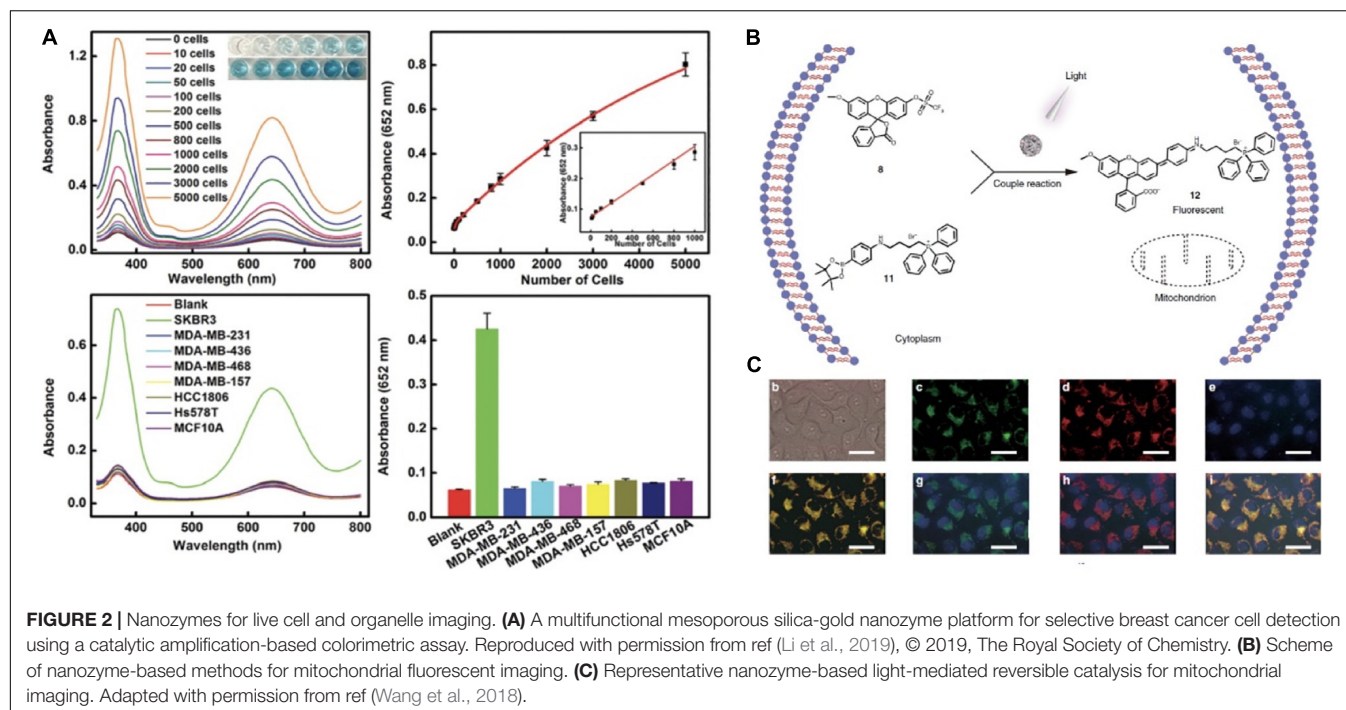


FIGURE 1 | Nanozymes for pathological tissue imaging. **(A)** Peroxidase nanozymes catalyze the oxidation of various peroxidase substrates (TMB, DAB, and OPD) in the presence of H_2O_2 to produce different color reactions. Adapted with permission from ref (Jiang B. et al., 2018), © 2018, Springer Nature. **(B)** M-HFn nanozymes specifically stained tumor tissues from different organs. Adapted with permission from ref (Fan et al., 2012), © 2012, Springer Nature. **(C)** Peroxidase nanozymes for the pathological identification of unstable atherosclerotic plaques from patients with symptomatic carotid disease. Reproduced with permission from ref (Liang and Yan, 2019), © 2019, American Chemical Society.

2018, Leong and co-workers engineered a mesoporous silica-gold nanocluster hybrid nanozymes with excellent peroxidase-like catalytic activity for selective detection of HER2-positive ($HER2^{2+}$) breast cancer cell (Li et al., 2019). Owing to their high catalytic performance, the prepared silica-gold hybrid nanozymes achieved the detection limit of 10 cells using colorimetric analysis. The hybrid nanozymes did not stain, or only slightly stained,

normal or lesion tissues, but strongly stained cancerous regions. Significantly, there was a clear distinction between cancerous cells and adjacent normal cells in representative sections (**Figure 2A**).

Besides enzyme-like activity, the unique physicochemical properties (such as luminescence, X-ray absorption, and paramagnetic properties) of nanozymes also have been widely



developed for pathological tissue imaging. For instance, Cai's group developed a folate receptor-targeting gold nanocluster as fluorescence enzyme mimetic nanoprobe for tumor tissues fluorescence visualizing detection. In the work, the intravenous dose used was 500 mg/kg for fluorescence imaging, and the concentration of 1.8 mM, 1 h was used for DAB staining (Hu et al., 2014). For the same tumor tissue slice, nanozyme staining and fluorescent staining were obtained simultaneously in a one-step incubation, and the results were mutually complementary. Thus, the developed fluorescence/nanozyme nanoprobe could provide a molecular colocalization diagnosis strategy within clinical tissue specimens, which efficiently avoids false-positive and false-negative results, and greatly improves the detection accuracy, credibility, and repeatability for cancer pathological diagnoses. Likewise, Zhang et al. also developed a gold nanozyme-based dark-field imaging assay as a novel immunohistochemical method for detecting HER2 overexpressed in breast cancer tissues (Lin et al., 2016). By quantitative analysis of the optical property of dark-field imaging, cancerous tissue can be quantitatively divided into four levels: “–, +, ++, and +++.”

Despite the fact that nanozyme-based staining methods have been broadly developed for pathological disease diagnosis, there are still many unresolved issues and challenges. The first is how to improve the enzyme-like activity of nanozymes. Since the catalytic activity of nanozymes is directly correlated with their detection sensitivity, the improvement of enzyme-like activity of nanozymes could help substantially improve the detection sensitivity of nanozyme-based staining methods. However, the issue of false positives would arise along with the improved enzyme-like activity (Wu et al., 2019).

In addition, the false positive issue would become even more severe due to the limited substrate specificity of nanozymes. We proposed a strategy to improve both the catalytic activity and the substrate specificity by introducing histidine residues onto the surface of Fe_3O_4 nanozymes to mimic the natural peroxidase enzymes (Fan et al., 2017). Juewen Liu engineered a specific nanozyme using molecular imprinting method to enhance the substrate selectivity and activity of enzyme mimics (Zhang et al., 2017). In addition, the oriented immobilization of the recognizing moieties to the surface of nanozymes could also reduce false positives greatly. Guo et al. constructed an inorganic/protein hybrid nanozyme by oriented immobilizing nature enzymes on the surface of inorganic graphene NPs (Liu Y. et al., 2019). The prepared nanohybrid nanozymes exhibited outstanding peroxidase-mimicking activity and excellent substrate selectivity. The second challenge for nanozyme staining method is how to quantitatively analyze the pathological staining results. Currently, the clinical pathological analysis mainly relies on experienced judgment, which is subjective, and variation between observers is high for certain categories of pathological diagnosis (Qian and Jiao, 2017). By combining the unique optical property and enzyme-like catalytic activities, nanozymes hold promise to achieve quantitative analysis for pathological disease staining diagnosis.

NANOZYMES FOR LIVE CELL AND ORGANELLE IMAGING

Cytological examination is an important means of clinical disease diagnosis (Bromberg et al., 2007; Mosterd et al., 2008;

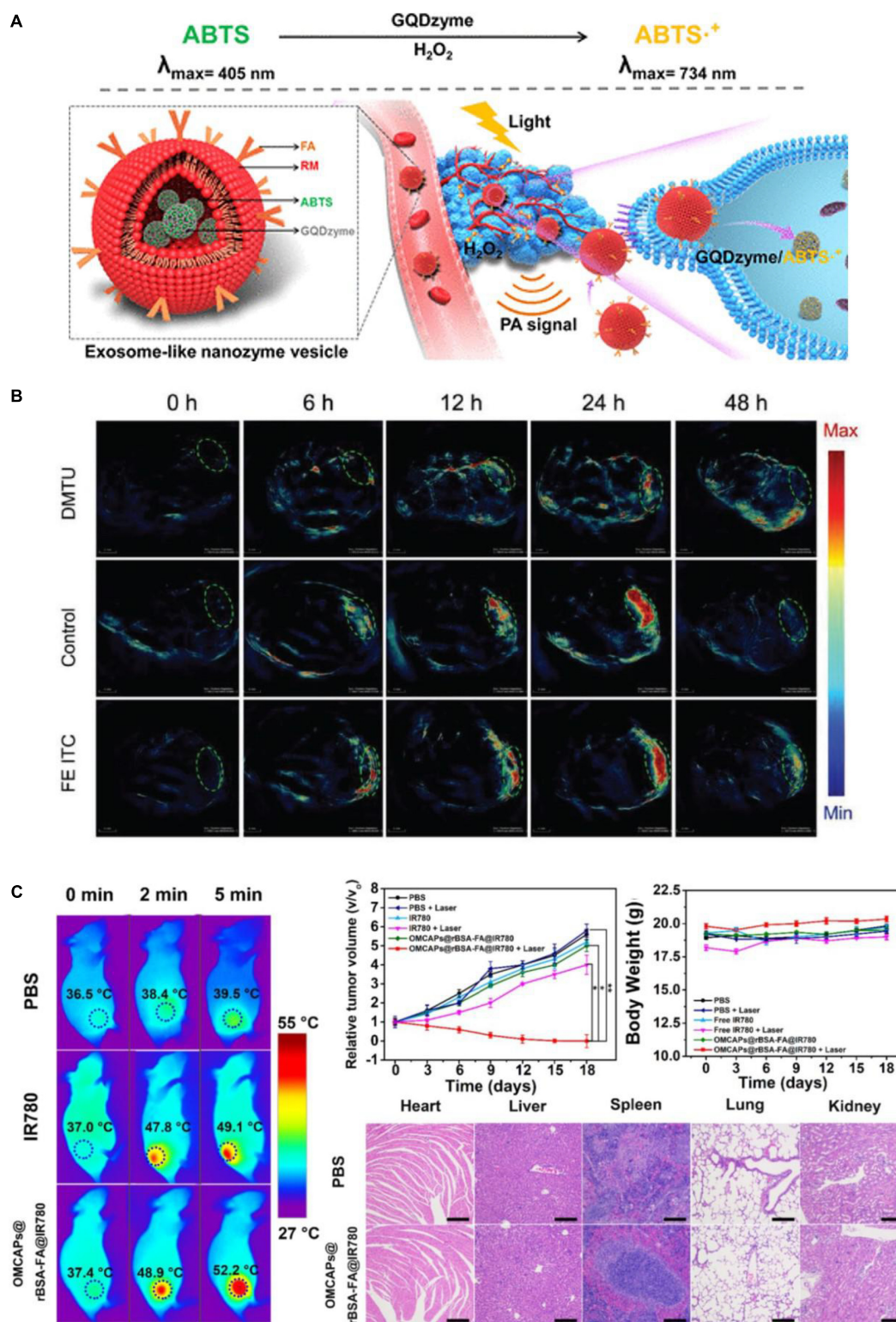


FIGURE 3 | Nanozymes for *in vivo* imaging of disease progression. **(A)** Schematic illustration of exosome-like nanozyme vesicles for the H_2O_2 -responsive catalytic photoacoustic imaging of tumors. Reproduced with permission from ref (Ding et al., 2019), © 2019, American Chemical Society. **(B)** Representative nanozyme-based tumor photoacoustic imaging images. Reproduced with permission from ref (Liu F. et al., 2019), © 2019, John Wiley and Sons. **(C)** Carbon-gold hybrid nanozymes for real-time imaging, photothermal/photodynamic and nanozyme oxidative therapy of tumors. Reproduced with permission from ref (Zhang et al., 2019).

Hao et al., 2011; Venugopal and Prasad, 2015). Exfoliated cells from blood, cerebrospinal fluid, spinal fluid, chest water and mucous liquid can provide a large amount of clinical information (including cell morphology, cell type, and cell proportion, etc.), which can be used for cancer screening (Schiffman et al., 2000; Dillner et al., 2008), CNS hematologic malignancies (Bromberg et al., 2007) anemia diagnosis (Hao et al., 2011), and Langerhans cell granulomatosis detection (Mosterd et al., 2008).

Currently, the most commonly used cytological detection methods are flow cytometry, cytological smear and nucleic acid testing. These traditional methods are characterized by high technical requirements, time consuming or high cost. Nanozymes-driven color reaction can be used for qualitative and quantitative analysis of cytological features. Trau et al. extended the application of nanozymes to the detection of circulating tumor cells (CTCs) (Li et al., 2017). The targeting antibody-conjugated Fe₃O₄ nanozymes simultaneously achieved CTC magnetic isolation and visualization by catalyzing the oxidation of colorimetric substrate TMB into blue colored products. In addition, the visualized CTCs can be further quantified using UV-vis measurement. The developed nanozyme platform successfully detected 13 melanoma CTCs per mL blood within 50 min, and the concentration of Fe₃O₄ nanozymes used was about 0.2 mg/ml for TMB colorimetric development. Later, Wang et al. (2018) also developed an Fe₃O₄ NPs-based ultrasensitive electrochemical CTCs detection strategy (Tian et al., 2018). Under the optimized experimental conditions, the proposed nanozyme cytosensor exhibited significant analytical performance for MCF-7 CTCs detection with a detection limit of 6 cells mL⁻¹ with a linear range from 15 to 45 cells mL⁻¹ at the acceptable stability condition and reproducibility. Recently, nanozyme-based detection strategies have been broadly developed for the cytological detection of breast cancer cell (Li et al., 2019), cervical cancer cells (Yu et al., 2013; Maji et al., 2015), human chronic myelogenous leukemia cell (Ge et al., 2014), melanoma tumor cell (Li et al., 2017), and squamous cancer (Wang et al., 2014) etc.

In addition to detecting CTCs, researchers also employed the catalytic activity of nanozymes to design real-time detection probes for organelle imaging in living cells. For example, Qu et al., designed a heterogeneous palladium nanozyme that could effectively mediate the bioorthogonal reactions *in situ* through light and thus realized the specific imaging of mitochondria in living cells (Wang et al., 2018) (Figures 2B,C). Beside CTCs and organelle imaging detection, there are also several other nanozymes-based colorimetric methods for specific disease imaging, including jaundice (Santhosh et al., 2014), acquired immune deficiency syndrome (Lin et al., 2017), diabetes (Tianran et al., 2014), infectious disease (Kim et al., 2014; Duan et al., 2015), and neurodegenerative disease (Wang C. I. et al., 2012; Farhadi et al., 2014). Thus, compared to traditional methods (such as PCR, cell flow cytometry, and ELISA), nanozymes methods exhibit more broaden prospect for live cell and organelle imaging because nanozyme assay is more fast, cost-effective and much easier to operate.

NANOZYMES FOR *IN VIVO* IMAGING

In addition to enzyme-mimicking activity, nanozymes also exhibit fluorescence, electricity, paramagnetic properties and other unique physicochemical properties. By employing the unique physicochemical properties, nanozymes also have been broadly developed for *in vivo* monitoring and imaging of disease. For example, we utilized the unique *r*₂ relaxivity of iron nanozymes and achieved tumor *in vivo* magnetic resonance imaging (MRI) after we achieved the *in vitro* tumor tissue imaging by using the peroxidase-like activity of iron-based nanozymes with a single-dose of ¹²⁵I-M-HFn NPs containing 45 μg HFn, 500 μCi ¹²⁵I, and 11.2 μg Fe by intravenously injection (Zhao et al., 2016). We also designed a quantum-dot-based nanozyme vesicle for *in vivo* H₂O₂-responsive catalytic photoacoustic imaging of nasopharyngeal carcinoma (Ding et al., 2019). In this work, graphene quantum dots showed intense peroxidase activity and effectively catalyzed the peroxidase substrate 2,2'-azino-bis (3-ethylbenzthiazoline-6-sulfonic acid) diammonium salt (ABTS) into its oxidized form. The oxidized ABTS then exhibited strong near-infrared (NIR) absorbance, rendering it to be an ideal contrast agent for photoacoustic imaging. In the study, GQDzyme was at a dose of 100 μg/mL, 100 μL by an intravenously injection (Figure 3A). Jiang X. et al. (2018) achieved tumor phototherapy and simultaneous photoacoustic/thermal imaging and computed tomography by using a developed iridium oxide catalase nanozyme with extraordinary photothermal conversion efficiency and X-ray absorption coefficient showing a typical example of fully exploiting the multifunctional properties of nanozymes for tumor imaging and treatment. The BSA-IrO₂ NPs used in the study was 1.5 mM, 200 μL via an intravenously injection (Jiang X. et al., 2018).

Nanozyme probes have also been broadly developed for disease therapeutic monitoring. For example, in 2019, Chen's group prepared a tumor-microenvironment-activated nanozyme-mediated theranostic nanoreactor for imaging-guided combined tumor therapy (Liu F. et al., 2019). In their work, the constructed activatable nanoreactors achieved non-invasive imaging of tumor progression by using nanozyme-mediated photoacoustic imaging signal and photothermal therapy (PTT) function and the AMP NPs were at a dose of 10 mg/kg, 200 μL (Figure 3B). Cui's group also prepared a mesoporous carbon-gold hybrid nanozyme probe for real-time imaging, photothermal/photodynamic and nanozyme oxidative therapy of tumors (Zhang et al., 2019). The results demonstrated that the synthesized nanozyme probes revealed excellent tumor targeting efficacy, long tumor retention, and favorably diagnostic and therapeutic effect for tumor (Figure 3C).

Besides cancer imaging diagnosis, nanozymes also have been broadly exploited for many other disease imaging such as infections, inflammation and some neurological diseases. For example, Rotello et al., reported a gold NPs-based charge-switchable nanozyme for bioorthogonal imaging of biofilm-associated infections (Tonga et al., 2015). In this work, the developed gold nanozymes could penetrate and accumulate inside the acidic microenvironment of biofilms and achieved

imaging detection of the biofilm-associated infections arising from different and/or mixed bacteria species. Zhao et al. fabricated MnO₂ nanozymes as the intracellular catalytic DNA circuit generators for versatile imaging of DNA base-excision repair in living cells (Chen et al., 2017). MnO₂ nanosheet was used not only as a DNA nano-carrier but also a DNAzyme cofactor supplier. In this study, DNAzyme strands are blocked via the hybridization with the damaged bases-containing excision probes, which could be recognized by the corresponding base-excision repair enzymes in living cell. The detection signal could be 40-fold amplified by integrating several sets of probes with a dose of 20 µg mL⁻¹ MnO₂ nanozymes. Likewise, Yang et al. (2018) reported a nanozyme tag enabled chemiluminescence imaging probe for simultaneous multiplex imaging of cytokines. The prepared chemiluminescence nanozyme probe provides a novel and universal nanozyme-labeled multiplex immunoassay strategy for high-throughput detection of relevant biomarkers and further disease diagnosis. Thus, nanozymes open novel avenues for monitoring the initiation and progress of diseases by combining the unique physicochemical properties and enzyme-like catalytic activities of nanozymes.

SUMMARY AND OUTLOOK

The emergence of nanozymes uncovers the biological effects of inorganic nanomaterials. Nanozymes thus can be used as an alternative of natural enzymes because of their capability to address the limitations of natural enzymes such as low stability, high cost, and difficult storage. Over the past decade, nanozyme-based probes have been widely developed for disease imaging and diagnosis from *in vitro* to *in vivo*. The typical nanozymes for disease imaging diagnosis are summarized in **Supplementary Table S1**.

Despite the remarkable advantages of nanozymes, there still remains plenty of limitations while put nanozymes into practical clinical application, such as poor dispersibility, easy sedimentation after surface modification, limited catalytic types, poor substrate selectivity, and potential nanotoxicity. To further drive the rapid development of nanozyme-based imaging agents for disease diagnosis, substantial breakthroughs are expected by overcoming the following challenges: (1) Rational design and surface modification are still remain critical challenges to improve their substrate selectivity and

dispersibility of nanozymes. Thus, both experimental and computational studies should be combined together to aid in the process of nanozyme design and surface modification. (2) A detailed understanding of the relationship between the catalytic properties and the *in vivo* biological behaviors of nanozymes is necessary. It is because the size, morphology and surface property of nanozymes have a direct impact on their catalytic activity and thus determine the *in vivo* biological behaviors of nanozymes. (3) A systematic evaluation of the biological fates and the biocompatibility of nanozyme systems (including the cytotoxicity, *in vivo* uptake and behavior, biodistribution, immunogenicity, blood compatibility, and tissue compatibility) should be performed when administrated into living organisms, since the biocompatibility and biodegradability are the common concerns when move these systems into clinical practice. (4) Developing standards and reference materials. Although nanozymes have shown a broad range of applications from *in vitro* biological detection to *in vivo* imaging diagnosis, there are rare basic concepts and the corresponding standards on nanozyme research. Therefore, nanozymes performance should be fully normalization according to their size, shape, modification to compare with each other when used for disease imaging diagnosis.

AUTHOR CONTRIBUTIONS

PW, TW, ML, and XY researched the literature and wrote the review. All authors revised and polished the review.

FUNDING

This work was supported by the National Key R&D Program of China (2017YFA0205501), the National Natural Science Foundation of China (81722024 and 81571728), the Key Research Program of Frontier Sciences (QYZDY-SSWSMC013), and the Youth Innovation Promotion Association (2014078).

SUPPLEMENTARY MATERIAL

The Supplementary Material for this article can be found online at: <https://www.frontiersin.org/articles/10.3389/fbioe.2020.00015/full#supplementary-material>

REFERENCES

- Ali, S. S., Hardt, J. I., Quick, K. L., Kim-Han, J. S., Erlanger, B. F., Huang, T. T., et al. (2004). A biologically effective fullerene (C60) derivative with superoxide dismutase mimetic properties. *Free Radic. Biol. Med.* 37, 1191–1202. doi: 10.1016/j.freeradbiomed.2004.07.002
- André, R., Natálio, F., Humanes, M., Leppin, J., Heinze, K., Wever, R., et al. (2011). V2O5 nanowires with an intrinsic peroxidase-like activity. *Adv. Funct. Mater.* 21, 501–509. doi: 10.1002/adfm.201001302
- Bromberg, J. E. C., Breems, D. A., Kraan, J., Bikker, G., van der Holt, B., Smitt, P. S., et al. (2007). CSF flow cytometry greatly improves diagnostic accuracy in CNS hematologic malignancies. *Neurology* 68, 1674–1679. doi: 10.1212/01.wnl.0000261909.28915.83
- Chen, F., Bai, M., Cao, K., Zhao, Y., Wei, J., and Zhao, Y. (2017). Fabricating MnO₂ nanozymes as intracellular catalytic DNA circuit generators for versatile imaging of base-excision repair in living cells. *Adv. Funct. Mater.* 27:1702748. doi: 10.1002/adfm.201702748
- Chen, T., Zou, H., Wu, X., Liu, C., Situ, B., Zheng, L., et al. (2018). Nanozymatic antioxidant system based on MoS₂ nanosheets. *ACS Appl. Mater. Interfaces* 10, 12453–12462. doi: 10.1021/acsami.8b01245
- Chi, M., Chen, S., Zhong, M., Wang, C., and Lu, X. (2018). Self-templated fabrication of FeMnO₃ nanoparticle-filled polypyrrole nanotubes for peroxidase mimicking with a synergistic effect and their sensitive

- colorimetric detection of glutathione. *Chem. Comm.* 54, 5827–5830. doi: 10.1039/c8cc01574k
- Comotti, M., Della Pina, C., Matarrese, R., and Rossi, M. (2004). The catalytic activity of “naked” gold particles. *Angew. Chem. Int. Ed.* 43, 5812–5815. doi: 10.1002/anie.200460446
- Dai, Z., Liu, S., Bao, J., and Ju, H. (2009). Nanostructured FeS as a mimic peroxidase for biocatalysis and biosensing. *Chemistry* 15, 4321–4326. doi: 10.1002/chem.200802158
- Dillner, J., Rebolj, M., Birembaut, P., Petry, K. U., Szarewski, A., Munk, C., et al. (2008). Long term predictive values of cytology and human papillomavirus testing in cervical cancer screening: joint European cohort study. *BMJ* 337:a1754. doi: 10.1136/bmj.a1754
- Ding, H., Cai, Y., Gao, L., Liang, M., Miao, B., Wu, H., et al. (2019). Exosome-like nanozyme vesicles for H₂O₂-responsive catalytic photoacoustic imaging of xenograft nasopharyngeal carcinoma. *Nano Lett.* 19, 203–209. doi: 10.1021/acs.nanolett.8b03709
- Dong, J., Song, L., Yin, J. J., He, W., Wu, Y., Gu, N., et al. (2014). Co₃O₄ nanoparticles with multi-enzyme activities and their application in immunohistochemical assay. *ACS Appl. Mater. Interfaces* 6, 1959–1970. doi: 10.1021/am405009f
- Duan, D., Fan, K., Zhang, D., Tan, S., Liang, M., Liu, Y., et al. (2015). Nanozyme-strip for rapid local diagnosis of Ebola. *Biosens. Bioelectron.* 74, 134–141. doi: 10.1016/j.bios.2015.05.025
- Fan, J., Yin, J. J., Ning, B., Wu, X., Hu, Y., Ferrari, M., et al. (2011). Direct evidence for catalase and peroxidase activities of ferritin–platinum nanoparticles. *Biomaterials* 32, 1611–1618. doi: 10.1016/j.biomaterials.2010.11.004
- Fan, K., Cao, C., Pan, Y., Lu, D., Yang, D., Feng, J., et al. (2012). Magnetoferritin nanoparticles for targeting and visualizing tumour tissues. *Nat. Nanotechnol.* 7, 459–464. doi: 10.1038/nnano.2012.90
- Fan, K., Wang, H., Xi, J., Liu, Q., Meng, X., Duan, D., et al. (2017). Optimization of Fe₃O₄ nanozyme activity via single amino acid modification mimicking an enzyme active site. *Chem. Comm.* 53, 424–427. doi: 10.1039/c6cc08542c
- Fan, K., Xi, J., Lei, F., Wang, P., Zhu, C., Yan, T., et al. (2018). In vivo guiding nitrogen-doped carbon nanozyme for tumor catalytic therapy. *Nat. Commun.* 9:1440. doi: 10.1038/s41467-018-03903-8
- Farhadi, K., Forough, M., Pourhossein, A., and Molaei, R. (2014). Highly sensitive and selective colorimetric probe for determination of L-cysteine in aqueous media based on Ag/Pd bimetallic nanoparticles. *Sens. Actuators. B Chem.* 202, 993–1001. doi: 10.1039/C4TA03990D
- Gao, L., and Yan, X. (2016). Nanozymes: an emerging field bridging nanotechnology and biology. *Sci. China. Life Sci.* 59, 400–402. doi: 10.1007/s11427-016-5044-3
- Gao, L., Zhuang, J., Nie, L., Zhang, J., Zhang, Y., Gu, N., et al. (2007). Intrinsic peroxidase-like activity of ferromagnetic nanoparticles. *Nat. Nanotechnol.* 2, 577–583. doi: 10.1038/nnano.2007.260
- Ge, S., Liu, F., Liu, W., Yan, M., Song, X., and Yu, J. (2014). Colorimetric assay of K-562 cells based on folic acid-conjugated porous bimetallic Pd@Au nanoparticles for point-of-care testing. *Chem. Comm.* 50, 475–477. doi: 10.1039/c3cc47622g
- Hao, J. J., Qiu, Y. N., Zhou, D. F., Xiao, Y., Liu, Q., and Jin, R. M. (2011). Comparisons of clinical features of chronic aplastic anemia and myelodysplastic syndrome in children. *China. J. Contem. Pediatr.* 13, 867–869. doi: 10.1111/j.1600-0714.2011.01024.x
- He, S., Shi, W., Zhang, X., Li, J., and Huang, Y. (2010). β -cyclodextrin-based inclusion complexes of CoFe₂O₄ magnetic nanoparticles as catalyst for the luminol chemiluminescence system and their applications in hydrogen peroxide detection. *Talanta* 82, 377–383. doi: 10.1016/j.talanta.2010.04.055
- Herget, K., Hubach, P., Pusch, S., Deglmann, P., Götz, H., Gorelik, T. E., et al. (2017). Haloperoxidase mimicry by CeO₂-x nanorods combats biofouling. *Adv. Mater.* 29:1603823. doi: 10.1002/adma.201603823
- Hu, A. L., Deng, H. H., Zheng, X. Q., Wu, Y. Y., Lin, X. L., Liu, A. L., et al. (2017). Self-cascade reaction catalyzed by CuO nanoparticle-based dual-functional enzyme mimics. *Biosens. Bioelectron.* 97, 21–25. doi: 10.1016/j.bios.2017.05.037
- Hu, D., Sheng, Z., Fang, S., Wang, Y., Gao, D., Zhang, P., et al. (2014). Folate receptor-targeting gold nanoclusters as fluorescence enzyme mimetic nanoprobes for tumor molecular colocalization diagnosis. *Theranostics* 4, 142–153. doi: 10.1016/j.thno.2014.07.266
- Huang, X. L. (2018). Hydrolysis of phosphate esters catalyzed by inorganic iron oxide nanoparticles acting as biocatalysts. *Astrobiology* 18, 294–310. doi: 10.1089/ast.2016.1628
- Hyon Bin, N., Jung Hee, L., Kwangjin, A., Il, P. Y., Mihyun, P., In Su, L., et al. (2010). Development of a T1 contrast agent for magnetic resonance imaging using MnO nanoparticles. *Angew. Chem. Int. Ed.* 46, 5247–5247. doi: 10.1002/ange.200604775
- Jiang, B., Duan, D., Gao, L., Zhou, M., Fan, K., Tang, Y., et al. (2018). Standardized assays for determining the catalytic activity and kinetics of peroxidase-like nanozymes. *Nat. Protoc.* 13, 1506–1520. doi: 10.1038/s41596-018-0001-1
- Jiang, X., Zhen, W., Liu, Y., Lin, L., and Tian, H. (2018). BSA-IrO₂: Catalase-like nanoparticles with high photothermal conversion efficiency and X-Ray absorption coefficient for anti-inflammation and tumor theranostics. *Angew. Chem.* 130, 10309–10313. doi: 10.1002/ange.201804466
- Jiang, B., Yan, L., Zhang, J., Zhou, M., Shi, G., Tian, X., et al. (2019). Biomineralization synthesis of the cobalt nanozyme in SP94-ferritin nanocages for prognostic diagnosis of hepatocellular carcinoma. *ACS Appl. Mater. Interfaces* 11, 9747–9755. doi: 10.1021/acsami.8b20942
- Kim, M. I., Ye, Y., Woo, M. A., Lee, J., and Park, H. G. (2014). A highly efficient colorimetric immunoassay using a nanocomposite entrapping magnetic and platinum nanoparticles in ordered mesoporous carbon. *Adv. Healthc. Mater.* 3, 36–41. doi: 10.1002/adhm.201300100
- Korschelt, K., Ragg, R., Metzger, C. S., Klunker, M., Oster, M., Barton, B., et al. (2017). Glycine-functionalized copper (II) hydroxide nanoparticles with high intrinsic superoxide dismutase activity. *Nanoscale* 9, 3952–3960. doi: 10.1039/c6nr09810j
- Kuchma, M. H., Komanski, C. B., Colon, J., Teblum, A., Masunov, A. E., Alvarado, B., et al. (2010). Phosphate ester hydrolysis of biologically relevant molecules by cerium oxide nanoparticles. *Nanomedicine* 6, 738–744. doi: 10.1016/j.nano.2010.05.004
- Kwon, H. J., Cha, M. Y., Kim, D., Kim, D. K., Soh, M., Shin, K., et al. (2016). Mitochondria-targeting ceria nanoparticles as antioxidants for Alzheimer's disease. *ACS Nano* 10, 2860–2870. doi: 10.1021/acsnano.5b08045
- Leng, B., Zou, L., Jiang, J., and Tian, H. (2009). Colorimetric detection of mercuric ion (Hg²⁺) in aqueous media using chemodosimeter-functionalized gold nanoparticles. *Sens. Actuators. B Chem.* 140, 162–169. doi: 10.1016/j.snb.2009.03.074
- Li, B., Chen, D., Wang, J., Yan, Z., Jiang, L., Duan, D., et al. (2014). MOFzyme: intrinsic protease-like activity of Cu-MOF. *Sci. Rep.* 4:6759. doi: 10.1038/srep06759
- Li, J., Wang, J., Wang, Y., and Trau, M. (2017). Simple and rapid colorimetric detection of melanoma circulating tumor cells using bifunctional magnetic nanoparticles. *Analyst* 142, 4788–4793. doi: 10.1039/c7an01102d
- Li, M., Lao, Y. H., Mintz, R. L., Chen, Z., Shao, D., Hu, H., et al. (2019). A multifunctional mesoporous silica-gold nanocluster hybrid platform for selective breast cancer cell detection using a catalytic amplification-based colorimetric assay. *Nanoscale* 11, 2631–2636. doi: 10.1039/c8nr08337a
- Liang, F., Musto, C. J., and Suslick, K. S. (2010). A simple and highly sensitive colorimetric detection method for gaseous formaldehyde. *J. Am. Chem. Soc.* 132, 4046–4047. doi: 10.1021/ja910366p
- Liang, M., and Yan, X. (2019). Nanozymes: from new concepts, mechanisms, and standards to applications. *Acc. Chem. Res.* 52, 2190–2200. doi: 10.1021/acs.accounts.9b00140
- Lin, F., Tian, Y., Rong, Y., Lou, D., Zhang, X., Meng, W., et al. (2016). Enzyme catalysis enhanced dark-field imaging as a novel immunohistochemical method. *Nanoscale* 8, 8553–8558. doi: 10.1039/c5nr08232c
- Lin, X. D., Liu, Y. Q., Tao, Z. H., Gao, J. T., Deng, J. K., Yin, J. J., et al. (2017). Nanozyme-based bio-barcode assay for high sensitive and logic-controlled specific detection of multiple DNAs. *Biosens. Bioelectron.* 94, 471–477. doi: 10.1016/j.bios.2017.01.008
- Liu, F., Lin, L., Zhang, Y., Wang, Y., Sheng, S., Xu, C., et al. (2019). A tumor-microenvironment-activated nanozyme-mediated theranostic nanoreactor for imaging-guided combined tumor therapy. *Adv. Mater.* 31:1902885. doi: 10.1002/adma.201902885
- Liu, Y., Zheng, Y., Chen, Z., Qin, Y., and Guo, R. (2019). High-performance integrated enzyme cascade bioplatfrom based on protein-BiPt nanochain@graphene oxide hybrid guided one-pot self-assembly strategy. *Small* 15:1804987. doi: 10.1002/smll.201804987

- Liu, Y., Zhu, G., Bao, C., Yuan, A., and Shen, X. (2014). Intrinsic peroxidase-like activity of porous CuO micro-/nanostructures with clean surface. *Chinese J. Chem.* 32, 151–156. doi: 10.1002/cjoc.201300683
- Maji, S. K., Mandal, A. K., Nguyen, K. T., Borah, P., and Zhao, Y. (2015). Cancer cell detection and therapeutics using peroxidase-active nanohybrid of gold nanoparticle-loaded mesoporous silica-coated graphene. *ACS Appl. Mater. Interfaces* 7, 9807–9816. doi: 10.1021/acsami.5b01758
- Mondal, S. S., and Holdt, H. J. (2016). Breaking down chemical weapons by metal-organic frameworks. *Angew. Chem.* 55, 42–44. doi: 10.1002/anie.201508407
- Mosterd, K., Van Marion, A., and Van Steensel, M. A. (2008). Neonatal langerhans' cell histiocytosis: a rare and potentially life-threatening disease. *Int. J. Dermatol.* 47, 10–12. doi: 10.1111/j.1365-4632.2008.03950.x
- Mu, J., Wang, Y., Zhao, M., and Zhang, L. (2012). Intrinsic peroxidase-like activity and catalase-like activity of Co₃O₄ nanoparticles. *Chem. Comm.* 48, 2540–2542. doi: 10.1039/c2cc17013b
- Natalio, F., Andre, R., Hartog, A. F., Stoll, B., Jochum, K. P., Wever, R., et al. (2012). Vanadium pentoxide nanoparticles mimic vanadium haloperoxidases and thwart biofilm formation. *Nat. Nanotechnol.* 7, 530–535. doi: 10.1038/nnano.2012.91
- Nath, I., Chakraborty, J., and Verpoort, F. (2016). Metal organic frameworks mimicking natural enzymes: a structural and functional analogy. *Chem. Soc. Rev.* 45, 4127–4170. doi: 10.1039/c6cs00047a
- Nirala, N. R., Khandelwal, G., Kumar, B., Prakash, R., and Kumar, V. (2017). One step electro-oxidative preparation of graphene quantum dots from wood charcoal as a peroxidase mimetic. *Talanta* 173, 36–43. doi: 10.1016/j.talanta.2017.05.061
- Peng, C., Hua, M. Y., Li, N. S., Hsu, Y. P., Chen, Y. T., Chuang, C. K., et al. (2019). A colorimetric immunosensor based on self-linkable dual-nanozyme for ultrasensitive bladder cancer diagnosis and prognosis monitoring. *Biosens. Bioelectron.* 126, 581–589. doi: 10.1016/j.bios.2018.11.022
- Qian, B., and Jiao, L. (2017). Application of multiplexed immunofluorescent staining and multi-spectral imaging in histological studies. *China. J. His. Cyt.* 26, 373–382. doi: 10.16705/j.cnki.1004-1850.04.010
- Ragg, R., Natalio, F., Tahir, M. N., Janssen, H., Kashyap, A., Strand, D., et al. (2014). Molybdenum trioxide nanoparticles with intrinsic sulfite oxidase activity. *ACS Nano* 8, 5182–5189. doi: 10.1021/nn501235j
- Roy, P., Lin, Z. H., Liang, C. T., and Chang, H. T. (2012). Synthesis of enzyme mimics of iron telluride nanorods for the detection of glucose. *Chem. Comm.* 48, 4079–4081. doi: 10.1039/c2cc30833a
- Sahoo, P. C., Jang, Y. N., and Lee, S. W. (2013). Enhanced biomimetic CO₂ sequestration and CaCO₃ crystallization using complex encapsulated metal organic framework. *J. Cryst. Growth.* 373, 96–101. doi: 10.1016/j.jcrysgro.2012.11.043
- Santhosh, M., Chinnadaya, S. R., Kakoti, A., and Goswami, P. (2014). Selective and sensitive detection of free bilirubin in blood serum using human serum albumin stabilized gold nanoclusters as fluorometric and colorimetric probe. *Biosens. Bioelectron.* 59, 370–376. doi: 10.1016/j.bios.2014.04.003
- Schiffman, M., Herrero, R., Hildesheim, A., Sherman, M. E., Bratti, M., Wacholder, S., et al. (2000). HPV DNA testing in cervical cancer screening - results from women in a high-risk province of costa rica. *JAMA* 283, 87–93. doi: 10.1001/jama.283.1.87
- Singh, N., Savanur, M. A., Srivastava, S., D'Silva, P., and Mughesh, G. (2017). A redox modulatory Mn₃O₄ nanozyme with multi-enzyme activity provides efficient cytoprotection to human cells in a Parkinson's disease model. *Angew. Chem.* 56, 14267–14271. doi: 10.1002/ange.201708573
- Su, H., Liu, D. D., Zhao, M., Hu, W. L., Xue, S. S., Cao, Q., et al. (2015). Dual-enzyme characteristics of polyvinylpyrrolidone-capped iridium nanoparticles and their cellular protective effect against H₂O₂-induced oxidative damage. *ACS Appl. Mater. Interfaces* 7, 8233–8242. doi: 10.1021/acsami.5b01271
- Su, L., Dong, W., Wu, C., Gong, Y., Zhang, Y., Li, L., et al. (2017). The peroxidase and oxidase-like activity of NiCo₂O₄ mesoporous spheres: Mechanistic understanding and colorimetric biosensing. *Anal. Chim. Acta* 951, 124–132. doi: 10.1016/j.aca.2016.11.035
- Sun, M., Xu, L., Qu, A., Zhao, P., Hao, T., Ma, W., et al. (2018). Site-selective photoinduced cleavage and profiling of DNA by chiral semiconductor nanoparticles. *Nat. Chem.* 10, 821–830. doi: 10.1038/s41557-018-0083-y
- Talib, P., Dowding, J. M., Sanjay, S., Brian, W., Eric, H., Karakoti, A. S., et al. (2010). Nanoceria exhibit redox state-dependent catalase mimetic activity. *Chem. Comm.* 46, 2736–2738. doi: 10.1039/B922024K
- Tarnuzzer, R. W., Colon, J., Patil, S., and Seal, S. (2005). Vacancy engineered ceria nanostructures for protection from radiation-induced cellular damage. *Nano Lett.* 5, 2573–2577. doi: 10.1021/nl052024f
- Tian, L., Qi, J. X., Qian, K., Oderinde, O., Cai, Y. Y., Yao, C., et al. (2018). An ultrasensitive electrochemical cytosensor based on the magnetic field assisted binanozymes synergistic catalysis of Fe₃O₄ nanozyme and reduced graphene oxide/molybdenum disulfide nanozyme. *Sens. Actuators. B Chem.* 260, 676–684. doi: 10.1016/j.snb.2018.01.092
- Tianran, L., Liangshuang, Z., Liangqia, G., Fengfu, F., and Guonan, C. (2014). Seeing diabetes: visual detection of glucose based on the intrinsic peroxidase-like activity of MoS₂ nanosheets. *Nanoscale* 6, 11856–11862. doi: 10.1039/c4nr03393k
- Tokuyama, H., Yamago, S., Nakamura, E., Shiraki, T., and Sugiura, Y. (1993). Photoinduced biochemical activity of fullerene carboxylic acid. *J. Am. Chem. Soc.* 115, 7918–7919. doi: 10.1021/ja00070a064
- Tonga, G. Y., Jeong, Y., Duncan, B., Mizuhara, T., Mout, R., Das, R., et al. (2015). Supramolecular regulation of bioorthogonal catalysis in cells using nanoparticle-embedded transition metal catalysts. *Nat. Chem.* 7, 597–603. doi: 10.1038/nchem.2284
- Venugopal, S. B., and Prasad, S. (2015). Cytological diagnosis of osteoblastoma of cervical spine: a case report with review of literature. *Diagn. Cytopathol.* 43, 218–221. doi: 10.1002/dc.23175
- Vernekar, A. A., Das, T., and Mughesh, G. (2016). Vacancy-engineered nanoceria: enzyme mimetic hotspots for the degradation of nerve agents. *Angew. Chem.* 55, 1412–1416. doi: 10.1002/ange.201510355
- Wang, C. I., Chen, W. T., and Chang, H. T. (2012). Enzyme mimics of Au/Ag nanoparticles for fluorescent detection of acetylcholine. *Anal. Chem.* 84, 9706–9712. doi: 10.1021/ac300867s
- Wang, W., Jiang, X., and Chen, K. (2012). Iron phosphate microflowers as peroxidase mimic and superoxide dismutase mimic for biocatalysis and biosensing. *Chem. Comm.* 48, 7289–7291. doi: 10.1039/c2cc32429f
- Wang, F., Zhang, Y., Du, Z., Ren, J., and Qu, X. (2018). Designed heterogeneous palladium catalysts for reversible light-controlled bioorthogonal catalysis in living cells. *Nat. Commun.* 9:1209. doi: 10.1038/s41467-018-03617-x
- Wang, T., He, J., Duan, D., Jiang, B., Wang, P., Fan, K., et al. (2019). Bioengineered magnetoferritin nanozymes for pathological identification of high-risk and ruptured atherosclerotic plaques in humans. *Nano Res.* 12, 863–868. doi: 10.1021/acs.nano.5b07408
- Wang, T., Wang, J., Ye, Y., Ping, S., Yi, Y., Wang, T., et al. (2017). Co₃O₄/reduced graphene oxide nanocomposites as effective phosphotriesterase mimetics for degradation and detection of paraoxon. *Ind. Eng. Chem. Res.* 56, 9762–9769. doi: 10.1021/acs.iecr.7b02223
- Wang, X., Liu, D., Li, J., Zhen, J., and Zhang, H. (2015). Clean synthesis of Cu₂O@CeO₂ core@shell nanocubes with highly active interface. *NPG Asia. Mater.* 7:e158. doi: 10.1038/am.2014.128
- Wang, Y. L., Zhang, Y., Su, Y., Li, F., Ma, H. M., Li, H., et al. (2014). Ultrasensitive non-mediator electrochemical immunosensors using Au/Ag/Au core/double shell nanoparticles as enzyme-mimetic labels. *Talanta* 124, 60–66. doi: 10.1016/j.talanta.2014.02.035
- Wei, L., Yu-Sang, L., Jing, Y., Lihua, Z., Zhengdan, L., Heqing, T., et al. (2010). Ultrasensitive fluorometric determination of hydrogen peroxide and glucose by using multiferroic BiFeO₃ nanoparticles as a catalyst. *Talanta* 81, 901–907. doi: 10.1016/j.talanta.2010.01.035
- Wu, L., Li, G. H., Xu, X., Zhu, L., Huang, R. M., and Chen, X. Q. (2019). Application of nano-ELISA in food analysis: recent advances and challenges. *Trends. Anal. Chem.* 113, 140–156. doi: 10.1016/j.trac.2019.02.002
- Wu, Y., Song, M., Xin, Z., Zhang, X., Zhang, Y., Wang, C., et al. (2011). Ultra-small particles of iron oxide as peroxidase for immunohistochemical detection. *Nanotechnology* 22:225703. doi: 10.1088/0957-4484/22/22/225703
- Xing, L., Qi, W., Huihui, Z., Lichun, Z., Yingying, S., and Yi, L. (2012). BSA-templated MnO₂ nanoparticles as both peroxidase and oxidase mimics. *Analyst* 137, 4552–4558. doi: 10.1039/C2AN35700C

- Xue, J., Song, H., Zhao, H., Wei, B., Zhang, L., and Yi, L. (2012). Well-redispersed ceria nanoparticles: promising peroxidase mimetics for H₂O₂ and glucose detection. *Anal. Methods* 4, 3261–3267. doi: 10.1039/c2ay25511a
- Yang, F., Hu, S., Zhang, Y., Cai, X., Huang, Y., Wang, F., et al. (2012). A hydrogen peroxide-responsive O₂ nanogenerator for ultrasound and magnetic–resonance dual modality imaging. *Adv. Mater.* 24, 5205–5211. doi: 10.1002/adma.201202367
- Yang, Z., Zhong, Y., Tang, X., Li, J., and Gao, W. (2018). Nanozyme tags enabled chemiluminescence imaging immunoassay for multiplexed cytokine monitoring. *Chem. Comm.* 54, 13813–13816. doi: 10.1039/c8cc07779g
- Yu, C. J., Chen, T. H., Jiang, J. Y., and Tseng, W. L. (2014). Lysozyme-directed synthesis of platinum nanoclusters as a mimic oxidase. *Nanoscale* 6, 9618–9624. doi: 10.1039/c3nr06896j
- Yu, T., Youhui, L., Zhenzhen, H., Jinsong, R., and Xiaogang, Q. (2013). Incorporating graphene oxide and gold nanoclusters: a synergistic catalyst with surprisingly high peroxidase-like activity over a broad pH range and its application for cancer cell detection. *Adv. Mater.* 25:2510. doi: 10.1002/adma.201370115
- Zhang, A., Pan, S., Zhang, Y., Chang, J., Cheng, J., Huang, Z., et al. (2019). Carbon-gold hybrid nanoprobe for real-time imaging, photothermal/photodynamic and nanozyme oxidative therapy. *Theranostics* 9, 3443–3458. doi: 10.7150/thno.33266
- Zhang, T., Cao, C., Tang, X., Cai, Y., Yang, C., and Pan, Y. (2016). Enhanced peroxidase activity and tumour tissue visualization by cobalt-doped magnetoferritin nanoparticles. *Nanotechnology* 28:045704. doi: 10.1088/1361-6528/28/4/045704
- Zhang, W., Hu, S., Yin, J. J., He, W., Lu, W., Ma, M., et al. (2016). Prussian blue nanoparticles as multienzyme mimetics and reactive oxygen species scavengers. *J. Am. Chem. Soc.* 138, 5860–5865. doi: 10.1021/jacs.5b12070
- Zhang, X., He, S., Chen, Z., and Huang, Y. (2013). CoFe₂O₄ nanoparticles as oxidase mimic-mediated chemiluminescence of aqueous luminol for sulfite in white wines. *J. Agric. Food Chem.* 61, 840–847. doi: 10.1021/jf3041269
- Zhang, Z., Liu, B., and Liu, J. (2017). Molecular imprinting for substrate selectivity and enhanced activity of enzyme mimics. *Small* 13, doi: 10.1002/smll.201602730
- Zhao, Y., Liang, M., Li, X., Fan, K., Xiao, J., Li, Y., et al. (2016). Bioengineered magnetoferritin nanoprobe for single-dose nuclear-magnetic resonance tumor imaging. *ACS Nano* 10, 4184–4191. doi: 10.1021/acsnano.5b07408
- Zheng, C., Ke, W., Yin, T., and An, X. (2016). Intrinsic peroxidase-like activity and the catalytic mechanism of gold@ carbon dots nanocomposites. *RSC Adv.* 6, 35280–35286. doi: 10.1039/c6ra01917j

Conflict of Interest: The authors declare that the research was conducted in the absence of any commercial or financial relationships that could be construed as a potential conflict of interest.

Copyright © 2020 Wang, Wang, Hong, Yan and Liang. This is an open-access article distributed under the terms of the Creative Commons Attribution License (CC BY). The use, distribution or reproduction in other forums is permitted, provided the original author(s) and the copyright owner(s) are credited and that the original publication in this journal is cited, in accordance with accepted academic practice. No use, distribution or reproduction is permitted which does not comply with these terms.



The Fate of SWCNTs in Mouse Peritoneal Macrophages: Exocytosis, Biodegradation, and Sustainable Retention

Ping-Xuan Dong^{1,2*}, Xinfeng Song^{1,2}, Jiwei Wu^{1,2}, Shuqin Cui^{1,2}, Guizhi Wang², Lianying Zhang³ and Hanwen Sun^{1,2*}

¹ Shandong Provincial Engineering Laboratory of Novel Pharmaceutical Excipients, Sustained and Controlled Release Preparations, Dezhou University, Dezhou, China, ² College of Medicine and Nursing, Dezhou University, Dezhou, China, ³ College of Life Science, Dezhou University, Dezhou, China

OPEN ACCESS

Edited by:

Michael Ming-Yuan Wei,
Texas Commission on Environmental
Quality, United States

Reviewed by:

Rui-Lin Liu,
Xian Jiaotong University, China
Weisi Song,
Arizona State University, United States

*Correspondence:

Ping-Xuan Dong
leaf-1210@163.com
Hanwen Sun
hanwen916@163.com

Specialty section:

This article was submitted to
Nanobiotechnology,
a section of the journal
Frontiers in Bioengineering and
Biotechnology

Received: 16 September 2019

Accepted: 03 March 2020

Published: 20 March 2020

Citation:

Dong P-X, Song X, Wu J, Cui S,
Wang G, Zhang L and Sun H (2020)
The Fate of SWCNTs in Mouse
Peritoneal Macrophages: Exocytosis,
Biodegradation, and Sustainable
Retention.
Front. Bioeng. Biotechnol. 8:211.
doi: 10.3389/fbioe.2020.00211

The understanding of toxicological and pharmacological profiles of nanomaterials is an important step for the development and clinical application of nanomedicines. Carbon nanotubes (CNTs) have been extensively explored as a nanomedicine agent in pharmaceutical/biomedical applications, such as drug delivery, bioimaging, and tissue engineering. The biological durability of CNTs could affect the function of CNTs-based nanomedicines as well as their toxicity in cells and tissues. Therefore, it is crucial to assess the fate of nanomedicine in phagocytes. Herein, we investigated the candidate fate of acid-oxidized single-walled carbon nanotubes (SWCNTs) in non-activated primary mouse peritoneal macrophages (PMQ). The sodium dodecyl sulfate polyacrylamide gel electrophoresis (SDS-PAGE) results showed that the intracellular SWCNTs continued growing from 4 to 36 h in PMQ. After replacing the exposure medium, we found the exosome induced by SWCNTs on the surface of macrophages according to scanning electron microscope (SEM) observation. The near-infrared (NIR) absorption increase of the supernatant samples after post-exposure indicates that SWCNTs exocytosis occurred in PMQ. The decreasing intracellular SWCNTs amount suggested the incomplete biodegradation in PMQ, which was confirmed by Raman spectroscopy and transmission electron microscopy (TEM). The combined data reveal that SWCNTs could be retained for more than 60 h in macrophages. Then sustainable retention of SWCNTs in primary macrophages was coexist with exocytosis and biodegradation. The findings of this work will shed light on the bioimaging, diagnosis and other biomedical applications of CNTs-based nanomedicines.

Keywords: SWCNTs, primary macrophages, exocytosis, biodegradation, sustainable retention

INTRODUCTION

Carbon nanotubes and other graphene-based materials have attracted considerable interest in many biomedical applications such as bioimaging, drug carrier and NIR-responsive cancer therapy (Yoo et al., 2015; Sajid et al., 2016). In 1991, Sumio Iijima discovered the carbon nanotubes (CNTs), which have been classified into single-wall carbon nanotubes (SWCNTs) and multi-walled carbon nanotubes (MWCNTs) based on the number of graphene layers. SWCNTs consist of a single long wrapped graphene sheet, while the MWCNTs have several graphene layers. SWCNTs

diameters range from 0.4 to 2 nm, while MWCNTs diameters range from 2 to 100 nm. All CNTs were high aspect ratio tubular structures with lengths varying between 0.2 micrometer and few micrometers (Sajid et al., 2016). Owing to their dominant structural, optical and electronic properties, carbon nanotubes have attracted attention for applications such as drug delivery, photoacoustic imaging, and diagnosis (De la Zerda et al., 2008; Al-Qattan et al., 2018). With the increasing production and biomedical application of nanoparticles, the probability occupational exposure and biological consumption rises. Carbon nanotube toxicity is regarded as one of the major concerns for therapeutic application (Kagan et al., 2005; Nel et al., 2006; Ema et al., 2016; Bishop et al., 2017). CNT *in vivo* toxicity research showed that SWCNTs or MWCNTs were engulfed by macrophages, which induced inflammatory response, granulomas formation, fibroblast focus, and potential carcinogenicity in the pulmonary organs of marine animals (Lam et al., 2004; Shvedova et al., 2008, 2013; Moller et al., 2014; Sargent et al., 2014). Additionally, inflammation, genotoxicity, oxidative stress, malignant transformation are induced by CNTs in lung epithelial cells, mesothelial cells and neurons cells (Kisin et al., 2007; Belyanskaya et al., 2009; Lindberg et al., 2009; Moller et al., 2014; Sargent et al., 2014). Significant quantities of these nanoparticles were recognized and engulfed by macrophages in the liver and spleen when the nanomaterials entered bodies (Pescatori et al., 2013; Feliu et al., 2016). The chronic toxicity mediated by nanoparticles to macrophages then increased with the consumption and long-term retention of these nanoparticles. Therefore, assessing the fate of nanoparticles consumed by macrophages of nanoparticles would lead to a better design and functionality of nanoproducts, including toxicity control (Oh and Park, 2014; Requardt et al., 2019).

Biodegradation of CNTs and other nanoparticles has been the subject of several studies (Feliu et al., 2016). Studies have shown that the carboxylated SWNTs were completely degraded through enzymatic catalysis with horseradish peroxidase (HRP), producing CO₂ gas over a period of 10 days (Allen et al., 2008, 2009). Human neutrophil enzyme myeloperoxidase (MPO) catalyzes the biodegradation of SWCNTs *in vitro*, resulting in a lower pulmonary inflammatory response in mice generated by biodegraded nanotubes (Kagan et al., 2010). The degradation of SWCNTs was mediated with human eosinophil peroxidase (EPO) *in vitro* and activated eosinophils *ex vivo* (Andon et al., 2013). Biodegradation of CNTs could be also mediated by oxidative metabolism in several bacteria species (Zhang et al., 2013). While within macrophage, a persistent inflammation cell, SWCNTs were digested by superoxide peroxynitrite oxidase and respiration burst, which was mediated by chemicals such as phorbol myristate acetate (PMA) activation (Kagan et al., 2014; Hou et al., 2016). The ability of biodegradation of CNTs in non-activated macrophages has not been documented.

The fate of nanoparticles was also modulated by exocytosis in mammalian cells (Sakhtianchi et al., 2013; Oh and Park, 2014). Exocytosis nanomaterials were reported containing DNA-wrapped SWCNTs (Jin et al., 2008, 2009), D-penicillamine coated quantum dots (Jiang et al., 2010), gold nanoparticles (Oh and Park, 2014), cerium dioxide nanoparticles (Strobel et al., 2015),

and silica nanoparticles (Chu et al., 2011). The exocytosis mechanism of SWCNTs mediated through the activation of P2×7 receptor, an ATP-gated membrane receptor in macrophages Raw264.7 (Cui et al., 2016). The intracellular SWCNTs in RAW264.7 showed a rapid excretion over time of exposure, short SWCNTs (195 nm) were expelled faster than long (630 nm) and middle (390) length SWCNTs (Cui et al., 2017). In primary macrophages, the question that whether SWCNTs exocytosis is involved in the final fate of SWCNTs after CNTs exposure has not been explored.

The water-soluble tetrazolium/formazan (WST-1) measurement demonstrated that SWCNTs (10–50 µg/mL) induced cytotoxicity at 24 h in Raw264.7 by decreasing cell viability (Dong et al., 2012). While in the primary macrophages, 10–50 µg/mL SWCNTs showed no significant cytotoxicity, but impaired the phagocytic function and accessory cell function (Dong et al., 2013). In this context, the present study was designed to assess the possible fate of SWCNT in primary macrophages with a low dose exposure (10 µg/mL). The reason for using this cell is that macrophages are distributed throughout most of the body, scrutinizing for foreign particles, such as nanomaterials. Additionally, primary macrophages have an increased number of opportunities to encounter and engulf CNTs. A number of studies have shown that CNTs residing in murine lung tissues for 2–3 months cause epithelioid granulomas and pulmonary fibrosis with uptake by macrophages (Lam et al., 2004; Wang P. et al., 2013). Exocytosis, biodegradation, sustainable retention or concomitant or any combined could be the potential final fate of SWCNTs in macrophages. Determining the fate of CNTs details in primary macrophages would be significant for gaining a better understanding of CNT toxicity, their durable time *in vivo* and desired medical applications.

In this study, we employed murine peritoneal macrophages, a primary macrophage, to investigate the fate of SWCNTs after 10 µg/mL exposure, since this concentration cause none cell death *in vivo* and *in vitro* (Hong et al., 2015). We measured the intracellular SWCNTs amount using SDS-PAGE (Wang et al., 2009) at different time points in macrophages exposed SWCNTs. Meanwhile, we monitored the amount of SWCNTs in the culture medium supernatant using ultraviolet-visible-near infrared (UV-vis-NIR) spectroscopy after the removal of the SWCNTs exposure solution. We characterized the degradation of SWCNTs structure with Raman microscopy. The intracellular SWCNTs were characterized by SDS-PAGE and TEM.

EXPERIMENTAL SECTION

Materials and Reagents

SWCNTs (CNTs purity > 95%, SWCNT purity > 90%, ash < 1.5 wt%) synthesized by chemical vapor deposition (CVD) method were originally obtained from Chengdu Organic Chemicals Co., Ltd. (SiChuan, China). The detailed information can be found on the company website: <http://www.timesnano.com/>. All ingredients for the culture media were purchased from Gibco. All ingredients for the media were purchased from Hyclone Inc. (Waltham, MA, United States).

Animals

Female Kunming mice were purchased from Charles River Laboratories (Beijing, China) and bred and housed under pathogen free conditions in the animal care facility.

This study was carried out in accordance with the principles of the Basel Declaration and recommendations of guidelines for experimental animals, the Institutional Animal Care and Use Committee of Peking University. The protocol was approved by the Institutional Animal Care and Use Committee of Peking University. Mice at 6–8 weeks of age were used for cell preparation.

Preparation of SWCNTs Solutions and Characterization

The water solution of SWCNTs was prepared according the procedure described previously (Dong et al., 2012). Briefly, 10 mg of SWCNTs were sonicated (KQ-500DV, 100 kHz, 60 kHz) in 40 mL of concentrated $\text{H}_2\text{SO}_4/\text{HNO}_3$ at a ratio of 3:1 in a 100 mL test tube for 24 h at 40–50°C. The resultant suspension was then diluted with deionized water and filtered through a membrane (0.22 μm), followed by a wash with deionized water until the pH changed to neutral. Then a 1 mg/mL SWCNTs solution in deionized water was made after sonication for 2 min (KQ-500DV, 40 kHz). For TEM characterization, SWCNTs were diluted to 10 $\mu\text{g/mL}$, precipitated onto a copper net, and then dried for imaging with a Hitachi H-7500 transmission electron microscopy at 80 kv (Tokyo, Japan). The hydrodynamic size distribution and surface charges of SWCNTs were characterized using a Zetasizer Nano (Malvern Instruments, Malvern, United Kingdom).

Primary Macrophages Collection and Culture

Mouse peritoneal macrophages were collected and determined using the protocol described previously (Wan et al., 2006, 2013; Dong et al., 2013). In brief, two or three mice were injected intra-peritoneally with a thioglycolate (TG) broth (3% wt/vol; 1 mL/mouse; Difco Laboratories, Livonia, MI, United States) 3 days before cell collection in order to elicit the macrophages into the peritoneal cavity. Cells were plated onto Corning 6-well tissue culture plates at $0.5\text{--}1 \times 10^6$ cells/well and then incubated at 37°C, 5% $\text{CO}_2/95\%$ air, and 95% humidity for 4 h to allow the macrophages to adhere to the surfaces. The surfaces were then washed twice with D-PBS to remove all non-adherent cells, and the macrophage layer was cultured in a complete RPMI-1640 (c-RPMI) medium, consisting of RPMI-1640 and 10% heat deactivated fetal bovine serum (FBS) supplemented with 20 mM L-glutamine and 100 U/ml penicillin/streptomycin. The resulting macrophage purity was > 95%, as determined by CD11b staining analysis.

Quantification SWCNTs in Primary Macrophages by SDS-PAGE Gel Electrophoresis

First, peritoneal macrophages were exposed with a low dose (10 $\mu\text{g/mL}$) SWCNTs. After incubation, SWCNTs uptake and

preservation in primary macrophages was determined by SDS-PAGE according to the method described previously (Wang et al., 2009; Cui et al., 2017). Briefly, macrophages were washed three times with D-PBS to remove extra SWCNTs. Then 160 μL cell lysis buffer containing 1% SDS, 1 mM MgCl_2 and 1 mM CaCl_2 was added for lysing the cells. After a short (2 min) sonication in an ultrasonic probe tip sonicator (JY92-IIN, Ningbo Scientz Biotechnology Co., Ltd. Zhejiang, China), the cell lysates was performed with SDS-PAGE gel electrophoresis using a Bio-Rad Mini Protean Tetra electrophoresis chamber. Twenty microliters cell lysate samples were loaded and then electrophoresed at 120 v for 2 h. We used 4% stacking gels to seal the loading well for 30 min and scanned the gel using a UMAX scanner. We quantified the integrated optical densitometry (IOD) of a SWCNTs band on the gel using Gel pro software (version 4.0). The same concentration of SWCNTs (125 $\mu\text{g/mL}$) was also loaded onto a loading well in each electrophoresis, which was used as a standard for control the cell lysates. The primary peritoneal macrophages were believed to be terminally differentiated cells, without any proliferation *ex vivo*. To eliminate the effect of difference cell numbers within each experiment, the SWCNTs band intensity was normalized against the calculated SWCNTs standard. Then the ratio of IOD was calculated as the SWCNTs band in cells against the standard SWCNTs brand.

Determination of SWCNT in Cell Supernatant by NIR Spectroscopy

Macrophages were exposed with 10 $\mu\text{g/mL}$ SWCNTs for 12 h and then washed 3 times with D-PBS, followed by incubation with a fresh c-RPMI culture. The cell supernatant was collected at indicated time points for NIR spectroscopy analysis. The NIR spectra were acquired by using a Cary 5000 UV-Vis-NIR spectrophotometer (Varian, Palo Alto, United States).

Scanning the Surface of Macrophages After SWCNTs Exposure

To explore the interactions between exocytosis SWCNTs and the cell membrane, peritoneal macrophages post-exposure with SWCNTs at same time points were investigated with SEM. First, cells cultured on sterilized coverslips were exposed to SWCNTs. After incubation in a fresh c-RPMI culture, cells were fixed with 2.5% glutaraldehyde in PBS overnight. After washing with D-PBS twice, the cells were washed with pure ethanol (100%) for 10 min and dried. After coating with platinum, the surfaces of the macrophages were observed with Hitachi SU8000 SEM (Hitachi, Tokyo, Japan).

Raman Spectroscopy Assessment of SWCNTs Within Peritoneal Macrophages

After exposure with SWCNTs and incubation with fresh c-RPMI, primary macrophages were fixed onto a glass bottom cell culture dish (Nest Scientific, Rahway, NJ, United States) using 4% paraformaldehyde. Next, the Raman spectrum of SWCNTs within cells was detected using an inVia Raman microscope spectrometer (Renishaw Plc., Gloucestershire, United Kingdom).

with a 633 nm laser source. We obtained the changes in the D and G band intensity throughout the degradation process at the spectrum range of 800–1800 cm^{-1} . All Raman spectra were recorded for 10 s at 10% laser power, using a 50 L objective. For each sample, at least 70 spectra were recorded.

Ultrathin Section of *in situ* Macrophages for SWCNTs Examination

Cells at a concentration of 1×10^6 were exposed to 10 $\mu\text{g}/\text{mL}$ SWCNTs for 12 h in a glass bottom cell culture dish. After incubation in fresh c-RPMI for 12–48 h, the cells were fixed *in situ* with 2.5% glutaraldehyde for 10 min at room temperature and stored at 4°C overnight. Then cells were post-fixed *in situ* with 1% of osmium tetroxide at room temperature for 2 h, followed by dehydration and resin embedding. Ultrathin sections of macrophages were cut by using a Leica EM UC6 ultramicrotome (Wetzlar, Germany) and settled on 200-mesh carbon-coated copper grids. After staining with uranyl acetate and lead citrate, the samples were observed with a Hitachi H-7650 TEM (Hitachi, Tokyo, Japan).

Transmission Electron Microscopy (TEM)

To detect the morphology of the residual SWCNTs within primary macrophages at 12–36 h, the cell lysis of macrophages post-exposure was observed on a Hitachi H-7500 TEM (Hitachi, Tokyo, Japan).

Statistical Analysis

The data were expressed as the mean \pm standard deviation (SD), and the difference between groups was evaluated using Student's *t*-test, with the significance level set at $*p < 0.05$ or $**p < 0.01$.

RESULTS AND DISCUSSION

Characterization of SWCNTs

Stable SWCNTs physiologic solutions have been helpful for biomedical application, such as tumor-targeted multifunction, drug delivery and immunomodulator (Villa et al., 2008; Pescatori et al., 2013; Bhattacharya et al., 2015). Acid-functionalized SWCNTs (AF-SWCNTs) were better dispersed in c-RPMI than non-treated SWCNTs (Figure 1A). The suspension was stable for days without any obvious precipitation, while the non-treated SWCNTs suspension showed precipitation at the same concentration (10 $\mu\text{g}/\text{mL}$). TEM images showed that AF-SWCNTs presented fibrillar tube shape and retained the structural integrity of the carbon nanotubes (Figure 1B). After acid-oxidation, most SWCNTs were 200–1000 nm in length and separated into bundles, and a few aggregated into clusters. Dynamic light scattering data also dominated the average hydrodynamic diameters (HD) of functionalized SWCNTs at 400nm, while a few were more than 1000 nm (Figure 1C) in water solution. The zeta potentials were changed to -44.1 mv (in pH 12) from -23.2 mv (in pH 2), which indicated many negative charges existed on the surface of SWCNTs (Supplementary Figure S1). The well dispersion in aqueous media depended

on the carboxyl and hydroxyl groups around the sidewalls of SWCNTs and the surface negative charges (Dong et al., 2013; Cui et al., 2016). SWCNTs had little (0.056 wt%) iron content through inductively coupled plasma mass spectrometry (ICP-MS) measurement (Dong et al., 2012).

Cellular Internalization of SWCNTs in Primary Peritoneal Macrophages

To investigate the SWCNTs internalized in primary macrophages, we employed an SDS-PAGE to quantify the amount of SWCNTs in cells. With gel electrophoresis, the SWCNTs in cell lysates could deposit as a sharp black band in the stacking gel, while cellular proteins could be stripped off the SWCNTs and dispersed in the resolving gel (Wang et al., 2009). We first determined the standard curve of the amount of SWCNTs against the band intensity by SDS-PAGE using a bovine serum albumin (BSA) and SWCNTs mixtures at 16–500 $\mu\text{g}/\text{mL}$. The standard curve showed a good linear relationship ($R^2 = 0.9993$), as shown in Supplementary Figure S2.

SDS-PAGE results indicated that the SWCNTs accumulation in primary macrophages increased with the exposure time prolonged. The ratio of IOD increased to 0.81 ± 0.12 (36 h exposure) from 0.20 ± 0.06 (4 h exposure) (Figure 2A). The amount of SWCNTs within primary macrophages increased to 20.3 μg (36 h) from 5 μg (4 h). The results of bright field imaging directly showed that SWCNTs within the cells tended to increase with prolonged exposure (Figure 2B). These data suggest that SWCNT internalization by mouse primary macrophages is a persistent process during 4–36 h exposure. While the intracellular SWCNTs in RAW showed an elevated peak at 8 h, which was followed by a rapid excretion over time of exposure (Cui et al., 2017). This difference may be dependent on the different susceptibility and enzyme system between primary cells and cancer cell lines (Wang et al., 2011).

Exocytosis of SWCNTs in Primary Macrophages

Several studies have demonstrated that CNTs and other nanoparticles were repelled from cells following their uptake (Jin et al., 2009; Wang Y. et al., 2013; Strobel et al., 2015; Cui et al., 2017). Exocytosis of nanoparticles impacts both their toxicity and the efficiency of therapeutic delivery (Sakhtianchi et al., 2013).

To determine the fate of SWCNTs in primary peritoneal macrophages, we observed the exocytosis of SWCNTs following their uptake using SEM, TEM, and NIR spectroscopy. SEM images indicated that a large number of exosomes were located on the primary macrophage surface at different time points after removing the SWCNTs solution (Figure 3A). SEM observations showed that clusters of 50–100 nm exosomes and 100–400 nm extracellular vesicles (EVs) were secreted extracellularly by the primary macrophages at 24 and 36 h post exposure after 6 h SWCNTs exposure (Figure 3A). No exosome or EV was found on the surface of control primary macrophages (Supplementary Figure S3). Under TEM examination, multivesicular endosomes (MVEs) were found (Figure 3B), which generate exosomes when

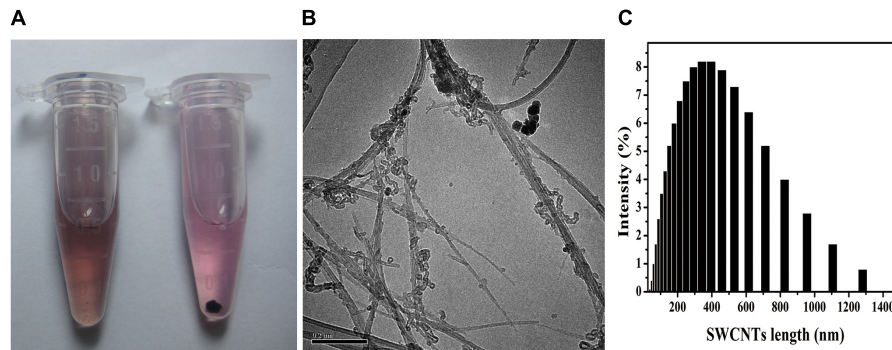


FIGURE 1 | SWCNTs suspension, TEM images, and hydrodynamic size distribution. **(A)** Suspension in c-RPMI of acid-functionalized SWCNTs (AF-SWCNTs, Left) and non-treated SWCNTs (Right). **(B)** Representative TEM image of AF-SWCNTs. Scale bar = 0.2 μm . **(C)** Hydrodynamic size (HDS, nm) distribution in water.

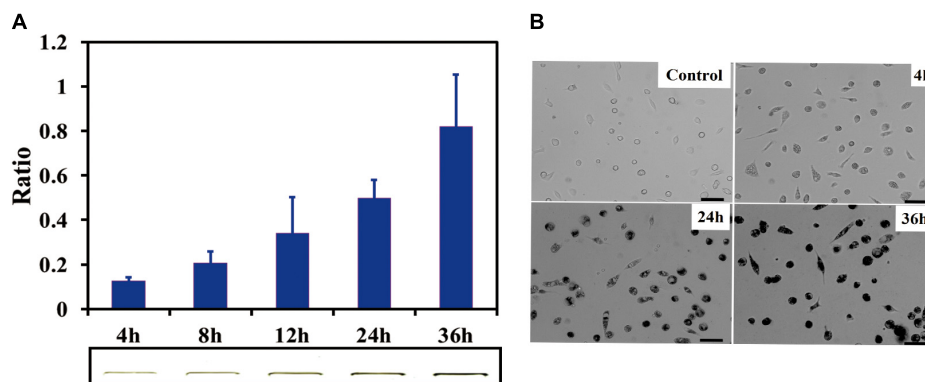


FIGURE 2 | Cellular uptake of SWCNTs in primary macrophages. **(A)** Relative quantification of cellular uptake of SWCNTs in mouse peritoneal macrophages in a time-dependent manner. In the lower panel shows corresponding representative SWCNTs in gel. **(B)** Representative microscopy images of cell cultured after 10 $\mu\text{g/mL}$ SWCNT exposure for 0, 4, 24, and 36 h. The darker the color is the more SWCNTs are within individual cells at the low cell density area. Scale bar = 30 μm . For **(A)**, data are presented as the mean of three independent experiments. Error bars represent the standard errors.

they fuse with the plasma membrane (Tkach and Thery, 2016). SWCNT-containing vesicles near cell membrane were also found to be released to extracellular spaces (Figure 3B), which were also reported in macrophage cell line-RAW264.7 (Cui et al., 2017). Then, the SWCNTs-containing vesicles were as small as exosomes (50–100 nm) and EVs (100–400 nm) (Figure 3A) in primary macrophages, where several aggregating together (Figure 3B). However, the released SWCNTs in RAW264.7 were 400–1000 nm in length, and located in lysosomes (late endosome), with sized about 1 μm (Cui et al., 2017). Therefore, the data suggest that the exocytosis of shorter SWCNTs (<50 nm) could have been facilitated by exosomes and EVs in primary macrophages, while exocytosis of long SWCNTs fibers (400–1000 nm) may be produced by late endosomes. Meanwhile, the morphology of macrophages gradually changed to a large and flat shape from a rounded shape with the increased post-exposure time (Supplementary Figure S4). These images indicate the SWCNTs exposure induced exosome and other EVs formation and secretion in primary macrophages. Consistent with this, Zhu et al. (2012) reported that magnetic iron oxide nanoparticles (MIONs) induced exosome secretion from the mice alveolar macrophages

in a dose-dependent manner. The exosomes induced by MIONs affected the exocytosis and degradation of MIONs nanoparticles (Zhu et al., 2012).

To verify SWCNTs expulsion into the extracellular environment, the supernatant was analyzed after removing the exposure solution using a typical NIR spectra of carbon nanotubes, by which we characterized the metallic band (M1, ~ 965 nm) and semiconducting transition absorbing band (S2, ~ 1155 nm) (Cherukuri et al., 2004). Data showed that absorption increased in the S2 band over a time period of 8–24 h after exposure, but absorption in S2 band then decreased at 48 h (Figure 3C). There was no significant cell death after explosion with the same concentration for 24 h, as reported previously (Dong et al., 2013), which allowed us to rule out the influence of cell death on the release of intracellular SWCNTs. SEM images showed that phagocytosis of tangled SWCNTs occurred in primary macrophages after removing the exposure solution (Figure 3D). The results suggest there was a sustained internalization of SWCNTs following the exocytosis, since the primary macrophage could take up latex beads after exposure of SWCNTs, which was also reported by previous research

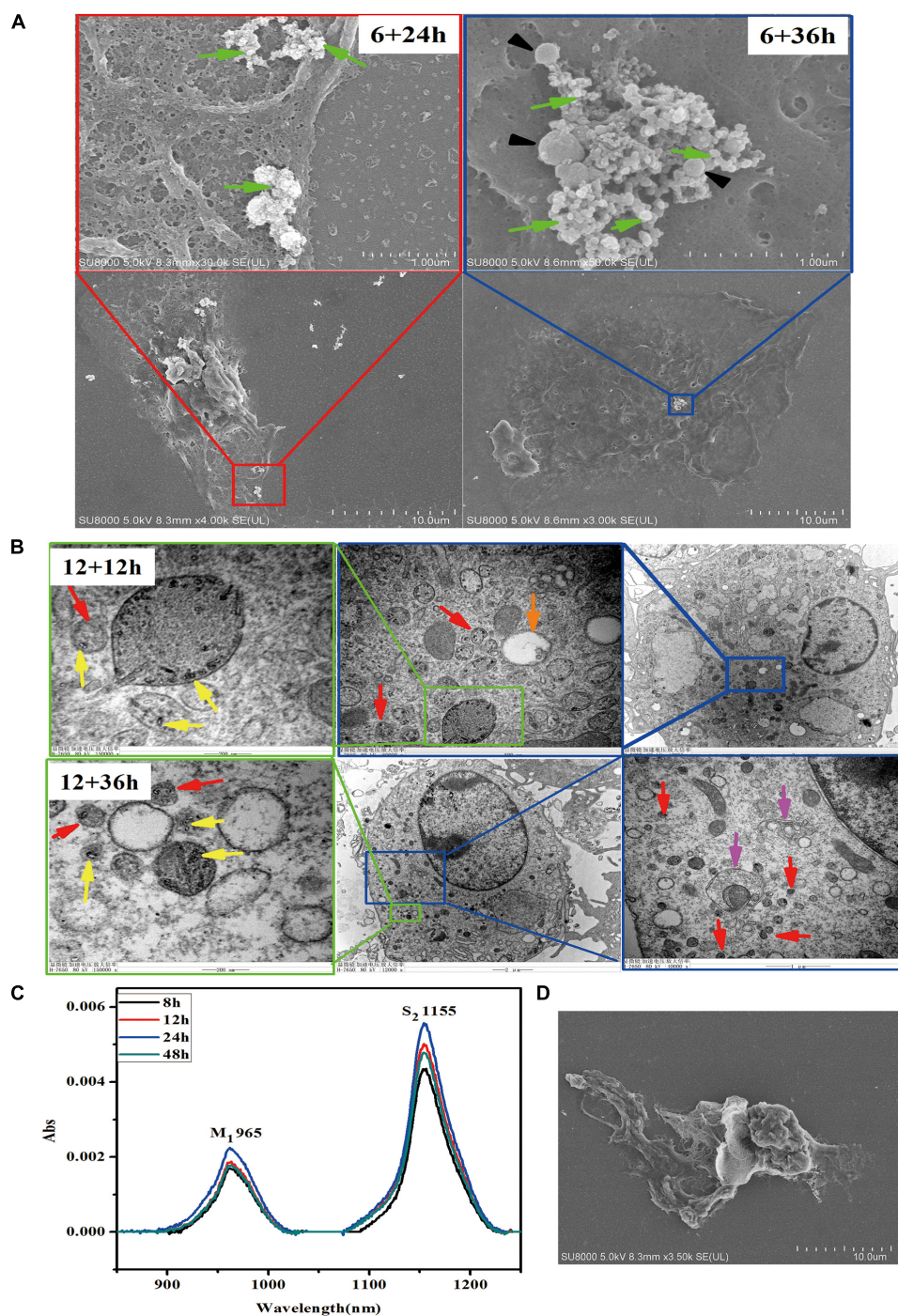


FIGURE 3 | Exocytosis of SWCNTs by primary peritoneal macrophages. **(A)** Representative SEM images of exosome (green arrows) and extracellular vesicles (black arrowheads) on the surface of primary peritoneal macrophages at 24 h (Left) and 36 h (Right) after 6 h SWCNT exposure. **(B)** TEM images showing the SWCNTs (yellow arrows), small vesicles (red arrows), multivesicular bodies (MVBs, orange arrows) and autophagosome/autolysosome (pink arrows) in primary macrophages at 12 h (up panels) and 36 h (bottom panels) after removing 12 h SWCNTs (10 μ g/mL) exposure. **(C)** NIR spectra of the supernatant of SWCNTs at different time (8–48 h). **(D)** SEM image of primary macrophages phagocytosis tangled SWCNTs.

(Dong et al., 2013). Similarly, the titanium dioxide nanoparticles excreted from neural stem cells could be re-taken by cells (Wang Y. et al., 2013).

P2 \times 7 receptor played a crucial role in regulation exocytosis of SWCNTs in macrophages RAW264.7, which can be activated by ATP and inhibited by oxidized ATP (OATP) (Cui et al., 2016).

But in this study, ATP/OATP cannot affect the quantified the SWCNTs in primary PMQ (data not shown), which indicates that other mechanisms but not P2 \times 7 receptor pathway could regulate the exocytosis in the primary macrophage.

Biodegradation of SWCNTs in Primary Macrophages

The observed reduction of supernatant SWCNTs made us to question whether there was an increase of SWCNTs within primary macrophages. To this end, we measured the intracellular SWCNTs amounts after replacing the exposure solution with fresh culture medium. SDS-PAGE gel results indicated that 86, 87, 79, and 63% of the internalized SWCNTs in primary macrophages remained within cells respectively at 8, 12, 24, and 48 h after removing the exposed SWCNTs. The amount of SWCNTs in primary macrophages decreased with the prolonged post-exposure time. At 24 and 48 h post-exposure the amount of SWCNTs within cells decreased significantly compared with the intracellular SWCNTs with 12 h SWCNTs exposure (* $p < 0.05$, ** $p < 0.01$) (Figure 4A). The reduced amount of SWCNTs suggests that degradation in primary macrophages could be occurring.

In addition, typical Raman spectra of SWCNTs in primary macrophages presents a characteristic tangential-mode G-band at 1580 cm⁻¹ (± 10) and a characteristic disordered mode D-band at 1340 cm⁻¹ (± 10). A marked loss of the G-band and increase of D-band at 48 h post-exposure (Figure 4B) would indicate that the existence of a biodegradation process of CNTs. The characteristic D/G band intensity ratio is correlated with the degree of structural defects during degradation (Liu et al., 2010; Nunes et al., 2012). The results in this study showed that the defect sites on the side-walls and the I_D/I_G ratio of SWCNTs increased in a time dependent manner after changed with fresh culture medium (Figure 4C). The I_D/I_G ratio of SWCNTs increased from 0.38 (± 0.08) to 0.44 (± 0.09), 0.59 (± 0.08), 0.61 (± 0.10) at 12, 24, and 48 h, respectively, following a 12 h exposure (Figure 4D). The Raman data of SWCNT in cells were consistent with the SDS-PAGE results. The results indicate that there was an occurrence of SWCNTs partial biodegradation in the murine peritoneal macrophages without any chemical stimulation.

The mechanism of CNTs biodegradation was reported to relate with several peroxidases and reactive oxygen species (ROS) (Kagan et al., 2014; Yang et al., 2019). The results of ROS generation in primary macrophages with 2',7'-dichlorofluorescein diacetate (DCF-DA) assay showed no significant changes after SWCNTs exposure (data not shown). The biodegradation of SWCNTs was found by several natural enzymes, such as HRP, MPO, and EPO *in vitro* and *ex vivo* (Allen et al., 2008; Kagan et al., 2010; Andon et al., 2013). Previous studies showed that HRP (a plant-derived enzyme), MPO (neutrophils-derived) and EPO (expressed in eosinophils) combined with superoxide (such as H₂O₂) played an important role in degradation of SWCNTs *ex vivo* or in neutrophils and eosinophils (Kagan et al., 2010; Andon et al., 2013). Poly(ethylene glycol)PEG functionalized SWCNTs could be defunctionalized and biodegraded in neutrophil by MPO/H₂O₂ system or by hypochlorite and its' product hypochlorous acid (HOCl)

(Vlasova et al., 2012; Bhattacharya et al., 2014). While the macrophages expressed low level of MPO and EPO (Dale et al., 2008). It was reported that the macrophages "digest" SWCNTs by superoxide/peroxynitrite oxidative induced by NADPH oxidase (Kagan et al., 2014; Ding et al., 2017; Yang et al., 2019), which could be accelerated by PMA stimulation (Kagan et al., 2014; Hou et al., 2016). Then more details about the mechanism of biodegradation of SWCNTs in none stimulation primary macrophages should be better study in future.

Residual SWCNTs Within Post-exposure Primary Macrophages

Although exocytosis and biodegradation processes coexist in primary macrophages, there were still 63% of intracellular SWCNTs residual within cells (Figure 4A). We detected morphological changes of SWCNTs remaining in cells using SEM and cell lysate TEM characterizations. The SEM images indicated the presence of approximately 5 μ m long, fiber-like SWCNTs and tangle SWCNTs in the primary macrophages (Figure 5A). These SWCNTs protruded from the surface of the macrophages and wrapped within the cell membrane structure (white arrows in Figure 5A). As a result, these SWCNTs are tightly connected with cell membrane and can't be removed through washing. These SWCNTs made a remarkable contribution to the amount of SWCNTs within the cells, as showed in Figure 4A. The lysate of post-exposure macrophages TEM images showed that after 36 h post-exposure the SWCNTs underwent structural deformation, increasing of fragmentation and loss of fibrous structure (Figure 5B), when compared with their original appearance (Figure 1B). The data also verified the presence of SWCNTs biodegradation in primary macrophages, as shown in Figure 3, while the long tubular structure of SWCNTs still defined (Figure 5A). With prolonged time post-exposure, the morphology of primary macrophages also gradually changed from a small spheroidal shape to a large, flat shape also (Supplementary Figure S3). The results indicated that acid-functional long SWCNTs sustainable retention in primary macrophages for days. The bio-durability of SWCNTs was reported that depended on the surface functionalization. SWCNTs with acid function undergo 90-day degradation while the ozone-treated and aryl-sulfonated SWCNTs do not degrade *in vitro* (Liu et al., 2010). Nunes et al. (2012) reported the presence of a partial biodegradation of MWCNT-NH₃⁺ by microglia in the motor cortex after 14 days post-cortical administration.

The data of SDS-PAGE, Raman (Figure 4) and SEM and TEM (Figure 5) indicated that CNTs' length maybe another factor affects the bio-durability in macrophages. Long fibrous MWCNTs with tens of micrometers could be seen protruding from the macrophages, which elicited an inflammatory response *in vivo* and *in vitro*, as reported previously (Muhlfeld et al., 2012; Murphy et al., 2012). Long, but not short/tangled, CNTs were deposited in the pulmonary airspaces and caused pleural inflammation and chest wall lesions (Murphy et al., 2012, 2013). IL-1 β release in macrophages depended on the length of exposed CNTs, as long CNTs were frustrated phagocytosis by macrophages (Murphy et al., 2012). Long exposure of MWCNTs

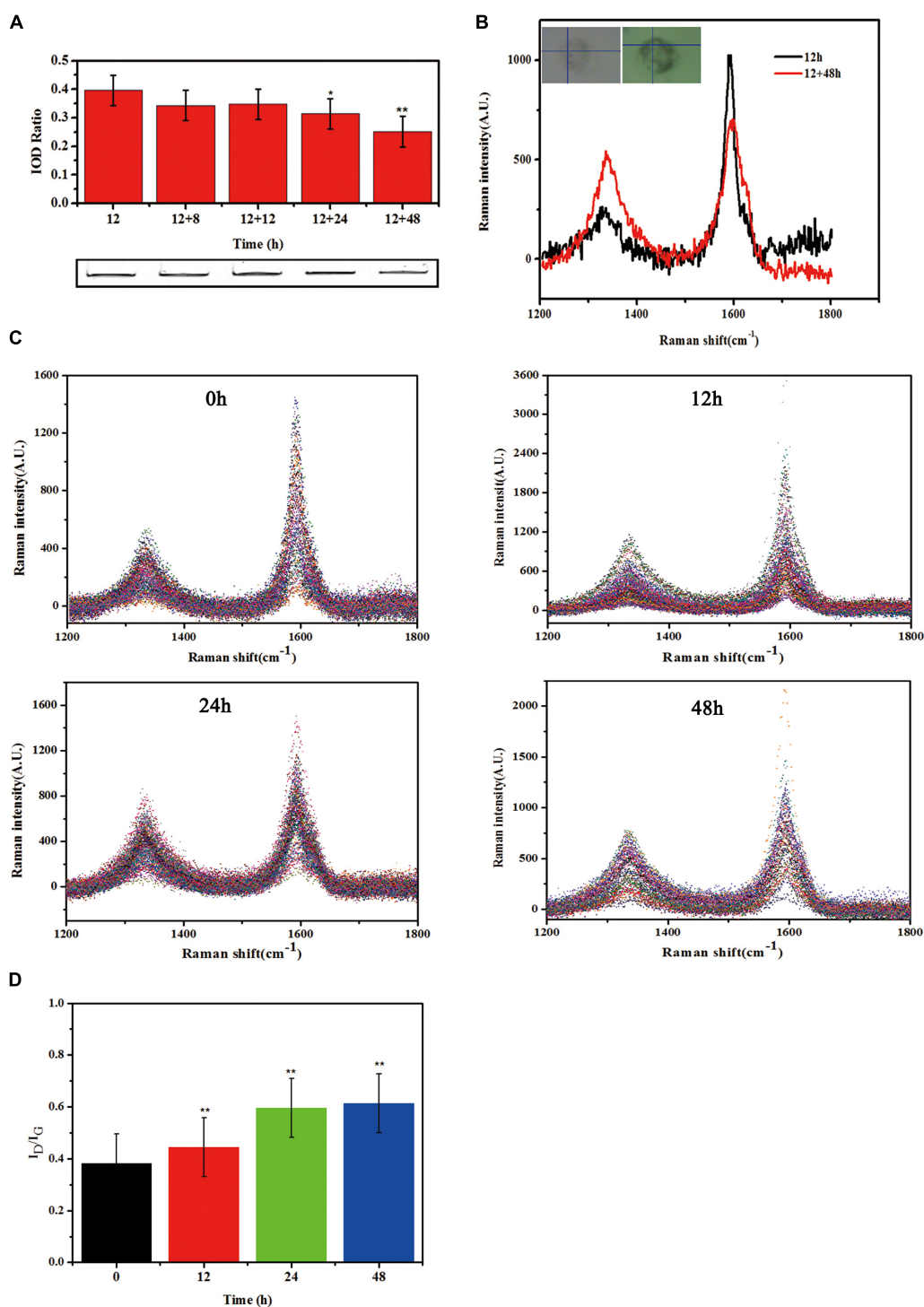


FIGURE 4 | Biodegradation of SWCNTs in primary macrophages. **(A)** Measurement the amount of SWCNTs by SDS-PAGE gel analyses within primary macrophages at extending time period of 8, 12, 24, and 48 h after removing exposure solutions. The amount of SWCNTs within cells decreased at 24 and 48 h significantly compared with the time point of 12 h SWCNTs exposure (* $p < 0.05$, ** $p < 0.01$). **(B)** Representative Raman spectra (excitation, 633 nm) of SWCNTs in primary macrophages at 12 h (black line) exposure and then 48 h (red line) after changing to fresh c-RPMI medium. Corresponding cell images and sampling sites were shown as insets. **(C)** Collated Raman spectra as acquired from the macrophages just changing fresh c-RPMI (0 h) (left up), 12 h (right up), 24 h (left bottom) and 48 h (right bottom). **(D)** Quantitative I_D/I_G ratios of SWCNTs suggesting dramatic changes in the carbon structure of the nanotubes in primary macrophages. The intensity ratio between D and G bands (I_D/I_G) indicated was calculated from the average intensities of D and G bands at each time point ($n = 102$, $n = 96$, $n = 121$, and $n = 70$ spectra used for calculation at each time point, respectively. Average intensity of G band was normalized to 1. The means and standard deviations of I_D/I_G were given. (** $p < 0.01$).

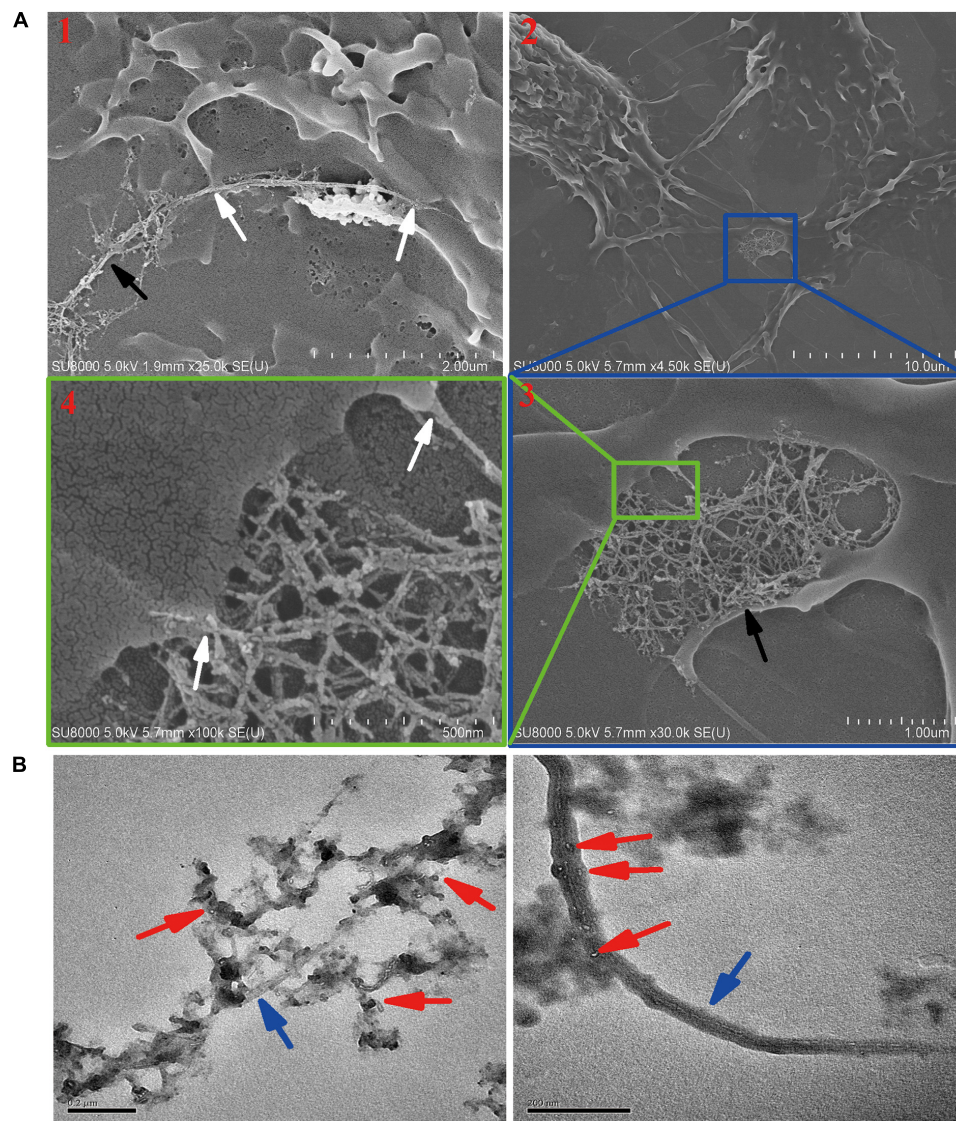


FIGURE 5 | Characterization the residual SWCNTs within post-exposed primary macrophages by SEM and TEM. **(A)** SEM images showing long and tangled SWCNTs (black arrow) connected with cell membrane (white arrow) at 24 h after 12 h SWCNTs exposure. Image #1 and 2, 3, 4 were obtained at two different cells. **(B)** TEM images showing SWCNTs after exposed in primary macrophages 12 h (left) and with 36 h post-exposure (right). Blue arrows point to SWCNTs with long fiber-like shape; Red arrows point to degraded fragments of SWCNTs. Scale bar in TEM images = 200 nm.

induced a prolonged presence of inflammatory cytokines IL-6 and TNF- α in alveolar macrophages, whereas short MWCTNs stimulated fibrosis and collagen secretion (Wang et al., 2010; Muhlfeld et al., 2012). All the data indicates that long and tangled CNTs present different mechanisms of toxicity. It indicated that short CNTs were suggested for biomedical application to reduce the biopersistence and inflammatory response in biosystems.

Engineered nanomaterials could also be recognized and cleared as “pathogens” by immune-competent cells, such as macrophages (Farrera and Fadeel, 2015). Our results show that the fate of SWCNTs in primary macrophages is a complicated process, consisting of simultaneous uptake, exocytosis, biodegradation and retention. Clearance of long

fiber CNTs is a much slower process than for short CNTs and compact particles in macrophages (Murphy et al., 2013; Landry et al., 2016). It is necessary to understand the potential toxicity of the residual CNTs within cells as the retention time prolongs. Autophagosomes/autolysosomes in cytoplasm (**Figure 3B**) indicate also autophagy in primary macrophages induced by CNTs, as reported previously (Wan et al., 2013; Cohignac et al., 2018). It has also been reported that complete degradation of CNTs produces only CO₂ molecules, with fully biocompatible CNTs (Allen et al., 2008, 2009). However, the degradation of CNTs may produce some toxic by-products, such as polyaromatic hydrocarbons and other in-rich aromatic rings molecules (Nunes et al., 2012; Zhang et al., 2013). Therefore,

it is worth considering the toxicology effects of the degrading mixture. There has been considerable interest in carcinogenicity of CNTs, as they are high aspect ratio materials and persistent in cells and tissues (Luanpitpong et al., 2016b). Rigid long MWCNTs can cause mesothelioma, while frustrated phagocytosis is a mechanism of CNT-induced carcinogenesis (Poland et al., 2008; Takagi et al., 2012). Chronic exposure of CNTs to epithelial cells induces cell changes to cancer-like cells and malignant tumor cells (Wang et al., 2011; Luanpitpong et al., 2016a).

CONCLUSION

In conclusion, the study has investigated the fate of SWCNTs in primary macrophages. Our results showed that mouse peritoneal macrophages internalized SWCNTs in a time-dependent manner, utilizing phagocytosis. After the removal of the SWCNTs exposure solution, the amount of SWCNTs in the suspension increased during the first 24 h. The exosomes and extracellular vesicles induced by SWCNTs were observed on the surface of post-exposure macrophages. The data indicates that the exocytosis of SWCNTs from macrophages occurred, and an uptake following the exocytosis was also observed. However, the biodegradation of SWCNTs within primary macrophages also occurred after the removal of the exposure solution. The connection of long and tangled SWCNTs was also examined by SEM and TEM images. All data showed that exocytosis, uptake, biodegradation and sustainable retention of SWCNTs co-exist in primary macrophages. Long acid-functional SWCNTs were suggested for longer biopersistence in primary macrophages. Understanding the fate and retention time of CNTs in cells and living organism may facilitate the assessment of CNTs health risks and the design of CNTs agents for improved application in bioimaging, drug delivery, and cancer therapy.

REFERENCES

- Allen, B. L., Kichambare, P. D., Gou, P., Vlasova, I. I., Kapralov, A. A., Konduru, N., et al. (2008). Biodegradation of single-walled carbon nanotubes through enzymatic catalysis. *Nano Lett.* 8, 3899–3903. doi: 10.1021/nl802315h
- Allen, B. L., Kotchey, G. P., Chen, Y., Yanamala, N. V., Klein-Seetharaman, J., Kagan, V. E., et al. (2009). Mechanistic investigations of horseradish peroxidase-catalyzed degradation of single-walled carbon nanotubes. *J. Am. Chem. Soc.* 131, 17194–17205. doi: 10.1021/ja9083623
- Al-Qattan, M. N., Deb, P. K., and Tekade, R. K. (2018). Molecular dynamics simulation strategies for designing carbon-nanotube-based targeted drug delivery. *Drug Discov. Today* 23, 235–250. doi: 10.1016/j.drudis.2017.10.002
- Andon, F. T., Kapralov, A. A., Yanamala, N., Feng, W., Baygan, A., Chambers, B. J., et al. (2013). Biodegradation of single-walled carbon nanotubes by eosinophil peroxidase. *Small* 9, 2721–2729, 2720. doi: 10.1002/smll.201202508
- Belyanskaya, L., Weigel, S., Hirsch, C., Tobler, U., Krug, H. F., and Wick, P. (2009). Effects of carbon nanotubes on primary neurons and glial cells. *Neurotoxicology* 30, 702–711. doi: 10.1016/j.neuro.2009.05.005
- Bhattacharya, K., El-Sayed, R., Andón, F. T., Mukherjee, S. P., Gregory, J., Li, H., et al. (2015). Lactoperoxidase-mediated degradation of single-walled carbon nanotubes in the presence of pulmonary surfactant. *Carbon* 91, 506–517. doi: 10.1016/j.carbon.2015.05.022

DATA AVAILABILITY STATEMENT

The datasets generated for this study are available on request to the corresponding author.

ETHICS STATEMENT

The animal studies were approved by the Institutional Animal Care and Use Committee of Peking University.

AUTHOR CONTRIBUTIONS

P-XD and HS designed the study. P-XD performed the experiments and analyzed the data. XS, JW, SC, and GW contributed reagents, materials, and analysis tools. P-XD wrote the manuscript. LZ revised the final manuscript. All authors have read and approved the final manuscript.

FUNDING

This work was supported by the National Natural Science Foundation of China (21806019 and 21607021). This work was also supported by the Foundation of State Key Laboratory of Environmental Chemistry and Ecotoxicology, Research Center for Eco-Environmental Sciences (KF2012-02).

SUPPLEMENTARY MATERIAL

The Supplementary Material for this article can be found online at: <https://www.frontiersin.org/articles/10.3389/fbioe.2020.00211/full#supplementary-material>

- Bhattacharya, K., Sacchetti, C., El-Sayed, R., Fornara, A., Kotchey, G. P., Gaugler, J. A., et al. (2014). Enzymatic ‘stripping’ and degradation of PEGylated carbon nanotubes. *Nanoscale* 6, 14686–14690. doi: 10.1039/c4nr03604b
- Bishop, L., Cena, L., Orandle, M., Yanamala, N., Dahm, M. M., Birch, M. E., et al. (2017). *In vivo* toxicity assessment of occupational components of the carbon nanotube life cycle to provide context to potential health effects. *ACS Nano* 11, 8849–8863. doi: 10.1021/acsnano.7b03038
- Cherukuri, P., Bachilo, S. M., Litovsky, S. H., and Weisman, R. B. (2004). Near-infrared fluorescence microscopy of single-walled carbon nanotubes in phagocytic cells. *J. Am. Chem. Soc.* 126, 15638–15639. doi: 10.1021/ja0466311
- Chu, Z., Huang, Y., Tao, Q., and Li, Q. (2011). Cellular uptake, evolution, and excretion of silica nanoparticles in human cells. *Nanoscale* 3, 3291–3299. doi: 10.1039/c1nr10499c
- Cohignac, V., Landry, M. J., Ridoux, A., Pinault, M., Annangi, B., Gerdil, A., et al. (2018). Carbon nanotubes, but not spherical nanoparticles, block autophagy by a shape-related targeting of lysosomes in murine macrophages. *Autophagy* 14, 1323–1334. doi: 10.1080/15548627.2018.1474993
- Cui, X., Wan, B., Yang, Y., Ren, X., and Guo, L. H. (2017). Length effects on the dynamic process of cellular uptake and exocytosis of single-walled carbon nanotubes in murine macrophage cells. *Sci. Rep.* 7:1518. doi: 10.1038/s41598-017-01746-9
- Cui, X., Wan, B., Yang, Y., Ren, X., Guo, L. H., and Zhang, H. (2016). Crucial role of P2X7 receptor in regulating exocytosis of single-walled carbon nanotubes in macrophages. *Small* 12, 5998–6011. doi: 10.1002/smll.201602410

- Dale, D. C., Boxer, L., and Liles, W. C. (2008). The phagocytes: neutrophils and monocytes. *Blood* 112, 935–945. doi: 10.1182/blood-2007-12-077917
- De la Zerda, A., Zavaleta, C., Keren, S., Vaithilingam, S., Bodapati, S., Liu, Z., et al. (2008). Carbon nanotubes as photoacoustic molecular imaging agents in living mice. *Nat. Nanotechnol.* 3, 557–562. doi: 10.1038/nnano.2008.231
- Ding, Y., Tian, R., Yang, Z., Chen, J., and Lu, N. (2017). NADPH oxidase-dependent degradation of single-walled carbon nanotubes in macrophages. *J. Mater. Sci. Mater. Med.* 28:7. doi: 10.1007/s10856-016-5817-z
- Dong, P. X., Wan, B., and Guo, L. H. (2012). *In vitro* toxicity of acid-functionalized single-walled carbon nanotubes: effects on murine macrophages and gene expression profiling. *Nanotoxicology* 6, 288–303. doi: 10.3109/17435390.2011.573101
- Dong, P. X., Wan, B., Wang, Z. X., Guo, L. H., Yang, Y., and Zhao, L. (2013). Exposure of single-walled carbon nanotubes impairs the functions of primarily cultured murine peritoneal macrophages. *Nanotoxicology* 7, 1028–1042. doi: 10.3109/17435390.2012.694487
- Ema, M., Gamo, M., and Honda, K. (2016). A review of toxicity studies of single-walled carbon nanotubes in laboratory animals. *Regul. Toxicol. Pharmacol.* 74, 42–63. doi: 10.1016/j.yrtph.2015.11.015
- Farrera, C., and Fadeel, B. (2015). It takes two to tango: understanding the interactions between engineered nanomaterials and the immune system. *Eur. J. Pharm. Biopharm.* 95, 3–12. doi: 10.1016/j.ejpb.2015.03.007
- Feliu, N., Docter, D., Heine, M., Del Pino, P., Ashraf, S., Kolosnjaj-Tabi, J., et al. (2016). *In vivo* degeneration and the fate of inorganic nanoparticles. *Chem. Soc. Rev.* 45, 2440–2457. doi: 10.1039/c5cs00699f
- Hong, G., Diao, S., Antaris, A. L., and Dai, H. (2015). Carbon nanomaterials for biological imaging and nanomedicinal therapy. *Chem. Rev.* 115, 10816–10906. doi: 10.1021/acs.chemrev.5b00008
- Hou, J., Wan, B., Yang, Y., Ren, X. M., Guo, L. H., and Liu, J. F. (2016). Biodegradation of single-walled carbon nanotubes in macrophages through respiratory burst modulation. *Int. J. Mol. Sci.* 17:409. doi: 10.3390/ijms17030409
- Jiang, X., Röcker, C., Hafner, M., Brandholt, S., Dörlich, R. M., and Nienhaus, G. U. (2010). Endo- and exocytosis of zwitterionic quantum dot nanoparticles by live hela cells. *ACS Nano* 4, 6787–6797. doi: 10.1021/nn101277w
- Jin, H., Heller, D. A., Sharma, R., and Strano, M. S. (2009). Size-dependent cellular uptake and expulsion of single-walled carbon nanotubes: single particle tracking and a generic uptake model for nanoparticles. *ACS Nano* 3, 149–158. doi: 10.1021/nn800532m
- Jin, H., Heller, D. A., and Strano, M. S. (2008). Single-particle tracking of endocytosis and exocytosis of single-walled carbon nanotubes in NIH-3T3 cells. *Nano Lett.* 8, 1577–1585. doi: 10.1021/nl072969s
- Kagan, V. E., Bayir, H., and Shvedova, A. A. (2005). Nanomedicine and nanotoxicology: two sides of the same coin. *Nanomedicine* 1, 313–316. doi: 10.1016/j.nano.2005.10.003
- Kagan, V. E., Kapralov, A. A., St Croix, C. M., Watkins, S. C., Kisin, E. R., Kotchey, G. P., et al. (2014). Lung macrophages "digest" carbon nanotubes using a superoxide/peroxynitrite oxidative pathway. *ACS Nano* 8, 5610–5621. doi: 10.1021/nn406484b
- Kagan, V. E., Konduru, N. V., Feng, W., Allen, B. L., Conroy, J., Volkov, Y., et al. (2010). Carbon nanotubes degraded by neutrophil myeloperoxidase induce less pulmonary inflammation. *Nat. Nanotechnol.* 5, 354–359. doi: 10.1038/nnano.2010.44
- Kisin, E. R., Murray, A. R., Keane, M. J., Shi, X. C., Schwegler-Berry, D., Gorelik, O., et al. (2007). Single-walled carbon nanotubes: geno- and cytotoxic effects in lung fibroblast V79 cells. *J. Toxicol. Environ. Health A* 70, 2071–2079. doi: 10.1080/15287390701601251
- Lam, C. W., James, J. T., McCluskey, R., and Hunter, R. L. (2004). Pulmonary toxicity of single-wall carbon nanotubes in mice 7 and 90 days after intratracheal instillation. *Toxicol. Sci.* 77, 126–134. doi: 10.1093/toxsci/kfg243
- Landry, M., Pinault, M., Tchankouo, S., Charon, E., Ridoux, A., Boczkowski, J., et al. (2016). Early signs of multi-walled carbon nanotubes degradation in macrophages, via an intracellular pH-dependent biological mechanism; importance of length and functionalization. *Part Fibre Toxicol.* 13:61. doi: 10.1186/s12989-016-0175-z
- Lindberg, H. K., Falck, G. C., Suhonen, S., Vippola, M., Vanhala, E., Catalan, J., et al. (2009). Genotoxicity of nanomaterials: DNA damage and micronuclei induced by carbon nanotubes and graphite nanofibres in human bronchial epithelial cells *in vitro*. *Toxicol. Lett.* 186, 166–173. doi: 10.1016/j.toxlet.2008.11.019
- Liu, X., Hurt, R. H., and Kane, A. B. (2010). Biodurability of single-walled carbon nanotubes depends on surface functionalization. *Carbon N. Y.* 48, 1961–1969. doi: 10.1016/j.carbon.2010.02.002
- Luanpitpong, S., Wang, L., Castranova, V., Dinu, C. Z., Issaragrisil, S., Chen, Y. C., et al. (2016a). Induction of cancer-associated fibroblast-like cells by carbon nanotubes dictates its tumorigenicity. *Sci. Rep.* 6:39558. doi: 10.1038/srep39558
- Luanpitpong, S., Wang, L., Davidson, D. C., Riedel, H., and Rojanasakul, Y. (2016b). Carcinogenic potential of high aspect ratio carbon nanomaterials. *Environ. Sci. Nano* 3, 483–493. doi: 10.1039/c5en00238a
- Moller, P., Christophersen, D. V., Jensen, D. M., Kermanizadeh, A., Roursgaard, M., Jacobsen, N. R., et al. (2014). Role of oxidative stress in carbon nanotube-generated health effects. *Arch. Toxicol.* 88, 1939–1964. doi: 10.1007/s00204-014-1356-x
- Muhlfeld, C., Poland, C. A., Duffin, R., Brandenberger, C., Murphy, F. A., Rothen-Rutishauser, B., et al. (2012). Differential effects of long and short carbon nanotubes on the gas-exchange region of the mouse lung. *Nanotoxicology* 6, 867–879. doi: 10.3109/17435390.2011.626533
- Murphy, F. A., Poland, C. A., Duffin, R., and Donaldson, K. (2013). Length-dependent pleural inflammation and parietal pleural responses after deposition of carbon nanotubes in the pulmonary airspaces of mice. *Nanotoxicology* 7, 1157–1167. doi: 10.3109/17435390.2012.713527
- Murphy, F. A., Schinwald, A., Poland, C. A., and Donaldson, K. (2012). The mechanism of pleural inflammation by long carbon nanotubes: interaction of long fibres with macrophages stimulates them to amplify pro-inflammatory responses in mesothelial cells. *Part Fibre Toxicol.* 9:8. doi: 10.1186/1743-8977-9-8
- Nel, A., Xia, T., Madler, L., and Li, N. (2006). Toxic potential of materials at the nanolevel. *Science* 311, 622–627. doi: 10.1126/science.1114397
- Nunes, A., Bussy, C., Gherardini, L., Meneghetti, M., Herrero, M. A., Bianco, A., et al. (2012). *In vivo* degradation of functionalized carbon nanotubes after stereotactic administration in the brain cortex. *Nanomedicine* 7, 1485–1494. doi: 10.2217/nnm.12.33
- Oh, N., and Park, J. H. (2014). Surface chemistry of gold nanoparticles mediates their exocytosis in macrophages. *ACS Nano* 8, 6232–6241. doi: 10.1021/nn501668a
- Pescatori, M., Bedognetti, D., Venturelli, E., Menard-Moyon, C., Bernardini, C., Muresu, E., et al. (2013). Functionalized carbon nanotubes as immunomodulator systems. *Biomaterials* 34, 4395–4403. doi: 10.1016/j.biomaterials.2013.02.052
- Poland, C. A., Duffin, R., Kinloch, I., Maynard, A., Wallace, W. A., Seaton, A., et al. (2008). Carbon nanotubes introduced into the abdominal cavity of mice show asbestos-like pathogenicity in a pilot study. *Nat. Nanotechnol.* 3, 423–428. doi: 10.1038/nnano.2008.111
- Requardt, H., Braun, A., Steinberg, P., Hampel, S., and Hansen, T. (2019). Surface defects reduce Carbon Nanotube toxicity *in vitro*. *Toxicol. In Vitro* 60, 12–18. doi: 10.1016/j.tiv.2019.03.028
- Sajid, M. I., Jamshaid, U., Jamshaid, T., Zafar, N., Fessi, H., and Elaissari, A. (2016). Carbon nanotubes from synthesis to *in vivo* biomedical applications. *Int. J. Pharm.* 501, 278–299. doi: 10.1016/j.ijpharm.2016.01.064
- Sakhtianchi, R., Minchin, R. F., Lee, K. B., Alkilany, A. M., Serpooshan, V., and Mahmoudi, M. (2013). Exocytosis of nanoparticles from cells: role in cellular retention and toxicity. *Adv. Colloid Interface Sci.* 201–202, 18–29. doi: 10.1016/j.cis.2013.10.013
- Sargent, L. M., Porter, D. W., Staska, L. M., Hubbs, A. F., Lowry, D. T., Battelli, L., et al. (2014). Promotion of lung adenocarcinoma following inhalation exposure to multi-walled carbon nanotubes. *Part Fibre Toxicol.* 11:3. doi: 10.1186/1743-8977-11-3
- Shvedova, A. A., Kisin, E., Murray, A. R., Johnson, V. J., Gorelik, O., Arepalli, S., et al. (2008). Inhalation vs. aspiration of single-walled carbon nanotubes in C57BL/6 mice: inflammation, fibrosis, oxidative stress, and mutagenesis. *Am. J. Physiol. Lung Cell. Mol. Physiol.* 295, L552–L565. doi: 10.1152/ajplung.90287.2008
- Shvedova, A. A., Tkach, A. V., Kisin, E. R., Khaliullin, T., Stanley, S., Gutkin, D. W., et al. (2013). Carbon nanotubes enhance metastatic growth of lung carcinoma via up-regulation of myeloid-derived suppressor cells. *Small* 9, 1691–1695. doi: 10.1002/sml.201201470

- Strobel, C., Oehring, H., Herrmann, R., Forster, M., Reller, A., and Hilger, I. (2015). Fate of cerium dioxide nanoparticles in endothelial cells: exocytosis. *J. Nanopart. Res.* 17:206. doi: 10.1007/s11051-015-3007-4
- Takagi, A., Hirose, A., Futakuchi, M., Tsuda, H., and Kanno, J. (2012). Dose-dependent mesothelioma induction by intraperitoneal administration of multi-wall carbon nanotubes in p53 heterozygous mice. *Cancer Sci.* 103, 1440–1444. doi: 10.1111/j.1349-7006.2012.02318.x
- Tkach, M., and Thery, C. (2016). Communication by extracellular vesicles: where we are and where we need to go. *Cell* 164, 1226–1232. doi: 10.1016/j.cell.2016.01.043
- Villa, C. H., McDevitt, M. R., Escorcía, F. E., Rey, D. A., Bergkvist, M., Batt, C. A., et al. (2008). Synthesis and biodistribution of oligonucleotide-functionalized, tumor-targetable carbon nanotubes. *Nano Lett.* 8, 4221–4228. doi: 10.1021/nl801878d
- Vlasova, I. I., Vakhrusheva, T. V., Sokolov, A. V., Kostevich, V. A., Gusev, A. A., Gusev, S. A., et al. (2012). PEGylated single-walled carbon nanotubes activate neutrophils to increase production of hypochlorous acid, the oxidant capable of degrading nanotubes. *Toxicol. Appl. Pharmacol.* 264, 131–142. doi: 10.1016/j.taap.2012.07.027
- Wan, B., Fleming, J. T., Schultz, T. W., and Sayler, G. S. (2006). *In vitro* immune toxicity of depleted uranium: effects on murine macrophages, CD4+ T cells, and gene expression profiles. *Environ. Health Perspect.* 114, 85–89. doi: 10.1289/ehp.8085
- Wan, B., Wang, Z. X., Lv, Q. Y., Dong, P. X., Zhao, L. X., Yang, Y., et al. (2013). Single-walled carbon nanotubes and graphene oxides induce autophagosome accumulation and lysosome impairment in primarily cultured murine peritoneal macrophages. *Toxicol. Lett.* 221, 118–127. doi: 10.1016/j.toxlet.2013.06.208
- Wang, L., Luanpitpong, S., Castranova, V., Tse, W., Lu, Y., Pongrakhananon, V., et al. (2011). Carbon nanotubes induce malignant transformation and tumorigenesis of human lung epithelial cells. *Nano Lett.* 11, 2796–2803. doi: 10.1021/nl2011214
- Wang, L., Mercer, R. R., Rojanasakul, Y., Qiu, A., Lu, Y., Scabilloni, J. F., et al. (2010). Direct fibrogenic effects of dispersed single-walled carbon nanotubes on human lung fibroblasts. *J. Toxicol. Environ. Health A* 73, 410–422. doi: 10.1080/15287390903486550
- Wang, P., Nie, X., Wang, Y., Li, Y., Ge, C., Zhang, L., et al. (2013). Multiwall carbon nanotubes mediate macrophage activation and promote pulmonary fibrosis through TGF- β /Smad signaling pathway. *Small* 9, 3799–3811. doi: 10.1002/smll.201300607
- Wang, R., Mikoryak, C., Chen, E., Li, S., Pantano, P., and Draper, R. K. (2009). Gel electrophoresis method to measure the concentration of single-walled carbon nanotubes extracted from biological tissue. *Anal. Chem.* 81, 2944–2952. doi: 10.1021/ac802485n
- Wang, Y., Wu, Q., Sui, K., Chen, X. X., Fang, J., Hu, X., et al. (2013). A quantitative study of exocytosis of titanium dioxide nanoparticles from neural stem cells. *Nanoscale* 5, 4737–4743. doi: 10.1039/c3nr00796k
- Yang, M., Zhang, M., Nakajima, H., Yudasaka, M., Iijima, S., and Okazaki, T. (2019). Time-dependent degradation of carbon nanotubes correlates with decreased reactive oxygen species generation in macrophages. *Int. J. Nanomed.* 24, 2797–2807. doi: 10.2147/IJN.S199187
- Yoo, J. M., Kang, J. H., and Hong, B. H. (2015). Graphene-based nanomaterials for versatile imaging studies. *Chem. Soc. Rev.* 44, 4835–4852. doi: 10.1039/c5cs00072f
- Zhang, L., Petersen, E. J., Habteselassie, M. Y., Mao, L., and Huang, Q. (2013). Degradation of multiwall carbon nanotubes by bacteria. *Environ. Pollut.* 181, 335–339. doi: 10.1016/j.envpol.2013.05.058
- Zhu, M., Tian, X., Song, X., Li, Y., Tian, Y., Zhao, Y., et al. (2012). Nanoparticle-induced exosomes target antigen-presenting cells to initiate Th1-type immune activation. *Small* 8, 2841–2848. doi: 10.1002/smll.201200381

Conflict of Interest: The authors declare that the research was conducted in the absence of any commercial or financial relationships that could be construed as a potential conflict of interest.

Copyright © 2020 Dong, Song, Wu, Cui, Wang, Zhang and Sun. This is an open-access article distributed under the terms of the Creative Commons Attribution License (CC BY). The use, distribution or reproduction in other forums is permitted, provided the original author(s) and the copyright owner(s) are credited and that the original publication in this journal is cited, in accordance with accepted academic practice. No use, distribution or reproduction is permitted which does not comply with these terms.

Advantages of publishing in Frontiers



OPEN ACCESS

Articles are free to read
for greatest visibility
and readership



FAST PUBLICATION

Around 90 days
from submission
to decision



HIGH QUALITY PEER-REVIEW

Rigorous, collaborative,
and constructive
peer-review



TRANSPARENT PEER-REVIEW

Editors and reviewers
acknowledged by name
on published articles

Frontiers

Avenue du Tribunal-Fédéral 34
1005 Lausanne | Switzerland

Visit us: www.frontiersin.org

Contact us: info@frontiersin.org | +41 21 510 17 00



REPRODUCIBILITY OF RESEARCH

Support open data
and methods to enhance
research reproducibility



DIGITAL PUBLISHING

Articles designed
for optimal readership
across devices



FOLLOW US

[@frontiersin](https://twitter.com/frontiersin)



IMPACT METRICS

Advanced article metrics
track visibility across
digital media



EXTENSIVE PROMOTION

Marketing
and promotion
of impactful research



LOOP RESEARCH NETWORK

Our network
increases your
article's readership